CALIFORNIA INSTITUTE OF TECHNOLOGY

EARTHQUAKE ENGINEERING RESEARCH LABORATORY

MODERN DIGITAL SEISMOLOGY — INSTRUMENTATION, AND SMALL AMPLITUDE STUDIES IN THE ENGINEERING WORLD

BY

JOHN F. CLINTON

REPORT NO. EERL 2004-10

PASADENA, CALIFORNIA

APRIL 2004

Modern Digital Seismology — Instrumentation, and Small Amplitude Studies in the Engineering World

Thesis by

John F. Clinton

In Partial Fulfillment of the Requirements

for the Degree of

Doctor of Philosophy

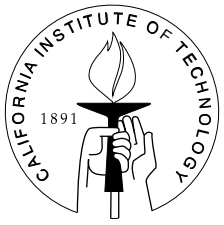

California Institute of Technology

Pasadena, California

2004

(Submitted May 24, 2004)

Acknowledgements

I would like to thank my advisor, Tom Heaton. Throughout my time at Caltech, he was continuously jovial, and gave me great encouragement. He has always been overly generous with his time, and I have learnt much from our frequent discussions.

I would like to acknowledge Jascha Polet and David Johnson from SeismoLab, who taught me a lot about the hardware and software issues, helped set up countless experiments, and were always helpful with data analysis and recovery. I also would like to thank Arnie Acosta and Erdal Safak for their help with obtaining data from the USGS array at Millikan Library. Mr. Isamu Yokoi from Tokyo-Sokushin was also extremenly helpful with all issues that arose with the VSE sensors. I would like to thank IRIS for purchasing the VSE-355G2 sensor.

The faculty and students of Civil Engineering also provided great support. In particular Brad Aagaard for the brains, Andy for the sharing the misery at 2am all first and second years long, Swami, Javier and Case for the laughs. And especially Case for the extensive proof-reading.

My mother-in-law, Maria Cua, helped out with minding Peete, letting us get some work done.

My parents, Peter and Margaret, so far away for these past years, have yet managed to share much of my Caltech experience, and helped me make it to the end.

But after everyone has gone home, Peete and Georgie were always there, and allowed me to too often not go home myself. Thanks for your patience and love. For what its worth, this is for both of you.

Abstract

The recording of ground motions is a fundamental part of both seismology and earthquake engineering. The current state-of-the-art 24-bit continuously recording seismic station is described, with particular attention to the frequency range and dynamic range of the seismic sensors typically installed. An alternative method of recording the strong-motions would be to deploy a velocity sensor rather than an accelerometer. This instrument has the required ability to measure the strongest earth motions, with enhanced long period sensitivity.

An existing strong motion velocity sensor from Japan was tested for potential use in US seismic networks. It was found to be incapable of recording strong motions typically observed in the near field of even moderate earthquakes. The instrument was widely deployed near the M8.3 Sept 2003 Tokachi-Oki earthquake. The dataset corroborated our laboratory observations of low velocity saturations. The dataset also served to show all inertial sensors are equally sensitive to tilting, which is widespread in large earthquakes. High-rate GPS data is also recorded during the event. Co-locating high-rate GPS with strong motion sensors is suggested to be currently the optimal method by which the complete and unambiguous deformation field at a station can be recorded.

A new application of the modern seismic station is to locate them inside structures. A test station on the 9^{th} floor of Millikan Library is analysed. The continuous data-stream facilitates analysis of the building response to ambient weather, forced vibration tests, and small earthquakes that have occurred during its lifetime. The structure's natural frequencies are shown to be sensitive not only to earthquake excitation, but rainfall, temperature and wind. This has important implications on structural health monitoring, which assumes the natural frequencies of a structure do not vary significantly unless there is structural damage.

Moderate to small earthquakes are now regularly recorded by dense, high dynamic range networks. This enhanced recording of the earthquake and its aftershock sequences makes possible the development of a Green's Function deconvolution approach for determining rupture parameters.

Contents

List of Figures

List of Tables

Chapter 1 Introduction

The last few years have seen the beginning of a new era in high dynamic range seismic instrumentation. 24-bit resolution (which translates to ~ 7 orders of magnitude) is now commonplace and becoming readily affordable. It is the standard for many seismic networks, and is increasingly common in engineering networks. Instruments are now designed to record over a wide frequency range to take advantage of this new resolution. It is also increasingly possible for networks to store large volumes of high sample rate continuous data at reasonable cost with relative ease. This thesis examines new research that has only become possible with the wealth of data that has recently become available to the community.

Two main issues are dealt with in this thesis:

1. What is the current system of seismological instrumentation. How does it work, how does it overlap, and how can it be improved?

2. What new applications are now possible with the modern instrumentation?

In addressing these issues, the following problems are explored:

a. understanding the best instrumentation for recording ground motions over the widest possible band of interest.

b. prediction of motions of a tall building structure from small motions of a nearby free-field station.

c. removing the total path effect from earthquake records: isolating which part of a record is due to the source, and then what can be learned from this source time function.

1.1 Seismological Instrumentation

Chapter 2 describes the typical specifications of a modern broadband seismic network station, using the California Integrated Seismic Network as an example. The benefits of introducing a strong motion velocity recording instrument in place of the accelerometer are

discussed.

In Chapter 3, an existing strong motion instrument with widespread usage in Japan is introduced, and a regime of laboratory tests is described which shows whether the instrument is capable of performing to the levels anticipated in Chapter 2. A major design flaw was exposed during the tests; the instrument as delivered was observed to be incapable of resolving strong motions above $15 cm/s$, well below the advertised clip level of $200 cm/s$, and the expected motions in the near field of large earthquakes.

Nonetheless, many of these instruments are deployed in modern networks in Japan, and were heavily excited by the shaking produced during the 25 September 2003 M8.3 Tokachi-Oki earthquake, located offshore of Hokkaido Island in Japan. The data produced during this event provided a dataset allowing a thorough analysis of the quality of data one may expect from the strong motion velocity instrument, and provides the basis for Chapter 4. Unfortunately, the problems observed in the laboratory experiments, documented in Chapter 3, were also observed in the field.

Widespread static offsets over hundreds of square kilometres also exposed the inability of the strong motion velocity sensor to improve on accelerometer recordings of static offset. Chapter 4 shows that recording high-rate GPS displacement alongside a strong motion instrument is very important if wide-band, $100 Hz$ — DC displacements are to be accurately recorded. The usefulness of the strong motion instrument in the network is also observed as motions saturate some sensors at up to $1000 km$ distance. Network-wide individual station health monitoring can also be performed by comparing the signals from the 2 co-located broadband and strong motion sensors during such large magnitude earthquakes.

In Chapter 5, modifications to the strong motion instrument are documented, as are the results of laboratory tests on this new instrument, which indicate the sensor now operates to the specifications first advertised.

1.2 Applications of Modern Instrument Data

1.2.1 Small Amplitude Studies for Buildings

When attempting to predict motions of a tall building structure from small motions of a nearby free-field station, the problem of how a structure's natural periods vary is fundamentally important. Small variations in this parameter have important consequences not only in modelling the structural response to ground motion, but also in determining the building stiffness.

Whilst there is a wealth of knowledge and research concerning structural dynamics, the earth-building system in general is not well understood. Chapter 6 investigates the question of whether the response of a building during strong motions can be predicted solely from knowing the response at a local base station. The installation of a 24-bit continuously recording accelerometer station within the California Integrated Seismic Network (CISN) on the 9^{th} floor of Caltech's Millikan Library, alongside other nearby ground CISN stations, facilitated this investigation.

1.2.2 Moderate Earthquake Source Inversions

Focal mechanism solutions are rapidly produced for many earthquakes recorded in the Southern California. The focal mechanism represents the orientation of the point source that best fits either the hypocentral motions (first motion solution) or the overall earthquake (moment tensor solution). If the source is constrained to be a double couple, then the plane of rupture can be either of the two conjugate planes described by this solution. Of course earthquakes will have a finite rupture area and consequently some directivity pattern. Knowing the pattern of the directivity can determine which plane on the focal sphere a rupture occurs on. Unfortunately, path and station effects obscure this directivity for even moderately large events (M$<$ 6). Chapter 7 introduces a method of deconvolving a 'point source' aftershock from the mainshock, which can provide an estimate of the source-time function of an earthquake, and indicate the directivity of the mainshock. An aftershock with the same epicentral location and focal mechanism as the mainshock is selected, which

will then have the same radiation pattern, path and site effects as the mainshock. This study is only possible with the quality (in particular the dynamic range) and density of stations in the CISN, which allows recordings of the mainshock and aftershocks at many stations with good signal to noise.

1.3 A Comment on Deconvolutions

This thesis includes various methods of solving the problem of deconvolution. The convolution operation, $*$, is a linear operator between two functions $G(t)$ and $u(t)$, and may be written as

$$x(t) = G(t) * u(t) \tag{1.1}$$

$$x(t) = \int_{-\infty}^{\infty} G(\tau)u(t-\tau)\,d\tau \tag{1.2}$$

where $x(t)$ is the convolution of the functions $G(t)$ and $u(t)$. In this work, the independent variable, t, will always refer to time.

An important property of the convolution operator is that its conjugate operator in the frequency domain is simply the multiplication operator. So

$$X(\omega) = G(\omega)U(\omega) \tag{1.3}$$

where $X(\omega)$, $G(\omega)$ and $U(\omega)$ are the Fourier Transforms of $x(t)$, $G(t)$ and $u(t)$, respectively, and ω is frequency.

[In practice, a discrete version of a Fourier Transform, the Fast Fourier Transform, or FFT, is used. The discrete inverse function is the Inverse Fast Fourier Transform, or IFFT.]

In Chapters 2-4, timeseries obtained from different seismometers will be analysed. In this case, $x(t)$ is the observed seismometer output, and $u(t)$ is the ground displacement, which when convolved with the instrument impulse response, or Green's function, $G(t)$, gives $x(t)$. In the frequency domain, $G(\omega)$ is known as the Transfer Function of the instrument. The problem is to recover the ground displacement by deconvolving it from the

known instrument response.

Due to the characteristics of the instrument response of broadband sensors, the output from a particular seismometer may be simple over a particular frequency range (i.e., $G(\omega)$ within this frequency range is not sensitive to frequency, and is a constant value). However, when considering very broadband signals, the instrument response is sensitive to frequency, and must be removed. This problem is traditionally performed in the frequency domain, where the Fourier Transform of the timeseries, $X(\omega)$, is divided by the Transfer Function $G(\omega)$ to get the FFT of the ground displacement, $U(\omega)$. $u(t)$ is then obtained by an IFFT

$$u(t) = IFFT\left[\frac{X(\omega)}{G(\omega)}\right] \tag{1.4}$$

A problem arises for broadband strong motion velocity instruments, where motions are large, records are short, and static offsets are expected. The frequency domain method does not give physically realistic solutions, as displacements and velocities must be zero before the earthquake occurs. Further, division in the frequency domain requires a high pass filter at low frequency to prevent numerical instability (division by zero). This removes the static offset. In this case a different approach to deconvolving the instrument response from the ground displacement is required— a time domain solution employing direct integration of the equivalent equation of motion for the sensor system is used

$$\ddot{x}(t) + 2\beta\dot{x}(t) + \omega_0^2 x(t) = G\ddot{u}(t) \tag{1.5}$$

These parameters will be defined in Chapter 3. Direct integration leads to

$$u(t) = \frac{1}{G}\left(\int x(t)\,dt + 2\beta\iint x(t)\,dt^2 + \omega_0^2\iiint x(t)\,dt^3\right) - At^2/2 - Bt - C \tag{1.6}$$

where A, B and C are constants of integration determined by initial conditions.

As t becomes large, the solution becomes unstable due to tilts and other sources of small trends in the record, but this is often not significant in the short duration of a strong motion record.

Finally, in Chapter 7, the problem of removing the path effects from a seismogram is

discussed using empirical Green's Functions. An earthquake timeseries on an instrument recording, $x(t)$, can be approximated as the convolution of response time functions from the source, $S(t)$, the path, $P(t)$, the site, $C(t)$ and the instrument, $I(t)$

$$x_m(t) \approx S_m(t) * P_m(t) * C_m(t) * I_m(t) \qquad (mainshock) \tag{1.7}$$

$$x_a(t) \approx S_a(t) * P_a(t) * C_a(t) * I_a(t) \qquad (aftershock) \tag{1.8}$$

It is assumed that a small aftershock, with similar focal mechanism to the mainshock, has a δ-function as source time function. If the mainshock and aftershock have a similar focal mechanism and location, then the path, site and instrument responses should be the same for both $x_m(t)$ and $x_a(t)$. Thus, one can assume

$$x_m(t) \sim S_m(t) * x_a(t) \tag{1.9}$$

The source time function of the mainshock, $S_m(t)$, can be approximated as the deconvolution of the aftershock time function from the mainshock time function. Solving this in the frequency domain requires a division by $X_a(\omega)$, which will cause instabilities as earthquakes timeseries have many near-zero amplitudes in the frequency domain. Thus an approach in the time domain is employed, using the definition of deconvolution (Equation 1.2) written as a series of vectors (outlined in Bracewell (1965)). As shown in the following set of equations, the convolution operator may be described as a matrix multiplication, with the matrix defined by the aftershock timeseries —

The 3 functions of Equation 1.9 can be written as

$$x_{m_i} = x_m(i\Delta t), \qquad i = 0, n_1 \tag{1.10}$$

$$x_{a_i} = x_a(i\Delta t), \qquad i = 0, n_2 \tag{1.11}$$

$$S_m = S_m(i\Delta t), \qquad i = 0, (n_1 - n_2) + 1 \tag{1.12}$$

and so the convolution in Equation 1.9 may be written as the serial product

$$x_{m_i} = \left(S_m * x_{a_i}\right)_i = \sum_{j=1}^{n_1} S_{m_j} x_{a_{i-j}} \Delta t \tag{1.13}$$

and the serial product can be re-written in matrix form, expanding x_a

$$\Delta t \begin{bmatrix} x_{a_0} & 0 & 0 & \dots & 0 \\ x_{a_1} & x_{a_0} & 0 & \dots & 0 \\ x_{a_2} & x_{a_1} & x_{a_0} & \dots & 0 \\ \vdots & \vdots & \vdots & \ddots & \vdots \\ x_{a_{n_2}} & x_{a_{n_2-1}} & x_{a_{n_2-2}} & \dots & x_{a_{n_1}} \\ 0 & x_{a_{n_2}} & x_{a_{n_2-1}} & \dots & x_{a_{n_1+1}} \\ \vdots & \vdots & \vdots & \ddots & \vdots \\ 0 & 0 & 0 & \dots & x_{a_{n_1-n_2}} \end{bmatrix} \begin{pmatrix} S_{m_1} \\ S_{m_2} \\ S_{m_3} \\ \vdots \\ S_{m_{n_1-n_2+1}} \end{pmatrix} = \begin{pmatrix} x_{m_1} \\ x_{m_2} \\ x_{m_3} \\ \vdots \\ x_{m_{n_1}} \end{pmatrix} \tag{1.14}$$

which is now in the form

$$[A]\{y\} = \{b\} \tag{1.15}$$

where $[A]$ is an n_1 x $(n_2 - n_1 + 1)$ matrix.

The deconvolution has now been re-written as a simple linear matrix inversion. Classical inversion techniques can be used to invert for the source time function vector, x. In Chapter 7, a damped least squares solution is used.

1.4 A Comment on Tilt

In many cases of strong motion, tilt is associated with heavy shaking, especially when static offsets are also present. Unfortunately, no matter what type of inertial instrument is used, whether an accelerometer, or a strong motion velocity-meter, tilt cannot be easily distinguished and removed from estimates of static offset, or indeed the true ground acceleration.

In strong motions, tilt can be caused by rotation of the ground due to tectonic displacements over a wide area, or can also be from local site failure, such as lateral spreading, or

liquefaction. It can also occur if the instrument shifts during a strong motion. The effect of tilt is to produce an offset in the acceleration timeseries. This offset can also be caused by an instrument malfunction, as has been observed for the FBA-23 (Iwan et al, 1985; Boore, 2001).

It is important to try to estimate the amount of tilt in a record. In a large thrust earthquake, there will be a tectonic tilt, which can affect the sensitive instruments. This tectonic tilt can be obtained from GPS.

To obtain the approximate tectonic tilt in a region, the change in elevation during the earthquake from 2 regional GPS stations, A and B, of known distance apart, L, is required (ΔZ_A and ΔZ_B). The relative change in vertical displacement between the two stations is determined, $\Delta Z_{A-B} = \Delta Z_A - \Delta Z_B$, and the tectonic tilt, θ_T is then

$$\theta_T = \frac{\Delta Z_{A-B}}{L} \tag{1.16}$$

The tilt measured from the seismometers, θ_S, can be determined using the static offset at the end of an acceleration trace Δ_{accn}, which can often be seen more clearly as the slope of the velocity trace (see Figure 3.6). The change in acceleration due to a tilt is simply $\Delta_{accn} = gsin(\theta_S)$ for horizontal channels, and $\Delta_{accn} = gcos(\theta_S)$ for the vertical channel, where g is the acceleration due to gravity, $981 cm/s^2$. This is summarised in Figure 1.1. Assuming small angles of tilt, $sin(\theta_S) \sim \theta_S$, $cos(\theta_S) \sim 1 - \theta_s^2$ — note there is generally no observed change to the vertical channels during small tilts — θ_S can then be measured from the horizontal channels as

$$\theta_S = \frac{\Delta_{accn}}{g} \tag{1.17}$$

If the tectonic tilt and the seismic tilt are of similar order of magnitude, then the tilt can be ascribed to the tectonic shift. Unfortunately, as was observed in the field for the M8.3 Tokachi-Oki earthquake in Japan, tilts in practice are typically far larger than that of the tectonic tilt. For stations located on poorer foundations (see Chapter 4 for data from the K-Net and WISE networks), the large tilts may be due to a local site failure such as liquefaction or lateral spreading. A further complication of this interpretation (illustrated in examples in Chapter 4), is that the largest permanent offsets often occur in the vertical

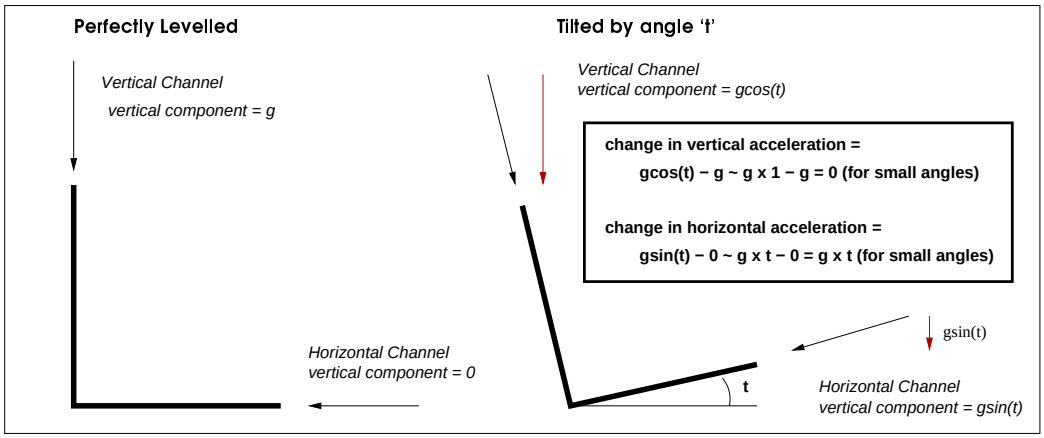

Figure 1.1: The effect of tilt on inertial seismometers.

acceleration timeseries. For tilting, the maximum changes are expected on the horizontal channels. Therefore, these examples strongly imply non-linear instrument behaviour.

Co-locating high sample rate GPS ($\geqq 1sps$) and an inertial seismometer may indeed be the optimal method to obtain a true representation of the ground movement at a site. Preliminary data from high rate GPS in Hokkaido Island will be used to demonstrate the potential of a station of this type.

Finally, an example of the sensitivity of an instrument to tilt is as follows: Assume a site undergoes an instantaneous tilt of magnitude θ about the N-S axis at time $t = 0$. The acceleration recorded by the E-W horizontal channel will be

$$a(t) = \ddot{u}(t) = g\theta \tag{1.18}$$

The N-S acceleration will be zero, as will the vertical acceleration if the tilt is small. The resultant E-W displacement is thus

$$u(t) = g\theta t^2/2 \tag{1.19}$$

Thus the rotation, or tilt, required to produce an error of only $5cm$ of displacement after

100s of an accelerometer record, is

$$\theta = \frac{5\text{x}2}{981\text{x}100^2} \quad (1.20)$$

$$= 1.02\text{x}10^{-6} rads \quad (1.21)$$

$$= 0.000058^o \quad (1.22)$$

So a tilt of only $1\mu rad$ will cause an error in the acceleration timeseries large enough to distort the true offset in displacement.

1.5 A Simple Methodology for Determining Displacement and Tilt Using Seismometers and GPS

Networks of GPS sensors are now commonplace in regions with plate boundaries. Measuring differential motion over the region gives important insight into the build-up of strain on faults. The movements of the plate boundaries drive the earthquake process, and so GPS networks and seismic networks tend to be located in the same region.

GPS is primarily installed to measure data at very long periods. Seismic data is insensitive to these extremely long period motions, with sensors designed to measure transient phenomena of short duration. With strong motion seismic sensors, it is difficult to resolve motions over 100s in duration.

In the past few years GPS displacement estimates have greatly improved, due to improvements in satellite infrastructure and number, developments in sensor placement and design, and better location algorithms. These improvements have also made it feasible to record GPS measurements at higher sampling rates. Current GPS sensors are capable of recording at up to 10sps (though practitioners have questioned whether this data is useful). Many networks are recording data at 1sps, with accuracy of about 2mm for the horizontal components, slightly less accurate for the vertical.

The different optimal location requirements, as well as the independent goals of the networks, mean seismic and GPS stations are rarely co-located. In Southern California,

this is beginning to change, with co-location of 2 new CISN (California Integrated Seismic Network) and SCIGN (Southern California Integrated GPS Network) stations (recording high rate GPS) which traverse the San Andreas Fault. GPS stations require a clear view of the sky, as well as good foundations, preferably bedded on hard rock. An important requirement for a seismic station is low noise levels, and so many stations are located on hard rock and sensors may also be buried. In practice, co-location of seismic sensors and GPS does not require the instruments to be as close as possible, since records from Tokachi-Oki shows useful data can be recovered even when the sensors are separated by $1km$.

$1sps$ high rate GPS Data from the M8.3 Tokachi-Oki earthquake was recorded for the entire GEONET network. Fortunately, the dense networks of both GPS and strong motion have overlap and some stations are very near each other.

Many investigators have tried to constrain seismic strong motion records using GPS offsets (Boore, 2001). The final co-seismic offset as measured from nearby GPS is used as a guide in determining the amount of tilt, as well as the onset of tilt. A similar approach with high-rate GPS data is possible, and can prove to be significantly more useful than the static offset alone. Previous studies were hampered by the fact the GPS stations were on the order of kilometers away from the seismic stations, so confidence in the correlation of the final offsets was low.

If the seismic and GPS stations are co-located, the permanent offset can be used to constrain the final offsets, and as $1sps$ data is shown in this thesis to reproduce seismic motions with periods greater than $2s$, the GPS can also constrain the onset and magnitude of tilting.

It is noted in this work that in order to optimally match the seismic arrivals, and the magnitudes of the motion, there is a need to match orientations of the horizontal seismic sensors to the GPS timeseries. In data analysed in Chapter 4, a station was shown to require a vertical rotation of over 30^o. Once this rotation has been made (if required), the two datasets can be inverted to solve for the three translations and two horizontal rotations. This is optimally done in the frequency domain, where the long period and static offsets from the GPS can be made to fully match the translational displacements, combining this

with the high frequency response of the inertial sensor. A damped least squares linear inversion with constraints can be used to determine the solution.

The inversion can simply be performed on each of the 2 horizontal components separately, or can include all the 3 components from the GPS and seismic sensor at once, which would use all the data available, though would also include any non-physical tilts observed in the vertical channel.

1.6 A Summary of Recommendations for Modern Station Design

The analysis in this section assumes all inertial sensors are near $144dB$ quality, and are recording onto a 24-bit datalogger, unless otherwise stated.

The particular sensor options for a modern network station are

- high-gain broadband velocity sensor (e.g., STS-2)
- low-gain strong motion velocity sensor (e.g., VSE-355G3)
- low-gain strong motion force balance accelerometers (e.g., FBA-23, EpiSensor)
- GPS

All seismic sensors are theoretically sensitive to motions ranging from $\sim 50Hz$ to DC. In reality the seismic sensors have optimal frequency ranges that do not encompass this entire range. GPS sensors record from $1Hz$ (potentially up to $10Hz$) to DC.

A summary of the sensor performance is as follows:

GPS: poor resolution at high frequency ($1sps - 10sps$ sampling interval), insensitive to motions below $2mm$ in horizontal channels, $4mm$ vertical. Does not clip, and is not sensitive to tilt.

high-gain broadband [*e.g., STS-2*]: no strong motion as clip levels are about $1cm/s$, difficult calibration, poor high frequency resolution beyond $20Hz$.

low-gain broadband [*e.g., VSE-355G3*]: no restraint on tilt, complex transfer function response, difficult calibration.

accelerometer [*e.g., EpiSensor*]: no restraint on tilt, poor long period response, simple

calibration, relatively cheap and small compared to broadband seismometers.

1.6.1 Station options

1. Stations Located on Structures

A typical current digital strong motion station located on a structure deploys a 24-bit accelerometer recording onto a 16-bit datalogger in a triggered mode. Structures commonly instrumented are buildings, bridges and dams.

Recording of 24-bit data ($\sim 144dB$) would be useful, as evidence from buildings continuously monitored at Caltech indicates that typical building noise levels are similar to the digitiser noise floor for a 16-bit accelerometer station, and a factor of 100 above the instrument noise for a 24-bit instrument. Monitoring structural noise can greatly improve understanding of structural response.

The noise levels at these sites are high enough that a broadband sensor would be redundant, as all motions above the station noise are recorded on-scale by the strong motion instrument. GPS requires an unobstructed view of the sky, so within a building, a roof site is the only option. Further, ambient displacements on structures are often large, which would make GPS noisy, and only be useful for strong motions. GPS may be important if it is used on a free-field site near the structure, where long-term displacements may be more accurately determined, and the free-field displacements from strong motion could be used as input motion to the building system.

The main decisions to consider for a structural station are thus:

a. Strong Motion Velocity Meter vs. Accelerometer: A velocity meter has the advantage of increased sensitivity at low frequencies, so more teleseismic and regional events can be recorded - this is especially useful if the station is operated in continuous mode, as these motions would fail to trigger a triggered setup. Transient displacement estimates are more stable as only a single integration is required to obtain displacement with frequencies above $0.0125Hz$. Accelerometers, however, have the advantages of being cheaper, smaller, lighter and easier to calibrate.

The FBA type instrument is best suited to a building instrumented with a large array of sensors, which need to be located in small spaces. If the building noise is well below the FBA type instrument noise floor at long periods, the strong motion velocity meter may be a useful option.

b. Triggered vs. Continuous: The decision to record data in a triggered mode implies some concern with the cost and time taken by data processing and storage. If a station can be placed within a modern seismic network, such as stations MIK and CBC in the CISN, data can be handled and made available with minimal extra work within the network. The advantages of continuous recording are clear from this thesis, studies of building response to ambient vibrations show the building is a dynamic system sensitive to environmental changes, as well as internal usage. Continuous recording also leads to recordings of small ground motions that would not trigger a system only designed to record large motions. These motions provide insight into building performance, and have obvious potential for a Green's Functions approach for the determination of building response to larger, potentially destructive ground motions.

In summary, for research value, the optimal 24-bit station within a structure would deploy a strong motion velocity sensor recording continuously.

2. Low-Noise Station

A typical field station within a modern broadband seismic network consists of 24-bit data-logger recording the output from both a strong motion FBA sensor and a high-gain broad-band velocity sensor.

The high-gain velocity sensor is shown to be capable of recording below the ambi-ent station noise for most station sites over a broad frequency band. Combined with a strong motion sensor, the two instruments effectively cover all ranges of motions from the strongest possible earthquake motions to the station noise level, over a very broad fre-quency range. The instruments are insensitive to static offsets, and so care must be taken in interpreting strong ground motions with associated static offset. Numerical instability an well as the inability of an inertial sensor to distinguish between ground displacement and

ground tilt cause this problem. One obvious way to measure the permanent displacement accurately is with GPS, which is now capable of recording to millimeter accuracy at 1*sps*. GPS also has no upper bound on the size of displacements that can be recorded.

Co-locating GPS with these very broadband seismic stations would produce a station with a dynamic range that encompasses the full range of earth motions, as well as unambiguously determining station displacements. This is the ideal configuration for a modern network using 24-bit technology.

In some cases within the CISN and in other networks, stations are composed of a single strong motion sensor placed alongside a 24-bit digitiser. This may be a typical configuration within denser urban regions where noise levels are so high they approach the limits of resolution for the strong motions sensors (and consequently little seismic data not recorded by a strong motion sensor would be recorded by a high-gain broadband sensor). In such a station, deploying a strong motion velocity sensor is significantly advantageous to using an FBA sensor, as more long period low amplitude signals, such as teleseisms, will be recorded at the station.

3. Adding Seismic Sensors to an Existing GPS Network

A current topic of interest is adding seismic sensors to existing GPS network stations. The question is what sort of sensors should be used. The goal of adding the new sensors is not to replicate the full-range broadband stations, but to record a broadband timeseries from a large earthquake. This is because technically GPS is limited to 1*sps*, and in any case, it would be insensitive to the small displacements at frequencies higher than 1*sps*. Addition of a strong motion instrument would mean the strong motion is recorded over a very broad frequency band.

The cheapest and simplest configuration would be to add an FBA type instrument operating in triggered mode. If its only aim is to record the strongest ground motions, the digitiser would not need to be 24-bit, 16-bit instruments would suffice. In this mode, the FBA type sensor would be the preferred option as the advantages of a velocity instrument (better high-frequency displacement, increased event resolution) are negated. However, a 24-bit instrument with continuous transmission to a network storage facility would have

many advantages. Firstly, the data from large earthquakes would still be recorded. Also, the existing strong motion network would become denser with a minimum of effort and cost, as the GPS stations are already setup and access rights to the site have already been established. For a network like CISN, this could have important benefits for many of the real-time data analysis and products.

If a continuous strong motion sensor was to be deployed alongside existing GPS, the ideal type would be the strong motion velocity sensor described in detail in this thesis. The increased sensitivity to small regional and teleseismic data makes this instrument a better alternative to the FBA-type sensors.

Chapter 2 A Strong Motion Velocity Meter in a Modern Seismic Network?

2.1 Introduction

Seismometry has seen huge advances in the past 30 years. The dynamic range of typical seismometers has increased from less than 5 orders of magnitude to more than 7, primarily because of the development of force feedback systems (Wielandt and Streckeisen, 1982; Iwan et al**,** 1985; Wielandt and Steim, 1986). Advances in recording systems have been even more dramatic; current 24-bit digitisers record over 7 orders of magnitude compared to the 3 orders of magnitude achievable by analogue recording devices (Trifunac and Todorovska, 2001a). The past 30 years have also seen the dramatic development of digital data communication, processing and storage, which has prompted the development of a plan for an Advanced National Seismic Plan (Heaton et al**,** 1989; Benz and Filson, 1998). These new capabilities allow us to devise new strategies to record ground motions. One such strategy, whose advantages are the subject of this Chapter, would be to deploy continuously telemetered strong motion velocity seismometers in place of existing triggered strong motion accelerometers.

The most critical role of strong motion networks is to provide on-scale recordings of potentially damaging motions over a broad frequency band. Because continuous analogue recording is extremely expensive and strong shaking is infrequent, strong motion seismographs were designed to record only during strong ground shaking. Furthermore, because of the limited dynamic range of recording devices, it was most efficient to record ground acceleration, since near-source strong ground motions have relatively flat acceleration spectra in the band from 0.3 to 3.0Hz.

The typical station specifications for a modern digital network are described, using the California Integrated Seismic Network, CISN, as an example. A CISN station con-

sists of two broadband seismometers, typically a high-gain velocity recording device, such as an STS-2 or a CMG-40T, and a strong motion accelerometer, such as an FBA-23, or EpiSensor. These instruments record on a 24-bit digitiser that has continuous, near-real-time telemetry of high sampled data (80-100sps) to the CISN centre at Caltech and USGS-Pasadena.

The main thrust of this Chapter is to discuss whether it would be better to deploy a velocity-recording strong motion instrument in place of existing force-balance accelerometers. Using a large suite of real Earth signals, the hypothetical long-period low-gain velocity seismometer (with a clipping level set to $\pm$5m/s) is compared to the existing $\pm$2g clipping Kinemetrics FBA-23 accelerometer.

It is shown that there are significant advantages in the deployment of the proposed instrument over an accelerometer —

• The velocity instrument would have several orders of magnitude greater sensitivity in the period band from 2s to several hundred seconds. This would allow the recording of

— long-period basin response from regional earthquakes as small as M3.0, and
— teleseismic ground motions from earthquakes as small as M6,

which could potentially lead to dense spatial recording of small amplitude motions that are not recorded by traditional strong motion networks.

• Furthermore, as well as allowing full recovery of ground acceleration, recovery of ground displacement is likely to be more stable from such a long-period low-gain broadband seismometer.

It is anticipated that a strong motion velocity seismometer would essentially be a low-gain version of existing broadband seismometers, such as the Weilandt-Streckeisen STS-2, and thus its cost would likely be similar to other broadband seismometers. Unfortunately, so would its size and weight. Thus the clear advantages would be offset by significantly poorer cost, size and weight than an accelerometer, which makes it somewhat unwieldy for dense building instrumentation.

At this stage it is pertinent to discuss the design of such an instrument. The STS-2 is designed to respond as a simple single degree of freedom oscillator with free period of 120s, with differential feedback, and so has output proportional to ground velocity from

120s to high frequencies. In reality, it consists of a mechanical pendulum with free period of 2s. The feedback electronics produce a heavily over-damped ($\sim$ 1000% of critical) output, and so the suspension displacement is proportional to ground velocity over a wide frequency band about this free period. Chapter 3 presents an investigation into a relatively new Japanese strong motion velocity recording sensor, the VSE-355G2. This instrument has a mechanical pendulum of about 3Hz with a similar feedback system. Unfortunately it is also slightly heavier (20kg), and larger (30cm x 30cm plan x 20cm high) than the STS-2.

A strong motion velocity seismometer could record a broader swath of Earth motions than are currently recorded by existing strong motion accelerometers. With a clipping level of $\pm$5m/s (a velocity magnitude greater than that of any seismic ground motion measured to date) it would recover on-scale all motions relevant to structural engineering, and it would record long-period motions with accelerations too small to be recorded by traditional accelerometers. It is estimated that direct recording of velocity with a dynamic range of 140dB would permit recording of broadband motions from regional and near-source events as small as M3.0. These broadband motions could be used to study path effects such as the amplification of long-period motions by basins. In addition, a strong motion velocity array should be capable of recording teleseisms as small as M6. This could lead to dense spatial recording of small amplitude motions that are not recorded by traditional strong motion networks.

Single differentiation of the raw velocity output would produce the acceleration records currently used by engineers. However, the real issue is not acceleration versus velocity, but is one of having accurate motion in the frequency band of interest. The velocity seismometer has the significant advantage that displacement estimates of ground motion would be obtained from a single integration of the raw data. Current strong motion velocity devices have flat responses up to 70Hz, so acceleration timeseries can be recovered up to this frequency, which is satisfactory for most engineering purposes, as few structures are damaged by energy at 70Hz. Further, as long as the longest frequencies in a signal are below the low frequency corner of the instrument ($\sim$ 100s — in effect excluding all but static offsets), single integration would result in smaller long period error than would a double integration, assuming a similar error in the true signal of velocity and acceleration. Single integration

thus leads to a more stable and conclusive set of displacement time series, especially with regard to static offsets. Even very small baselines or linear trends, which are difficult to isolate and remove in current strong motion records, can seriously distort the resultant displacement after double integration, often leaving its estimation more a matter of judgment rather than science (Boore, 2001). Resolving long-period motions associated with static displacements is somewhat more complicated, as will be discussed in Chapters 3 and 4. Essentially, as the instrument response of the strong motion sensor needs to be removed to recover the zero frequency static offset, the strong motion velocity meter provides no improvements over traditional accelerometers for this. As the velocity meter is also an inertial seismometer like the accelerometer, the sensor is also very sensitive to tilt. Small changes in tilt can significantly affect the derivation of ground displacement, as pointed out by Trifunac and Todorovska (2001b). In order to fully derive the translational displacements in the presence of tilt requires additional information from a co-located rotational meter, or a nearby true displacement meter, such as GPS.

The increased range of Earth recordings obtained from using the proposed strong motion velocity seismometer is demonstrated through comparisons of signal recovery with both a typical accelerometer, the Kinemetrics FBA-23, and a broadband velocity instrument, the Weilandt-Streckeisen STS-2. The performance of each device is illustrated by showing how their dynamic characteristics relate to a wide range of seismic motions, in terms of frequency content and acceleration amplitude. An in-depth description of the components of the complete seismographic system — which includes a digital recording device as well as the seismometer — and how the dynamic range is finally determined, is first presented.

2.2 A Typical CISN Station

The California Integrated Seismic Network (CISN), `www.cisn.org`, is the network source of most of the data used not only in this Chapter, but throughout the thesis. The CISN collates data from the Southern California Seismic Network (SCSN), the Northern California Seismic Network (NCSN), and many strong motion networks around the State of Califor-

nia. Data is available from the individual network data centre Web portals: the Southern California Earthquake Data Center (SCEDC), `www.scecdc.scec.org`, the Northern California Earthquake Data Center (NCEDC), `quake.geo.berkeley.edu`, and the Consortium of Organizations for Strong Motion Observation Systems (COSMOS) Strong Motion Virtual Data Center, `www.cosmos-eq.org`. CISN is a recent amalgamation of the three existing organisations. Most data herein is from the SCSN. This network has immensely benefited from the TriNet project (1997-2001). TriNet provided a dense, modern seismic information system for Southern California (Hauksson et al**,** 2001; Hauksson et al**,** 2003), with over 150 broadband stations. TriNet itself grew out of the first digital, co-ordinated broadband and strong motion seismic network in Southern California, TERRAscope (Kanamori et al**,** 1991), which comprised 28 stations.

The SCSN is designed to record on-scale motions from an M8 earthquake, as well as large teleseismic earthquakes and small regional motions. The entire network has a minimum earthquake detectability threshold of M1.8. This requires not only an even and relatively dense distribution of stations, but each station must also have a very large dynamic range, of about 10 orders of magnitude, or 200dB. Thus the typical station consists of two broadband force-balance seismometers, typically a high-gain velocity recording device, such as an STS-2 or a CMG-40T, and a low-gain strong motion accelerometer, such as an FBA-23, or EpiSensor. These instruments record on a 24-bit Quanterra digitiser — about 7 orders of magnitude dynamic range, or 138dB. A plot of the dynamic range of the typical sensor/datalogger configuration is in Figure 2.1, which also includes the average size of earthquake signals from events of various magnitudes and distances. A detailed explanation of how this plot was produced is in Sections 2.4 and 2.5. The digitiser has continuous, near-real time telemetry of high sampled data ($80 - 100sps$) to the data processing and archiving centres at the Caltech Seismological Lab, located in the South Mudd Laboratory at Caltech, and across the road from South Mudd, at the USGS Pasadena office, 525 S. Wilson Ave. The digitisers can also log the continuous (in a 3-week buffer) and triggered data locally in the event of a transmission breakdown.

The data processing centres receive continuous data from more than 1200 high sample channels (100sps, 80sps), and over 2000 lower sample channels (20sps, 1sps, 0.1sps,

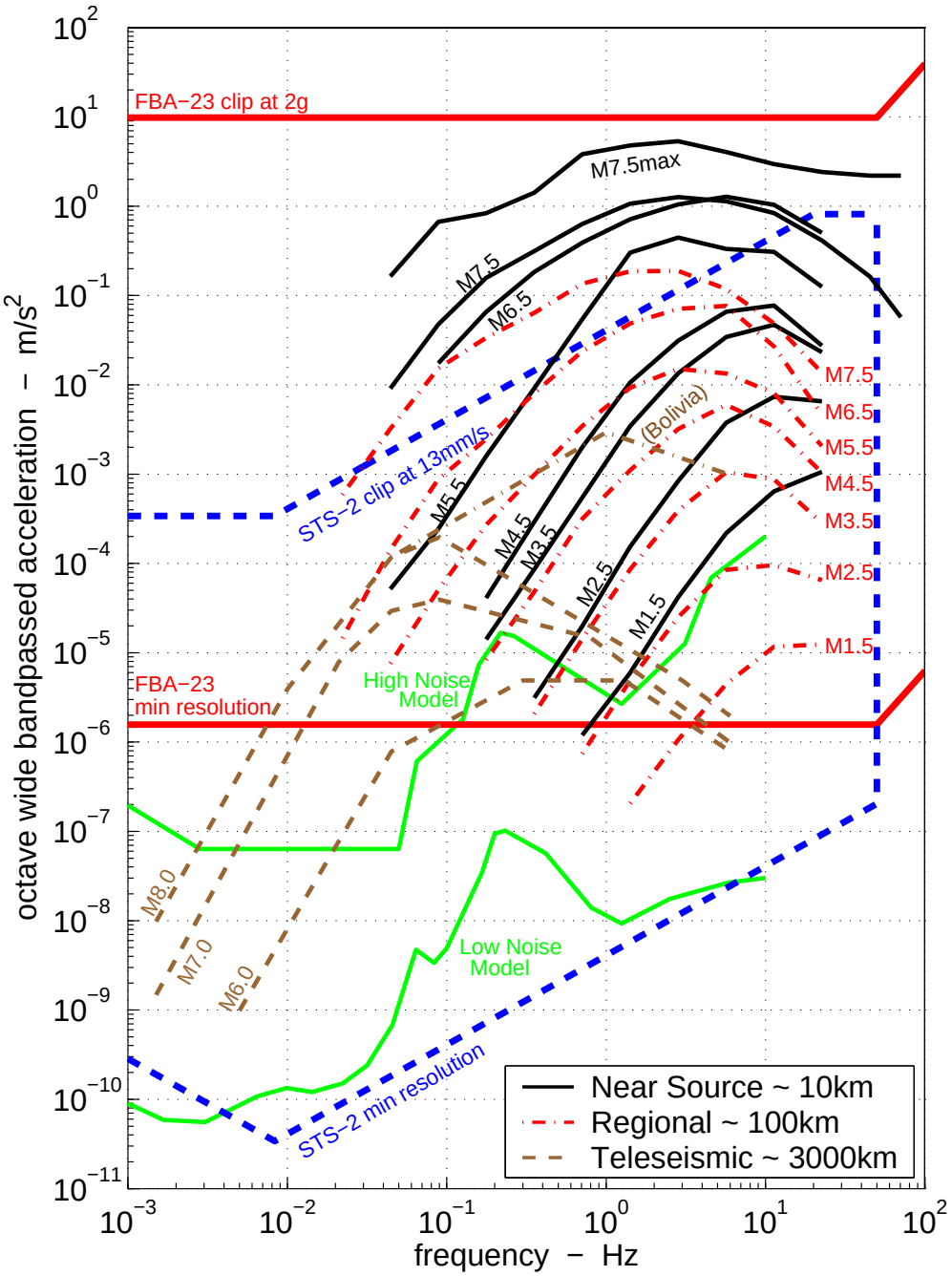

Figure 2.1: Frequency - amplitude plot for octave wide bandpasses of ground motion acceleration. A typical CISN station records all motions located between the FBA-23 clip and the STS-2 minimum resolution, encompassing the ~ 10 orders of magnitude required to cover the Earth's signals. Assumes 24-bit digitiser. Note that instrument limits are scaled down to account for the bandpassing of the event data. Ground motions recorded on-scale by the FBA-23 lie between the thick solid lines. The thick dashed lines give the dynamic range of the STS-2. Noise levels are the USGS High and Low Noise Models (Peterson, 1993).

health monitoring channels).

In certain cases, especially for stations in noisy areas, such as buildings, only a strong motion accelerometer is deployed with the 24-bit digitiser. This is the case at many of the stations around Caltech Campus, such as the Millikan Library (MIK), the Broad Center (CBC) and the USGS Building (GSA). Some other stations, such as the Caltech Athenaeum (CAC), have only an accelerometer alongside a 19-bit K-2 digitiser.

Other remote stations may only have a short period Mark Products L4-C vertical instrument with limited dynamic range of about $55dB$, primarily used for earthquake detection and location.

In total the SCSN currently has about 155 stations with both broadband and strong motion sensors, with about 55 stations with a single 3-component strong motion sensor. There are also about 140 stations with vertical component short period sensors only. A station location map for the entire SCSN is in Figure 2.2, and Figure 2.3 is a close up of the LA basin.

The data is stored in both a continuous format, at $20sps$, and in triggered 'event' format, at 80-$100sps$, at the Southern California Earthquake Data Center, SCEDC. The digitisers are all Quanterra models, the older dataloggers have a maximum sampling rate of $80sps$, the new models $100sps$. Triggered event data is available a few hours after an event is identified, and continuous data for the previous day is made available at 12AM GMT.

Summary tables of typical instruments and digitisers are in Tables 2.1 and 2.2. The instrument response for the broadband sensors is in Figure 2.4. The broadband instrument response is flat to velocity for all the instruments from about $7Hz$ (the other instruments have their high frequency cutoff all beyond $20Hz$) to $30s$ and further, up to $360s$. Beyond the long-period period corner, all sensors have a drop-off at a rate of $-12dB/oct$ to velocity, which means in this recording range, the instruments are flat to the differential of acceleration (the 'jerk'). At frequencies less then the high frequency cutoff, these instruments all respond essentially as single degree of freedom (SDOF) simple oscillators with differential feedback.

Data is available via a Web browser at `www.scecdc.scec.org/stp.html`, or from a stand-alone software version on the users computer, downloadable from `www.scecdc.`

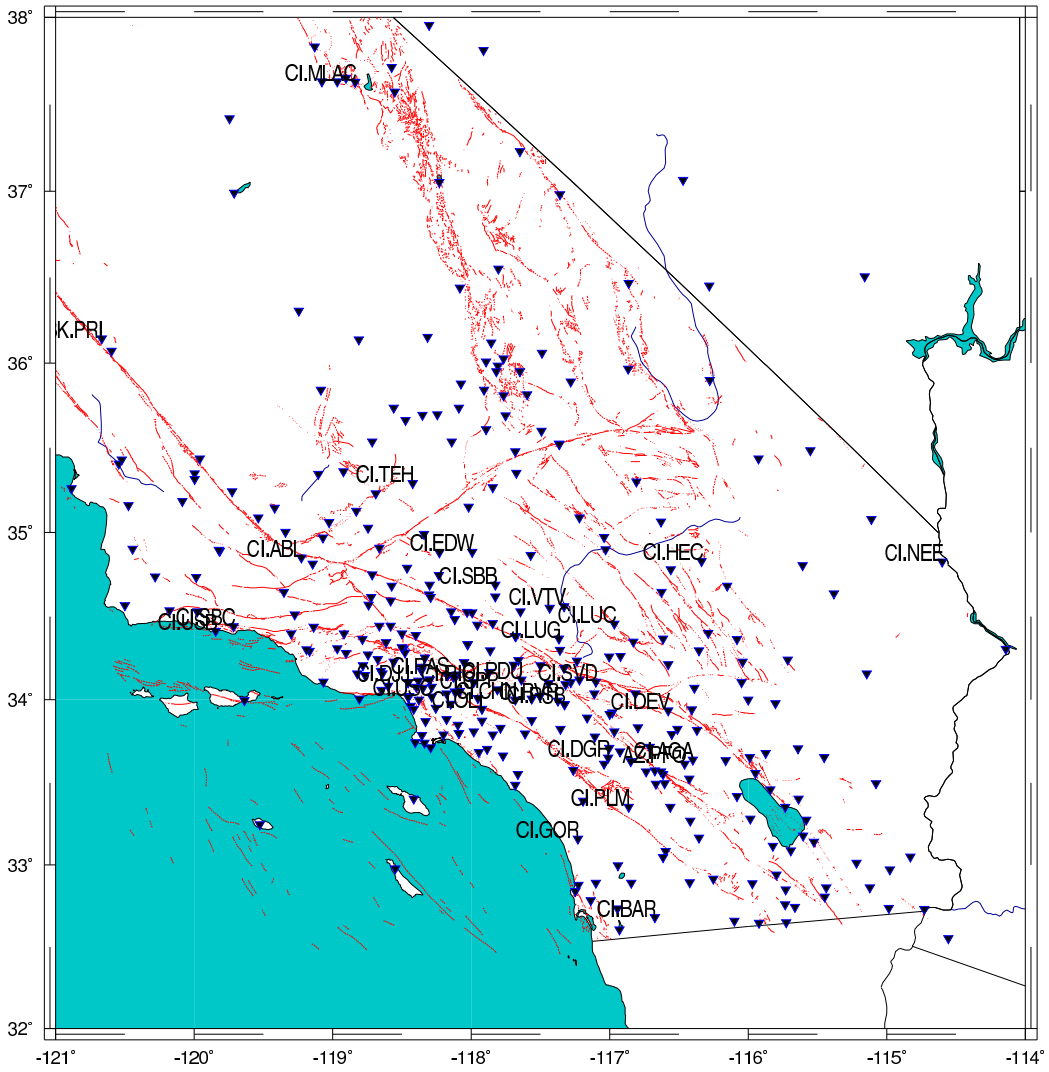

Figure 2.2: Southern California Seismic Network (SCSN) station map. Known faults are in light shade. A selection of station names is shown.

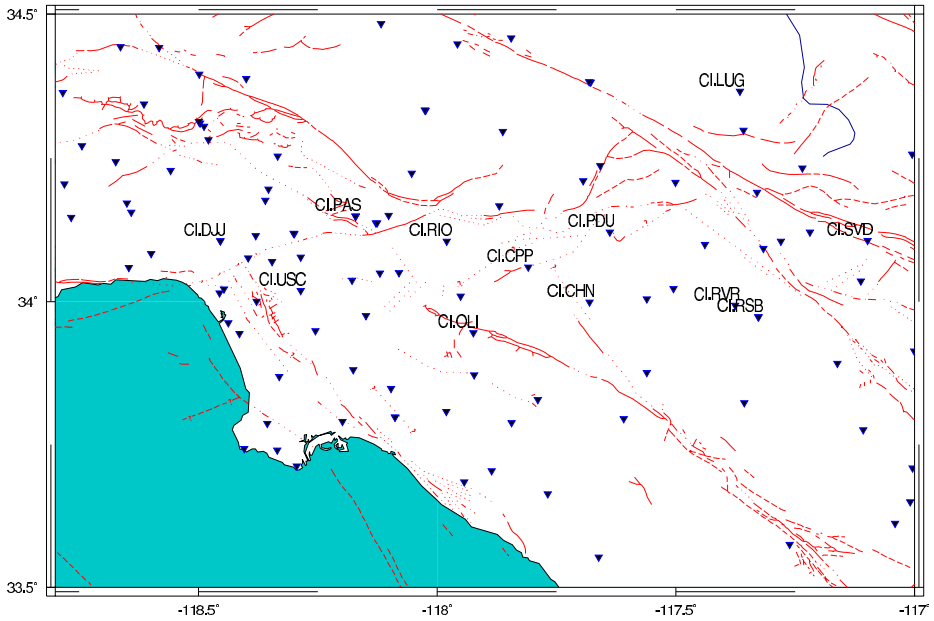

Figure 2.3: Southern California Seismic Network (SCSN) station map for the Los Angeles basin. Known faults are in light shade. CI.PAS is station at Kresge Lab., Pasadena.

Manufacturer	**Type**	**Freq. Range**	**Sensitivity**	**Clip Level**
High Gain Broad-Band Seismometers :				
Streckeisen	STS-1	0.0027-10Hz	2500 $V/m/s$ (vert)	$\sim 0.8 cm/s$
			2300 $V/m/s$ (horiz)	$\sim 0.8 cm/s$
Streckeisen	STS-2	0.0083-50Hz	1500 $V/m/s$	$1.3 cm/s$
Guralp	CMG-1T	0.0027-10Hz	1500 $V/m/s$	$\sim 1 cm/s$
Guralp	CMG-40T	0.033-50Hz	800 $V/m/s$	$\sim 1 cm/s$
Guralp	CMG-3ESP	0.0083-50Hz	2000 $V/m/s$	$\sim 1 cm/s$
Guralp	CMG-3T	0.0083-50Hz	1500 $V/m/s$	$\sim 1 cm/s$
Low Gain Broad-Band (Accelerometer/Strong Motion Velocity) :				
Kinemetrics	FBA-23	DC-50Hz	5 V/g	$2g$
Kinemetrics	EpiSensor	DC-180Hz	10 V/g	$2g$
Tokyo-Sokushin	VSE-355G3	$\sim$.01-70Hz	10 $V/m/s$	$\sim 200 cm/s$

Table 2.1: Summary of typical instruments used in the California Integrated Seismic Network. Abridged from Hauksson et al. (2001)

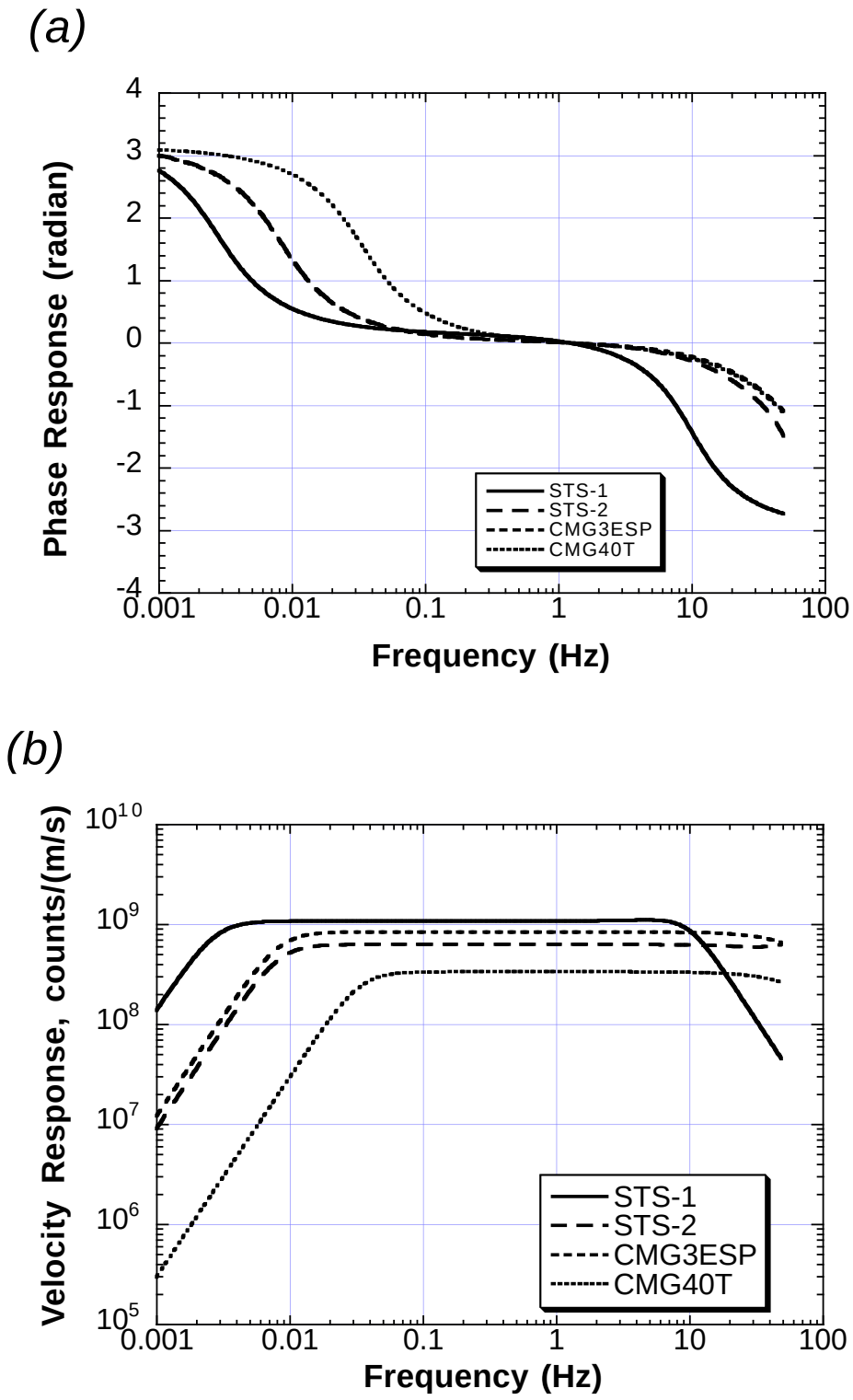

Figure 2.4: Response for typical broadband CISN instruments (from Hauksson et al. (2001)).

Manufacturer	Type	Site Recording	Channels	Max. SPS	Volts/cts
Quanterra	Q980	1.6Gb	9	80	$20/2^{23}$
Quanterra	Q380	1.6Gb	3	80	$20/2^{23}$
Quanterra	Q680	1.6Gb	6	80	$20/2^{23}$
Quanterra	Q4128	1.6Gb	8	100	$20/2^{23}$
Quanterra	Q730	1.6Gb	6	100	$16/2^{23}$
Quanterra	Q730E	280Mb	6	100	$16/2^{23}$
Quanterra	Q330	20Gb	6	200	$20/2^{23}$
Kinemetrics	K2	64Mb	4	100	$2.5/2^{23}$

Table 2.2: Summary of typical digitisers used in the California Integrated Seismic Network. Abridged from Hauksson et al. (2001)

`scec.org/ftp/programs/stp`. This later version can be opened using perl scripts for automated searching and downloading of data.

2.3 The Definition of Dynamic Range

Following Heaton (2003), the dynamic range, *DR*, of an instrument is defined as the ratio of the largest on-scale/linear measurement, M_{max} divided by the smallest measurement resolvable by the instrument, M_{min}:

$$DR = \frac{M_{max}}{M_{min}} \tag{2.1}$$

In the context of seismic instrumentation, the measurement is usually voltage output for a seismometer, or counts for a digitiser.

Traditionally, dynamic range is given in the units of decibels (dB), $\frac{1}{10}^{\text{th}}$ of a Bel. A Bel is defined as a base 10 logarithmic measure of energy per unit time, or power. Since the power of a signal is proportional to the square of the signal amplitude:

$$DR_{dB} = 10log_{10}\left[\frac{M_{max}}{M_{min}}\right]^2 dB \tag{2.2}$$

$$= 20log_{10}\left[\frac{M_{max}}{M_{min}}\right] dB \tag{2.3}$$

The Earth, for example, has about 10 orders of magnitude range in intensity from the largest motions from large earthquakes to the noise levels at the quietest sites (such as recorded at depth in a mine shaft in a seismically inactive region far from the ocean). Thus the dynamic range of the Earth is:

$$DR_{dB}(Earth) = 20log_{10}\left[\frac{10^{10}}{1}\right]dB \quad (2.4)$$

$$= 200dB \quad (2.5)$$

Similarly, m orders of magnitude dynamic range is equivalent to $(20*m)dB$.

Seismic recordings made on traditional recording paper have a maximum amplitude of about $10cm$, and a minimum resolution of about $0.1mm$. This is a dynamic range of 3 orders of magnitude, or $60dB$.

Modern seismometers record on digital recorders, which convert the analogue voltage seismometer output to digital counts. The nominal dynamic range is determined by the number of bits used to characterise the voltage. One bit is used to determine whether the signal is positive or negative, and each additional bit represents a factor of 2 in dynamic range, so dynamic range is 2^{n-1}. For a 24-bit digitiser, the dynamic range is 2^{23} or 8388608. This is $138.5dB$, or $138.5dB/20 \sim 7$ orders of magnitude.

[An alternative, quick way to determine the dynamic range of a digitiser in dB is $DR_{dB} = (\#bits-1)*6.02$, as each additional bit increases the dynamic range by $20log(2) = 6.02$.]

2.4 The Seismographic System

The range of amplitude and frequency recorded by a modern seismographic system is controlled by both the seismometer and the digitiser, or digital recorder. Ideally, the maximum gain of the datalogger ($2^{(n-1)}$counts for a n-bit system) should be reached when the instrument is at its clip level. If so, the minimum resolution of the seismographic system is determined by lowest resolution of the instrument and digitiser. Thus, the dynamic range

of the 2 components is investigated separately, to fully understand the dynamic range of the complete system.

Similarly, the behaviour of a system at clipping is dependent on the clipping characteristics of both the datalogger and sensor. With regards to the datalogger, many *n*-bit instruments simply cannot measure/output any more then 2^{n-1} counts, and will flat-line if the input signal is larger than this. Modern Quanterra 330 series instruments are in fact 27-bit sensors, though linearity of signal output is only guaranteed up to 24-bit. Thus the output can measure above 2^{23} or 8,388,608 counts. Similarly, the instruments manufacturers design the instruments only to guarantee linearity up to the advertised clip level. Once this has been exceeded, a range of signal errors can occur, ranging from the relatively innocuous (and this very difficult to recognise as incorrect) small drift away from linearity, to spikes, flat-lines and long-period instrument responses. Many of these will be observed in practice in the subsequent Chapters.

2.4.1 Dynamic Range of the Digital Recorder

Current state-of-the-art digital recorders employ 24-bit digitisers. The nominal dynamic range of such a device is about $140dB$. Theoretically, the dynamic range can exceed $140dB$ at low frequencies, since low frequency signals are oversampled and each point is the average of many samples. However, this dynamic range enhancement does not occur where the noise is characterised by a power density that increases as frequency decreases, i.e., some form of $1/f$ noise. This type of noise has a constant power in frequency bands of equal relative width (Wielandt and Streckeisen, 1982). Most electronic systems, in fact, are characterized by $1/f$ noise below 1Hz, and hence no resolution enhancement occurs (Joe Steim, personal communication, 2001). In practice, under normal operating temperatures, the dynamic range can indeed increase. For example, the Quanterra Q330, with $135dB$ nominal dynamic range, at 26°C records $136dB$ at $10Hz$, up to $142dB$ at $0.5Hz$, before dropping slightly at lower frequencies (Joe Steim, personal communication, 2001). As this is not a very large difference, I will assume, for the purposes of this work, a frequency-independent constant dynamic range of $140dB$, approximately 7 orders of magnitude, for

the digitiser.

2.4.2 Dynamic Range of Each Seismometer

— FBA-23

The clipping limit of the FBA-23 seismometer is $\pm 19.6 m/s^2$ ($\pm 2g$) up to its corner frequency of $50Hz$. By comparing ground motions recorded simultaneously with the FBA-23 and STS-2, it was established that the FBA-23 can resolve acceleration above the noise level of the instrument down to about $3\text{x}10^{-6} m/s^2$ across a broad band of frequencies (0.01 to $10Hz$). This is illustrated in Figures 2.13 and 2.14, from Section 2.5, which show the bandpassed records of a M8.1 event at $2900km$ epicentral distance. The FBA-23 noise at periods of about 100*s* and 50*s* are both of this level. For example, in Figure 2.14, the noise level is approximated as a sine wave with a 100*s* period and amplitude $5\text{x}10^{-5} m/s$:

$$\begin{aligned} \dot{u}_{noise} &= 5\text{x}10^{-5} \sin 2\pi f \tau \quad \text{m/s} \\ &= 5\text{x}10^{-5} \sin(6.28\text{x}10^{-2})\tau \quad \text{m/s} \\ \Rightarrow \ddot{u}_{noise} &= 3.14\text{x}10^{-6} \cos(6.28\text{x}10^{-2})\tau \quad \text{m/s}^2 \end{aligned}$$

and thus the amplitude of this wave in acceleration is approximately $3.14\text{x}10^{-6} m/s^2$, $136dB$ below the clip level of $\pm 19.8 m/s^2$. This is less than the published $145dB$ for the frequency range 0.01 to $20Hz$ (`www.kinemetrics.com`), but could also be due to limitations of the digitiser.

Further evidence for this noise level can be seen in Figure 2.5. In this plot, real continuous ambient noise data from a selection of accelerometer/digitiser configurations in the SCSN is presented. On average, FBA channels record noise at about $136dB$ below the clip level, whilst the EpiSensor has a better dynamic range, nearer $140dB$. This general trend, with a relatively constant amplitude over a wide band-width, occurs for a variety of stations and digitisers, which indicates this observed noise line is the actual noise floor of the instrument, rather than station's local site noise, or digitiser noise.

For the purposes of this work, it is thus assumed the dynamic range of the FBA ac-

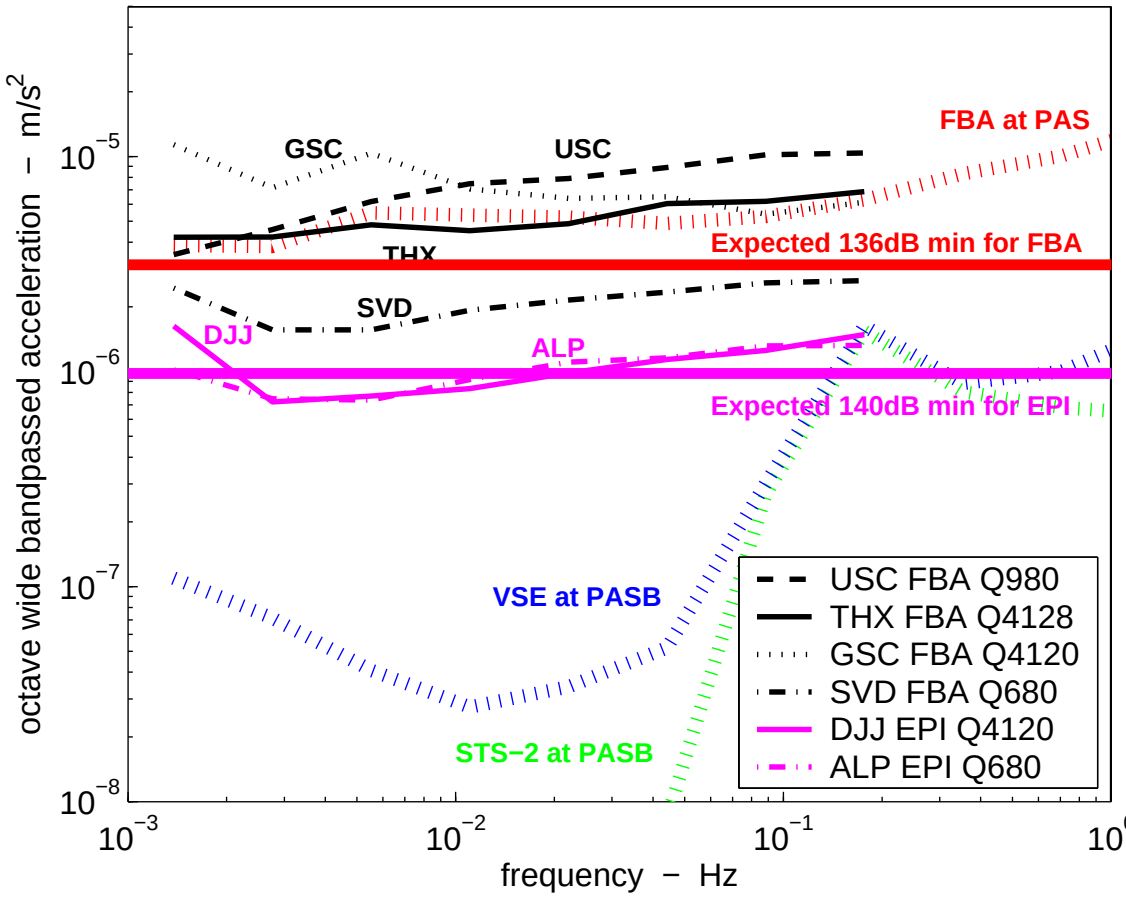

Figure 2.5: Comparison of noise floors for various accelerometer/digitiser configurations deployed in SCSN. All station data from a 3hour period on 1 April 2002. Also includes data from test station PASB, which at the time of the comparison, housed a Japanese Strong Motion Velocity Meter, the VSE-355G2, and an STS-2. PAS and PASB are essentially co-located.

celerometer is 136dB for the frequency range from 50Hz - DC.

— STS-2

Broadband seismometers such as the STS-2 have more complex characteristics. For seismic signals with periods shorter than the corner frequency (120s for an STS-2), they typically have clip levels that are given in both velocity and acceleration; in the case of the STS-2 this is $\pm 13 mm/s$ and $\pm 3.3 m/s^2$ ($\pm 0.34g$). Velocity clip levels are often given as peak-to-peak values, for the STS-2 this would be $26 mm/s$ peak-to-peak, hence the 1/2 peak-to-peak value is $13 mm/s$. The minimum resolvable motion for the STS-2 is not a simple function, or indeed directly related to the clip; in fact it is highly dependent on frequency, and is greater than 140dB for the frequency range of interest. The instrument noise level is published in the STS-2 manual (Streckeisen and Messgerate), and is shown in Figure 2.6.

— Strong Motion Velocity Meter

The hypothetical long-period, low-gain velocity instrument would have a similar type of response as the STS-2, with a corner frequency at 120s, and clip level at $\pm 5 m/s$ and $\pm 49 m/s^2$ ($\pm 5g$). Minimum resolution is assumed to be 140dB below the clip level, a similar value to both the STS-2 and FBA-23.

The dynamic characteristics of these three seismometers are summarised in Table 2.3, and illustrated in Figure 2.6.

Instrument Type	Free Period	Clip Level
FBA-23	0.02s (50Hz)	$\pm 19.6 m/s^2$ ($\pm$2g)
STS-2	120s (0.0083Hz)	min[$\pm$13mm/s, $\pm 3.3 m/s^2$ ($\pm$0.34g)]
strong motion velocity	120s (0.0083Hz)	min[$\pm$5m/s, $\pm 49 m/s^2$ ($\pm$5g)]

Table 2.3: Comparison of important properties of the instruments

The final response of the seismographic system is similar to the instrument response, but the system dynamic range at any frequency does not exceed 140dB due to the limitations

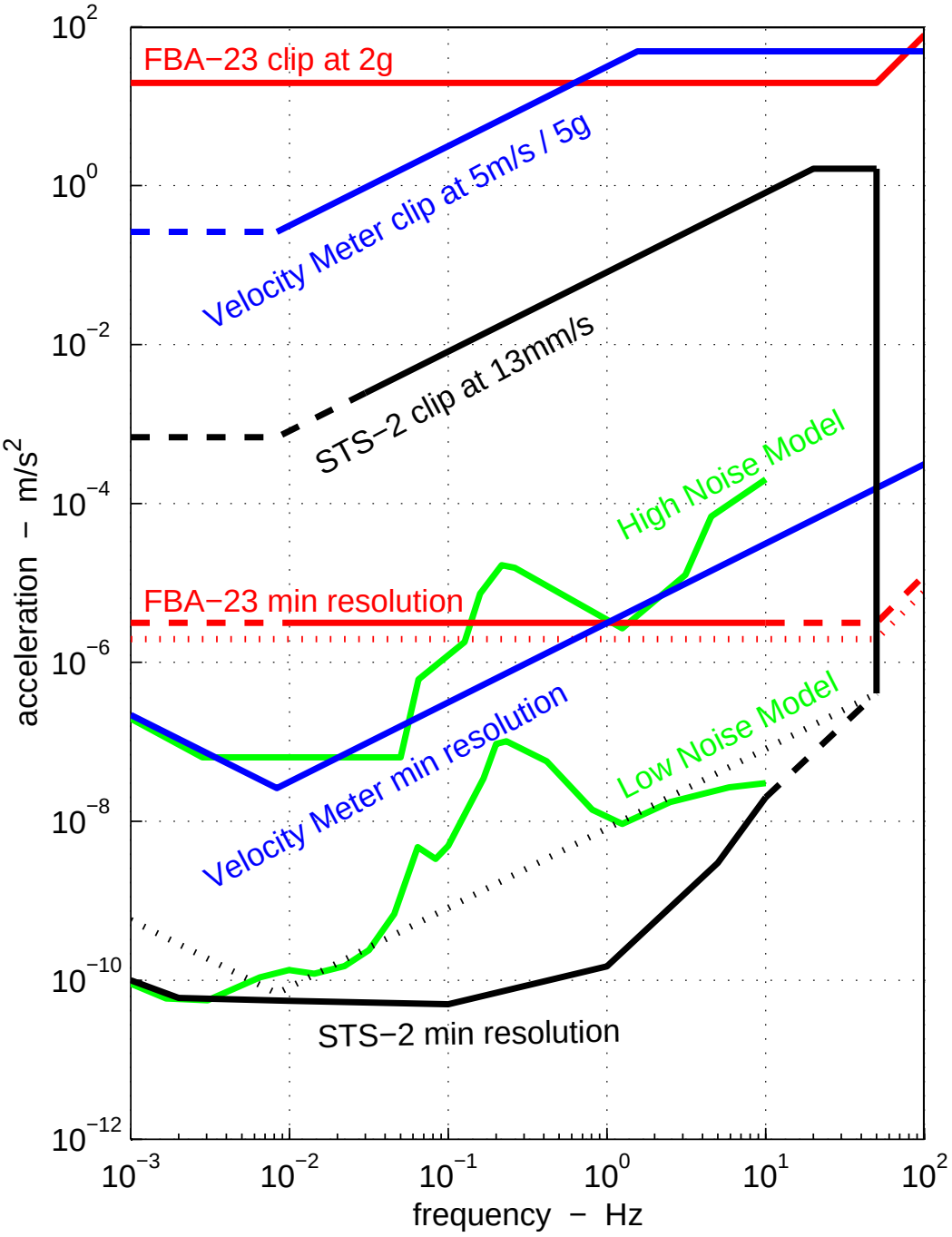

Figure 2.6: Instrument responses in terms of acceleration. Dashed lines indicate regions of uncertain instrument response. For the FBA-23 and STS-2, dotted lines indicate areas 140*dB* below instrument clipping levels. Noise levels are the USGS High and Low Noise Models (Peterson, 1993).

of the digitiser. For the three instruments, only the system response for the STS-2 system is affected.

Note that for brevity and simplicity, hereafter the combined seismographic system comprising both the instrument and digitiser is referred to simply as the ‘instrument’ or the ‘seismometer’.

2.5 Strong Motion Instrument Comparisons Using Recorded Earthquake Signals

The hypothetical strong motion velocity meter is compared with the Kinemetrics FBA-23 accelerometer, and the Weilandt-Streckeisen STS-2 broadband velocity seismometer. To show the range of motions typically recorded on-scale and above the instrument noise of each instrument, their performance in frequency and amplitude of acceleration is plotted in relation to a broad range of Earth signals typically of interest to engineers and seismologists. Measured signal strengths of each record are not power spectra of the broadband time series, but discrete octave-wide bandpasses. This allows the inconsistencies in the power spectra associated with arbitrarily picking a duration for the transient earthquake signals (Aki and Richards, 1980) to be ignored. Although this also means the complexity of the overall broadband signal is ignored (and will then in general under-represent the final strength of the record), bandpassing facilitates a better relation of the instrument limits to signal strength.

2.5.1 Assembly of the Earthquake Database

The earthquake signals selected were divided into magnitude-distance bins, summarised in Table 2.4. For each distance, the bins vary in increments of one magnitude unit, for example, the M6.5 bin incorporates data from M6.0 to M6.9 events. The three distance bins represent near-source, regional and teleseismic recordings.

The records in the near-source database were generally limited to data from within 10*km* distance from the projection of rupture onto the Earth’s surface. Event magnitudes

1. NEAR SOURCE : data within $0-20km$ **of epicenter (or surface projection of rupture)**				
Magnitude	**#stations**	**#records**	**events**	**instruments — data source**
M7.5	26	78	Chi-Chi ′99	A800,A900 Geotech — CWB Taiwan
	5	14	Koaceli ′99	SMA-1(5xGSR-16) — ERD,Kandilli
M6.5	9	26	Northridge ′94	SMA-1 (3xFBA-23) — UCSB
	14	41	Imp. Valley ′79	SMA-1 (3xDCA-10) — UCSB
	1	3	Coalinga ′83	SMA-1 — UCSB
M5.5	3	8	3	8 x FBA-23 — TriNet
M4.5	28	84	20	32 x FBA-23, 52 x STS-2 — TriNet
M3.5	10	62	21	32 x FBA-23, 30 x STS-2 — TriNet
M2.5	12	108	35	108 x STS-2 — TriNet
M1.5	8	42	12	42 x STS-2 — TriNet

2. REGIONAL : data within $90-110km$ **of epicenter (or surface projection of rupture)**				
Magnitude	**#stations**	**#records**	**events**	**instruments — data source**
M7.5	16	48	Chi-Chi ′99	A800,A900 Geotech — CWB Taiwan
	2	6	Koaceli ′99	6 x GSR-16 — ERD Turkey
M6.5	4	12	2	12 x STS-2 — TriNet
M5.5	11	51	7	24 x FBA-23, 27 x STS-2 — TriNet
M4.5	13	52	5	10 x FBA-23, 42 x STS-2 — TriNet
M3.5	13	96	23	96 x STS-2 — TriNet
M2.5	12	66	20	66 x STS-2 — TriNet
M1.5	10	39	12	39 x STS-2 — TriNet

3. TELESEISMIC : data about $3000km$ **(27°) from epicenter, records usually** $20sps$ **(or equivalent), up to 1 hour duration)**				
Magnitude	**#stations**	**#records**	**events**	**instruments — data source**
M8	19	57	9	STS-1,2, KS5400,3600 — IRIS GSN
M7	20	60	7	STS-1,2, KS5400,3600 — IRIS GSN
M6	13	39	8	STS-1,2, KS5400,3600 — IRIS GSN

Table 2.4: Summary of waveform data included in each Magnitude-Distance bin. For the teleseismic datasets — M8 is represented by events in the range M7.6 - M8.0, at 21° - 31° and 33 - 480*km* depth, with 2 additional records from the M8.2 637*km* deep focus Bolivia event at 20° — M7 is represented by events in the range M6.8 - M7.4 at 23° - 29° and 10 - 185*km* depth — M6 is represented by events all of M6 at 25° - 29° and 10 - 49*km* depth.

range from M7.5 down to M1.5. Records were obtained from the SCEDC database (then TriNet) (`www.trinet.org`; `www.scecdc.scec.org/stp.html`) (Hauksson et al, 2001). Due to a sparsity of data from events of M6 and above, the distance limit was relaxed to include records under 20*km* from the projection of rupture. For these larger events, data is also included from the Southern California Earthquake Center (SCEC) Strong Motion Data Base (SMDB) (now part of COSMOS, `http://db.cosmos-eq.org/`) for historic events, with records from predominantly analogue instruments, and from Taiwanese (Lee et al, 1999; Uzarski and Arnold, 2001) and Turkish (`www.koeri.boun.edu.tr`; `www.deprem.gov.tr`; Youd et al, 2000) data centers for timeseries from recent large earthquakes outside of Southern California.

The regional database was represented by records at a distance of about 100*km*. Event magnitudes range from M7.5 down to M1.5. As with the near-source database, the distance bin was relaxed to include records within $85 - 110km$ of the projection of rupture onto the Earth's surface for the sparse data sets from the larger magnitude events. The data sources were the same as those for the near-source database.

Records in the teleseismic database were limited to signals recorded at about 3000*km* epicentral distance. Data from M8 to M6 events were used, obtained from the IRIS-GSN Web site (`www.iris.washington.edu`).

Each bin contained records from a wide sampling of events and stations in order to obtain reasonable median values of peak amplitude. The only event which contained data which seriously deviated from the median was the M8.2 deep focus Bolivia event, which is treated separately.

All timeseries from broadband velocity instruments were differentiated to acceleration.

2.5.2 Recovery of Earth Signals

Once the database was assembled, each individual timeseries was passed through octave-wide bandpass filters. The absolute maxima of each bandpass for each record was recorded, as illustrated for 2 very different signals in Figure 2.7 and Figure 2.8. The maximum frequency for the bandpasses for each magnitude-distance bin was determined by the Nyquist

value of the timeseries. The minimum frequency was more subjectively chosen as the frequency where the signal intensity was similar to the background noise.

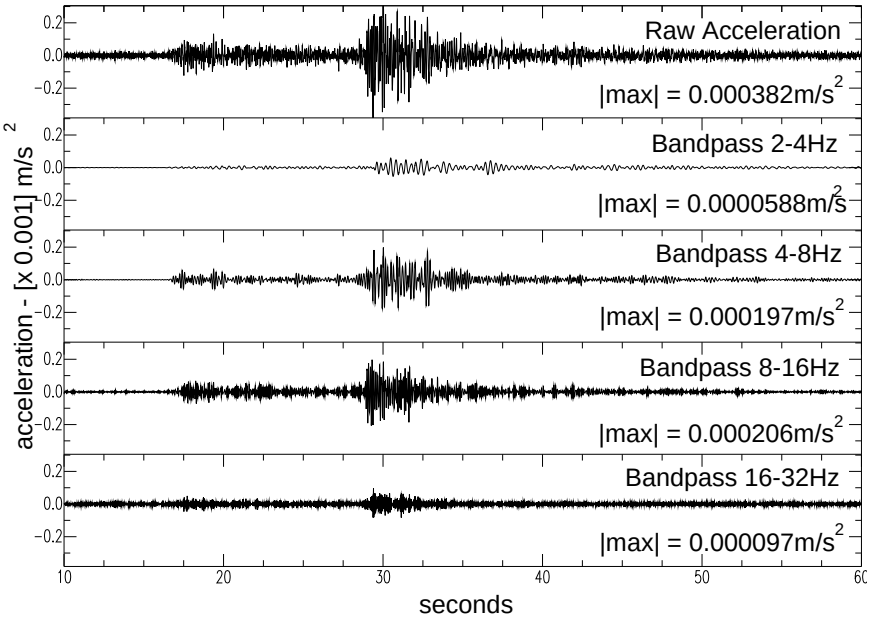

Figure 2.7: Sample bandpasses for M3.5 at 100*km* (acceleration records from 3 February 1998 event, recorded at Station LKL on the 80*sps* N-S component channel of an STS-2.

For each bandpass of a magnitude-distance bin, the geometric mean of all the absolute maxima was calculated. When combined with the geometric means from the other bandpasses in the same bin, a curve is obtained which represents the octave-wide frequency content typical of ground motions for that bin. This is demonstrated for the M3.5 at 100*km* magnitude-distance bin in Figure 2.9.

The frequency-amplitude curves for all the magnitude-distance bins are shown in Figure 2.1. In this Figure, also shown are the dynamic range performances of the instruments typically installed at a CISN station. Figure 2.10 includes the hypothetical low-gain velocity meter.

The limits of the individual instruments to the broadband signals have been discussed (see Figure 2.6). The ground motion data plotted has been bandpass filtered, and to account for this, there is a need to modify, or calibrate, the broadband instrument clip levels for an octave-wide clip level. To do this, first a number of broadband timeseries are chosen which are close to clipping each instrument (generally within 20% of saturation). These records

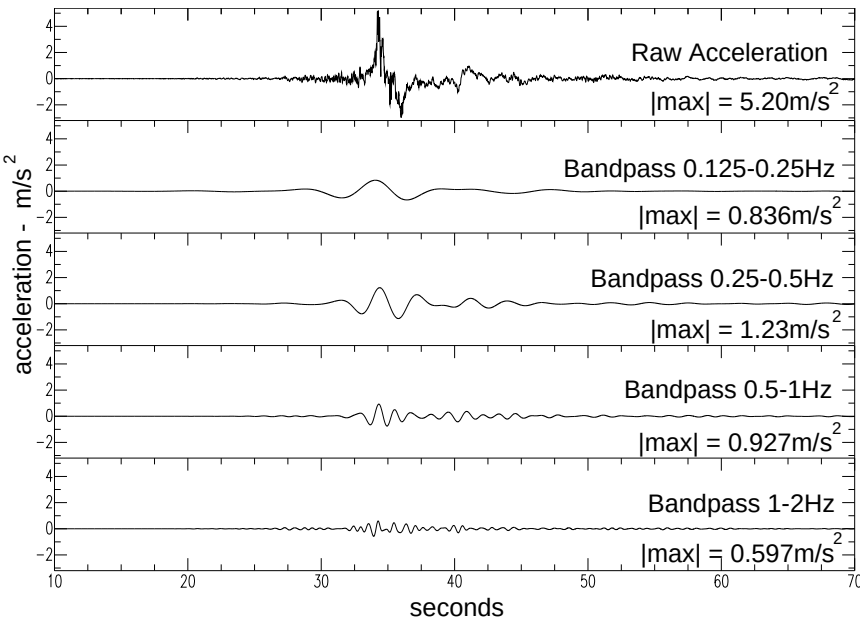

Figure 2.8: Sample bandpasses for M7.5 at 10*km* (acceleration records from 21 September 1999 Chi-Chi earthquake, recorded at Station T076 on the 200*sps* Z component channel of a Geotech A900).

are then filtered in octave-wide bandpasses. To calibrate the instruments, the bandpass with the highest velocity (for the broadband STS-2 seismometer) or acceleration (for the FBA-23) is selected, this maximum value is scaled by the reciprocal of the percentage the timeseries came to the clip level for the instrument. This new value is the calibrated clip level for the bandpassed data. The inherent uncertainty in this method was reduced by performing this for a number of records of varying spectral content. Typically this reduced the broadband clipping levels by about 50% .

Finally, the New High and Low Noise Models from Peterson (1993) were superimposed onto Figures 2.1 and 2.10.

The 'M7.5Max' line on Figures 2.1 and 2.10 was derived from some of the largest near-source waveforms ever recorded, including data from the recent Chi-Chi, Taiwan, and Kocaeli, Turkey events. The line is constructed using the absolute maxima of each bandpass for the M7.5 at 10*km* dataset (not the geometric mean). From all these records, it is clear that both the $\pm 19.6 m/s^2$ FBA-23 and hypothetical low-gain velocity instrument are unlikely to clip in the event of most conceivable Earth motions. In this regard, both

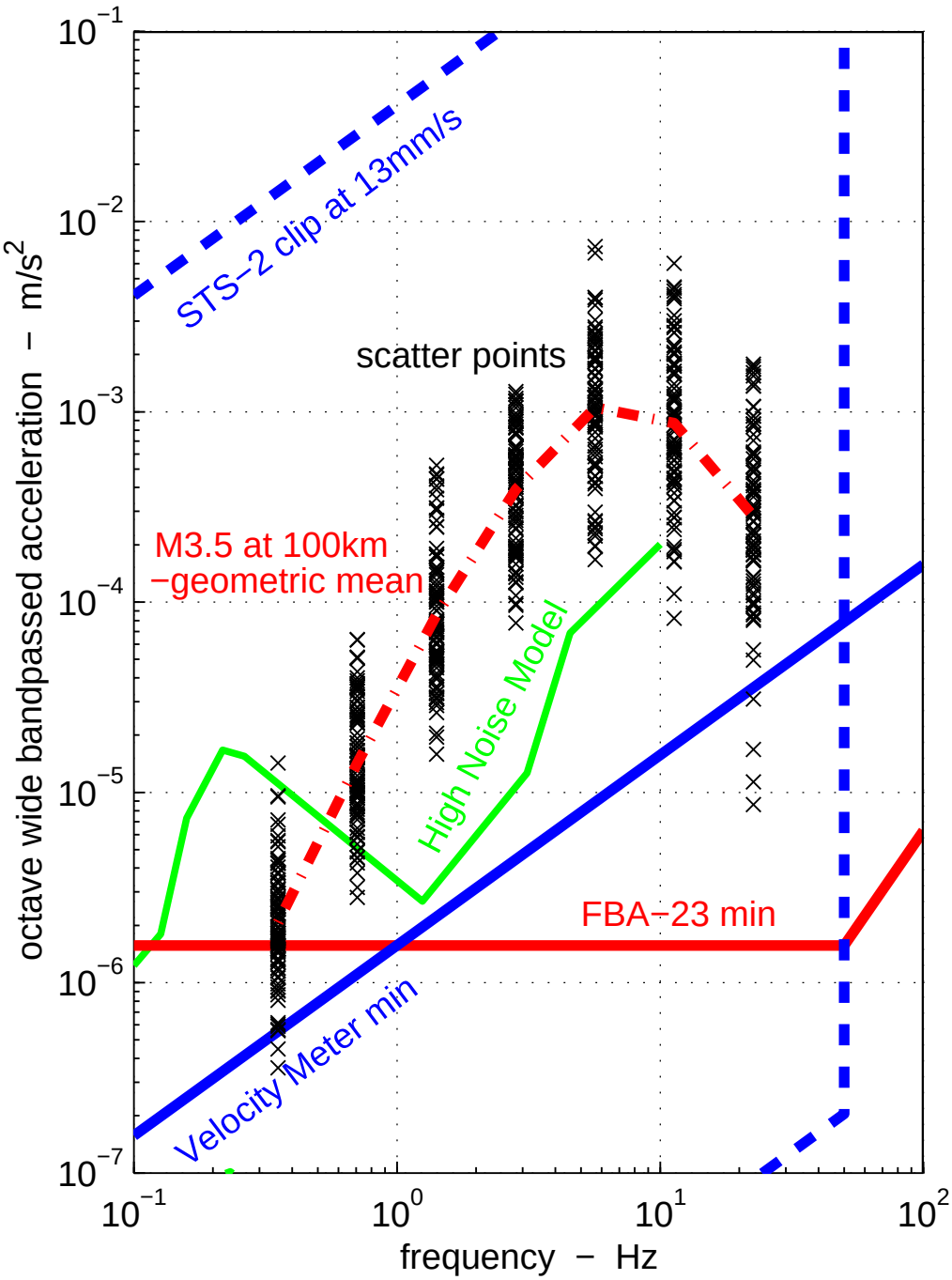

Figure 2.9: Data scatter and geometric mean for M3.5 at 100*km*. The crosses are the individual data points from each timeseries (as in Figure 2.7), and their geometric mean is represented by the thick dashed-dotted line. Instrument and noise lines are similar to Figure 2.6.

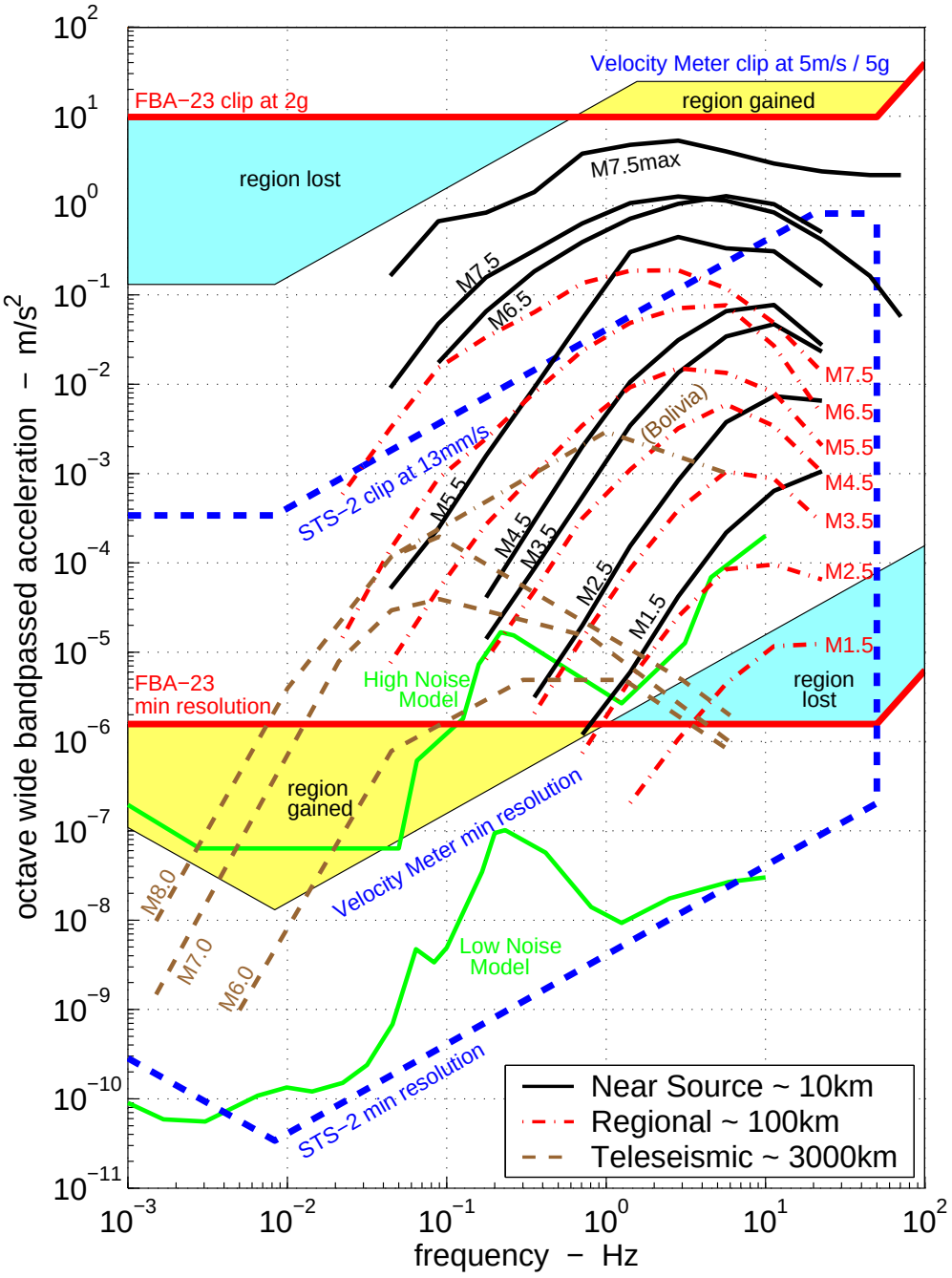

Figure 2.10: Frequency - amplitude plot — showing advantages of recording strong motion velocity. As Fig 2.1, with on-scale motions recorded by the hypothetical low-gain broadband seismometer lying between the solid blue lines. The areas shaded light blue are regions of frequency-amplitude space that are recorded by the FBA-23, but not recorded by the hypothetical low-gain broadband seismometer. Areas shaded yellow are regions of frequency-amplitude space that are recorded by the hypothetical low-gain broadband seismometer, but not recorded by the FBA-23. (*see text for further explanation*)

instruments would be equally effective in recording the strong motion data gathered to date.

The yellow shading in Figure 2.10 indicates regions of frequency-amplitude space that can be recorded by the hypothetical instrument, but are not presently recorded by the accelerometer. For the same dynamic range, the low-gain velocity instrument would record a larger range of Earth signals at periods greater than $1Hz$ than the accelerometer. The potential of this hypothetical device for measuring long-period motions from basin amplifications of small, local earthquakes is obvious. Teleseismic energy at longer periods, as well as energy from smaller events at teleseismic distances, would also be recorded. Regions of frequency-amplitude space presently recorded by the accelerometer, but not recorded by the hypothetical instrument, are indicated by the blue shading in Figure 2.10.

Note that the lines of geometric mean are not representative for some large, deep teleseismic events. The teleseismic database includes the M8.2 9 June 1994 $637km$ deep focus Bolivia event, and the median line for data from this event alone is also plotted on Figure 2.10. Records from this earthquake contain interesting high frequency energy not present at teleseismic distances during shallower events.

2.5.3 Recovery of Acceleration

High frequency acceleration signals derived from a single differentiation of an STS-2 velocity timeseries are examined to demonstrate the likelihood of good recovery of acceleration data from the hypothetical instrument. Figure 2.11 presents a comparison of acceleration records from an STS-2 and an FBA-23. The record in question, from a M4.5 Northridge aftershock on 27 January 1994, recorded by the nearby SCSN station at Calabasas (CALB), had a recorded peak velocity (STS-2) of $1.24cm/s$, within 95% of clipping the instrument. There is a close correlation of these signals, even near the clipping limit of the STS-2. A similar capability to recover ground acceleration from the hypothetical instrument is anticipated.

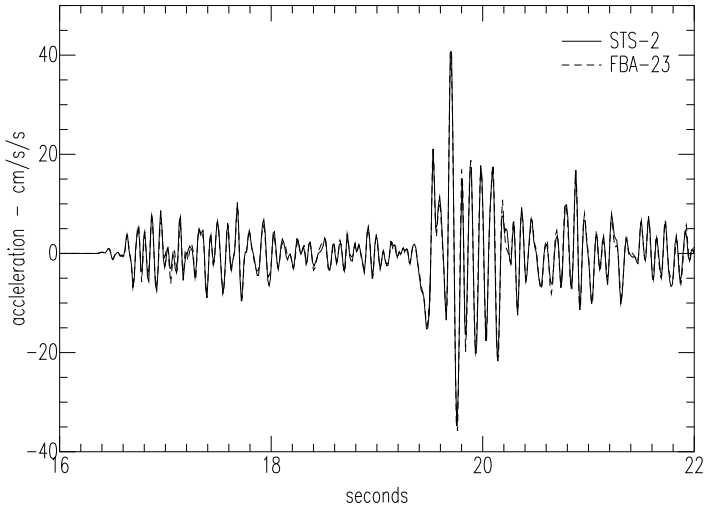

Figure 2.11: Comparison of acceleration records from a differentiated STS-2 (solid line) and an FBA-23 (dashed line). The records are from a M4.5 Northridge aftershock on 27 January 1994 recorded at Calabasas, CALB, N-S Component, 12km from the epicenter. Timeseries are from 80sps channels, with a low-pass filter at 20Hz.

2.6 'Strong Motion' Recordings at Teleseismic Distances

The global seismic network and database IRIS-GSN (`www.iris.washington.edu`) has 1sps accelerometer channels (mainly FBA-23's) at many stations to record long-period data from the largest earthquakes. These events may cause motions that may over-drive the current broadband seismometers, even at teleseismic distances. Figures 2.12, 2.13 and 2.14 show an example of long-period motions recorded by this channel. The recordings are from station SNZO in New Zealand, and are from the M8.1 25 March 1998 event located near Balleny Island, at a distance of 2900km. The instruments at the station are a Geotech KS-36000-i down-hole seismometer (similar to the STS-2) and an FBA-23. This record is within 15% of clipping a $\pm 13 cm/s$ STS-2 — the earthquake actually clipped a Guralp CMG-3T (station SBA) and a Geotech/Teledyne KS-54000 (station VNDA) both set to about $\pm 9 mm/s$ and both at a distance of 1700km from the epicenter in Antarctica. It is clear from the records that the FBA-23 is capable of recording the event well out to periods up to about 50 seconds. This clearly shows the usefulness of the strong motion instrument

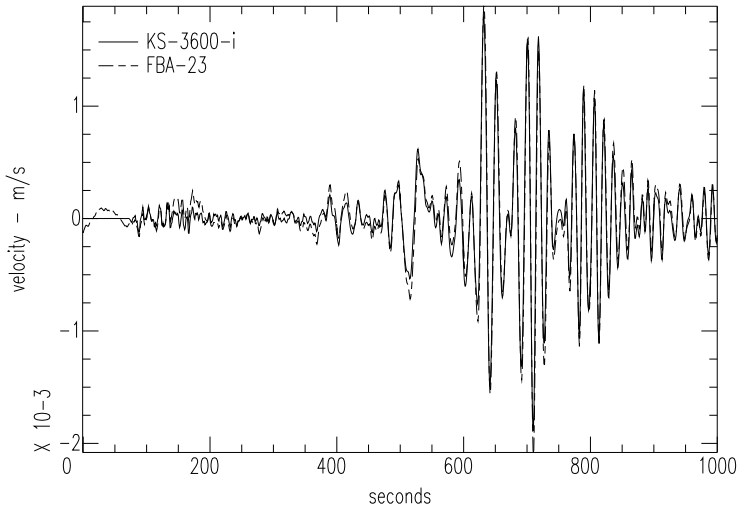

Figure 2.12: Velocity time series of 1*sps* integrated FBA-23 (dashed line - high-pass filter at 300*s*) and the 20*sps* KS-36000-i (solid line - decimated to 1*sps*) recording of the Z-component of the M8.1 Balleny Island earthquake from IRIS-GSN Station SNZO at 2900*km*.

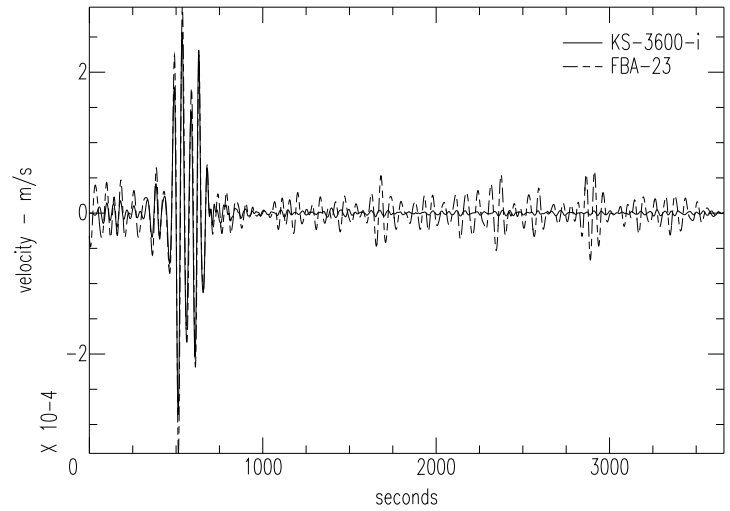

Figure 2.13: As Figure 2.12, but with a bandpass from 37.5 to 75 seconds, clearly showing the FBA-23 recording (dashed line) is capable of recovering long-period motion up to 50 seconds.

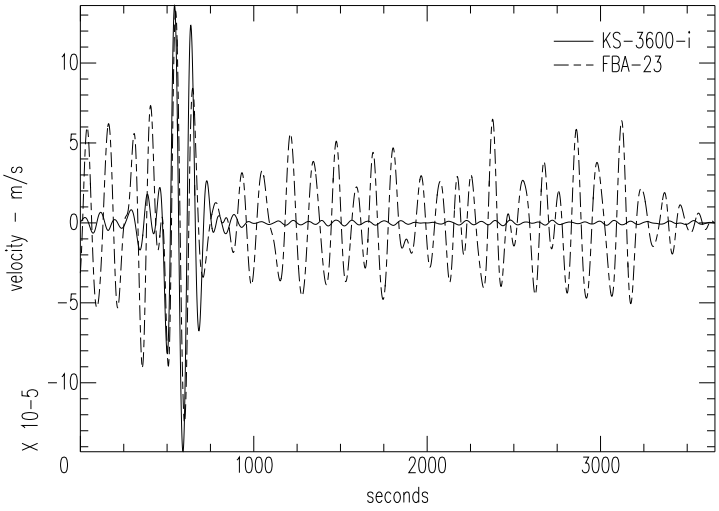

Figure 2.14: As Figure 2.12, but with a bandpass from 75 to 150 seconds, showing the FBA-23 recording (dashed line) is not easily resolved above the instrument noise at these amplifications.

at the IRIS-GSN stations, especially in the event of a great M9 earthquake, which could clip the high-gain broadband instruments for great distances. A low-gain velocity recording device would be ideally suited to deployment in future IRIS-GSN stations, as well as in the proposed Advanced National Seismic System.

2.7 Summary

Although the existing strong motion accelerometers generally perform well, several undesirable features of their response could be remedied by utilizing a strong motion sensor with a better long-period response.

Two main issues are addressed. The first issue is that records from accelerographs must be integrated twice to recover ground displacement. This double integration is an unstable procedure. In order to achieve reasonable displacements we often need to apply numerous adhoc assumptions. The second issue is that the accelerations from long-period signals (periods longer than 10 seconds) are very small. Even with $140dB$ of dynamic range, the signal-to-noise ratio of accelerometer records is poor for distant earthquakes. Potentially

valuable basin effects from small local earthquakes are also not recorded by the current accelerometers.

It is shown that both these problems would be alleviated by employing the hypothetical strong motion velocity instrument described here. This instrument would better utilize the large dynamic ranges — currently up to 7 orders of magnitude — available to the instrument designer by virtue of modern 24-bit digitisers.

The seismological community would benefit from this richer range of recorded motion, as many current networks built and maintained (in mostly urban areas) by the earthquake engineering community include only strong motion accelerometers. With the deployment of an instrument of the type discussed here, a station would record increased long-period data from near-source events of small magnitudes, medium-sized regional events and larger teleseisms. Continuous telemetry from a dense network of these strong motion stations would also aid development and the eventual reliability of a future real-time earthquake early warning system.

Using the proposed instrument, the engineering community would have access to reliable estimates of near-source ground displacements without compromising the quality of acceleration records. Improved measurements of the near-source displacement records would be of important use for the development of future structural design codes, though as will be illustrated in subsequent Chapters, permanent displacements are as difficult to recover with this instruments as they are from accelerometers. Further, the strong motion velocity meter is equally sensitive to tilt as any other inertial sensor.

A strong motion velocity seismometer would essentially be a low-gain version of existing broadband seismometers, such as the Weilandt-Streckeisen STS-2. Thus its cost would also be similar to other broadband seismometers, which at current prices is many times more than current $140dB$ accelerometers. Unfortunately, so would its size and weight. Thus the clear advantages are likely to be offset by significantly greater cost, size and weight than an accelerometer, which would make it unwieldy for dense building instrumentation.

Chapter 3 Examination of a Strong Motion Velocity Instrument

3.1 Introduction

This report documents the investigation into the performance of the tri-axial VSE-355G2 Strong Motion Velocity Seismometer, purchased with IRIS funds in late 2001. The instrument is manufactured by Tokyo Sokushin Co. Ltd., Office 2-22-9, Nishi-Nipporim Arakawa-Ku, Tokyo, 116-0013 Japan (`www.to-soku.co.jp`). Photographs of the instrument are in Figure 3.1.

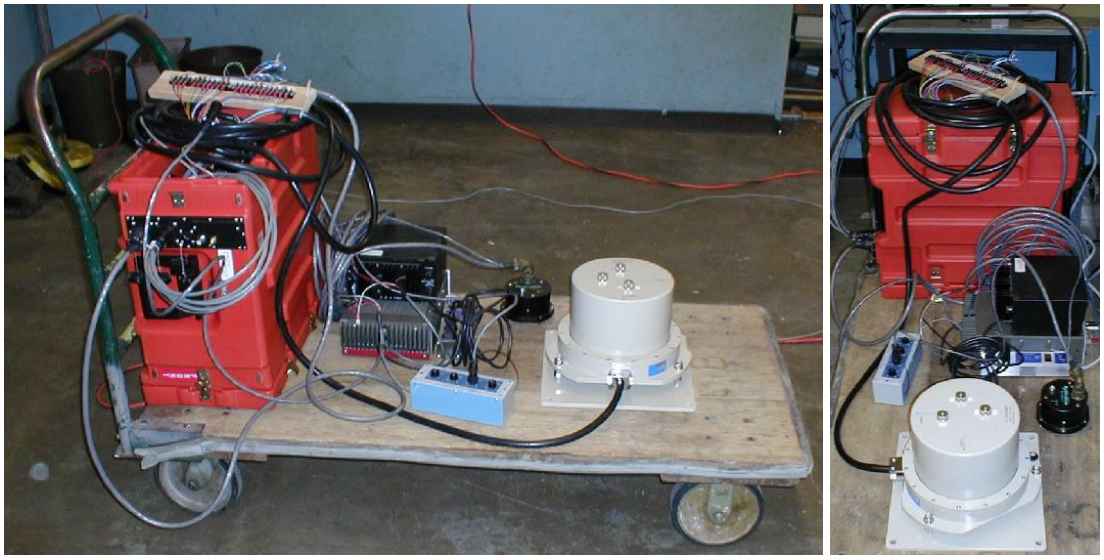

(a) Side view (b) Front view

Figure 3.1: VSE photo - Cart Test setup. VSE-355G2 is the large silver cylindrical instrument at the front of the cart, the EpiSensor is the small black cylindrical instrument just behind the VSE in the middle of the cart. A Q4120 datalogger (large rectangular box) is located at the back of the cart.

The instrument measures velocity as the standard output, from a heavily over-damped

mechanical pendulum and a feedback loop proportional to the pendulum displacement. A built-in calibration coil can provide known acceleration input for determination of the instrument sensitivity and frequency characteristics.

The performance of the instrument was determined by

- comparing earthquake signals and noise levels from the VSE-355G2 and a Streckeisen STS-2, co-located with the seismometer, in order to calibrate and obtain the sensitivity of the instrument.
- determining the system response to a known input, through the calibration coil, in order to estimate the equivalent SDOF instrument response.
- placing the instrument alongside an accelerometer on a laboratory cart and running the cart along the floor, in order to determine the actual instrument clip level (setup as in Figure 3.1).

A major design error was discovered during the original testing regime, the instrument was found to 'clip', or undergo non-linear behaviour, at velocities of only $15 cm/s$, significantly below the advertised clip level of $200 cm/s$ and also well below the expected velocities during large earthquakes. Exhaustive consultation and re-testing, involving many on-site visits from Tokyo-Sokushin, as well as independent tests carried out both here in the US and Japan, followed the discovery. A chronological list of the tests performed on the instrument are contained in Appendix A.

To obtain a satisfactory result from the cart tests which determine a broadband clipping level, the manufacturer had to replace and redesign the feedback and the suspension of the instrument. Once it had been established the instrument performed to the initial specifications in terms of strong motion recording, in late 2003, all the initial tests performed in 2001/2002 were repeated again with the new instrument. After the overhaul, the manufacturer changed the name from the VSE-355G2 to the VSE-355G3. The overhaul does change the characteristic response of the instrument somewhat, though it is still designed, and is in compliance with, the original specifications.

Results and background discussion relating to the instrument performance in general, and the results from the initial set of tests comprise this Chapter. Chapter 4 presents an analysis of the performance of the VSE-355G2 during the M8.3 Tokachi-Oki earthquake. The results of the tests on the VSE-355G3 are presented in Chapter 5.

The VSE-355G2 instrument, as received in 2001, has been operational in Japan for a number of years. It has been deployed at a number of stations (> 45) as the strong motion sensor in conjunction with an STS-2 (or similar) seismometer in the Freesia Broadband Seismic Network, or F-Net [`www.fnet.bosai.go.jp`]. The VSE-355G, an earlier version of the VSE-355G2, comprises the rest of the strong motion sensors (~ 80 stations in total). The manufacturer also has these and other strong motion velocity-meters deployed in other networks around Japan, which do not freely distribute their data. Data from F-Net shows the ability of the instrument to resolve motions beyond even hundreds of seconds from large teleseismic events. Data from the M8.3 23 September 2003 Tokachi-Oki earthquake off Hokkaido Island is analysed in Chapter 4, which shows how existing instruments in the network also perform poorly when motions reach over $15 cm/s$.

The instrument is currently deployed alongside a Guralp CMG-1T at California Integrated Seismic Network (CISN) station CRP, the Robinson Pit at Caltech. The planned longterm deployment for the instrument is at a new 3-channel CISN Station, within $1/2$ a kilometre of the existing TriNet Station SVD near San Bernadino, in close proximity to the San Andreas Fault.

3.2 A Note on Removing the Instrument Response

The problem of removing the instrument response from data is often ignored if the frequency band of interest is inside a region of flat response of the seismometer. In this case the record in counts (as output by the datalogger) is simply divided by the station gain, giving the ground acceleration (for an accelerometer) or ground velocity (for a typical broadband sensor or strong motion velocity-meter). The station gain, G, is determined from the sensitivity, or gain, of the sensor (G_s), and the gain of the datalogger (G_d). Table 3.1 gives some typical examples.

Sensor	G_s	**Datalogger**	G_d *(cts/Volt)*	**Station Gain, G**
STS-2	$1500V/m/s$	Q4120	$2^{23}/20$	$6,291,456cts/cm/s$
STS-2	$1500V/m/s$	Q730	$2^{23}/16$	$7,864,320cts/cm/s$
STS-1	$2500V/m/s$	Q4120	$2^{23}/20$	$10,485,760cts/cm/s$
STS-1	$2500V/m/s$	Q730	$2^{23}/16$	$13,107,200cts/cm/s$
EpiSensor	$10V/g$	Q4120	$2^{23}/20$	$4,275.5cts/cm/s^2$
EpiSensor	$10V/g$	Q730	$2^{23}/16$	$5,344.4cts/cm/s^2$
FBA-23	$5V/g$	Q4120	$2^{23}/20$	$2,137.8cts/cm/s^2$
FBA-23	$5V/g$	Q730	$2^{23}/16$	$2,672.2cts/cm/s^2$
FBA-23	$5V/g$	K2	$2^{18}/1.5$	$890.7cts/cm/s^2$
VSE-355G2	$10V/m/s$	Q4120	$2^{23}/20$	$41,943.0cts/cm/s$
VSE-355G2	$10V/m/s$	Q730	$2^{23}/16$	$54,428.8cts/cm/s$

Table 3.1: Typical Station Gains

Gains for some other instruments and dataloggers, as well as the frequency ranges for which the sensors have flat response, can be found in Tables 2.1 and 2.2.

Following Kanamori (2002) and Heaton (2003), the equation of motion for a simple seismometer is

$$\ddot{x}(t) + 2\beta\dot{x}(t) + \omega_0^2 x(t) = G\ddot{u}(t) \tag{3.1}$$

where $x(t)$ is the displacement response of the seismometer,

$u(t)$ is the displacement of the ground,

ω_0 is the natural frequency of the seismometer, *radians*,

$\omega_0 = 2\pi f$, f is the natural frequency of the seismometer, *Hz*,

$\beta = 2\zeta\omega_0$, ζ is the damping ratio.

In this case, the frequency response of the instrument to ground motion displacement, I_d, is found by taking the Fourier Transform of Equation 3.1:

$$I_d(\omega) = \frac{X(\omega)}{U(\omega)} = \frac{G\omega^2}{\omega^2 - 2i\beta\omega_0\omega - \omega_0^2} \tag{3.2}$$

or, in terms of frequency, f:

$$I_d(f) = \frac{X(f)}{U(f)} = \frac{Gf^2}{f^2 - 2i\beta f_0 f - f_0^2} \tag{3.3}$$

In this case, the response of the instrument when $f > f_0$ is $I_d(f) \approx G$, so is flat to displacement.

Accelerometer: Similarly, the frequency response of the instrument to ground motion acceleration, I_a, can be expressed as:

$$I_a(f) = \frac{X(f)}{-f^2 U(f)} = \frac{-G}{f^2 - 2i\beta f_0 f - f_0^2} \tag{3.4}$$

In this case, the response of the instrument when $f < f_0$ is $I_d(f) \approx G/f_0^2$, so is flat to acceleration. This is the case of the typical accelerometer. The natural frequency, f_0 of modern accelerometers is usually $50Hz$ or greater. This frequency is above the maximum frequency of interest in many cases in seismology and engineering, and is above the range of interest in this work. Thus, for accelerometer records with frequencies ranging from $50Hz$ to DC (or static offset), simple removal of the station gain is all the instrument correction that is required to obtain acceleration. This is illustrated by Figures 3.5 — 3.10 in the next Section. The ground displacement $u(t)$ as determined from the accelerometer output, $x(t)$, is then:

$$u(t) = \iint x(t)\, dt^2 + At + B \tag{3.5}$$

The initial conditions at time $t = 0$ are $u(0) = \dot{u}(0) = 0$ and $x(0) = \dot{x}(0) = 0$ (both ground and instrument response displacements and velocities are zero), so solving for the 2 constants of integration, $A = B = 0$. This is valid as long as pre-event noise is recorded by the datalogger, and this noise is significantly below the signal strength, a satisfactory assumption for large dynamic range stations in all but the noisiest locations for a wide range of ground motions.

The displacement derived from accelerometers is often unstable at long periods, as a double integration is required. Accelerations at long periods are very small, so the signal to noise is not good. Further, any small errors in the initial condition assumption that velocity and displacement are zero in the sensor timeseries cause large errors in the resultant displacement.

Even worse is the problem of bias in the initial baseline of acceleration:

$$\ddot{u}(t) = x(t) + C + Dt \tag{3.6}$$

where C is a baseline shift, and D is a linear trend.

The constants C and D can be very small, but are also double integrated:

$$u(t) = \iint x(t)\,dt^2 + Dt^3/3 + Ct^2/2 + At + B \tag{3.7}$$

So as time grows, a small baseline error will grow as a cubic or quadratic time-function. A baseline shift even of the order of the count level of the datalogger will cause instability with increasing time.

Strong Motion Velocity Meter: For the typical broadband instrument, such as the STS-2 and the VSE-355G2, the output can be modelled as a simple near critically damped oscillator with differential feedback. Thus the final output $y(t) = \dot{x}(t)$, and Equation 3.1 becomes:

$$\ddot{y}(t) + 2\beta\dot{y}(t) + \omega_0^2 y(t) = G\ddot{u}(t) \tag{3.8}$$

The frequency response of the instrument to ground motion velocity, I_v, is:

$$I_v(f) = \frac{Y(f)}{if U(f)} = \frac{Gf^2}{f^2 - 2i\beta f_0 f - f_0^2} \tag{3.9}$$

So in this case, when $f > f_0$, $I_v(f) \approx G$, so the output is flat to velocity. The natural frequency of broadband instruments ranges from about 56s for the VSE-355EI to 360s for the STS-1 and CMG-1T. So for all signals with frequency content greater than f_0, removal of the instrument gain is all the processing required. (In reality there is also a corner at high frequencies, dependent on the instruments, but as the main interest is in recovering ground displacements, not high frequency accelerations, this is ignored here.) In the near-field of large earthquakes, static offsets are an expected occurrence, which have an infinite, or DC frequency that is important to measure. To recover this part of the waveform requires

removal of the instrument response.

There are many methods to remove the instrument response over the entire frequency range. The most complete method is to remove individual poles and zeros as determined from the sensor transfer function and other decimation / filtering operations performed by the feedback and A/D conversions of the datalogger (Scherbaum, 2001). This is because the manufacturers of the dataloggers include other complexities like anti-alias filters. These poles and zeros are described in the SEED files that are associated with some data-sets. As these are not available for all data-sets, two simple methods are described here. Both assume the sensor operates as a simple single degree of freedom (SDOF) seismometer, which is fully described by a gain factor, damping (ζ) and corner or natural frequency (f_0). For an SDOF, at the corner frequency, there are 2 poles corresponding to a change in slope in the frequency domain of $12dB/octave$. An example for the VSE-355G2, with corner at $93.2s$, is in Figure 3.13.

The two methods are (i) time domain solution (ii) frequency domain solution:

3.2.1 Time Domain Deconvolution: Direct Integration

Re-stating Equation 3.8

$$\ddot{y}(t) + 2\beta\dot{y}(t) + \omega_0^2 y(t) = G\ddot{u}(t) \tag{3.10}$$

Directly integrating, and summing all the constants, gives:

$$\dot{y}(t) + 2\beta y(t) + \omega_0^2 \int y(t)\,dt - A = G\ddot{u}(t) \tag{3.11}$$

Integrating two more times to get ground displacement, $u(t)$:

$$u(t) = \frac{1}{G}\left(\int y(t)\,dt + 2\beta \iint y(t)\,dt^2 + \omega_0^2 \iiint y(t)\,dt^3\right) - At^2/2 - Bt - C \tag{3.12}$$

For the initial conditions at time $t = 0$, assume that the seismometer response ($\dot{y}(0)$, $y(0)$, $\int y(t)\,dt\big|_{t=0}$, $\iint y(t)\,dt^2\big|_{t=0}$ and $\iiint y(t)\,dt^3\big|_{t=0}$) as well as the ground ($\dot{u}(0)$ and $u(0)$)

are at rest at the start of the record. As for the accelerometer, this is physically correct if the record contains pre-event noise, from a station with continuous data recording, or for a triggered station with a pre-trigger buffer. Again, poor signal-to-noise ratio in a record may introduce some error here:

$$u(t) = \frac{1}{G}\left(\int y(t)\,dt + 2\beta \iint y(t)\,dt^2 + \omega_0^2 \iiint y(t)\,dt^3\right) \tag{3.13}$$

Thus, instead of just removing the gain and integrating the output from the broadband instrument, $y(t)$, two extra terms involving the integral and double integral of the seismometer displacement $x(t)$ (recall $y(t) = \dot{x}(t)$) are required to get the deconvolved timeseries. The constants 2β and ω^2, on which the magnitude of these integral terms depend, are dependent on the equivalent SDOF each sensor best approximates, and so are sensor dependent. Table 3.2 shows the instrument constants derived from the appropriate SDOF for the commonly used broadband instruments analysed in this work. For an STS-1, with very long equivalent free period, the constants are small: $2\beta = 0.02468/s$ and $\omega_0^2 = 0.0003046 rad/s^2$ but for the VSE-355EI, with a relatively short free period of $T_0 = 56s$, the constants are an order of magnitude larger. Clearly as the natural frequency becomes higher, the proportion of the deconvolved signal due to the higher-order integrals increases. Nonetheless, even for the STS-1, as the length of the timeseries becomes longer, the deconvolved signal becomes more unstable.

Sensor	T_0 *(s)*	ζ *(%)*	2β $(1/s)$	ω_0^2 (rad/s^2)
VSE-355EI	56	65	0.1459	0.01259
VSE-355G	80	65	0.1021	0.006169
VSE-355G2	80	65	0.1021	0.006169
VSE-355G2 *	93.5	65	0.0836	0.004516
VSE-355G3	80	65	0.1021	0.006169
VSE-355G3 *	105.5	60	0.07147	0.003547
STS-2	120	70.7	0.07404	0.002742
STS-1	360	70.7	0.02468	0.0003046
CMG-1T	360	70.7	0.02468	0.0003046

Table 3.2: Typical broadband sensor constants, based on equivalent SDOF dynamic characteristics. * indicates equivalent SDOF as determined from laboratory testing.

This method is ideal for deconvolving the instrument response from transient signal like a large earthquake, which may record permanent ground displacements. Though the DC offset is not recorded by the sensor, it can be closely approximated as long as the permanent offset occurs within a short time. This is shown in Figure 3.2, which presents 3 components of data from a station 257km from the epicenter of the 25 September 2003 M8.3 Tokachi-Oki earthquake. Nearby GPS data indicates lateral offsets of $10cm$ EW and $-5cm$ NS, and $-2cm$ vertical offset. It is shown using the integration scheme of Equation 3.13, assuming zero initial conditions, gives static offsets similar the GPS. The 'raw' displacement does not include any static offset component.

As the initial velocities, displacements, and integrals of displacements are in fact known (in a band limited sense), these initial conditions could possibly be used to reduce error:

$$A = \dot{y}(0) + 2\beta y(0) + \omega_0^2 \int y(t)\,dt\Big|_{t=0} \tag{3.14}$$

$$B = y(0) + 2\beta \int y(t)\,dt\Big|_{t=0} + \omega_0^2 \iint y(t)\,dt^2\Big|_{t=0} \tag{3.15}$$

$$C = \int y(t)\,dt\Big|_{t=0} + 2\beta \iint y(t)\,dt^2\Big|_{t=0} + \omega_0^2 \iiint y(t)\,dt^3\Big|_{t=0} \tag{3.16}$$

So a more complete solution uses Equation 3.12 where the constants are defined in Equations 3.14, 3.15 and 3.16.

In Figure 3.2 data representing the integration using the initial conditions, Equation 3.12, are also included. This form is observed to lead to instability in 2 of the 3 components, without any improvement on the other component. This is because the sampling rate is $100sps$, and so any small changes in the count level of the first 2 elements of the timeseries lead to non-physically large accelerations once differentiated, and so constant A in Equation 3.12 becomes large. Decimation of the data, and tapering of the initial conditions, caused the resultant displacements to converge to the form from Equation 3.13, without any improvement in the longterm stability of the solution. As this method involves ad-hoc judgments about the character of the initial conditions themselves, henceforth time domain deconvolutions will only use the zero initial condition form of Equation 3.13.

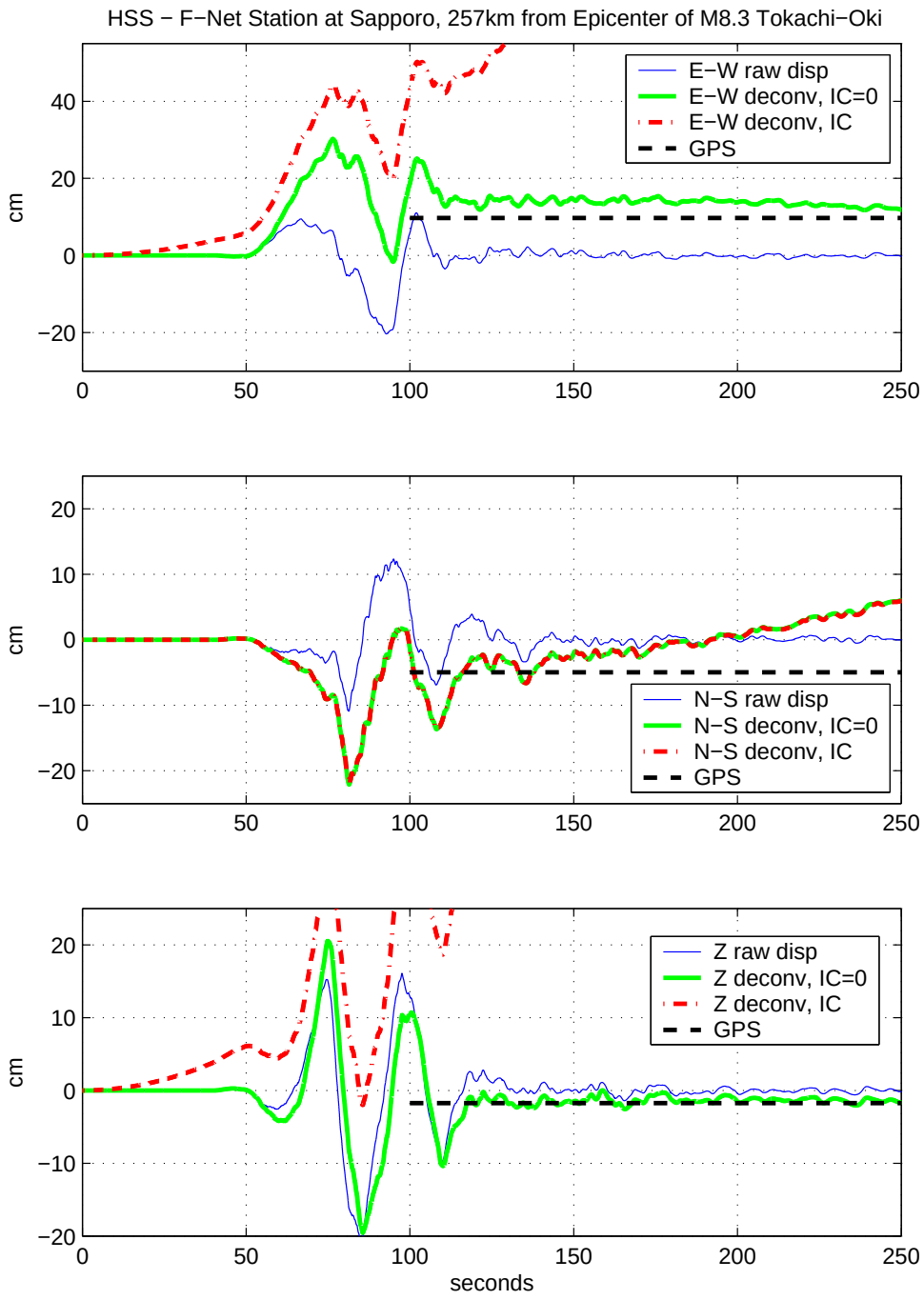

Figure 3.2: Time domain deconvolution of a strong motion record. VSE-355G2 at Station HSS, Sapporo town, 257km from epicenter of M8.3 Tokachi-Oki earthquake. Nearby GPS Station SAPPORO provides expected permanent offsets. 'Raw' displacement, simply gain removed and integrated raw VSE output, is observed to have zero static offset, contrary to the GPS data. Deconvolution using integration scheme of Equation 3.13, with zero IC's, gives best results. Using the initial conditions given in Equation 3.12 leads to instabilities.

3.2.2 Frequency Domain Deconvolution, Division by the Instrument Response

Another way of expressing the response of a single degree of freedom oscillator, $x(t)$, is as a convolution of the ground motion, $u(t)$, and the impulse response of the oscillator, $G(t)$:

$$x(t) = \ddot{u}(t) * G(t) \tag{3.17}$$

The convolution operator in the time-domain is equivalent to multiplication in the frequency domain:

$$X(\omega) = -\omega^2 U(\omega) G(\omega) \tag{3.18}$$

So the ground displacement, $u(t)$, can be found by an inverse FFT of $X(\omega)/[G(\omega).\omega^2]$.

This method is useful for very long timeseries, especially when analysing the noise content of a signal, or teleseismic waves. For strong motions with possible static offsets, it is unsatisfactory. To prevent numerical instabilities in the frequency domain division step, a low frequency cutoff must be chosen. Even if this cutoff is at a very long period, this will remove the static offset. This is illustrated in Figure 3.3.

In Figure 3.4 data is presented from the M6.5 San Simeon earthquake, 22 December 2003, as observed at Caltech CRP on a VSE-355G3. A 15*min* period from the E-W component is analysed, and the data is deconvolved using the two techniques described here. In this instance, though both the deconvolution appear stable in velocity even after 15*mins* (though the time-domain deconvolved velocity has a small static offset), the displacement records exhibit long period wandering, which produces different long period behaviour as seen in the FFT of the signals. High frequency behaviour is also attenuated in the the time domain method, likely because the deconvolution provides displacement at 1*sps*, which does not contain all the high frequency energy of 1*sps* velocity.

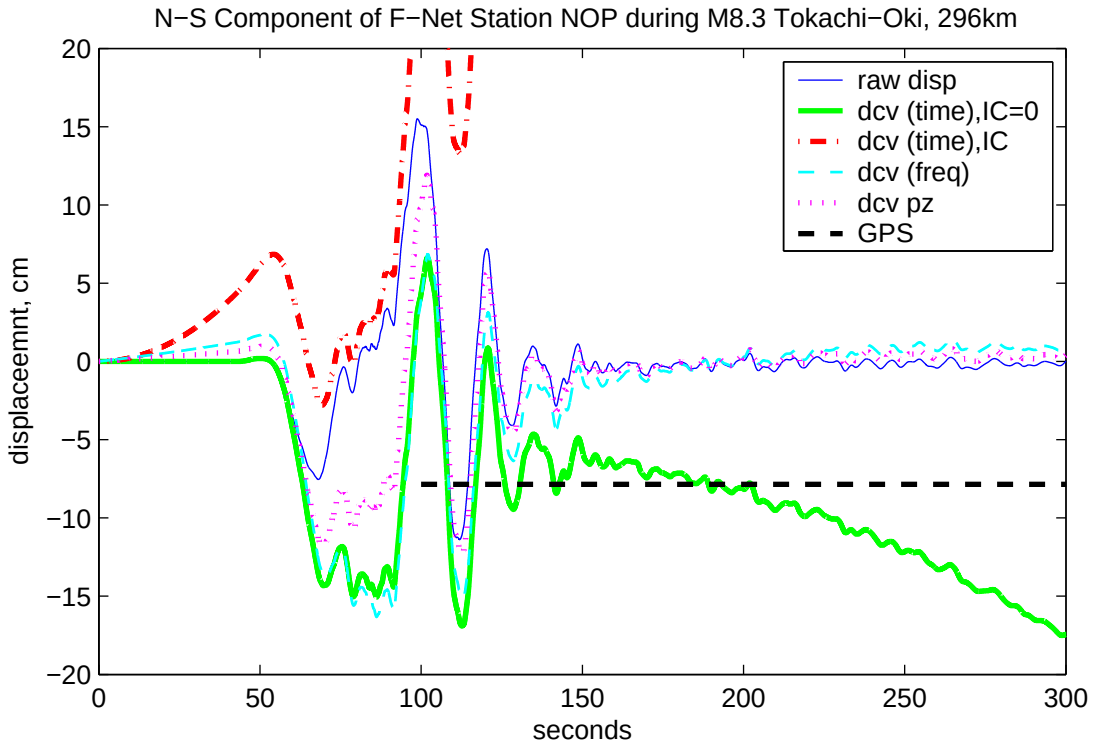

Figure 3.3: Comparison of time and frequency domain deconvolution for a strong motion record. VSE-355G2 at Station NOP, 296km from epicenter of M8.3 Tokachi-Oki earthquake. Nearby GPS Station TAKINOUE provides expected permanent offset of $-8cm$ ($8cm$ south). 'Raw' displacement, simply gain removed and integrated raw VSE output, shown to have zero static offset. Time domain deconvolution using integration scheme of Equation 3.13, with zero IC's, gives best results, with good correlation with GPS, though timeseries becomes instable after $160s$. Using the initial conditions in the time domain (Equation 3.12) leads to instabilities. Frequency domain deconvolutions, using both the SEED pole-zeros and the equivalent SDOF instrument response, approximate the deconvolved time domain response, but both produce no static offset.

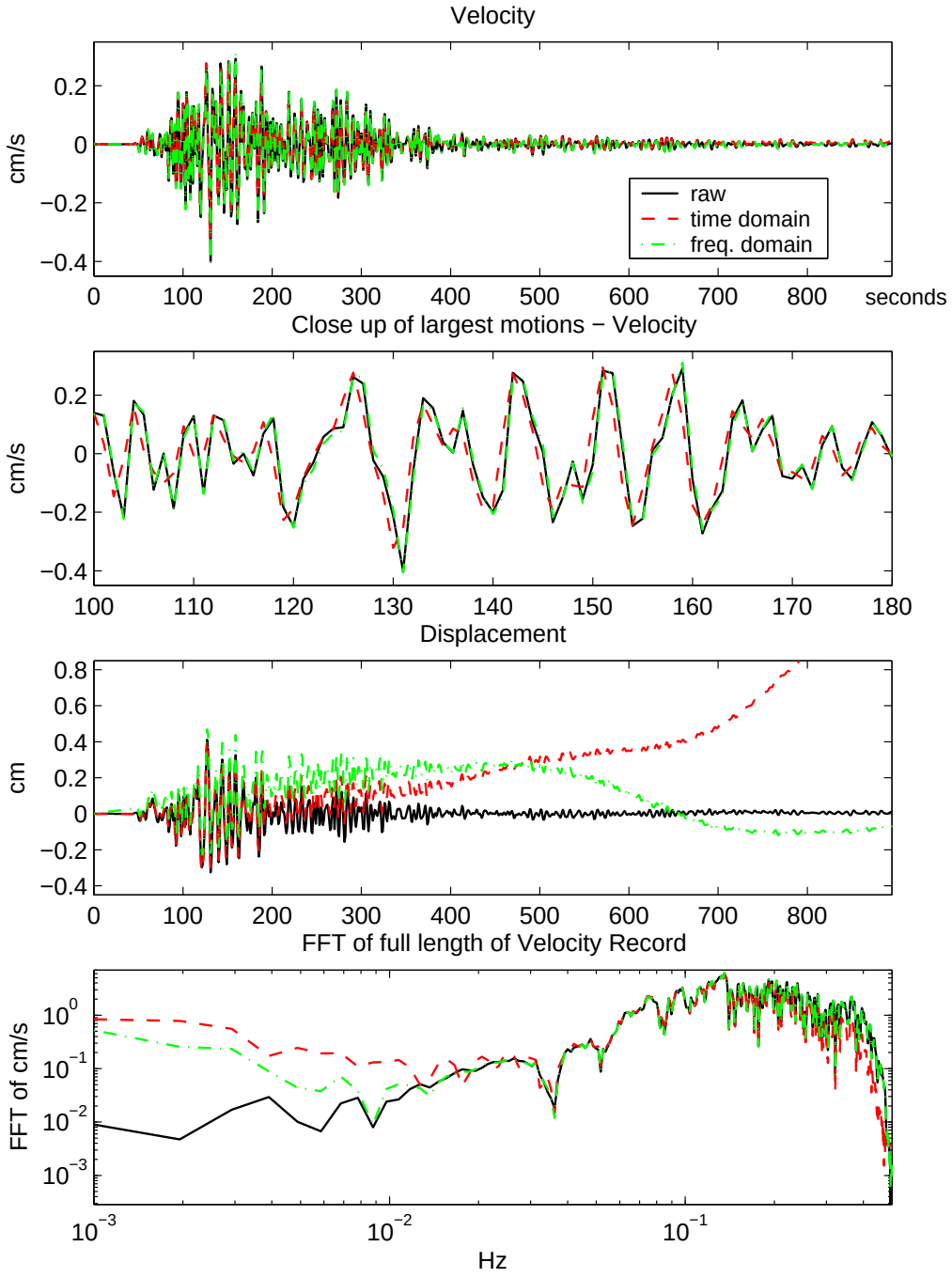

Figure 3.4: Time and frequency domain deconvolution comparison for regional motions: M6.5 San Simeon earthquake, 22 December 2003, at CRP, 323*km* distant. Recorded on a VSE-355G3. 15*min* of data from E-W component, comparing raw output (with pre-event mean and instrument gain removed), with the same output with a time domain deconvolution and a frequency domain deconvolution. Note from the FFT, the time domain deconvolution differs considerably at low frequencies, due to effect of offset at end of timeseries (Figure 3.4), and also has attenuation of high frequencies close to the Nyquist at 0.5*Hz*.

3.3 Synthetic Responses for the VSE-355G2 and FBA-23

In the course of this and the next two Chapters, the response of the various instruments to many different types of input motions is investigated. These inputs are in the form of controlled calibration coil voltages, laboratory tests of simplified, yet typical ground motions expected in large earthquakes, and actual ground motions. In this section, the synthetic output of the VSE-355G2 and the FBA-23, typical and representative of both strong motion velocity sensors, and accelerometers, are produced. It will be demonstrated that in the ideal case, both sensors can reproduce the input motions.

A given ground motion synthetic is generated, then convolved with the equivalent SDOF response that best approximates the seismometer. The FBA-23 SDOF is $f_0 = 50Hz, \zeta = 0.707$, and the VSE-355G2 SDOF is $T_0 = 94s$ and $\zeta = 0.65$. Deconvolutions using time domain integration are provided for the VSE.

Figures 3.5—3.10 present the 3 components of ground motion data, the FBA response, the VSE response, and the deconvolved VSE response, to the idealised ground motions. The FBA response is always multiplied by ω_0^2, following Equation 3.4, to account for the gain correction. The raw output from the accelerometer is shown as the acceleration timeseries for the FBA in all the Figures. It is noted this is nearly identical to the ground motion acceleration input, and deviates only at high frequencies approaching and above the $50Hz$ corner frequency. The VSE output is proportional to input ground velocity over a wide frequency band, but as these sample inputs all contain discontinuities and static offset, there are static frequency components of the motion which are not recorded by the raw VSE output, and thus the VSE output is not similar to the ground input velocity. The instrument response is then deconvolved from all of the raw VSE displacement timeseries by the time-domain direct integration method described by Equation 3.13. For these idealised ground motions, with no background noise, zero initial conditions, no instrument malfunction, and no tilting, the integration scheme produces the exact response.

All synthetics are generated using the SAC2000 'FUNCGEN' command, with $0.005Hz$ sampling frequency (200 samples per second). δ-functions are one time step only. All 'events' begin at $20s$. High amplitude, high frequency vibrations after the 'event' is finished

in the deconvolved VSE acceleration timeseries are not physical.

The synthetic ground motions investigated are —

1. δ-function in acceleration (*Figure 3.5*). This is a typical calibration coil input, and will be seen again in this Chapter, and Chapter 5.

2. step-function in acceleration (*Figure 3.6*). This is another typical calibration coil input, and will be seen again in this Chapter, and Chapter 5. This function is also produced as an error in certain accelerometers during strong, and sometimes even ambient, ground motions (Iwan et al, 1985). This step-function is also the response of an inertial sensor to a sudden tilt of the ground. Both the VSE and the FBA displacements are affected by this phenomenon. As can be seen in the Figure, resultant displacements will very strongly influenced by a small offset in acceleration. In Chapter 1, it is noted that a tilt of only $1\mu rad$ will produce an offset of $5cm$ in displacement after $100s$. In the laboratory experiments, this property of the response is used in calibration of the VSE, independent of the calibration coil — by adjusting the levelling screws, a tilt is imparted to the instrument, causing the response seen by the VSE. Modelling this output constrains the actual SDOF parameters of the VSE, a physical compliment to the calibration coil test.

3. ramp in acceleration, with static offset (*Figure 3.7*). A linear ramp, starting at $20s$ and lasting $5s$, causes a static offset of $0.1cm/s^2$. This is a more physically realistic model for a ground tilt, as it is not instantaneous, though the actual instrument responses are very similar to Figure 3.6, the step function in acceleration. Many examples of this motion will be seen in timeseries from the M8.3 Tokachi-Oki earthquake, in Chapter 4.

4. step in displacement (*Figure 3.8*). A static offset in displacement is modelled. This is a model for instrument response to ground deformation without measurable tilt, such as may occur in lateral spreading, or a tectonic co-seismic slip.

5. ramp in displacement, with static offset (*Figure 3.9*). A linear ramp lasting $5s$ from starting at $20s$ causes a static offset in displacement of $20cm$. This is equivalent to 2 equal and opposite δ-functions, the first positive at $20s$, , the second negative at $25s$, in acceleration. This is a more physically realistic model for a ground deformation, though the actual instrument responses are very similar to Figure 3.8, the step function in acceleration. Examples of this will also be seen in Chapter 4.

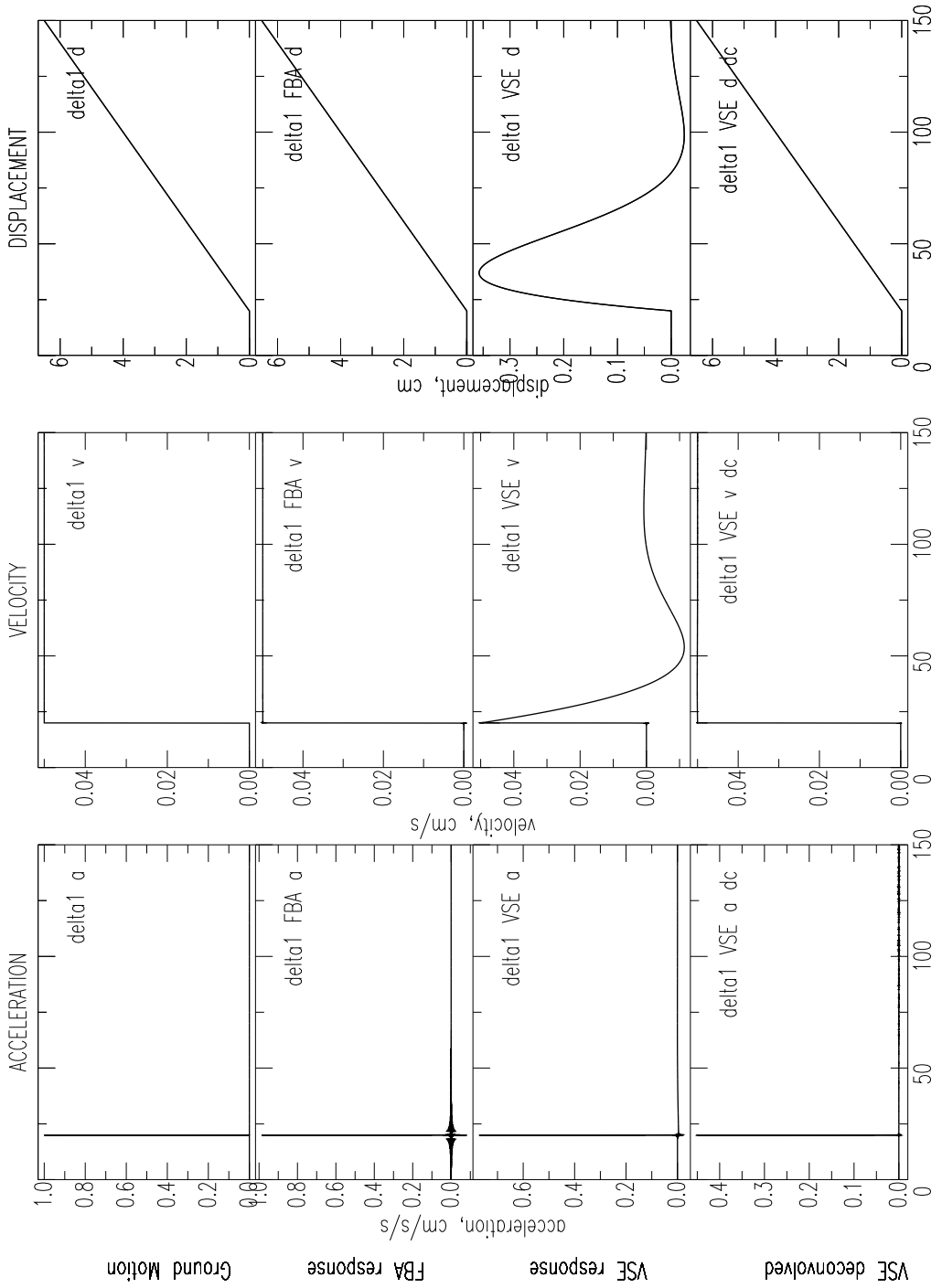

Figure 3.5: Synthetic instrument response to δ-function in acceleration. Typical calibration coil input. Top 3 plots: acceleration, velocity and displacement from input δ-function; 2^{nd}: FBA response; 3^{rd}: VSE response; Bottom: VSE response deconvolved (using direct integration in time domain).

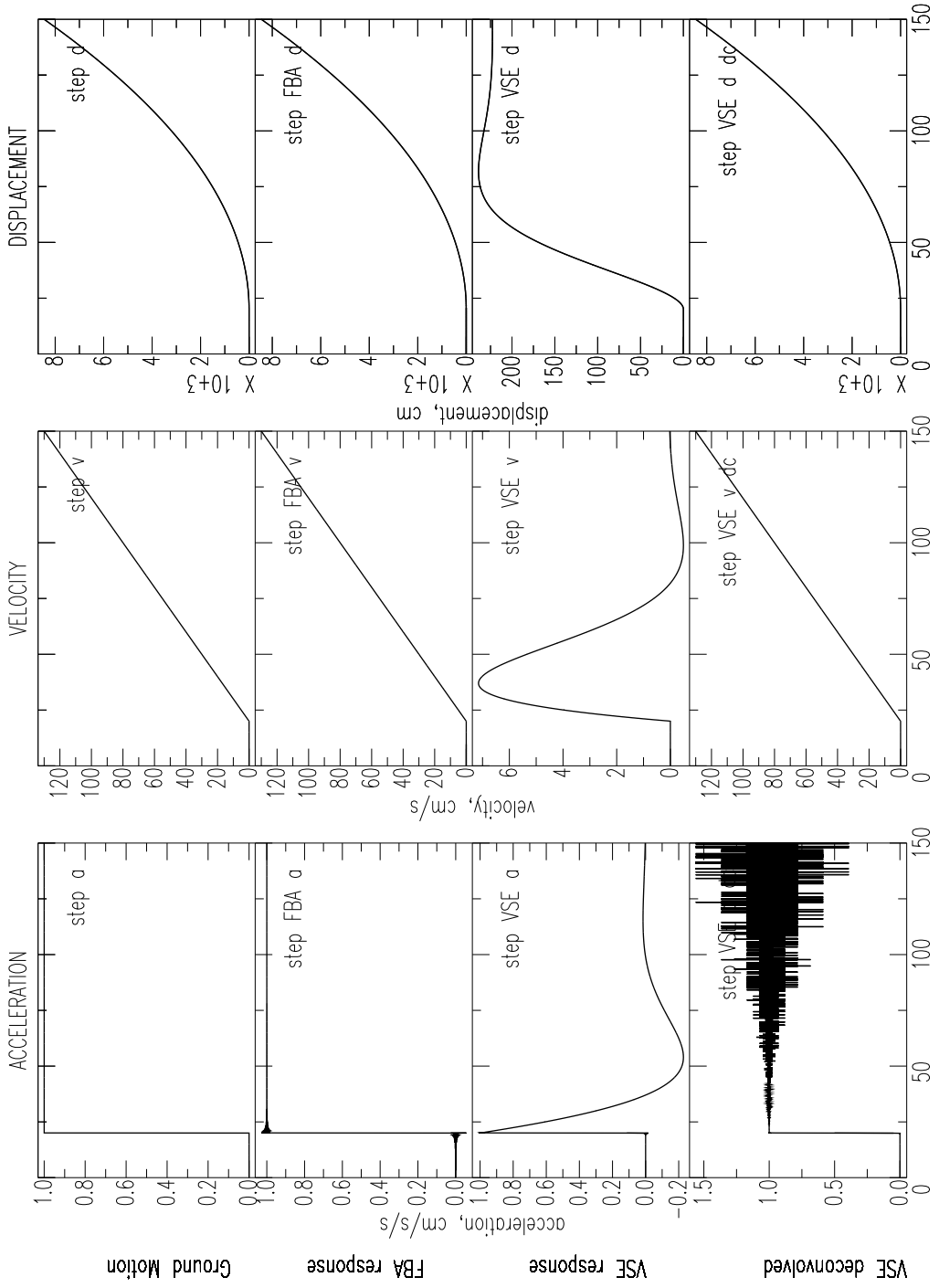

Figure 3.6: Synthetic instrument response to step function in acceleration. Typical calibration coil input, also represents an instantaneous tilting of the ground, or a typical instrument error seen in accelerometers. Top 3 plots: acceleration, velocity and displacement from input step function; 2^{nd}: FBA response; 3^{rd}: VSE response; Bottom: VSE response deconvolved (using direct integration in time domain).

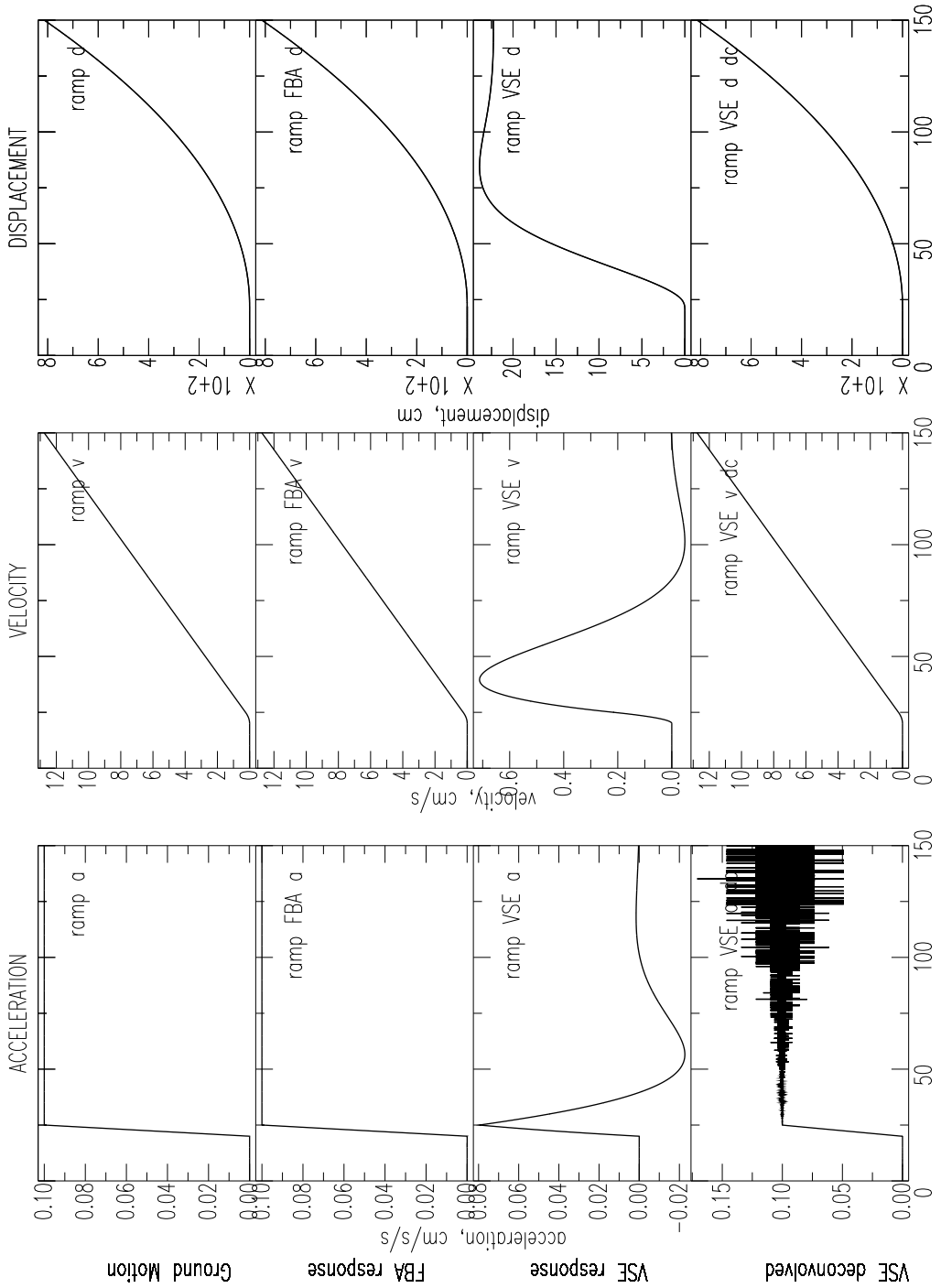

Figure 3.7: Synthetic instrument response to a static offset in acceleration, with 5*s* ramp. instrument response to a physically more realistic ground tilt. Top 3 plots: acceleration, velocity and displacement from input ramp function; 2^{nd}: FBA response; 3^{rd}: VSE response; Bottom: VSE response deconvolved (using direct integration in time domain). Note this acceleration of $0.1 cm/s^2$ is caused by a tilt of only 0.0058^o ($0.000102 rad$), yet causes over 8*m* displacement after 130*s*.

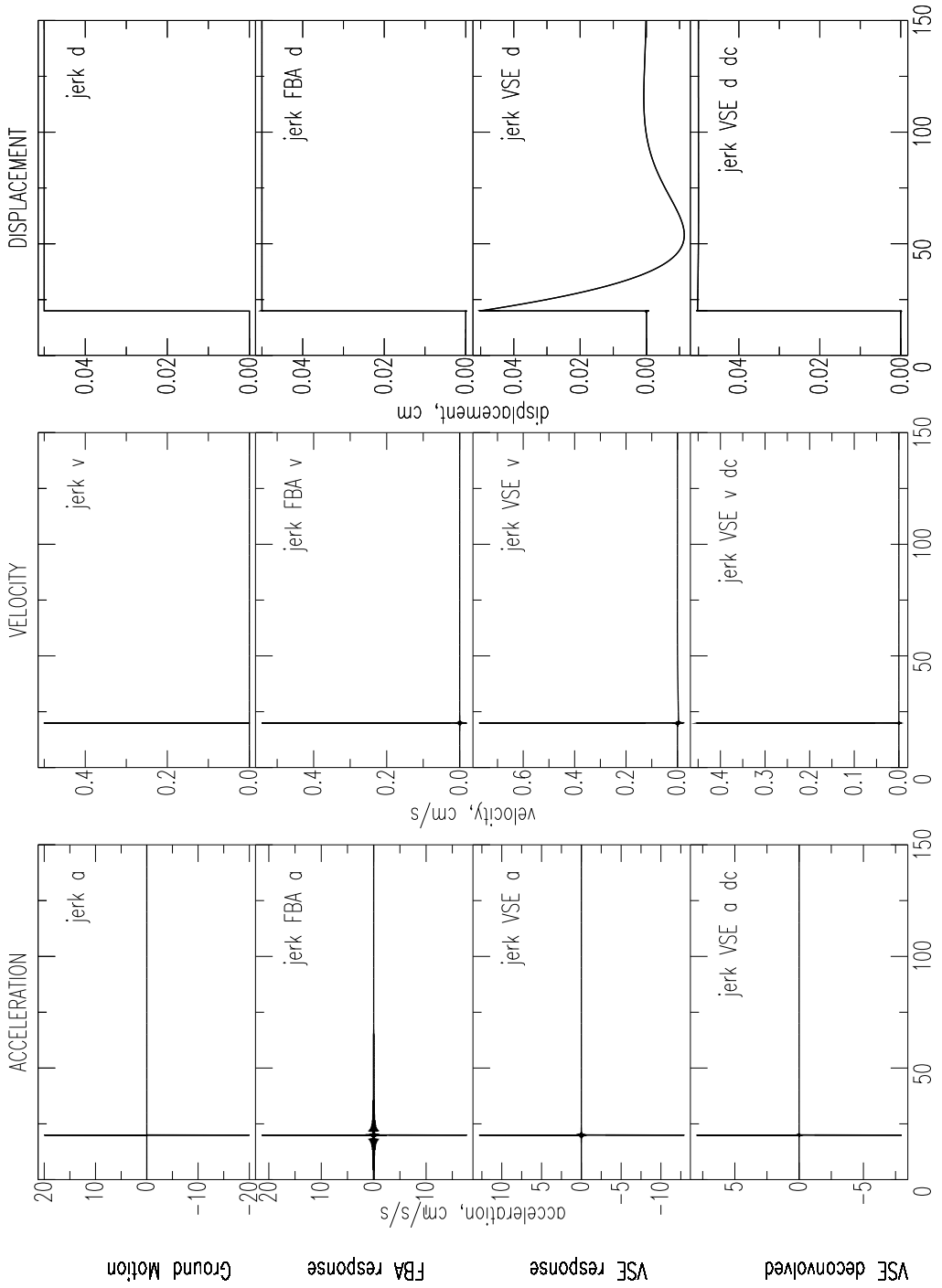

Figure 3.8: Synthetic instrument response to step function in displacement (a 'jerk' in acceleration). Response to a static offset in ground motions. Top 3 plots: acceleration, velocity and displacement from input jerk-function; 2^{nd}: FBA response; 3^{rd}: VSE response; Bottom: VSE response deconvolved (using direct integration in time domain).

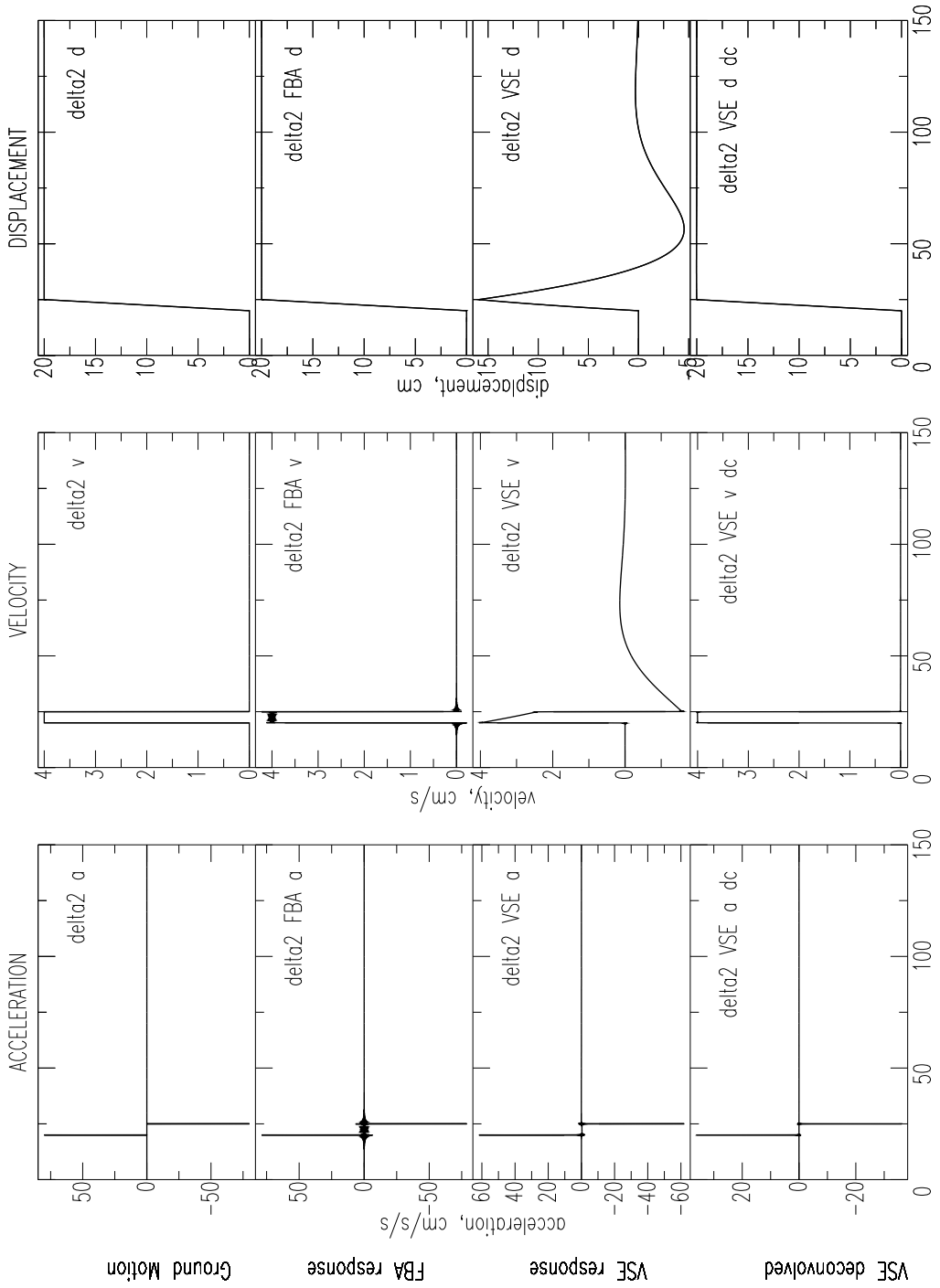

Figure 3.9: Synthetic instrument response to static offset in displacement, with ramp. Physically more realistic than a step in displacement. Top 3 plots: acceleration, velocity and displacement from input function; 2^{nd}: FBA response; 3^{rd}: VSE response; Bottom: VSE response deconvolved (using direct integration in time domain).

6. VSE cart test: displacement of 8m in 10s (*Figure 3.10*). This models a 'perfect' run of the cart test described in this Chapter and Chapter 5. A ramp in velocity from $20s - 22s$ produces a velocity of $1cm/s$, maintained for $8s$ before returning to zero velocity at $30s$, producing a permanent displacement of $8m$ over the $10s$. This produces a simple raw VSE output, but this shape is never recovered in practice, primarily due to tilting over the floor during the displacement.

3.4 Instrument Design and Specifications

The Operation Manual (Tokyo Sokushin Co. Ltd., 2002b) supplied with the instrument reports the following instrument specifications for the VSE-355G2:

$$\begin{aligned}
\textit{frequency range:} &\quad 0.012 \leftrightarrow 70Hz (0.0143 \leftrightarrow 83.3secs) \\
\textit{clip levels:} &\quad \pm 200kine (\pm 2m/s) \\
&\quad \pm 2000gal (\pm 2g, \pm 19.8m/s^2) \\
\textit{sensitivity:} &\quad 100mV/kine, 50mV/kine^2). \\
\textit{maximum output voltage:} &\quad \pm 20V \\
\textit{resolution:} &\quad 10^{-6} gal
\end{aligned}$$

The design of the instrument is described in a document sent through personal communication with the manufacturer (Tokyo Sokushin Co. Ltd., 2002a). The instrument measures velocity as the standard output. The mechanical pendulum is described as having a natural frequency of $3Hz$ and is heavily over-damped, about 10000% of critical, and so the suspension displacement is proportional to ground velocity over a wide frequency band about this free period, from $70Hz$ to $83s$.

The feedback loop is proportional to the displacement of the pendulum, and so the instrument output measures ground velocity within this frequency band. At periods beyond $83s$, the expected response drop-off would be $3dB/octave$, but in earlier models of the instrument, this was found to lead to instabilities with DC offsets, and the VSE-355G2 (and G3) includes an integration circuit in the feedback loop to provide signal drop-off at $6dB/octave$. With such a corner, the instrument may be modeled at long periods as an

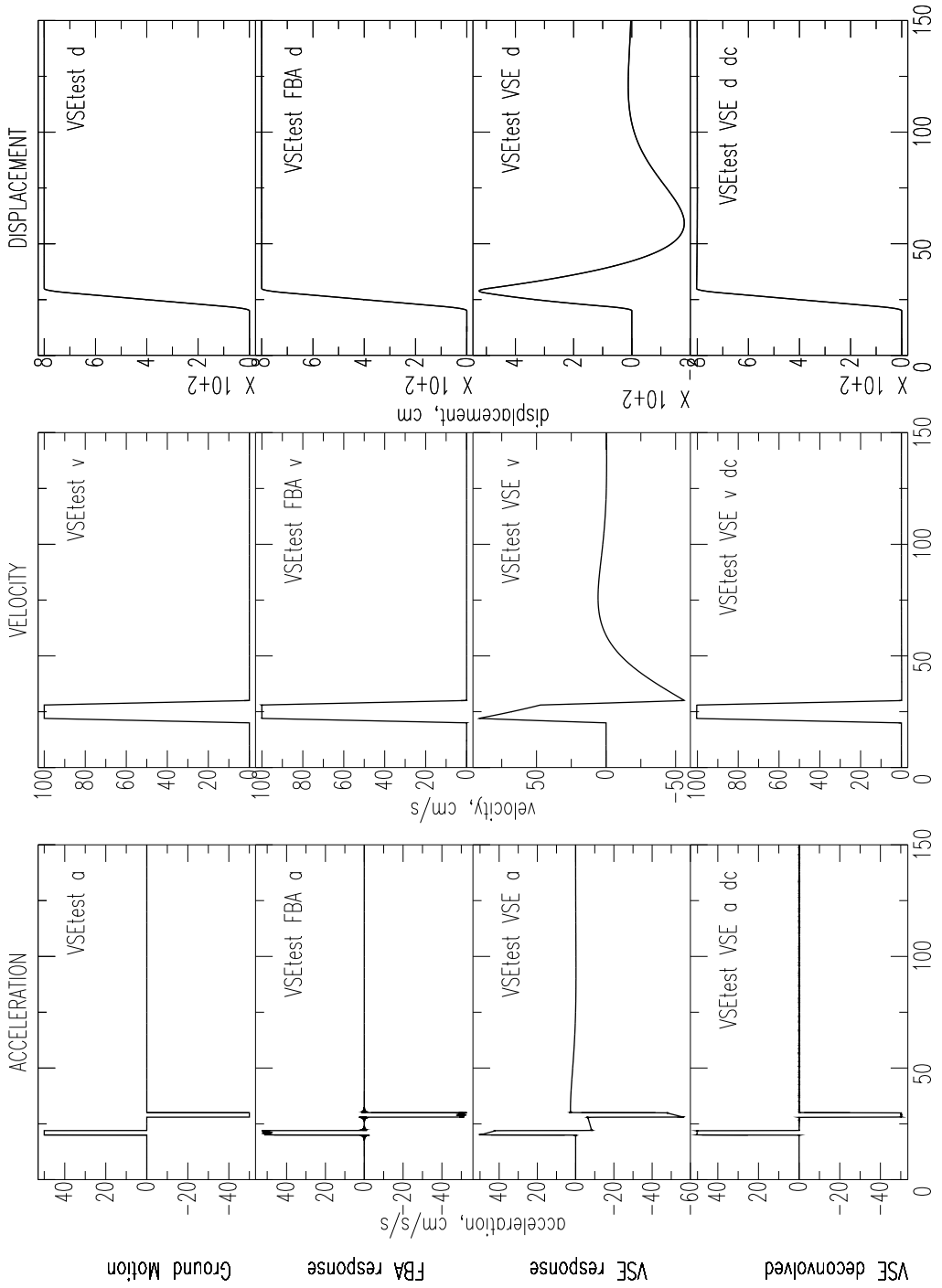

Figure 3.10: Synthetic instrument response to idealised cart test, where a displacement of $8m$ is reached over $10s$ with a constant velocity of $1m/s$. Top 3 plots: acceleration, velocity and displacement from input function; 2^{nd}: FBA response; 3^{rd}: VSE response; Bottom: VSE response deconvolved (using direct integration in time domain).

SDOF with velocity output. This is a similar response to an STS-1 or STS-2. This modeling approximation allows us to determine an equivalent SDOF response for the instrument which is useful in measuring the true long period motion of the ground, deconvolved from the instrument response.

A note on the installation: the horizontal channels had to be interchanged on the VSE-355G2 (and G3, as only components internal to the casing were modified), so N-S output channels actually represent the E-W motion, and vice-versa. This is due to the definition of polarity for the VSE-355G2, which required a clockwise rotation of 90 degrees in order to agree with the standard alignment of other instruments (such as the STS-2 or EpiSensor). In fact this unorthodox polarity is characteristic of all Tokyo-Sokushin products, which is shown in Chapter 4 to cause confusion within seismic networks in Japan - when these instruments are used to investigate static displacements, the results often end up being 90^o or 180^o out of phase with nearby records.

Also, the operational manual supplied by the manufacturer was unclear and insufficient for correct and efficient installation — at least for the English version. Clarification, and indeed correction of the manual required some correspondence with the company and its representatives. Another major source of difficulty involved resolving the pin connections for use with Quanterra dataloggers.

The operation manual does not explicitly state the effective natural frequency of the instrument, nor the effective instrument damping. Both are useful, though not essential, in removing the instrument response in order to recover actual displacements, and correct long period motions beyond about 90*s*. One could also use the published Transfer Function, though this is shown to differ from the observed response of the VSE-355G2 instrument, as well as for the modified G3 version.

3.5 Test Data and Analysis

3.5.1 Instrument Sensitivity

The sensitivity of the instrument was determined by comparing data from the VSE-355G2 instrument with data from a Streckeisen STS-2 located on the same pier and recording onto the same $144dB$ Quanterra digitiser.

The instruments were located at Kresge Laboratory, recording onto a Q4128 digitiser, operating as test station PASB in the SCSN. The signals compared were from a small local earthquake, as well as the background noise. The local earthquake was the 16 March 2002 M4.6 event $35.5km$ WNW of Santa Barbara Island, at a distance of $145km$ from PASB. Noise data was taken from a 3hour segment beginning at 08:00 UTC on 16 March 2002.

Records of the raw counts (with mean removed) were band-passed between 0.5–1s for the local earthquake records, and between 5–10s for the noise (measuring the microseisms). In the band-passes described, the time-series were almost identical after multiplication of the VSE records by a scalar constant. For both noise and small earthquake signals, this constant was found to be ~ 150 E-W, ~ 141 N-S and ~ 143 for the Z component. The published STS-2 sensitivity of $15V/cm/s$ is assumed to be correct (quality control for this instrument is generally very high, within 1% of the manufacturer's published sensitivity of $15V/cm/s$). The published VSE-355G2 sensitivity is $100mV/cm/s$, so our expected constant should be 150. For the 3 components there is 0% error E-W, 6% error N-S and 4.5% error in the Vertical component.

Figure 3.11 shows the broadband FFT's of the M4.6 event records for the 3 components, scaled by the above values. The only other processing of the raw counts is to remove the mean of the data.

The Q4128 datalogger gain, G_d, is $40V/2^{24}cts$, equivalent to $419430cts/Volt$. If the Operation Manual sensitivity of $100mV/cm/s$ for the VSE-355G2 sensitivity is assumed to be correct, then the nominal gain is $41,943cts/cm/s$. Similarly, for the STS-2, the sensitivity is $15V/cm/s$, and thus the nominal gain is $6,291,450cts/cm/s$. Subsequent plots in cm/s have been scaled by these gain factors. These values are summarised in Table 3.1.

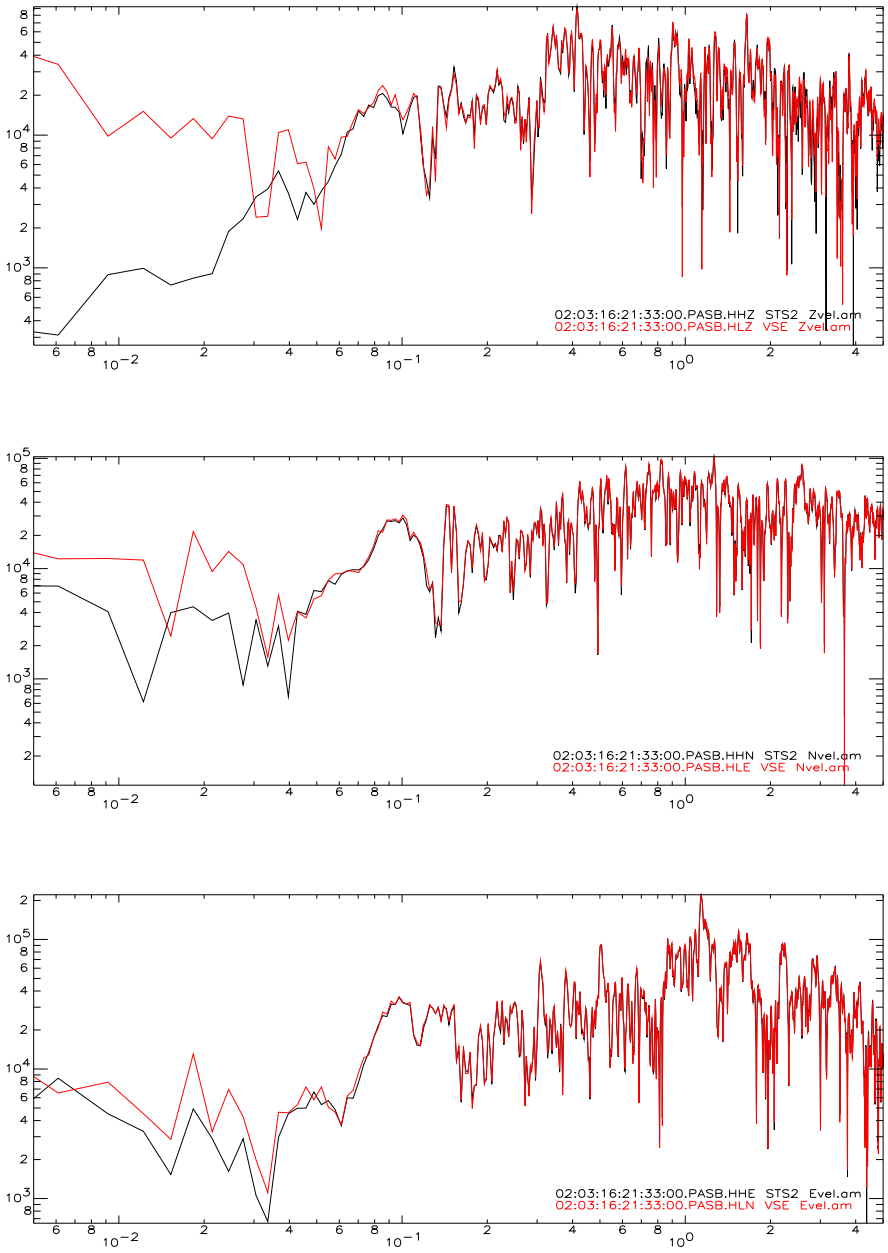

Figure 3.11: Sensitivity scaling: FFT of data recorded at PASB on 03/16/02 for M4.6 event at 145km. Y-axis is FFT of raw counts, X-axis frequency in Hz. Lighter shaded lines are the VSE output in counts multiplied by a sensitivity factor. *(see text on Instrument Sensitivity)*, black is STS-2 output in counts. Top plot is Z, middle is N-S, bottom is E-W component.

3.5.2 Instrument Response

The calibration coil internal to the instrument is used to estimate the equivalent SDOF instrument response at long period. In this test a known current function from a signal generator is applied over the calibration coil, which applies the same function in acceleration to each of the 3 sensors individually.

The SDOF mass displacement response, $G(t)$, to a δ-function in acceleration is:

$$G(t) = \frac{H(t-t_0)}{\omega_d} e^{-\beta(t-t_0)} \sin \omega_d (t-t_0) \tag{3.19}$$

(*Gt* in this case is the same function as described in Equation 3.17 — This solution is observed as the displacement response of the VSE in Figure 3.5.)

$H(t-t_0) =$ *amplitude of a step function at time* t_0 $[\dot{H}(t-t_0) = \delta(t-t_0)]$;

$H = 0$ *if* $t < t_0, H = H$ *if* $t \geq t_0$

where:

$\omega_0 =$ *natural frequency*

$\beta =$ $\omega_0 \zeta$, $\zeta =$ *damping ratio*

$\omega_d =$ *damped natural frequency* $= \omega_0 \sqrt{1-\zeta^2}$

But as the VSE has a velocity transducer, the output is in velocity. So, the VSE response, $V(t)$ to a δ-function in acceleration is:

$$V(t) = \frac{dG(t)}{dt} = \frac{H(t-t_0)}{\omega_d} [-\beta e^{-\beta(t-t_0)} \sin \omega_d (t-t_0) + \omega_d e^{-\beta(t-t_0)} \cos \omega_d (t-t_0)] \tag{3.20}$$

(This solution is observed as the velocity response of the VSE in Figure 3.5.)

The integral of a δ-function is a step function (which is often the applied current function to a calibration test), the SDOF displacement solution, $D(T)$, to a step input in acceleration is:

$$D(t) = \int G(t)dt = \frac{H(t-t_0)}{\omega_0^2} [1 - e^{-\beta(t-t_0)} \cos \omega_d (t-t_0) - \frac{\beta e^{-\beta(t-t_0)}}{\omega_d} \sin \omega_d (t-t_0)] \tag{3.21}$$

(This solution is observed as the displacement response of the VSE in Figure 3.6.)

So the VSE response to a step function in acceleration is simply $\frac{dD(t)}{dt} = \frac{d[\int G(t)dt]}{dt} = G(t)$, given by Equation 3.19. (This solution is observed as the velocity response of the VSE in Figure 3.6.)

In this case a signal generator was used to apply a step function in Voltage to the calibration, equivalent to a step in acceleration. Thus the raw velocity proportional output should match the shape described by Equation 3.19. The equivalent SDOF response of each of the 3 sensors was estimated by graphically finding the best fit to the VSE-355G2 calibration test output, varying the amplitude and starting time of the step function $H(t–t_0)$, the natural period, $T_0(= 2\pi/\omega_0)$ and damping ζ. The results are shown in Figure 3.12. The top 3 sub-plots of the Figure show the velocity output from the instrument, with the mean of the pre-event noise (in this case the event is the first step) and the gain of $41943 cts/cm/s$ removed from the records. The model is the best fit solution to Eqn. 3.19. The bottom 3 sub-plots are the integral of the velocity output, and the model is the fit to Eqn. 3.21 using the same variables. Note there is permanent offset to this plot, which is inversely proportional to the natural frequency, ω_0.

The natural period of the instrument was found to be $93.2s$ in the East-West component, $93.0s$ in the North-South component for the horizontal sensors, and $94.6s$ for the vertical component. The damping was estimated to be at 65% of critical damping for each of the 3 sensors.

Most subsequent VSE-355G2 data presented in the Chapter now not only will have the gain factor removed, but also have this instrument response removed (using a frequency domain deconvolution).

A comparison of this equivalent instrument response with the published instrument transfer function (Tokyo Sokushin Co. Ltd., 2002a) is in Figure 3.13. There is close correlation between the two, though the actual corner period is longer for the transfer function. The transfer function is:

$$F(i\omega) = \frac{-35 * 10^3}{\left(7007 - \frac{19.46}{\omega^2}\right) + i\left(\omega - \frac{504.4}{\omega}\right)} \qquad [V/m/s] \tag{3.22}$$

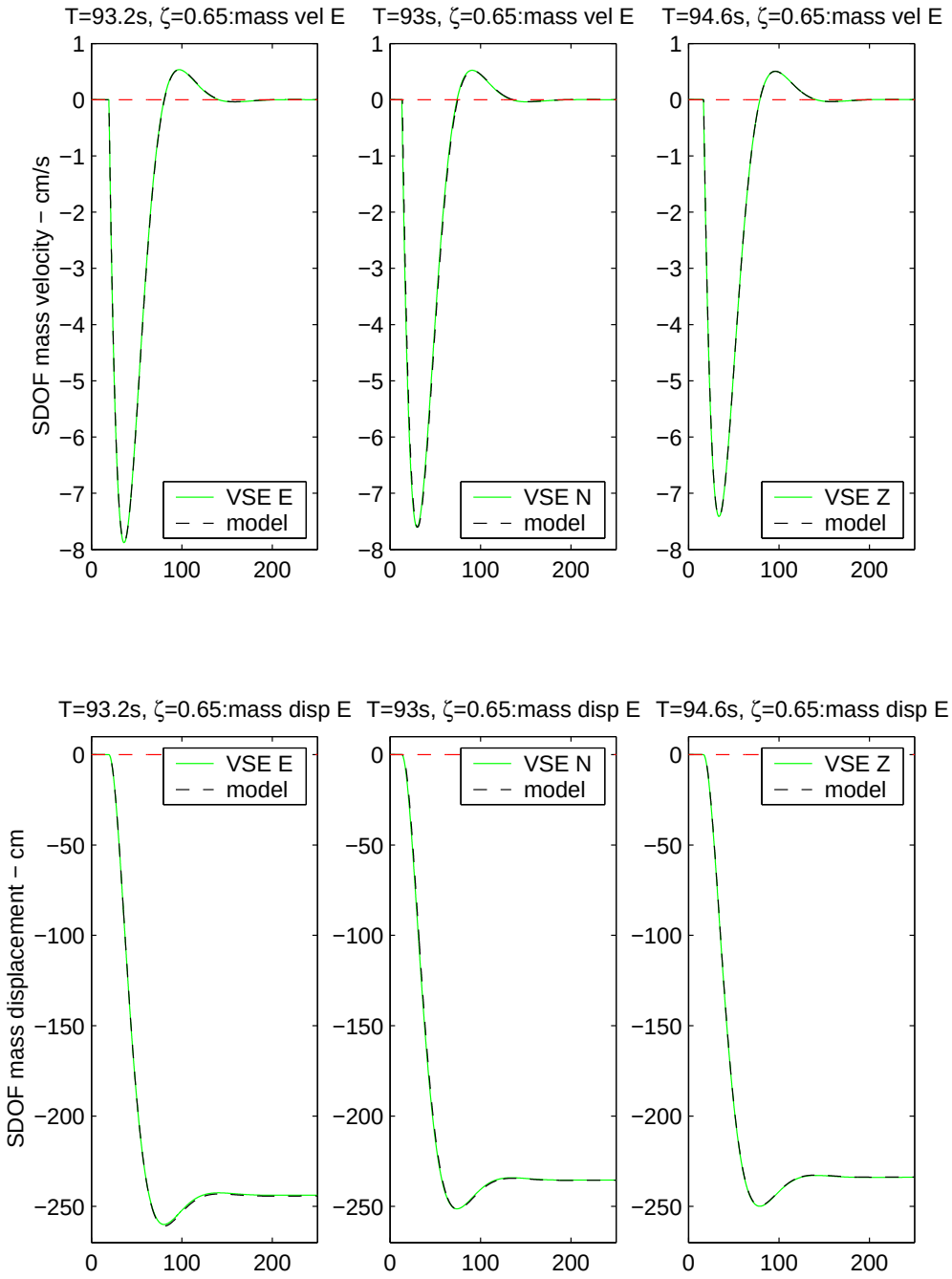

Figure 3.12: Calibration coil response for the VSE-355G2.

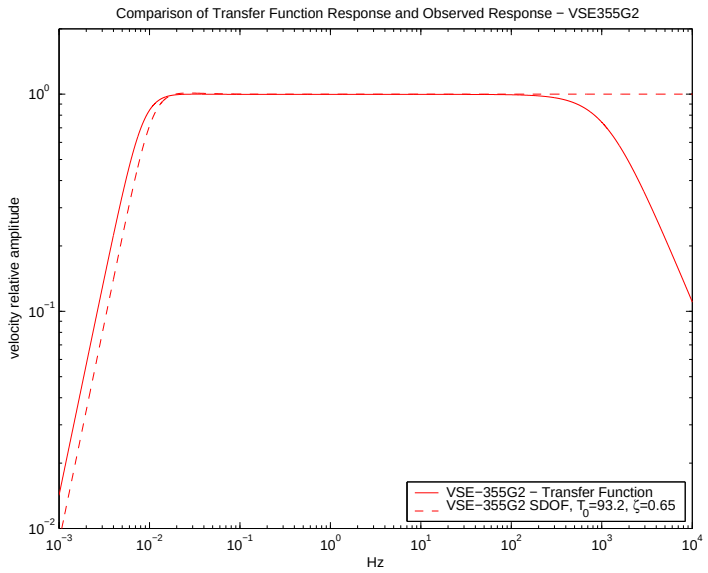

Figure 3.13: Comparison of the theoretical response from the Transfer Function and the observed calibration coil test result.

3.5.3 Instrument Resolution

Figures 3.14, 3.15 and 3.16 show FFT's of ground velocity from co-located VSE-355G2 and STS-2 instruments at PASB, and nearby FBA-23 and STS-1 sensors at PAS, over a 3hour period of noise for the 3 components. The instrument responses have been removed from the records after a bandpass from $0.00125Hz$ — $0.5Hz$ ($2s$ — $800s$).

At periods below $10s$ the VSE-355G2 instrument performs similarly to the STS-1 and STS-2, but above $10s$ through to the instrument corner near $93s$, and out towards $1000s$ the instrument is not capable of resolving the background noise at PAS. At these frequencies, instrument noise saturates the signal at about an order of magnitude higher than the noise at PAS. FBA noise above $10s$ is about 2 orders of magnitude higher than that of the VSE.

In fact in Figure 3.14 the instrument noise of the accelerometer saturates the signal completely over the frequency band here, with no background noise being measured. This noise level is similar for the N-S and Z components, so this instrument data is omitted from Figures 3.15 and 3.16 to remove clutter.

At high frequencies from $1Hz$ — $50Hz$ (see Figure 3.17), a similar lack of resolution for the accelerometer is observed, while the VSE-355G2 instrument noise appears slightly

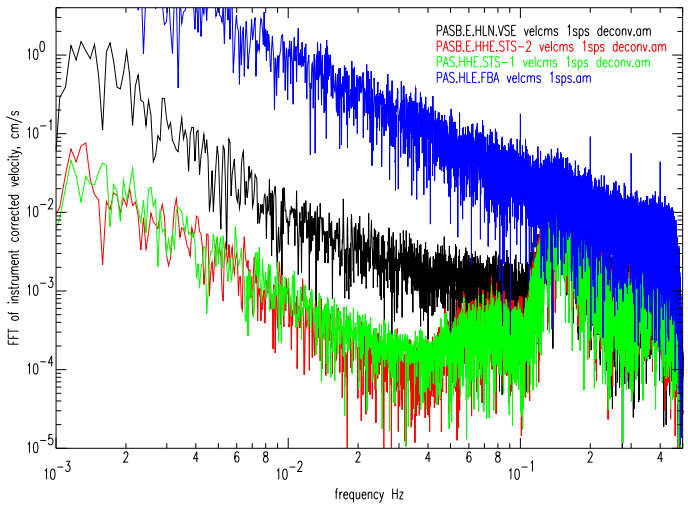

Figure 3.14: Resolution of E-W component. FFT of noise data. The dark trace in the middle is the VSE (PASB), the darker bottom trace is the STS-2 (PASB), and the lighter bottom trace is the STS-1 (PAS). The dark top trace is the FBA-23 (PAS). Instrument response deconvolved.

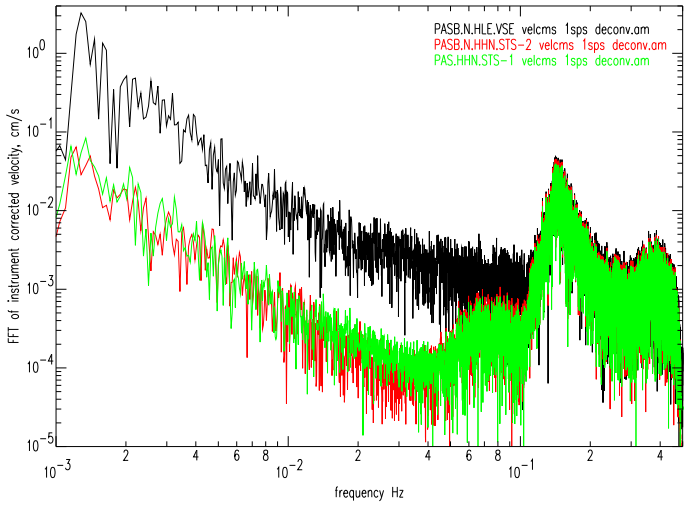

Figure 3.15: Resolution of N-S component — as Figure 3.14.

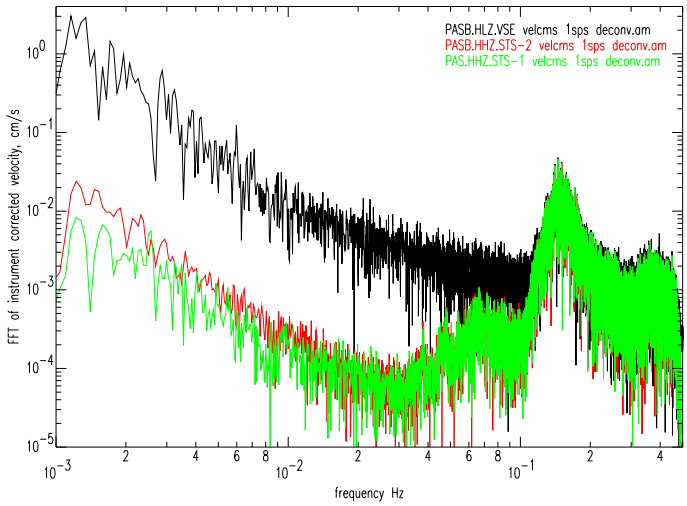

Figure 3.16: Resolution of Z component — as Figure 3.14.

above the background station noise, as seen from the STS-2. The STS-1 response is not sensitive to frequencies above $10Hz$. From Figure 2.10, the FBA is expected to have similar sensitivity to the VSE at about $1Hz$. In Figure 3.17, this is clearly not the case. This is explained by the fact the FBA is not operating well below the $144dB$ assumed in Figure 2.10.

Figure 2.10 presents a frequency-amplitude plot in terms of octave wide band-passes in acceleration. Data from a range of ground motions were plotted along with the band-pass adjusted recording limits of an FBA-23, an STS-2 and a hypothetical strong motion velocity recording device, with limits of $5m/s$ / $5g$ and corner at $120s$ (similar to the VSE-355G2). Figure 3.18 re-presents much of this plot, and includes the additional data presented in this report.

In this Figure 3.18, ground motions recorded on-scale by the FBA-23 lie between the solid red lines. On-scale motions recorded by the hypothetical low-gain broadband seismometer (again similar to the VSE-355G2 analysed in this report) lie between the solid blue lines. The dashed blue lines give the dynamic range of the STS-2. Noise levels are the USGS High and Low Noise Models (Peterson, 1993). The (deconvolved) data discussed in this report are represented by the lines labeled A-D. The dashed red line A is the FBA-23 noise. The dotted-dashed blue line B is the VSE-355G2 noise. The dashed green line C is

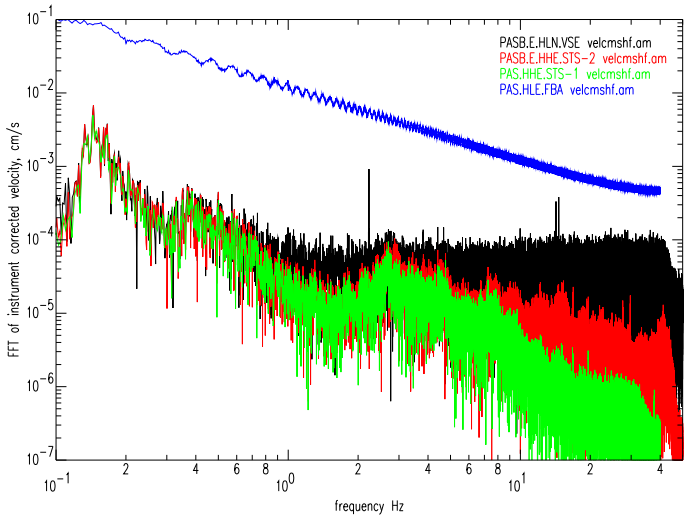

Figure 3.17: Typical resolution of instrument at high-frequency — as Figure 3.14.

the STS-2 noise. The dotted green line D is the STS-1. All this data is from the 3hour time window recorded at Kresge Laboratory. The solid brown line E represents the band-passes from the M7.8 14 November 2001 Qinghai-Xinjiang event recorded by a VSE-355G2 at 38^o in Japan (discussed in Section 3.6).

The VSE-355G2 noise (line B) follows the proposed instrument resolution of the $5m/s$ instrument closely, which indicates the instrument is performing close to the published sensitivities, which corresponds to a dynamic range near $144dB$ if the expected clip was reached (with the clip at $15cm/s$, the instrument is recording at less than $120dB$ dynamic range). The noise attributed to the instrument may also be due to datalogger noise, as this is also at the limit of resolution for the datalogger. At very high frequencies, from $10Hz$ to $50Hz$, the STS-2 records a noise level just below the expected VSE minimum and the actual VSE response is just above this minimum, which reflects the observations in Figure 3.17.

The resolution of the VSE-355G2 is only slightly above the station noise as recorded by the STS-2 and STS-1 (lines C and D, respectively) from $10Hz$ out to about $10s$, and is exactly equal for the microseisms. At longer periods, once again the VSE-355G2 is not able to resolve motions at the noise level of this station.

The FBA-23 represented by line A is not performing at $144dB$ — it is a full order of

magnitude above the expected noise level at $10Hz$, and about a factor of 2 above this level from $10s$ to $1000s$.

Figure 3.19 is a reproduction of a segment of Figure 3.18, and contains only the experimental noise floors from the FBA-23, the VSE-355G2 and the STS-2, along with some Earth signals. The noise from the FBA-23 is nearly 3 orders of magnitude higher ($\sim 60dB$) than the VSE-355G2 at $100s$, and nearly 2 orders higher ($\sim 40dB$) at $10s$. They are equivalent at about $10Hz$. Thus, between $10Hz$ and $1000s$, the region between the dotted red and the dashed-dotted blue lines represents areas of amplitude-frequency space which are recorded by the VSE-355G2 and not by the FBA-23. There is a large portion of teleseismic signals, and also some energy from small local events in this region. This clearly shows the benefit of the VSE-355G2 instrument.

As an aside, it was noted that the dynamic range of the accelerometer at this station was not at its expected level near $140dB$. This warranted a further investigation into the long period response of a collection of accelerometer / datalogger configurations in TriNet/CISN, to determine whether or not this was an isolated occurrence. Three different $3hour$ blocks of noise data were collected for each station, and after octave wide band-passing of the data, the averages are shown in Figure 3.20. this is the same figure as Figure 2.5, where it was used to estimate the average FBA-23 noise floor. PAS / PASB data shown in Figure 3.19 is again reproduced, as the thick dotted lines. Data from stations with an FBA-23 are in black, stations with an EpiSensor are in maroon. This station sample indicates the FBA-23 dynamic range is generally less than $135dB$, whilst the EpiSensor dynamic range is generally closer to $144dB$, and as the published EpiSensor dynamic range is $155dB$, the noise floor may be from the datalogger and not the instrument. The EpiSensor is a better alternative to the FBA-23 for observing teleseismic motions, though it is still significantly noisier than the VSE.

3.5.4 Instrument Clipping

During the VSE-355G2 calibration test it was observed that the applied current would saturate the instrument response at about $600,000cts$, equivalent to $1.43V$ or $14.3cm/s$.

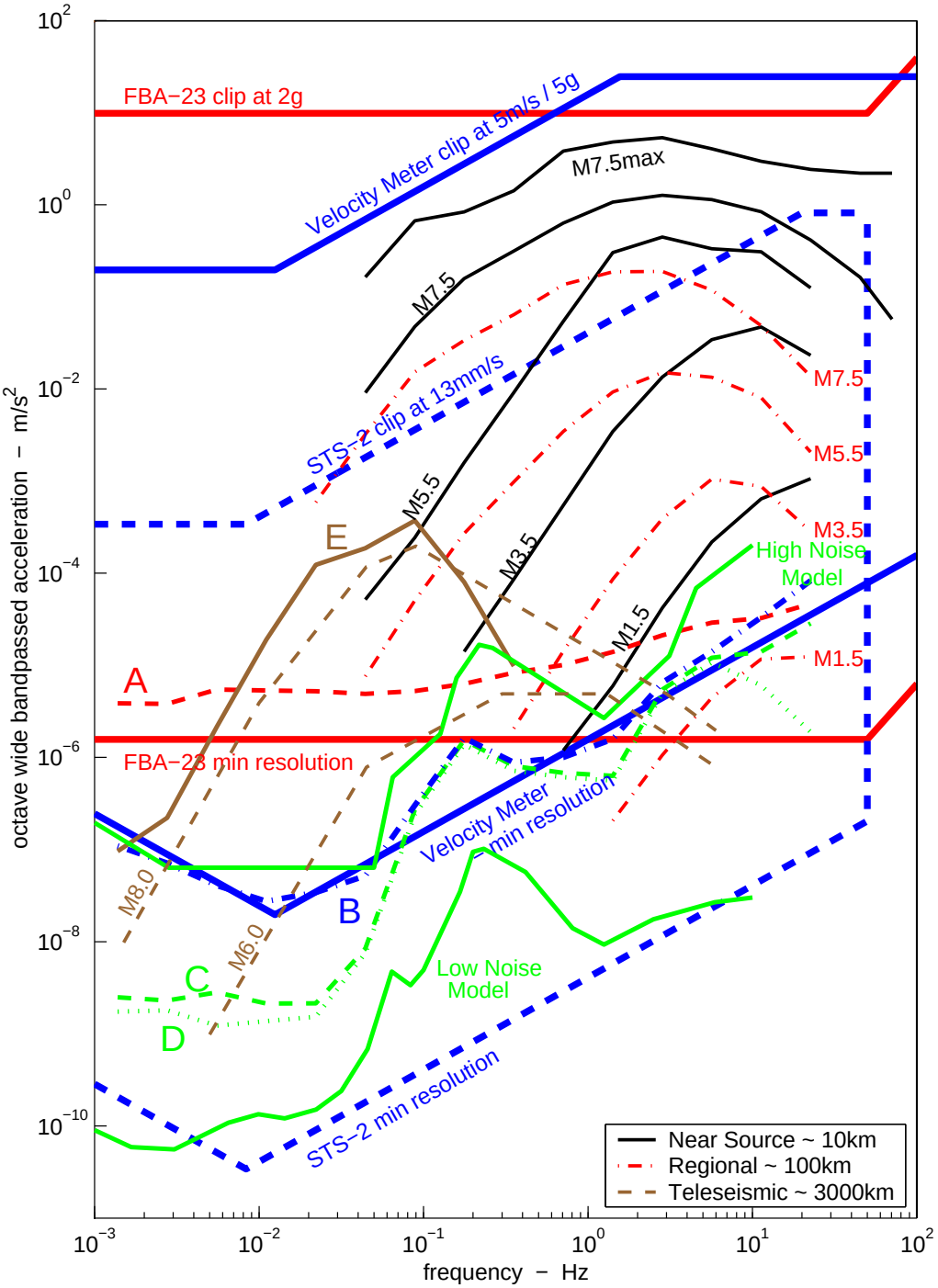

Figure 3.18: Frequency - amplitude plot for octave wide band-passes of ground motion acceleration. Includes typical signals and theoretical instrument limits. Deconvolved noise data from PAS, PASA are represented by lines annotated with letters A-D. A: FBA-23, B: VSE-355G2, C: STS-2, D: STS-1. Line E is teleseismic signal from M7.8 Qinghai recorded on VSE-355G2 in Japan at 4220*km*. (*see text on Instrument Resolution for further explanation.*)

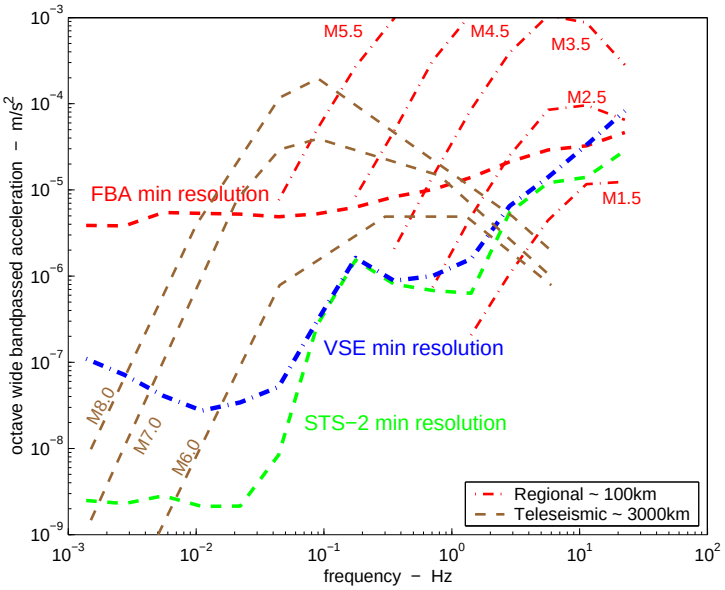

Figure 3.19: Close-up of noise floors of Fig. 3.18, showing minimum sensitivity of instruments at Pasadena.

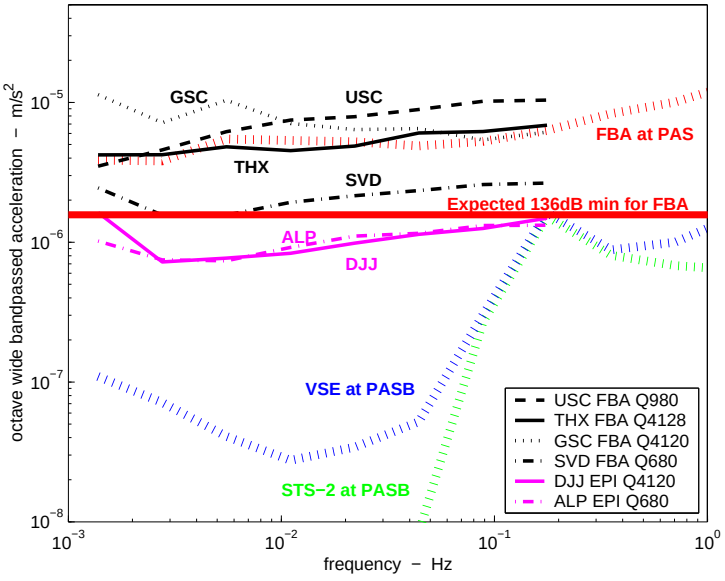

Figure 3.20: Similar to Fig. 3.18. Comparison of noise floors for various accelerometer deployed in TriNet.

This is well below the maximum voltage of $20V$ (or maximum velocity of $2m/s$). In order to get on-scale data for the calibration test, the resistance over the coil was increased until the applied voltage was below this level.

The problem prompted further investigation to confirm whether this was a defect of the instrument or simply a problem confined to the calibration coil. A cart test experiment was developed, in which the instrument would record large velocities of an order seen in strong ground motion records (over $1m/s$). This involved placing the instrument alongside an EpiSensor, both connected to a Quanterra datalogger also on the cart, and robustly moving the apparatus along a laboratory floor (see Figure 3.1 for test layout). The instrument was indeed observed to clip at about $\pm 15cm/s$.

Figure 3.21 illustrates the problem. On this and subsequent plots, the in-plane velocity output from the VSE-355G2 is compared to the in-plane velocity recovered from the EpiSensor. In order to best observe clipping, the VSE output is not deconvolved, and just has the instrument gain removed. Also included in Figure 3.21 are the accelerations recovered from the VSE-355G2 and the EpiSensor. In Figure 3.21, whenever the recorded velocity is greater than about $\pm 15cm/s$, there is a clipping of the VSE. Other differences in the velocity records are attributed to inexact orientation, tilt and differential vibrations on the cart which occur over the course of the test. Accelerations from the EpiSensor are well below $50cm/s^2$ ($5\%g$) and thus the instrument clip level in acceleration ($200\%g$). This is also well below the VSE-355G2 (and G3) clip level in acceleration (at high frequencies, the VSE sensors will clip at $2g$).

The characteristics of the clipping observed in the cart test in Figure 3.21 and during the calibration tests in Figure 3.22 are unlike that of a datalogger clip, where, for the Q4120, the maximum number of counts is reached and the output simply 'flat-lines' until the ground motions return below the datalogger clip level. In these cases, the output will spike above the clip level of about $15cm/s$, but very soon after the excursion will return sharply to the clip level amid some high frequency vibration before resting near $15cm/s$ for a few seconds. For the cart test, the high frequency vibrations cause large acceleration spikes not recorded by the EpiSensor. This behaviour seems to indicate the mechanical seismometer mass has reached its displacement limit and has crashed onto the side rests. This same

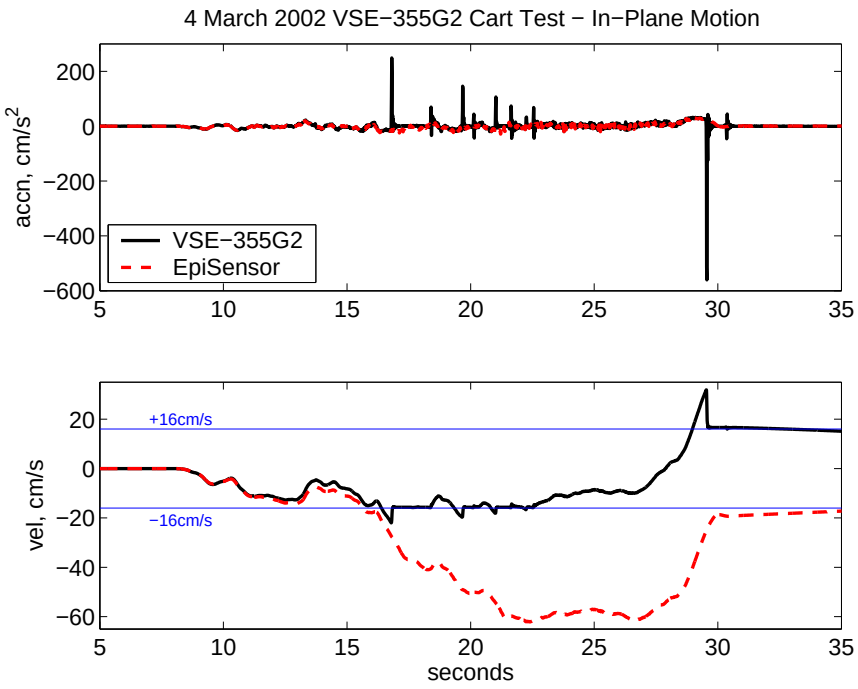

Figure 3.21: VSE and EpiSensor Cart Test results, April 2002. The VSE clips whenever velocities are greater than $\pm 15 cm/s$.

behaviour is observed in the calibration tests with a simple step input (Figure 3.22), where after about 45*s* the velocity would slowly drop back to zero with a shape similar to the step response of the instrument. For the cart test, with a more complicated input, once the actual velocity (as observed in the EpiSensor) changes direction, the instrument returns back on-scale, although of course it records incorrect magnitudes of motion. Any instrument response is drowned out by these subsequent motions. Data presented from strong motions in Chapter 4 show when there are large, high frequency velocity reversals, as is typical of large earthquakes, there is almost no 'resting' at the clip level. Note also that in Figure 3.21, after an initial clip has occurred, if subsequent absolute velocity change exceeds $30 cm/s$, clipping occurs again as the mechanical seismometer appears to hit the opposite side rest due to the peak-to-peak velocity limit being reached. This occurs even though the actual velocity does not appear to have reversed direction.

After correspondence with the manufacturer, the source of the low clipping was identified as a problem with the power regulator, which prevented the final stage amplifier from

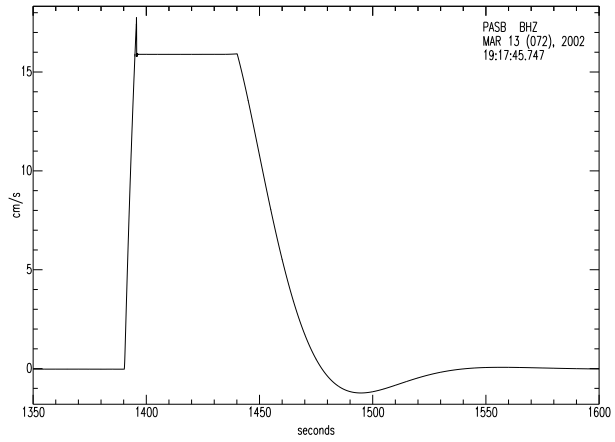

Figure 3.22: Calibration coil test results, March 2002, with clipping above $16 cm/s$.

working correctly. The Vice-President of the company, Mr. Isamu Yokoi, visited Caltech on 6/18/02 and 6/19/02 to rectify the problem. Once this problem had been corrected, the cart test was repeated. The test showed improved performance, with good VSE-355G2 correspondence with the EpiSensor data up to 30cm/s (Fig. 3.23). On tests that went above this speed, clipping once again occurred (Fig. 3.24). It is noted that for unknown reasons, the behaviour of the instrument after clipping is different to the previous tests (such as in Fig. 3.21). The clip level here is defined to be at the point where the instrument output departs suddenly and significantly from the accelerometer path, or indeed from its own smooth path. This occurs at about $-50 cm/s$ and again at $+30 cm/s$, where the VSE seems to spike sharply, then increase linearly with time, until the absolute velocity (as seen from the EpiSensor) begins to decrease. No explanation for this behaviour is presented. Once again, the test is of a robust nature, and the differing longterm trends which appear over the course of the records may be attributed to inexact seismometer orientation or differential tilt during the test.

Initially the manufacturer believed the problems observed in the laboratory at Caltech were isolated to this instrument, and were not representative of all VSE-355G2 instruments. A search of the Japanese Freesia Broadband Seismic Network (F-Net) database in 2001 did not find any recordings with this instrument which had velocities greater than $6 cm/s$,

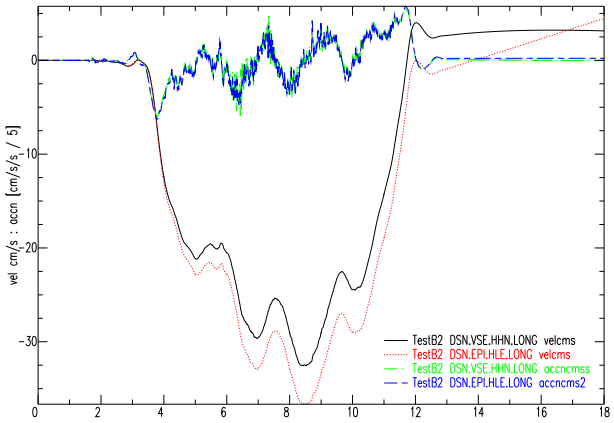

Figure 3.23: VSE and EpiSensor Cart Test results, June 2002. No clipping observed at this speed, below 40cm/s.

so this could not be independently confirmed. The M8.3 Tokachi-Oki earthquake hit the south-east of Hokkaido Island in Japan on 25 Sept 2003, providing a large set of strong ground motions, with a number of VSE instruments (including the VSE-355G2) within 200km of the epicentre. Their performance indicates strange non-linear behaviour above 15cm/s is not limited to the model at Caltech. A complete analysis of the performance of the VSE series of instruments during this earthquake is included in Chapter 4.

Following the discovery of the problem, and the initial failure to fully rectify the sensor, a protracted set of visits and correspondence occurred. In mid-2003, an instrument which appeared to satisfy the initial design specifications was tested and deployed within the CISN. Chapter 5 summarises these tests and presents the instrument performance of the VSE-355G3.

3.5.5 Spurious Resonances

FFT's of the noise data collected by the VSE-355G2 indicated the presence of some spurious resonances at frequencies beyond 2Hz, in all 3 components, as illustrated in Figure 3.25. Data was collected at PASB on 24 March 2002 from 08:00 — 11:00 UTC. These 'spikes' were not observed by the co-located STS-2 or nearby STS-1. Resonances were

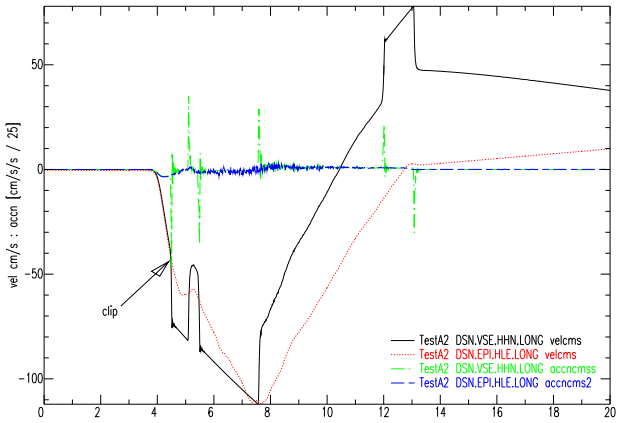

Figure 3.24: VSE and EpiSensor Cart Test results, June 2002. Clipping observed at near 40cm/s, with unexplained linear increase in velocity after clip until true velocity reverses.

observed at 2.225Hz, 14.235Hz and 14.63Hz on the E-W component, 2.225Hz, 12.01Hz and 12.405Hz on the N-S component, and 12.405Hz and 14.63Hz on the vertical component. The very narrow bandwidth of the 'spikes' indicate that if the resonance is due to the mechanical system (and not part of the electronic feedback circuit), it is characterised by very high Q, or low damping.

It is noted these resonances no longer appear in the VSE-355G3 model.

3.6 Recovery of Teleseismic Data

Figures 3.26, 3.27 and 3.28 show the potential of the VSE-355G2 to record long-period motion from giant earthquakes that may saturate the 13mm/s STS-2 even at teleseismic distances. These records are from the 14 November 2001 M7.8 Qinghai-Xinjiang Border Region, China, recorded at Station ZMM, Japan, a distance of 4220km (38°). The maximum velocity is 2mm/s, within 16% of the instrument clip level. The station is part of the Freesia Broadband Seismic Network (F-Net), Japan [`www.fnet.bosai.go.jp`]. In Figure 3.27 we observe the VSE-355G2 is very capable of recording long period motions over 100s for these large events. The FFT in Figure 3.28 indicates this may be valid even out to

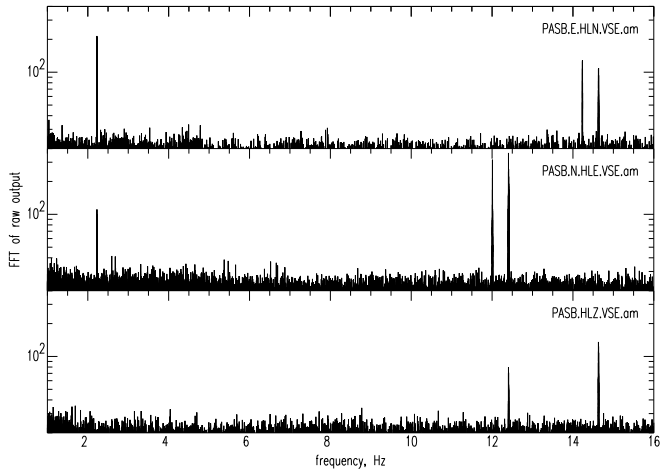

Figure 3.25: FFT of raw VSE-355G2 background noise, indicating presence of spurious resonances.

longer periods. This follows from similar observations made using accelerometer data in Figures 2.12 — 2.14 , though it is noted the accelerometer was not capable of this level of resolution beyond about 50*s*.

3.7 Summary

This Chapter documents the investigation into the performance of the tri-axial VSE-355G2 Strong Motion Velocity Seismometer, purchased with IRIS funds in late 2001. The instrument is manufactured by Tokyo Sokushin Co. Ltd. The instrument measures velocity as the standard output, from a heavily over-damped mechanical pendulum and a feedback loop proportional to the pendulum displacement.

The investigation confirms the instrument generally adheres to the manufacturer's specifications, though a very significant problem of a lower than expected clipping level was discovered. As the most critical function of a strong motion seismometer is to record on-scale all ground motions, this is a major flaw. The instrument was observed to produce a highly non-linear response once velocities exceeded $15cm/s$, with high frequency velocity

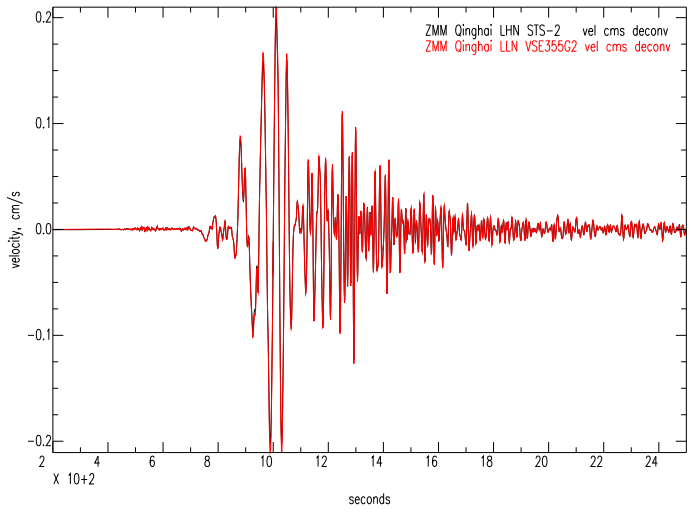

Figure 3.26: Deconvolved (frequency domain) velocity time-series of VSE-355G2 versus co-located STS-2 from Station ZMM recording M7.8 Qinghai, China event, 14 November 2001 at 4221*km* (38°). Data from the F-Net, Japan.

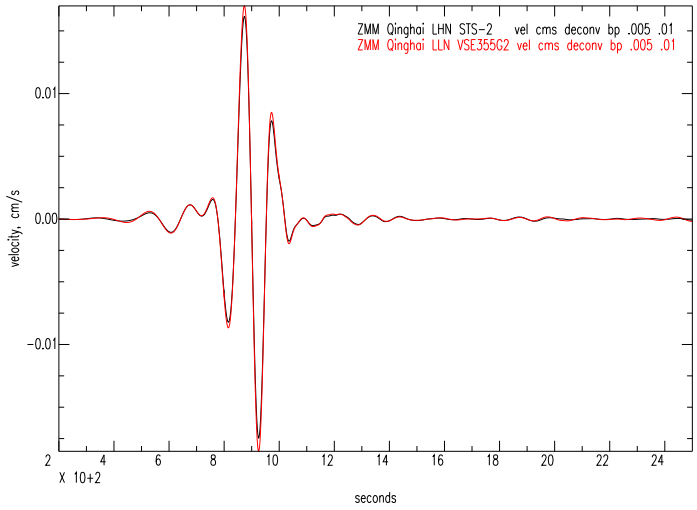

Figure 3.27: Station ZMM, M7.8 Qinghai event: bandpass from 100 to 200*s*, data is deconvolved (frequency domain).

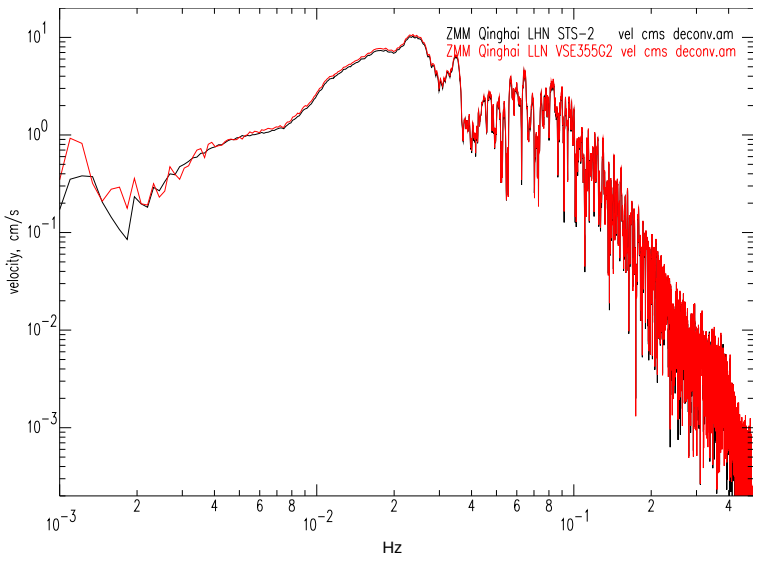

Figure 3.28: Station ZMM, M7.8 Qinghai event: FFT of broadband data, data is deconvolved (frequency domain). Y-axis is FFT of the velocity time-series (cm/s) from Figure 3.26.

jumps preceding a flatline in velocity until a velocity reversal occurred. This is under 5% of the expected clip level of $200 m/s$, and is well below expected, and previously observed, strong motion velocities. The manufacturer produced many fixes to the instrument to rectify the problem, which are discussed in Chapter 5. The new model of the instrument has been renamed the VSE-355G3.

The initial model as delivered, and its predecessor, the VSE-355G, provide the strong motion backbone of the Freesia Broadband Network (F-Net) in Japan, and other Tokyo-Sokushin strong motion velocity instruments are also widely deployed in other Japanese networks. Instrument performance from the M8.3 Hokkaido earthquake is included in Chapter 4.

These initial tests demonstrated the ability of the instrument to resolve long period ($>$ 30s) motions was much better than that of a strong motion accelerometer — the instrument had good response even at 100's of seconds. The instrument noise measured at PAS was only slightly above that of the station noise out to 10s, and remained within an order of magnitude at 100s (well over 2 orders of magnitude better than the FBA-23). With the instrument clip at only 5% of $2 m/s$, the instrument operated near $120 dB$ dynamic range. If

the clip was as expected with this level of sensitivity, the dynamic range would be $144dB$. Instrument sensitivities were within 6% of manufacturer's specifications. All 3 components were approximated as SDOF systems with $T_0 \sim 94s$ and $\zeta = 0.65$.

It is further noted from the investigation that the EpiSensor is a better alternative to the FBA-23 for observing weak regional and teleseismic earthquakes, though it is still significantly noisier than the VSE. For the same 24-bit dataloggers, the FBA-23 dynamic range is generally less than $135dB$, whilst the EpiSensor records closer to $144dB$.

Chapter 4 Strong Motion Velocity Instrument Performance in 2003 M8.3 Tokachi-Oki Earthquake

4.1 Introduction

The M8.3 Tokachi-Oki earthquake hit the South-East side of the Northern Japanese island of Hokkaido on 04:50AM on the morning of the 26^{th} September 2003, local time (25 September at 19:50:06.2, UTC). The epicentre was about 145km SSW of the the town of Kushiro, 41.775^{o}Lat, 143.904^{o}Long, at a depth of $27km$ (`neic.usgs.gov`). The reverse-thrust earthquake occurred on a fault at the plate interface between the over-riding North American plate, which extends into the North-East corner of the Eurasian land-mass, including Hokkaido Island, and the subducting Pacific plate. Tectonic measurements indicate that at this boundary, the Pacific plate moves WNW at a rate of about $8.2cm/year$ relative to the the North American plate (`earthquake.usgs.gov`).

This earthquake occurred in a region extraordinarily well instrumented, and provided an excellent set of strong motion records and GPS displacements. Three large networks operate strong motion instrumentation under the National Research Institute for Earth Science and Disaster Prevention, NIED (Okada et al, 2003). Currently, all NIED data is openly available to the community through their Web-site (`www.bosai.go.jp`). One of these networks, FREESIA, or F-NET, operates Tokyo-Sokushin VSE-355G and VSE-355G2 instruments. Independent of NIED, another network, the Warning Information System of Earthquakes (WISE, `www.ceri.go.jp`), operated by the Structural Division of the Civil Engineering Research Institute of Hokkaido, in Sapporo, provides about 140 single instrument stations also with Tokyo-Sokushin strong motion velocity (VSE-355EI) instruments.

This Chapter evaluates the field performance of VSE series of instruments during the

earthquake. Some major areas of concern, highlighted in the previous two Chapters, are investigated. The ability of the instrument to recover ground displacements is investigated by comparing the permanent offsets after strong motion has passed with the GPS network in the region. It is obvious that the Tokyo Sokushin sensors, with corners at about 56s for the VSE-355EI, and at about 94s for the VSE-355G and VSE-355G2, have problems recovering large static offsets even using the time-domain deconvolved timeseries. They are also highly sensitive to tilt, in a similar manner to accelerometers (shown in Figure 3.7). The character of the instrument during strong motion is also investigated. In all cases where the VSE-355G2 records velocities above $17cm/s$ (though only at 2 stations), the timeseries is observed to be unstable. This was also observed in the laboratory (Figure 3.21). In this event, spikes are also often observed in the timeseries, though unlike in the cart test clipping, only a very short (if any) flat-line is seen. Only one VSE-355G instrument was subjected to velocities above $10cm/s$, and it performed without apparent problem reaching $21.7cm/s$ (Station URH in Figure 4.35). Many VSE-355EI in the WISE array recorded motions above $10cm/s$, some even above $100cm/s$ — the network is more dense, and as the stations are located on structures, the response is often dominated by the structural resonances, unlike the 40m deep F-Net vaults. This local, large effect means the WISE array may not be readily compared with data from the free-field stations. Static offsets are also more unstable, partly due to this as well as the short corner frequency at 56s.

The usefulness of the strong motion sensor in a broadband network is also discussed. All high-gain broadband instruments are saturated within a 500km radius, and some instruments out to a distance of nearly 1000km are clipped. An earthquake of this magnitude has strong motion signals with good signal-to-noise thousands of kilometers from the epicenter for a $144dB$ quality sensor. Consequently, comparing the broadband and strong motion signals from large events for all stations within a network is demonstrated to be a useful way to determine the operational health the network. In this network, the VSE sensors and some broadband instruments (the STS-1 and CMG-1T), show evidence of signal non-linearities at levels well below their expected clip level. The broadband sensors also exhibit a lot more variability in signal calibration than the widely deployed STS-2.

4.2 The Available Networks

A map of Japan with all the NIED and WISE station locations is presented in Figure 4.1. Figure 4.2 shows the same data for Hokkaido Island. The characteristics of a typical station in each network is described as follows:

4.2.1 F-Net

This is a 'full-range' seismographic network, with every station consisting of a broadband instrument as well as a strong motion instrument. Each of the 6 channels are recorded with 27-bit dataloggers (originally the Quanterra Q680 was used, but to ensure compatibility with other networks, a Japanese manufactured digitiser is now used). There are about 80 stations throughout Japan, spaced at about 100km intervals. The instruments are co-located in tunnels $30 - 50m$ deep to reduce noise. Data is continuously telemetered to NIED in Tsukuba and archived. The dynamic and frequency range covered by these stations are very similar to a typical CISN station in Southern California. 100Hz data is available.

4.2.2 K-Net

'Kyoshin Net' is a dense strong motion network consisting of over 1000 accelerometer stations at free-field sites at intervals of 20km covering the country. These instruments are located on the ground surface. The stations have K-NET95 accelerometers, with 144dB dynamic range and a clip of 2g. Frequency bandwidth is from about 20Hz to DC. The on-site digitiser is 24bits with a sampling frequency of 100Hz. Data is triggered, with automatic dial-in once an event has been recorded. Most K-Net stations are located on thick sedimentary sites in urban areas.

4.2.3 KiK-Net

'Kiban Kyoshin-Net' is also a nationwide strong motion Network, with about 650 stations. Each station consists of an up-hole and down-hole accelerometer, with 6 channels of data. The depth of the boreholes range from a minimum of 100m, to a maximum of 2000m.

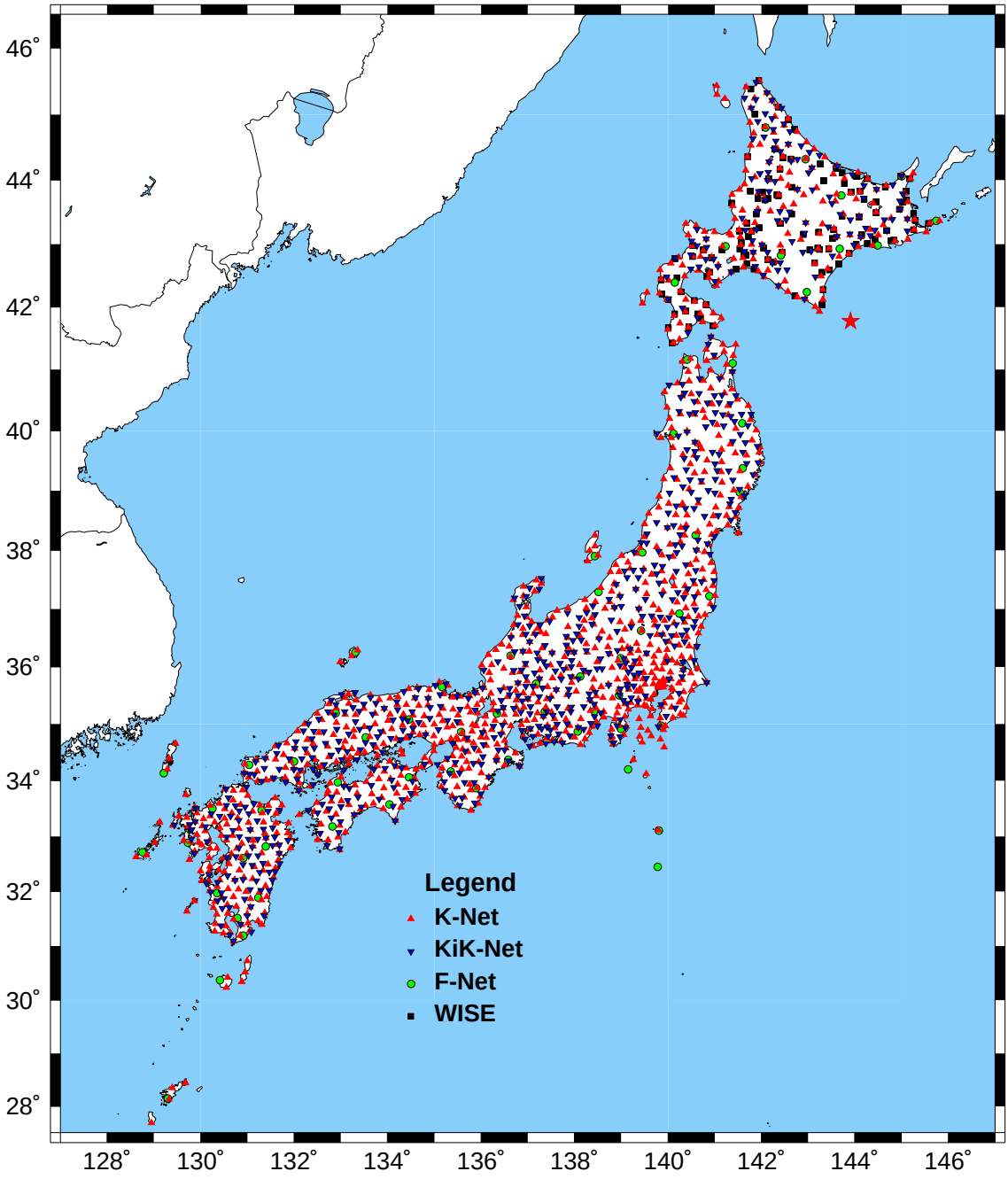

Figure 4.1: Strong motion stations in Japan: F-Net, K-Net, KiK-Net and WISE. Star indicates M8.3 Epicenter.

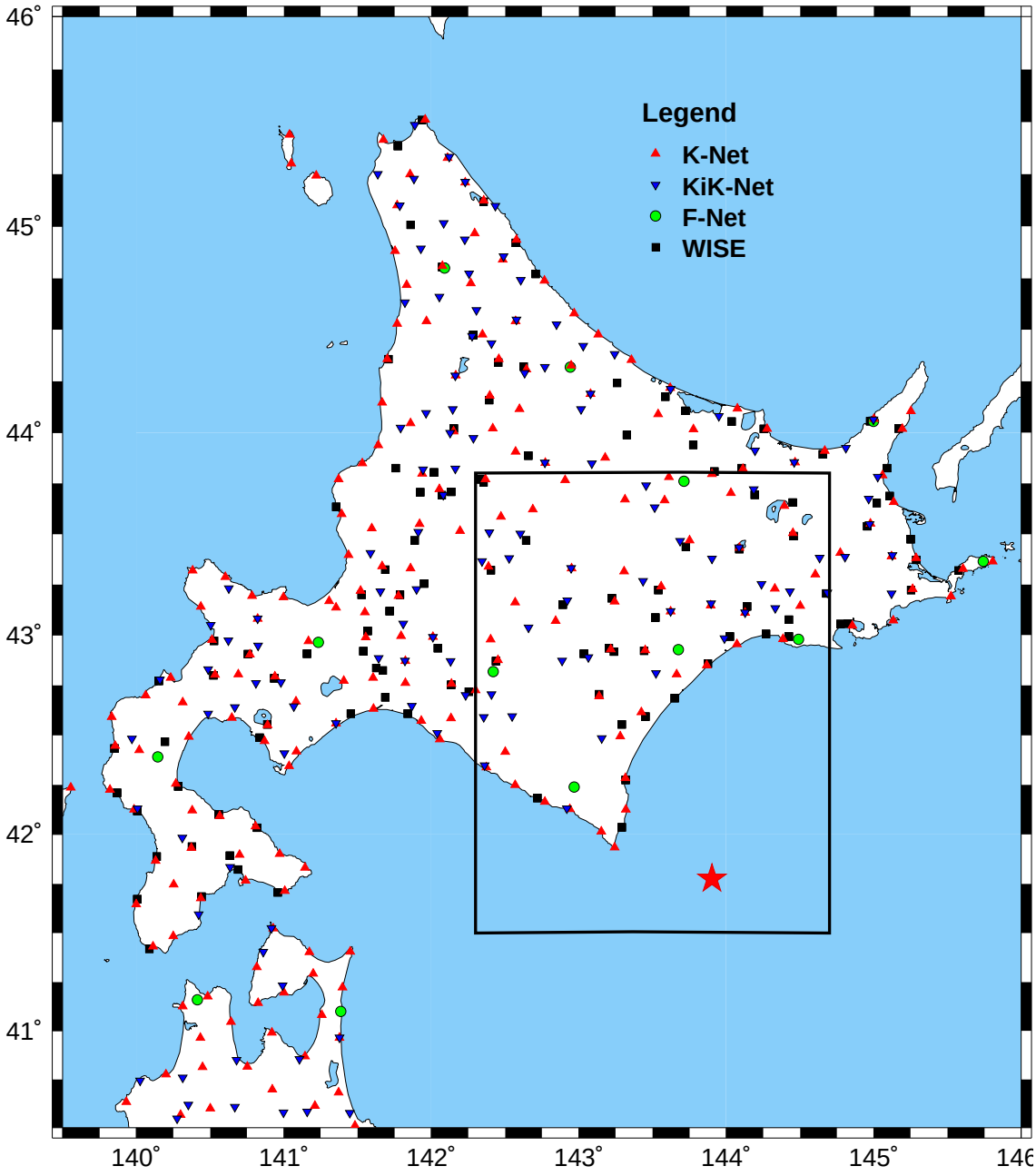

Figure 4.2: Strong motion stations in Hokkaido: WISE Network, F-Net, K-Net and KiK-Net stations. Star indicates M8.3 Epicenter. Box is outline of the boundaries of the south-eastern Hokkaido Plot, Figure 4.11.

The modal depth is about 300m. KiK-Net stations piggy-back on the existing Hi-Net (high sensitivity network) boreholes, and so are located mainly on rock or thin sedimentary sites. Instrumentation is the same as in the K-Net sites, with K-Net95 accelerometers, though sampling is at 200Hz. Automatic dial-in ISDN phone line transmission is used to retrieve the data, as in K-Net.

4.2.4 WISE

The Warning Information System of Earthquakes (WISE) is a strong motion network consisting of VSE-355EI instruments in single sensor stations, with 16-bits dataloggers digitising at 100Hz (*personal communication, Isamu Yokoi, 2003*). The 140 stations, approximately at 40km spacing, are at important civil infrastructure locations throughout Hokkaido, such as highway embankments, dams and bridges. Unfortunately, a station list with details of the structure being monitored by each sensor, and the proximity of the sensor to the structure, is not available. The timeseries data indicates many of the sensors are located on the structures, as there are strong resonances dominating the response. The VSE-355EI is a velocity strong motion seismometer, like the VSE-355G2 but with a more limited frequency range, from 0.0188Hz (56s) to 100Hz. The dynamic range is just below the VSE-355G2, at 136dB (`www.to-soku.co.jp/english.html`), with expected clip at 200cm/s. The digitiser is only 16bits, so the output data has only about 90dB dynamic range. ISDN packet lines are used to transmit data once the sensor has triggered in near-real time. The network was primarily developed to rapidly determine damage levels of critical civil infrastructure on the island in the event of a large earthquake.

Stations from all 4 of these networks obtained multiple records from within 100km of epicenter.

4.3 Static Offset — GPS and Seismometers

In Japan, the Geographical Survey Institute measures crustal deformation using GEONET, the GPS Earth Observation Network. This is a dense network of GPS stations located throughout the country. GPS data is collected and distributed to the public through their Web-site `mekira.gsi.go.jp/ENGLISH/index.html`. Data from the Website is available in Cartesian co-ordinates (X,Y,Z) at a sampling rate of 1 sample per day.

The method outlined in Strang and Borre (1997), which employs a reference ellipsoid, is used to convert these Cartesian co-ordinates to a latitude, longitude and height. The reference ellipsoid selected is the World Geodetic System (1984) ellipsoid, with ellipsoid parameters $a = 6378137m$ and $1/f = 298.257223568$; a is the major axis length (the radius of earth at the equator), and f is the dimensionless flattening of the earth. The Matlab function TOGEOID.M, from `kom.auc.dk/~borre/matlab/sat_cons/`, is used to perform the conversion.

The deformation in *cm* along the lines of latitude (corresponds to E-W component) and longitude (N-S) are then determined from the relative change in the geographical co-ordinates. At $43.5^{o}Latitude$, the length of a degree of latitude is $111.102km$ and the length of a degree of longitude is $80.877km$ (National Geospatial-Intelligence Agency, `pollux.nss.nima.mil/calc/degree.html`).

There is some variation between each daily recording that appears to be due to measurement error. Thus, to reduce this, an average co-ordinate change over the seven days before and after the earthquake is used. Figure 4.3 shows the variation over this period for several stations at varying distances from the epicenter. For simplicity, it is assumed all the drift that occurs is due to the dynamic tectonic movement associated with the earthquake rupture, and the displacement caused by aftershocks is negligible. This assumption is satisfactory for the accuracy involved in this study, though Figure 4.4 shows there is significant further displacements at nearby stations due to the M7.1 aftershock.

The GPS displacement field can be compared to the displacement field from the strong motion records once these calculations have been made. As there is static offset, the instrument responses of each seismometer need to be removed. This deconvolution is performed

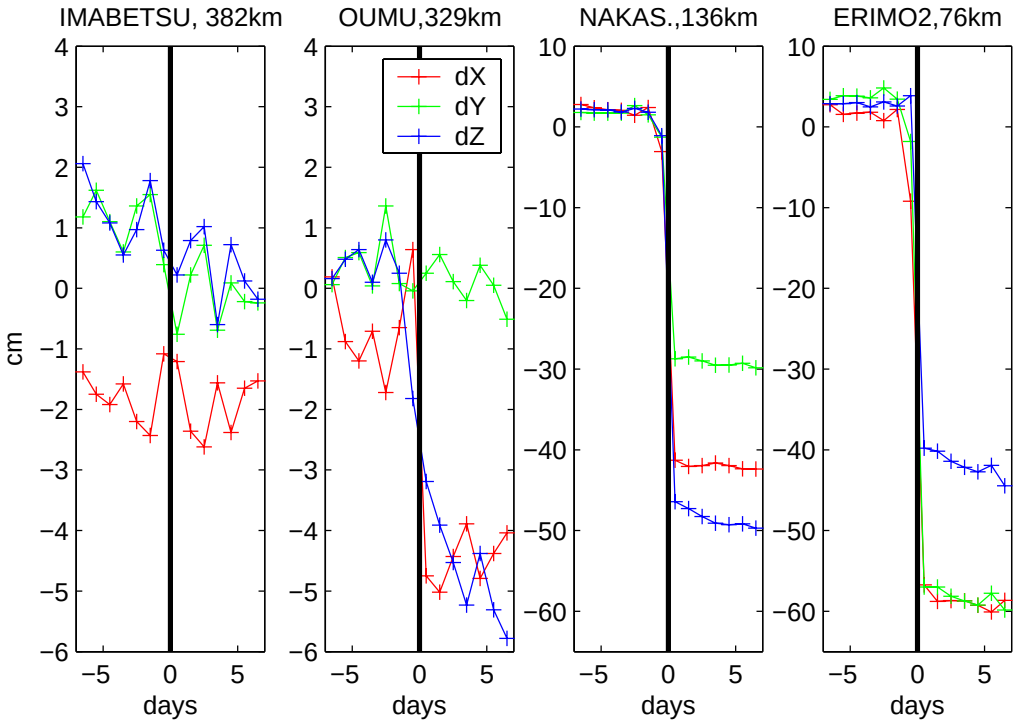

Figure 4.3: Variation of GPS readings at 4 stations of varying distance from the mainshock, in the week before and the week after the M8.3 earthquake. Data is 1 sample/day, obtained from the Web.

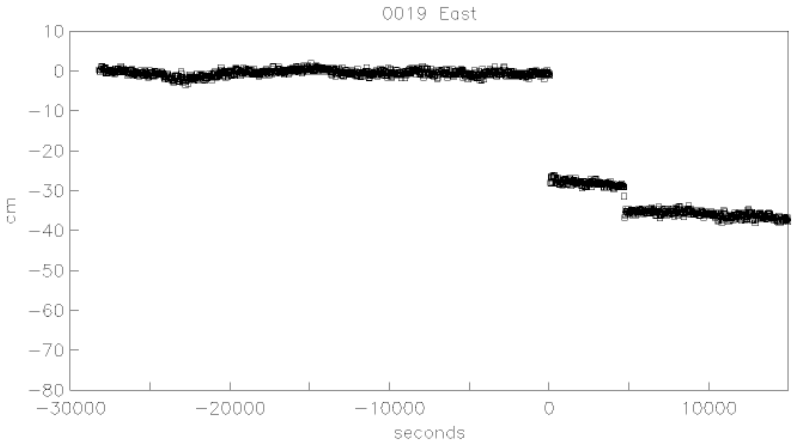

Figure 4.4: Variation of GPS sampled every 30*s* at station Erimo1 (closest stations to mainshock) from a 12.5*hr* period centered around the mainshock. E-W only. Note large offsets mainshock as well as M7.1 aftershock. From K. Larson (*personal communication*)

by a time domain direct integration of the equivalent equation of motion for the seismometer. The method is described in detail in Chapter 3. As illustrated in Figures 3.5 — 3.10, as the accelerometers have very high natural frequencies, only the instrument gain needs to be removed, and then the signal is integrated twice to recover displacement. For the VSE sensors, the output, $y(t)$, can be converted to ground displacement, $u(t)$ using Equation 3.12, reproduced here —

$$u(t) = \frac{1}{G}\left(\int_0^T y(t)\,dt + 2\beta \iint_0^T y(t)\,dt^2 + \omega_0^2 \iiint_0^T y(t)\,dt^3\right) \tag{4.1}$$

Strong motion VSE sensors are deployed by both the F-Net (with more recent VSE-355G and VSE-355G2), and the WISE Network (all stations deploy older VSE-355EI sensors). There are 13 F-Net stations in the Hokkaido region, and over 100 Hokkaido strong motion stations. After removal of the pre-event mean from the whole signal $y(t)$, the ground displacement $u(t)$ is determined from Equation 4.1. As the VSE-355EI has a much shorter equivalent natural period (56s compared to $\sim 94s$), the parameters β and ω_0^2 are significantly larger, and so are the sizes of the double and triple integral terms, and consequently the permanent displacements are less stable.

The permanent offsets for all the records from the seismometers tend to be unstable. With increasing time, every record becomes unstable. Some records become unstable as soon as the strong motion begins, due to instrument malfunction, clipping, or tilting, others develop numerical instabilities after the strong motion has passed, and the permanent offset can then be more easily estimated. A final estimation of permanent offset for each record is always somewhat subjective. After about 100s, most records have developed quadratic or at least linear trends, which can swamp the physically plausible offsets. Usually, an offset is taken from about $30s - 100s$ after the strong motion begins, which in the near-field region is after the strongest motions, and the majority of the co-seismic static offset, have occurred. Even when the quality of the displacement record is good, the accuracy of any offset is at best of the order of $0.5cm - 2cm$. Permanent offsets are determined independently of the nearby GPS stations to reduce estimation bias.

Figure 4.5 shows a map of Hokkaido island, where the length and direction of the

arrows emanating from each station represents the static horizontal offsets due to the earthquake. The black arrows are from GPS stations, and the blue and green arrows represent the estimated final horizontal offsets from the WISE and F-Net VSE seismometers respectively. Figure 4.6 presents the vertical components of the final offset for each station. For the VSE stations, a circle surrounding the station indicates a static displacement value was too difficult to estimate, usually due to wild trends leading to non-physically large displacements occurring near the onset of motions. This indicates instrument malfunction, or, in certain regions close to the epicenter, ground failure. Some examples of stations with this response will be shown in the next Section (e.g. Station KMU in Figure 4.23)

It is obvious that in general the VSE instruments do not give an accurate view of the permanent ground displacements as measured by the GPS. The longer period VSE-355G/G2 sensors, located in vaults, perform better than the WISE sensor, although as is shown later, some of these instruments clip at low velocities near the epicenter. It is very difficult to estimate static offset from the WISE VSE-355EI, as the sensors have a comparably short period, and are located at noisy civil infrastructure sites. Though the magnitudes are generally of similar order as the GPS, the azimuths tend to wildly differ from the GPS. Resonances from the structures dominate many WISE records. Another obvious problem is selecting permanent offsets before the major displacements have been recorded — many WISE records are unstable, with large tilts occurring shortly after the strong motion begins. Even if the selected static deformation estimate before instabilities dominant is correct for that time, it may not be the final offset for that site. This may partly explain why motions appear to be the opposite direction for many WISE stations. Another complication is there is strong evidence that the WISE VSE instruments are not oriented correctly. In particular, the E-W and N-S components seem to be recording west and south as positive at certain sites, opposite to the standard convention. Further, in (rectangular) structures, the horizontal channels are usually aligned parallel to the external walls, or main structural orientation. In the case of buildings, bridges and dams, this may not coincide with East and West. Also, all Sokushin instruments have default horizontal channel polarity which produces a negative N-S channel output (or S-N), and this needs to be accounted for in any network, which can easily be forgotten. The individual station timeseries analyses in the next section illus-

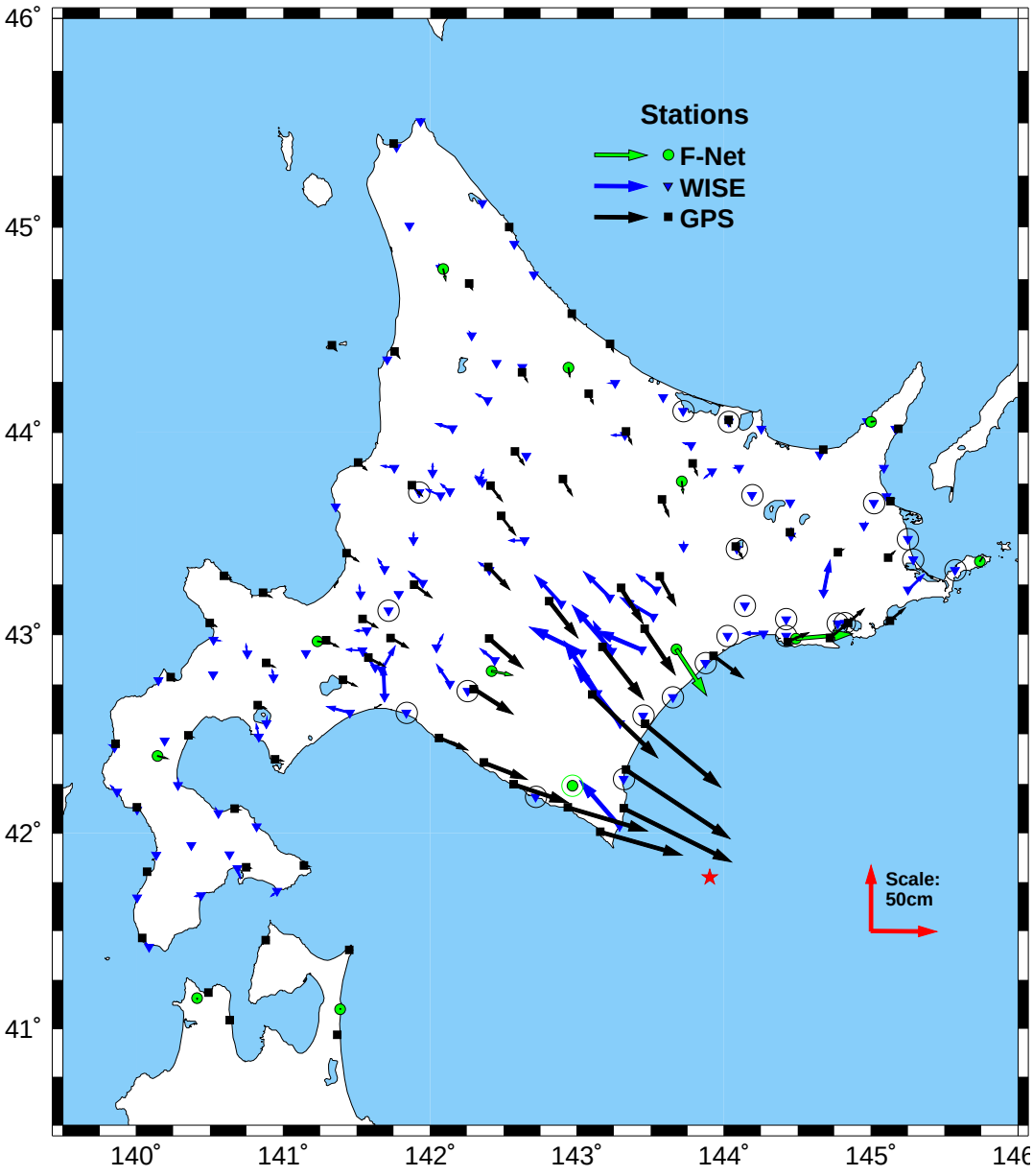

Figure 4.5: Comparison of static horizontal offset due to M8.3 Tokachi-Oki earthquake, as recorded from GPS and strong motion velocity instruments (deconvolved). A circle around a station indicates static offset cannot be estimated, or is non-physically large, indicating serious ground failure or instrument malfunction.

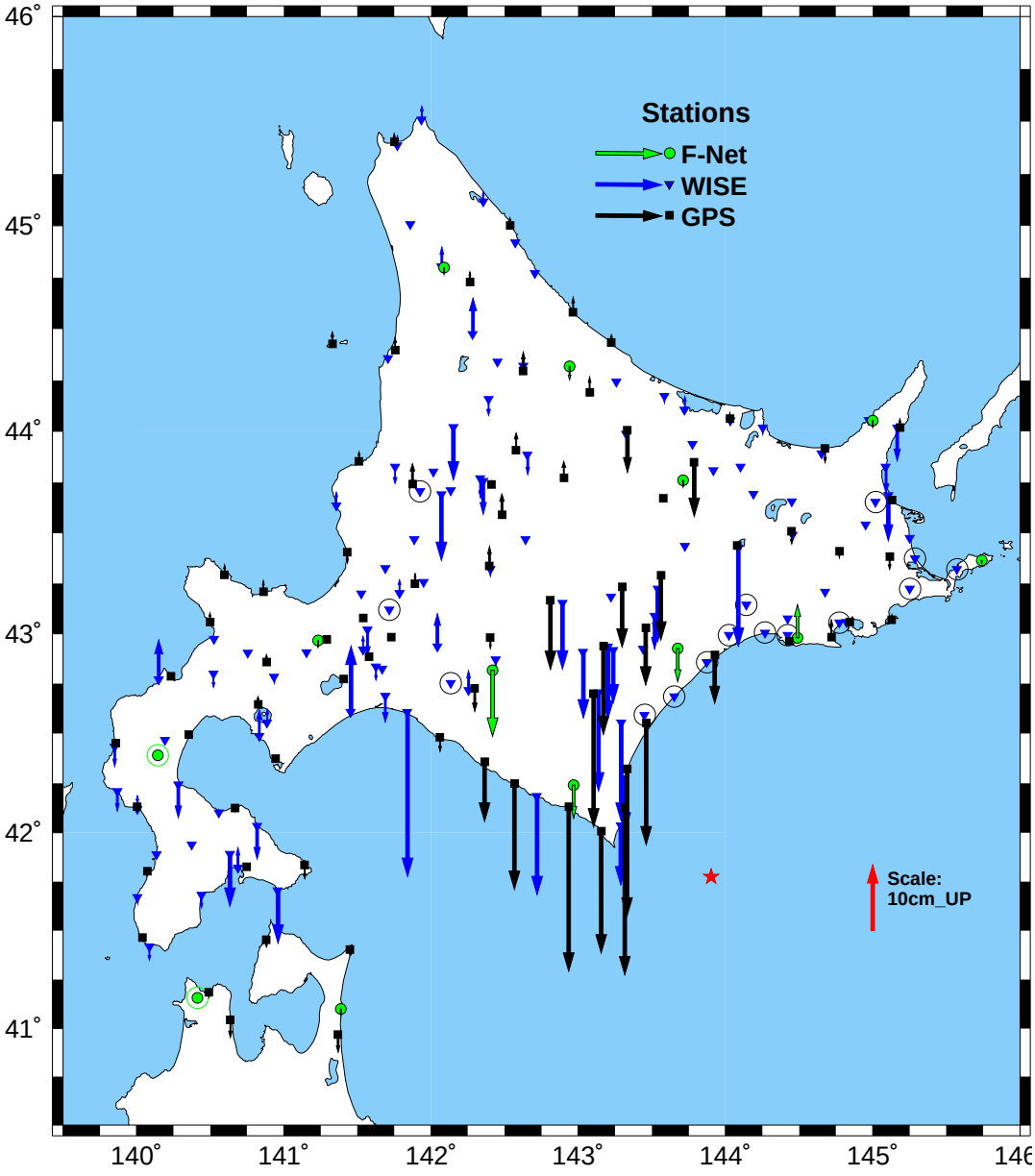

Figure 4.6: Comparison of static vertical offset due to the M8.3 Tokachi-Oki earthquake, as recorded from GPS and strong motion velocity instruments (deconvolved). A circle around a station indicates static offset cannot be estimated, or is non-physically large, indicating serious ground failure or instrument malfunction.

trate evidence for all these problems. It will also be shown that some stations have reversed polarity for both horizontal channels (see Figure 4.42), which explains why many stations have almost exactly reversed azimuth in Figure 4.5. The vertical stations are all properly oriented, and this produces a better displacement field. This improved data quality exposes other deficiencies away from the epicenter in the north and south-west of Hokkaido, where large differences in magnitude and orientation of the final vertical offset of the seismometers is observed with the GPS in Figure 4.5. Note this cannot be blamed on ground tilt, as this would not be widespread at these distances, and further the vertical component is not sensitive to small tilts.

In order to observe how the VSE sensors compare to the accelerometers in terms of static displacement recovery, some K-Net and KiK-Net accelerometer data near the epicentral region were also integrated up to displacement. These data are presented alongside the GPS and VSE static offsets in Figures 4.7 and 4.8. As expected, the double integration leads to serious instabilities commonly observed in accelerometers. This is a well-known problem, and may be due to non-linear behaviour of the accelerometer (though this has not been noted before for this particular instrument), or may be due to a real tilting of the ground (Iwan et al, 1985; Boore, 2001) from the serious and widespread ground failure associated with the event. Even so, many stations, including even the relatively noisy surface free-field K-Net stations close to the epicenter, have remarkable good final estimations.

In particular, the down-hole KiK-Net sites, at depths of over $100m$, are shown as yellow arrows with black outline, show excellent correlation with the GPS field.

Figures 4.9 and 4.10 present the VSE data for the entire island again, but without any instrument correction. For the F-Net stations, continuous data is available, and to estimate the permanent offset, the average displacement from a $10s$ period long after the strong motion shaking is over $(590 - 600s)$ is used. For the WISE Strong Motion Array, data is available for $200s$, so after a single integration, the permanent offset is defined as the average displacement of the last $10s$ $(190s - 200s)$. As expected for instruments insensitive to DC offsets, all F-Net stations, and almost all VSE-355EI stations, have very stable final offsets on all channels after the single integration. It is noted that not all these are zero offsets though. Permanent offsets are observed at numerous stations, even far away from

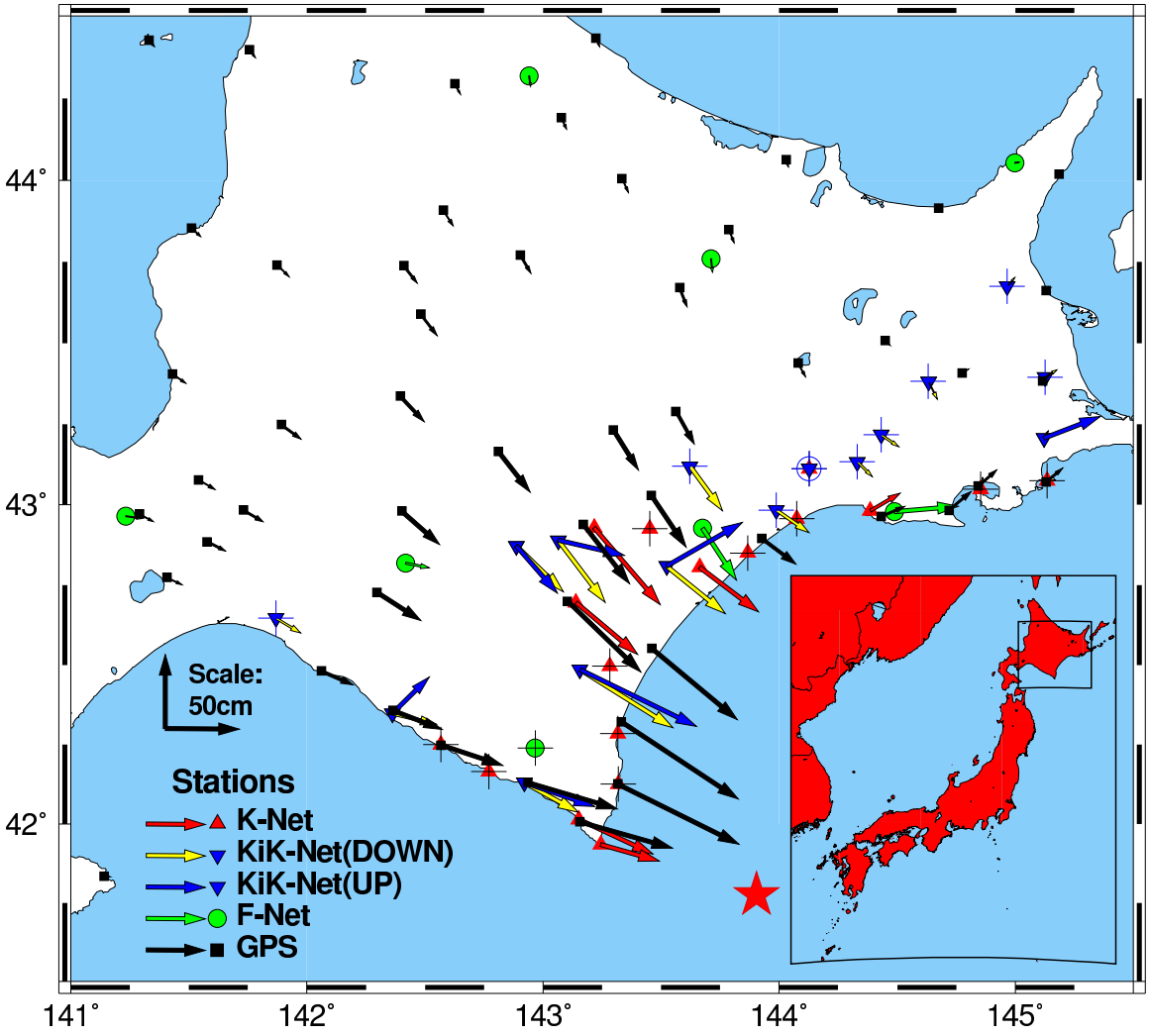

Figure 4.7: Comparison of static horizontal offset due to the M8.3 Tokachi-Oki earthquake, as recorded from GPS, velocity instruments (deconvolved), and accelerometers (deconvolved). Circle around a station indicates it was impossible to estimate a static offset, suggesting serious ground failure or instrument malfunction (for KiK-Net down-hole, '+' indicates impossible to estimate static offset).

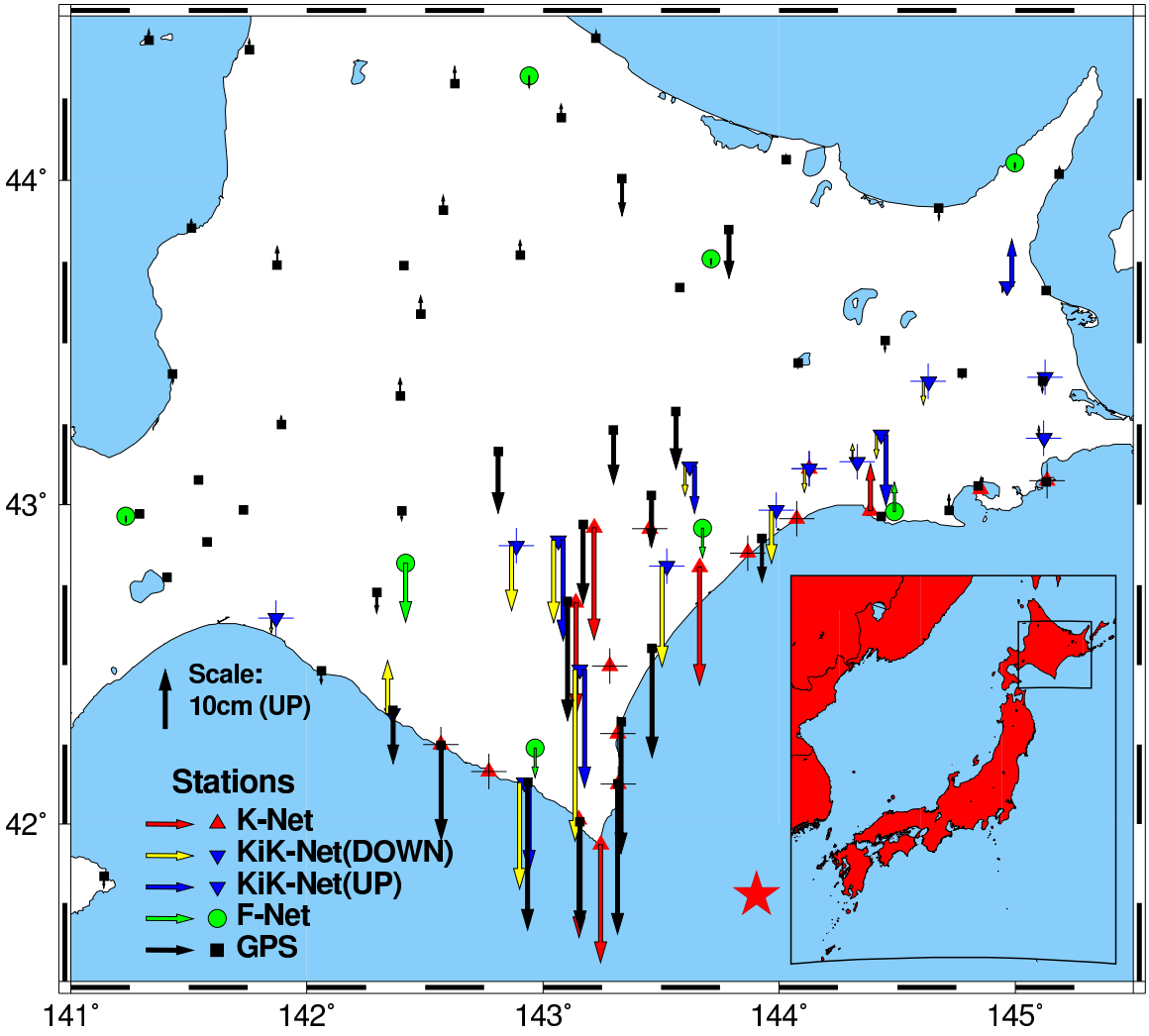

Figure 4.8: Comparison of static vertical offset due to the M8.3 Tokachi-Oki earthquake, as recorded from GPS, velocity instruments (deconvolved), and accelerometers (deconvolved). Circle around a station indicates it was impossible to estimate a static offset, suggesting serious ground failure or instrument malfunction (for KiK-Net down-hole, '+' indicates impossible to estimate static offset).

the mainshock, which recorded peak velocities well under the low clip level of $15cm/s$. These offsets most likely indicate poor instrument performance. One example is from the F-Net VSE-355G2 at station HID, in the south-center of the island.

Recording GPS positions at high frequencies, for example at about $1sps$, is a current area of research. During this earthquake, all the GEONET GPS stations were recording locally at this rate. Unfortunately, without a local power supply back-up at the stations, as there were widespread power outages in the near-field of the event, many stations briefly lost power after a few seconds of strong motion, as parts of the national grid failed. Many stations thus do not record a full uninterrupted time series for the event.

The daily GPS data point for each station is composed of an average of all the high-rate measurements, which minimises as far as possible the many errors, such as atmospheric effects, instantaneous satellite configuration etc. For the high-rate $1sps$ GPS data, no such averaging is possible, so much care must be taken when analysing the data. As there is some concern to quality (and interpretation) of the $1sps$ data, as well as the sheer volume of data this would present, this data is not readily made available. Through personal communication with Kristine Larson, who has obtained and worked on this $1sps$ data, several GPS stations in the near field are seen to have displacement time-series very similar to nearby seismic data. In future, if GPS recording at high sample rates, and seismic instruments are co-located, a general inversion would be possible, solving for for the three linear degrees of freedom, and two rotational degrees of freedom (defined by rotation about the horizontal axes). At this time, this would be the optimal station configuration for recording ground motions.

Larson et al. (2003) presents data showing that seismic deformations recorded during the M7.9 Denali earthquake in November 2002 are indeed similar to nearby high-rate GPS,with similar long period waves being observed by both sensors. The Tokachi-Oki dataset has a far greater network density, and much improved station quality. Further, displacements of over $1m$ are widespread over a very large area encompassing many diverse types of seismic stations. This dataset provides ample information to produce and test an inversion scheme to determine translations and rotations measured at a site using both GPS and seismic records.

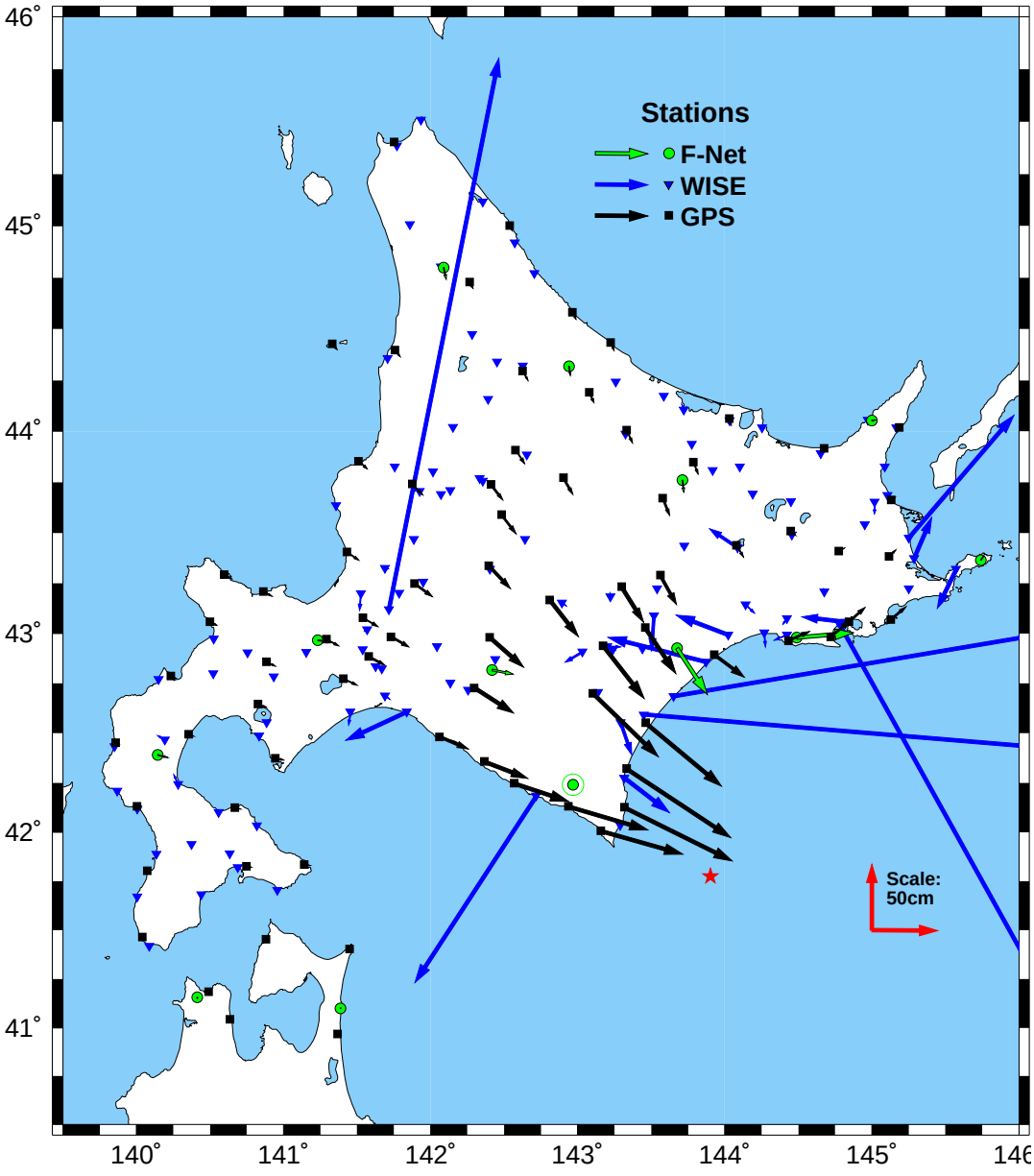

Figure 4.9: Comparison of static horizontal offset as recorded from GPS and strong motion VSE velocity instruments (no deconvolution). Black arrows: GPS, blue: WISE stations, green: F-Net. As expected, without deconvolution, VSE sensors show no static offset unless instrument malfunction or serious site failure occurs.

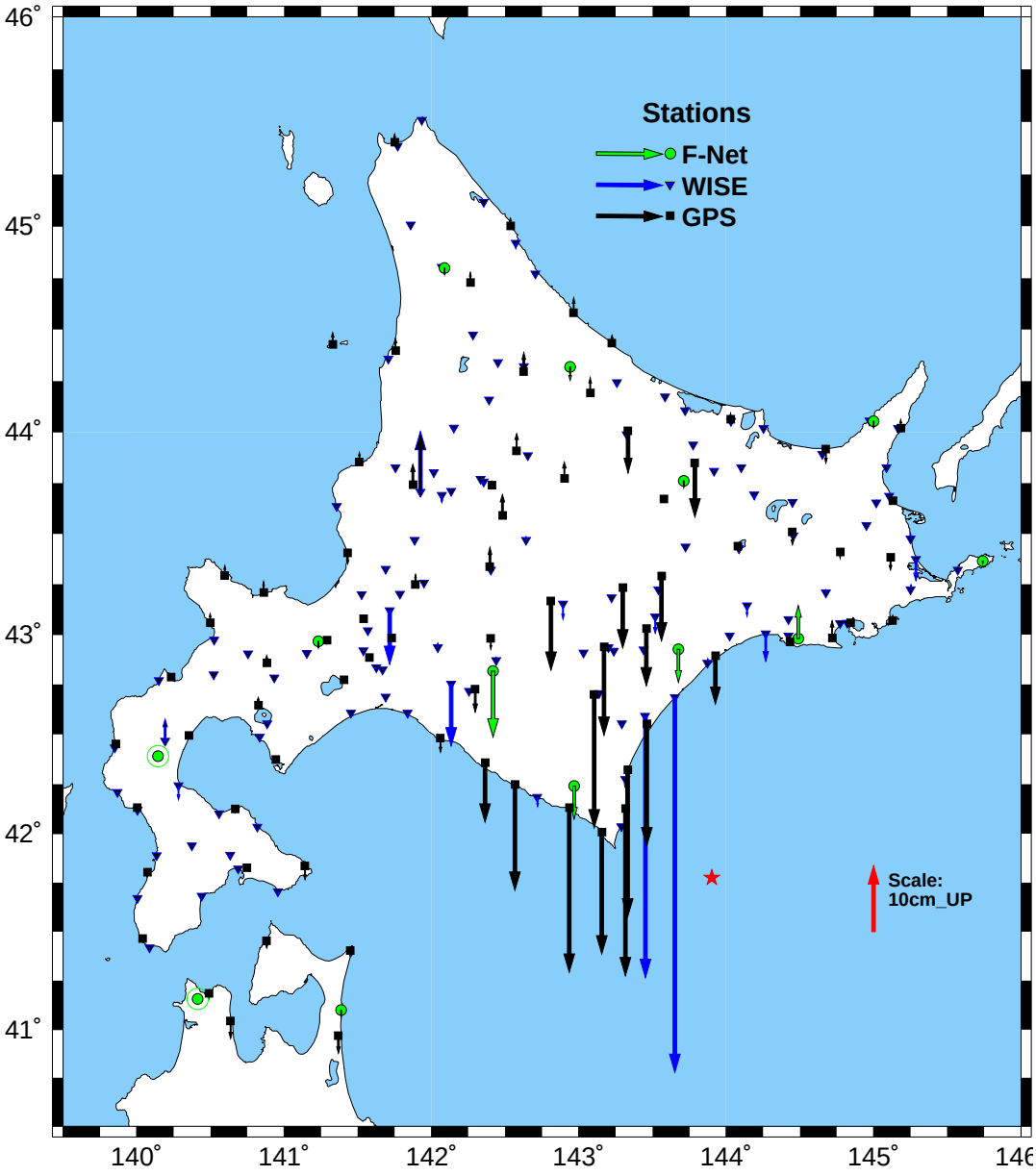

Figure 4.10: Comparison of static vertical offset as recorded from GPS and strong motion VSE velocity instruments (no deconvolution). Black arrows: GPS, blue: WISE stations, green: F-Net. As expected, without deconvolution, VSE sensors show no static offset unless instrument malfunction or serious site failure occurs.

An example of a high-rate GPS record will be presented later in the Chapter (Figure 4.44), where the similarity of the GPS displacement timeseries with that from nearby accelerometers is illustrated.

4.4 Strong Motion around Hokkaido

In this section the VSE performance in general is evaluated from timeseries analysis. Regions nearest the epicenter with a high density of stations, are selected for a comparison of records from the various sensors. The VSE series instruments are compared to each other, as well as to nearby data from accelerometer and GPS stations. By analysis of the individual timeseries, both the dynamic and static performance of the sensor can be evaluated. For the VSE-355G2, errors similar to those observed in the laboratory are repeated during the strong motions.

Though there are two networks that deploy Sokushin VSE instruments — F-Net and WISE — the most reliable indication of the performance of the instrument can be determined from the F-Net stations, as they contain sensors exactly the same as the model tested at Caltech (VSE-355G2), or the most recent predecessor (VSE-355G). Plus, these stations are located at quiet free-field vault sites. Unfortunately, there are few of them in the region of largest motions. The F-Net stations KSR and KMU (both with VSE-355G2 sensors) recorded the strongest velocities, though both instruments exhibit large velocity spikes consistent with low clipping instrument malfunction observed at Caltech. The largest motions that seem to be uncorrupted are from URH (VSE-355G), with peak velocity of $21.7 cm/s$.

All subsequent timeseries data in this sections have the instrument responses removed using the time domain method, unless stated otherwise. Timing is not synchronised between network stations, but is synchronised within networks.

In general the VSE range of instruments have a similar capacity to recover permanent displacements as accelerometers. The F-Net VSE-355G/G2 instruments, once deconvolved, are about as reliable as the K-Net and up-hole KiK-Net accelerometers. Unfortunately only a few of these instruments are located in the near-field. The WISE VSE-355EI are less capable, which may be due to being located at extremely noisy sites, having inexact

orientations, as well as having a short corner period.

The regions investigated in detail are all located in East Hokkaido, as shown in Figure 4.11. Altitude is included on this map. A range of mountains sweep southwards from the centre of the island to the southern tip closest to the epicenter. Assuming relief correlates with station site quality, this tip is the only area with many hard rock stations looked at in detail in the following analysis. It is probably no coincidence that static displacements are well recovered from this region. Unfortunately, only accelerometers are located here. Flat topography, possibly indicating basin geology, dominate the other selected regions, where ground failure was widely reported in the aftermath of the mainshock. This is reflected in general from the displacements in these regions seemingly being contaminated by large tilts.

The damage to civil infrastructure in the near-field cited in this section is from an EQE/ABS Consulting Reconnaissance Report,
`www.eqe.co.jp/pressservice/pressreport/2003Tokachi/tokachi_reportE.pdf`.
Fortunately the region was relatively sparsely populated, with few towns with large structures. Some structures, such as town halls and schools, were damaged. Widespread liquefaction and lateral spreading caused foundation failure of roads, railroads, structures, bridges and ports. A tsunami washed many fishing boats onto the ports. In general though, thanks to the sparse population and infrastructure and the good quality of construction technique (partly due to the known earthquake risk and thick wall construction for insulation against the harsh climate), damage from this large earthquake was limited.

Chapter 1 includes a discussion on how tectonic tilt can be measured from GPS, and then compared to local tilts determined by linear and quadratic trends in the seismic records. Many tilts observed in the field appear not to be due to the tectonic tilt, as they are many times larger. This is shown to include KiK-Net down-hole sites.

4.4.1 Stations near Kushiro town

There is a cluster of stations around the fishing town of Kushiro, the largest town on the East Coast of Hokkaido, about 145*km* directly North of the epicenter (Figure 4.12). F-

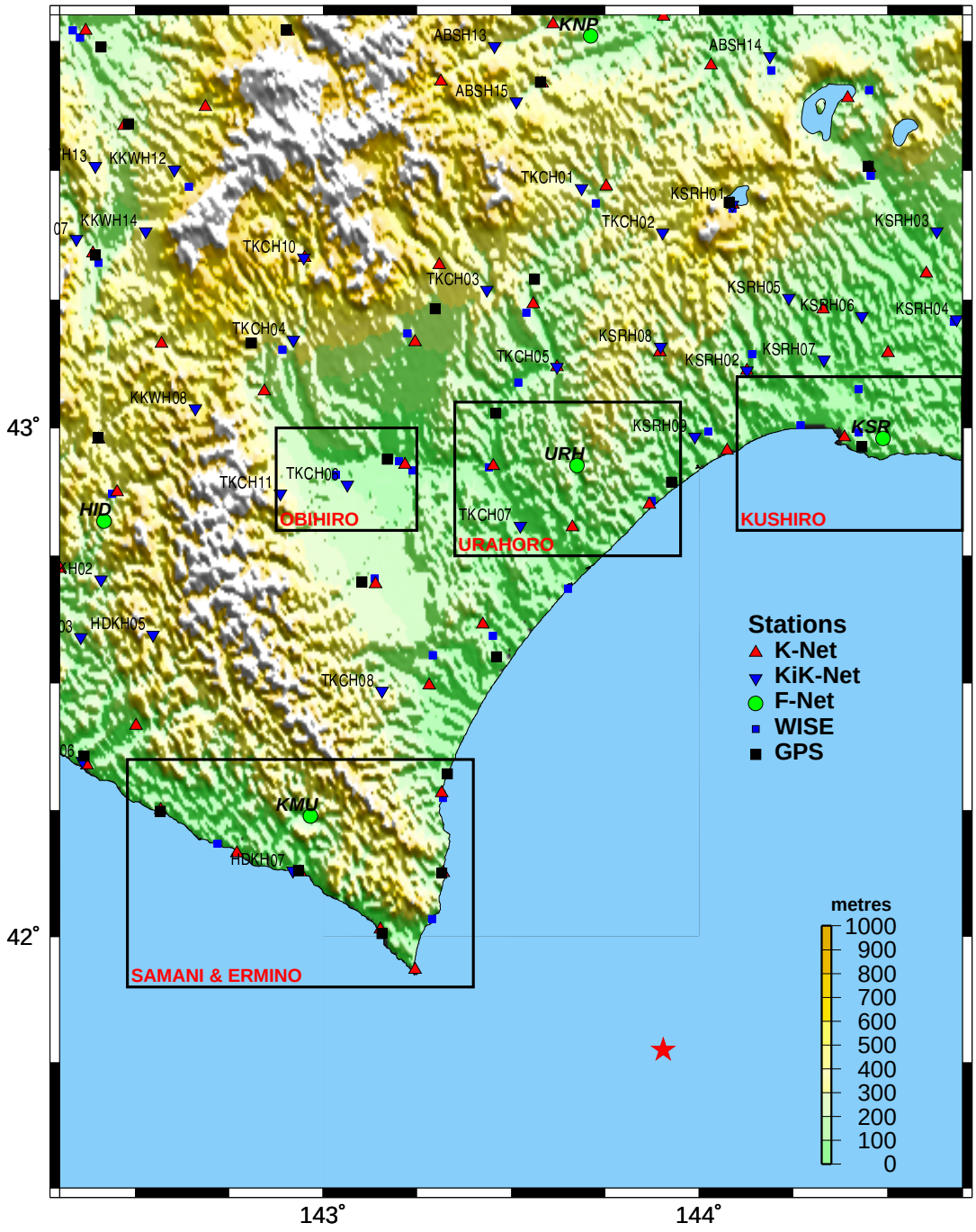

Figure 4.11: Topography and strong motion stations in East Hokkaido. Elevation in *m*. Station names for F-Net and KiK-Net stations. Star indicates M8.3 Epicenter. Boxes outline the regions where stations are compared in detail.

Net station KSR, K-Net station HKD077, and 3 WISE stations, i902k004, i907k002, and i907k003, are all within 15*km* kilometres of each other. GPS station Kushiroshi is also located in the town. Liquefaction was reported at the fishing port, and ceilings at the local airport collapsed.

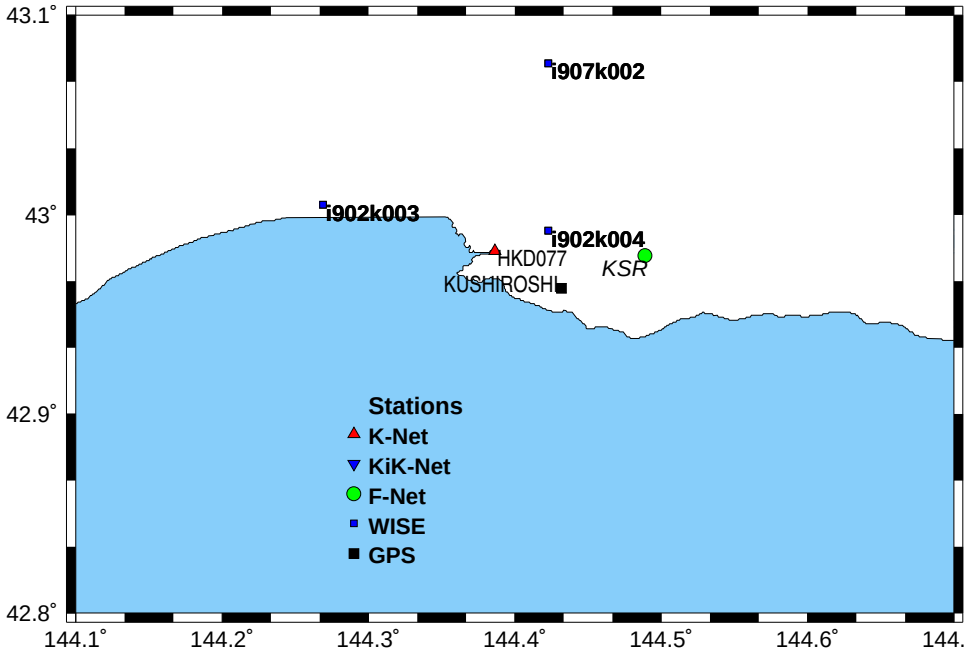

Figure 4.12: Stations near Kushiro town. Blue stations from WISE, green: F-Net, red: K-Net, black: GPS. All stations are within 15*km* of each other, and about 145*km* from the epicenter.

The F-Net station KSR has a VSE-355G2. Figure 4.13 shows the strong motion portion of the velocity trace during the earthquake. There appears to be a non-linearity in the E-W component, when the velocity swings from $-20cm/s$ rapidly to $+16cm/s$, at which stage a high frequency spike is recorded. Note the N-S component, as well as the negative E-W component, reach greater velocities (max. $23.6cm/s$), without any obvious non-linearity. Clearly a spike like this could also be caused by the sensor being struck by an object during the strong station, but this is unlikely as the spike is not observed in the other 2 components. Also, it is curious the spike occurs at about the same velocity that caused the problems in the lab. Further, spikes at this frequency are observed at the other F-Net station with a VSE-355G2, KMU, as described in the next case study.

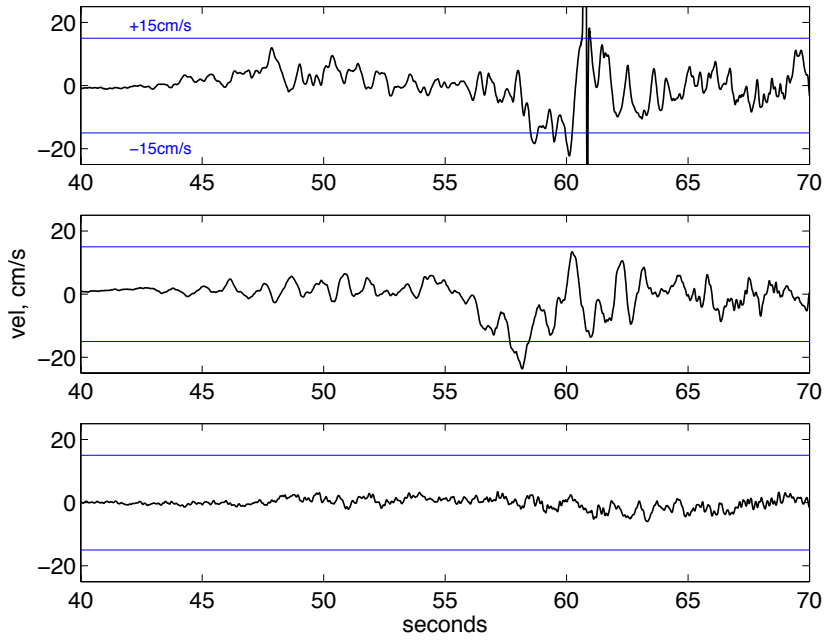

Figure 4.13: Close up of velocity trace showing F-Net KSR VSE-355G2 clipping during M8.3 earthquake. Only E-W component clips, with a high frequency spike at 61*s*. N-S component reaches 23.6cm/s without clipping. Top: E-W; middle: N-S; bottom: vertical.

Figures 4.14, 4.15 and 4.16 present the deconvolved acceleration, velocity and displacement records from all the Kushiro town stations. Timing is not synchronised between networks. In the figures, WISE station i902k003 clearly has a strong resonance frequency, which indicates it is located at a structure, and does not have a free-field response. The response at high frequencies is dominated by the structural response, as seen from the velocity and acceleration. Due to this resonance, velocities over 150cm/s, and accelerations over 0.4*g*, are recorded (without clipping) for this VSE-355EI.

The acceleration and velocity traces are very noisy for all the stations other than the F-Net KSR — from this group of stations, only KSR is located at a quiet site. Nonetheless, velocities of similar size to the KSR spike are observed at the other stations. The acceleration spike caused by the velocity jump at KSR is anomalously high though, near 6*g*, many times larger than any other peaks at KSR, or at any other nearby station.

The GPS station Kushiroshi records a static offset of 16.1*cm* to the East, 7.09*cm* to the North and 1.2*cm* of uplift. In Figure 4.16, it is clear no instrument exactly recovers this

displacement once the strong shaking has stopped. The K-Net station HKD077 and the F-Net station KSR displacements are similar to the GPS offset about $30-40s$ after strong motion begins, after which the time domain integration scheme becomes unstable, or the land tilts, causing the observed non-physical deviations. The E-W F-Net channel, shown to clip in Figure 4.13, is initially similar to the K-Net station, but becomes unstable after $60s$, when the clipping occurs. Permanent offsets are difficult to estimate from the WISE stations, which have very unstable displacement timeseries.

Figures 4.17 and 4.18 are similar to Figures 4.15 and 4.16, but a bandpass filter between $50s$ and $5s$ has been applied, to remove the static offset and the high frequecy components that are highly variable from site to site. In these plots, the K-Net and the F-Net stations (the only stations assured to be in free-field sites) are very similar for all 3 components. The WISE station i902k003 has a response dominated by a $3-4s$ resonance, the structural resonance previously mentioned. The two other WISE stations have similar Z-component velocities and displacements, but it seems the N-S channel on i902k004 and the E-W channel on i907k002 are inverted, as well as the i907k002 E-W channel. These problems illustrate why the displacement field from the WISE network in Figure 4.5 is characterised by highly variable azimuths not commensurate with the GPS.

4.4.2 Stations near Samani town

There are a number of stations in the vicinity of the small fishing village of Samani, near the South-East tip of Hokkaido, one of the regions closest to the epicenter — see Figure 4.19. This section analyses waveforms from the stations nearby and to the west of Samani village: F-Net station KMU, K-Net stations HKD109 and HKD108 (HKD110 did not record during the event), KiK-Net station HDKH07, and WISE station i306k003, are all within $20km$ of each other, except HKD108, which is about $30km$ directly west of KMU. Stations to the East, the closest set of stations to the epicenter, are discussed in the next subsection. Schools in this region reported minor damage.

The F-Net station KMU, at Kamikineusu, has a VSE-355G2. Figure 4.20 shows the strong motion portion of the velocity trace during the event. All 3 channels on the sensor

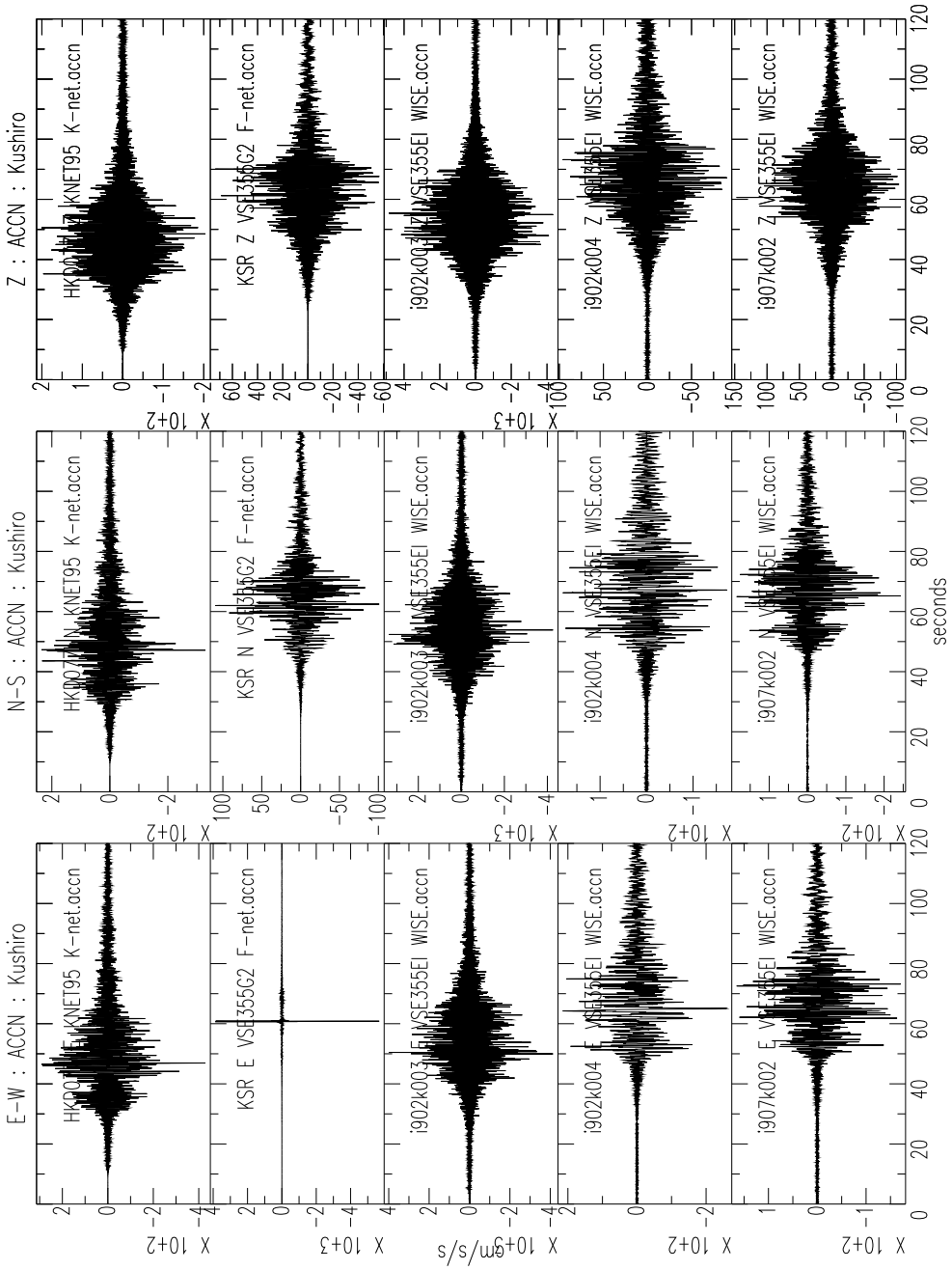

Figure 4.14: Acceleration timeseries from the stations located near Kushiro town. Note the anomalously large acceleration spike at KSR E-W component.

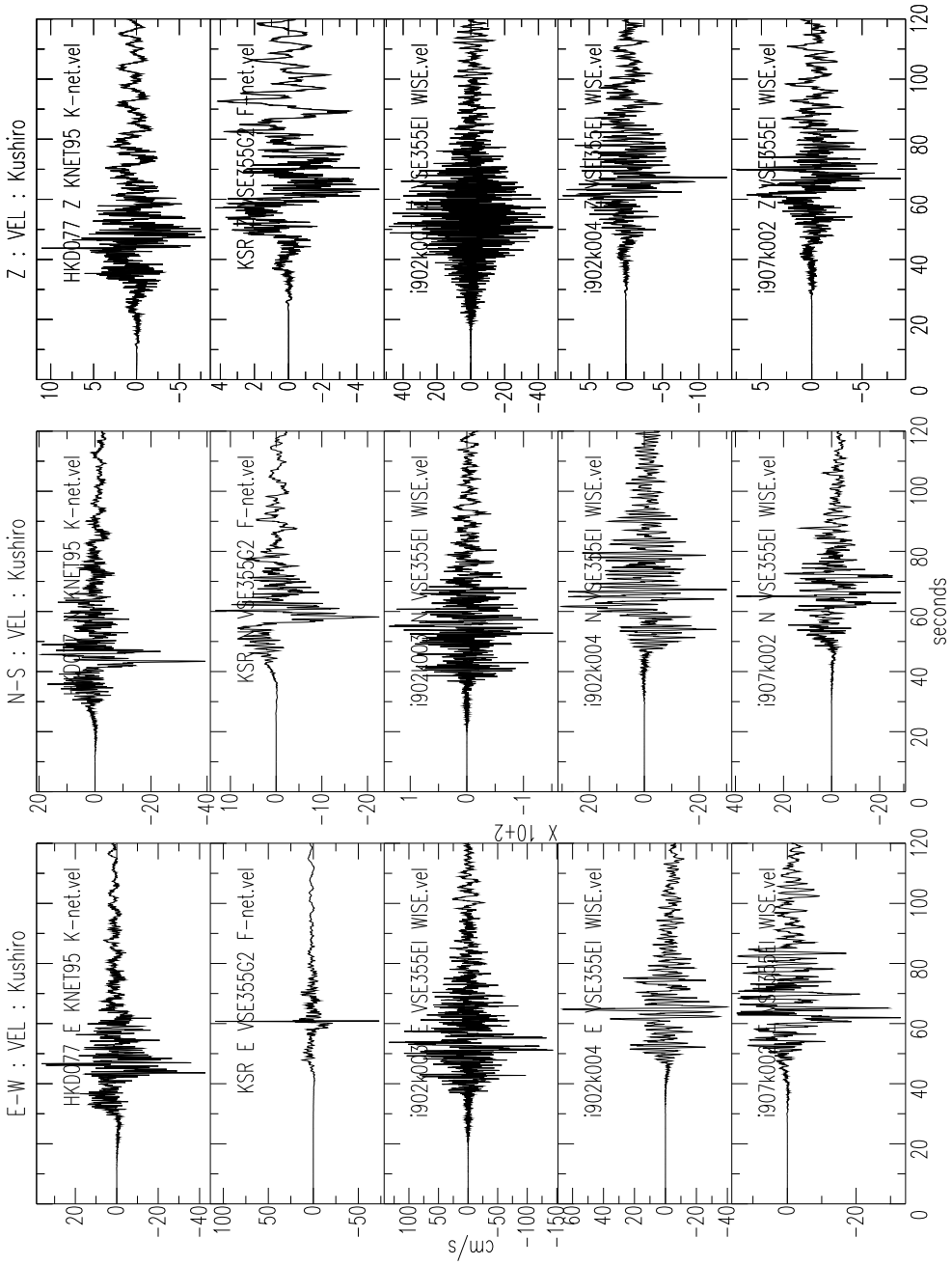

Figure 4.15: Velocity timeseries from the stations located near Kushiro town. Note the anomalously large velocity spike at KSR E-W component.

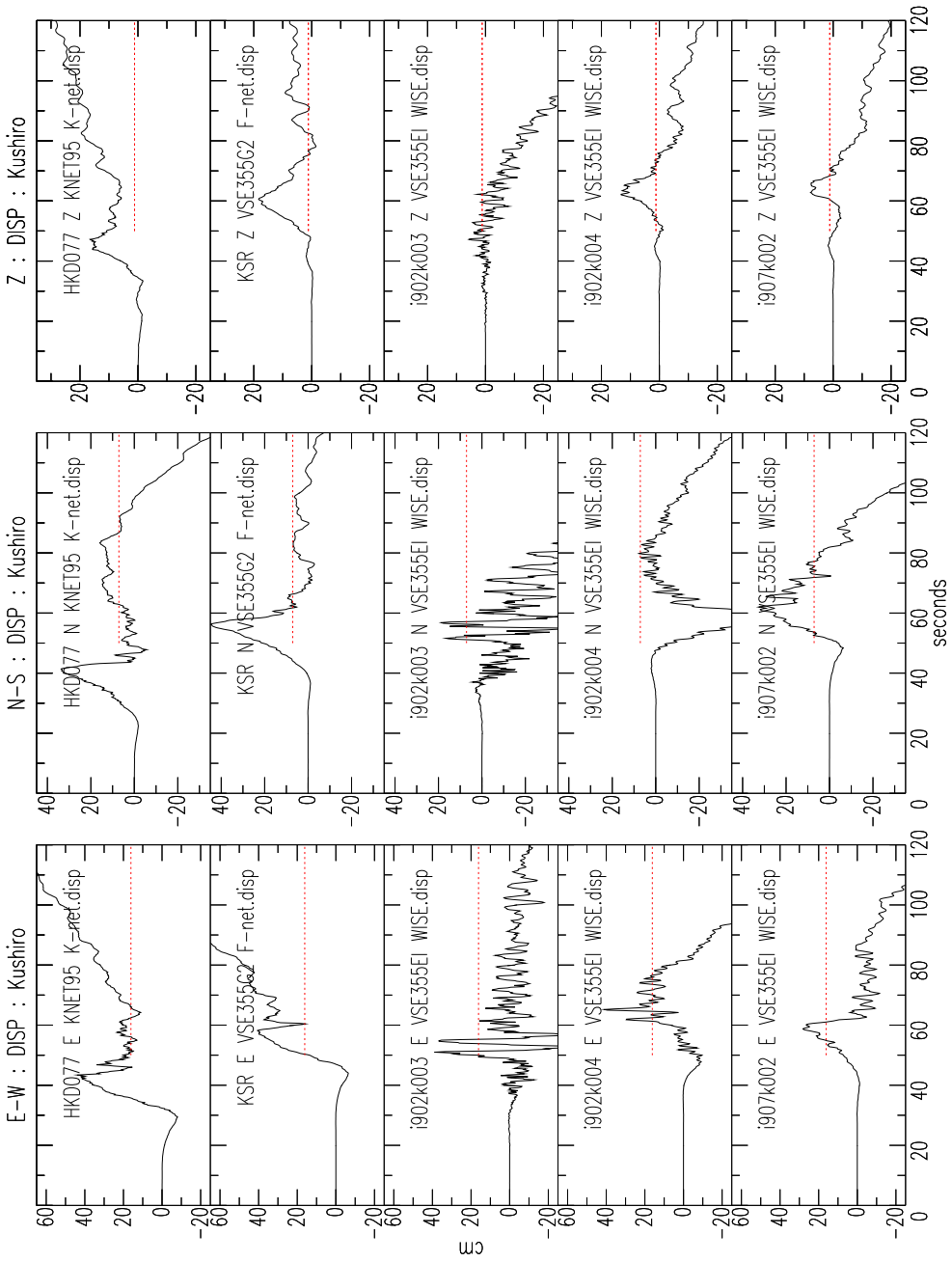

Figure 4.16: Displacement timeseries from stations near Kushiro town. GPS Stn Kushiroshi offsets are 16.1*cm* East, 7.09*cm* North and 1.2*cm* uplift, indicated by the dotted lines. No seismometer measures this change exactly. The K-Net components show similar displacements after 70*s*, although then the signal deviates. The F-Net N and Z components are also close to the static offset after about 90*s* before deviating, and the E component, has similar to behaviour to the K-Net E component until clipping occurs at $\sim 60s$. WISE instruments all perform poorly.

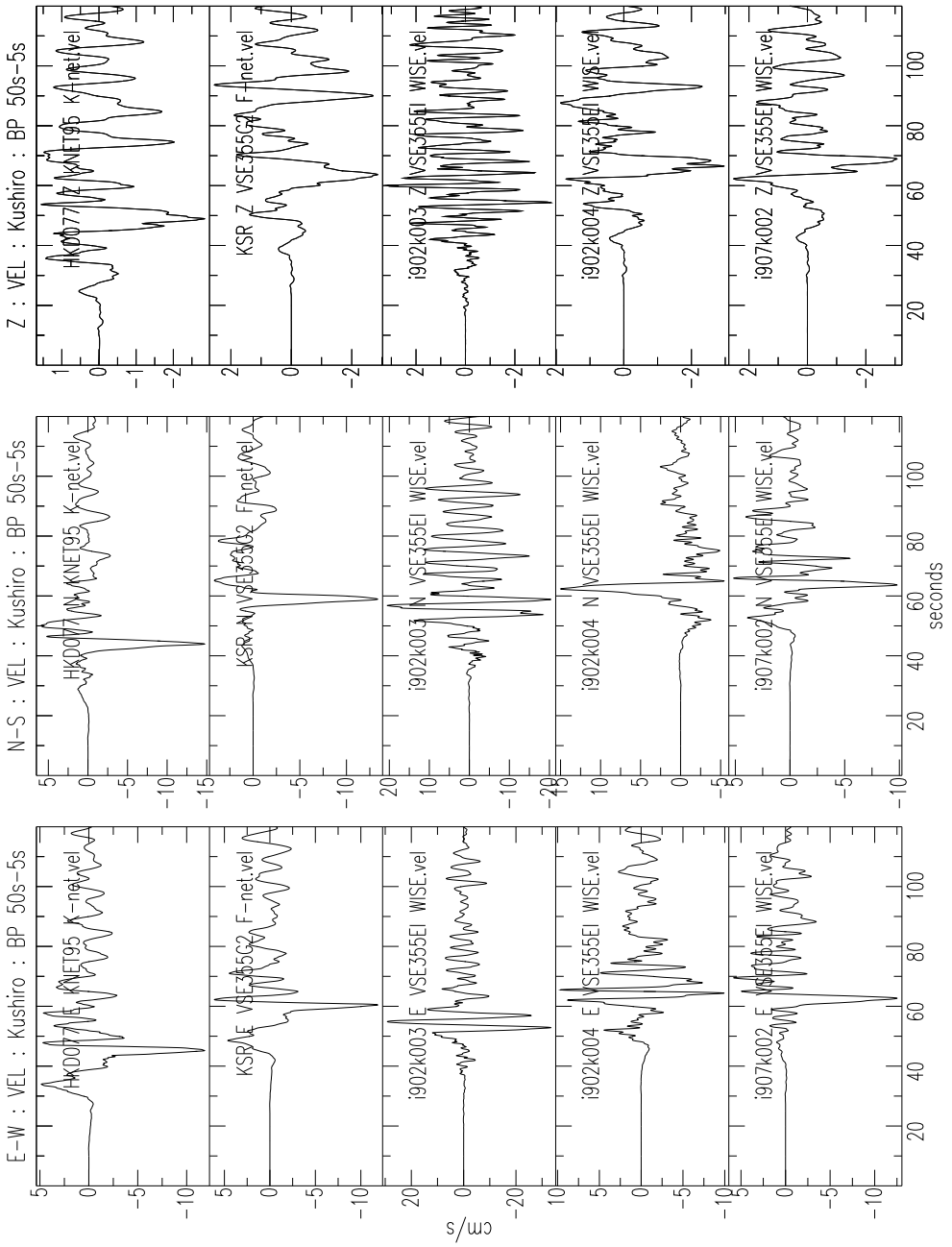

Figure 4.17: Velocity timeseries from the stations located near Kushiro town. Bandpass from 50s — 5s. Note similarities between K-Net (top trace) and F-Net (2^{nd} trace) stations, the free-field sites. WISE station i902k003 is dominated by a structural resonsnace at $\approx 3.5s$

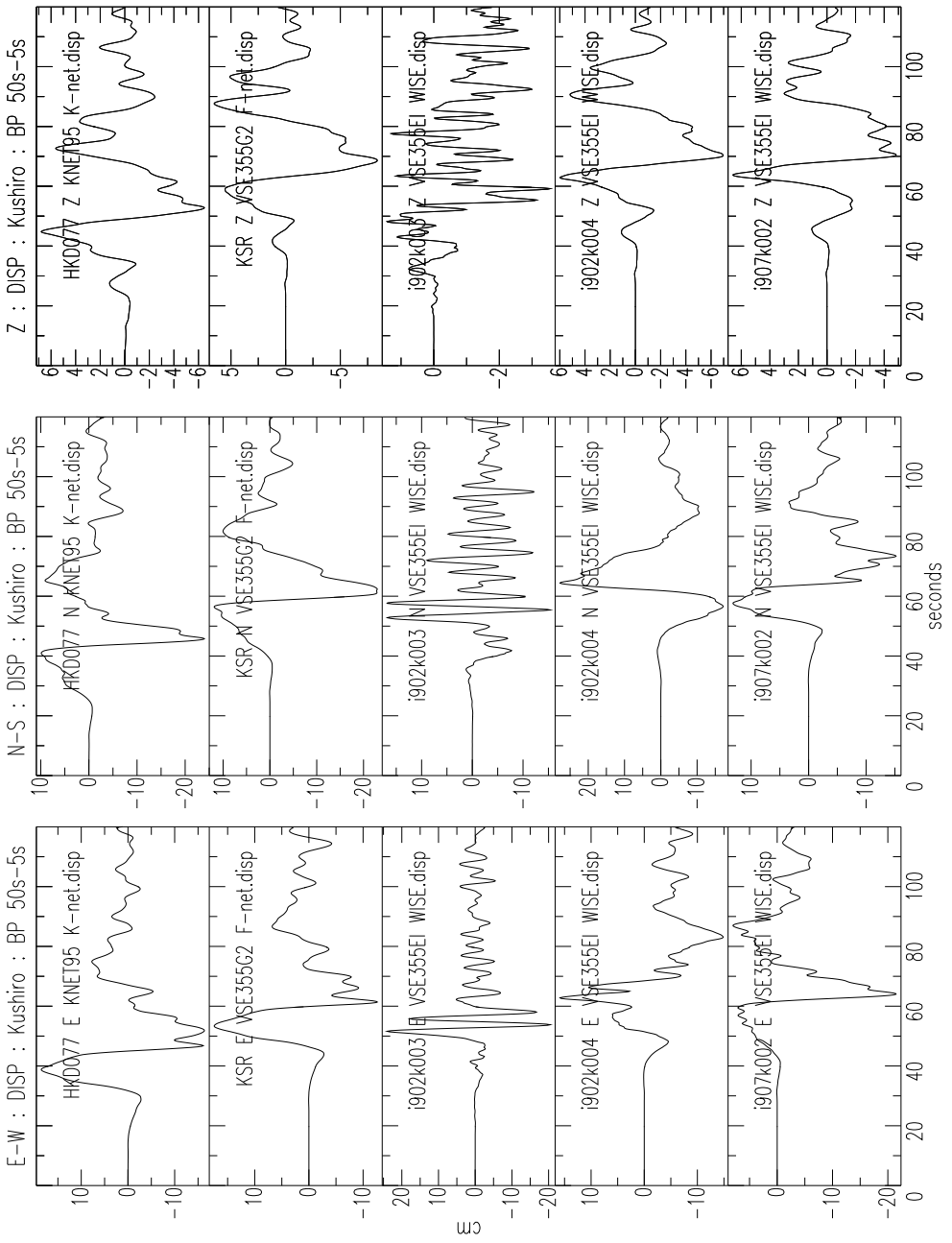

Figure 4.18: Displacement timeseries from the stations located near Kushiro town. Band-pass from 50*s* — 5*s*. Note similarities between K-Net (top trace) and F-Net (2^{nd} trace) stations, the free-field sites. i902k003 is dominated by a structural resonance. i902k004 N-S and i907k002 E-W appear to be inverted.

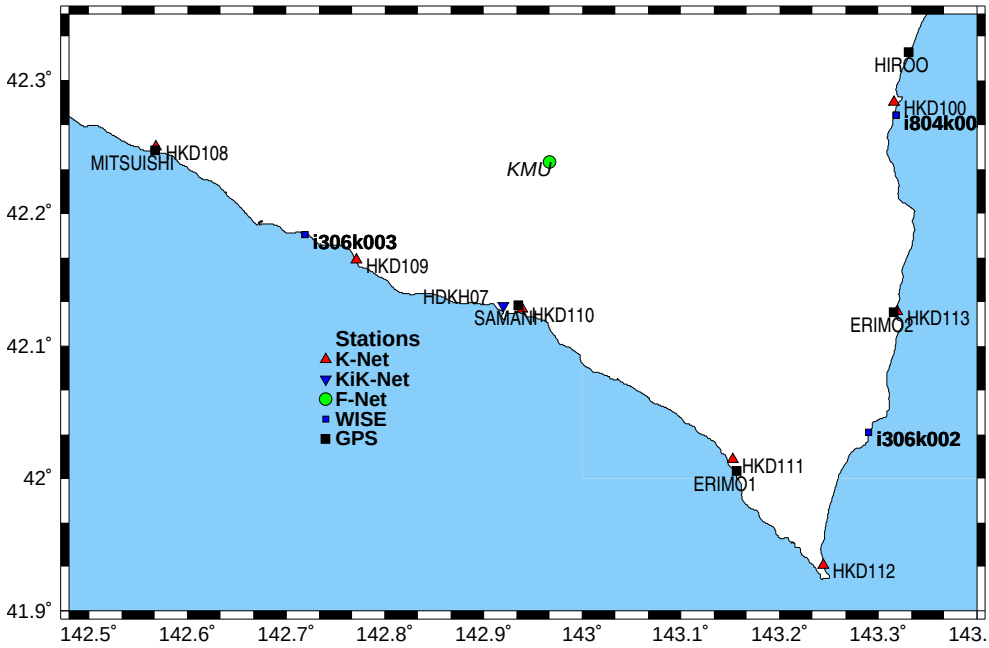

Figure 4.19: Stations near Samani and Erimo towns. Blue stations from WISE, green: F-Net, red: K-Net, black triangle: KiK-Net, black square: GPS. The villages are near the GPS stations with the same name. Station KMU is 94*km* from the epicenter.

show some corruption, a 'clip' occurs when the velocity exceeds $\sim \pm 16 cm/s$ — as seen by the spikes in velocity, often followed by a short rest at this 'clip velocity', as if the mechanical pendulum is resting at its maximum displacement 'stop'. This is similar to the behaviour observed at Caltech, though in the lab the rest at clip velocity was longer (Figure 3.21). This may be due to the violent high frequency velocity cycles characteristic of this strong motion — velocity reversals move the pendulum away from the 'stops' back 'on-scale'. These velocity reversals were not present in our cart tests — the cart was pushed with monotonically increasing displacement, with much smaller changes in accelerations. The likelihood of these clips being caused by external objects banging the sensor is small, as at times only certain channels clip at a given instant, and, unlike at station KSR, there are very many clip spikes on all 3 components.

Figures 4.21, 4.22 and 4.23 present the acceleration, velocity and displacement records from all the Kushiro town stations. Timing is not synchronised between networks. For the F-Net station KMU, the clipping is observed to produce non-physical (at least from

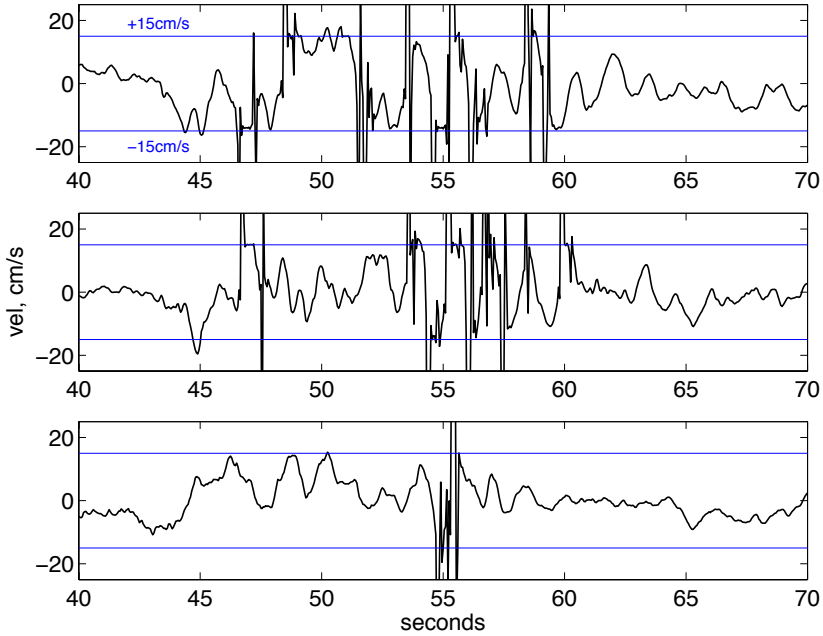

Figure 4.20: Close up of velocity trace showing F-Net KMU VSE-355G2 clipping during M8.3 earthquake. Clipping occurs when velocities are greater than $\sim \pm 15 cm/s$, with short plateau at this level after clip, until a velocity reversal. Top: E-W; middle: N-S; bottom: vertical.

the earthquake) high frequency spikes in the acceleration record of at least $3g$ in every channel. The clips do not have much obvious impact on the displacement time series, as stable (though incorrect) static displacements are recorded on 2 channels.

The velocity and acceleration timeseries from the down-hole KiK-Net site look very much like the up-hole with a lowpass filter. The filtered velocity and displacement traces, with bandpass of $50s$ to$5s$, in Figures 4.24 and 4.25 show this is indeed the case. The K-Net station has a linear trend in velocity beginning during the strongest motion, which is a good indication of tilting at the site. The slope of the velocity is $\sim 0.2 cm/s^2$, equivalent to a tilt of 0.01^o. A tilt 10 times bigger, of 0.1^o would cause the linear trend observed at the WISE station. The tectonic tilt in the region can be determined from the GPS stations at Samani and Mitsuishi. The elevation change due to the earthquake is $-22.2cm$ at Samani, and $-14.4cm$ at Mitsuishi, so there is a rise of $7.8cm$ from Samani to Mitsuishi. Samani is about $10km$ south, and about $30km$ east of Mitsuishi, so the maximum tectonic tilt (Equation 1.16) should be in the N-S component, and be of the order of 0.00045^o, with tilting to the north,

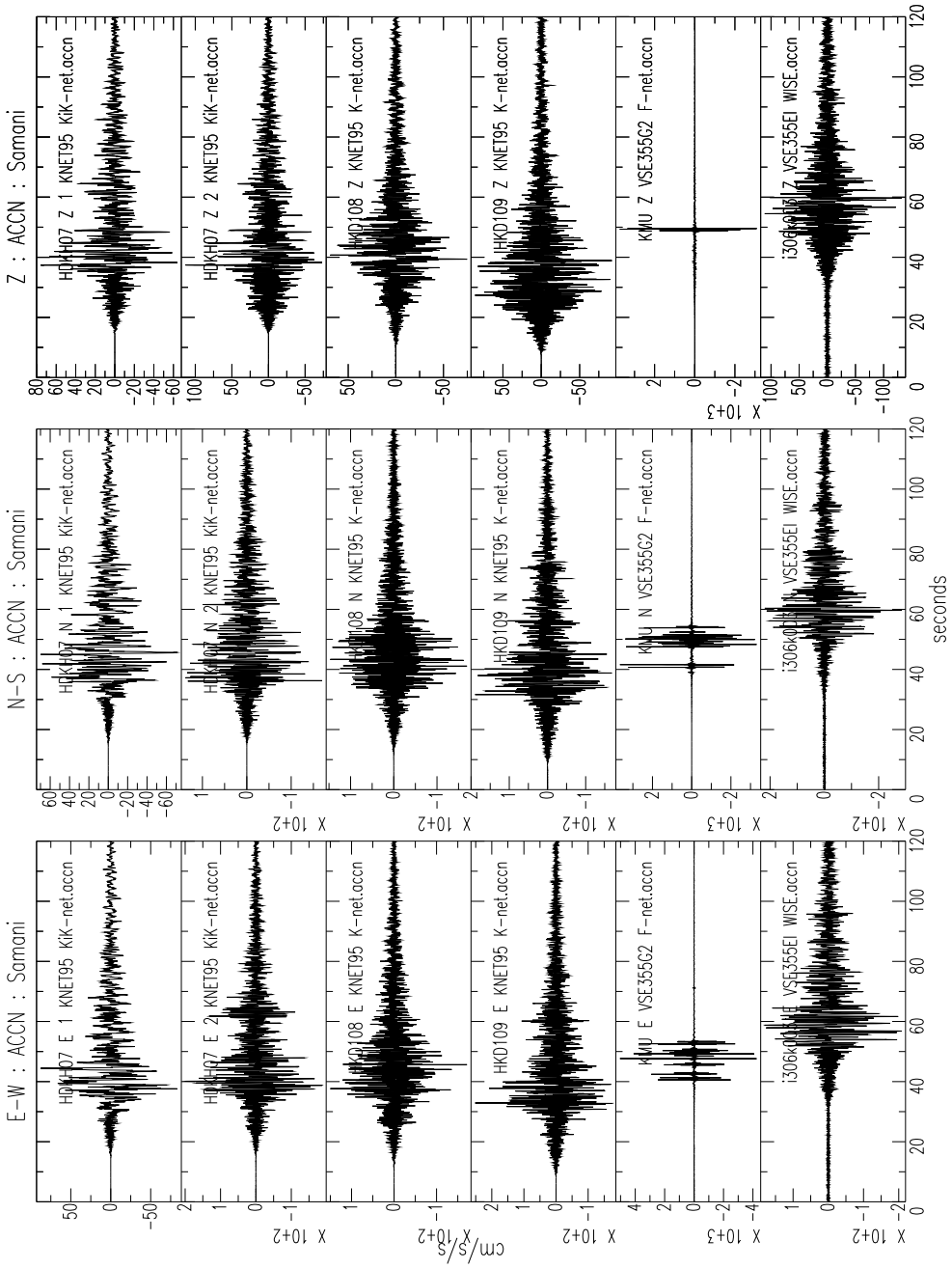

Figure 4.21: Acceleration timeseries from the stations located near Samani town. Note the anomalously large acceleration spikes in all KMU channels. KiK-Net stations: '1': Down-Hole, '2': Up-Hole.

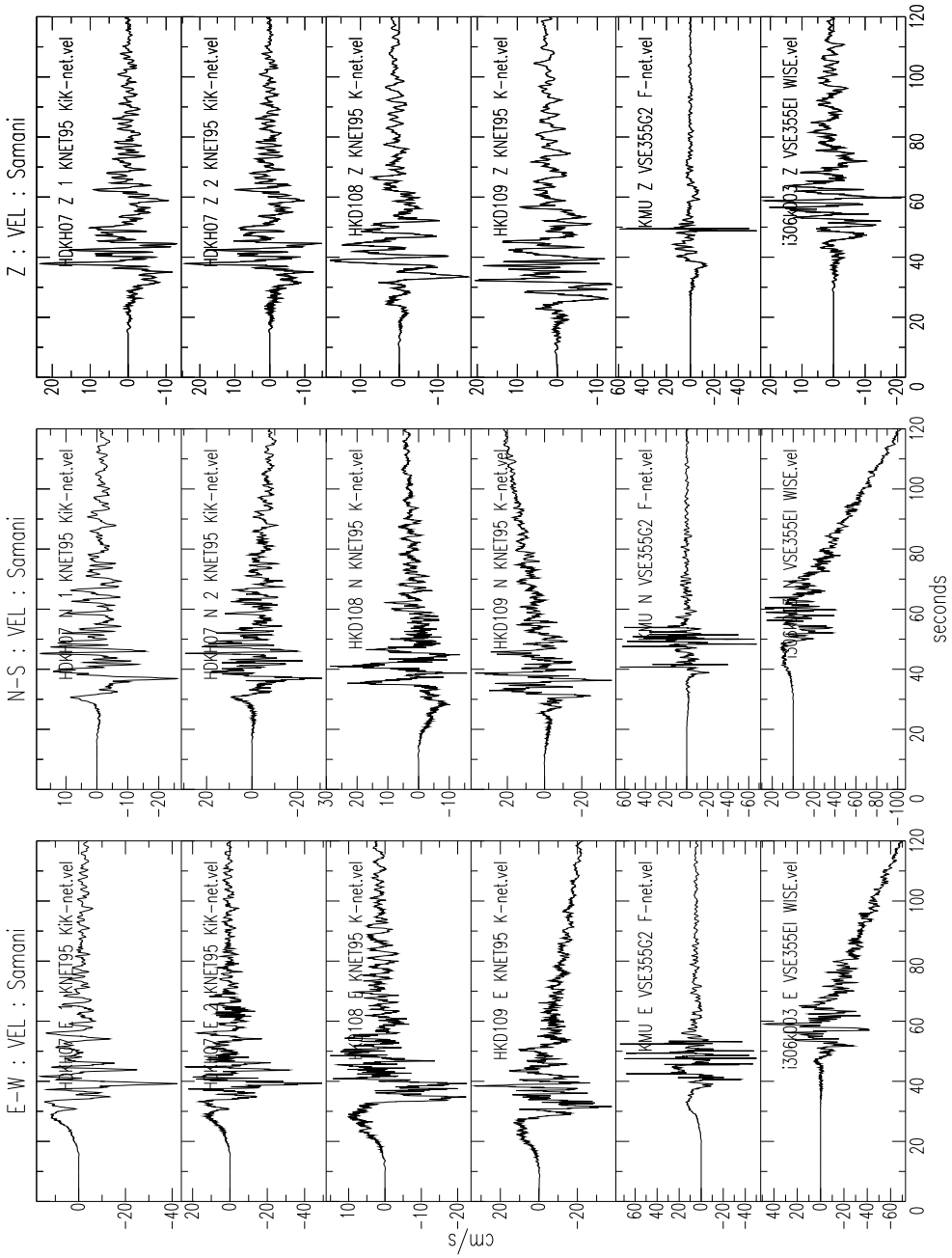

Figure 4.22: Velocity timeseries from the stations located near Samani town. Note the anomalously large velocity spikes in all KMU channels. KiK-Net stations: ‘1’: Down-Hole, ‘2’: Up-Hole.

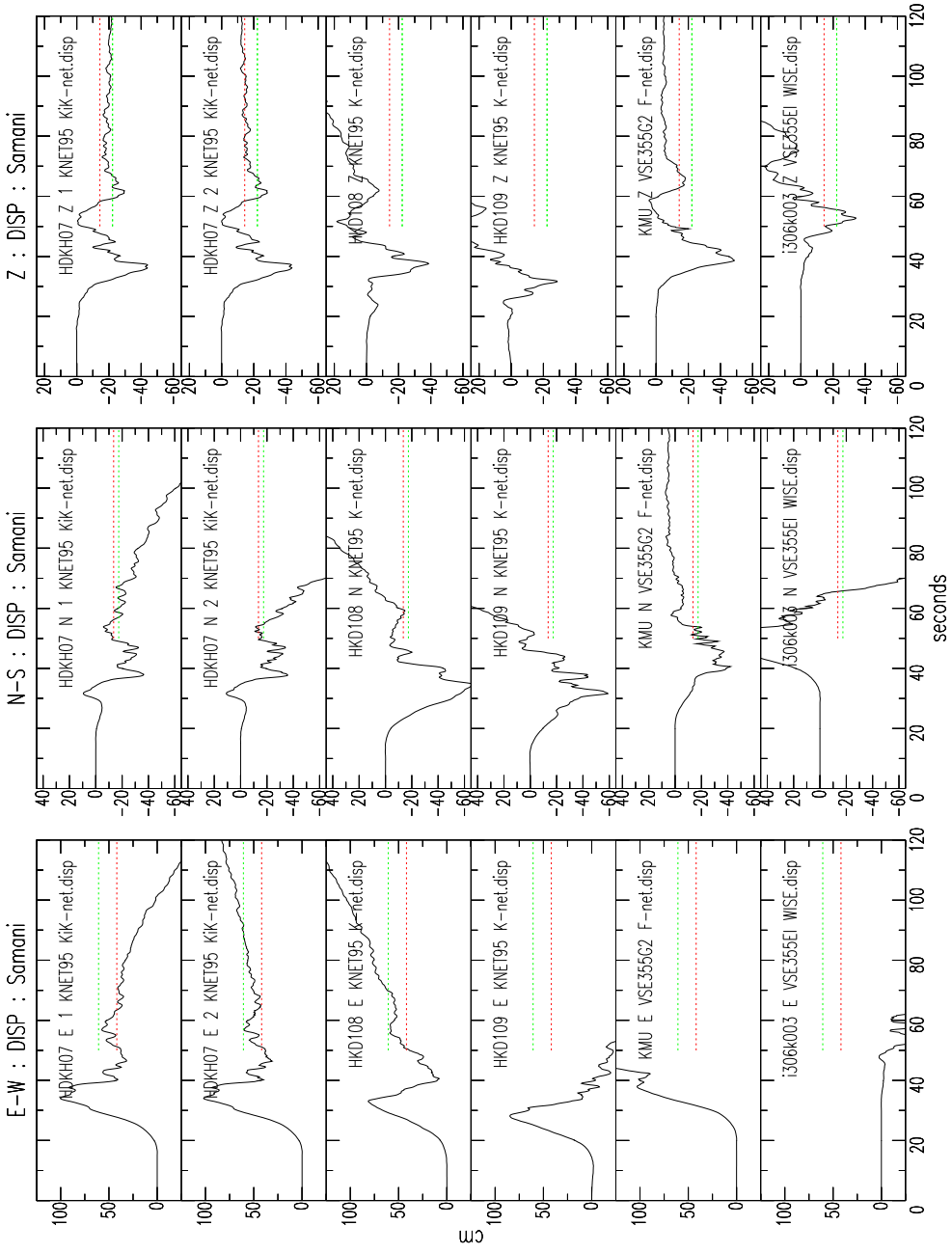

Figure 4.23: Displacements from stations near Samani town. GPS stations Samani records 60.7*cm* East, 17.4*cm* South and 22.2*cm* vertical drop, Mitsuishi records 41.8*cm* East, 13.6*cm* South and 14.4*cm* vertical drop, with similar final displacements for HKD111, and HKD109 after $\sim 70s$ (although then the signal deviates). The VSE instruments perform poorly, only KMU N-S and Z have stable offsets, which differ from GPS. KiK-Net stations: '1': Down-Hole, '2': Up-Hole.

leading to positive offsets for the N-S channels. The tilts observed in practice are well over an order of magnitude higher than this, and for the WISE station, in the other direction.

In Figure 4.23, the KiK-Net stations also appear to suffer some tilt, though for the E-W channels, do so in opposite directions. If it assumed the general form of the deviation from the permanent offset is due to a quadratic function, as expected for a tilt, the tilt can be estimated using Equation 1.19. For the N-S down-hole KiK-Net channel, a displacement of $-70cm$ occurs from time $50s$ to $100s$. This is equivalent to 0.0033^o, and not only is this still an order of magnitude higher then the tectonic tilt, it is in the wrong direction. The tectonic tilt has a negligible effect at these levels of displacements.

The GPS station Samani records a static offset of $60.7cm$ to the East, $17.4cm$ to the South and $22.2cm$ of vertical drop. In Figure 4.23, it is clear no instrument nearby recovers the horizontal displacements once the strong shaking has stopped. Both the up-hole and the down-hole KiK-Net station HDKH07 do record a large, stable permanent offset for the vertical channel, of $15cm$ drop up-hole, and $19.8cm$ drop down-hole. These are remarkably similar to the Samani GPS station only a few km away. In contrast, although the VSE-355G2 F-Net instrument recorded a relatively stable static offset in 2 components, both components are at least $15cm$ offset from the closest GPS.

The WISE station i306k003 has a very sharp change in velocity at $70s$, when a large linear trend begins. The displacement timeseries in Figure 4.25 show that after about $70s$, both the E-W and N-S components have a sharp change in displacement that is not consistent with other station displacements, deviating away from the expected zero displacements observed for the other instruments. The onset of this unusual behaviour coincides with a small amplitude long period response in the velocity, which is very similar to the response of the instrument to a step in acceleration. This was illustrated in the lab in the top sub-figure of Figure 3.12. The resultant integrated output, as seen in the lower subplot, has a permanent offset, which explains the observed displacement for these channels. [Note these are VSE-355EI, with corner frequency at $55s$, not the $\sim 80s$ period of the VSE-355G2.] This could arise from some instrument error, or severe ground failure at the site.

Kristine Larson (*personal communication*) has determined the $1sps$ high-rate GPS data from Mitsuishi. In Figure 4.26, this GPS data and the K-Net station HKD106 displacement

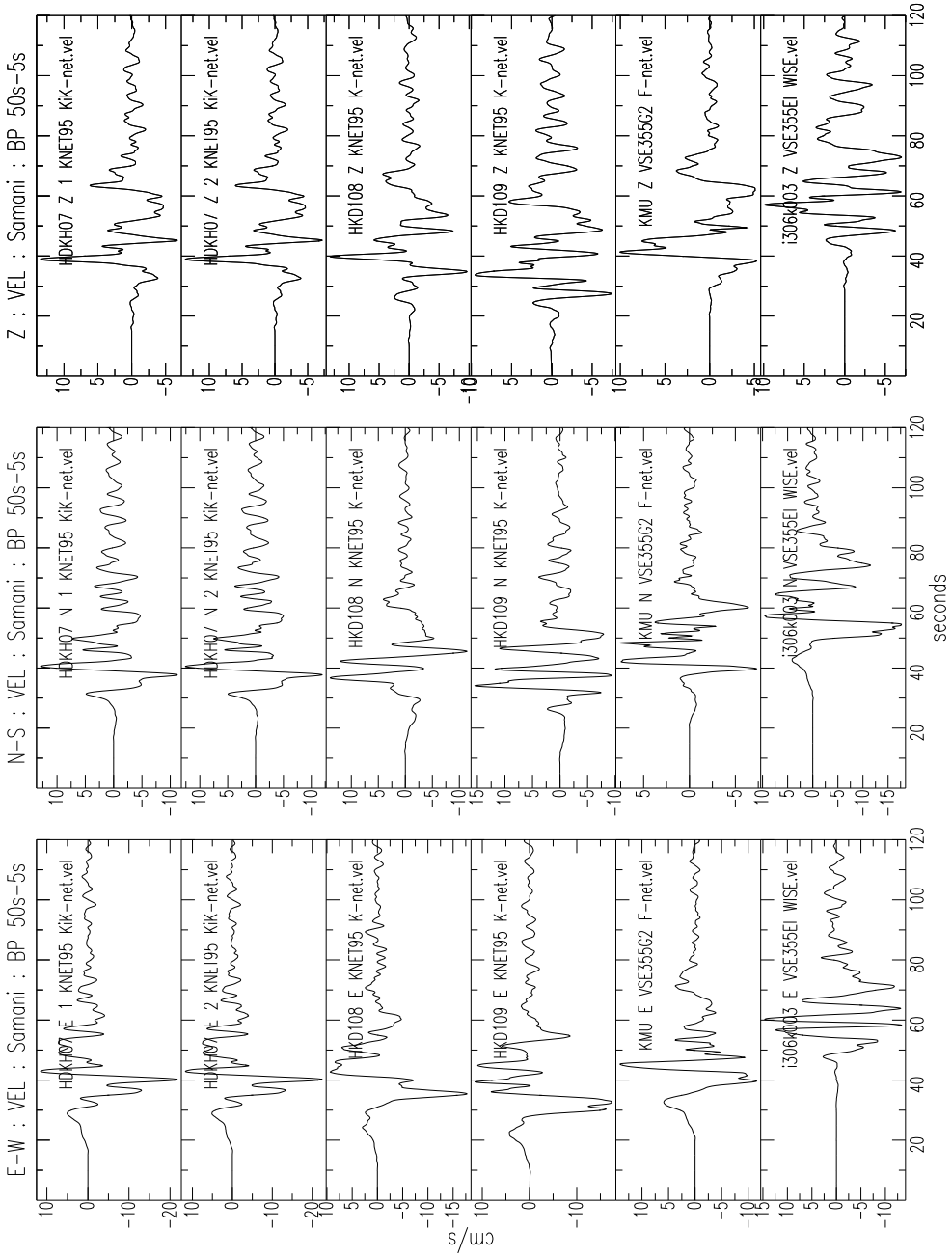

Figure 4.24: Velocity timeseries from the stations located near Samani town. Bandpass from 50*s* — 5*s*. Note similarities between KiK-Net (top 2 traces), K-Net (3^{rd}, 4^{th} traces) and F-Net (bottom trace) stations, at free-field sites. KiK-Net stations: '1': Down-Hole, '2': Up-Hole.

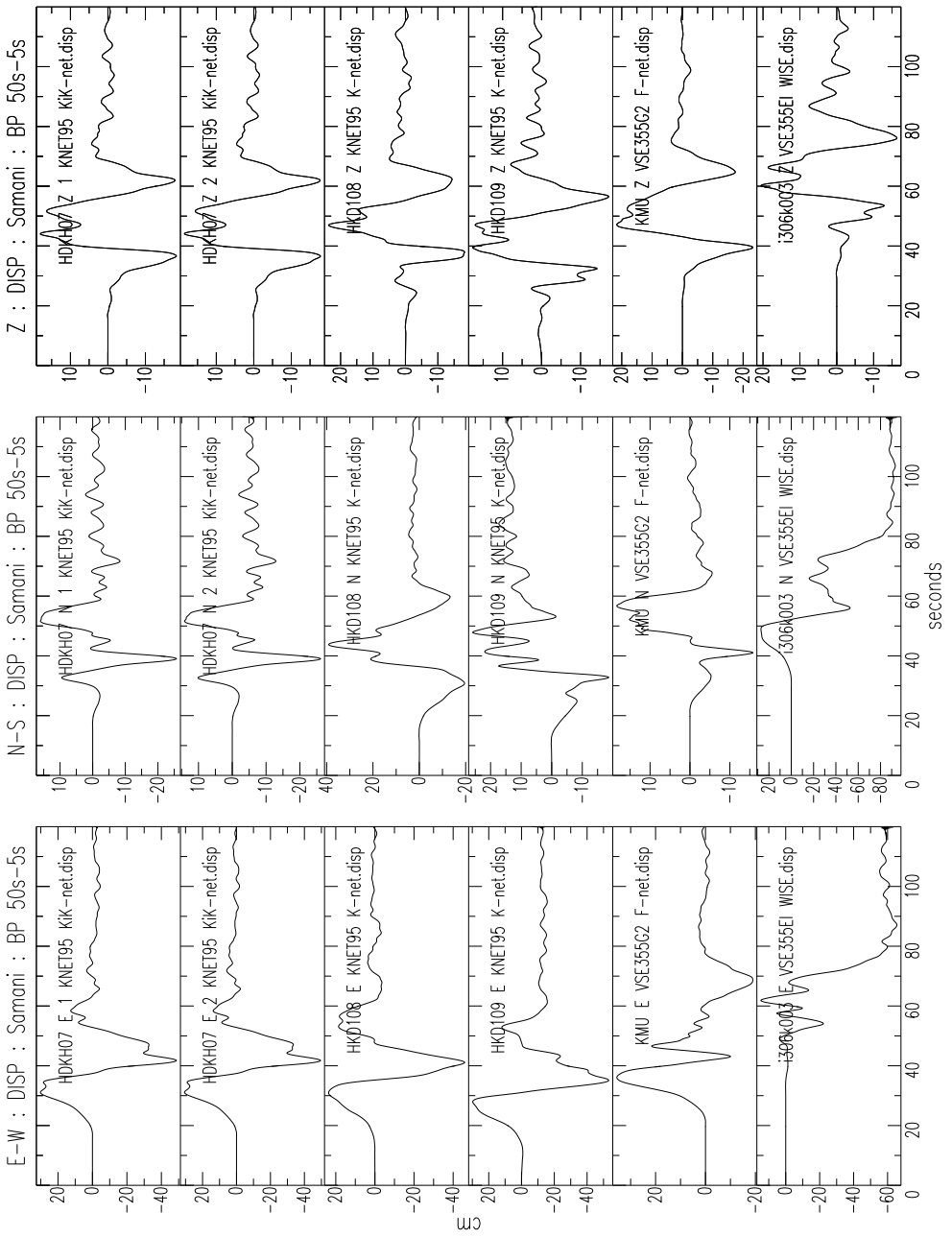

Figure 4.25: Displacement timeseries from the stations located near Samani town. Band-pass from 50s — 5s. Note similarities between KiK-Net (top 2 traces), K-Net (3^{rd}, 4^{th} traces) and F-Net (bottom trace) stations, at free-field sites. KiK-Net stations: '1' : Down-Hole, '2': Up-Hole.

timeseries are compared. These stations are within 1km of each other. The K-Net station has apparent tilt, which distorts the records after about 50s of motion. The GPS station suffered a power outage about 20s after the strong motion began, but regained transmission after about 170s, recording the static offset for the earthquake.

In the early part of the motions, which is well recorded by both sensors, the displacements are similar, especially for the Vertical motions. The timing and shape of the E-W motion are also similar, though the peak magnitude of the initial swing is reduced from about 100cm on the GPS to about 85cm in the accelerometer. The N-S motions are quite different for both stations. It is expected large offsets in this direction would take place concurrently with the E-W component. This is the case for the K-Net station, though the GPS station does not record large N-S motion for about 10s after the E-W motions begin, which is the same time as the Vertical motion begins. Further investigation showed that if the horizontal components of the accelerometer is rotated, a much better fit can be obtained. The timing problem was also resolved, once the GPS leap seconds were taken into account, and actual trigger times were found for the accelerometers. Figure 4.27 presents this rotated data. Amplitudes and phase are very well matched. Tilting is clearly a problem at this site, though for the E-W channels, the offset at 80s, just before the tilting becomes large, is very similar to the 7day GPS average. For the N-S component, the accelerometer displacements deviated from the GPS very early on in the strong motion, before the 1sps GPS data is lost, indicating tilting concurrent with the onset of the strong motion. If this quality data can be determined for the entire timeseries, timeseries for both rotations about the horizontal axes, and the 3 translations, can be well determined by inversion methods.

4.4.3 Stations near Erimo

The closest region to the epicenter is located to the East of Samani, near Erimo town. There are a number of K-Net and Wise stations along the coastline in this area (see Figure 4.19). The largest displacements were recorded at these stations. Figures 4.28 and 4.29 present the deconvolved displacement and bandpassed velocity timeseries respectively.

The K-Net station HKD111 is very close to the GPS station Erimo1 (Figure 4.19). The

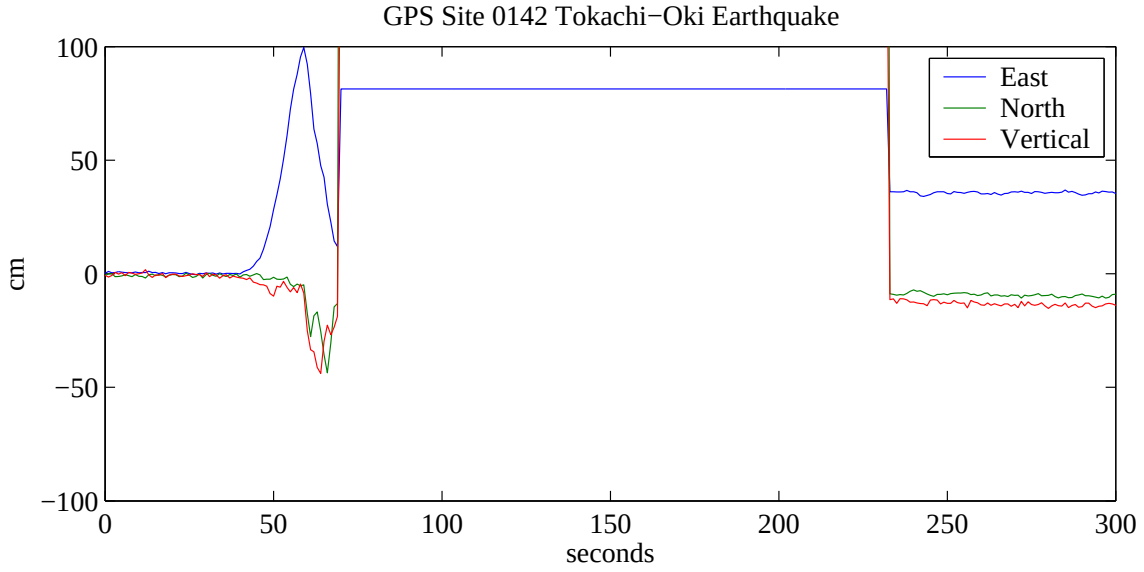

(a) 1*sps* GPS at Mitsuishi

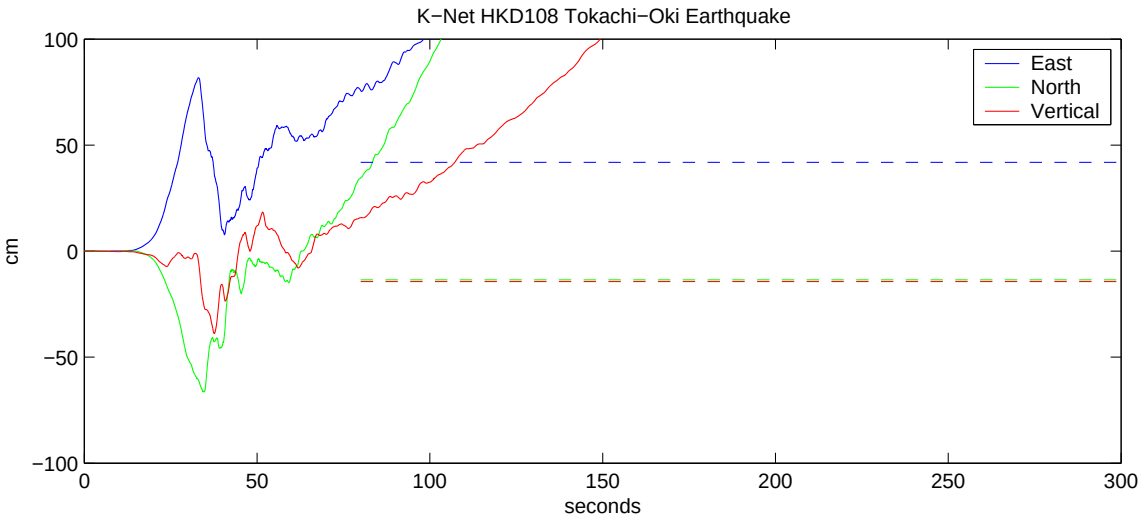

(b) 100*sps* Accelerometer at HKD108

Figure 4.26: High-rate GPS vs. accelerometer displacement timeseries for K-Net and GPS stations at Mitsuishi. GPS timing is 13*s* fast. 7*dy* average GPS offsets included on K-Net plot. high-rate GPS data was lost after 25*s* of the strong motion, and recovered about 170*s* later.

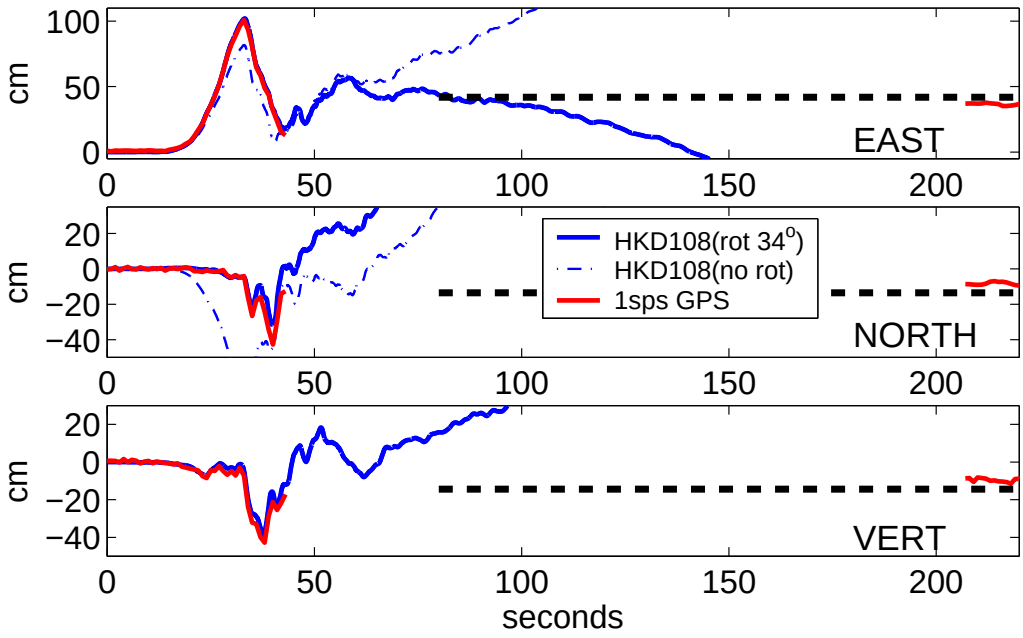

Figure 4.27: High-rate GPS vs. accelerometer displacement timeseries for K-Net and GPS stations at Mitsuishi. Accelerometer horizontal channels are rotated 34^o clockwise to best fit GPS. 7*dy* average GPS offsets included.

GPS station records a static displacement of 62.7*cm* to the East, 17.3*cm* to the South and 18.9*cm* of vertical drop. The final offsets estimates at this K-Net station are 48.4*cm* East, 18.1*cm* south, and 6.5*cm* vertical drop (though in retrospect, from Figure 4.28, this could easily have been chosen as $-20cm/s$, but the static offsets were estimated independently of the GPS). These are remarkably similar to the GPS. K-Net station HKD112 is the closest station to the epicenter, and is about 15*km* south-east of Erimo1, at the South-Eastern-most tip of Hokkaido. Permanent offsets determined at this station are also remarkably free of tilt, and are very similar to HKD111. The 2 other K-Net stations and the WISE stations located on the Eastern coastline, all show very large tilts, which in some cases even causes large non-physical trends on the vertical component.

Bandpassed velocities for these stations shown in Figure 4.29 confirm the similarity of K-Net stations HKD111 and HKD112, and show once again WISE stations may have inverted horizontal orientations. Motions from the WISE station i804k004 do not appear to be from a VSE-355EI instrument, as they are much smaller in magnitude than other nearby motions, and have higher frequency content.

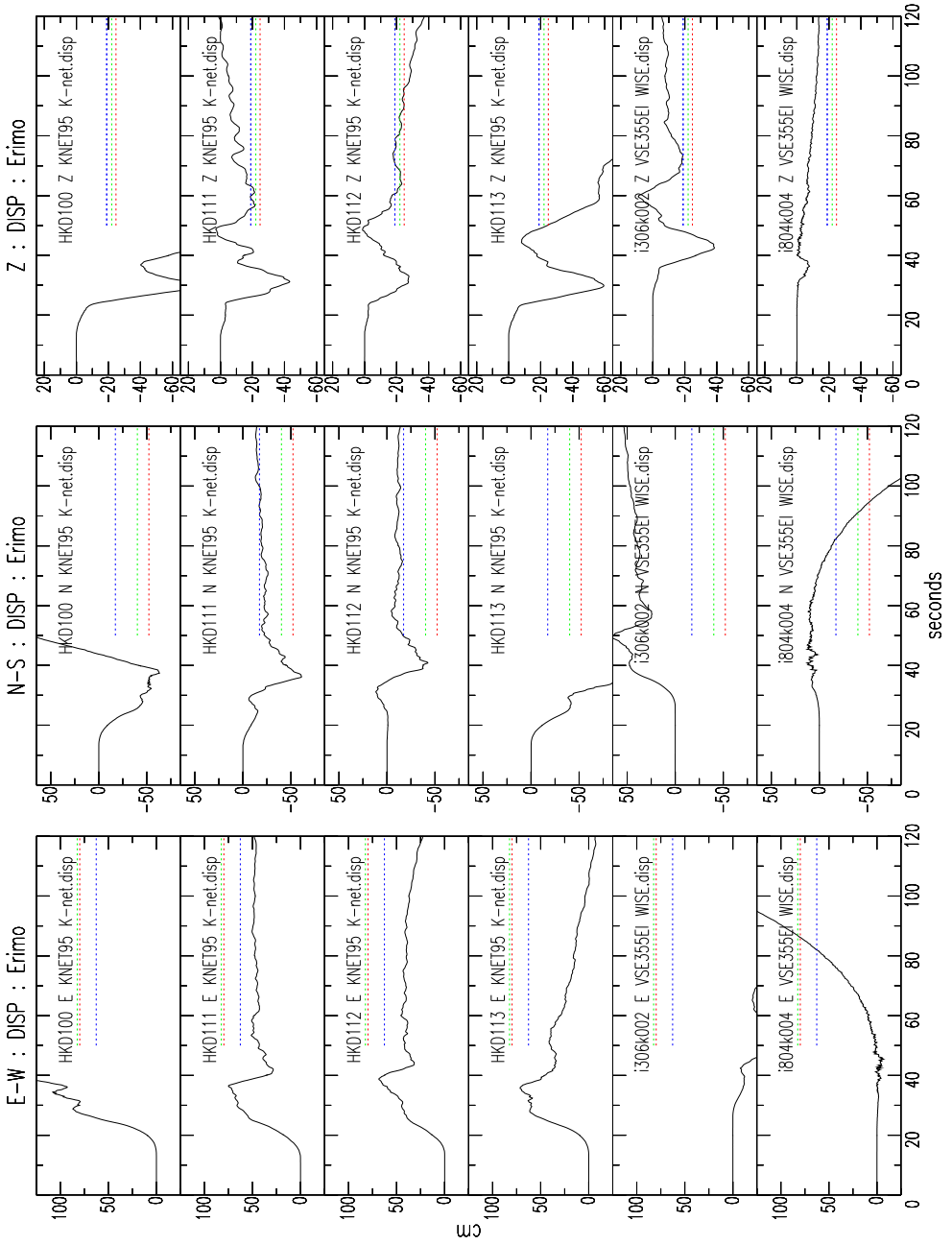

Figure 4.28: Displacements from stations near Erimo town. GPS station Erimo2 records 82.4*cm* East, 40.1*cm* South and 22.9*cm* vertical drop, Erimo1: 62.7*cm* East, 17.3*cm* South and 18.9*cm* vertical drop, Hiroo: 79.8*cm* East, 52.2*cm* South and 24.7*cm* vertical drop. All are plotted in horizontal lines. K-Net stations HKD111 and HKD112 have very similar final displacements for N-S and Z channels. Other stations perform poorly.

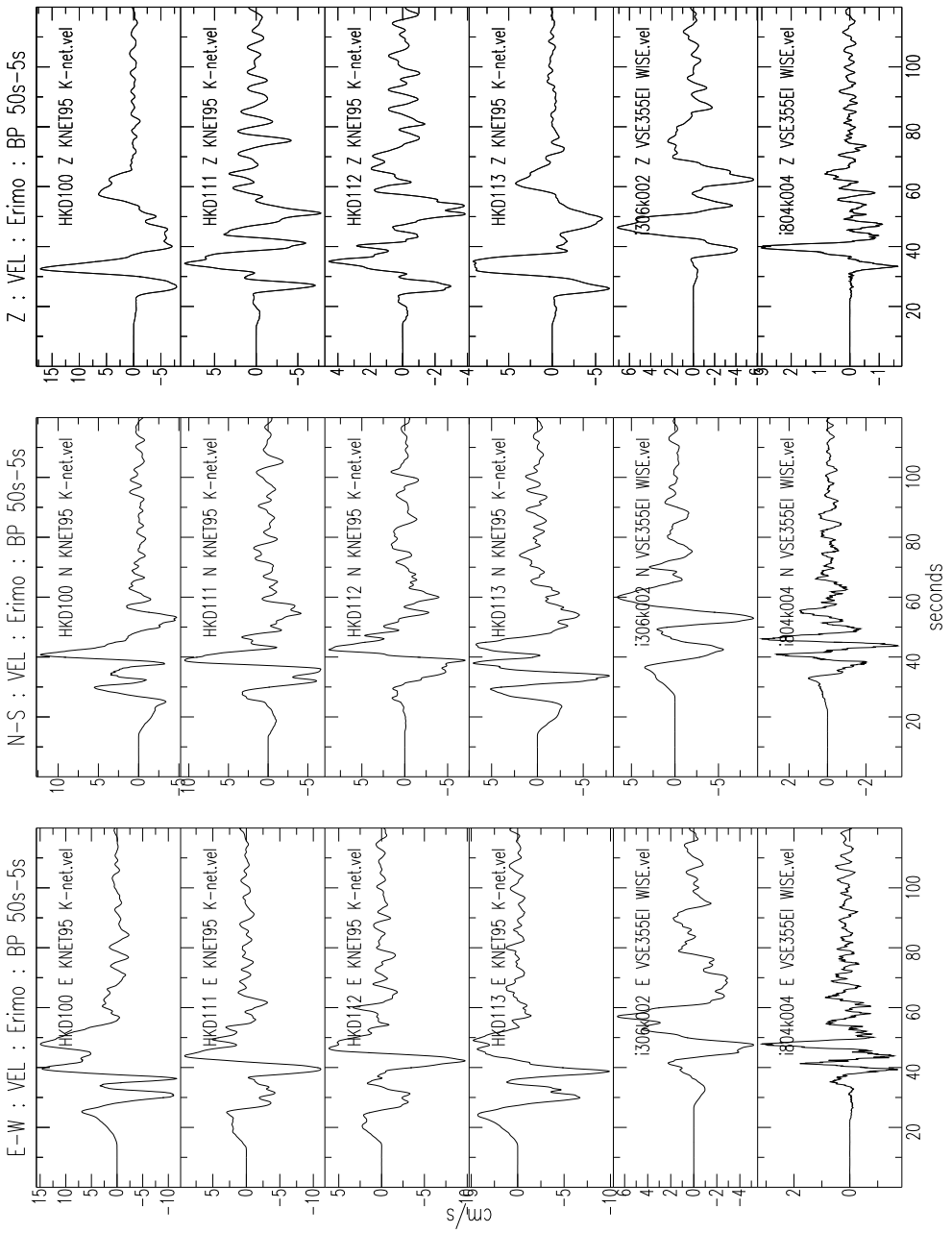

Figure 4.29: Velocity timeseries from the stations located near Erimo town. Bandpass from 50*s* — 5*s*. Note similarities for all K-Net stations, WISE i306k002 may have horizontal channels inverted, i804k004 has an unexplained response.

Kristine Larson (*personal communication*) has again determined the 1sps high-rate GPS data from Erimo1. In Figure 4.30, this GPS data and the K-Net station HKD111 displacement timeseries are compared. The stations are just over 1km apart. This GPS station suffered a power outage after 25s of strong motion, and did not regain transmission until the evening, after the major aftershocks had occurred. Before this occurred, the E-W and vertical components very closely match, though once again the magnitudes of the E-W peaks are slightly lower for the seismic sensor. The N-S motions are similar, though as with the data in Figure 4.26, large offsets begin at the same time as E-W offset occurs for the accelerometer, and not until the vertical motions begin for the GPS. Figure 4.31 presents the same data with the a clockwise rotation of 20^o for the horizontal channels of the accelerometer, and the same timing corrections as made for Figure 4.27. The fit is much improved, with excellent phase and amplitude correspondence between the two sensors. Tilt is minor at the accelerometer station, as can be seen by the relatively stable displacements after the strong motion has passed. Even so, the 7day GPS averages do not closely match the final accelerometer timeseries displacements.

4.4.4 Stations near Urahoro

There are a number of stations in the vicinity of Urahoro, the F-Net station which records the highest velocities without any large spikes. This station is in a wide basin area in East Hokkaido (see Figure 4.32). This section analyses waveforms from the stations nearest Urahoro: F-Net station URH, K-Net stations HKD086 and HKD091, KiK-Net station TKCH07, and WISE stations i807k002 and i902k001. All these stations are within 20km of URH, which is 129km from the epicenter. This region suffered major structural damage during to the earthquake — landslides, widespread liquefaction and lateral spreading damaged infrastructure, and a tsunami caused significant damage at the local ports. Ground failure was not limited to the coastal areas.

Figures 4.33, 4.34 and 4.35 present the acceleration, velocity and displacement records from all the Urahoro region stations. Timing is not synchronised between stations. URH is deployed with a VSE-355G sensor. No channel from this station clips — there are no

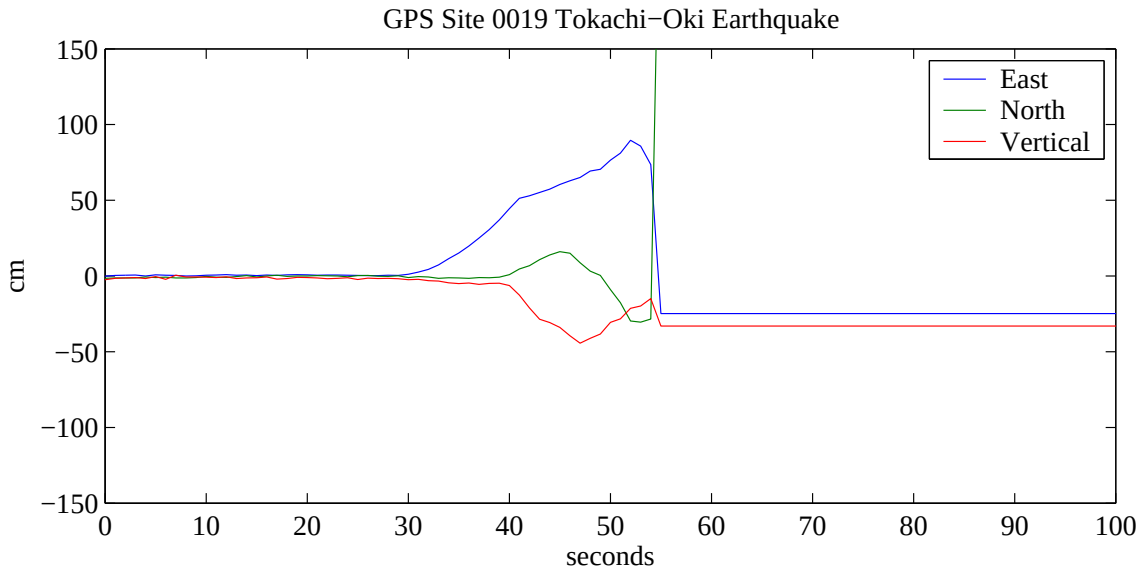

(a) 1*sps* GPS at Erimo1

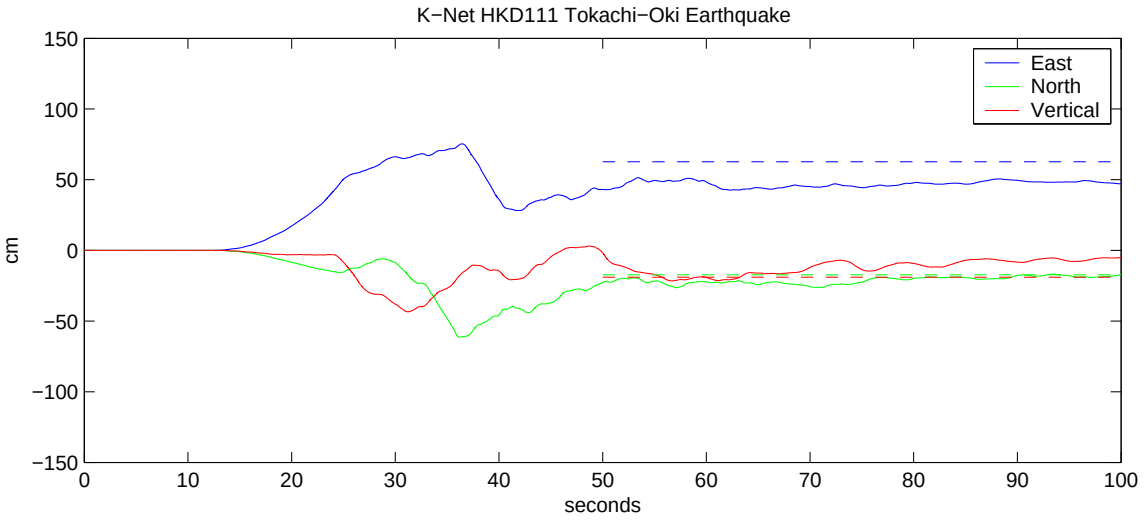

(b) 100*sps* Accelerometer at HKD111

Figure 4.30: High-rate GPS vs. accelerometer displacement timeseries for K-Net and GPS stations at Erimo. GPS timing is 13*s* fast. 7*dy* average GPS offsets included on K-Net plot.

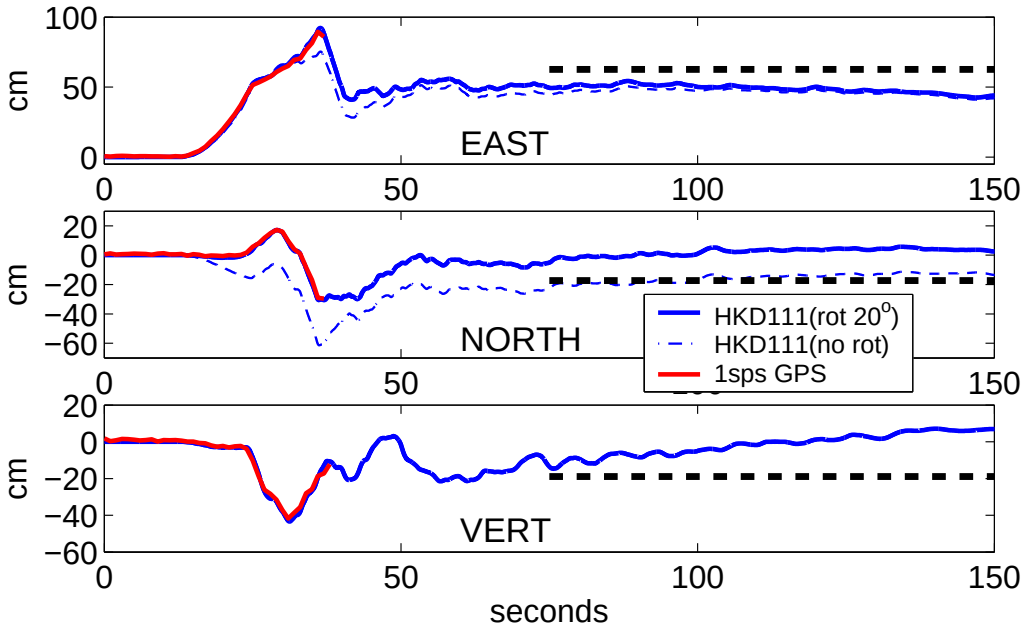

Figure 4.31: High-rate GPS vs. accelerometer displacement timeseries for K-Net and GPS stations at Erimo1. Accelerometer horizontal channels are rotated 20^o clockwise to best fit GPS. 7*dy* average GPS offsets included.

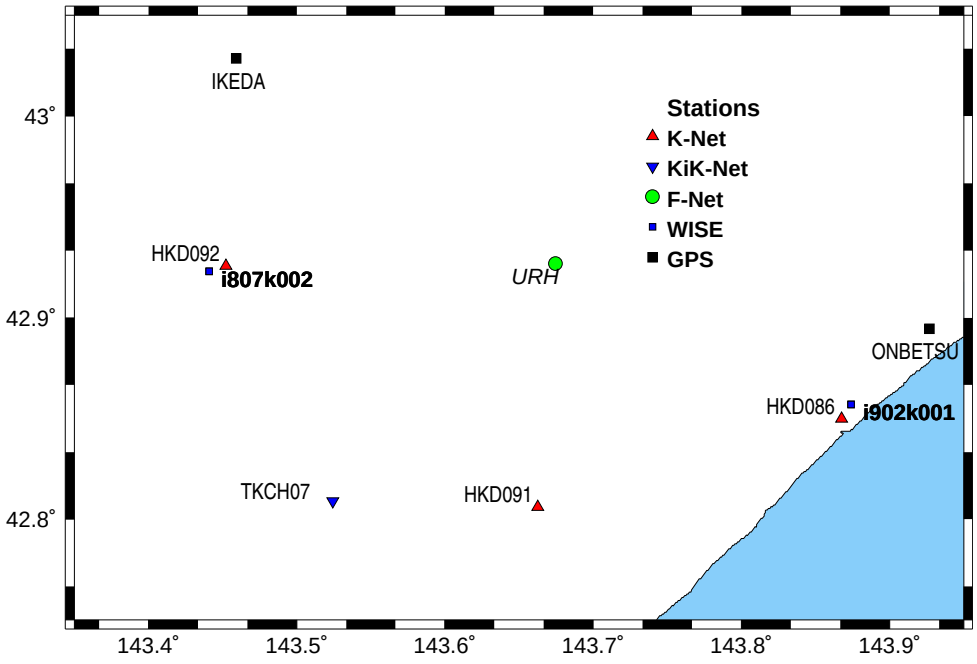

Figure 4.32: Stations near Urahoro. Blue stations from WISE, green: F-Net, red: K-Net, black triangle: KiK-Net, black square: GPS. All stations plotted are within 20*km* of URH, which is 129*km* from the epicenter.

unusually large high frequency peaks in either the velocity or acceleration timeseries. The maximum velocity is on the E-W component, recording $21.7 cm/s$. This level of velocity caused stations KSR and KMU to clip. Peak velocities on the other components are $17.4 cm/s$ N-S, and $12.9 cm/s$ Vertical.

This set of acceleration timeseries illustrates the variability in peak magnitude between closely spaced stations. At URH, accelerations are small, maximum $70 cm/s^2$, a little smaller but similar to the TKCH07 down-hole. Though these stations are buried, the other stations also have large variability, ranging from $750 cm/s^2$ to $250 cm/s^2$.

Velocities are quite large in this region. The N-S components of the up-hole KiK-Net station, and the WISE station i902k001 both record over $100 cm/s$.

All the accelerometers incur tilting during the earthquake. The stations all are located in wide flat basin, where widespread ground failure has been documented. Even the down-hole KiK-Net channels at TKCH07 show signs of tilting. GPS from the region indicates overall displacement of the order of $30 cm$ to the South-East, with a vertical drop of $\sim 8 cm$. The tectonic tilt from the differential vertical GPS is of the order of 0.0004^o, similar to previous observations. Trends observed in the E-W components of the velocity timeseries at TKCH07 up-hole and down-hole, HDK091 and i902k001 would be caused by tilts of the order of 0.1^o. HKD092 has a similar tilt, but only in the N-S direction. Even though there is major tilt in the E-W direction for the TKCH07 down-hole, N-S and Z channels record stable permanent offset comparable to the GPS. In the middle of all these tilting stations, the F-Net station URH produces very stable displacements comparable to GPS for all 3 channels.

Station HKD086, the K-Net instrument located on the coastline, has a very strange response, not easily interpreted by simple tilting alone. Figure 4.38 presents 3 components of acceleration and velocity timeseries data for the initial part of the record. From about $30s$ into the record, frequency content changes dramatically, with very little high frequency content, associated with serious tilting in all three components. In the N-S direction, this fall of $800 cm/s$ is observed in only $15s$, which corresponds to a tilt of over 3^o. In Figure 4.34, this tilt changes direction for all 3 components, indicating large, rapidly changing tilts. This appears to be a site that is liquefying. This is consistent with the widespread

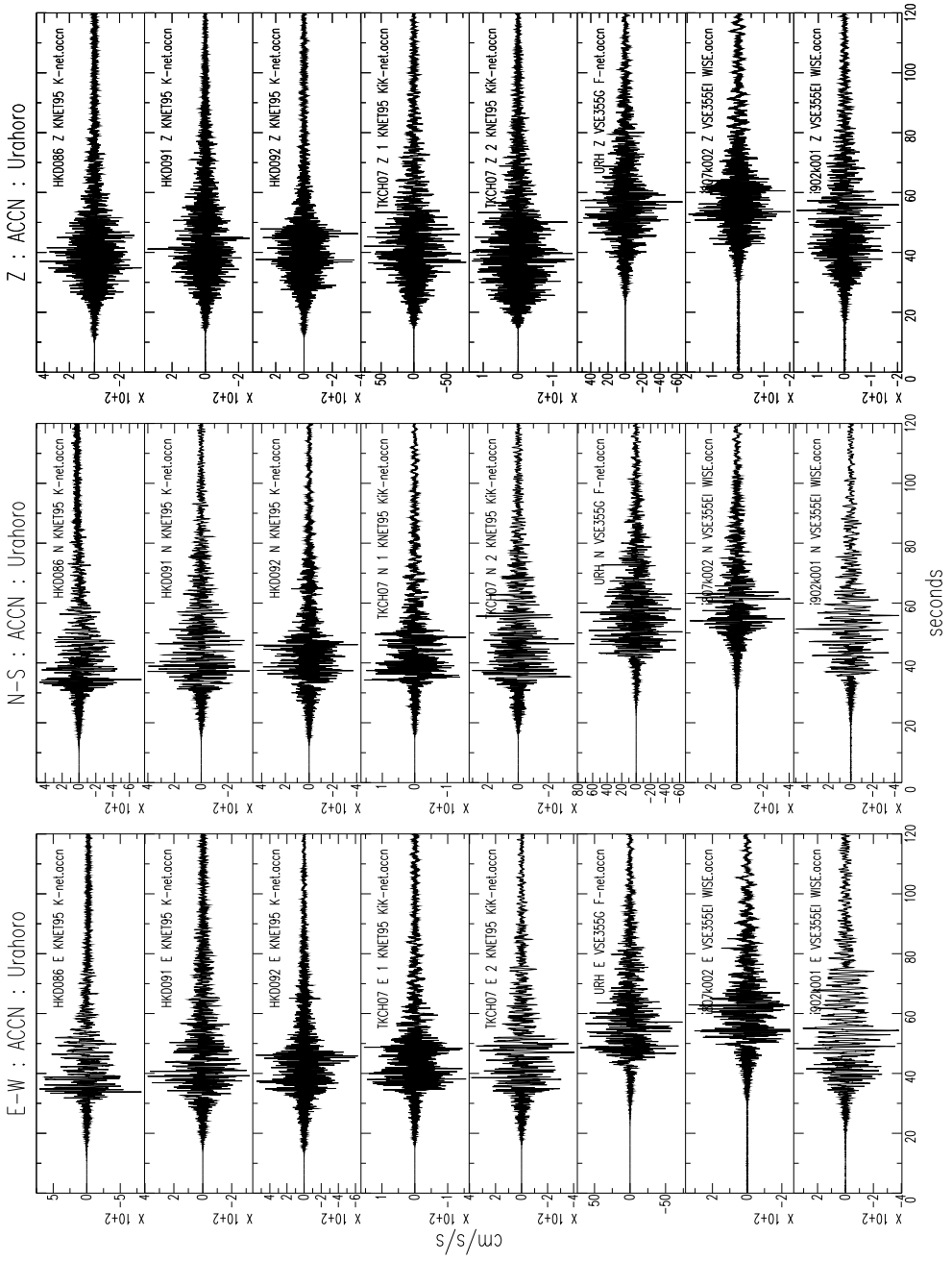

Figure 4.33: Acceleration timeseries from the stations located near Urahoro. Note the large variation acceleration magnitudes between these closely located stations. KiK-Net stations: ‘1’: Down-Hole, ‘2’: Up-Hole.

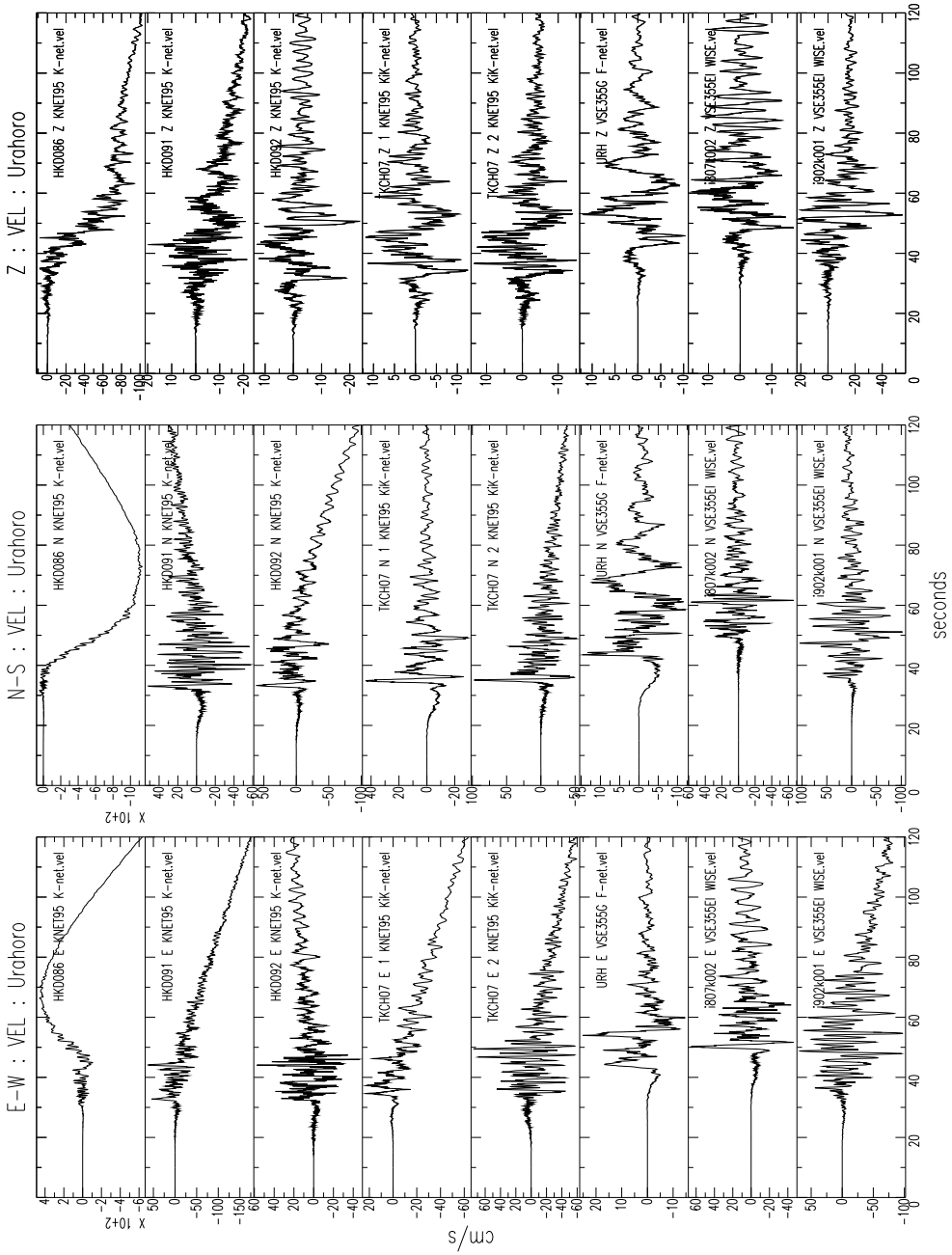

Figure 4.34: Velocity timeseries from the stations located near Urahoro. Tilting clearly affects all accelerometers bar N and Z KiK-Net down-hole. K-Net HKD086 liquefies. VSE i807k002 has resonances. KiK-Net stations: ‘1’: Down-Hole, ‘2’: Up-Hole.

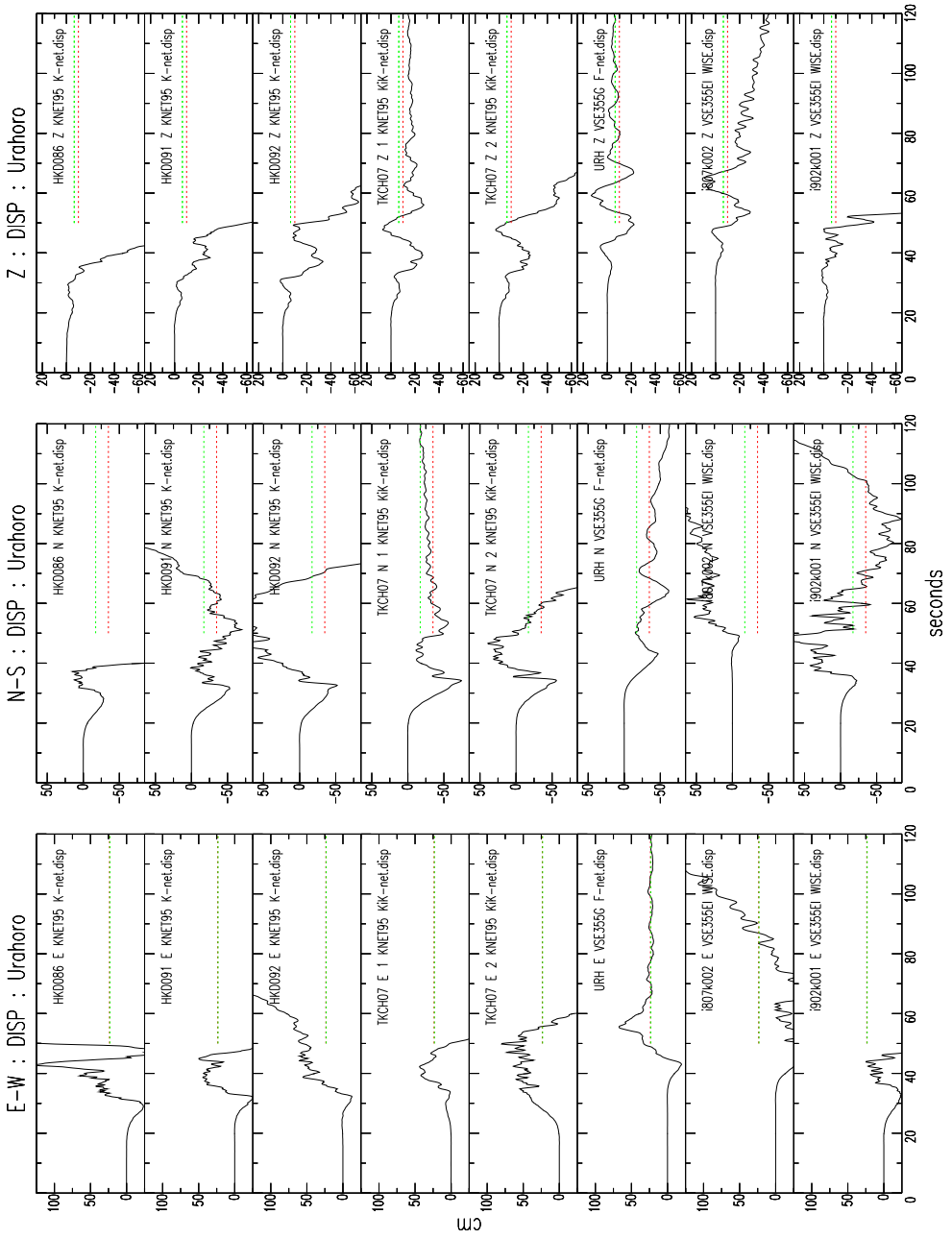

Figure 4.35: Displacements from stations near Urahoro. GPS stations — Ikeda: 23.6*cm* East, 34.9*cm* South, 10.0*cm* vertical drop, Onbetsu: 23.1*cm* East, 17.2*cm* South, 6.5*cm* vertical drop. Significant tilting for all accelerometers, including KiK-Net. F-Net station URH has good correlation with GPS . KiK-Net stations: ‘1’: Down-Hole, ‘2’: Up-Hole.

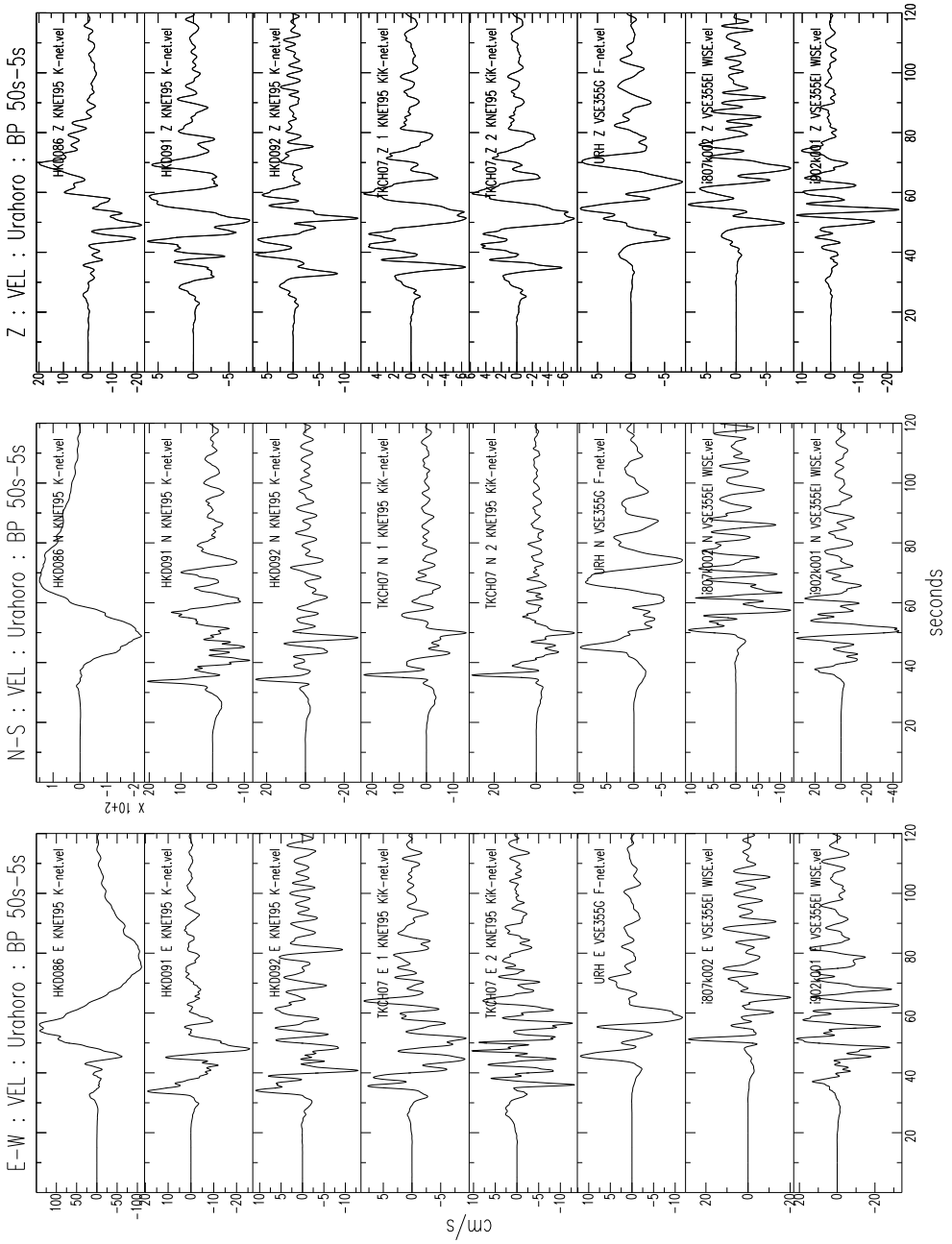

Figure 4.36: Velocity timeseries from the stations located near Urahoro. Bandpass from 50*s* — 5*s*. Note basin resonance at most stations, not apparent at URH. KiK-Net stations: '1': Down-Hole, '2': Up-Hole.

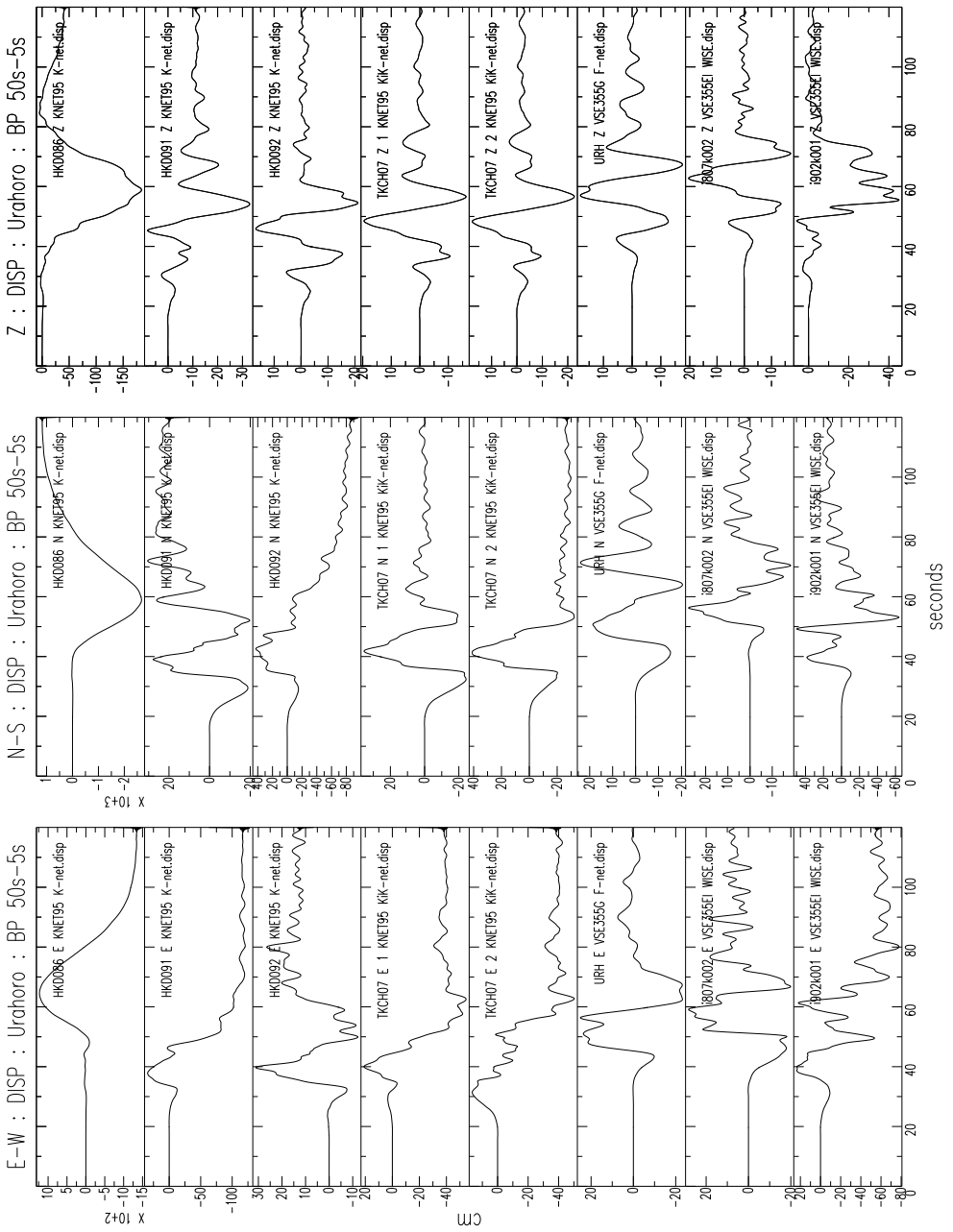

Figure 4.37: Displacement timeseries from the stations located near Urahoro. Bandpass from 50*s* — 5*s*. In this area, the 2 WISE stations appear correctly oriented. KiK-Net stations: '1': Down-Hole, '2': Up-Hole.

ground failure reported in this region.

A spectrogram of each component from the acceleration timeseries is presented in Figure 4.39. Each vertical line in the plot represents an FFT of 10*s* of the data beginning at the time it is plotted. It is clear from the plot that as the event progresses, the high frequency content is severely reduced, especially on the horizontal components.

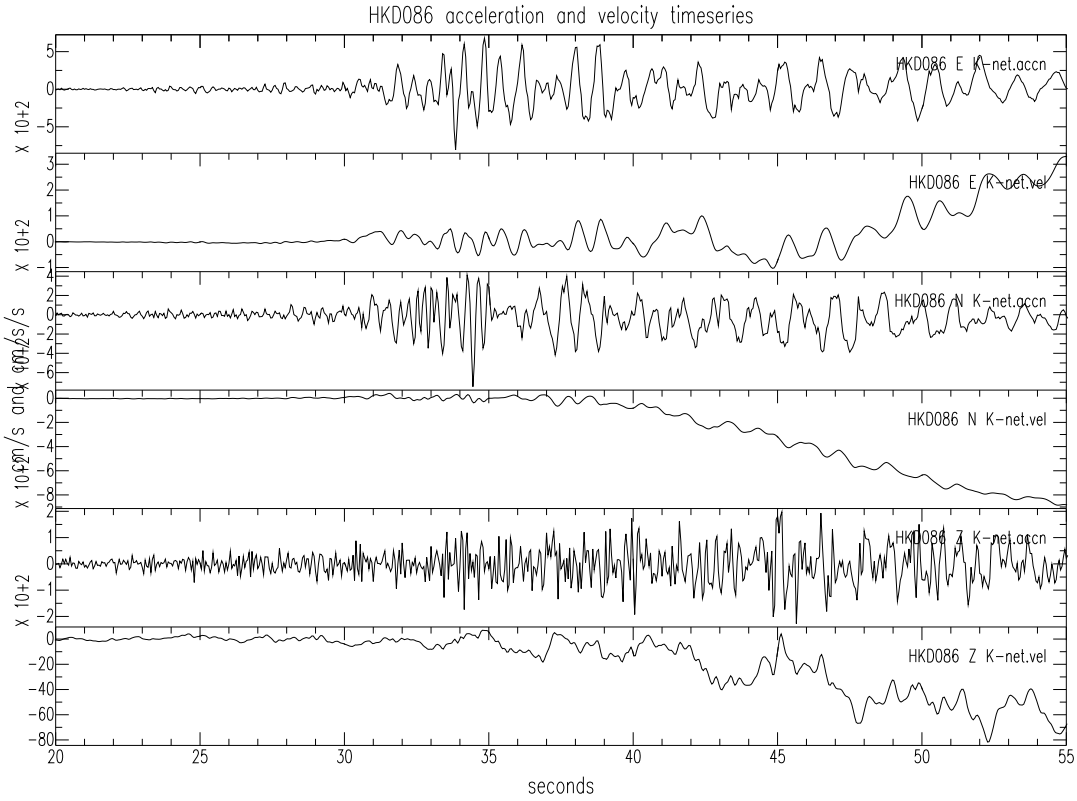

Figure 4.38: Velocity and acceleration timeseries from liquefaction site HKD086, K-Net. See Fig 4.32 for location. Note change in frequency content in the acceleration timeseries, and consequent very large tilts for all three components. One hypothesis is that liquefaction occurred at this site.

Figure 4.40 shows a similar spectrogram plot for nearby K-Net station HKD091, which does not have liquefaction. though dominant frequencies may also be low, there is not a complete attenuation of high frequencies like at HKD086.

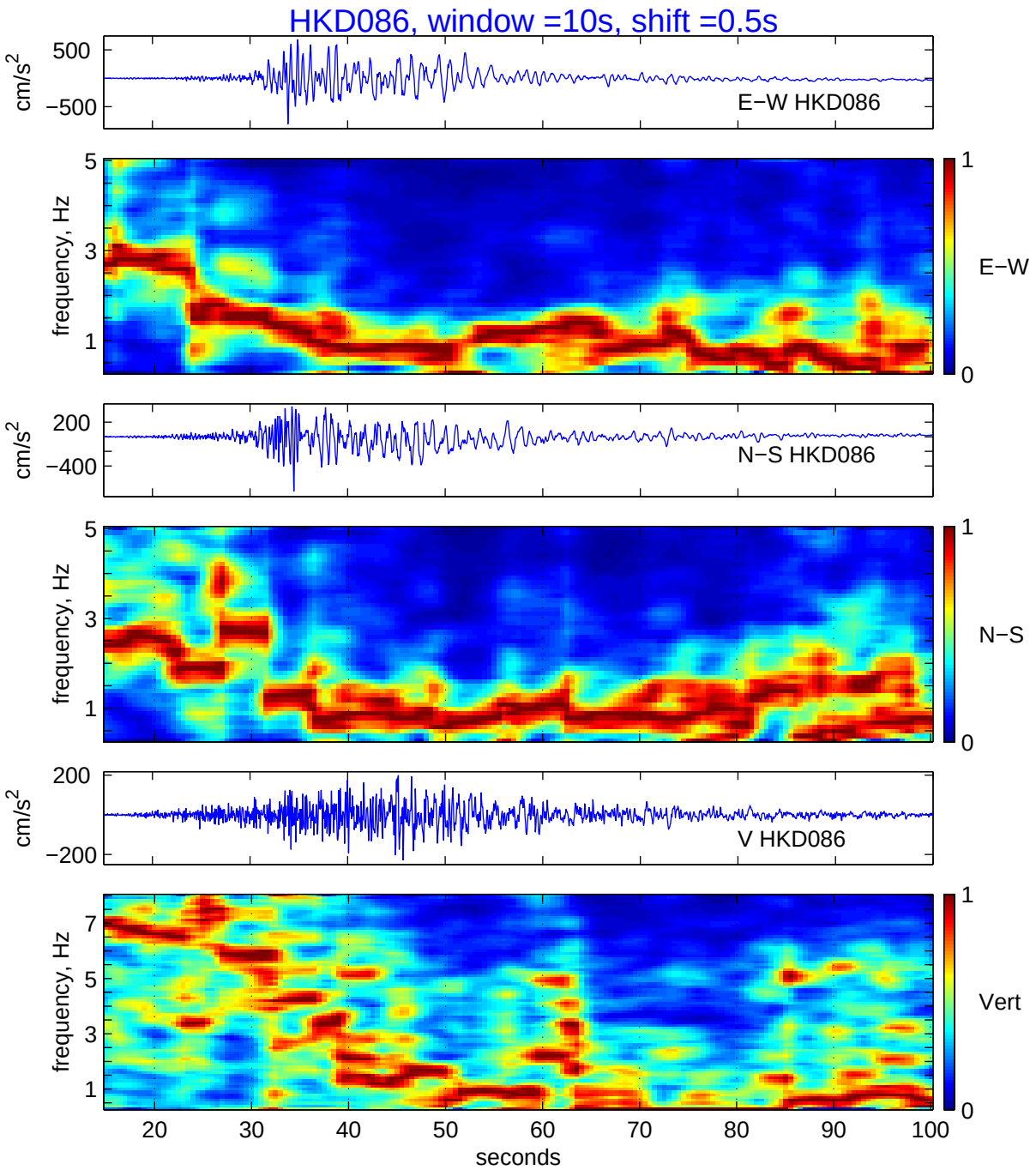

Figure 4.39: Acceleration timeseries and spectrogram for liquefaction site HKD086, K-Net. See Fig 4.32 for location. Frequency drop after about 30*s*, as site liquefies, with all high frequency attenuated.

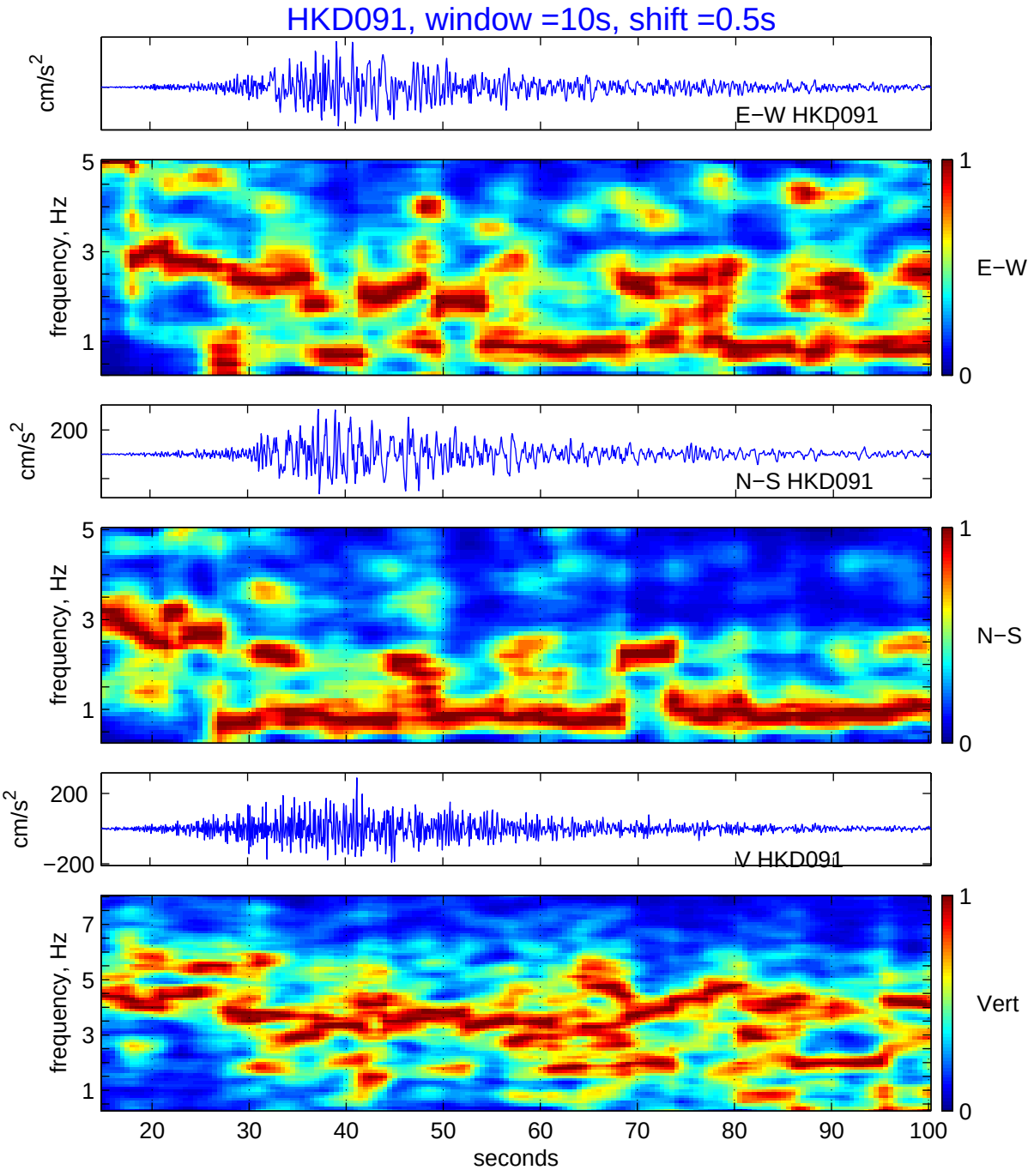

Figure 4.40: Acceleration timeseries and spectrogram for site HKD091, K-Net. See Fig 4.32 for location. Though tilting occurs at this site, no liquefaction occurs, and high frequencies are present in all components.

4.4.5 Stations near Obihiro

In Figures 4.7 and 4.8, it is clear the WISE stations to the West of Urahoro, in the wide flat basin, have recorded motions that appear to be of the correct order of magnitude, but with reversed polarities on the horizontal components. To investigate this, a cluster of stations around the town of Obihiro are examined. There are 3 WISE stations (i801k001, i801k004, i806k002), 2 KiK-Net stations (TKCH06, TKCH11), 1 K-Net (HKD095) and 1 GPS (Obihiro) stations within a few *km* of the town, which is about 160km from the epicenter — as shown in Figure 4.41. From the map in Figure 4.11, all the station are shown to lie in the flat basin, except KiK-Net TKCH11, which lies on the foothills of the mountain.

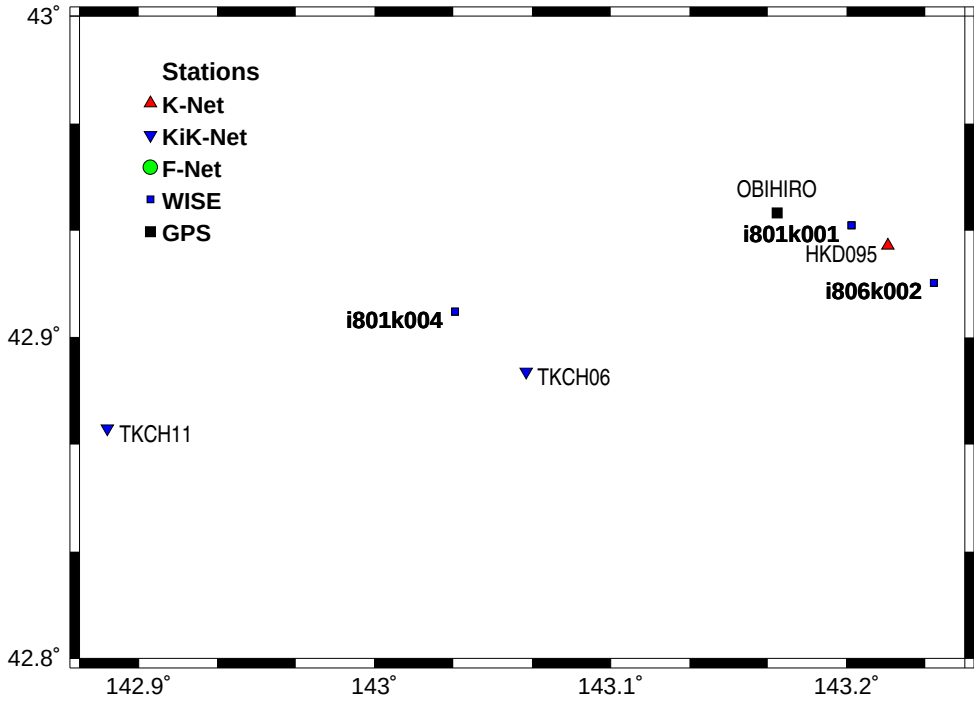

Figure 4.41: Stations near Obahiro. Blue stations from WISE, red: K-Net, black triangle: KiK-Net, black square: GPS. All stations plotted are within 15*km* of KiK-Net station TKCH06, which is 162*km* from the epicenter.

Figures 4.42, 4.43 show the band-passed velocity, and deconvolved displacement from these 8 sensors. Timing is not synchronised between networks. From the displacement timeseries, the WISE stations do all have the opposite polarity for the horizontal motions.

When we look at the velocity timeseries, these timeseries still appear reversed. Noting the similarity of the waveforms, and the close proximity of the stations, this is conclusive evidence that the polarity of the waveforms are reversed. Although the WISE stations once again do not provide a clear displacement field, the magnitudes of the best-guess offsets in Figures 4.7 are in general agreement with the GPS. Nonetheless, these examples do provide another reason for suggesting the WISE network is not appropriate for investigations into permanent ground displacement. Indeed, it also may be inappropriate to use this network to come to any conclusions regarding the functionality of the VSE series of seismometers in general.

Figure 4.42 also serves to illustrate again the stability and GPS compatibility of the displacements produced by the down-hole KiK-Net accelerometers. With very little tilt occurring at depths, the accelerometers perform very well. All the K-Net and WISE stations have unstable tilted displacements, with the surface KiK-Net instruments also showing some tilting. Even though the GPS station at Obihiro is $\sim 15km$ from TKCH06, and $\sim 30km$ from TKCH11, both KiK-Net down-hole sensor record static displacement almost identical to the GPS.

It is also interesting to note that though the static displacements from the 2 down-hole sites are very similar, the overall character of the ground motion is not. Kristine Larson (*personal communication*) has again determined the $1sps$ high-rate GPS data from Obihiro. In Figure 4.44, this GPS data and the 2 KiK-Net down-hole displacement timeseries are compared. The GPS and the TKCH06 site are located in the basin, where there are large displacement long period resonances measured both by the $1sps$ GPS, and the down-hole at $227m$ depth. These resonant waves are not seen at the nearby TKCH11 down-hole at $100m$ depth, located on the mountain side at the edge of the basin.

A spectrogram of the acceleration timeseries from both up-hole and down-hole from TKCH06, and the down-hole only from TKCH11, is presented in Figure 4.46. Each vertical line in the plot represents an FFT of $10s$ of the data beginning at the time it is plotted. The low frequency basin waves which dominate the TKCH06 station response are clearly observed in the spectrograms.

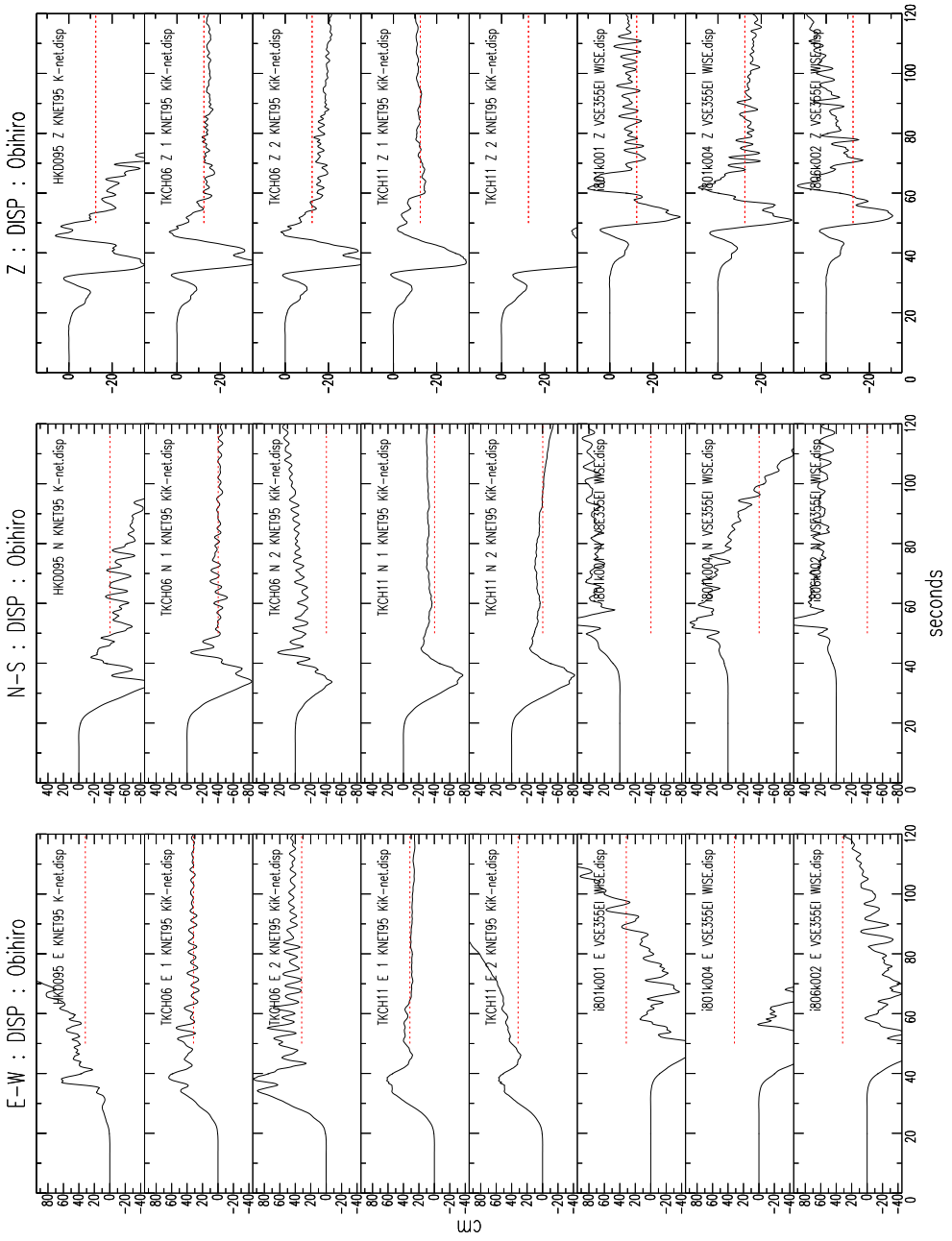

Figure 4.42: Displacements from stations near Obihiro. GPS Stn — Obihiro 31.7*cm* East, 40.3*cm* South, 12.4*cm* vertical drop. KiK-Net accelerometers, especially down-hole, have remarkably stable final offset, similar to GPS. KiK-Net stations: ‘1’: Down-Hole, ‘2’: Up-Hole.

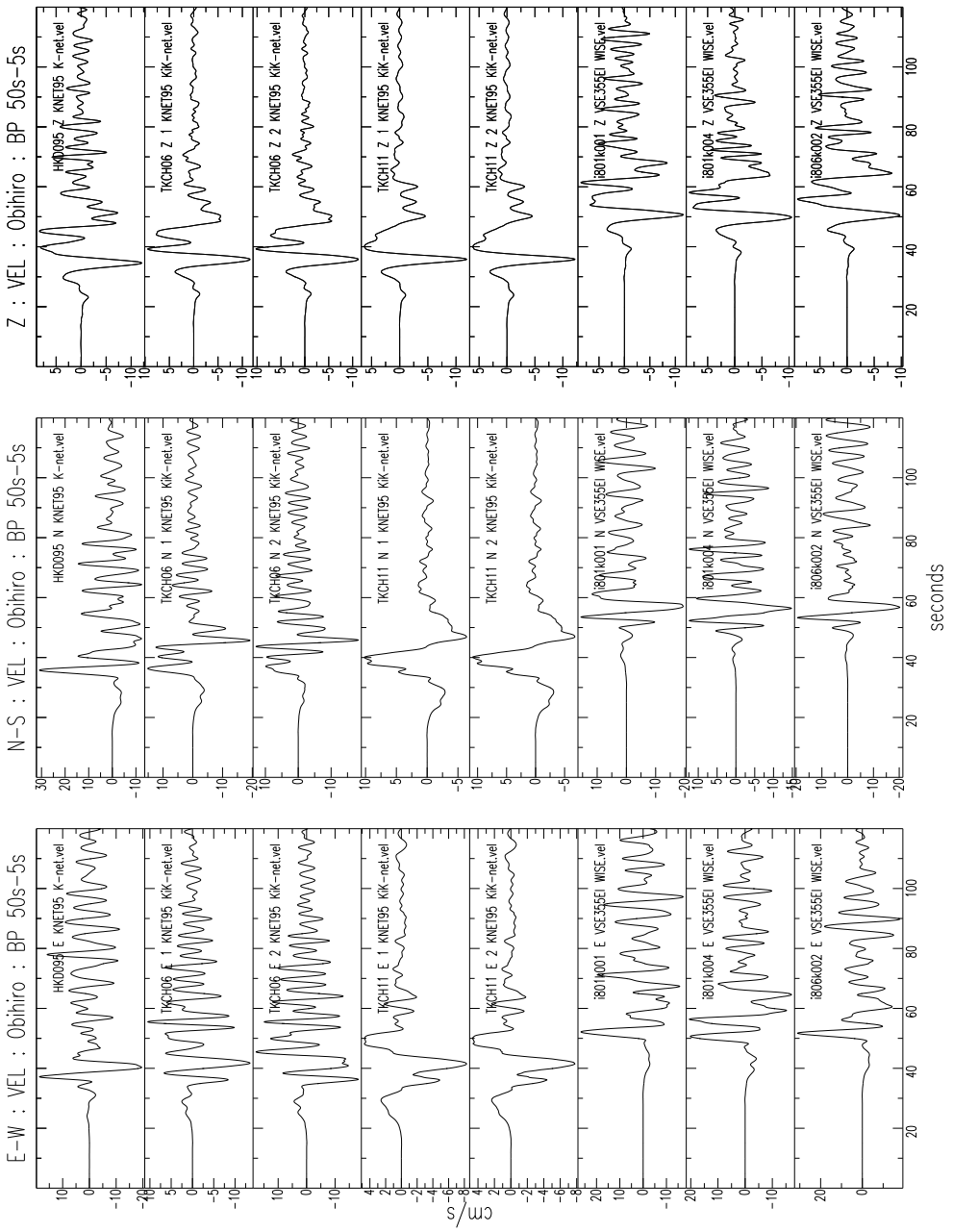

Figure 4.43: Velocity timeseries from the stations located near Obihiro. Bandpass from 50*s* — 5*s*. All stations in basin have large amplitude long period resonances at about 4*s*, which are not present on basin edge station TKCH11.

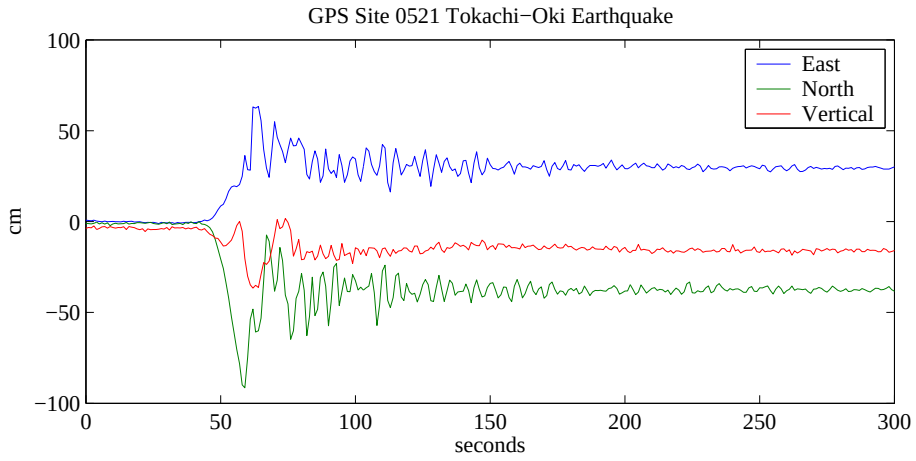

(a) 1*sps* GPS at Obihiro (Basin)

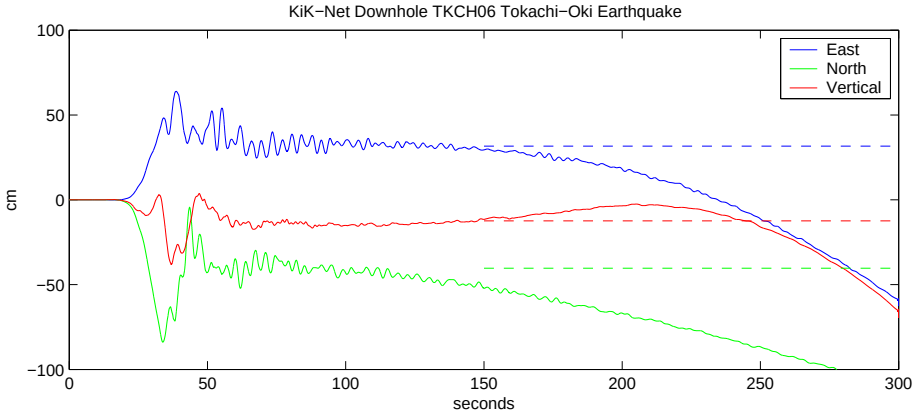

(b) 100*sps* accelerometer at TKCH06 down-hole (basin)

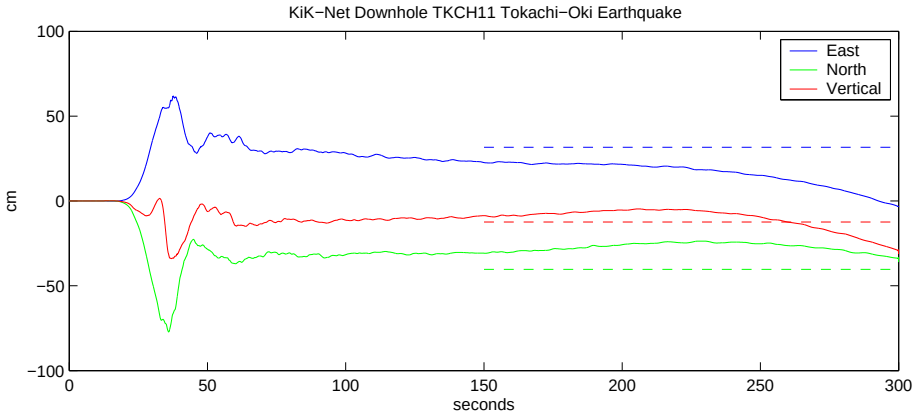

(c) 100*sps* accelerometer at TKCH11 down-hole (rock)

Figure 4.44: High-rate GPS vs. accelerometer displacement timeseries for KiK-Net and GPS stations near Obihiro. GPS timing is 13*s* fast. 7*dy* average GPS offsets included on KiK-Net plots.

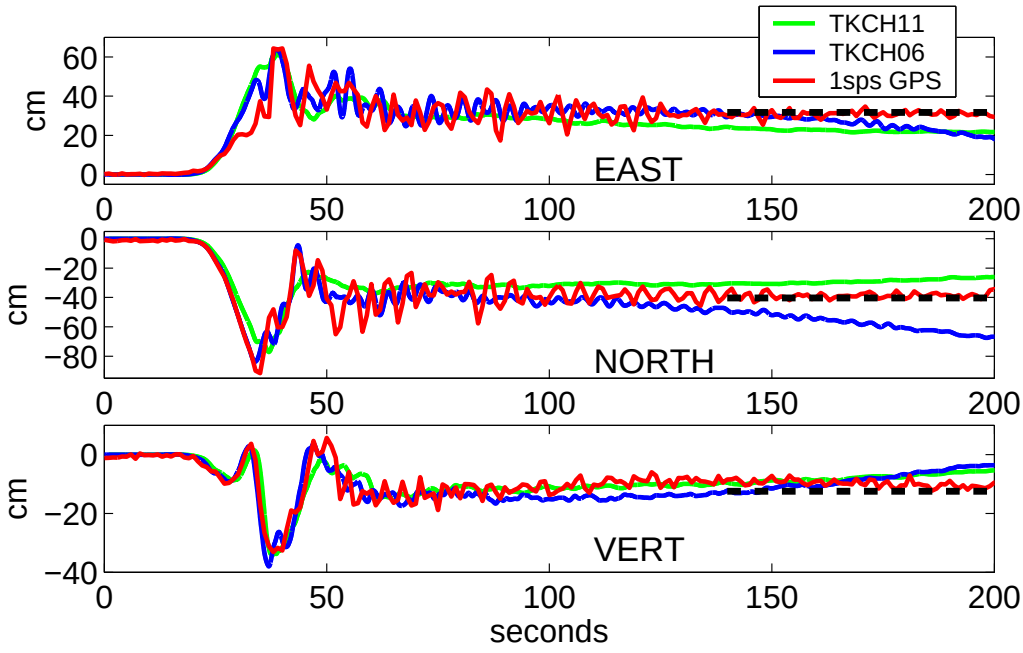

Figure 4.45: High-rate GPS vs. accelerometer displacement timeseries for KiK-Net and GPS stations near Obihiro. Accelerometer horizontal channels are not rotated. 7*dy* average GPS offsets are included.

4.5 Other F-Net stations on Hokkaido

The performance of the F-Net VSE-355G/G2 instruments in the near-field was not excellent, so the performance of the other F-Net stations on Hokkaido were analysed. After KMU, URH and KSR, the next closest station to the epicenter was HID, at 169*km* distance. This VSE-355G2 station recorded peak velocities of 16.6cm/s without the high frequency spikes seen at KMU and KSR. Upon deconvolution though, it appears this instrument also tilted. Figure 4.47 presents the displacement and velocity timeseries for both the deconvolved and un-deconvolved records. Deconvolved horizontal velocity timeseries have non-physical linear trends after 30*s* of strong motion, which is consistent with unexpected static offset in un-deconvolved horizontal displacements (see Figure 3.6. In the E-W component, this trend corresponds to a tilt of 0.01^o, much larger than the tectonic tilt as observed closer to the rupture. At this distance from the epicenter, with the vault setting, this size of tilting is unusual. It is likely this is a non-linear sensor response.

Figures 4.48 and 4.49 presents velocities and displacements from the remaining F-Net

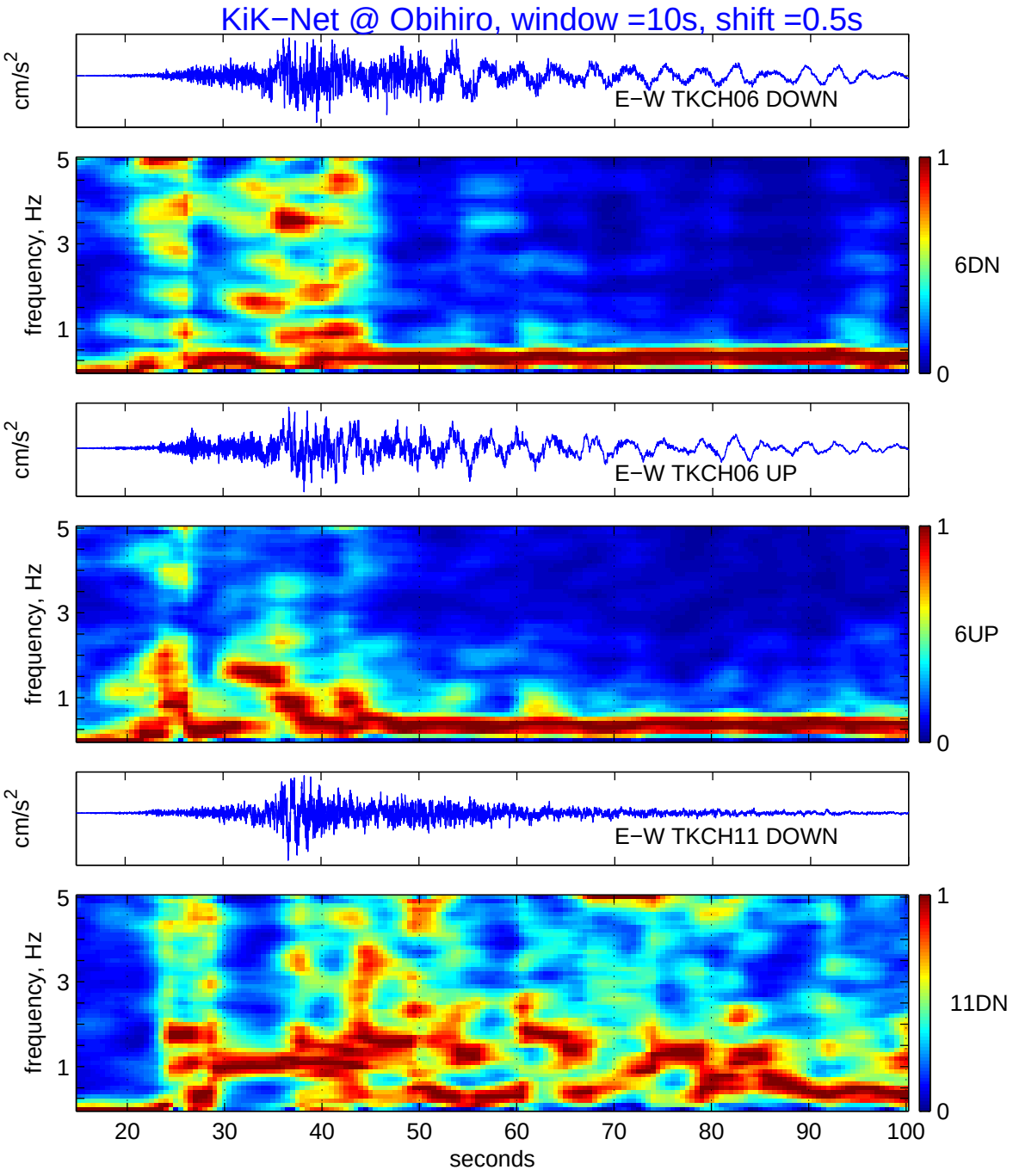

Figure 4.46: Acceleration timeseries and spectrogram for E-W component of KiK-Net sites TKCH06 and TKCH11. See Fig 4.41 for location. TKCH06 is located in the middle of the basin, and its response is dominated by basin waves, TKCH11 is on mountainous basin edge, and does not have these basin waves.

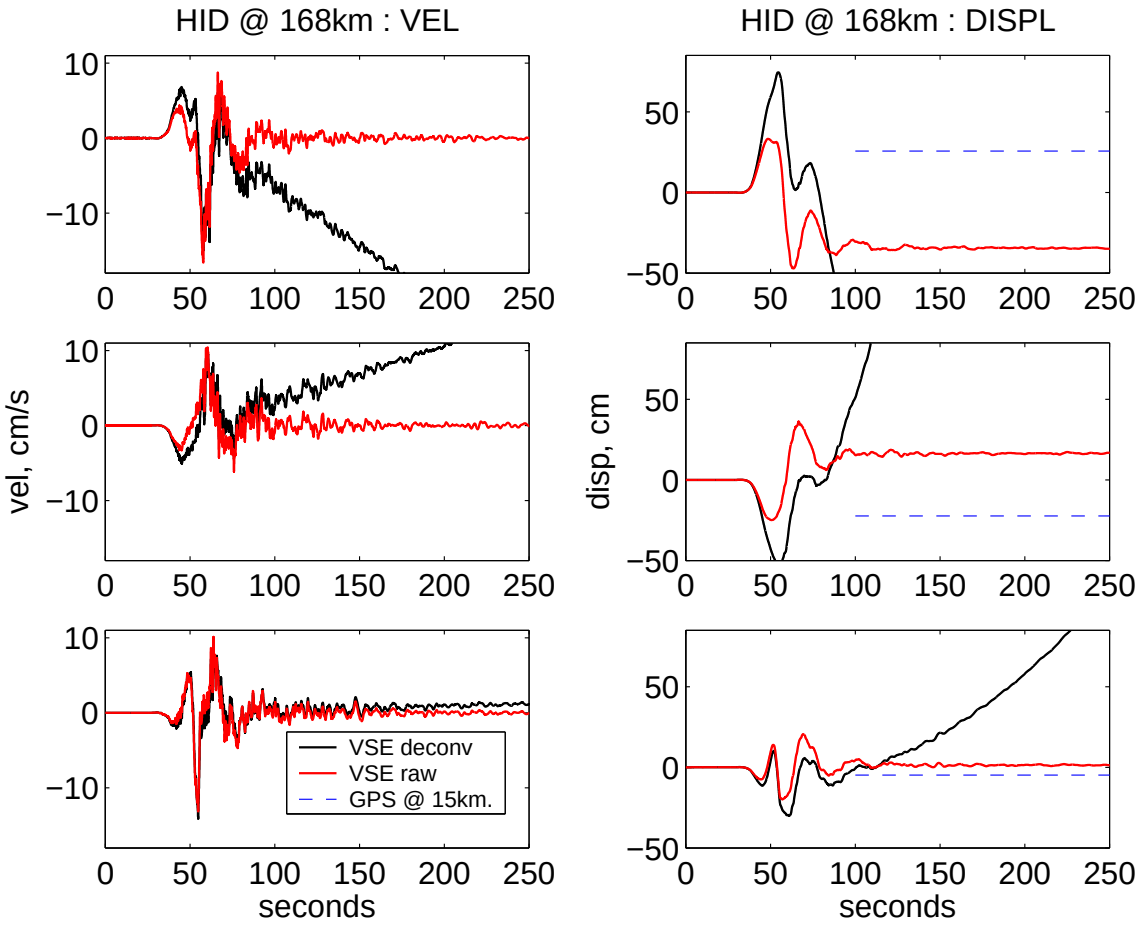

Figure 4.47: Comparison of deconvolved and raw velocity and displacement timeseries from VSE-355G2 at F-Net station HID, 169*km* from epicenter. GPS from Biratori station. Instrument performs poorly — note static offset in horizontal components of undeconvolved data. At this distance, and considering the station is location in a 30m deep vault, tilting is unlikely to be responsible. Note max velocity of 16.6cm/s is reached without clip. Top: E-W; middle: N-S; bottom: vertical.

stations on Hokkaido Island. Their locations can be seen on the map of Japan in Figure 4.50. The nearest GPS station to each station provides the expected static offset plotted. In general, the VSE does a good job in matching the GPS static offset, though tilts are observed even at large distances under small motions. This may be due to problems with sensor installation, or an unexpected non-linear sensor response. [Note these timeseries are 250*s* long, previous plots were only 120*s* long.]

Station IMG houses the only other VSE-355G sensor on Hokkaido, and the displacement derived from the sensor appears to be corrupted by tilting. It is not as stable as URH, which saw much larger motions and offsets, yet gave very good static offsets (see Figure 4.35). The East Component of KNP reached $15.1 cm/s$ velocity, and this station also exhibits tilting after this value is reached, similar to at HID. The corresponding displacement is also not stable.

4.6 Teleseismic Motion around Japan

The earthquake provides an excellent opportunity to observe how large events may saturate broadband networks over a large area. As the F-Net network consists of stations with co-located broadband and strong motion (all VSE-355G/G2) instruments, velocities from both sets of instruments can be directly compared. In this study, for all earthquakes investigated, all F-Net data is obtained from the F-Net Website `www.fnet.bosai.go.jp/`. Each station's dataset comprises of channels from both the high-gain broadband sensor data, and the low-gain strong motion velocity sensor. A 45*min* time period of 1*sps* data, beginning at the onset of rupture is downloaded. The only processing of the data is the removal of the mean of the trace, and division by the station gain, as determined by sensitivity from SEED response files available on the F-Net Web-site. All F-Net instruments have a response flat to velocity between at least 0.0125*Hz* (80*s*) and 10*Hz*. The instruments deployed in F-Net at the time of the earthquake consist of STS-1's, STS-2's and CMG-1T's for the broadband sensor, and VSE-355G's and VSE-355G2's for the strong motion sensor. A summary of the instrument properties is in Table 2.1. As discussed in the previous Section, the VSE-355G is an earlier version of the VSE-355G2, with a similar frequency range, but lower dynamic

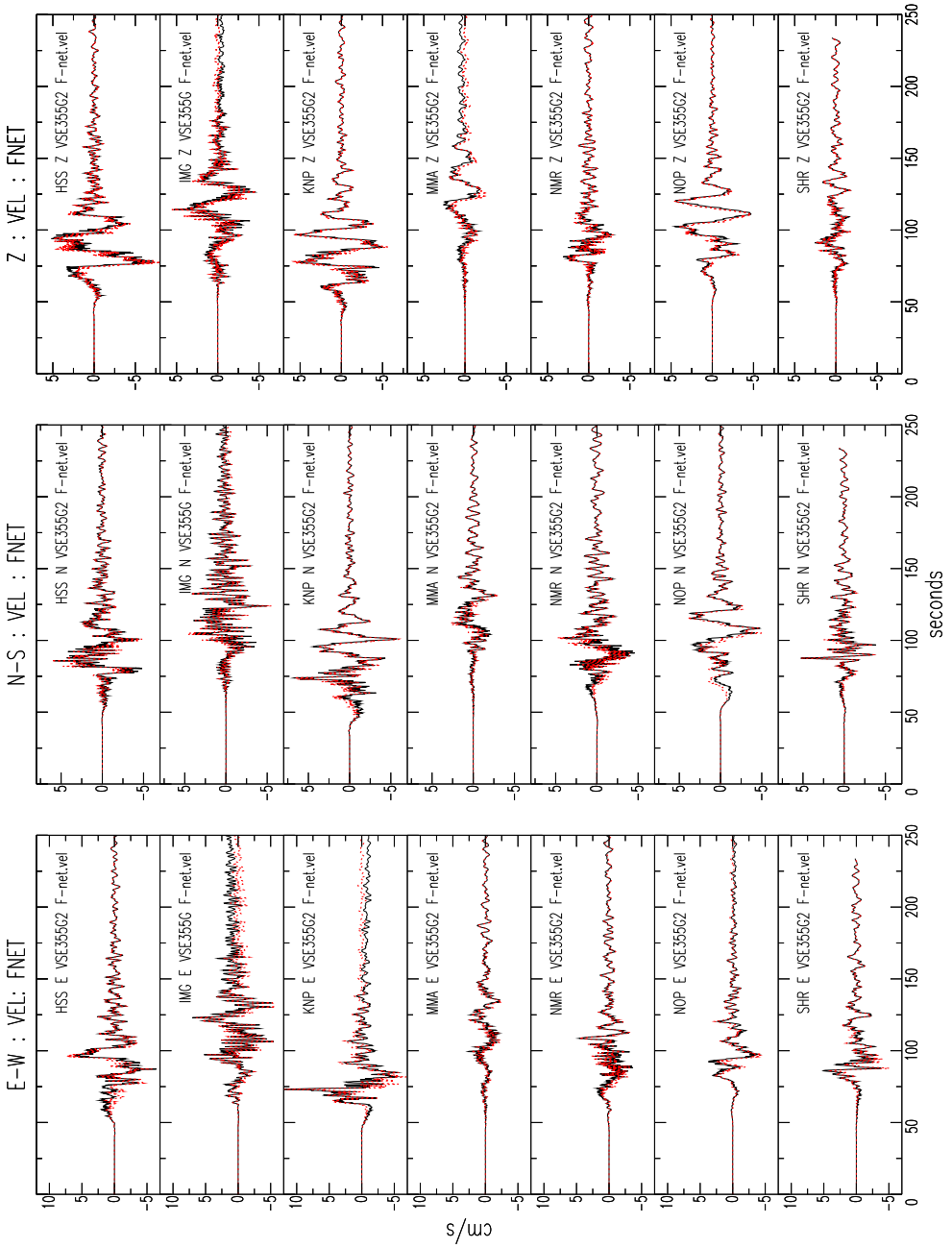

Figure 4.48: Velocity timeseries from other F-Net stations on Hokkaido Island. Solid lines are deconvolved data, dotted are raw VSE output. Max. velocity at KNP E-W component, where 13.1cm/s raw velocity is output, which is 15.1cm/s when deconvolved. No clipping is apparent. Very minor tilting is apparent over the 250s

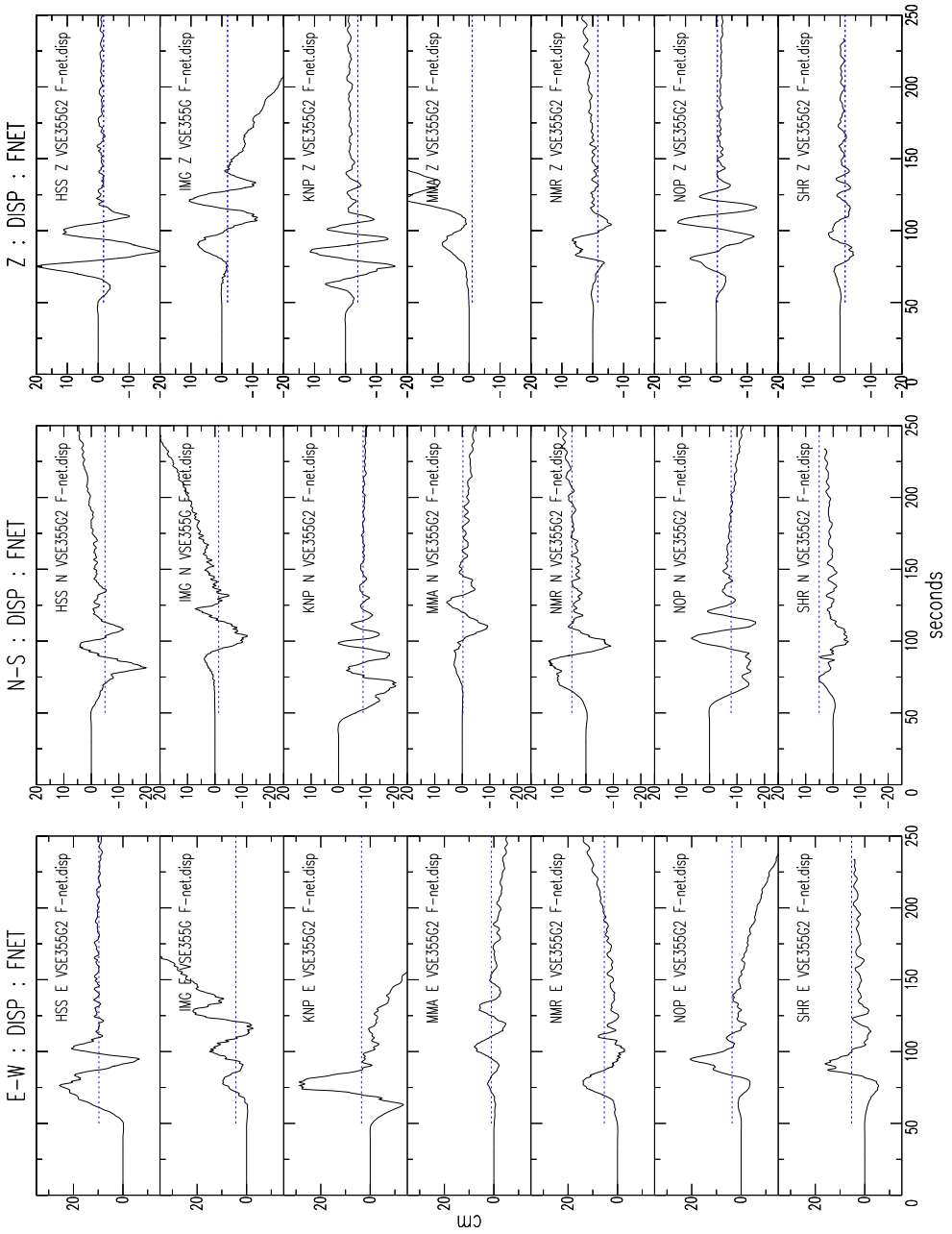

Figure 4.49: Displacement timeseries (deconvolved) from other F-Net stations on Hokkaido Island. Static offsets from nearest GPS stations are plotted as dotted lines.

range.

Figure 4.50 presents a summary plot of F-Net station performance throughout Japan during the M8.3 mainshock. Station performance is parameterised in the following manner:

Each of the 3 components is represented by a ratio K —

$$K_E = \frac{max(VSE[EW]velocity)}{max(Broadband[EW]velocity)} \tag{4.2}$$

$$K_N = \frac{max(VSE[NS]velocity)}{max(Broadband[NS]velocity)} \tag{4.3}$$

$$K_Z = \frac{max(VSE[Z]velocity)}{max(Broadband[Z]velocity)} \tag{4.4}$$

A station's performance can then be defined by the two parameters K_{max} and K_{min} —

$$K_{max} = max(K_E, K_N, K_Z) \tag{4.5}$$

$$K_{min} = min(K_E, K_N, K_Z) \tag{4.6}$$

For small motions below the broadband clip levels, and above the strong motion noise level, it is expected that $K_{max} \sim K_{min} \sim 1$. Due to some variation in instrument performance and calibration (station response files are being continuously maintained and updated, and quality control may not be perfect), a 'well operating station', observing motions within the fore-mentioned range, is defined as one with —

$$0.85 < K_{min}, \qquad \text{and} \qquad K_{max} < 1.15 \tag{4.7}$$

This allows a variation of 15% between the peak velocities from both sensors. A station with $K_{max} > 1.15$ has either clipped, has incorrect station gains, or a technical problem. A station with $K_{min} < 0.85$ has incorrect station gains, or a technical problem.

[Incorrect station gains are likely as quality control is not perfect - on the Web-site there are differences in sensors between the overall station summary table, and the individual station pages. Further, returned data would sometimes have incorrect starting values, beginning minutes into the record, and on a few occasions station coordinates on SAC files had different values to all station maps. eg: station SRN: 42.979N, 144.489E SAC header,

36.1987N, 136.6332E from station Web-page. A list of the stations with this problem is: AOG, KSR, HJO, NKG, NOP, OSW, SAG, SHR, SIB, SRN, STM, TYS, YNG. At another station, KZK, the broadband and strong motion are so different, it appears they are from different regions of Japan.]

In Figure 4.50, these 3 states are represented by colour symbols for each station. The closest station with un-clipped correct broadband recording of the event is HRO, with an STS-2, at 568*km*, with peak velocity of $0.69cm/s$. The most distant station in the network that has a broadband instrument clipped, is station NAA, with an STS-1, at 924*km* distance. The E-W component of the VSE records $0.85cm/s$, whilst the E-W STS-1 component clips at $0.76cm/s$ (see Figure 4.51). Figure 4.52 plots comparisons for all 3 components of the velocity and integrated displacement. It is noted there is no 'instrument response' in the displacement trace. This instrument response would be a long period signal in the clipped channel, similar to that observed in Figure 3.5, which is the response of the VSE to a δ-function in acceleration. This response is typically observed in sensor clipping, and its absence suggests the clipping at this channel may be due to datalogger saturation, rather than a sensor response.

In Figure 4.53 (SBT at 569*km*, with an STS-1) and Figure 4.54 (TYM at 834*km*, with an STS-1), clipping can be observed in the velocity trace. The integrated displacement timeseries contains the long period response attributed to the sensor clipping described above. It may be caused by a sudden deceleration of the mechanical sensor as it hits its 'stop', the limit of displacement of the pendulum.

Clipping of the broadband instruments due to shaking occurs at the stations indicated in Table 4.1. As discussed, stations as far away as 924*km* from the epicenter record velocities near 1cm/s and clip the STS-1. Though there are numerous other stations further away from the epicenter, which have $K_{max} > 1.15$ - as seen in Figure 4.50 — peak velocities are well below the broadband clip levels, and the high K_{max} is due to some station error. These stations are not included in Table 4.1.

In order to investigate whether these differences between the broadband and strong motion are caused by the strong motions or a systematic station error, F-Net data from smaller events (with subsequently smaller motions at distance), is analysed in a similar

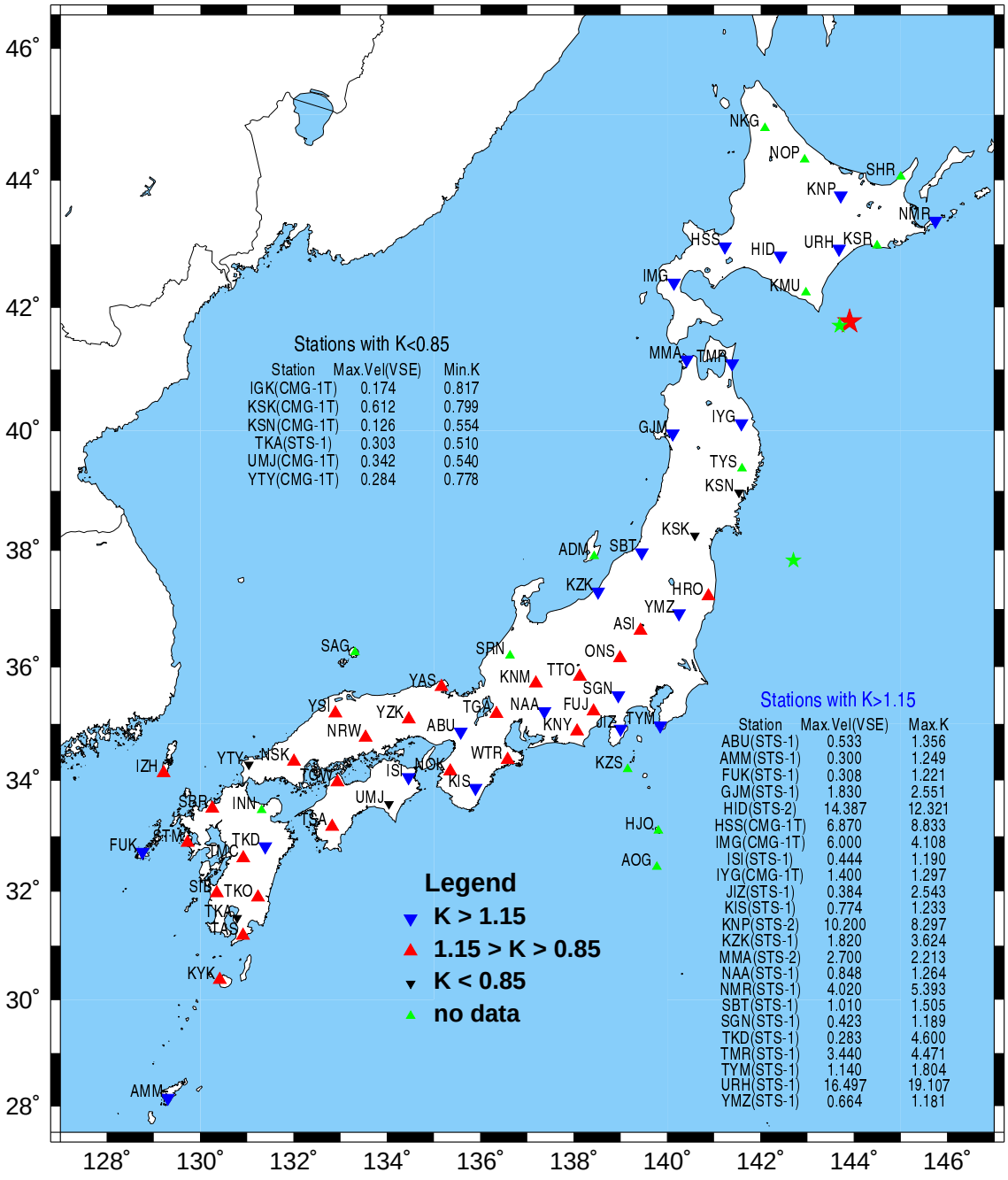

Figure 4.50: Comparison of velocity from F-Net instruments during M8.3 Tokachi-Oki earthquake. K: the ratio of maximum VSE (strong motion) velocity to maximum broadband velocity. This is determined for each of the 3 channels at each station. If $K > 1.15$ for any channel: generally indicates the broadband instrument has clipped, but can indicate incorrect station gain, or an instrument malfunction. $K < 0.85$: suggests instrument malfunction or other station problem. If $0.85 < K < 1.15$: the station appears well calibrated, in working order, and has not clipped. Problem stations have broadband instrument, max. observed VSE velocity (cm/s), and max/min K from all 3 channels tabulated.

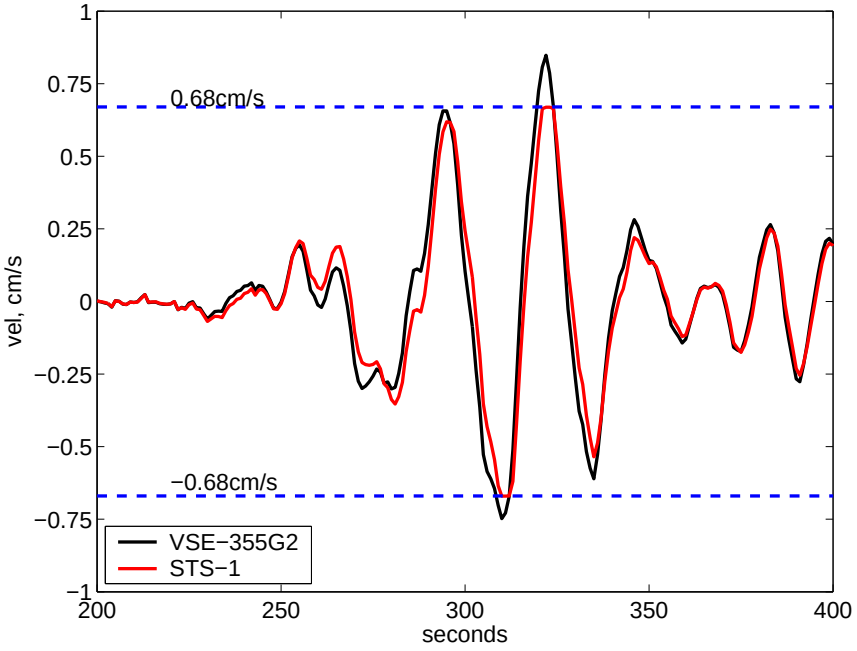

Figure 4.51: STS-1 E-W component from F-Net station NAA recording of M8.3 Tokachi-Oki, at 924km. STS-1 clips at 0.79cm/s.

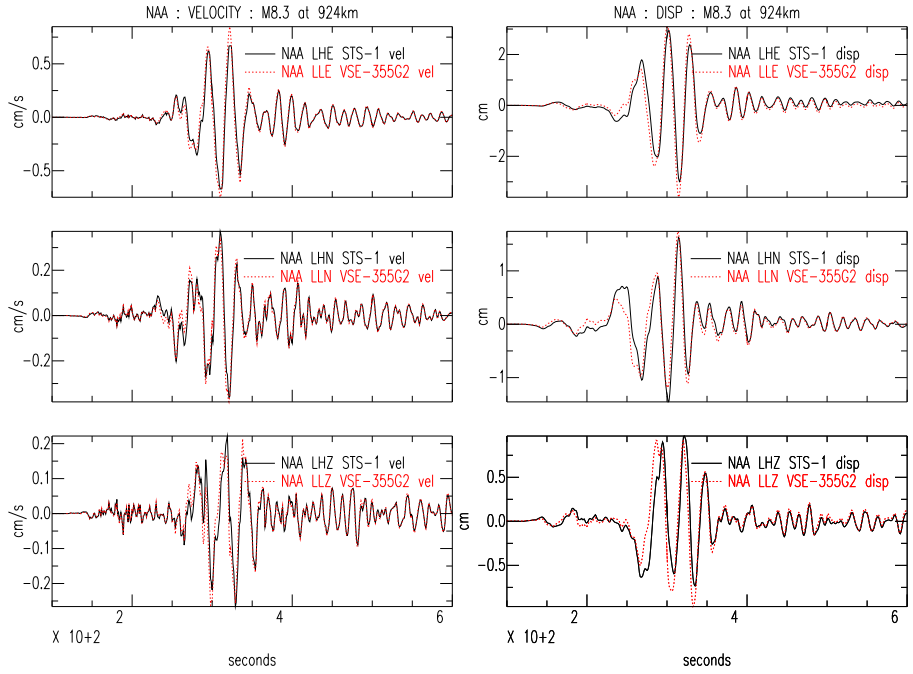

Figure 4.52: F-Net station NAA recording of M8.3 Tokachi-Oki, at 924km. 3 components of velocity and integrated displacement. Though STS-1 E-W component clips, no long period response observed in displacement, indicating saturation occurs in datalogger, not instrument.

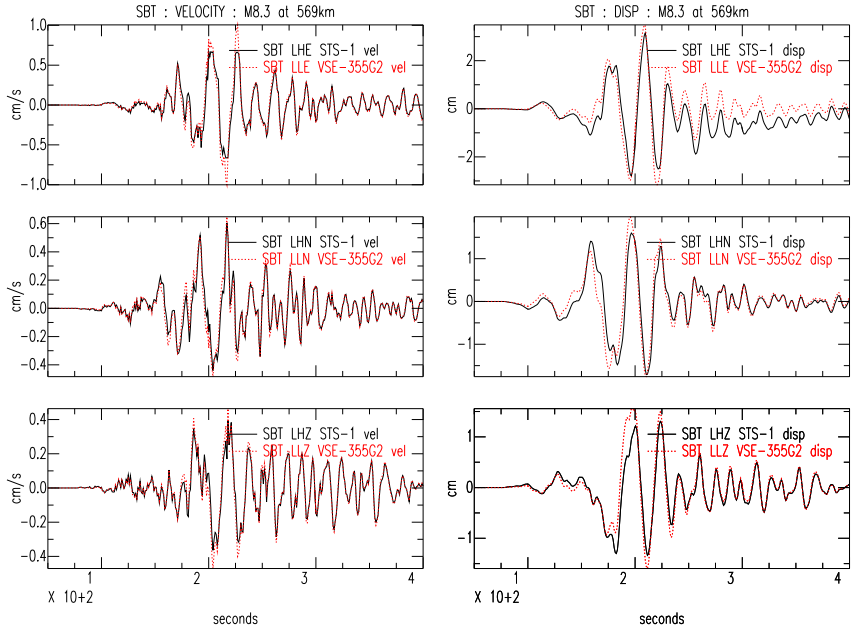

Figure 4.53: F-Net station SBT recording of M8.3 Tokachi-Oki, at 569*km*. All 3 components, in velocity and displacement. Clip in STS-1 E-W component, long period response observed in E-W displacement.

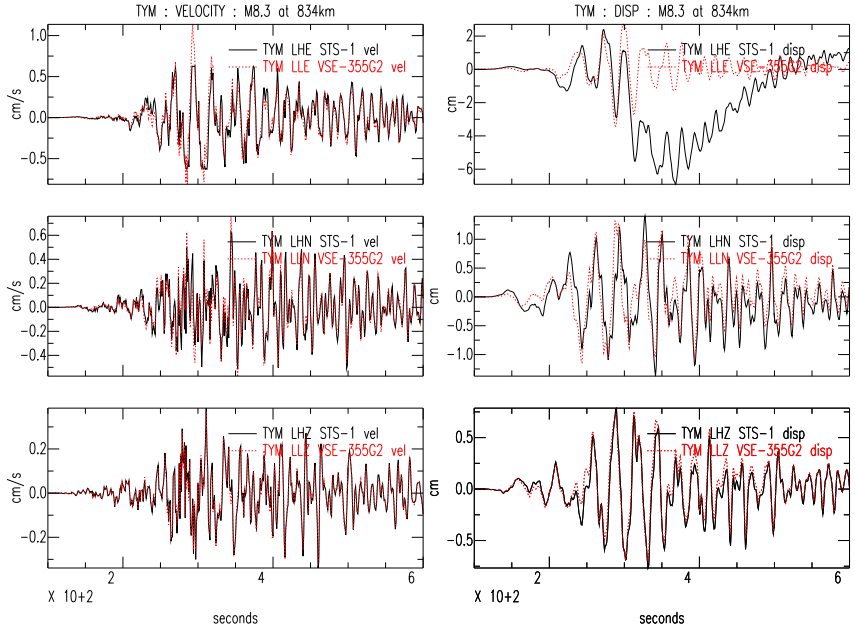

Figure 4.54: F-Net station TYM recording of M8.3 Tokachi-Oki, at 834*km*. All 3 components, in velocity and displacement. Clip at STS-1 E-W component, long period response observed in E-W displacement.

Station	**Distance (*km*)**	**Max VSE Velocity (*cm*/*s*)**	**Broadband Sensor**
URH	129	16.50	STS-1 **clips**
HID	169	14.39	STS-2 **clips**
KNP	221	10.20	STS-2 **clips**
TMR	223	3.44	STS-1 **clips**
NMR	232	4.02	STS-1 **clips**
HSS	257	6.87	CMG-1T **clips**
IYG	268	1.40	CMG-1T **clips**
MMA	300	2.70	STS-1 **clips**
IMG	318	6.00	CMG-1T **clips**
KSN	355	poor data	*wrong timing — ignore*
GJM	378	1.83	STS-1 **clips**
KSK	483	0.61	CMG-1T *NO CLIP*
HRO	568	0.69	STS-2 *NO CLIP*
SBT	569	1.01	STS-1 **clips**
YMZ	624	0.66	VSE-355G2 **clips**
KZK	679	1.82	STS-1 *DIFFERENT RECORDS?*
TYM	834	1.14	STS-1 **clips**
KNM	891	0.89	STS-2 *NO CLIP*
NAA	924	0.85	STS-1 **clips**

Table 4.1: Summary of F-Net station performance within 1000km of Tokachi-Oki

manner. Figure 4.55 presents data from the largest aftershock of the Tokachi-Oki earthquake, a M7.1 occurring $1hr, 18mins$ after the mainshock, very close to the epicentral area. Velocities from this earthquake were much smaller than from the mainshock, but still many stations to the west, up to a distance of $270km$, at IMG, have velocities over $1cm/s$, which is likely to clip the broadband instruments. Stations do not clip towards the north, even though they are closer to the epicenter. This is likely an indication that the directivity of the rupture was towards the West. Figure 4.56 is developed from F-Net data recorded from a M6.8 10 October 2003 earthquake located offshore of East Honshu.

Comparing all 3 maps shows there are many stations with pathological errors repeated for all earthquakes. Often the error appears to be simply a case of a difference in channel gains, as the strong motion and broadband signals for the same component are essentially a scalar multiple of each other. In some cases though, the errors are associated with unexpected instrument behaviour. This occurs both in the strong motion, and the high-gain broadband instruments (in the case of the high-gain broadband sensors, it is noted that from this dataset these errors only are observed for the STS-1 and CMG-1T, and not in the STS-2). One such example is in Figure 4.57, from station TKA at $1631km$, which the Z channel seems to have the same signal, with incorrect station gain. The magnitudes of the velocities recorded by the VSE are similar to those from nearby stations. The STS-1's reported gain seems too high if it clips at a minimum level of $0.59cm/s$. A permanent offset is also recorded on the displacement. This is associated with a broadband response to a step in acceleration, as illustrated in Figure 3.6. The large difference in magnitudes for the Z component is observed with both the M7.3 and M6.8 events. The STS-1 at TKD at $1487km$ from the M8.3(Figure 4.58) also shows similar behaviour, though in this case, STS-1 N-S and Z velocities appear too low. Again, the displacement timeseries show some non-linearity in the response, this time though an unknown long period wave (too long to be the instrument response illustrated in Figures 3.6 or 3.5) is observed in the N-S and Z channels. This performance is repeated again for both the M7.3 and M6.8 events.

A final example illustrates poor behaviour from a VSE-355G2, again during the M8.3, from station YMZ, at $624km$ (Figure 4.59). Here, though the velocity timeseries look identical, with the STS-1 not clipping at over $0.4cm/s$, the integrated displacements show the

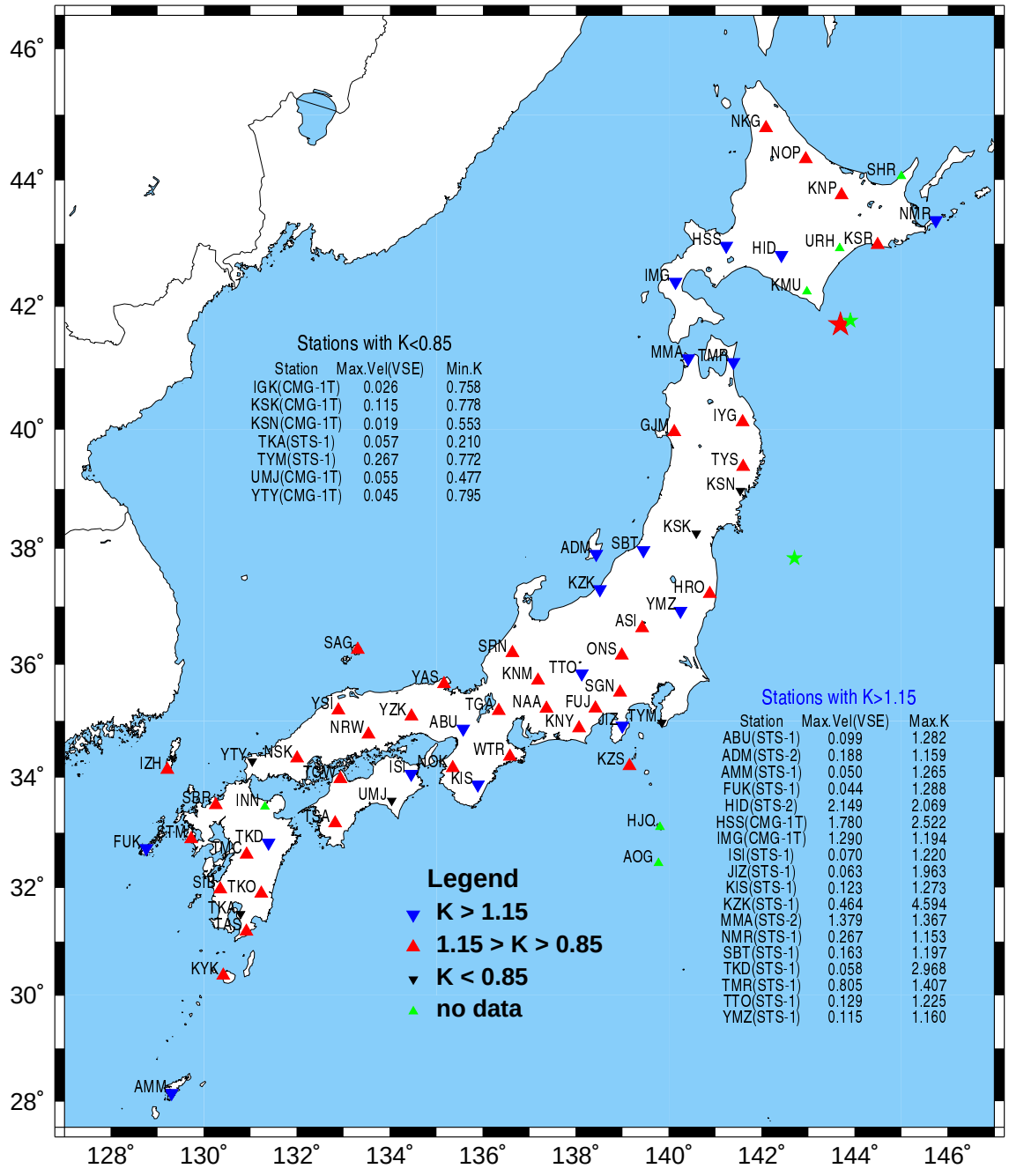

Figure 4.55: As Figure 4.50 for M7.1 25 September 2003 event, an aftershock of Tokachi-Oki.

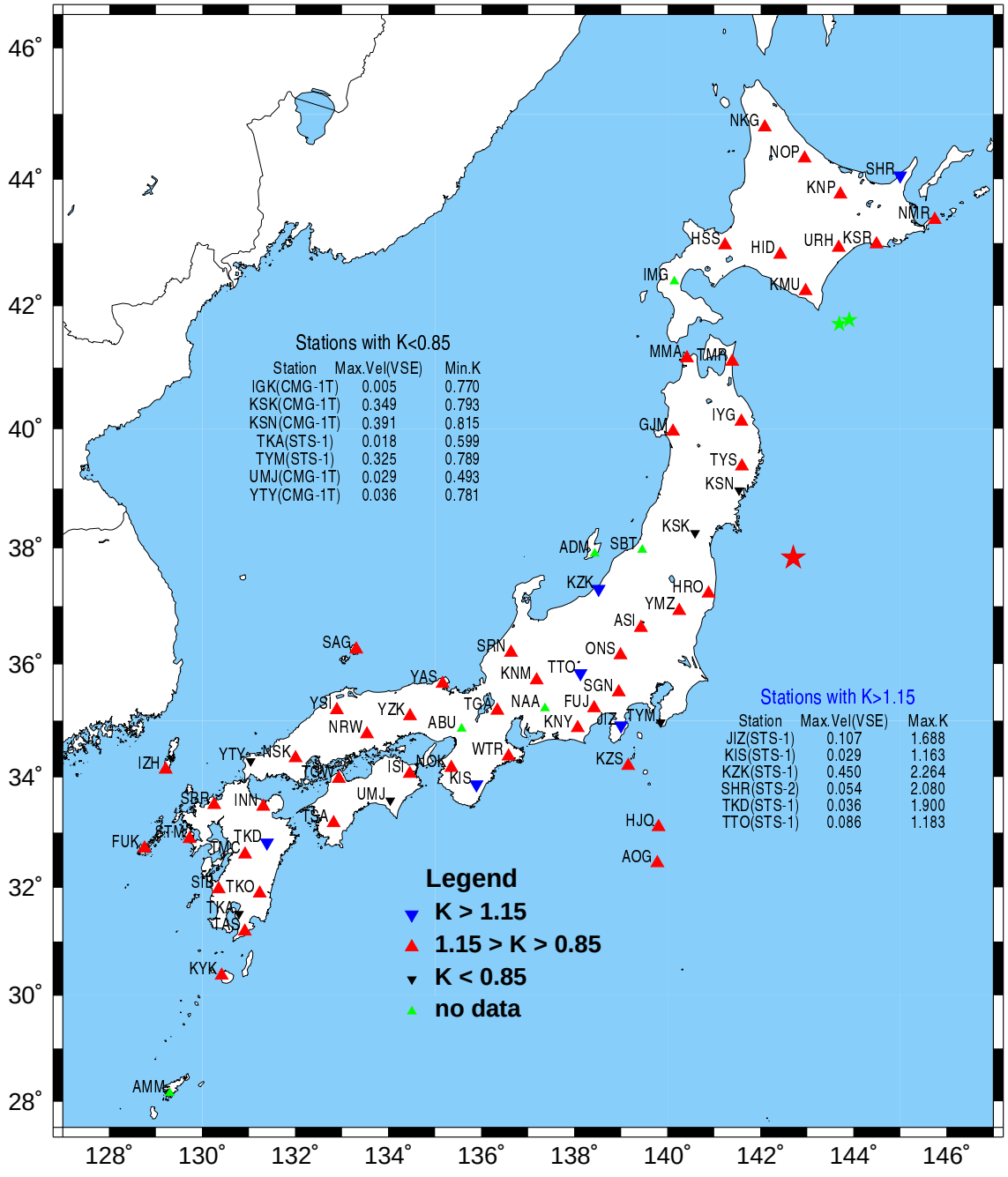

Figure 4.56: As Figure 4.50 for M6.8 10 October 2003 event, located off Honshu Island

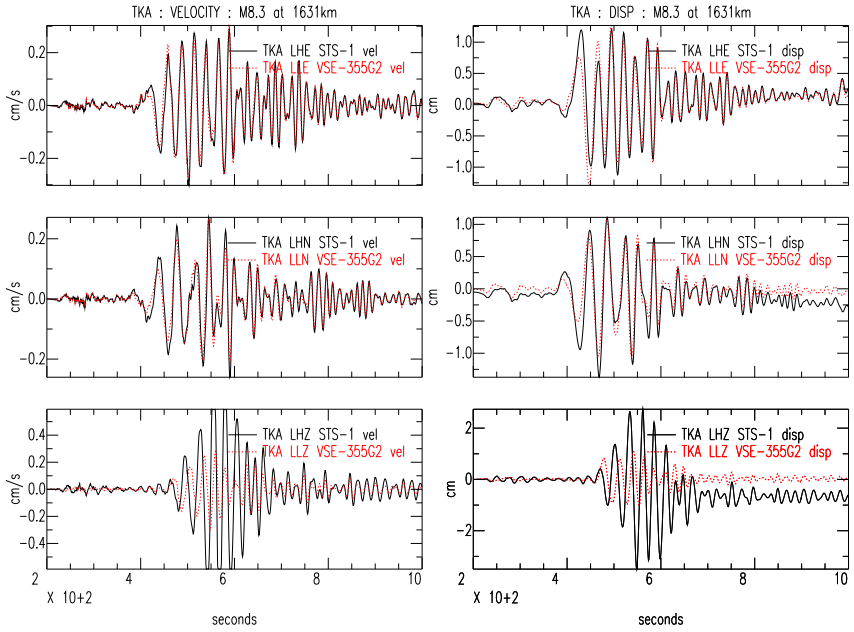

Figure 4.57: F-Net station TKA recording of M8.3 Tokachi-Oki, at 1631*km*. All components, in velocity and displacement. STS-1 Z component appears to have a low station gain, so velocity is too high, with unexplained static offset in corresponding displacement. Also STS-1 drift in N-S displacement.

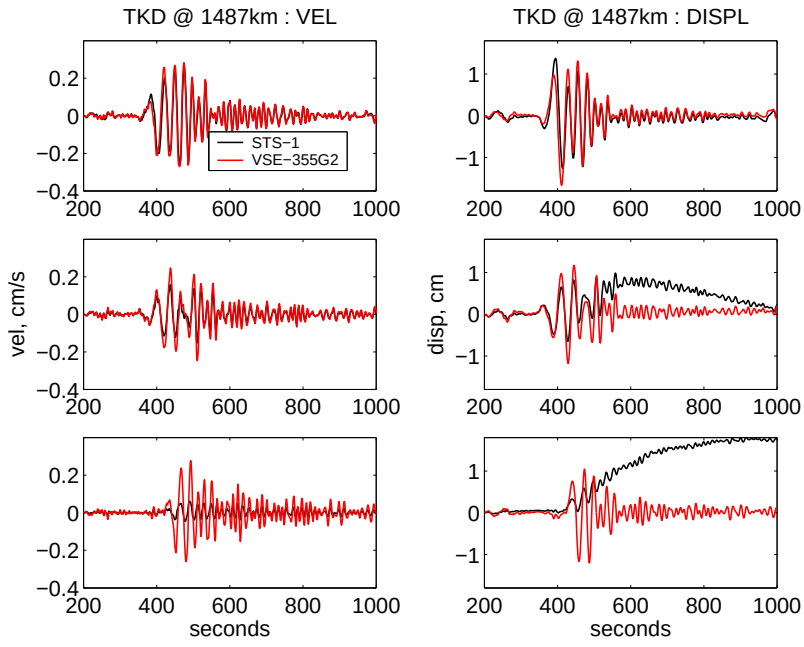

Figure 4.58: F-Net station TKD recording of M8.3 Tokachi-Oki, at 1487*km*. All components, in velocity and displacement. STS-1 Z and N-S component station gains appear to be too high. Unexplained long period drift in displacements. Top: E-W; middle: N-S; bottom: vertical.

VSE has recorded a permanent offset of near 2*cm* that is not physically realistic. Figure 3.6 shows a similar VSE response to a step in acceleration. These observations at YMZ cannot be due to tilt as the offset occurs only on the vertical channel, which is much less sensitive to tilt than the horizontal channels.

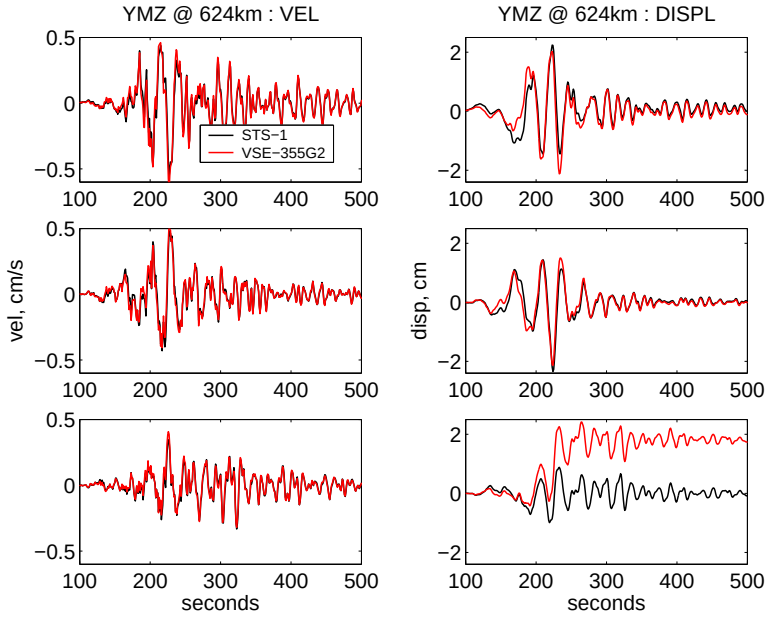

Figure 4.59: F-Net station YMZ recording of M8.3 Tokachi-Oki, at 624*km*. All components, in velocity and displacement. VSE-355G2 Z component performance, similar offset in displacement to a step in acceleration. This also occurs in the M6.8 event, at 239*km*, with max. vel of $0.22 cm/s$. Top: E-W; middle: N-S; bottom: vertical.

Tables 4.2 and 4.3 present a summary of the station information for each earthquake. Instrument types, and K_{max}, K_{min} and peak strong motion velocity are given for each of the 3 earthquakes.

Though not directly relevant to the performance of the VSE, this dataset provides insight into the field performance of the broadband instruments. A general indication of where the actual clip levels of the broadband instruments in the field occur can be obtained by plotting the maximum strong motion velocity against the maximum broadband velocity, as shown in Figure 4.60. From the 3 events, there is a total of 185 station recordings, or 555 channels each of broadband and strong motion.

There is a lot of clutter about the black line in Figure 4.60, so in Figure 4.61, the same data is plotted this time with peak broadband velocity against the ratio of peak broadband

Station	Broad-Band	Strong Motion	Lat	Lon	M8.3				M7.1				M6.8			
					Dist	Kmax	Kmin	VSEmx	Dist	Kmax	Kmin	VSEmx	Dist	Kmax	Kmin	VSEmx
ABU	STS-1	VSE-355G2	34.9	135.6	1072	*1.36*	1.09	0.533	1055	*1.28*	1.08	0.099	-	-	-	-
ADM	STS-2	VSE-355G2	37.9	138.4	-	-	-	-	367	*1.16*	1.03	0.188	-	-	-	-
AMM	STS-1	VSE-355G	28.2	129.3	2010	*1.25*	1.18	0.300	1992	*1.26*	1.20	0.050	-	-	-	-
AOG	STS-2	VSE-355G2	32.4	139.8	-	-	-	-	-	-	-	-	654	1.02	1.00	0.057
ASI	STS-2	VSE-355G2	36.6	139.4	690	1.06	1.04	0.640	674	1.09	1.05	0.111	320	1.04	1.03	0.146
FUJ	STS-1	VSE-355G2	35.2	138.4	870	1.01	0.92	0.512	854	1.13	1.02	0.141	480	1.14	1.05	0.094
FUK	STS-1	VSE-355G	32.7	128.8	1674	*1.22*	1.12	0.308	1655	*1.29*	1.03	0.044	1388	1.12	1.00	0.021
GJM	STS-1	VSE-355G2	40.0	140.1	378	*2.55*	2.20	**1.830**	359	1.08	0.95	0.465	325	1.09	1.01	0.450
HID	STS-2	VSE-355G2	42.8	142.4	169	*12.32*	6.95	**14.387**	162	*2.07*	1.34	**2.149**	554	1.06	0.95	0.132
HJO	STS-2	VSE-355G2	33.1	139.8	-	-	-	-	-	-	-	-	587	1.03	0.98	0.052
HRO	STS-2	VSE-355G	37.2	140.9	568	1.09	1.03	0.692	554	1.12	1.06	0.133	174	1.06	1.02	0.315
HSS	CMG-1T	VSE-355G2	43.0	141.2	257	*8.83*	5.21	**6.870**	246	*2.52*	1.54	**1.780**	584	*1.15*	1.07	0.072
IGK	CMG-1T	VSE-355G	24.4	124.2	2652	0.92	*0.82*	0.174	2634	0.93	*0.76*	0.026	2302	0.89	*0.77*	0.005
IMG	CMG-1T	VSE-355G	42.4	140.1	318	*4.11*	3.53	**6.000**	303	*1.19*	1.06	**1.290**	-	-	-	-
INN	STS-2	VSE-355G2	33.5	131.3	-	-	-	-	-	-	-	-	1138	1.03	1.02	0.024
ISI	STS-1	VSE-355G2	34.1	134.5	1192	*1.19*	1.08	0.444	1174	*1.22*	1.04	0.070	853	1.13	1.02	0.039
IYG	CMG-1T	VSE-355G2	40.1	141.6	268	*1.30*	0.89	**1.400**	250	1.03	0.93	0.303	272	1.02	0.94	0.254
IZH	STS-2	VSE-355G2	34.1	129.2	1542	1.06	1.01	0.341	1523	1.05	1.02	0.056	1282	1.07	1.00	0.044
JIZ	STS-1	VSE-355G2	34.9	139.0	874	*2.54*	1.04	0.384	859	*1.96*	0.95	0.063	464	*1.69*	1.00	0.107
KGM	CMG-1T	VSE-355G	26.8	128.2	2198	1.05	1.01	0.223	2180	1.06	1.00	0.040	1832	1.07	1.03	0.008
KIS	STS-1	VSE-355G2	33.9	135.9	1125	*1.23*	0.94	0.774	1108	*1.27*	0.98	0.123	756	*1.16*	0.94	0.029
KMU	CMG-1T	VSE-355G2	42.2	143.0	-	-	-	-	-	-	-	-	490	1.03	0.99	0.161
KNM	STS-2	VSE-355G2	35.7	137.2	891	1.05	0.96	**0.893**	873	1.04	0.95	0.137	546	1.07	0.95	0.068
KNP	STS-2	VSE-355G2	43.8	143.7	221	*8.30*	5.01	**10.200**	228	1.11	0.98	0.418	664	1.02	1.00	0.097
KNY	STS-2	VSE-355G2	34.9	138.1	920	1.04	1.02	0.467	904	1.11	1.01	0.105	530	1.09	0.95	0.093
KSK	CMG-1T	VSE-355G	38.3	140.6	483	0.94	*0.80*	0.612	466	0.81	*0.78*	0.115	191	0.84	*0.79*	0.349
KSN	CMG-1T	VSE-355G	39.0	141.5	-	-	-	-	355	0.58	*0.55*	0.019	163	0.88	*0.81*	0.391
KSR	STS-2	VSE-355G2	43.0	144.5	-	-	-	-	156	1.03	1.02	0.602	592	1.06	0.93	0.099
KYK	STS-2	VSE-355G2	30.4	130.4	1750	1.10	1.05	0.336	1732	1.08	0.94	0.053	1401	1.07	0.96	0.013
KZK	STS-1	VSE-355G2	37.3	138.5	679	*3.62*	2.52	**1.820**	662	*4.59*	1.93	0.464	374	*2.26*	1.64	0.450
KZS	STS-2	VSE-355G2	34.2	139.2	-	-	-	-	1015	1.04	0.99	0.100	587	1.03	0.98	0.182
MMA	STS-2	VSE-355G2	41.2	140.4	300	*2.21*	2.12	**2.700**	281	*1.37*	1.02	**1.379**	419	1.13	1.00	0.252
NAA	STS-1	VSE-355G2	35.2	137.4	924	*1.26*	0.99	**0.848**	907	1.14	1.02	0.145	-	-	-	-
NKG	STS-2	VSE-355G2	44.8	142.1	-	-	-	-	367	1.06	1.04	0.449	776	1.05	0.94	0.081
NMR	STS-1	VSE-355G2	43.4	145.7	232	*5.39*	3.18	**4.020**	249	*1.15*	1.07	0.267	666	1.12	1.08	0.056
NOK	STS-2	VSE-355G2	34.2	135.4	1130	1.07	1.01	0.553	1112	1.05	1.02	0.103	777	1.08	1.03	0.037
NOP	STS-2	VSE-355G2	44.3	142.9	-	-	-	-	296	1.00	0.98	0.373	721	1.05	1.01	0.110
NRW	CMG-1T	VSE-355G	34.8	133.5	1194	1.08	1.01	0.378	1175	1.04	0.98	0.079	890	1.09	1.01	0.037
NSK	STS-2	VSE-355G2	34.3	132.0	1329	1.08	1.00	0.373	1310	1.05	1.00	0.057	1038	1.04	0.99	0.034

Table 4.2: Summary of F-Net station performance during large earthquakes in Autumn, 2003. Epicenters plotted on maps in Figures 4.50, 4.55 and 4.56. Distances of station from epicentre are in *km*, maximum velocities are from the strong motion instrument, in cm/s.

Station	Broad-Band	Strong Motion	Lat	Lon	M8.3				M7.1				M6.8			
					Dist	Kmax	Kmin	VSEmx	Dist	Kmax	Kmin	VSEmx	Dist	Kmax	Kmin	VSEmx
ONS	CMG-1T	VSE-355G	36.2	139.0	756	0.95	0.91	0.564	739	0.96	0.87	0.086	380	0.96	0.90	0.103
OSW	STS-2	VSE-355G2	27.1	142.2	-	-	-	-	1627	1.03	1.00	0.017	1192	1.04	1.01	0.018
SAG	STS-2	VSE-355G2	36.3	133.3	-	-	-	-	1083	1.05	1.02	0.071	853	1.05	1.02	0.054
SBR	STS-1	VSE-355G	33.5	130.3	1512	1.14	1.09	0.308	1493	1.09	1.04	0.050	1224	1.10	1.04	0.030
SBT	STS-1	VSE-355G2	38.0	139.5	569	*1.50*	1.07	**1.010**	552	*1.20*	1.05	0.163	-	-	-	-
SGN	STS-1	VSE-355G2	35.5	138.9	819	*1.19*	1.01	0.423	803	1.09	1.02	0.081	423	1.09	1.02	0.103
SHR	STS-2	VSE-355G2	44.1	145.0	-	-	-	-	-	-	-	-	718	*2.08*	1.07	0.054
SIB	STS-2	VSE-355G2	32.0	130.4	1622	1.05	1.01	0.347	1604	1.05	1.00	0.065	1301	1.02	0.99	0.025
SRN	STS-2	VSE-355G2	36.2	136.6	-	-	-	-	865	1.03	0.99	0.116	569	1.07	1.00	0.095
STM	STS-2	VSE-355G2	32.9	129.7	1594	1.06	1.05	0.335	1575	1.04	1.03	0.050	1299	1.03	1.02	0.028
TAS	STS-2	VSE-355G2	31.2	130.9	1650	1.06	0.97	0.335	1632	1.04	1.03	0.053	1308	1.04	0.96	0.017
TGA	STS-2	VSE-355G2	35.2	136.3	985	1.05	0.96	0.762	967	1.05	0.99	0.137	641	1.04	1.00	0.061
TGW	STS-2	VSE-355G2	34.0	132.9	1295	1.05	1.03	0.331	1276	1.07	1.03	0.091	979	1.03	1.02	0.030
TKA	STS-1	VSE-355G2	31.5	130.8	1631	1.00	*0.51*	0.303	1613	0.94	*0.21*	0.057	1296	0.90	*0.60*	0.018
TKD	STS-1	VSE-355G2	32.8	131.4	1487	*4.60*	1.07	0.283	1469	*2.97*	1.10	0.058	1168	*1.90*	1.02	0.036
TKO	STS-2	VSE-355G2	31.9	131.2	1572	1.04	1.02	0.372	1554	1.05	1.00	0.077	1237	1.03	0.99	0.025
TMC	STS-2	VSE-355G2	32.6	130.9	1535	1.07	0.99	0.306	1516	1.07	1.05	0.066	1218	1.05	0.99	0.027
TMR	STS-1	VSE-355G2	41.1	141.4	223	*4.47*	2.29	**3.440**	204	*1.41*	1.21	**0.805**	380	1.10	0.98	0.213
TSA	CMG-1T	VSE-355G	33.2	132.8	1366	1.05	1.00	0.363	1348	1.10	1.02	0.080	1034	1.03	1.01	0.036
TTO	STS-1	VSE-355G	35.8	138.1	828	1.11	1.03	0.666	812	*1.23*	1.00	0.129	464	*1.18*	0.99	0.086
TYM	STS-1	VSE-355G2	35.0	139.8	834	*1.80*	0.97	**1.140**	820	1.13	*0.77*	0.267	408	0.90	*0.79*	0.325
TYS	STS-2	VSE-355G2	39.4	141.6	-	-	-	-	314	1.06	1.00	0.348	197	1.05	0.97	0.361
UMJ	CMG-1T	VSE-355G	33.6	134.0	1257	0.79	*0.54*	0.342	1240	0.79	*0.48*	0.055	914	0.83	*0.49*	0.029
URH	STS-1	VSE-355G	42.9	143.7	129	*19.11*	13.68	**16.497**	-	-	-	-	572	1.08	1.01	0.144
WTR	STS-2	VSE-355G2	34.4	136.6	1042	1.04	0.86	0.773	1026	1.04	1.02	0.137	672	1.06	1.03	0.043
YAS	STS-2	VSE-355G2	35.7	135.2	1019	1.05	1.00	0.530	1000	1.03	0.98	0.106	715	1.05	1.03	0.064
YMZ	STS-1	VSE-355G2	36.9	140.2	624	*1.18*	1.14	0.664	608	*1.16*	1.02	0.115	239	1.12	1.00	0.219
YNG	STS-2	VSE-355G2	24.4	123.0	-	-	-	-	2705	1.03	1.01	0.037	2384	1.07	1.01	0.013
YSI	STS-2	VSE-355G2	35.2	132.9	1206	1.05	1.01	0.391	1187	1.07	1.04	0.062	926	1.07	1.03	0.057
YTY	CMG-1T	VSE-355G	34.3	131.0	1400	0.96	*0.78*	0.284	1381	0.93	*0.80*	0.045	1121	0.95	*0.78*	0.036
YZK	CMG-1T	VSE-355G	35.1	134.5	1108	1.06	1.03	0.410	1090	1.04	1.02	0.091	798	1.03	1.01	0.059
ZMM	STS-2	VSE-355G2	26.2	127.3	2299	1.08	0.97	0.194	2281	1.07	0.94	0.029	1936	1.04	*0.85*	0.009

Table 4.3: Table 4.2 continued. Summary of F-Net station performance during large earthquakes in Autumn, 2003. Epicenters are located in Figures 4.50, 4.55 and 4.56.

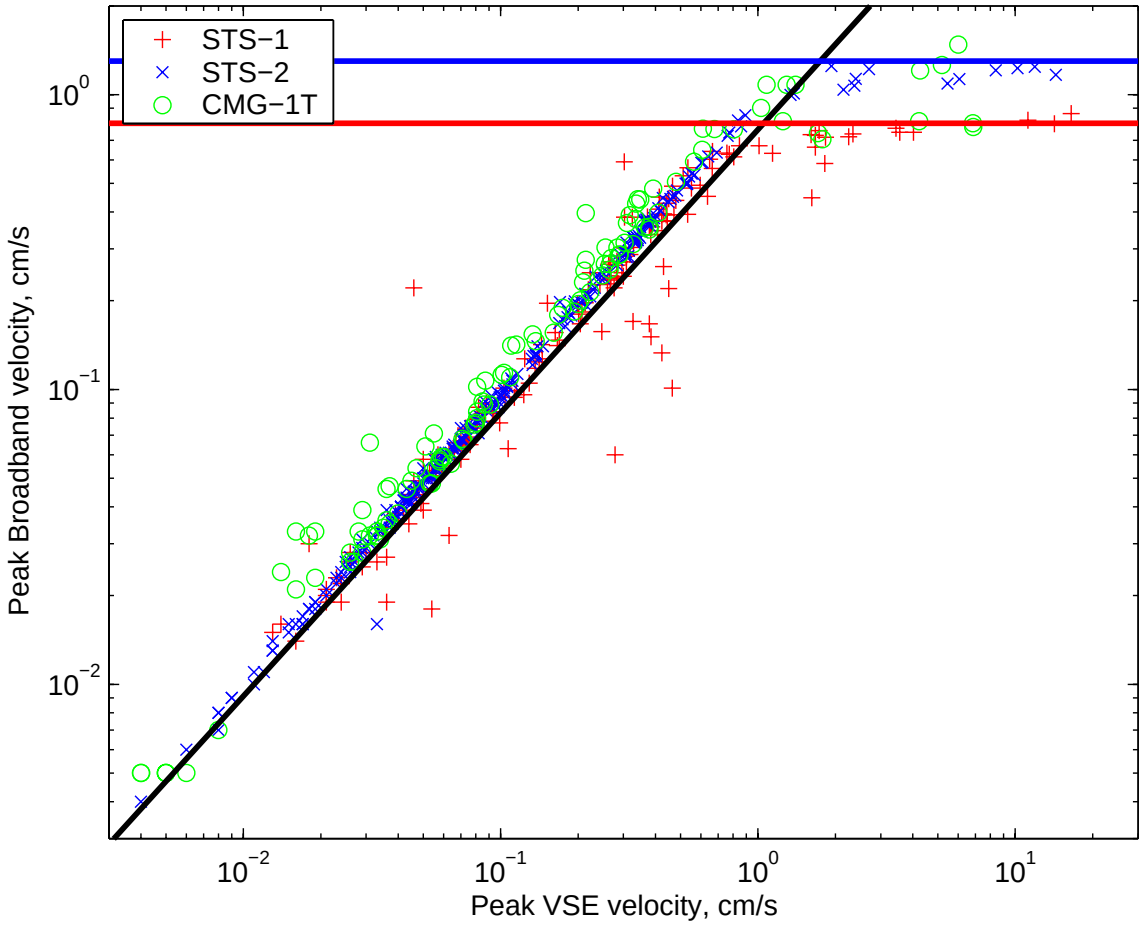

Figure 4.60: F-Net data from the 3 earthquakes: Comparison of peak broadband velocity against peak strong motion (VSE) velocity for each of 555 channels. Stations with STS-1 represented by: red plus; STS-2: blue cross; CMG-1T: green circles. The black line represents equal velocities for both instruments, the line on which data below clip is expected to fall on. Blue line is expected clip for STS-2 (and CMT-1T), at $1.3 cm/s$, red line is expected clip for STS-1, at $0.8 cm/s$

velocity to peak strong motion velocity for each component (equivalent to $1/K_E$, $1/K_N$ and $1/K_Z$). It is clear there is a lot of variation for the CMG-1T stations, though there is a bias to ratios above 1. There is some cluster of events just above a ratio of 1.6, which is the expected ratio if an STS-1 gain has been assigned to the CMG-1T. [From Table 2.1, we see sensitivity of STS-1 is $\sim 2500V/m/s$, and an STS-2 and CMG-1T have $1500V/m/s$, a ratio of 1.66.] The STS-1 also has a lot of variation, though ratios tend to be less than 1, and some clustering below a ratio of 0.6, which is consistent with a station gain of the STS-1 replaced with that of an STS-2. The STS-2 has much less variation, and has an average ratio of ~ 1.

The ratios for all instruments tend to drop sharply as they approach the expected clip levels, which indicates clipping. In fact, many of the instruments seem to clip at levels below the expected clip, but for the STS-1 and STS-2, the clip occurs within 80% of the expected clip for almost all instruments. This is observed in Figure 4.61 with the clustering of STS-2 channels between the two vertical blue lines, and for the STS-1 channels between the two vertical red lines. It is noted there is no exceedance of the expected clip for any of these channels. In contrast, the CMG-1T has a much broader range of apparent clipping, from $0.7cm/s$ to $1.45cm/s$.

In order to investigate the mean and standard deviation for the broadband stations below clipping, all data within 80% of the STS-2 clip for the STS-2 channels, and within 80% of the STS-1 clip for the CMG-1T and STS-1 channels is disregarded. The resultant data set may be summarised as:

	STS-2	STS-1	CMG-1T
# channels	252	141	96
$\left[\frac{peakBBvel}{peakVSEvel}\right]$ mean	0.971	0.930	1.116
$\left[\frac{peakBBvel}{peakVSEvel}\right]$ std. deviation	0.049	0.384	0.232

These means and standard deviations confirm that in this network, the STS-2 is a more consistent and reliable instrument then the STS-1 and CMG-1T.

It is noted that since all broadband components are compared with the the VSE-355G/G2, they are thus also sensitive to any variations from the VSE sensor calibration.

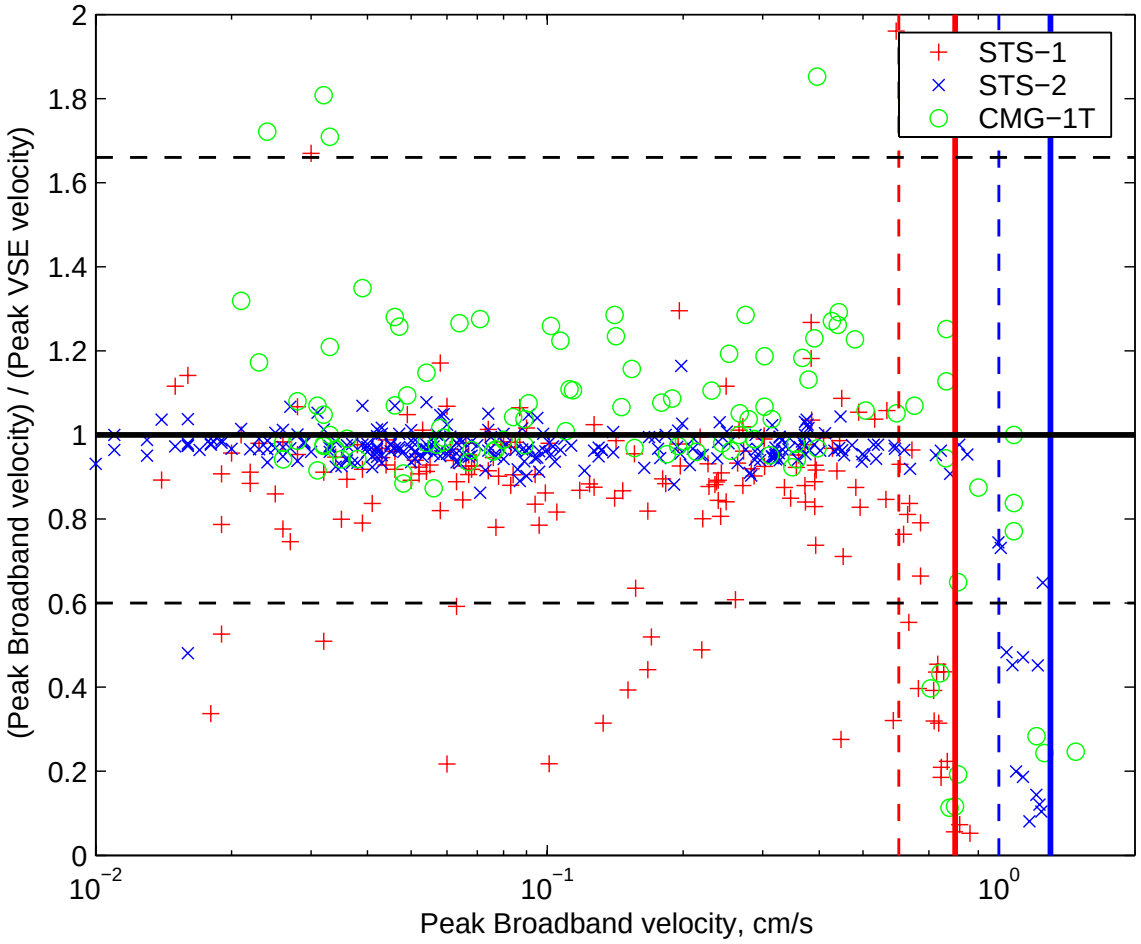

Figure 4.61: F-Net data from the 3 earthquakes: Comparison of peak velocity ratios against peak broadband velocity for each of 555 channels. STS-1: red plus; STS-2: blue cross; CMG-1T: green circles. The solid black line is expected ratio, 1. Dotted lines are expected ratios if simple instrument gain errors have occurred. Blue line: expected clip for STS-2, CMT-1T ($1.3 cm/s$), red line: expected clip for STS-1 ($0.8 cm/s$). Dotted red, blue lines are at 80% of these clip levels.

Figure 4.62 shows there is no correlation between component and deviation from expected behaviour. Any correlation trends more with instrument type, as seen in Figure 4.61.

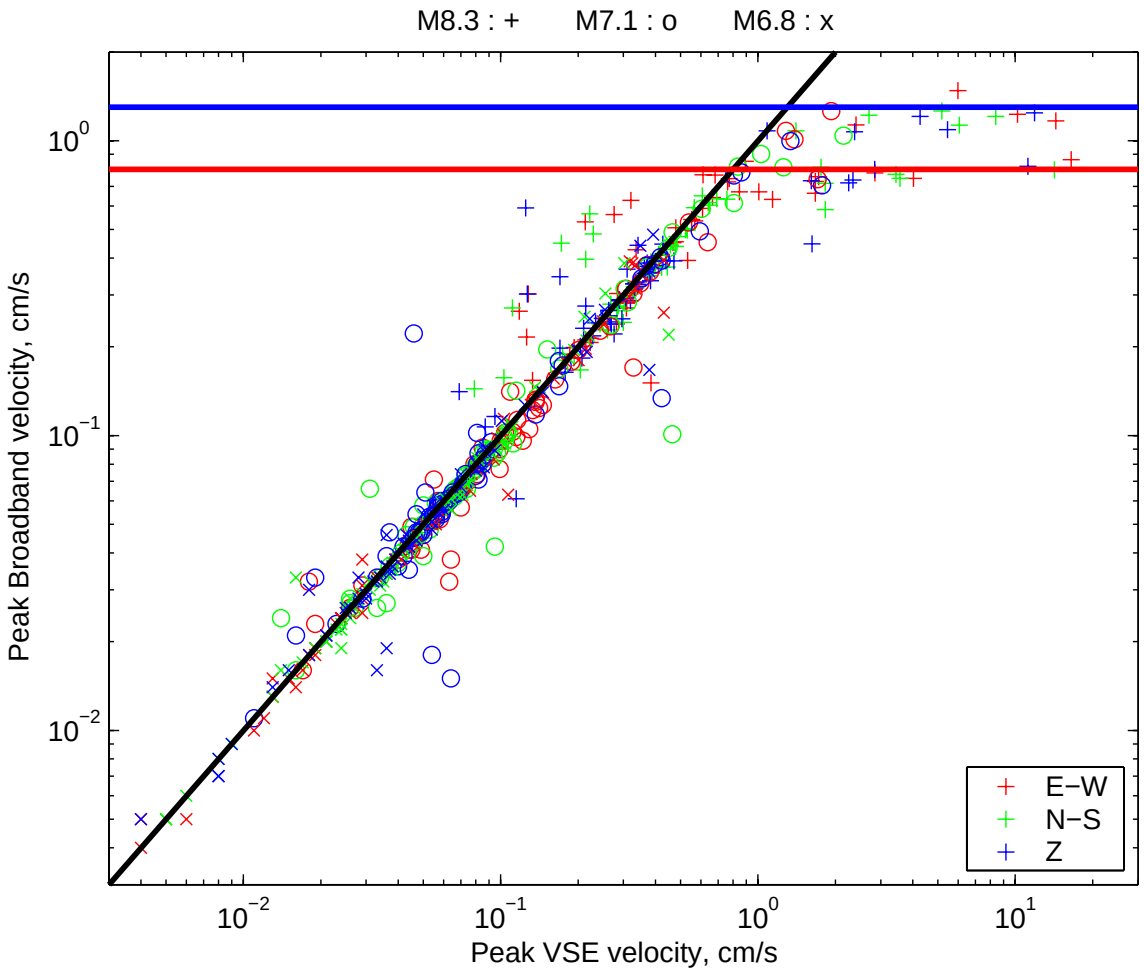

Figure 4.62: F-Net data from the 3 earthquakes: Comparison of peak broadband velocity against peak strong motion (VSE) velocity for each of 555 channels. As Figure 4.60, with colours representing channel orientations rather than broadband instrument type. Observe no error trending with individual components.

Finally, this dataset can be used to observe how the velocity decays with distance from the epicenter. Figure 4.63 shows on a log scale there appears to be a roughly linear decay of velocity with distance. The distance range here is from 100km to 3000km. A least squares fit to the data shows this decay rate of velocity amplitude with distance varies in the form of $vel \propto 1/r^n$, with n varying from 1.65 (M6.8) to 1.26 (M7.1). This is roughly consistent with the expected values of 1.42 (rock sites) and 1.62 (basin sites), developed from regression

analysis using a catalogue of southern California events (Cua, 2004).

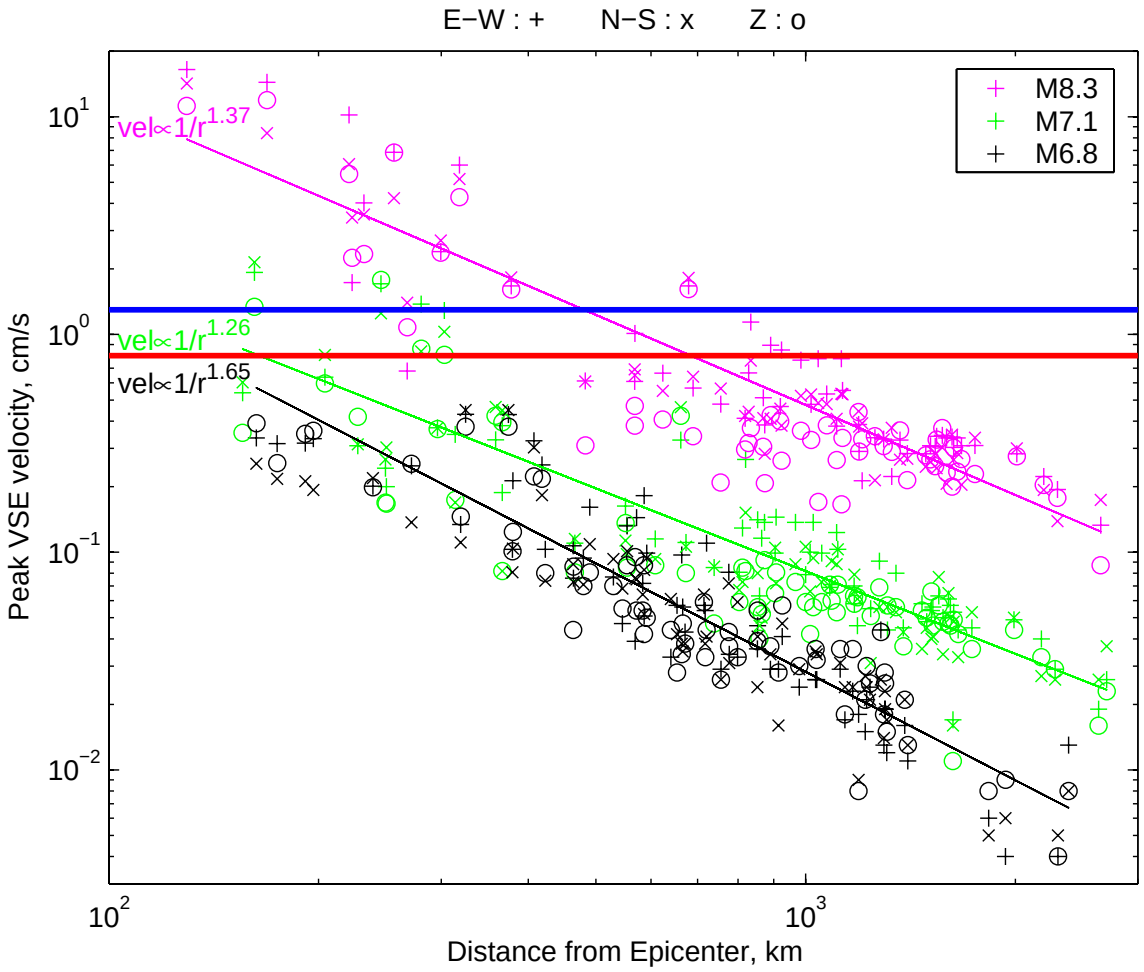

Figure 4.63: Comparison of peak strong motion velocity against distance from the epicenter for the three earthquakes, using F-Net data. Blue line: expected STS-1 and CMG-1T clip, red line: expected STS-1 clip. In M8.3, signals out to 1000km clip the STS-1. Compare ratios of velocity decay with distance to relationship of $vel \propto 1/r^n, n = 1.42(rock), 1.62(basin)$ from Cua (2004).

4.7 Summary

The many results of the analysis of the strong and weak motions recorded over Japan from the M8.3 25 Sept 2003 Tokachi-Oki earthquake are summarised below —

• Seismic data is available from 4 main networks. Nationwide Networks run by NIED are: 1. F-Net — a 24-bit broadband network with strong motion (VSE-355G/G2) and

high-gain velocity sensors co-located in vaults. About 100 stations throughout Japan, separated by about 100km. 2. K-Net — a dense 24-bit strong motion accelerometer network with 1000 stations nationwide, at 20km intervals. Free-field sites, but often noisy urban locations. 3. KiK-Net — an up-hole down-hole network of 24-bit accelerometers, with minimum borehole depth of 100m. 650 stations nationwide, located a quiet sites, often hard-rock. A final network local to Hokkaido run by the Civil Engineering Research Institute of Hokkaido consists of over 100 16-bit stations of strong motion VSE255EI instruments, with a corner at 56s. Stations are located on civil infrastructures such a road embankments, bridges, and large buildings.

• F-Net VSE-355G2 instruments, identical to the instrument tested in this thesis, also exhibit low clip levels during the earthquake. As in the lab, once velocities reach about 16cm/s, spikes in frequency associated with non-physical ground displacements occur. Only 2 VSE-355G2 recorded velocities significantly above this clipping velocity, and both had this problem (Figures 4.13 and 4.20). Another recorded 16.6cm/s and did not clip (Figure 4.47). A VSE-355G recorded 25cm/s without clipping, though this was the only sensor of this type to measure velocities above 14cm/s (Figure 4.29). VSE-355EI sensors in the WISE network record over 100cm/s without clipping (Figure 4.15).

• GPS data is recorded by GEONET, and is freely available over the Web at a sample rate of one data point per day. Many seismic stations are located in close proximity to GPS stations, and large permanent offsets are recorded ($> 1m$) over a wide area (Figures 4.5 and 4.6). These well recorded large displacements provide an important dataset for understanding how permanent displacements may be determined during strong ground motions.

• Strong motion seismic data, whether recorded by accelerometers or strong motion velocity sensors, is very sensitive to ground tilts, which cannot be readily distinguished from ground translation. A tilt of 0.003^o in an accelerometer, or strong motion velocity instrument, will produce a 10cm offset from the true displacement after only 20s. Tilts larger than this are widespread in the observed seismic data.

• The expected tectonic tilts are determined from the vertical co-seismic deformation between GPS stations. In the most severely displaced regions, these tilts are very small (of

the order of 0.0005^o). This is too minor to significantly obscure permanent displacements of many *cm*, widespread over most of the island of Hokkaido. As many seismic stations do have offsets compatible with larger tilts, they may be due to local site failure. Landslides, lateral spreading, and liquefaction were indeed observed over large regions near the epicenter.

• In sites where little ground tilting occurs, such as many down-hole KiK-Net and vaulted F-Net stations, and also some up-hole KiK-Net K-Net stations, permanent ground displacements from the seismic data is very similar to displacements measured by GPS (Figures 4.28, 4.35 and 4.42).

• high-rate GPS ($1sps$) is not freely available from GEONET, but was obtained for a sample of station from Kristine Larson. Preliminary analysis of this dataset shows excellent correlation with GPS for many stations. A methodology to combine the high-rate GPS data and the seismic data, which is easily affected by tilting, can lead to a complete understanding of ground motions — translations and displacements, at a given site.

• There are numerous KiK-Net sites in the region, where very small amounts of tilt is observed by the deep down-hole sensors, with the up-hole sensors recording local site tilting due to a variety of effects, which could include liquefaction and lateral spreading. In general, tectonic tilts determined from GPS data are shown to be almost negligible compared to the observed tilts.

• Though the WISE network is very dense, with many strong motion velocity sensors in the near source region (F-Net only has 4 stations that record over $10cm/s$), this network is unfortunately inappropriate for the studies undertaken here. Sensor component alignment appears to be unreliable. Also, the sensors are not located in 'free-field' sites (as this network is installed to monitor civil infrastructure) many have obvious structural resonances, or suffer site failure. Further, the sensor characteristics are not as broadband as other sensors used in this study, with a corner at $56s$ instead of at least $80s$. This increases the sensor noise for permanent displacement estimation.

• Regional ground motions from Tokachi-Oki observed over the length of Japan by the broadband F-Net stations show that high-gain broadband instruments have all saturated within $500km$ of the rupture, and some saturate at distances up to $1000km$ from the epicen-

ter (Figure 4.50).

• The Tokachi-Oki, and other large earthquakes, provide an excellent dataset for estimating the state-of-health of the sensors in a seismic network. By comparing timeseries from the broadband and strong motion sensors, which have been excited above the noise level over a very broad area, incorrect station gains, or faulty sensors, can be readily identified. Pathological errors in station gains were found for the CMG-1T and STS-1 broadband sensors. It is not known whether this is characteristic of the sensor, or is isolated to F-Net in particular (Figures 4.50, 4.55, 4.56 and 4.61).

• The large number of saturated broadband instruments provide insight into the overall performance of broadband sensors at levels near clipping. The STS-2 and STS-1 are shown to reliably clip at, or within 80%, of their expected clip levels ($1.3 cm/s$ and $0.8 cm/s$ respectively). There was a larger variation in clipping for the CMG-1T (Figure 4.61).

Chapter 5 Modifications to the VSE-355G2 — The VSE-355G3

5.1 Introduction

In Chapter 3 the VSE-355G2 instrument was introduced, and the major problem with a low clipping level was exposed. In Chapter 4, this problem was observed by the same instrument in the field during the M8.3 Tokachi-Oki earthquake. This Chapter summarises the modifications made to the instrument by the manufacturer, and provides laboratory and station data which indicates that the instrument is now performing to original specifications.

During the modification and re-testing process, low clip levels were found in the vertical channel once the horizontal problem seemed to have been corrected. The cart test was run in a elevator in Japan, as the set-up at Caltech did not easily facilitate this type of test.

Cart test data now shows impressive strong motion performance from the VSE-355G3, with motions exceeding $200 cm/s$ being recorded linearly by the instrument. The dynamic range of the instrument has not been compromised by the modifications, and retains similar performance to the VSE-355G2.

The equivalent SDOF determined from the calibration testing indicates the instrument has a different response from the VSE-355G2, with a longer equivalent free period of about $105s$ now observed. This is well in excess of the range specified by the manufacturer of only $80s$. Damping is slightly lower at 65% of critical. There much better correlation with the observed SDOF response and the expected theoretical Transfer Function response than is shown for the VSE-355G2.

The instrument is currently deployed within the CISN alongside a CMG-1T at CRP, the Caltech Robinson Pit.

5.2 Modifications

The instrument has been modified internally once, and fully overhauled twice. Both overhauls involved an engineer from Tokyo Sokushin visiting Caltech, and removing the existing suspension and feedback for all 3 components, replacing them with new sensors and feedback circuitry.

The first internal modification occurred in 18 June 2002, after Sokushin had identified the source of the low saturation velocities as a fault with the power regulator in the electronic feedback system which prevented the final stage amplifier from operating correctly. This attempt to increase the clip level to the expected level of $200cm/s$ only succeeding in moving the observed clip from $15cm/s$ to $40cm/s$ (see Figs 3.21 and 3.24).

A full overhaul took place on 11-12 November 2002. This was again in response to the low clipping levels. Cart tests subsequent to this showed the low clip level problem had been resolved for the two horizontal components, but not for the vertical component (Figure A.3(b)). Also, there was significant cross-coupling between all three components (Figure A.3(a)).

After investigation, Tokyo Sokushin reported that both problems were caused by a mechanical problem — the suspension spring in the Z-axis being unable to adequately resist the large velocities. This was fixed, as evidenced by elevator tests performed in Japan, where the vertical component was subjected to $\sim 1m/s$ velocities without any problems (Figure A.4).

On 15-16 Sept 2003, this same modification was incorporated into the Caltech sensor, which again involved replacing all 3 sensors. Cart tests subsequently confirmed the clip level was acceptable for the horizontal components, recording linearly beyond $2m/s$. Without the ability to perform an elevator test at Caltech, the vertical component could not be excited up to 2m/s. Velocities up to about $10cm/s$ were successfully recorded. Cross-axis sensitivity seemed to have been eliminated.

At this stage, with the apparent success of the instrument in strong motion, calibration tests were performed. These tests produced large permanent offsets in raw velocity output from simple step-function excitations that should not result in permanent offsets

(Figures A.7 and A.8, the expected response shown in Figure 3.5).

Once again the manufacturer visited Caltech, where it was discovered from careful analysis of the response of a similar VSE-355G3 instrument in Japan, that the errors were produced by incorrect pin connections between the sensor and the datalogger. When this was repaired, the instrument performed well in the calibration tests. At this stage, a full series of tests were repeated to confirm compliance with the sensor specifications. An in-depth chronological list of site visits by Sokushin, including results, and important milestones in the testing regime, are presented in Appendix A.

5.3 Test Analysis

5.3.1 Instrument Clipping

After all the repairs had been completed, by September 2003, the VSE-355G3 was observed to perform well in the cart test. A typical result is seen in Figure 5.1(a). The 'raw' output only is plotted, with nominal station gains removed, and acceleration data integrated to velocity. All three channels, the in-plane motion in the direction of the cart displacement, the out-of-plane, and the vertical, have very similar timeseries for both sensors. Figure 5.1(b) presents the large in-plane motions only, in acceleration, velocity and displacement. Also included in this plot is the time-domain deconvolution solution for the VSE-355G3. The deconvolved motion maps the EpiSensor's motions extremely well. In the velocity time-series, the maximum recorded deconvolved velocity is $211 cm/s$, which exceeds specifications. After the motion has ended, the deconvolved VSE-355G3 velocity records a near-zero velocity, reflecting the true physical position of the sensor, and indicates little tilting has occurred. The similarities in the displacement timeseries are also obvious, and the lack of tilt in the VSE-355G3 is reflected by a very steady final displacement of about $-16.4m$ being recorded. This is about the same distance traversed in the test (it was not precisely measured). This Figure can be compared to the theoretical solution of a similar cart test shown in Figure 3.10. This example has the least tilt of all the runs performed, in other tests, as seen in the subsequent plots, tilt seriously distorts both sensors'

translational response.

In the suite of tests which included the above data, clipping was observed only well beyond the $2m/s$ level, near $2.5m/s$. No cross coupling was observed, though some large offsets were observed in the 'zero' level for the horizontal channels. A plot of the entire suite of tests is in Figure A.6, showing a timeseries which consists of numerous cart tests, forwards and backwards along the hallway, and is interspersed with rotations of the VSE-355G3 sensor. The large offsets are caused by tilting of the instrument during both the translation and rotation — if tilts are large enough, they cannot be rectified by the sensor feedback. Figure A.11 shows a test subsequent to the discovery of the occurrence of the tilting, and the instrument's sensitivity to the problem. In this sequence of tests, whenever a tilt was observed after a displacement or rotation, the instrument was re-levelled. Re-levelling caused the background output level to return to zero.

In Figure 5.2, another example of a cart test is presented, from tests run in November, after all pin connection problems had been resolved. Again all three components are compared, also oriented to record in-plane motion, the out-of-plane and the vertical motion. All VSE-355G3 data has the instrument response removed using a time-domain deconvolution. Considering the rugged nature of the test, there is very good correlation of all components. Close correlation of large peak velocities over $175cm/s$ is recorded for the in-plane velocity. The effect of the tilt is severe, as seen by large linear trends in the out-of-plane velocity, which are similar for both sensors. Even so, the slope of the velocity is roughly $8cm/s^2$ for both sensors in the out-of-plane direction, which corresponds to a tilt of only 0.475^o (Equation 1.18), a small rotation. The effect of this tilt so strong it even affects the insensitive vertical components in both sensors. The permanent displacement is observed by the very similar in-plane displacement behaviour, with an offset of about -11m being recorded once the event is over, which correlates with the cessation of large accelerations and velocities. After this time, the large tilts cause immediate deviation of the displacement record. In the other components, displacements are expected to be small with little or no permanent offset. The large tilts, of the same order of magnitude as the in-plane tilts, cause large, non-physical displacements almost immediately after test begins.

The largest motions recorded in the correctly levelled sequence of cart tests are shown

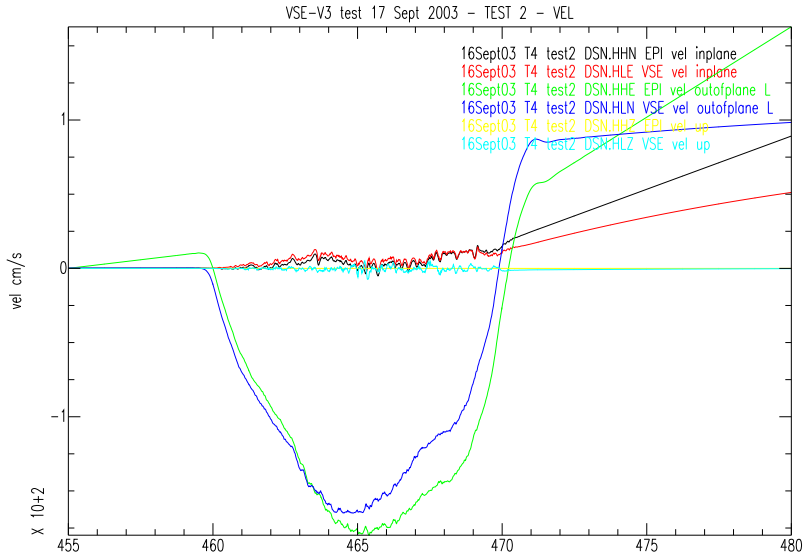

(a) All 3 components, raw velocity

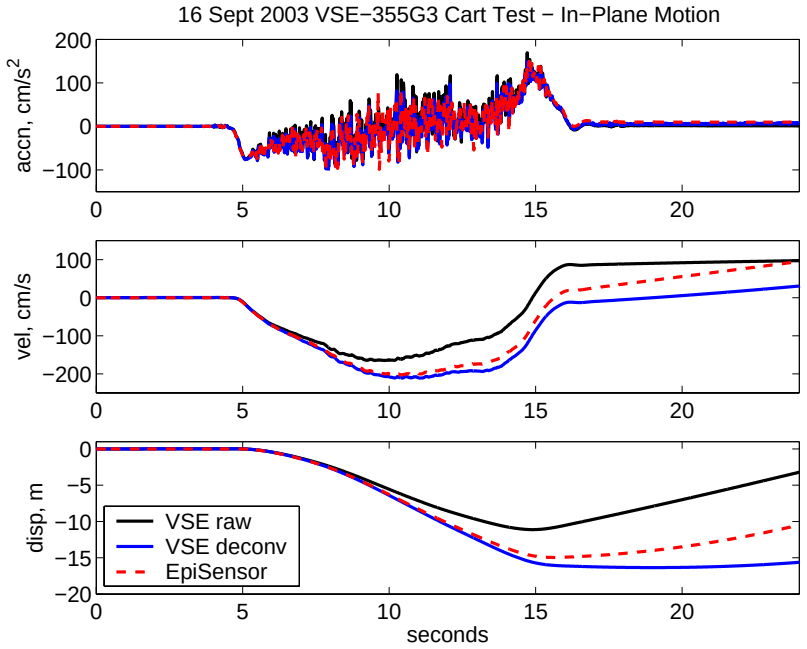

(b) In-plane components, EpiSensor: solid line, raw VSE: dotted, deconvolved VSE: dashed line

Figure 5.1: Typical Cart Test result for VSE-355G3, 16 September 2003. Very little tilting of VSE-355G3 over course of test, seen by relatively flat displacement after test is completed. An error in the pin connection led to the mis-labelling of in-plane/out-of plane components for both sensors.

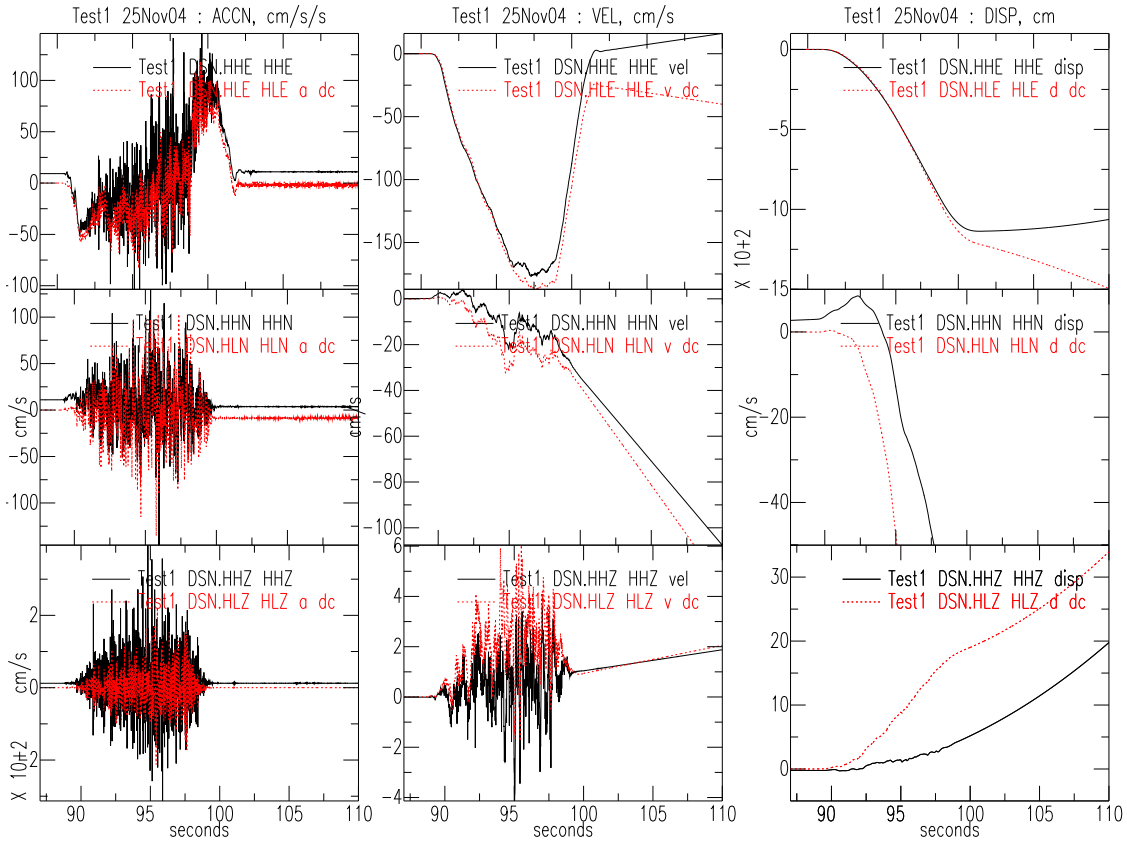

Figure 5.2: Typical Cart Test result for VSE-355G3, 25 November 2003. VSE-355G3 (dashed line) and the EpiSensor (solid) components are compared for in-plane motion (top), out-of-plane motion (middle) and vertical motion (bottom). Acceleration, velocity and displacement are all presented. VSE-355G3 data deconvolved using time domain integration. Large tilts observed in all components.

in Figure 5.3. The maximum 'raw' velocity in this case is $200 cm/s$, which, when deconvolved, reaches $256 cm/s$, well in excess of the minimum acceptable clipping velocity or $200 cm/s$. As the character of the deconvolved velocity is very similar to that of the EpiSensor (and EpiSensor accelerations are not near its clipping level), and $250 cm/s$ was the approximate speed estimated during the test, it is deduced that the VSE-355G3 is still recording linearly at this speed. Note tilts are also significant in this test, and are of a similar order as observed in Figure 5.2.

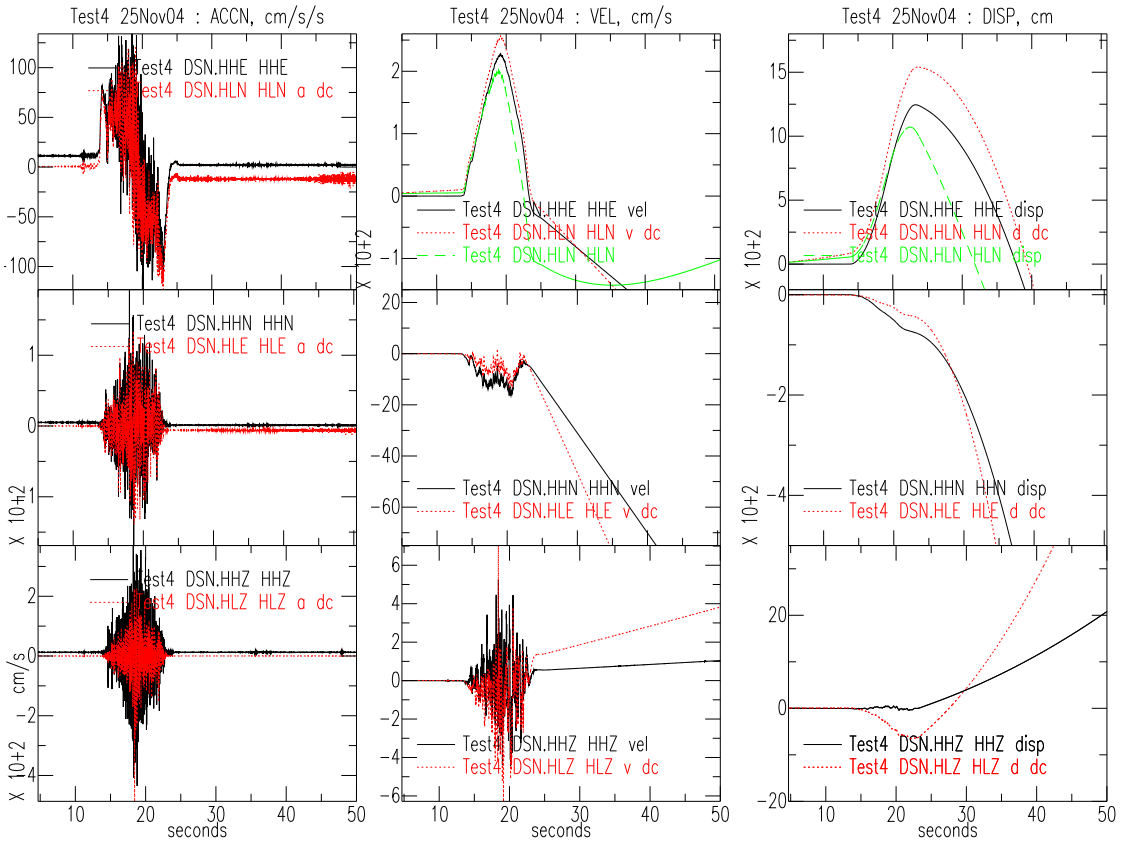

Figure 5.3: Typical Cart Test result for VSE-355G3, 25 November 2003. VSE-355G3 (dashed line) and the EpiSensor (solid) components are compared for in-plane motion (top), out-of-plane motion (middle) and vertical motion (bottom). Acceleration, velocity and displacement all presented. VSE-355G3 data deconvolved using time domain integration. Velocities in excess of $200 cm/s$ are recorded by both sensors.

Figure 5.3 provides a lower bound for the clipping level of the instrument. The tests where levelling was not closely monitored include data from cases where there were large

pre-event velocity offsets. When in-plane motions increase the large offset velocities further, clipping can be observed even if the true velocity is low. Figures A.5 and A.6 show some data from these tests, where clipping is observed at $243 cm/s$ for the N-S channel, and at $252 cm/s$ for the E-W channel. Once these velocities are reached, the sensor output flatlines. Note these are not deconvolved velocities; for this character of motion, the deconvolved velocities would be larger. This is well in excess of the expected clip level of $200 cm/s$.

5.3.2 Instrument Response

Once it had been determined that all the problems had been dealt with, calibration tilt tests were performed. [After the final overhaul, this included ensuring the clipping levels were satisfactory, no cross-coupling occurred during strong motions, and the pin connection problems were fixed.]

Figure 5.4 presents the output of the seismometer to a tilt produced by adjusting the levelling screw. The best fit SDOF solution is $T_0 = 105.5s, \zeta = 0.55$ E-W component, $T_0 = 105.2s, \zeta = 0.59$ N-S, and $T_0 = 105.8s, \zeta = 0.64$ Vertical. These SDOF's are significantly different from those of the VSE-355G2 (In Figure 3.12, all 3 components are shown to have a free period $\sim 93s$, and damping of 0.65).

The Transfer Function was supplied from the manufacturer in January 2004, given in the following form:

$$F(i\omega) = \frac{A1(i\omega)^3 + B1(i\omega)^2}{A2(i\omega)^4 + B2(i\omega)^3 + C2(i\omega)^2 + D2(i\omega) + E2} \tag{5.1}$$

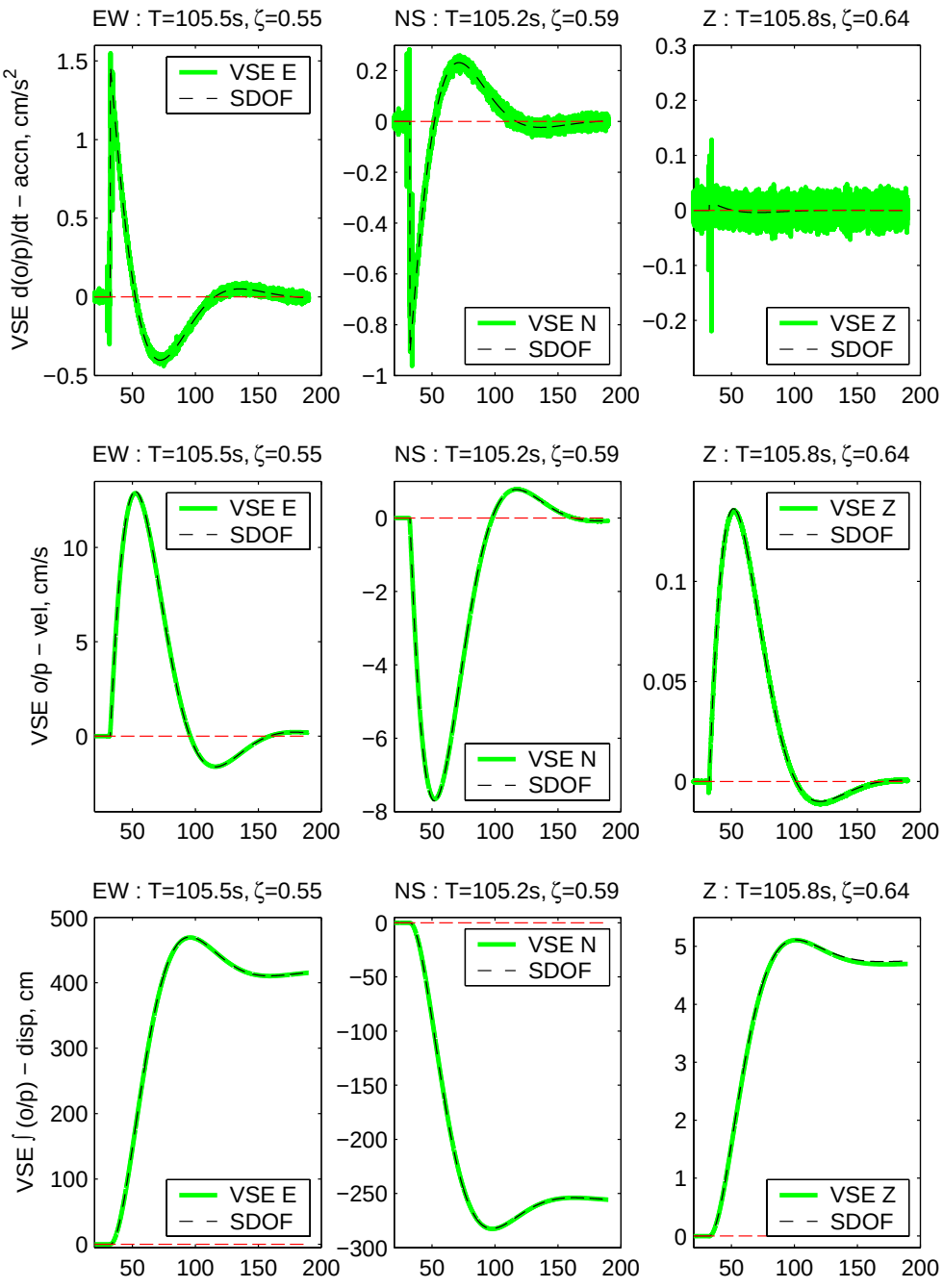

Figure 5.4: Response to a tilt, produced by adjusting the levelling screw, January 2004.

where each of these constants are defined as —

$$A1 = aA * Q * N \tag{5.2}$$

$$B1 = aA \tag{5.3}$$

$$A2 = Q * N \tag{5.4}$$

$$B2 = \left(1 + \frac{aA * B * G * K * Q * (R+N)}{m * R}\right) \tag{5.5}$$

$$C2 = \left(\frac{aA * B * G * K}{m * R} + \frac{aA * G * K * Q * (R+N)}{m * E * R}\right) \tag{5.6}$$

$$D2 = \left(P + \frac{aA * G * K}{m * E * R} + \frac{aA * g * Q * N}{m * F * C * D}\right) \tag{5.7}$$

$$E2 = \left(\frac{aA * g}{m * F * C * D}\right) \tag{5.8}$$

and —

$$aA = 500000V/m \quad ; \quad B = .7\text{x}10^{-9}\mu F$$

$$C = 2.2\mu F \quad ; \quad D = 4.4M\Omega$$

$$E = 2.778M\Omega \quad ; \quad F = 200K\Omega$$

$$G = 200 \quad ; \quad g = 20$$

$$K = 1.3M\Omega \quad ; \quad m = .03kg$$

$$N = 51\Omega \quad ; \quad Q = 32\mu F$$

$$R = 500K\Omega \quad ; \quad P = 355$$

This theoretical solution, determined from the characteristics of the mechanical sensor and the feedback control system, is shown in Figure 5.5, alongside a representative VSE-355G3 SDOF ($T_0 = 105.5s$, $\zeta = 0.60$). Also shown are the Transfer Function and equivalent calibration coil SDOF for the VSE-355G2. The longer period response, and lighter damping, of the VSE-355G3 is apparent. This is more clearly seen in Figure 5.6, a close up of the $\sim 100s$ corner. Also obvious is the better fit of the VSE-355G3 theoretical and experimental result, compared to the VSE-355G2. The manufacturer claims the behaviour of the Transfer Functions at high frequency ($> 100Hz$) is not correct. In the spec-

ifications, linearity is only expected out to 70*Hz*, and the behaviour above this frequency is not determined.

Figure 5.7 presents the SDOF for each individual channel of the VSE-355G3, as determined by the tilt test in Figure 5.4. All 3 components are shown to have a very similar response.

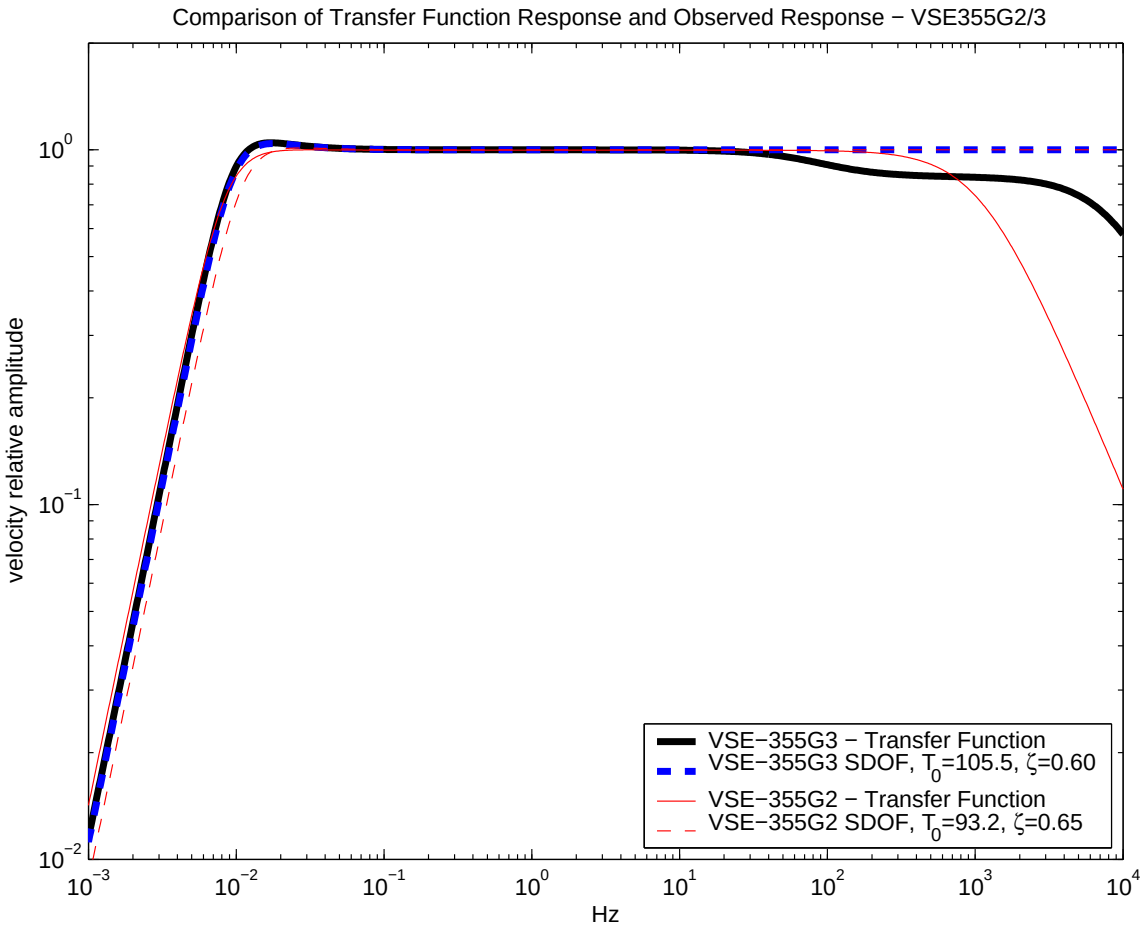

Figure 5.5: Comparison of the theoretical response from the Transfer Function and the observed calibration coil/tilt test results, for both the VSE-355G2 and VSE-355G3. Includes inaccurate high frequency response.

5.3.3 Instrument Sensitivity

For the VSE-355G3 sensitivity test, the instruments were located at the Robinson Pit, Caltech, recording onto a Q680 digitiser, operating as test station CRB. The instrument was

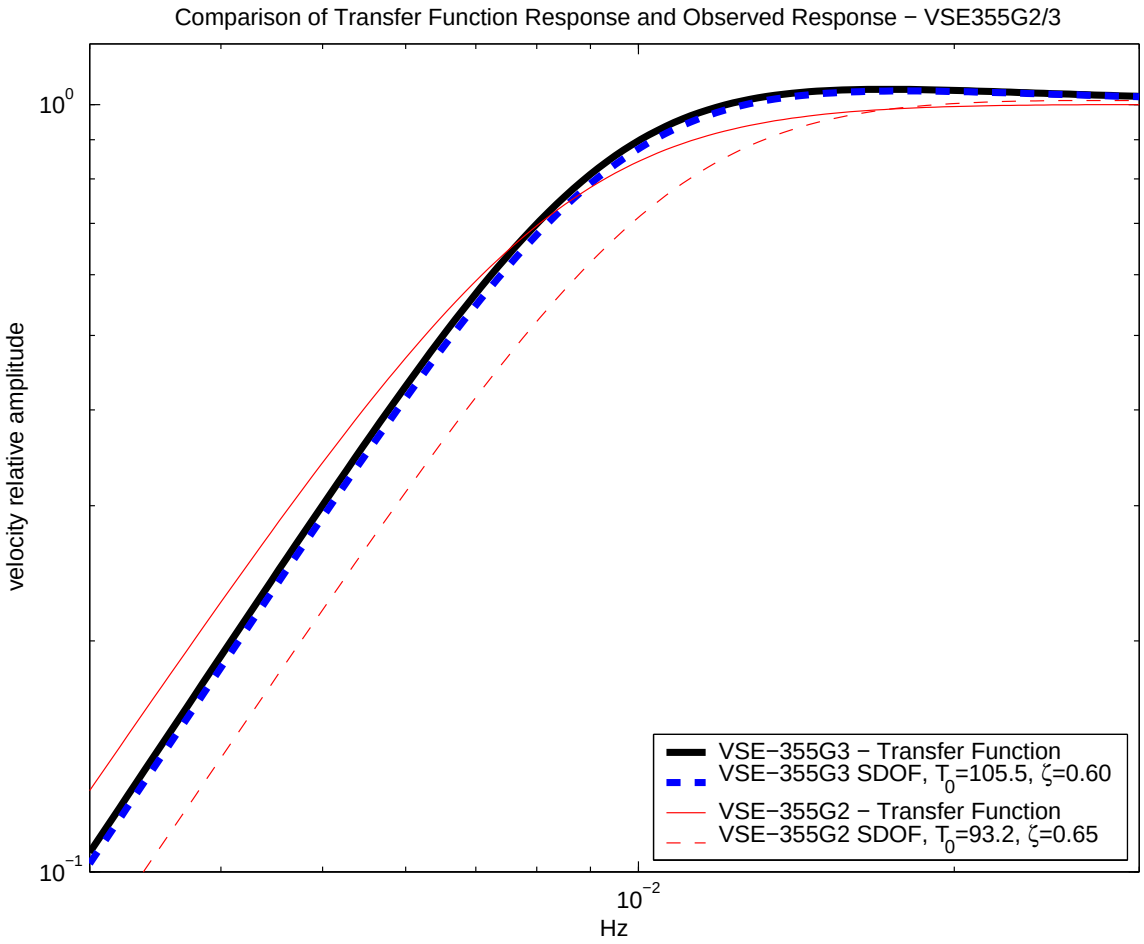

Figure 5.6: Comparison of the theoretical response from the Transfer Function and the observed calibration coil/tilt test results, for both the VSE-355G2 and VSE-355G3. Centred around the $\sim 100s$ corner frequency.

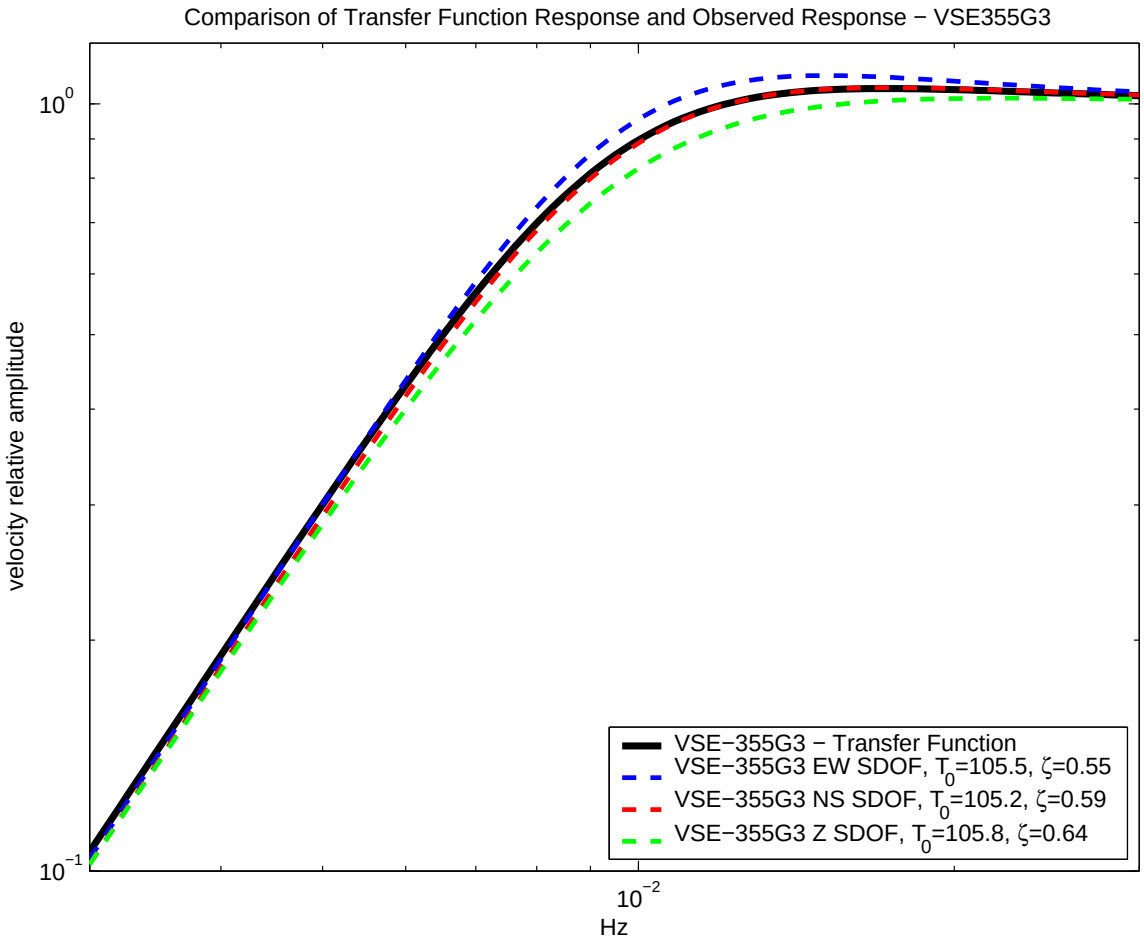

Figure 5.7: Comparison of the theoretical response from the Transfer Function and the observed calibration coil/tilt test results, including the individual responses for each VSE-355G3 channel.

initially deployed alongside an STS-2 on CRP, with an additional STS-2 and an FBA-23 on nearby test station CRPA (recording on a Q330). This setup was only deployed for a few days, as the STS-2's were required for use at other CISN stations. The STS-2 at CRP was replaced with a CMG-1T. CRPA was unreliable for comparisons as sensors and sensor position changed frequently.

Sensitivity versus STS-2

Unfortunately no small earthquakes with enough signal strength to record above the noise on all instruments occurred within the time-frame of this test, which was for ~ 2 weeks in mid-October 2003. However, upon examination of ambient noise, some peaks which appear to correspond to elevator use were observed. Time series around these peaks were bandpassed between $1-10Hz$, and scaled to get a best fit. The time-series (digital counts) were almost identical after multiplication of the VSE records by a scalar constant. This constant was found to be ~ 144 E-W, ~ 156 N-S and ~ 136.5 for the Z component.

As in the case of the VSE-355G2, the published STS-2 sensitivity of $15V/cm/s$ is assumed to be correct. The published VSE-355G2 sensitivity is $100mV/cm/s$, so our expected constant should be 150. For the 3 components there is 4% error E-W, 4% error N-S and 9% error in the Vertical component.

Figure 5.8 shows the timeseries for the 4 instruments during the larger elevator excitation, with the VSE scaled by the above values. The records are bandpassed between $1-10Hz$.

A comparison of noise levels can be seen in Figure 5.9, where the VSE is compared with the two co-located STS-2 instruments.

No parasitic resonances, including those observed for the VSE-355G2 (Figure 3.25), were observed out to $40Hz$, the limit of our digitising, for the VSE-355G3.

Calibration tests subsequent to these sensitivity tests were not satisfactory (see Figures A.7 and A.8) — the problem was found to be caused by poor pin connections. Thus, even though the data performs as expected, the observed signal at these tests may thus not be the true signal as recorded by a working VSE-355G3. After calibration tests were observed to be successful, a further sensitivity analysis was performed with the VSE-355G3

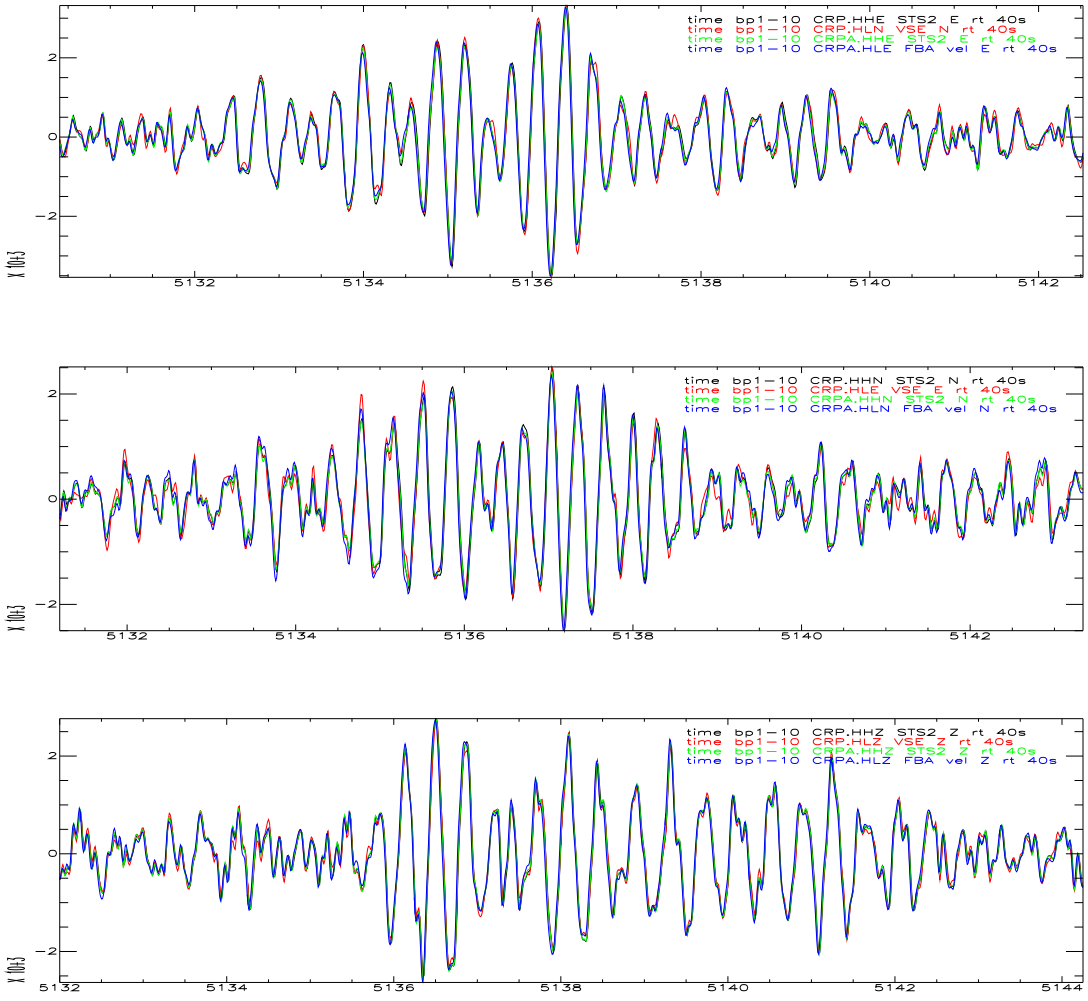

Figure 5.8: Sensitivity scaling: timeseries data for building noise recorded at CRP and CRPA, 18 October 2003, 18:25pm UTC. Bandpass from $1 - 10Hz$. Y-axis is raw counts, X-axis is seconds. STS-2 data is in raw counts, VSE is counts(VSE) x Sensitivity(VSE), FBA is counts(FBA) x Sensitivity(FBA). Top plot is E-W, middle is N-S, bottom is Z component.

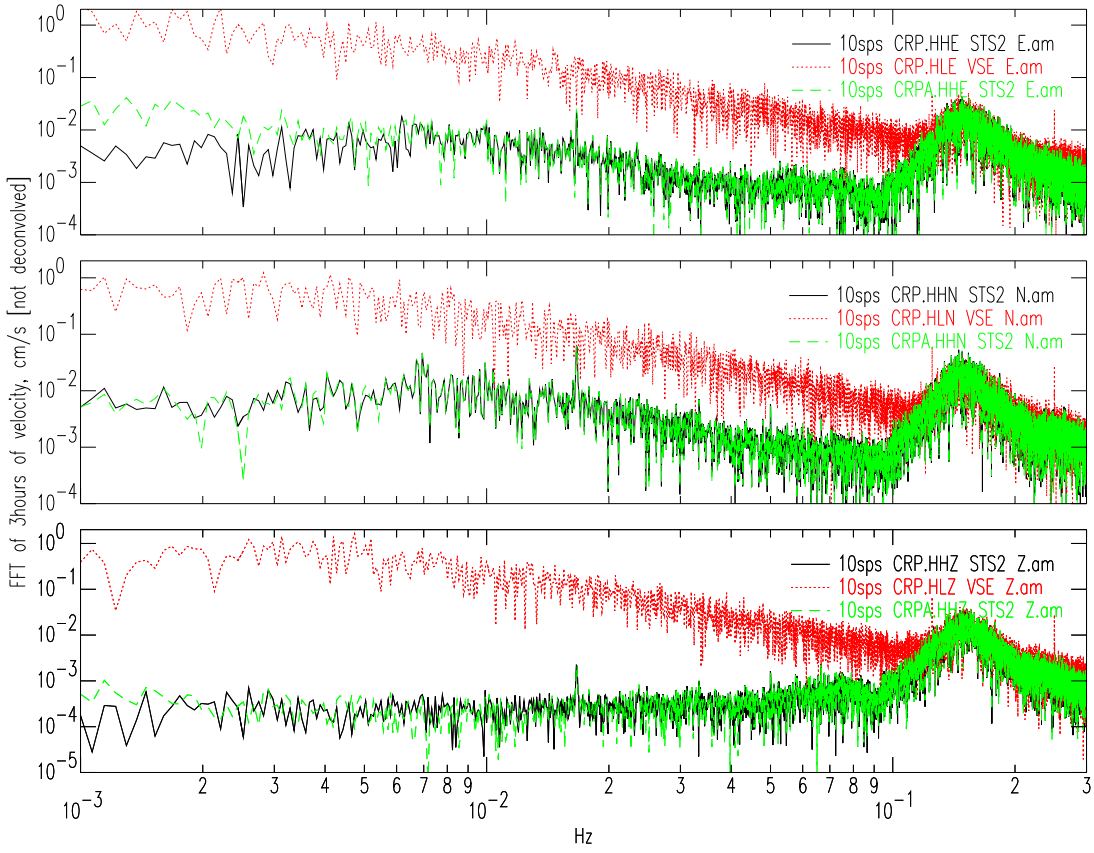

Figure 5.9: Noise: FFT of three hours of ambient data from VSE-355G3 and 2 STS-2's at CRP, CRPA. VSE-355G3 (dotted line) and the STS-2's have their instrument constants (gains) removed, but do not have the instrument response deconvolved.

alongside a CMG-1T.

Sensitivity versus CMG-1T

In late October 2003, the STS-2's at CRP and CRPA were replaced with CMG-1T's. Though this instrument has poorer reliability characteristics than the STS-2, as seen in Figure 4.61 for the Japanese F-Net network, the expected instrument gain of $150V/m/s$ will be assumed correct, which is the same gain as the STS-2. In Figure 5.10, bandpassed CRP data from the M6.5 San Simeon earthquake, 323*km* from the station, is compared for the 2 components. The scaling factors are 144.8 E-W; 162.4 N-S, and 131.0 Z. They are very similar to those determined in November 2003 using an STS-2, and correspond to a 3.5% error E-W, 8.2% error N-S (a little higher than the STS-2) and 12.6% error in the Vertical component (again a little higher than the STS-2). It is not known whether this reflects on a change in the VSE-355G3 sensitivity, or is due to sensitivity errors of the CMG-1T itself.

[The broadband San Simeon timeseries, and an FFT analysis for the VSE-355G3 E-W component of this same data is presented in Figure 3.4, showing the effect of different deconvolution schemes on data analysis.]

Figure 5.11(a) presents FFT data from a 3*hr* period of noise in February 2004. The noise level of the deconvolved VSE-355G3 response is just above the noise level of the station, as seen by the CMG-1T, for the horizontal channels for long periods from 8*s* out to 1000*s*. Though the VSE-355G3 vertical channel noise is lower than the horizontal noise at long periods, it is significantly higher than the CMG-1T vertical channel noise at these same periods (up to 2.5 orders of magnitude more).

A comparison of the higher frequencies for a short period of 1 minute of noise, can be seen in Figure 5.11(b), which has good correlation for each channel for both sensors. This recording is not the noise floor of the instruments, and is due to cultural noise, as the noise level is far higher than that expected for either instrument, as shown in Figure 5.12.

Figure 5.12 is a similar plot to Figure 3.19. This presents the amplitude of the CRP noise seen in Figures 5.11(a) and 5.11(b), in octave-wide bandpasses of the acceleration timeseries. USGS High and Low Noise Models, and the PAS/PASB VSE-355G2 noise

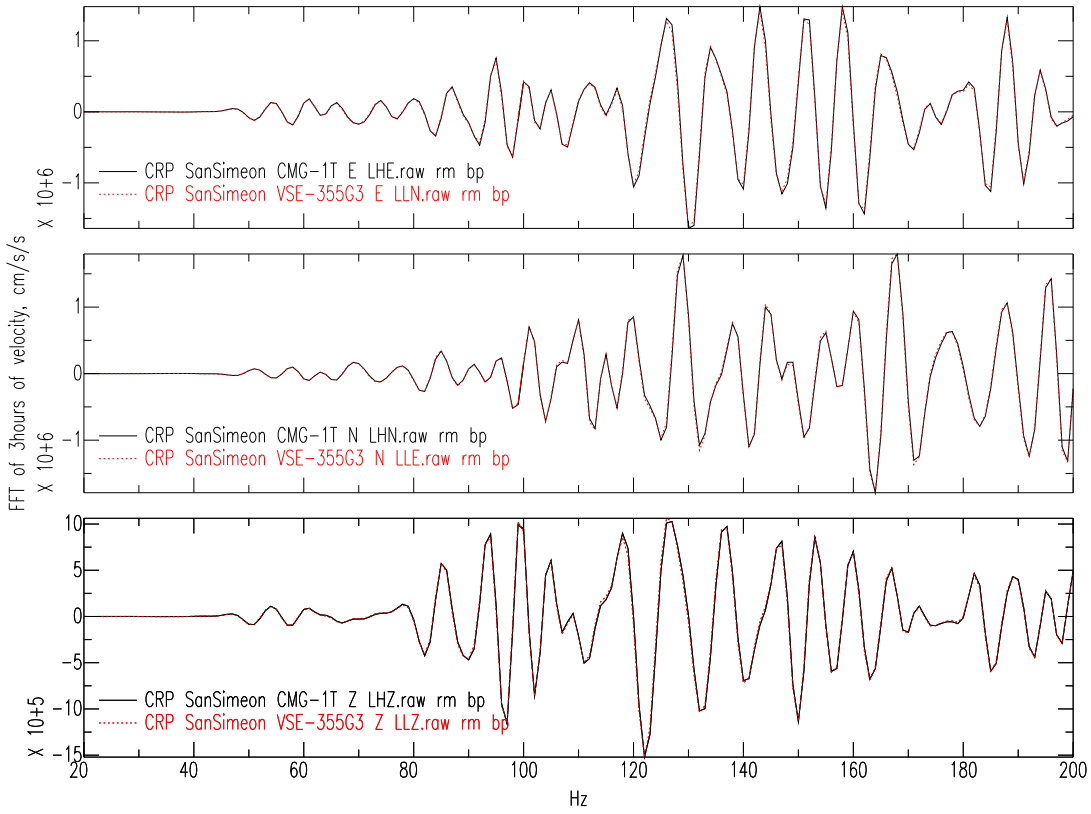

Figure 5.10: M6.5 San Simeon earthquake, 22 December 2003, at CRP, 323*km* distant. All 3 components from VSE-355G3 and CMG-1T (Top: E-W, Mid: N-S, Bottom: Z). Data is bandpassed from 5*s* – 20*s*, and the VSE-355G3 is scaled so that it best fits the CMG-1T. Scaling factors: 144.8 E-W; 162.4 N-S, and 131.0 Z.

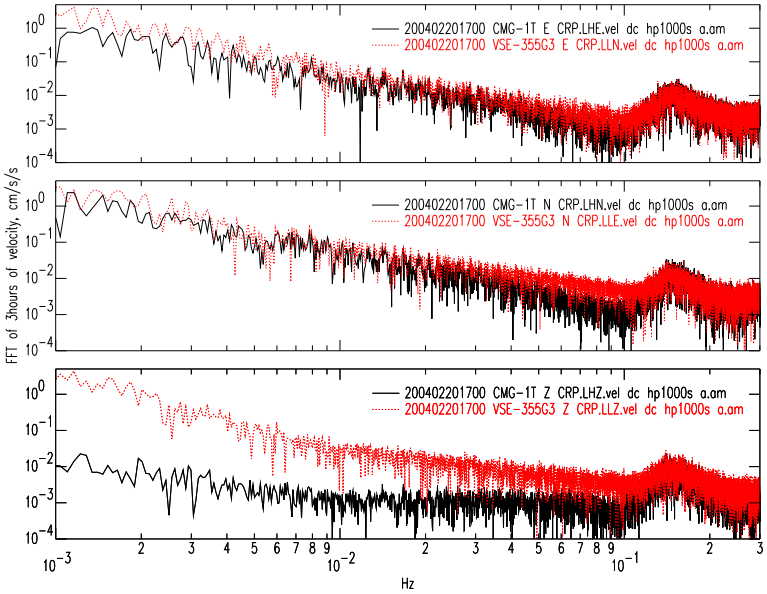

(a) Long period noise - 3*hrs* FFT (20 Feb 2004: 1AM-4AM PST)

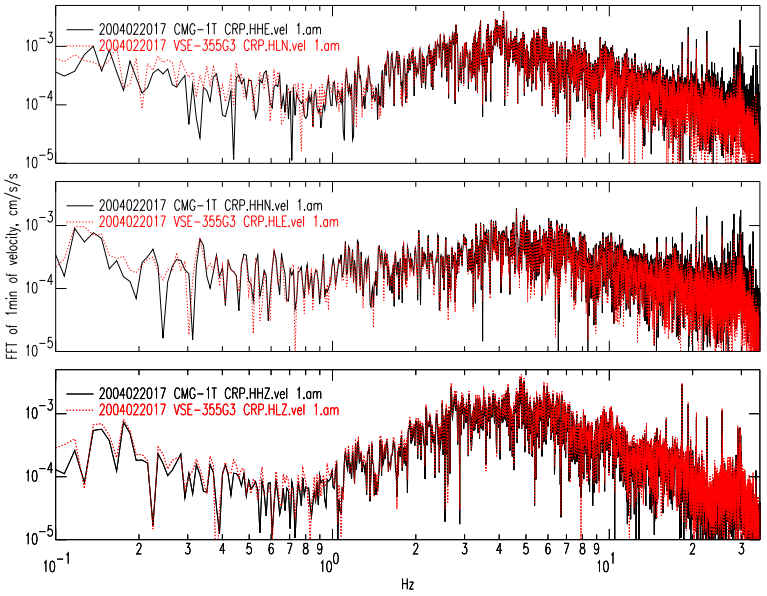

(b) High frequency noise - 1*min* FFT (20 Feb 2004: 01:27:00AM PST)

Figure 5.11: Ambient noise resolution for VSE-355G3 vs. CMG-1T. Sensors have default station gains removed, and instrument response removed, and long period data has a bandpass at 1000*s* to stabilise the FFT

floor results (from Figure 3.18) are also included. CRP is seen to be a very noisy station, higher than the High Noise Model at periods greater than 10*s*, and less than 1*s*, for all the horizontal channels. The high frequency data is clearly recording only the noise of the station, which is well above the resolution of the instrument, and so this is not determined for the VSE-355G3, and it can only be assumed to be similar to the VSE-355G2. For the long periods, the vertical CMG-1T does record a low noise level, well below the High Noise Model, and below the minimum resolution of the VSE-355G2 at PASB. This is still above the CMG-1T minimum resolution, which should be below the Low Noise Model at all frequencies higher the 500*s* (`www.guralp.com`), and so likely records the true station vertical noise level. This provides a good test for the VSE-355G3. The noise of the vertical VSE-355G3 is above the VSE-355G2 for all the frequency range. The CMG-1T horizontal channels are noisier than the VSE-355G3 vertical, but as the VSE-355G3 horizontal channels are both noisier than the resolution of the CMG-1T horizontal motions beyond 100*s*, this could be at the component resolution. As the vertical component is an order of magnitude more sensitive, this more likely due to tilting effects at these long periods, due to building straining. The vertical sensitivity is within an factor of 2 of the VSE-355G2 resolution, and consistently within a factor of 4 above the VSE-355G3 min resolution line, which is 7 orders of magnitude below the $2m/s$ expected clip level (assuming an operation of $140dB$). The instrument is thus operating at about $132dB$ dynamic range, and provides much improved longer period sensitivity to the typical 24-bit accelerometer, as represented by the PAS FBA-23 data. Note also that though the VSE-355G3 noise is about 2 times higher than the VSE-355G2 over a broad frequency range, the clip level has been raised by over a factor of 10.

5.4 Summary

The VSE-355G2 instrument as delivered to Caltech in 2001, has a performance generally similar to the manufacturer specifications, except for a significantly lower instrument velocity at clipping. This behaviour appears to have been confirmed from strong motions recorded in the M8.3 25 September 2003 Hokkaido earthquake.

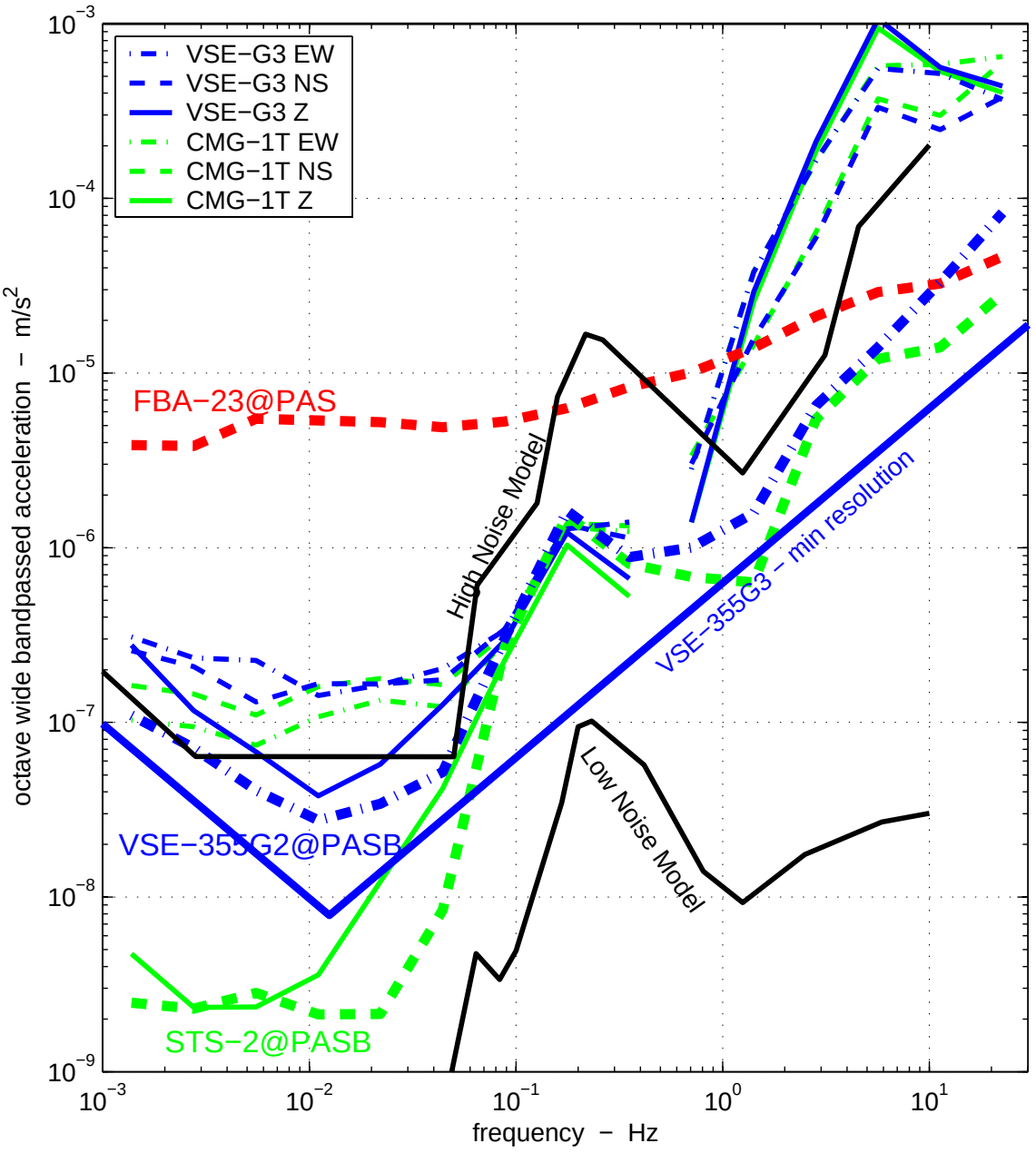

Figure 5.12: Station CRP channel sensitivity, February 2004, data from Figures 5.11(a) and 5.11(b). VSE-355G3 channels in blue, CMG-1T in green. Note both the vertical channels are significantly quieter than their horizontal counterparts. High and Low Noise USGS models included (Peterson, 1993). CRP is a very noisy site, with periods $> 20s, < 2s$ being slightly noisier than the High Noise model. Compare with data from PAS/PASB, with STS-1, FBA-23 and VSE-355G2, re-presented from Figure 3.19. PAS is a much quieter site. VSE-355G3 noise is about 2 times higher than the VSE-355G2 over a broad frequency range, though the clip level has been raised by over a factor of 10.

During the tests at Caltech, initially the clip velocity was observed at $15cm/s$, only 7% of the $200cm/s$ specified clip level. Clip level was estimated by translation of the instrument (alongside an accelerometer) along a laboratory floor. The manufacturer was informed, and after isolating the source of the low clipping to be a malfunctioning power regulator, a representative from Tokyo Sokushin visited Caltech to fix it. After the modifications, we repeated the cart test and observed clipping at about $40cm/s$, still only 20% of the specified clip level of $200cm/s$. After further tests in Japan, Tokyo Sokushin Engineers returned to Caltech and replaced mechanical and feedback systems for all 3 components. The strong motion cart tests then showed the horizontal components of the instrument did not clip until motions exceeded $200cm/s$. The vertical channel was shown to clip at about $15cm/s$, and there was serious cross-coupling between all channels. The manufacturer returned to Japan, and discovered the vertical suspension was insufficiently strong, and caused both problems. In Japan, the cart test was repeated in an elevator to demonstrate the ability of the vertical channels to recover strong motions. Sokushin returned to Caltech to replace all three sensor components with the redesigned seismometers. Tests then indicated satisfactory performance in strong motions from all three components. Further calibration tests indicated there was a problem with the pin connection from the sensor to the datalogger, with resultant very strange calibration test behaviour. Once the pin connections had been re-done, the calibration test output was consistent with expectation, and the general performance tests were repeated.

The VSE-355G3 instrument performance is now similar to, or in exceedance of, the manufacturer specifications. The ability to resolve long period ($> 30s$) motions is much better than that of a strong motion accelerometer, and the instrument has good response even at 100's of seconds. Instrument sensitivities, calibrated with an STS-2, are within 9% of manufacturer's specifications. Noise resolution was measured at the Caltech Robinson Pit, site of CISN Station PAS, and is found to track that of the CMG-1T and STS-2 out to $10s$, and remain at about an order of magnitude at $100s$. With the instrument clip at over $200cm/s$, the instrument is operating near $132dB$ dynamic range for a very broad band of frequency. All 3 components can be approximated as SDOF systems with $T_0 \sim 105s$ and $\zeta \sim 0.60$.

Compared to a typical accelerometer, the VSE-355G3 has been shown to have enhanced performance at long periods, and can produce very stable non-DC displacement timeseries. Once a signal with frequencies greater than 100*s* is produced, such as for some teleseismic waves, and for permanent displacement offsets, a deconvolution of the instrument response is required to reproduce the true ground motions. A time-domain integration of the time-series is shown to be an effective way to estimate the permanent offsets in strong ground motions. This method involves double integration of the time-series, which introduces the same sensitivity of the instrument to tilt, and small errors in baseline measurements as are observed with accelerometers.

From the viewpoint of event data retrieval in a seismological network, the VSE-355G3 is clearly an improvement to the existing accelerometers, though its extra weight and size are disadvantages. Within the CISN, which is not as constrained by these parameters as a typical strong motion network with sensors located throughout structures, it would ideally be used to replace the accelerometer sensors, particularly at stations with only a single (strong motion) sensor.

As with any inertial sensor, a strong motion velocity sensor cannot distinguish rotations from translations. This is a significant problem for any network which attempts to recover true ground displacement, as most ground displacements will be accompanied by some ground rotation involving the vertical direction. To determine the complete and correct translational and rotational movements at a site expected to experience strong motions requires the addition of a separate GPS sensor.

Chapter 6 Small Amplitude Studies in Structures

6.1 Introduction

The past few years have seen a proliferation of real-time structural monitoring testbeds. Analysis of the resulting data is leading towards a better understanding of building response. Current research at the California Institute of Technology into ambient, forced (Bradford et al, 2004) and earthquake vibration analysis of large concrete buildings, concrete dams (Alves and Hall, 2003) and wood-frame buildings (Camelo, 2003) indicates that during small shaking events, there is a measurable change in recorded natural frequencies of all these types of structures. In the case of wood-frame structures, natural frequencies may be reduced by a factor of two during stronger shaking, even without identifiable structural damage (Camelo, 2003). This non-linear structural softening is not well characterised or understood, and needs to be accounted for if real-time building monitoring is to be used effectively as a post-earthquake damage assessment tool.

This Chapter attempts to document the amount of frequency shifting in the instrumented large structures at the campus of the California Institute of Technology. The current state of instrumentation on campus is described, and the observed changes in fundamental frequencies are correlated with weather, earthquake history, and building usage.

The wandering of the natural frequencies of the Robert A. Millikan Library on the campus of the California Institute of Technology (Caltech) has been previously documented (Kuroiwa, 1967; Trifunac, 1972; Foutch, 1976; Luco et al, 1987; Chopra, 1995). Since its construction in 1967, a decrease in these resonant frequencies may be observed from yearly forced vibration experiments and from strong motion records. This frequency drop has been interpreted to be due to a corresponding softening in system stiffness. Recent ambient and forced vibration tests indicate the fundamental natural frequency of the structure

is now approximately 21% lower in the East-West direction and 12% lower in the North-South direction than was determined shortly after construction (Kuroiwa, 1967). Strong motion records indicate that the natural frequencies drop even further during moderately large events. In one such example, the M6.1 Whittier Narrows earthquake, located 19*km* from the library, the E-W and N-S natural frequencies decreased by 17% and 25% respectively, compared with forced vibration measurements prior to the event (Levine et al**,** 1988). The structure recovers stiffness somewhat after a moderately large shaking event, but due to lack of data in the immediate aftermath of these mainshocks, the recovery timeframe cannot be constrained. Further, Kuroiwa (1967) and others noted that the resonant frequencies drop measurably when the applied force during forced vibrations is increased — in 1966 during construction the fundamental E-W frequency dropped 3% when applied force was increased by a factor of 8.

Recent improvements in the quality and quantity of instrumentation in the building and at other sites on the Caltech campus have led to renewed investigation of the structure. Analysis of structural response to previously un-recorded ambient and small intensity ground motions are now possible.

Data is presented which indicates that not only do the natural frequencies change significantly during strong shaking — as evidenced by analogue recordings of large earthquakes in the recent past — but there are also measurable changes in the resonant frequencies of the buildings due to —

- forced vibrations using varying forces
- minor earthquake shaking
- weather conditions (rain and wind events, extremes in temperature)

These last two factors are shown to also affect the recently constructed Broad Center on the Caltech campus (the Broad Center has not yet been shaken, or subjected to strong earthquake motions).

The lowering of the natural frequencies during transient events in Millikan Library is likely due to a combination of two mechanisms, a non-linear softening of the superstruc-

ture itself, as well as an interaction of the structure with the surrounding soil. Changes in occupancy usage are also responsible for natural frequency changes. It is noted that the construction of partition walls for office space in three entire levels during the spring of 2003 occurs concurrently to a significant and permanent raising of the natural frequencies (though it is shown later the magnitude of the change in frequency cannot be solely explained by the relatively small increase in stiffness expected by the addition of the partition walls).

6.2 Historical Evidence for Natural Frequency Wandering — Millikan Library

The Robert A. Millikan Library is located at the center of campus at the California Institute of Technology (see Figure 6.1). It is a nine-story reinforced concrete building with a basement and an enclosed roof (housing air conditioning equipment), completed in 1967. The library is 21.0m by 22.9m in plan, and extends 43.9m above grade, and 48.2m above basement level. Inter-story heights are all 4.27m, except between the 1st and 2nd floors, which is 4.88m high. The roof wall is also 4.88m. The structural system consists of a moment frame with large stiff reinforced concrete shear walls (30.5cm thick) on the East and West sides of the building. These shear walls provide the predominant resistance to lateral forces in the North-South direction. A 30.5cm thick reinforced concrete inner core adds stiffness to the building, which along with the concrete moment frame, and the bolted pre-cast concrete window/wall panels, provide the lateral stiffness in the East-West direction. The foundation system is composed of a central pad 9.75m wide by 1.2m deep, which extends across the building to the shear walls on the East and West sides. Two foundation beams (2.74m wide by 0.61m deep) run parallel to the central pad under the North and South wall respectively. A series of stepped beams transfer loads from these foundation beams to the central pad. More detailed descriptions of the structural system may be found in Kuroiwa (1967), Foutch et al. (1975), Foutch (1976), and Luco et al. (1986). The alluvium under the foundation consists of medium to dense sands mixed with gravels, and bedrock lies at

a depth of about 275m. The water table appears to be at about 11*m* depth (Kuroiwa, 1967; Luco et al, 1987). Figures 6.2 and 6.3 show a North-South cross-section and a typical floor plan.

Figure 6.1: Millikan Library - View from North-East. The two dark coloured walls in the foreground comprise the 30.5*cm* thick east shear wall, which is somewhat narrower on the ground floor, due to walkway openings. The wall panels and concrete moment frame are visible on the north face

After the 1971 San Fernando earthquake, cracking and spalling of the concrete slabs located on the ground floor entry plaza was noted (Foutch and Jennings, 1978). Further, horizontal cracks along the pour line in the core shear walls between both the basement and 1st floor, and 1st and 2nd floors, have been observed in the emergency staircase in the North-South direction. Access to the East-West sides of the core shear wall is not possible. No further structural damage has been observed in the building.

In 1968, the building was instrumented with 2 permanent tri-axial Teledyne-Geotech RFT-250 accelerometers, located on the roof and basement. A 10 channel Kinemetrics CR-1 strong motion array was also installed in 1979, with channels on the basement, 6th floor, and roof. These systems have since been replaced by a 24-bit continuously recorded digital tri-axial accelerometer, the CISN (formerly TriNet) station MIK, on the 9th floor, and a 36 channel 19-bit triggered-accelerometer array run by the USGS, with a minimum

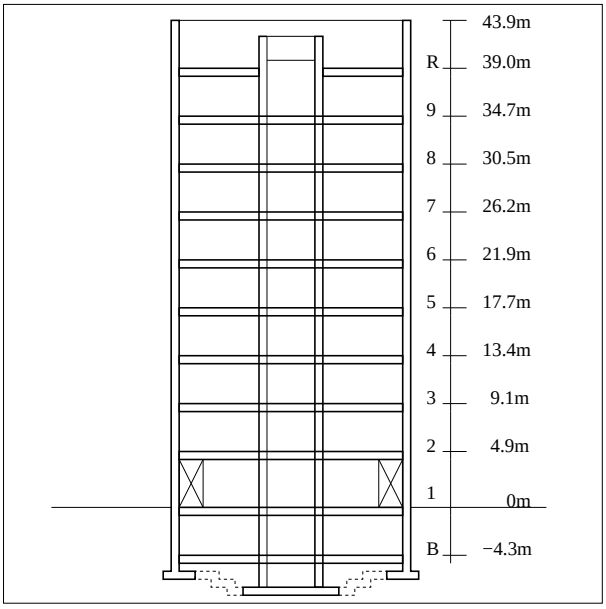

Figure 6.2: Millikan Library — North-South Section. Walkway openings on the ground floor, which cut through the shear walls, are represented by crosses.

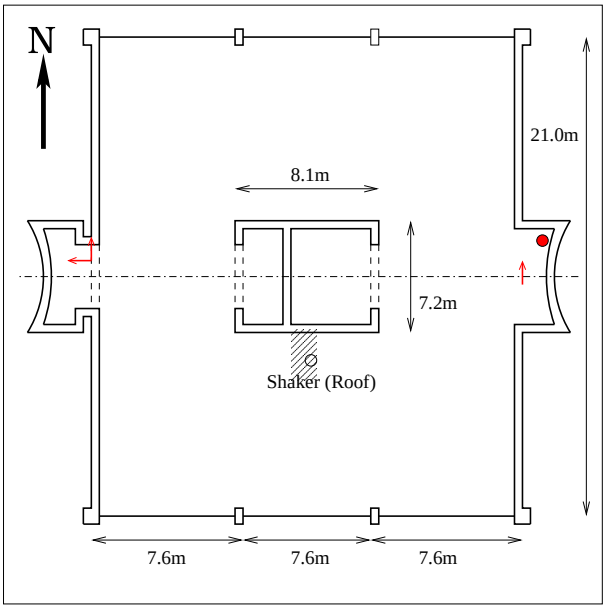

Figure 6.3: Millikan Library — Typical Plan View. The dark circle is the approximate position of CISN Station MIK on the 9th Floor, the arrows are the approximate positions and orientations of the 3 USGS channels on each floor (from 1 - Roof).

Event/Test	East - West				North - South			
	Nat Freq.	%diff1	%diff2	mx accn	Nat Freq.	%diff1	%diff2	mx accn
	Hz			cm/s^2	*Hz*			cm/s^2
forced vibrations, 1967	1.45	-	-	-	1.90	-	-	-
Lytle Creek, 1970 M5.3, Δ=57km	1.30	10.3	10.3	**49**	1.88	1.1	1.1	**34**
San Fernando, 1971 M6.6, Δ=31km	1.0	31.0	31.0	**306**	1.64	13.7	13.7	**341**
forced vibrations, 1974	1.21	16.6	16.6	-	1.77	6.8	6.8	-
Whittier Narrows, 1987 M6.1, Δ=19km	1.00	31.0	17.4	**262**	1.33	30.0	24.9	**534**
forced vibrations, 1988	1.18	18.6	2.5	-	1.70	10.5	4.0	-
Sierra Madre, 1991M5.8, Δ=18km	0.92	36.6	22.0	**246**	1.39	26.8	18.2	**351**
forced vibrations, 1993	1.17	19.3	0.8	-	1.69	11.1	0.6	-
Northridge, 1994 M6.7, Δ=34km	0.94	35.2	19.7	**143**	1.33	30.0	21.3	**512**
forced vibrations, 1994	1.15	20.6	1.7	-	1.67	12.1	1.2	-
forced vibrations, 1995	1.15	20.6	0.0	-	1.68	11.6	-0.6	-
Beverly Hills, 2001 M4.2, Δ=26km	1.16	20.0	-0.9	**9.3**	1.68	11.6	0.0	**11.8**
forced vibrations, 2002 - Full Weights	1.11	23.4	3.5	**3.6**	1.64	13.7	2.4	**8.0**
- 1/2 weights	1.14	21.4	0.9	**1.9**	1.67	12.1	0.6	**4.1**
Big Bear, 2003 M5.4, Δ=119km	1.07	26.2	6.1	**14.2**	1.61	15.3	3.6	**22.6**
continuous data average - May01-Nov03	1.19				1.72			
San Simeon, 2003 M6.5, Δ=323km	1.14	21.4	0.0	**20.4**	1.54	18.9	7.8	**14.3**

Table 6.1: Natural frequencies and peak roof accelerations from selected strong motion data and forced vibration experiments. **% diff1** is the difference between the recorded frequency and that obtained in the first forced vibration tests (Kuroiwa, 1967). **% diff2** is the difference between the recorded frequency and that obtained in the most recent forced vibration test prior to the event. A complete history is presented in Tables B.1, B.2, and references for all the tests are in Table B.3. Note the 1967 entry is representative of the results from all tests from 1967 up to the 1970 Lytle Creek Earthquake — the building was already fully loaded with books.

of 3 channels on each floor. A synchronised shaker was permanently installed on the roof of the building in the early 1970's, and is still used for forced vibration testing (Hudson, 1962).

Yearly modal analysis of the structure (using temporary deployment of Kinemetrics Ranger SS-1 seismometers) during Civil Engineering classes at Caltech, as well as the triggered event data from the RFT-250 and CR-1 arrays, have provided a relatively detailed history of the evolution of the dynamic properties of the building. A summary of the fundamental natural frequencies observed during strong shaking and selected forced vibration tests is presented in Table 6.1 (for a complete list and individual references, see Appendix B). Figures 6.4 and 6.5 present graphical interpretations of Table 6.1. In Figure 6.4, the natural frequencies are plotted against date of the observation, with a clear trend towards lower natural frequencies with increasing time, with major steps occurring during large earthquakes. Figure 6.5 plots frequency versus roof acceleration amplitude, on logarithmic axes. There is a clear pattern of frequency dropping with increasing excitation amplitude. The best fitting line is a good fit to the data, though there is still a very large variance.

Kuroiwa (1967) first observed variation in the natural frequencies, measuring small amounts of frequency lowering proportional to the applied force imparted by the shaker. This has been consistently observed since then. For example, in the tests carried out in July 2002 by Bradford et al. (2004), during shaking with full weights, a E-W natural frequency of $1.11Hz$ was measured, and during shaking with only 4 side weights, the natural frequency was $1.14Hz$ - a difference of $0.03Hz$, or 2.5%. This change in weights corresponds to a factor of nearly 2 difference in the amplitude of the rooftop sinusoidal acceleration, and a factor of 2.23 change in the applied force. Similar changes were observed in the N-S fundamental frequency. Thus with weight configurations variable in some of the forced tests (and unknown in some cases), this level of variability in reporting of results should be noted. It is assumed that the forced vibration test results in Table 6.1 are made with the shaker loaded with half-full weights, and the shaded area in Figure 6.4 is a band of the likely natural frequencies reflecting the error ($\pm 0.03Hz$) arising from this uncertainty in the experimental method.

The natural frequencies from strong shaking are determined from the free resonance

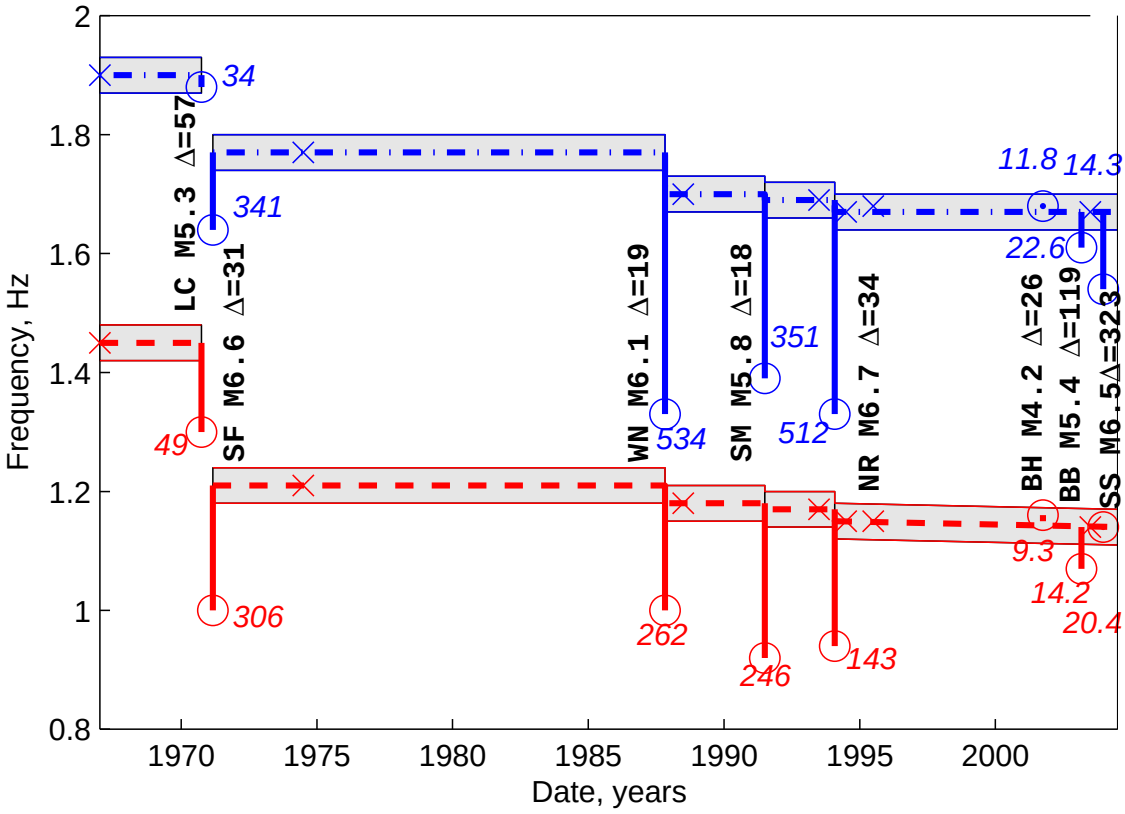

Figure 6.4: Graphical interpretation of Table 1 - Time vs. Frequency. Dashed lines are E-W natural frequencies, dashed-dotted are N-S natural frequencies, all from forced vibration testing. Shaded area is the likely region of natural frequencies taking into consideration errors in measurement, due to unknown shaker weight configuration and weather conditions for each test, and experimental error. Crosses indicate the actual time of a forced vibration measurement. Circles indicate the natural frequency estimated from the strong motion recording of the event, with the number in italics giving the peak acceleration recorded for the event (cm/s^2).

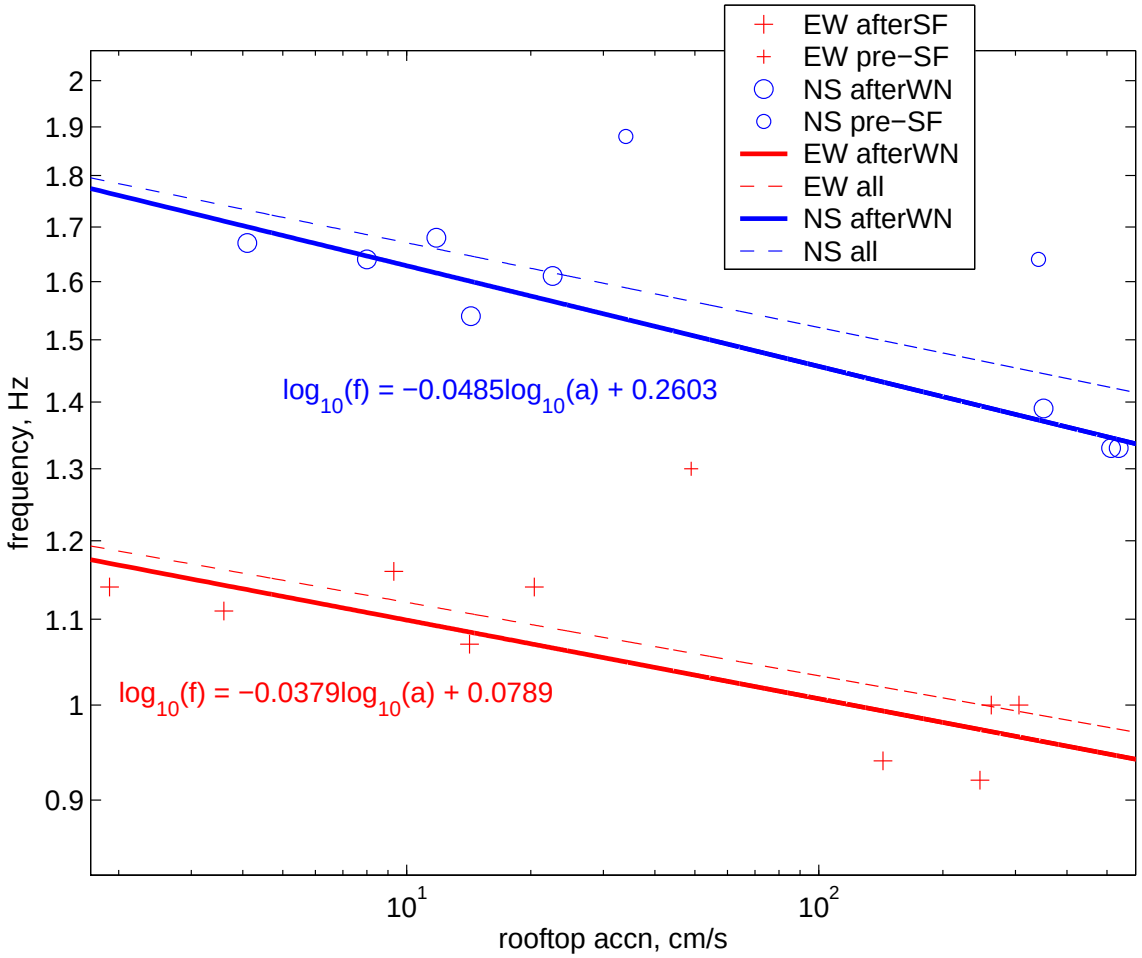

Figure 6.5: Graphical interpretation of Table 1 - Amplitude vs. Frequency, log scaling. For both E-W and N-S, the best fitting least squares solution for all the data is plotted in dashed lines. Outlying data from tests and earthquakes prior to main permanent natural frequency shift (pre- Whittier Narrows for N-S; pre- San Fernando for E-W) are removed from dataset for the solid line regressions, with labelled functional form.

of the structure (measured at the roof channels) after a large event. This is illustrated in Figure 6.6, which shows the response of the East-West Channels of the CR-1 array at Millikan to the 1987 M6.1 Whittier Narrows Mainshock (Levine et al, 1988).

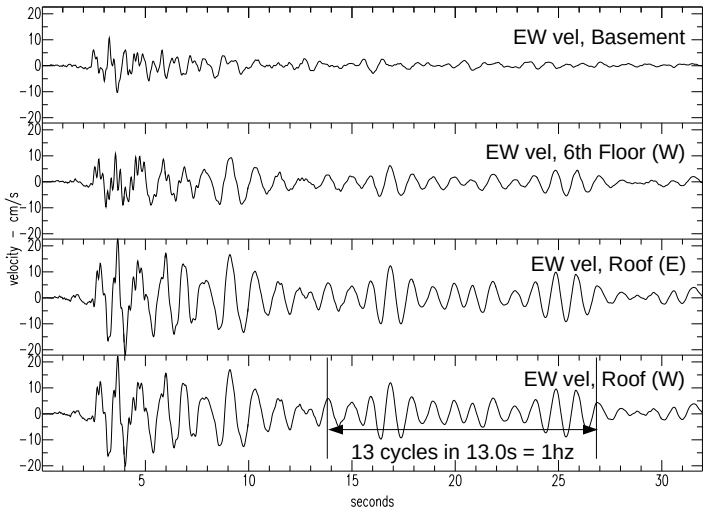

Figure 6.6: East-West components of CR-1 array in Millikan Library, recorded during the M6.1 Whittier Narrows earthquake $\Delta = 19km$ - velocity timeseries. The top trace is from the basement, the second is from the 6^{th} floor, and the last two are from the roof. The last trace includes a sample of how the fundamental frequency of the building is estimated, after the main energy (seen from the basement trace) has passed.

Table 6.1 shows the initial natural frequencies of the building at $1.45Hz$ in the E-W direction, and $1.90Hz$ in the N-S direction. For this initial test, and many subsequent tests, the higher order modes, including the first torsional frequency, are not clearly and unambiguously identified due to the poor signal to noise ratio for the recording systems of the time. (SMA-1's, CR-1's, and Ranger SS-1's all have dynamic range in the order of 3 orders of magnitude ($60dB$), compared with the $144dB$ resolution of the 24-bit instruments.) A further constraint on recovery of data at the higher modes is occupants would complain of 'motion sickness' when the library was shaken at higher frequencies during library hours.

The recorded history includes 4 large shaking events, all with roof accelerations of at least $340cm/s^2$ (over $34\%g$). Several smaller events, including the 1970 Lytle Creek earthquake, and some more recent events recorded on the digital instruments, with accelerations below $50cm/s^2$, are also included on Table 6.1 for comparison. During strong motion, the

natural frequencies temporarily fall by about 20%. Surprisingly, after each strong motion event, the structural system stiffens and natural frequencies return to near pre-earthquake levels, usually with a permanent drop in frequency of less than 2.5%. Some events have led to larger permanent decrease of all subsequent forced vibration resonant frequencies. In the most extreme case, the E-W fundamental frequency dropped permanently by 16.6% in tests subsequent to the San Fernando event.

East-West Fundamental Frequency

In the E-W direction, the lateral forces are primarily resisted by the elevator core and the concrete moment frame (and possibly also from the architectural facade of stiff window frames). Table 6.1 shows that the very first significant earthquake motion (from the 1970 M5.3 Lytle Creek earthquake, $\Delta = 57km$), with comparatively small rooftop accelerations of $49cm/s^2$, resulted in a decrease of 10.3% in the natural frequency as measured in the strong motion record. A further softening occurred during the larger magnitude, closer 1971 M6.6 San Fernando event ($\Delta = 31km$, peak roof accelerations = $306cm/s^2$), with the fundamental frequency measured at about $1.0Hz$ during the strong shaking. Subsequent forced vibration tests indicate the frequency dropped permanently by 16.6%, to $1.21Hz$, from these two events. No earthquake recorded since has generated E-W motions that exceeded the velocities and accelerations of the San Fernando event. Correspondingly, subsequent natural frequencies from strong motion and forced vibration do not show any significant loss of stiffness of the structural system. The most recent E-W natural frequency recorded from forced vibrations is $1.14Hz$ (Bradford et al, 2004). The general modeshape has remained constant throughout the history (Foutch, 1976; Bradford et al, 2004).

North-South Fundamental Frequency

For the N-S direction, with the lateral resistance provided by the massive shear walls, a different pattern emerges. Very little frequency loss occurs during the Lytle Creek event - even the strong motion record shows a shortening of only 1.1%. Instead, it is the San Fernando event, with rooftop accelerations of $341cm/s^2$, that causes the first major frequency

drop; natural frequencies from forced vibrations fell from 1.9Hz to 1.77Hz after the event. Modeshapes before and after San Fernando show major differences, before the earthquake, less than 3% of the peak displacement at the roof is attributed to basement rocking, yet after, and in subsequent tests, approximately 30% of the roof motion is due to basement rocking (Jennings and Kuroiwa, 1968; Foutch, 1976; Bradford et al, 2004). Another major decrease occurs during the 1987 M6.1 Whittier Narrows event ($\Delta = 19km$), where the highest rooftop accelerations ($534cm/s^2$) were recorded during the shaking. Figure 6.4 shows that this event caused the largest intra-event frequency drop (nearly 25%), with a 4% permanent decrease in forced frequencies. Subsequent natural frequency measurements from forced vibration tests are relatively constant, and no further softening beyond the 1.33Hz recorded in Whittier Narrows occurs during strong motions (including the Northridge earthquake). The most recent forced N-S natural frequency is 1.67Hz (Bradford et al, 2004).

East-West 2^{nd} Mode Frequency

At construction, the 2^{nd} E-W mode frequency was determined as 6.2Hz (Kuroiwa, 1967). During San Fernando, the frequency dropped to $\sim$ 4.95Hz (McVerry, 1980; Beck and Chan, 1995). Investigations subsequent to this earthquake have indicated the 2^{nd} mode varies from 4.17Hz (Beck and Chan, 1995) to 5.35Hz (Teledyne-Geotech-West, 1972). The most recent measured forced E-W 2^{nd} modal frequency is 4.93Hz (Bradford et al, 2004).

Response to Small Earthquakes

Table 6.1 also contains fundamental frequencies determined from shaking due to the small M4.2 Beverly Hills event ($\Delta = 26km$) in September 2001. Even though measured accelerations from the event are about double the accelerations from the sinusoidally excited forced vibration tests, the measured fundamental frequencies are higher than those from forced testing. This may be attributed to changes in the ambient pre-earthquake natural frequency due to climatic changes - and will be discussed in detail later.

The February 2003 M5.4 Big Bear event ($\Delta = 119km$) produced accelerations almost

double those from the M4.2 Beverly Hills event, and yet it had a more significant effect on the fundamental frequencies — the drop in frequency from Big Bear is much greater than double the drop observed in Beverly Hills. This suggests that the relationship between fundamental frequency and acceleration is non-linear. Further, it is observed that the fundamental frequency during the Big Bear event drops by 6.1% in the E-W direction, and only 3.6% in the N-S direction, even though the N-S accelerations are larger. This indicates that the E-W direction is more susceptible to softening under small excitations, and that larger motions are required to start significant softening in the N-S direction (the ambient data will corroborate this observation). The response of the library to this earthquake is studied in more detail later. Figure 6.5 indicates there is in general a linear relationship between the logarithm of the acceleration amplitude and logarithm of the frequency, though the scatter of the data is large, and, at least for the small amplitudes, may be due to the ambient variations in natural frequencies.

6.3 The Current System of Instrumentation at Caltech

There are currently 5 buildings on the Caltech campus with real-time telemetry of high-dynamic-range digital instrumentation. These are the Millikan Library, the Broad Center for the Biological Sciences, the USGS Building at 525 S. Wilson Ave, the Robinson Building and the Athenaeum. A dense array at Millikan Library is comprised of triggered digital accelerometers with dial-up data retrieval.

The Caltech Civil Engineering Department operated an older network of analog film-recording SMA-1's at a number of sites on and around the campus, as well as a 12-channel CR-1 at Millikan Library, which had been operational on campus since the 1970's. However, this network has not been maintained since the mid-1990's, and is currently not operational.

The digital stations currently operating at Caltech are described in the following subsections

6.3.1 Millikan Library (MIK, USGS-Caltech Array)

In January 1998 the USGS and Caltech Civil Engineering Department installed a 36 Channel dense network of FBA-11 accelerometers recording triggered event data on 2 19-bit Mt. Whitney dataloggers with dial-up data retrieval. A tri-axial EpiSensor accelerometer was also installed on the 9th floor of the structure and has been continuously transmitting 24-bit data since February 2001 to the Southern California Earthquake Data Center (SCEDC), as Station MIK in the California Integrated Seismic Network (CISN).

This improved sensor configuration prompted a detailed forced dynamic analysis (using the existing shaker located on the roof), which was performed in the Summer of 2002, (Bradford et al, 2004). The results of this study are summarised in Table 6.2. At the time of the tests, the approximate first mode frequencies during forced vibration (1/2 weights) are 1.14Hz for the East-West direction, 1.67Hz for the North-South direction, and 2.38Hz for the torsional mode.

	Millikan Library [Hz]			**Broad Center** [Hz]	
Orientation	1^{st} **Mode**	2^{nd} **Mode**	3^{rd} **Mode**	1^{st} **Mode**	2^{nd} **Mode**
East-West	1.14 [*1.19*]	4.93	7.83	2.67	3.01
North-South	1.67 [*1.72*]	7.22	?	2.43	2.81
Torsional	2.38 [*2.46*]	6.57	?	3.65	?

Table 6.2: Natural frequencies for the Millikan Library and the Broad Center. Millikan Library frequencies are from forced vibration tests, Summer 2002 (Bradford et al, 2004). For the 3 fundamental frequencies, in parentheses are the 2-year average frequencies from continuous ambient MIK data. Broad Center results are from the ambient vibration data from 14-days of continuous data during February 2003, and are preliminary (in the absence of a forced vibration modal analysis of the structure).

6.3.2 Broad Center (CBC)

The Broad Center is a 3-story structure with an irregular floor plan and 2 deep basements (see Figs 6.7 and 6.8). It was completed in the Summer of 2002, and has been instrumented since February 2003. The basements are enclosed by stiff shear walls, and the steel superstructure is braced with stiff unbonded braces in both the North-South and East-West directions.

Figure 6.7: Broad Center - View from South-West.

Figure 6.8: Broad Center - View from North-West. Structural core of the unbonded-brace frame is located below the parapet wall visible on the roof (Figure 6.9 contains a plan view).

The building houses a 24-bit CISN station, recording 8 channels of EpiSensor accelerometer data. Three tri-axial instruments are installed, all on the plan of the unbonded braced frame-line that is the structural core of the building. Two are located near the N-W intersection of the frame-line, one on the 1st floor, with the other on the roof. The final accelerometer, which only has its horizontal channels logged (the datalogger supports only 8 channels of data), is near the S-E intersection of the frame-line. All 8 channels comprise CISN station CBC. The instrument layout is illustrated by the schematic in Figure 6.9.

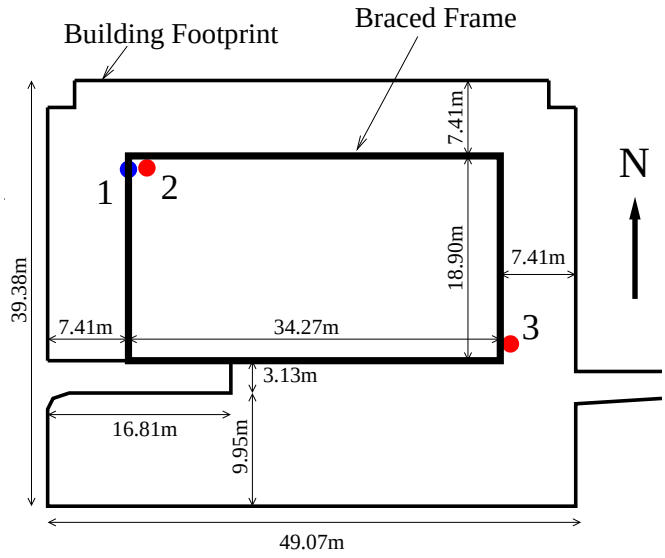

Figure 6.9: Broad Center — Schematic plan view showing placement of strong motion sensors. 1 is on First floor; 2 and 3 are located on the roof.

In the absence of a forced vibration modal analysis for the building, the natural frequencies were investigated using the CBC ambient data alone. The FFT amplitude spectra from 14 1-day recordings of ambient vibrations were stacked together, with obvious spectral peaks emerging. Table 6.2 presents the resonant frequencies determined by this analysis.Figure 6.10 shows the FFT's from each of the channels, with these selected frequencies highlighted. In both the E-W and N-S directions, 2 modal frequencies very close in frequency to each other are observed. A torsional mode is at 3.65*Hz*, clearly observed with out-of phase motions in the time-domain from both the E-W and N-S roof channels located in the N-W and S-E corners of the roof. A mode shape analysis using CBC data alone is not

possible as there is instrumentation at only 2 levels in the building. As the lowest E-W and N-S frequencies are relatively stronger than the higher E-W and N-S frequencies in the 1st floor, but much weaker at the roof, it is inferred that the lower frequencies likely correspond to a translational and rocking mode arising from soil-structure interaction, and the higher frequencies correspond to a structural shearing mode for the superstructure, which has large displacements at the roof, and small displacements at the 1st floor. Unfortunately, analysis of the displacement data from each channel, bandpassed around each natural frequency, does not fully support these conclusions. Further, it is very rare to observe individual natural frequencies clustered so close together in a structure. Potentially there could be a local effect in the building not yet appreciated. Ideally, further instrumentation and a forced vibration test are needed to confirm the dynamic properties of the structure.

6.3.3 525 S. Wilson Ave — USGS Office (GSA)

GSA is a 24-bit CISN station with a tri-axial EpiSensor accelerometer located in the basement of the 2-story wood-frame house (used as USGS Pasadena Offices). GSA data is currently used as a reference station for data from the Millikan Library and Broad Center. The station, operating since July 2000, is approximately 150*m* due West of the Millikan Library, and about 200*m* SSW of the Broad Center.

6.3.4 Robinson Building (CRP)

CRP is a 24-bit CISN station, located about 18*m* below grade, in the un-used Solar Telescope pit of the Robinson Building. It is currently used as a test station, and so can have a variety of instruments, though it always has one high-gain broadband (STS-2 or CMG-1) and one strong motion (EpiSensor or VSE-355G2) instrument deployed. It is the only station on campus with a high-gain digital instrument permanently deployed. It has been operational since March 2003, and is about 75*m* SW of Millikan Library.

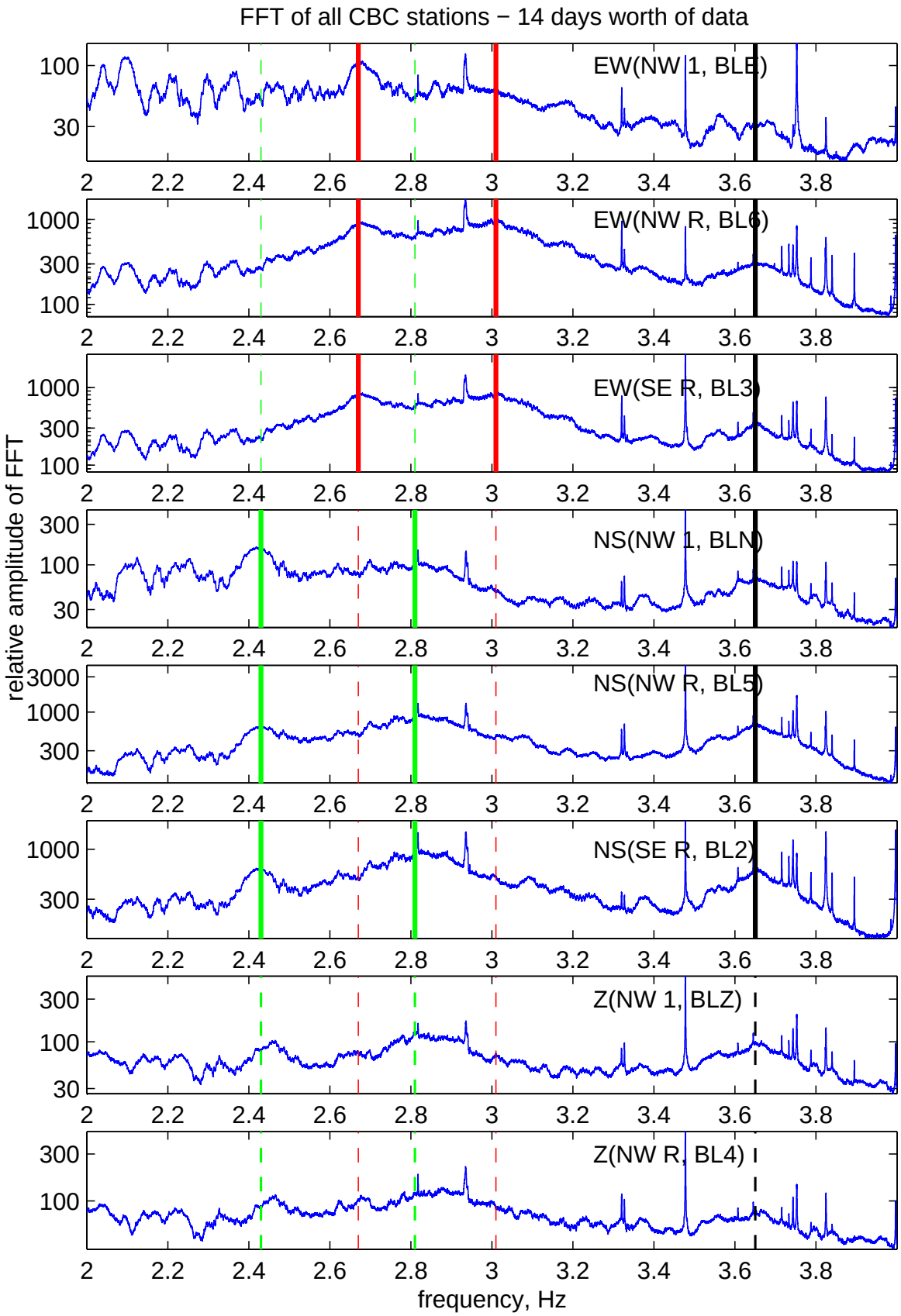

Figure 6.10: Broad Center — Stacked FFT data from 14days in February. Suspected natural frequencies shown by vertical bars: red - EW (2.67, 3.01Hz); green - NS (2.43, 2.81Hz), black - torsional (3.65Hz).

6.3.5 The Athenaeum (CAC)

CISN station CAC is a 19-bit K-2 datalogger with a tri-axial accelerometer deployed at the Athenaeum. Located in the basement, CAC occupies the same site as the old analog Athenaeum/Caltech station that has recorded earthquakes since the 1960's. Data is continuously telemetered to the CISN/SCEDC, but as the information is only 19-bit, only events that trigger on the network are permanently stored in the SCEDC.

Continuous and triggered data from these (and all other) CISN stations may be obtained from www.scecdc.scec.org/stp.html. Triggered data from some of the events recorded by the USGS-Caltech array on Millikan Library is available at nsmp.wr.usgs.gov/data.html.

6.4 Analysis of the Continuous Data Streams

As discussed in the previous section, two buildings on the Caltech campus, Millikan Library and the Broad Center, have continuous recording of data in the SCEDC from instruments located on the upper floors of a building. Thus these data streams can be used to analyse the evolution of each building's natural frequencies over the life of these stations, and at other interesting length scales. The natural frequency changes are correlated with weather data from the JPL Weather Station. This is the nearest digital continuously-monitored weather station, and it is located 8.5km North of the Caltech buildings at the Jet Propulsion Lab. Data is available from the start of continuous data storage from MIK, up to the end of November, 2003. This includes 2.5 years of data for MIK, and 10-months for CBC, which only started recording in mid-February 2003.

The JPL weather station logs data every second; the channels used for comparison are rainfall (cumulatively measured per day, mm), wind gusts (m/s), and temperature (^{o} Celsius). Subsequent plots present only total rainfall, maximum wind gusts and the maximum and minimum temperatures.

6.4.1 Entire Station Duration — MIK and CBC

Figure 6.11 is a spectrogram plot for the entire history of the station MIK, alongside JPL weather data. The three individual spectrogram sub-plots are centred about the three fundamental frequencies. Figure 6.12 plots the same data without scaling the peak of each 1 hour spectrogram slice to unity. Figure 6.13 is a similar spectrogram for the history of station CBC, and Figure 6.14 is the same without scaling of each slice. As the natural frequencies at CBC are not well-determined, individual spectrogram sub-plots are presented for each of the E-W and N-S channels, over a wide range of frequencies which encompass the observed spectral peaks.

Spectrograms are ideal for illustrating the evolution of the magnitude and frequency of any particular resonance, or energy over time. The spectrograms are colour plots with time on the x-axis, and frequency on the y-axis. At each point in the plot, the colour represents the intensity of the acceleration at MIK for the particular time and frequency. Each spectrogram is made by dividing the acceleration timeseries up into lengths of time (a slice) and taking the FFT of this time window. The magnitude of the FFT is then represented by a colour contour along the y-axis at the time on the x-axis to which the FFT corresponds (the mid-point slice time). Plotting this for each slice leads to the composite spectrogram. In Figures 6.11–6.14, the FFT length is 1-hour long, and there is no time overlap between slices. Each FFT has also been first smoothed over a frequency of $0.002Hz$ and then decimated to a sampling frequency of about $0.001Hz$. In these Figures, the acceleration amplitude scaling is linear for both MIK and CBC, with upper and lower bounds arbitrarily set to prevent unusual highs, such as the 22 Feb 2003 Big Bear earthquake, from swamping the colourbar.

As the three fundamental frequencies of Millikan Library are well separated and of large magnitude, the hourly peak in the FFT can be traced over time, as seen in Figure 6.15. Here the average of all the peaks is determined, and the deviation from this average is plotted. The daily average of the FFT peak is plotted as a thick line, with the hourly FFT peak as a thin line. The timing of small earthquake excitations, and forced vibration testing of the structure are highlighted by vertical bars. These are the source of the obvious large

deviations from the mean.

Figure 6.15 shows considerable variation in natural frequencies over the last 2 years. In particular notice the sensitivity of the fundamental E-W and torsional modes to rainfall, as evidenced by the large shifts during the winter months, when storms with several days of rainfall are a regular occurrence in Southern California. These rain events are infrequent during the summer months. The N-S mode does not seem to be as sensitive to the rainfall, and in general, it has smaller short-term deviations than the E-W and torsional modes. Also note a steady and unusual rise in the three fundamental frequencies during the spring of 2003, from April to July 2003. This occurs at the same time as a change in usage of 3 mid-level floors of the Library (3^{rd}, 4^{th} and 5^{th}), from housing library volumes to providing office space. The books were removed during the summer of 2002, with little apparent change in the natural frequencies. However, the construction of partition walls for the new offices in the spring/summer of 2004, coincides with the gradual rise of about 4% in E-W natural frequency. The rise is less pronounced in the N-S and torsional modes. The natural frequency of a building is proportional to the square root of its stiffness, so an increase of 4% in natural frequency is equivalent to an increase of 8% in stiffness. It does not seem plausible that such a large increase in stiffness can be attributed alone to the installation of partition walls (which only rise up to the false ceiling).

Discounting this recent lengthening trend, from the plots the following maximum variation for the daily average over the last 2 years are observed:

	E-W	N-S	Tors.
min	1.155Hz	1.71Hz	2.44Hz
max	1.215Hz	1.74Hz	2.55Hz
variation	0.06Hz	0.03Hz	0.10Hz
	5.1%	1.7%	4.4%

Figure 6.13 presents the first 10-months of data recorded at CBC. Table 6.2 indicates the suspected natural frequencies of the building. As these modes have not been well determined from a forced vibration test, a range in frequencies from $2.4Hz$ to $4.1Hz$ is presented for the N-S and E-W channels separately. There is significant machine noise,

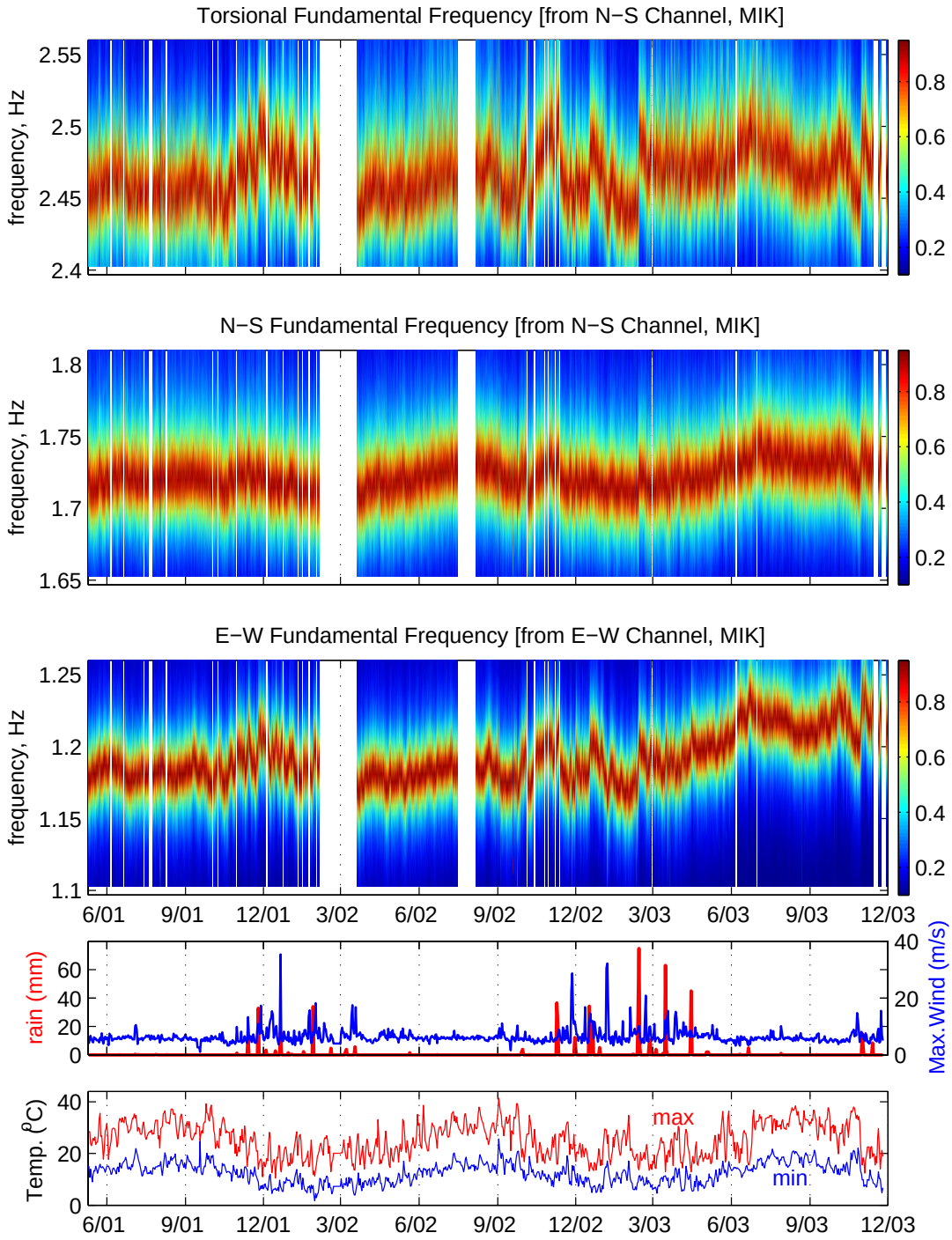

Figure 6.11: Spectrogram of natural frequencies as observed at MIK, for current station lifetime (May2001 - Nov2003). Spectrogram composed of 1 hour time windows, each scaled so max. is 1, and plotted with linear colourbar. Weather data is from JPL weather station ($\Delta = 8.5km$). Vertical breaks in data due to days with data glitches or no recorded data. Tick marks on x-axis correspond to 1^{st} of the month labelled underneath. The peaks in natural frequencies are observed to wander over the course of the 2.5 years. No longterm correlation with temperature is observed, though rain causes temporary lengthening of natural frequency.

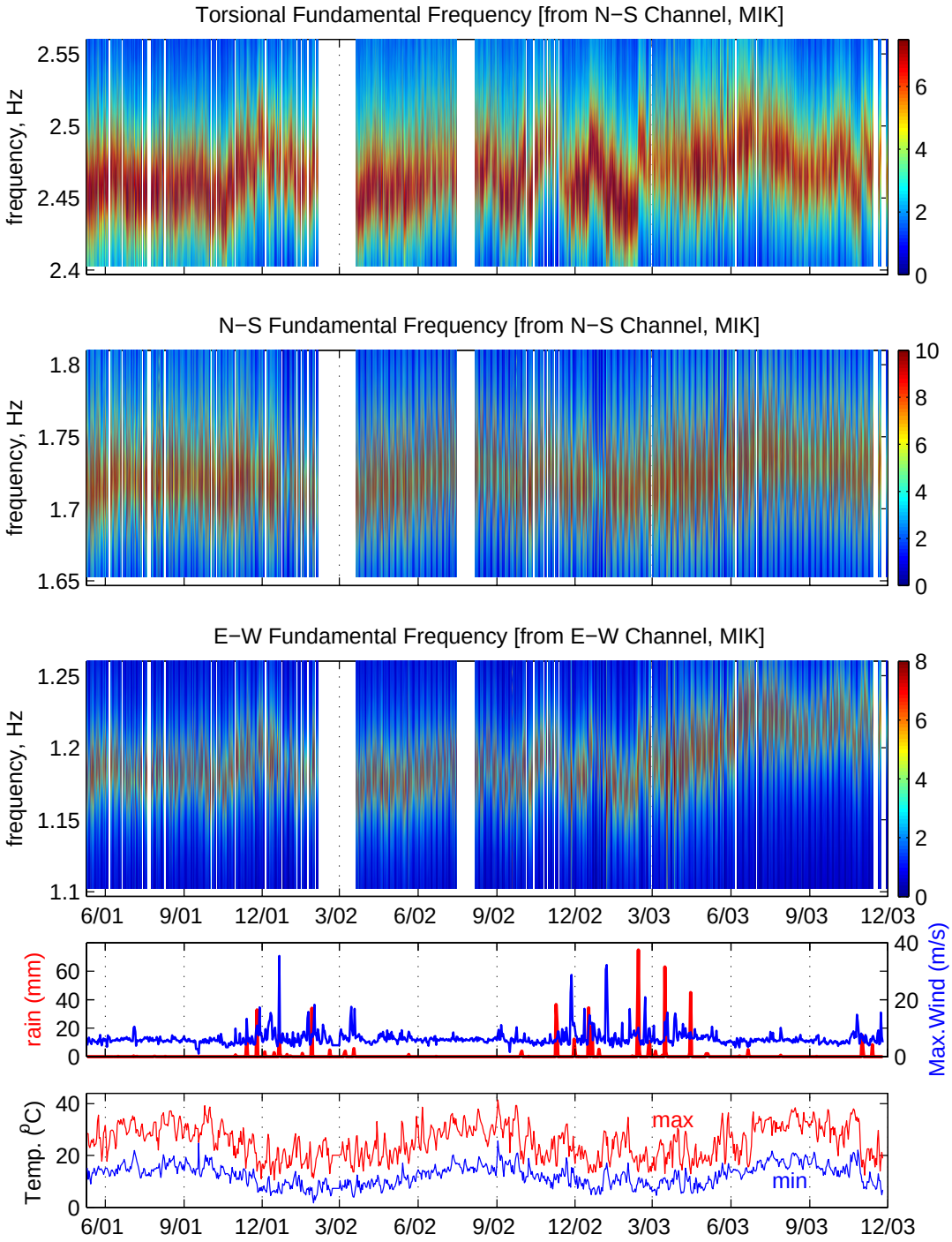

Figure 6.12: As Figure 6.11, no scaling of each spectrogram slice, linear colourbar

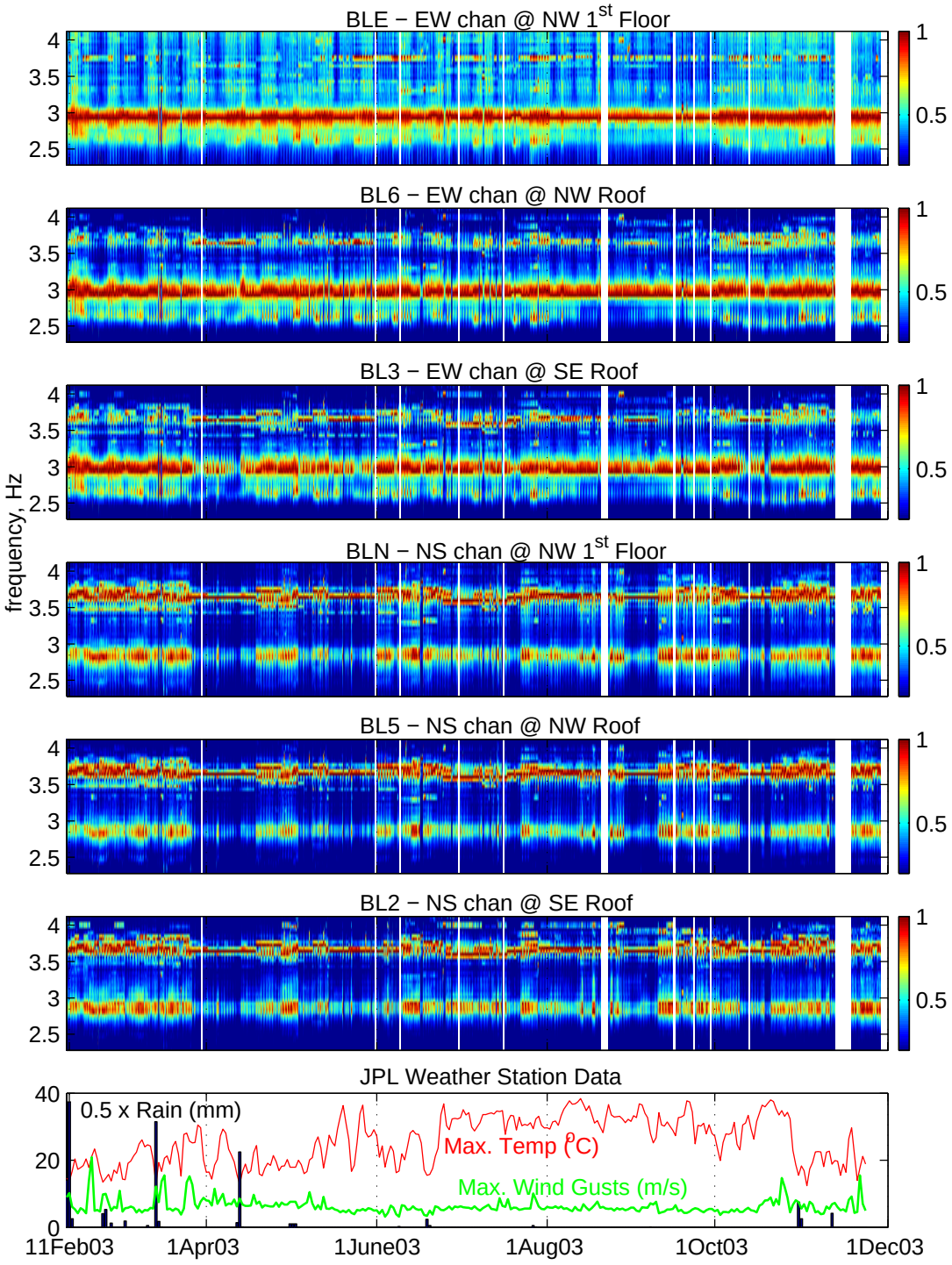

Figure 6.13: Spectrogram of all 6 horizontal channels at Station CBC, the Broad Center, for current lifetime of Station (Feb2003 - Nov2003). 1 hour spectrogram windows, no scaling, linear colourbar. Sharp red horizontal lines are due to machine noise in the building. Natural frequencies are represented by the broad peaks, near 2.6*Hz*, 3.0*Hz* and 3.6*Hz*, for the E-W channels, and near 2.4*Hz*, 2.8*Hz* and 3.6*Hz* for the N-S channels. Notice the 7*day* noise cycle with relative quiet on the weekends.

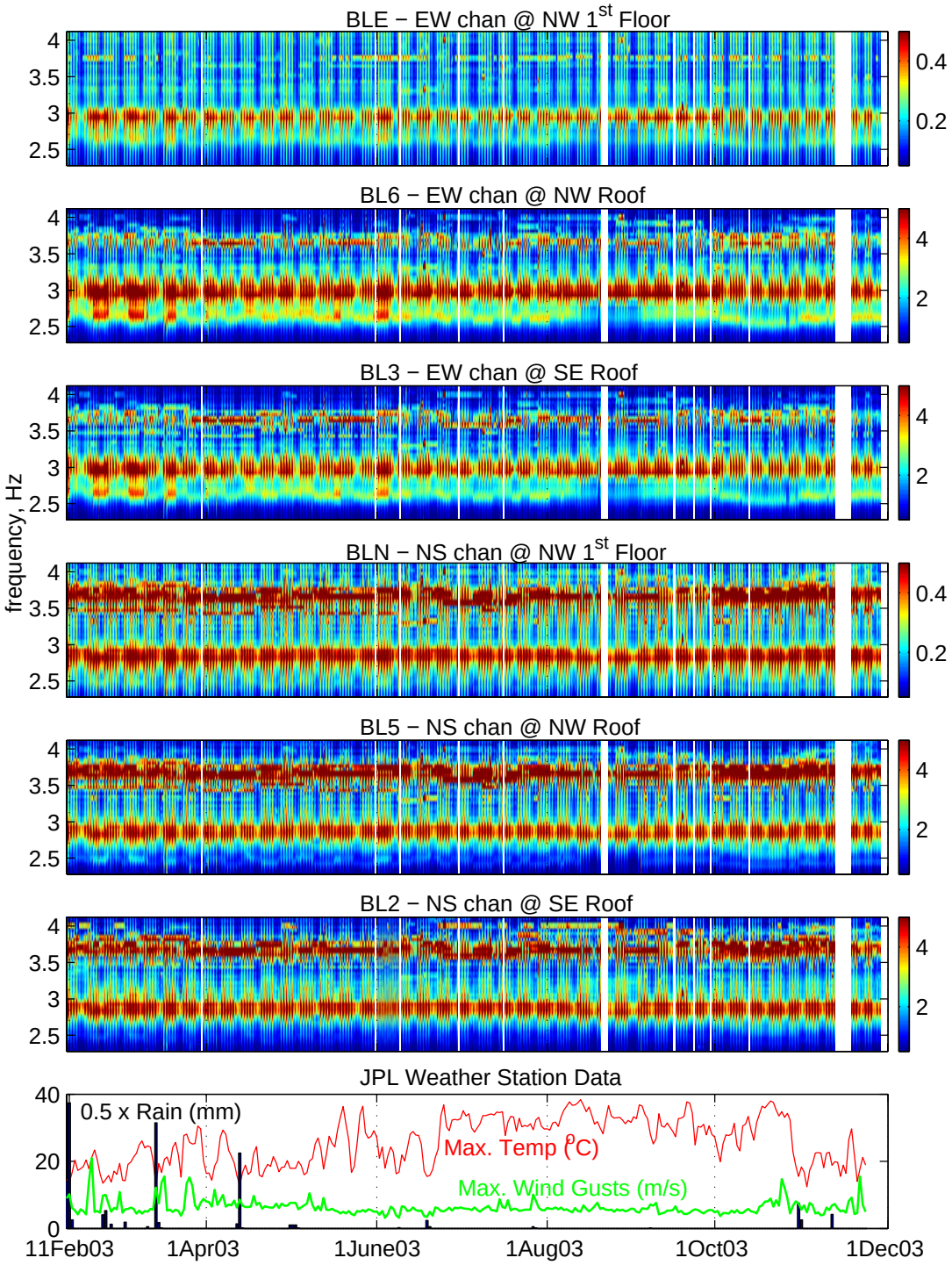

Figure 6.14: As Figure 6.13, no scaling of each spectrogram slice, linear colourbar

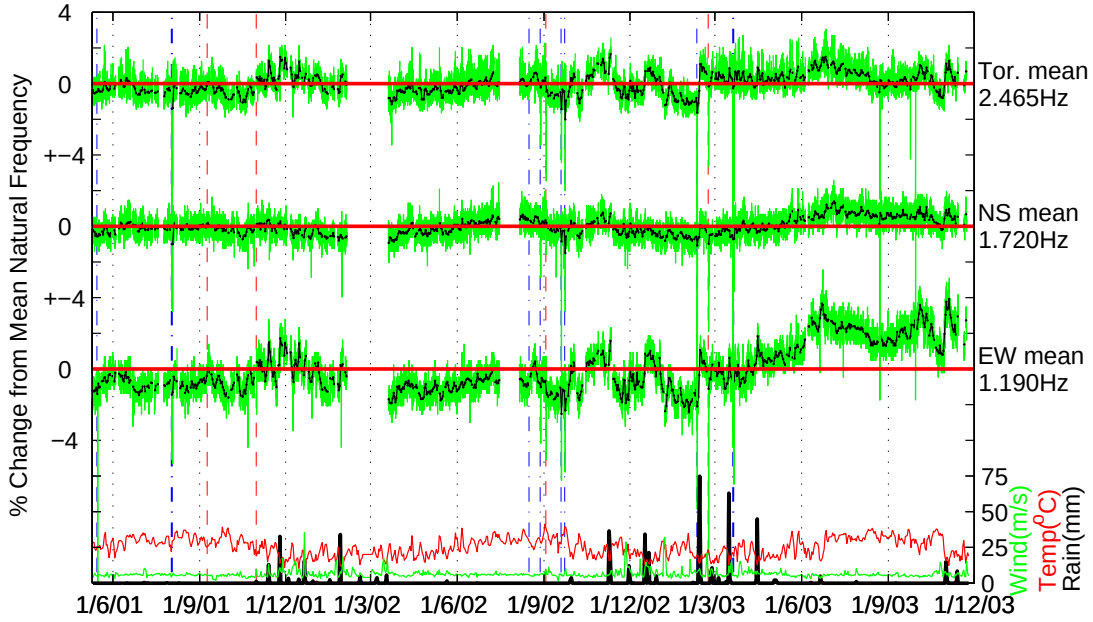

Figure 6.15: Deviation from the mean natural frequency for the 3 fundamental frequencies as recorded at MIK for station lifetime (May2001 - Nov2003). Fundamental frequencies for each hourly FFT are picked from the peaks in Figure 6.11, then the deviation from the average is determined. From the top down, the torsional, N-S and E-W frequencies are plotted. Hourly peak is shown in light thin line for each frequency, the thick black line tracks the daily average. The thick horizontal line is the average frequency. Rain, wind and temperature are plotted at the bottom. Vertical dashed-dot and dashed lines indicate days with forced vibration shaking of the library, and earthquakes with motions exceeding $2.5 cm/s^2$ at station MIK, respectively. These are responsible for the large deviations from the mean. [Earthquakes: 9/9/01:M4.2 Beverly Hills, $7 cm/s^2$; 30/10/01:M5.1 Anza, $2.8 cm/s^2$; 3/9/02:M4.8 Yorba Linda, $5 cm/s^2$; 22/2/03 M5.4 Big Bear, $18 cm/s^2$]. Note: forced vibration with full weights generates $8 cm/s^2$ at N-S fundamental mode.

characterised by the heavy horizontal red and yellow lines, near the natural frequencies at $3.65Hz$ (torsional), $2.81Hz$ (N-S) and $3.01Hz$ (E-W). It appears these frequencies are being driven by the machine noise, and so subtle shifts in their frequency over time would not be easy to interpret if it is indeed occurring.

The two lowest N-S and E-W frequencies, near $2.43Hz$ and $2.67Hz$ respectively, are not near any machine noise, and do seem to exhibit temporal changes similar to that seen in Millikan Library. Figure 6.16 presents a close-up of these lower frequencies for all the horizontal channels. Figure 6.17 presents the same data with no scaling of the colourbar. Large variations in signal strength over the time period are observed, with significant variation in the natural frequencies themselves. For the first 6-months, there is periodic variation, with period of the order of 2 weeks. After this, the predominant period of variation is much longer, on the order of months. The lowest E-W frequency seems to vary from $2.55Hz$ in mid October to $2.72Hz$ in early February, a variation of $\sim 6.5\%$. The lowest N-S frequency is of smaller amplitude to the lowest E-W mode, and thus is harder to observe above the ambient noise, and is only clearly visible on the N-W roof channel, BL5. It varies from $\sim 2.40Hz$ in mid October and $\sim 2.52Hz$ in early May, a variation of $\sim 4.9\%$. This N-S mode appears to disappear in late August, and in mid October drops to $2.4Hz$ for a number of weeks, coinciding with a large drop in the E-W lowest mode. Rainstorms, such as in early February and early November, clearly raise these resonant frequencies in a similar manner to what is observed in Millikan Library. The spectrograms also have a strong daily and weekly cycle, as much of the machinery is turned off during the nights and weekends.

6.4.2 Winter Storms — MIK

The temporal variations at MIK (Figure 6.15) can be partially explained by correlation with the rainfall data from the nearby JPL Weather Station. Figure 6.18 is a similar plot to Figure 6.15, focusing on the Winter of 2002/2003. In this 7-month period, heavy winds and rains were recorded. Each rainfall event prompts an immediate rise in the natural frequencies, which is largest in the E-W and torsional modes. After the storm, in the absence of other unusual excitation (such as windstorm, forced vibration test or earthquake), a gradual

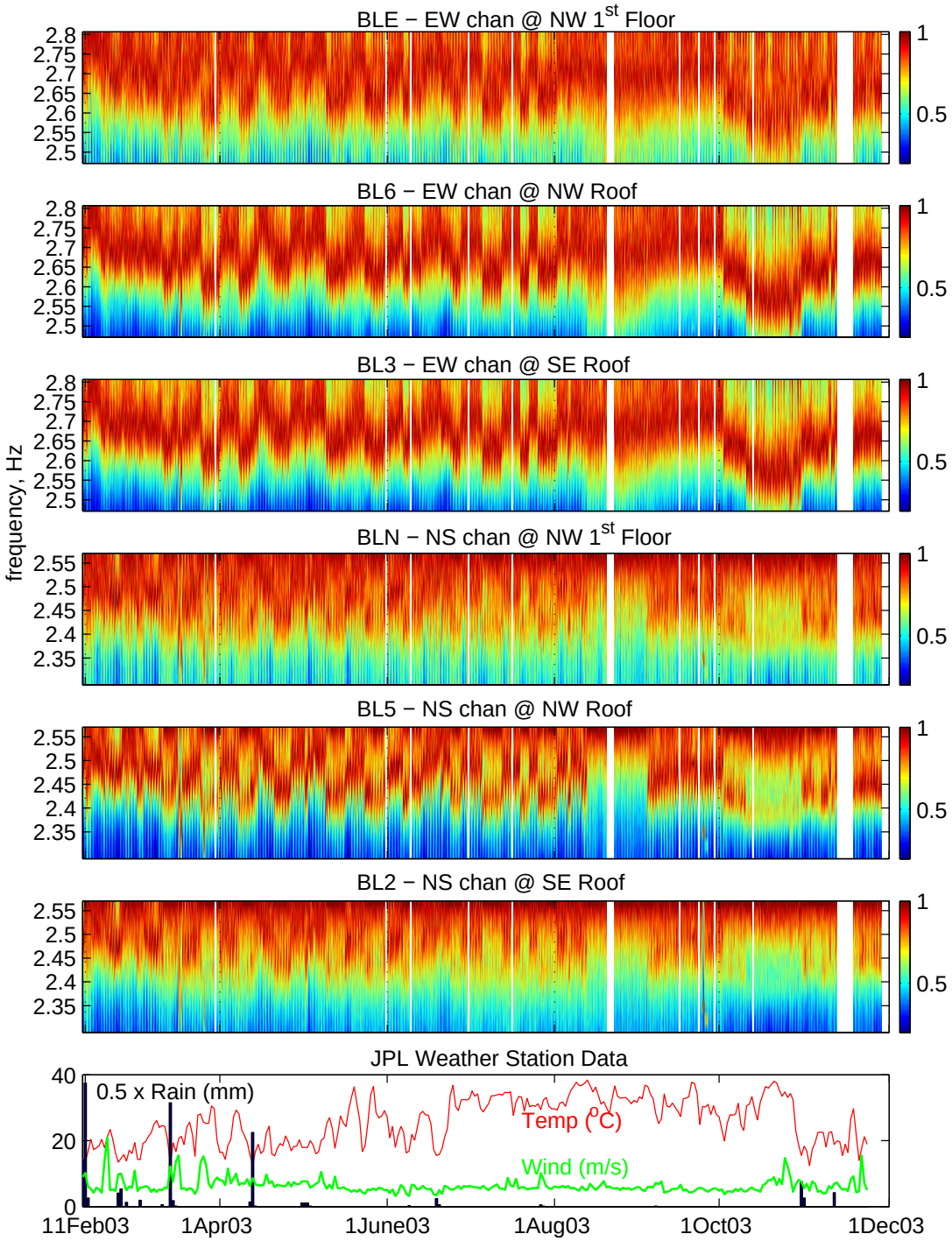

Figure 6.16: Spectrogram of fundamental frequencies for Broad Center, for current lifetime of Station CBC (Feb2003 - Nov2003). 1 hour window of spectrograms, scaled by max. value, linear colourbar. E-W channels centred around 2.67*Hz*, and N-S channels around 2.43*Hz*, the natural frequencies determined from stacking of 14-days of day long FFT's (Table 6.2). Note the rainfall seems to coincide with sudden rises in frequency, as observed at MIK.

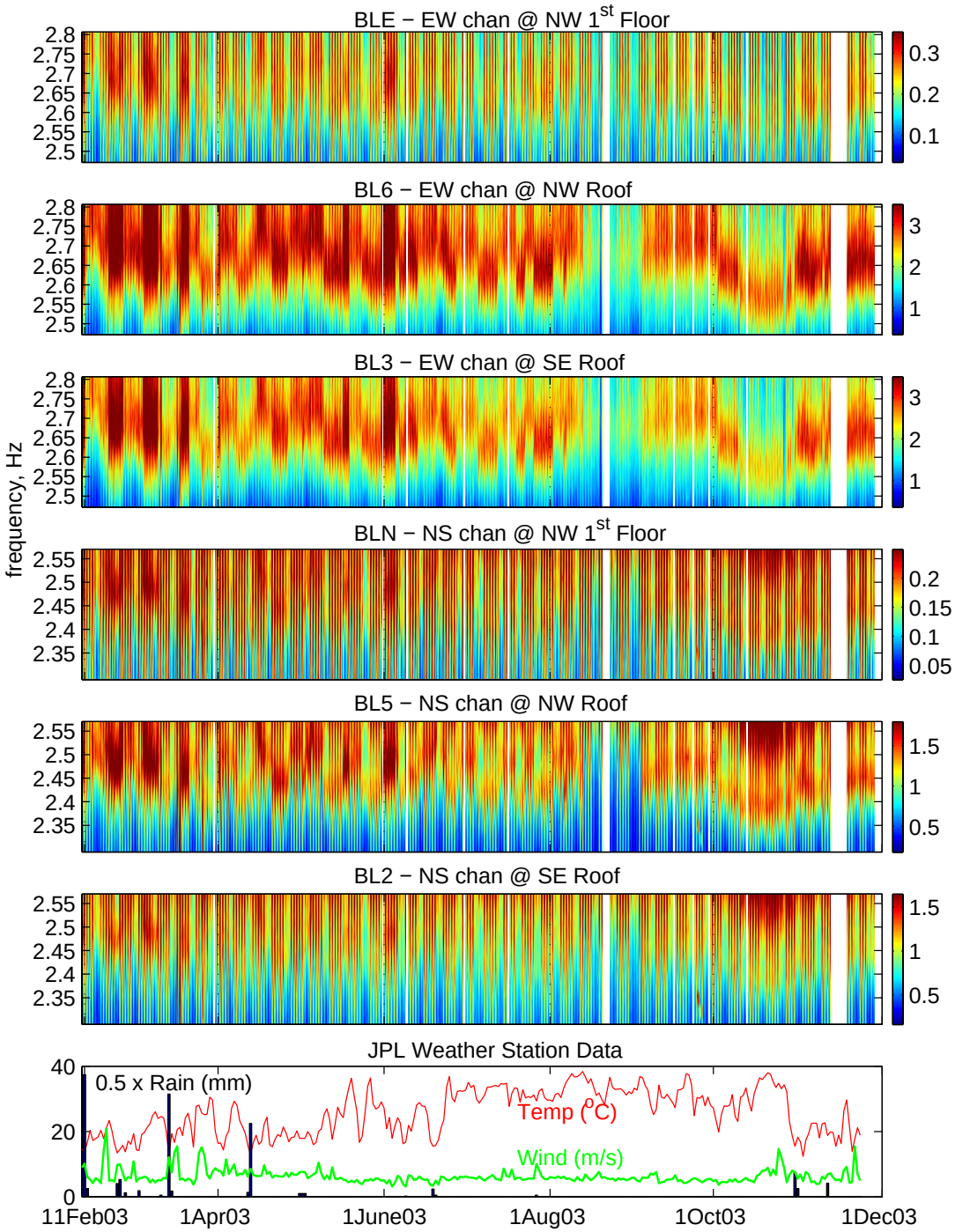

Figure 6.17: As Figure6.16, no scaling of spectrogram, linear colourbar.

recovery (on the order of about a week) of the frequencies to near the pre-rainfall levels is observed.

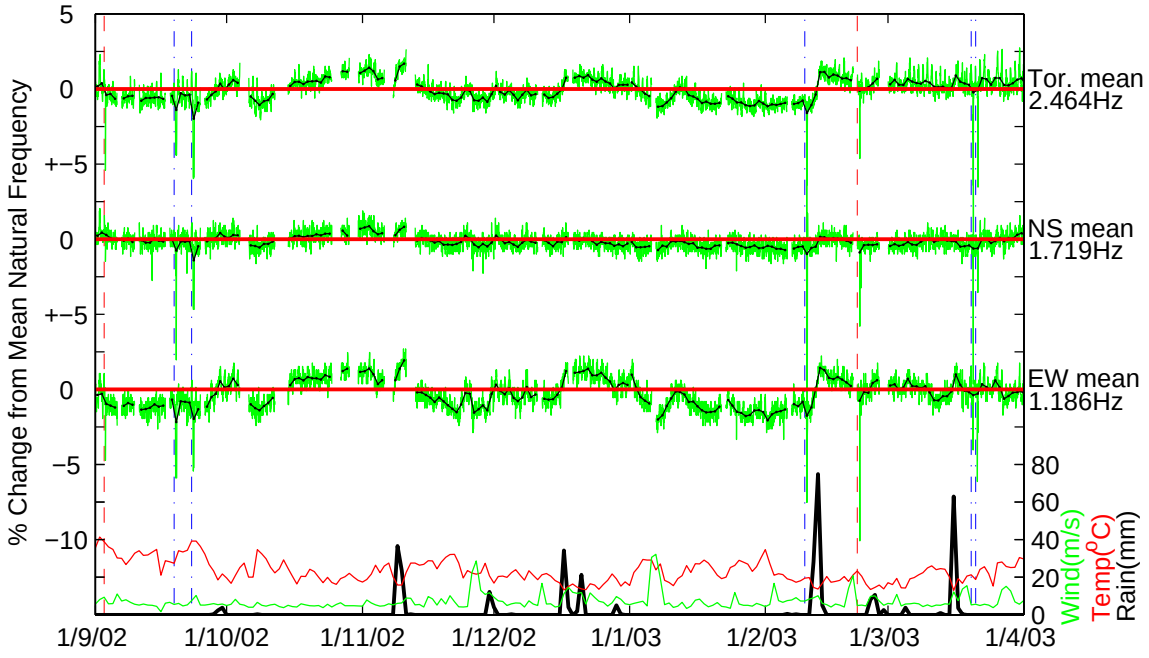

Figure 6.18: As Figure 6.15, with duration from September 2002 to March 2003, showing Millikan Library response to the storms recorded during the Winter season.

Figure 6.19 is a close-up of the period including the most severe storm since the installation of MIK, when over 100*mm* of rain fell over 2-days in early February 2003. This event caused a rapid and immediate rise of about 3% for the E-W and torsional natural frequencies, with a slow decay towards pre-rainfall levels over a 10 day period.

Figures 6.20 and 6.21 show a spectrogram of the E-W fundamental and 2^{nd} mode frequencies over the same time period, February 2003. An obvious rise in frequency of $\sim 3\%$ is observed in the 2^{nd} mode, with a similar return towards pre-rain frequencies as shown by the fundamental mode. The same trend is seen in Figures 6.22 and 6.23 during the rain events for the period of October - November 2003.

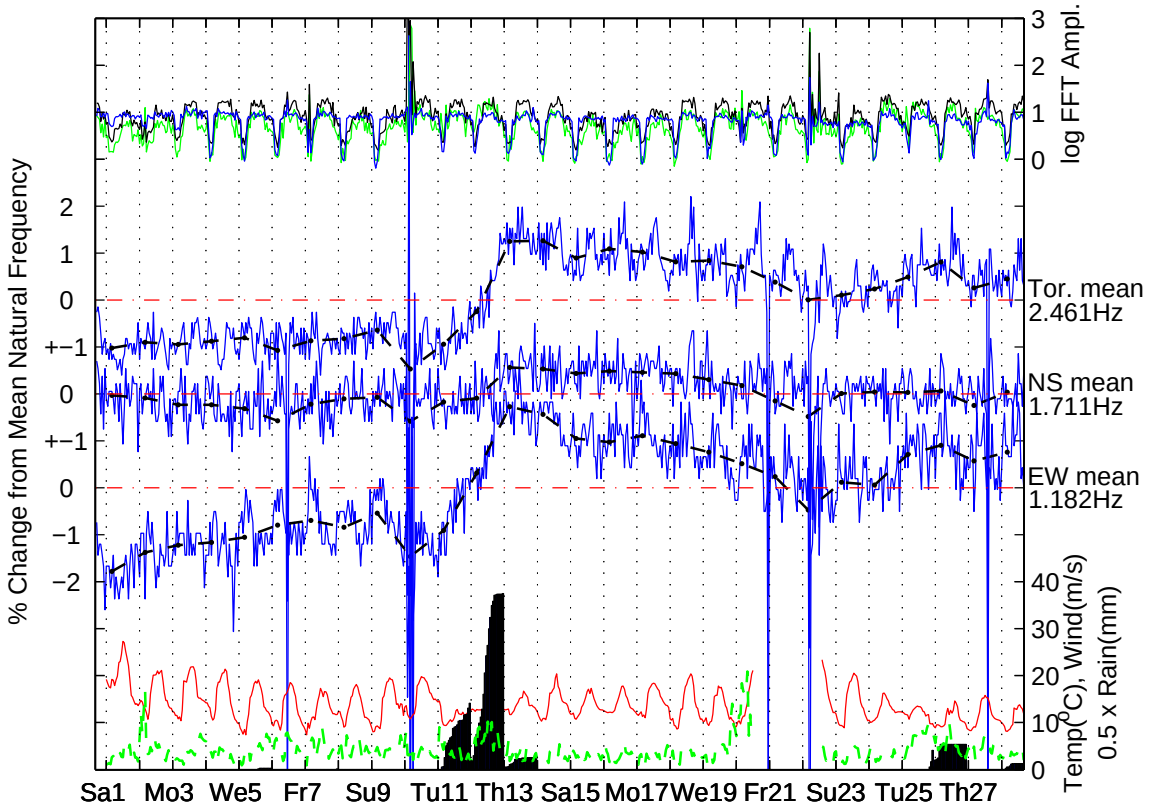

Figure 6.19: Deviation from the mean for the 3 natural frequencies of Millikan Library, for February 2003, including the major rainstorm from 11-12 February. In the centre of the plot, for each of the 3 natural frequencies, the horizontal dashed lines are the monthly average, the dashed-dotted lines are the daily average % deviation from this mean, and the solid light lines are the hourly % deviation from mean. At the bottom of the figure, the black bar data is the cumulative hourly rainfall (re-zeros at midnight). The solid line is the maximum hourly temperature, and the dashed line is the wind gust. On the top of the figure is the amplitude of each hourly FFT peak. The rainfall coincides with a very sharp rise in natural frequencies in the E-W and torsional modes, with slow return towards pre-rainfall levels afterwards. Dashed vertical lines represent the start of each new day (12AM PST). Frequency spikes are due to instrument glitches (6, 21, 27 February), vibration testing (10 February) and the Big Bear earthquake (22 February). FFT peaks fall at night, and on weekends. No major increase in excitation amplitude occurs during rainfall events not associated with high winds.

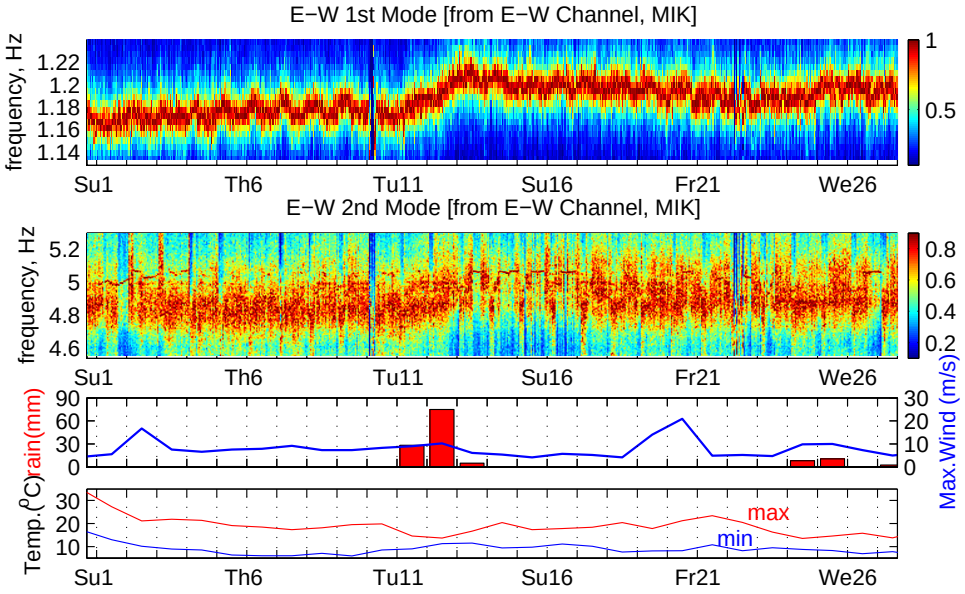

Figure 6.20: Spectrogram of Fundamental and 2^{nd} mode frequencies for E-W mode during February 2003, a time of heavy rainfall. 1 hour spectrogram windows, scaled by the maximum value, linear colourbar. JPL weather on bottom. Note correlation between rises in both natural frequencies and heavy rainfall.

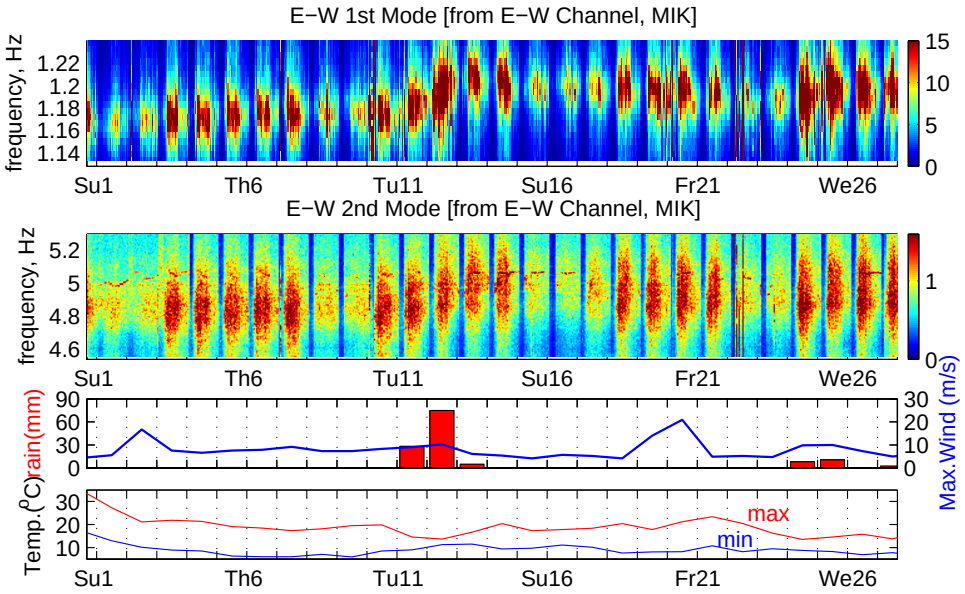

Figure 6.21: As Figure 6.20, with no scaling of each spectrogram, so variations of intensity of each frequency are apparent.

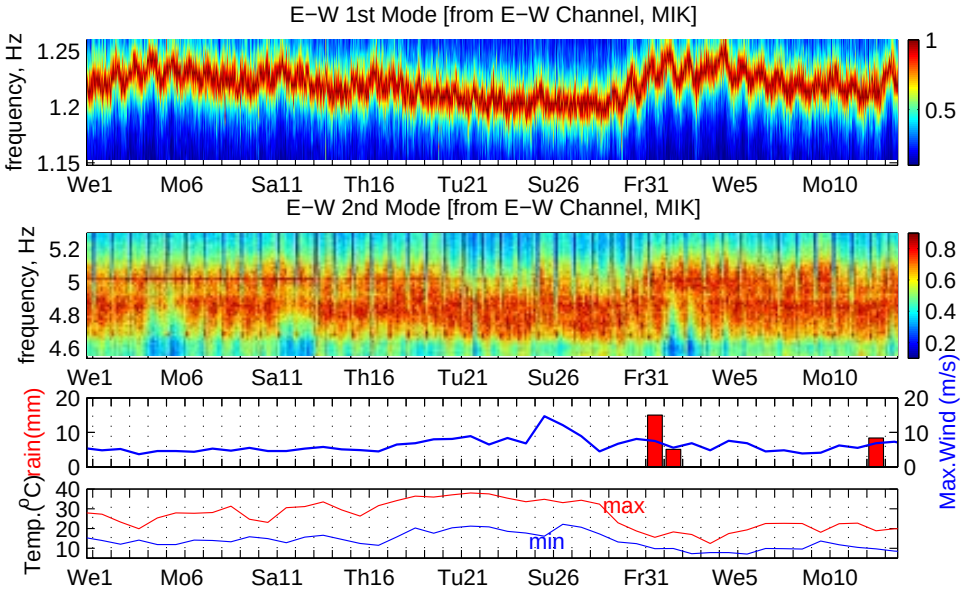

Figure 6.22: Spectrogram plot as Figure 6.20 for October - November 2003, when very hot temperatures and high winds caused widespread forest fires in Southern California, followed by heavy storms and cold weather. Again, note the correlation between rises in natural frequency and heavy rainfall.

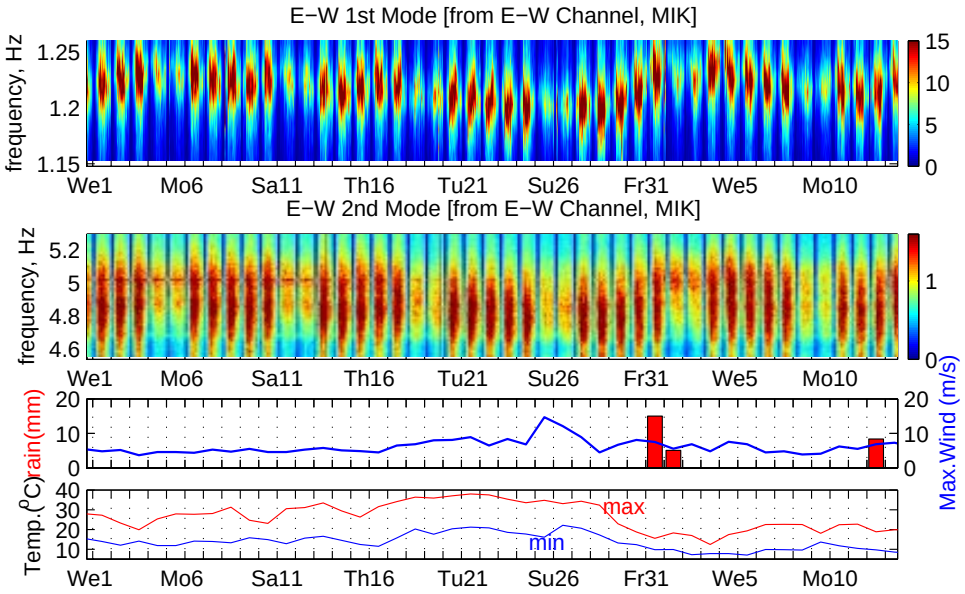

Figure 6.23: As Figure 6.22, with no scaling of each spectrogram, so variations of intensity of each frequency are apparent.

6.4.3 Santa Ana Winds — MIK

Strong winds can also influence the building, though they are usually accompanied with rainfall, which dominates the library's response. Between October and February, dry Easterly Santa Ana winds can affect the Pasadena area. In Figure 6.24, an example of such an intense Santa Ana windstorm (with no rainfall) is presented. The Library shows a sudden, significant drop in all the fundamental frequencies, in particular the E-W mode, which drops by about 3%. Amplitudes of the fundamental modes increase by about an order of magnitude during the windstorm, and the torsional mode increases about $1/2$ as much. Immediately after the event, the stiffness returns to near pre-event levels. This observation is consistent with the drops in natural frequency associated with increasing the weight in force vibration tests, which also increases the amplitude of excitation.

6.4.4 Diurnal Variation and High Temperatures — MIK

Figure 6.25 shows a typical example of the building response during hot weather, when there is significant daily variation of at least 1% for all three fundamental frequencies. This is likely due to both the changing weather conditions, and the daily building usage cycle. The air-conditioning in the building is turned off between the hours of 12pm and 4am, when the library is closed, and the elevators are also not in use. During the evening, the natural frequencies drop, and during the daytime, they increase again. On particularly hot days (such as the 1^{st} and 2^{nd} of September, 2002, in Figure 6.25, where temperatures reach 40^oC), there are higher frequency peaks. On cool, overcast and rainy days (such as in Figure 6.19), this diurnal variation is not as extreme. It is also clear that the torsional mode is more sensitive to temperature than the translational modes - this mode shows large increases in frequency above about 30^oC, whereas the other fundamental frequencies only show frequency increases at temperatures nearing 40^oC. Maximum daily variations can be as large as 3%.

These frequency increases during the day seem to be associated with thermal expansion of the concrete, but as the amplitudes of the ambient motion also increase by an order of magnitude during the day, are inconsistent with the general observation that natural

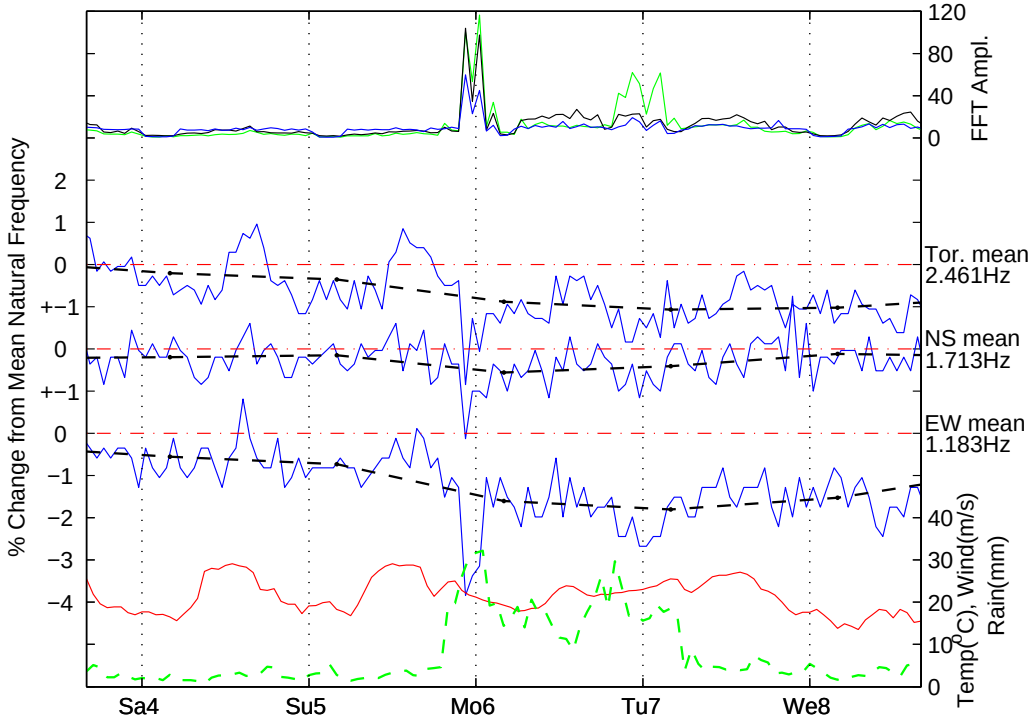

Figure 6.24: As Figure 6.19, for a 5-day period in January 2003, with a particularly intense wind storm (no rainfall). The natural frequencies of the Library dramatically shorten for the duration of the most intense windstorm, most notably in the E-W direction, but also significantly for the N-S and torsional modes. The smaller windstorm in the evening of January 6 appears slightly shifted in time from the response, this may be due to variations in the winds between the Library, and the weather station at JPL. The mean frequencies here are for the month of January.

frequencies drop as amplitude increases. For these amplitude levels, the thermal effects are larger than the excitation amplitude effects.

There does not appear to be any longterm trends associated with seasonal changes in temperature.

Figure 6.25 also includes hourly amplitudes of the FFT peaks, which show increased noise levels in the building associated with the working-hours usage of the building. In the evenings and weekends the building has less noise, as the air-conditioning and other machinery are not in operation.

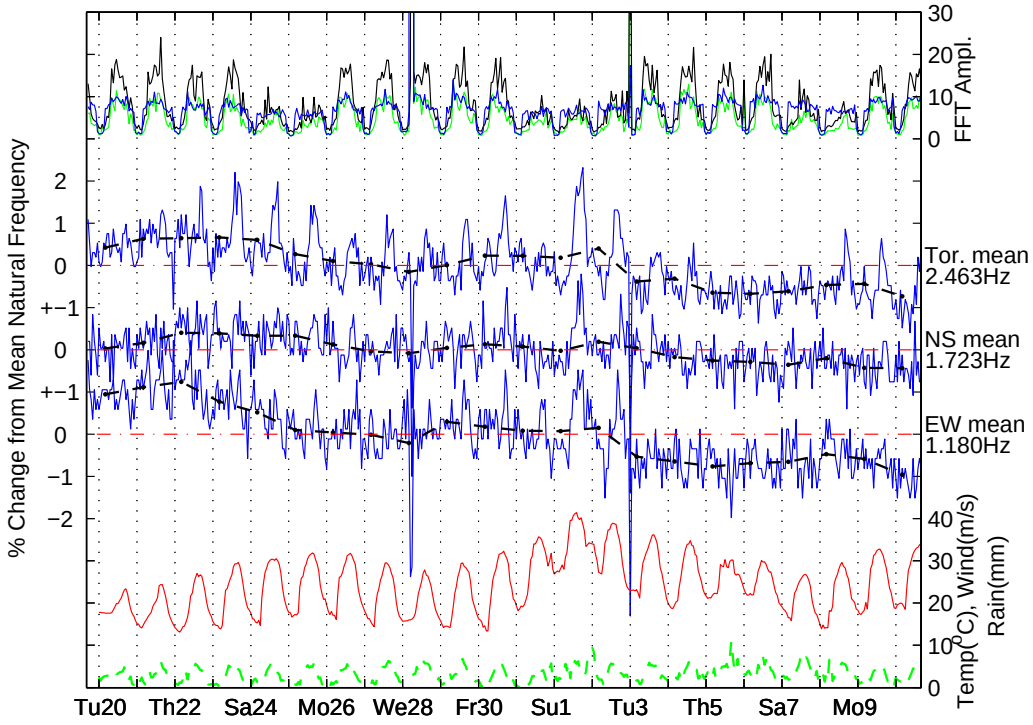

Figure 6.25: As Figure 6.19, for a 22-day period, late August — early September 2002. Typical daily variation during the summer months. Hourly maximum temperatures (solid lines) and the wind gusts (dashed lines) are shown on the bottom [no rainfall]. In the centre of the plot, the hourly smoothed FFT peaks are plotted for the 3 fundamental frequencies. Dashed lines are the daily averages, dashed-dotted lines are the mean for the time period. Above this is plotted the amplitude of the hourly FFT for all 3 fundamental modes. 26Aug: Vibration Testing; 3Sept: M4.8 Yorba Linda earthquake.

6.5 M5.4 22 February 2003 Big Bear Sequence

The moderate M5.4 Big Bear earthquake occurred at 4:19 AM PST on 22 February 2003, at a distance of 120*km* from the campus. At the time of the event, the stations GSA, MIK and CBC all were operational, and the USGS-Caltech array in Millikan Library also triggered. However, the basement channels and 2 channels recording the N-S directions on the east side of the building did not recover data due to refurbishment of parts of the building.

6.5.1 Millikan Library

USGS Triggered Data - Big Bear Earthquake

Figure 6.26 shows the timeseries for all the E-W channels, and the FFT of the records around the E-W modes: the E-W fundamental frequency is at 1.06*Hz* and the E-W 2^{nd} mode at 4.55*Hz*. These values are approximately 7% lower than the corresponding natural frequencies determined during forced vibrations (see Table 6.2). Further, the fundamental frequency is 11% below the ambient natural frequency of 1.19*Hz* (Figure 6.27) just before the earthquake, and the 2^{nd} mode is 6.2% below the pre-earthquake ambient frequency of 4.85*Hz* (Figure 6.20).

Note that the amplitude of the peak at 4.55*Hz*, which is identified as the second mode, is small at the 7^{th}, 8^{th} and 9^{th} floors; the timeseries between 8 and 12 seconds is rich in this frequency in the other floors. If we look at the modeshape for this frequency (see Figure 6.26), these floors are near a nodal point, and this explains why it is difficult to identify the 2^{nd} E-W mode using 9^{th} floor MIK data alone. This is seen in the small magnitude broad 2^{nd} mode peak in Figure 6.21.

Little excitation of other higher order modes was observed in the earthquake data, including the fundamental torsional mode, so no examination of their wander is attempted. Also note that no significant energy is present at the resonant frequencies in the reference site GSA record.

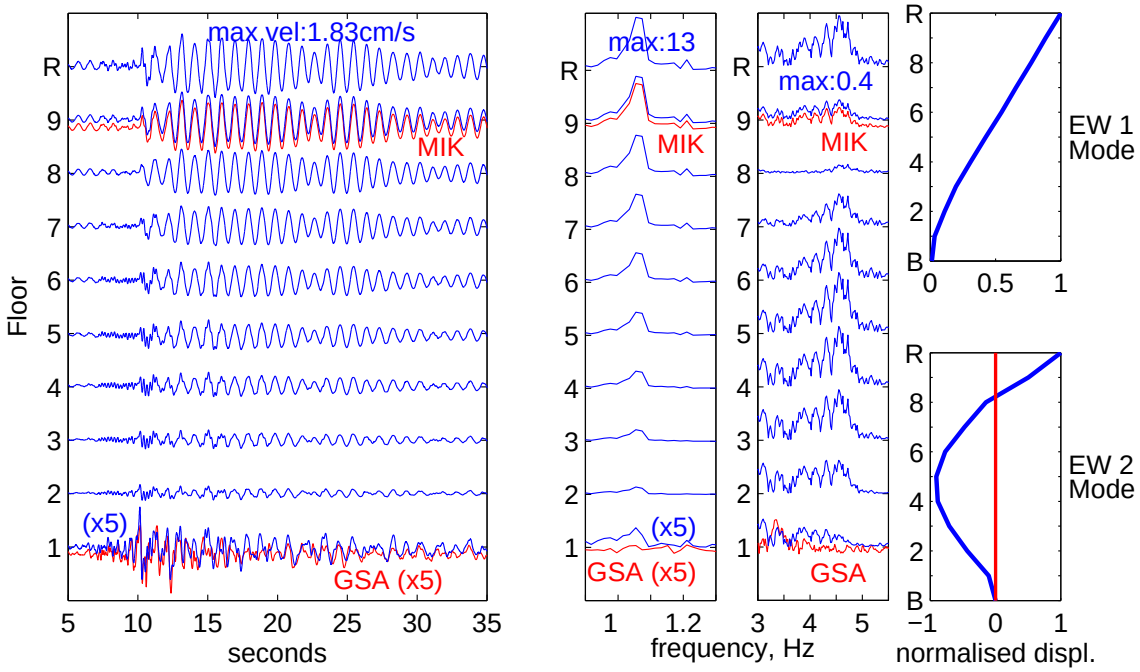

Figure 6.26: East-West components of USGS-Caltech array in Millikan Library, M5.4 Big Bear earthquake - velocity timeseries and FFT. Includes Floors 1-9 and Roof of Millikan Library as well as GSA ('free-field' site) and MIK (on 9th floor of Millikan Library), plotted underneath the 1st and 9th channels. FFT plots are centred around the fundamental frequency (1.06*Hz*) and 2nd mode frequency (4.55*Hz*) for the E-W direction. Also included are the modeshapes as identified from forced vibrations *(Bradford et al, 2004)* for the two E-W modes.

MIK Continuous Data: Big Bear Earthquake

The continuously recording strong motion channels from the 9th floor of Millikan provide an excellent opportunity to look at the wander in the Library's natural frequencies before, during and after the mainshock. Also observe how the structure regains its stiffness after minor shaking.

Figure 6.27 shows a spectrogram for the three fundamental frequencies and 2nd E-W mode frequency for a 60 minute period around the mainshock. FFT's are taken over a 30*s* period with 15*s* overlap. Although the frequency resolution is poor due to the short FFT length, observe that during the earthquake, the previously relatively stable frequencies all decrease by about 10%. Recovery from the earthquake to pre-earthquake levels appears to be almost instantaneous once the shaking has diminished. Aftershocks also shorten the frequencies, but by a lesser amount, commensurate to the smaller amplitudes of motion — for example, in Figure 6.28, a M4.1 aftershock occurs at 170*mins*, with a measurable decrease in frequency.

Figure 6.28 presents a similar spectrogram as Figure 6.27 for a 3 hour period around the same event, with FFT's taken over a 5 minute period with a 4 minute overlap. This provides improved resolution in the frequency domain, although resolution in the time domain is significantly diminished. The increased length also provides evidence that, though the natural frequencies are shortened a small amount in the immediate aftermath of an event, after about an hour, there is no perceptible difference between the pre- and post-event natural frequencies.

For this level of excitation, the structure regains its stiffness within minutes. This is in contrast to evidence (Udwadia and Trifunac, 1974) that suggests Millikan Library takes weeks or months to return to near pre-earthquake after undergoing strong motion. However, this observation is based on a minor shaking, whereas their observations were from San Fernando earthquake motions, which caused rooftop accelerations over 10 times greater than the Big Bear event. Thus, extrapolation of the Big Bear result to the large shaking that the building has been subjected to may not be valid. Note though that the previous work was based on single tests performed a few weeks and 22-months after the San Fernando earth-

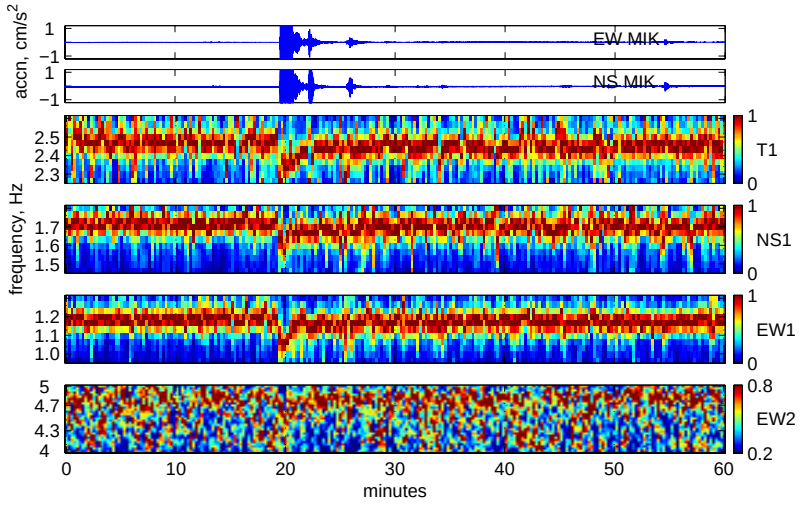

Figure 6.27: Acceleration data and resulting spectrograms for MIK from 12:00GMT to 13:00GMT 22 Feb2003. M5.4 Big Bear earthquake occurs at 12:19GMT. Max accn = 19.3cm/s^2 N-S, 10.9cm/s^2 E-W. Spectrograms are set around the 4 natural frequencies. 30s window spectrograms, with slices shifted by 15s. During the event, the fundamental frequencies shorten considerably during the shaking and aftershocks. Analysis of longterm behaviour, especially that of the 2^{nd} mode E-W, limited by poor resolution due to short FFT length (see Figure 6.28)

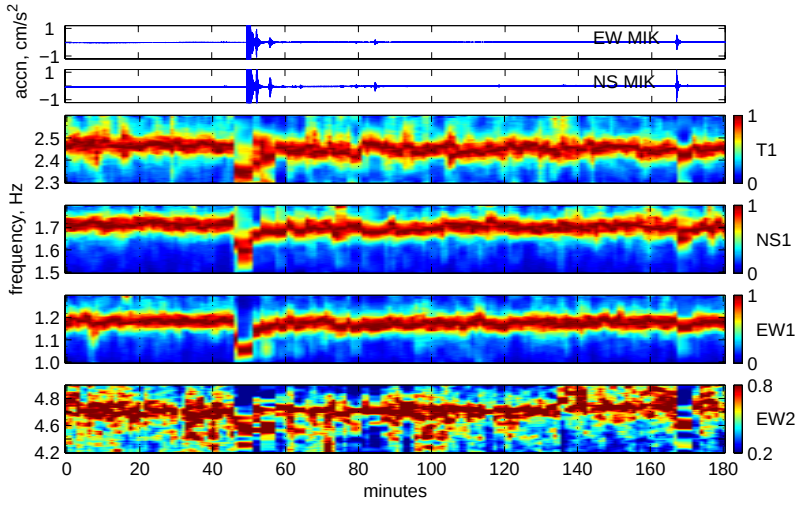

Figure 6.28: As Figure 6.27, but for MIK data from 11:30GMT to 14:30GMT, 5 minute window spectrograms, with slices shifted by 1 minute. M5.4 Big Bear earthquake occurs at 12:19GMT. During the event, as in Figure 6.27, we observe the fundamental frequencies shortening considerably. After shaking, over this time window there is no perceptible longterm shortening of the fundamental frequencies due to the earthquake. The event at 168 minutes is a M4.1 aftershock.

quake, where the observed decreases in the E-W natural frequency from pre-earthquake measurements were 18% and 12% respectively. The Big Bear data suggests the permanent change from the original natural frequency of 1.45Hz was about 12%. Udwadia and Trifunac (1974) show FFT segments from the tail of the strong motion record (about 80s after the initial triggering) that indicate the building is already returning to the pre-earthquake state. The differences in measurements may be explained by the many changing variables such as weather and test parameters, and may not necessarily be due to longterm 'healing' of the structure.

6.5.2 Broad Center

The continuous data from the Broad Center (CBC) provides another dataset for analysis of the impact of a small earthquake on the natural frequencies of a structure.

Figures 6.29 and 6.30 are 3-hour spectrograms of the 6 horizontal channels of CBC, with FFT's of a length of 5 minutes. These spectrograms have each FFT scaled to a maximum value of 1, so during the earthquake, the torsional mode disappears as the translational modes are predominantly excited. For each channel, a wide frequency band of acceleration spectra is plotted; a narrow band of displacement spectra centred on the fundamental frequency is underneath. Displacement spectra accentuates the energy in this frequency relative to the higher frequencies, and as these two fundamental frequencies are not driven by electrical or mechanical noise, fluctuations in frequency can be more easily observed.

During the earthquake, the natural frequencies all change considerably - it is not clear exactly which frequencies correspond to the values observed during the shaking as all 3 frequencies are so close together. It is clear that immediately after the earthquake, the frequencies return to their pre-earthquake levels.

6.6 A Linear Transfer Function Solution?

A simple method of modeling structural response to ground motions is to convolve the fundamental mode building response with a nearby reference recording of ground motion.

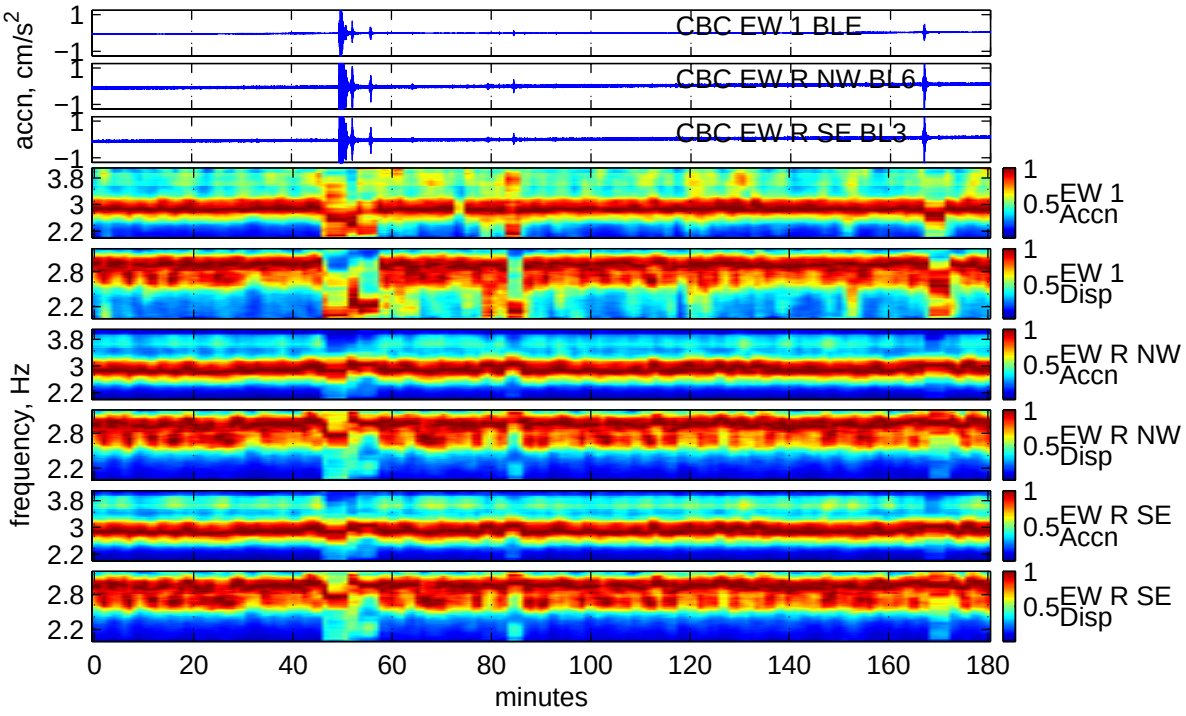

Figure 6.29: CBC E-W channels - acceleration timeseries and spectrograms from 11:30GMT to 14:30GMT, with FFT slices of 5 minutes length with each slice shifted by 1 minute. There are two spectrograms for each E-W channel — the first is a broad frequency range from acceleration data showing all identified modal frequencies. The second is a frequency band around the first mode only from displacement data to accentuate the behaviour of this the only mode without nearby machine noise (see Figure 6.13). M5.4 Big Bear earthquake occurs at 12:19GMT. Max accn = 14.8cm/s^2 at BL6, NW Roof. During the event, observe the fundamental frequencies shortening considerably. After shaking, over this time window there is no perceptible longterm shortening of the fundamental frequencies due to the earthquake.

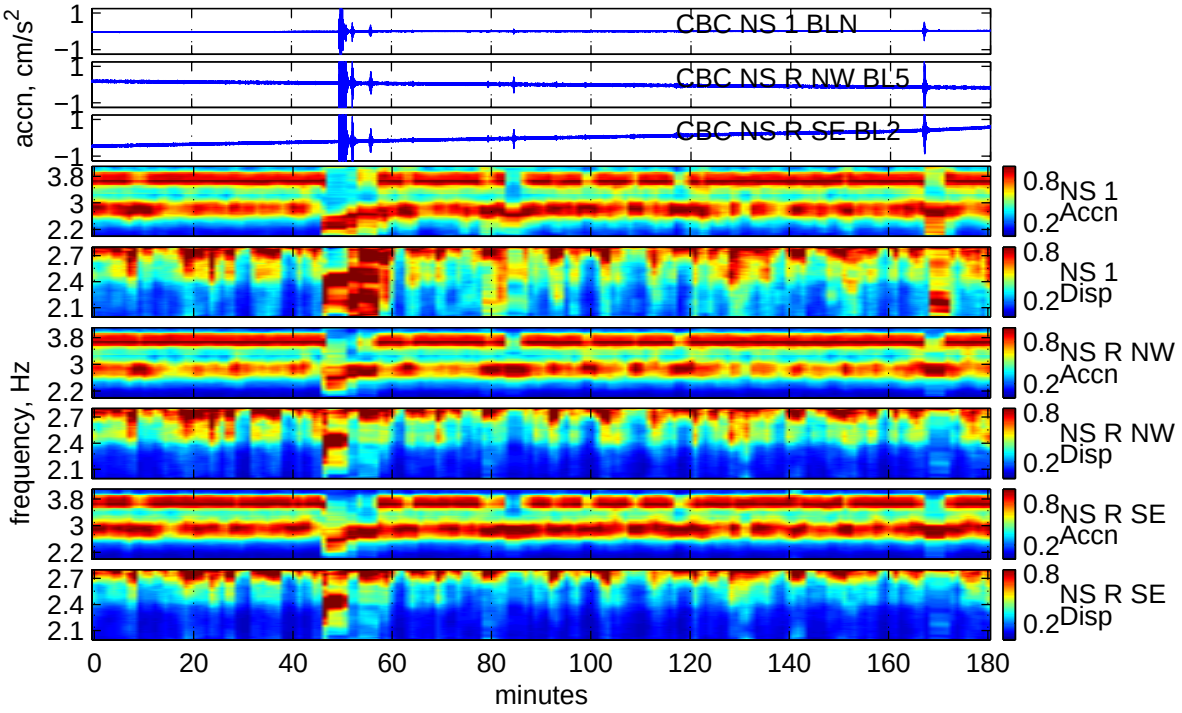

Figure 6.30: as Figure 6.29 — for CBC N-S channels. Max accn = 16.2cm/s^2 at BL5, NW Roof

There are obvious problems with this linear method during strong motion, since the fundamental frequency varies with excitation levels. Nonetheless, during small excitations, a linear response is expected.

A simple model is used which convolves the E-W acceleration ground motion at GSA with an impulse response of a single degree of freedom (SDOF) model representing the E-W fundamental frequency of Millikan Library. Amplitude amplification is determined using the participation factor of the first mode, assuming a mass matrix of equal floor mass, and modeshapes as determined from the forced vibration tests. This convolution gives the relative displacement of MIK to GSA, so we add to this the ground displacement at GSA. A constant damping ratio of 1.63% is employed, which is the value determined during the forced vibration tests (Bradford et al, 2004).

Figures 6.31 and 6.32 are examples of the results for 2 recent earthquakes. Figure 6.31 presents data from the 18 June 2003 M2.0 Pasadena earthquake (a foreshock of the bigger M2.6 event), 5km from Caltech, which had a maximum acceleration of 1.2cm/s^2 at MIK. Figure 6.32 presents data from the 22 February 2003 M5.4 Big Bear earthquake, 119km from Caltech, which had a maximum acceleration of 22.6cm/s^2 at MIK. Figure 6.31 shows that the model is improved if the ambient SDOF is used instead of the default forced vibration value (Note for this event, a default SDOF representing the second E-W mode is also included to help model the high frequency response). In Figure 6.32, where the behaviour of Millikan during the stronger motion is modelled, both the ambient and forced SDOF give a poor fit. In this case, the natural frequency has moved far from the ambient levels (as seen in Figure 6.26), and is best modelled using a natural frequency as determined from the strong motion records (1.06Hz). Note that though the character of the strongest motions is well modelled by this last SDOF, the low amplitude P-wave and coda motions are not well modelled as the natural frequency of the building seems to be evolving rapidly, as the excitation amplitude changes. These motions are small, and are certainly within what we would expect the linear response of the building, yet a single natural frequency cannot predict the motions of the building.

Current engineering practice has a single natural frequency assigned to the building, usually not even derived from experimental testing, but from formulae in the relevant design

code. This natural frequency is assumed constant for a wide range of ground motions. This data suggests this may not be the case even for weak motions.

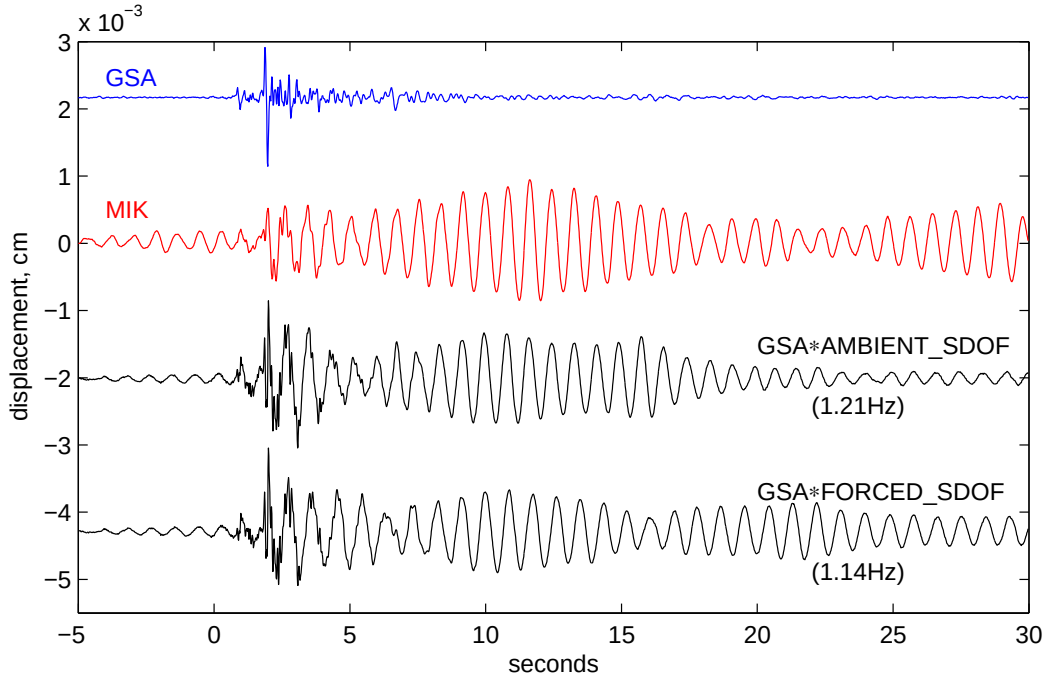

Figure 6.31: Prediction of MIK E-W motions using GSA E-W as input motion, for the M2.0 18 June 2003 Pasadena earthquake ($\Delta = 5km$). Motions recorded at GSA are convolved with an impulse response at a particular frequency. Damping is held constant at 1.63%. **Ambient_SDOF** uses the fundamental frequency as determined from FFT's of pre-event data ($1.21Hz$), **Forced_SDOF** uses the fundamental frequency as determined from Forced Vibration tests ($1.14Hz$). A 2^{nd} mode SDOF response is included for both models to reflect the high frequency components of the motions. During this very small amplitude motion, the natural frequency determined using the ambient data models the observations at MIK better than the forced vibration result.

6.7 Conclusions and Discussion

The data presented herein indicates that the dynamic behaviour of Millikan Library is determined by several external factors on very different timescales. There is significant wander in the translational and torsional natural frequencies of the structure. The determination of these frequencies is very dependent on the method/data used to estimate this frequency — whether we use ambient data, forced vibration data, or earthquake records.

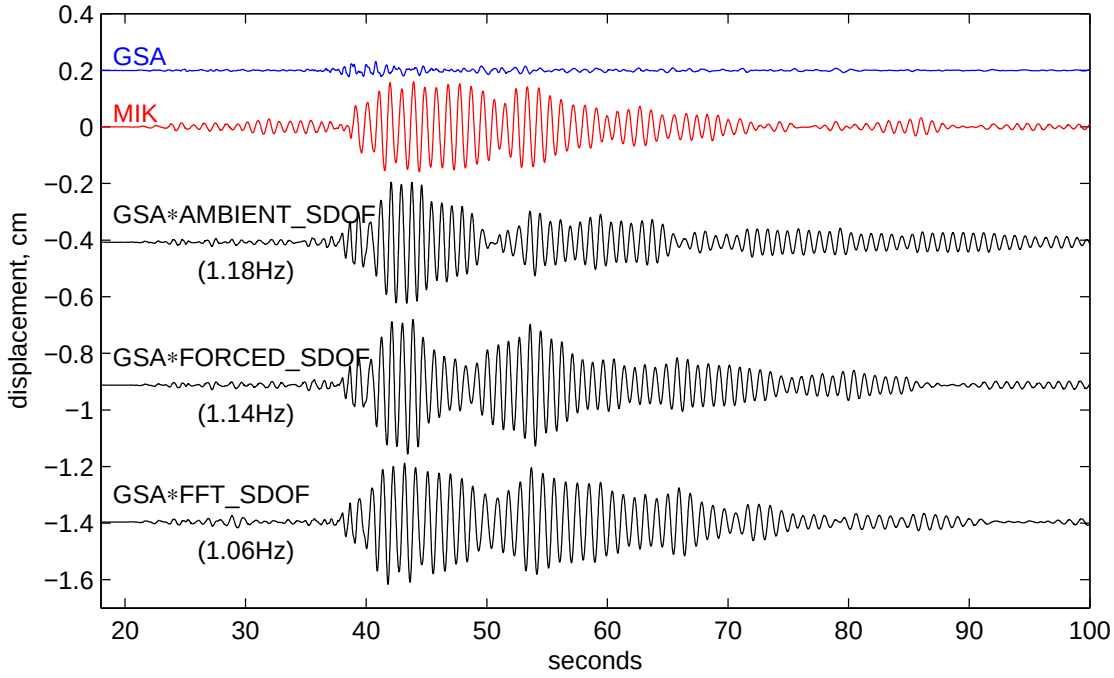

Figure 6.32: Prediction of MIK E-W motions using GSA E-W as input motion, for the M5.4 22 February 2003 Big Bear earthquake ($\Delta = 119km$). As Figure 6.31, with the **Ambient_SDOF** at $1.18Hz$, and **Forced_SDOF** at $1.14Hz$. Neither of these model the MIK observation well, so we include another SDOF, **FFT_SDOF**, with natural frequency at $1.06Hz$, as determined by the FFT peak of the strong motion record. This leads to a somewhat model of the observed motion. This shows that even during the moderate shaking generated from this relatively small and distant earthquake, a linear building model is inappropriate. A model that can have evolving natural frequencies will best represent the observed motions.

To the first order, there has been a significant permanent reduction in natural frequencies for the Millikan Library in the 36 years of its life, 22% E-W and 12% N-S. As the system mass did not change much during the lifespan [and removing the entire book collection from 3 of the lower floors is not shown to have an observable effect], this corresponds to a major decrease in system stiffness.

The large permanent frequency drops appear to be almost entirely caused by strong motions from moderate nearby LA Basin earthquakes. In particular, the 1971 San Fernando M6.6 earthquake had the largest effect, with permanent drops of 17% E-W and 7% N-S. For the E-W direction, the accelerations of this earthquake were not subsequently exceeded, and there are no more large permanent frequency drops. However, in the N-S direction, the San Fernando roof-top acceleration of $341 cm/s^2$ was exceeded with a recording of $534 cm/s^2$ during the 1987 M6.1 Whittier Narrows event. This caused a further permanent offset of 4%.

During the strong shaking, these moderate local events are shown to almost instantaneously shorten the frequencies by over 20%, without apparent structural damage. As there is only triggered data available, there is no clear evidence of the time-frame of stiffness recovery.

Smaller transient excitations also reduce the natural frequencies, such as forced shaking tests (by up to 7% with full shaker weights) and small earthquakes. Heavy rain can be seen to increase the E-W fundamental and 2^{nd} mode frequencies, and the torsional fundamental frequencies by up to 3% in a matter of hours, with little effect to the N-S fundamental frequency. Conversely, strong winds diminish all the natural frequencies by up to 3%, with inverse correlation with amplitude. The diurnal variation is of the order of $1-2\%$. On a day with a high temperatures near 40^oC, rising temperatures raise all the natural frequencies by a further $1-2\%$.

The recovery from these transient changes also varies. Certain moderate earthquakes have been shown to permanently shorten the observed frequencies - the 1971 M6.6 San Fernando event temporarily shortened the E-W fundamental frequency by 31%, and permanently by 16%. Subsequent earthquakes with similar ground motion magnitudes have also permanently reduced natural frequencies by a few percent. Small earthquake motions,

such as from the 2003 M5.4 Big Bear earthquake, reduce the ambient natural frequencies by 10% during the motion, with a full recovery within minutes. Similar observations are documented for the fundamental translational modes of the Broad Center.

For changes due to extreme weather, the recovery time can vary significantly. Any changes arising from wind and temperature only seem to last as long as the excitation, but for rain events the Library and the Broad Center slowly return to the pre-event fundamental frequencies over a time-span of about 1 week.

On a longer timescale, changing building usage can be responsible for large changes in the frequencies. Construction of partition walls to provide office space in 3 mid-level floors of the library over the period of 4-months is shown to coincide with an increase in frequencies during this same period — the E-W fundamental frequency is particular affected (4% increase over this period). It is noted that a 4% increase in natural frequency corresponds to a 8% increase in stiffness for the whole structure. This large stiffness increase cannot be realistically explained solely by placing partition walls in three middle floors.

The sources of all these observed wanders are not well understood. The different observed effects may be due to soil-structure interaction, super-structure non-linearities, or a combination of both.

For the particular case of Millikan Library, Chopra (1995) suggests that the the changes in the dynamic behaviour of the building during strong motion and weak forced shaking are associated with ‘cracking and other types of degradation of the so-called non-structural elements’. This mechanism does not account for the observed changes due to weather events.

The increases in natural frequency, and thus apparent increase in stiffness, during rain events may be caused by saturation of the soil. Though this could reduce the frictional resistance between the concrete and the soil at the foundation, which would lead to a more compliant system, reducing the natural frequencies. If the soil is dry before the event, saturation could also cause swelling of the soil, producing extra pressure against the sides of the foundations, reducing the amount of rocking and translation of the building. This attenuation of the base motions would lead to a stiffer system. Unfortunately, this does not explain why the E-W mode is most affected by the weather, but has very little rocking component

to its modeshape, yet the N-S mode, with 30% of the roof displacement for this modeshape being due to basement rocking (Appendix 3, Bradford et al, 2004), is not affected as much. Further, the gardens surrounding the building are heavily watered through out the year, so are likely to be near saturated year round. It is also noted the natural frequencies rise as soon as the rainfall event begins, or even beforehand. This could be due to to the fact the building is sensitive to pressure variations, but more likely it is because JPL weather station is 7*km* distant from Caltech, towards the mountains, and may receive its rainfall slightly delayed to to th Caltech Campus.

Stiffness changes in the super-structure during rain events should also be considered. Wetting of the concrete could potentially lead to expansion of the window/wall panels, and thus stiffen the E-W moment frames. This would explain why the E-W mode is most affected by rainfall. Slow recovery of pre-event stiffnesses would be determined by the drying process, which would be slow in the winter rainy season. Cycles of heating and cooling could have the same effect on the super-structure, but as heat is radiated quickly, this effect is transient.

Both mechanisms explain the observation that large rains not preceded by other events cause the largest increases in natural frequency. Rainfall events which closely follow the large events do not cause major changes themselves, as the soil or concrete is already in an expanded state.

The loss of natural frequency during heavy winds is consistent with the observations from previous investigators that as the amplitude of forced vibrations increases, the frequency drops. This is also consistent with the drop of frequency with increasing amplitude of earthquake excitation, from weak motions to strong motions, presented here.

The rise in frequency during hot weather is likely due to thermal expansion of the concrete stiffening the frame. All three fundamental frequencies are similarly affected by this. During the day, the ambient excitation is an order of magnitude larger than at night (when elevators and air conditioning are not in use, and the building is un-occupied), and so in the absence of this thermal expansion, the natural frequencies during the day would be expected to decrease.

The dramatic reduction in stiffness during moderate shaking could also be due to non-

linear soil-structure interaction - as there is no appreciable structural damage to Millikan during strong shaking. Measurement of pore-water pressures near the Library would help resolve the validity of this hypothesis. Another explanation would be that the bolted wall panels on the North and South sides of the structure, which provide resistance in the East-West direction, may loosen during stronger shaking. A single crack has been observed along pour lines on the North-South elevator core shear wall between the basement and 1st floor, and between the 1st and 2nd floors. Analysis of strain over the length of these cracks during different motions may also give insight into whether the loss of stiffness observed in the building may be due to rocking about these cracks. Potentially there are other cracks in the elevator core in the East-West walls, but these walls are covered by architectural features, and cannot be investigated.

The wandering in the natural frequencies is significant for the engineering community. In engineering practice, a linear structural behaviour is assumed for ambient and small motions, but this is clearly not the case. Further, as real-time structural health monitoring is becoming a reality, these unexpectedly large variations in the fundamental parameter of building response need to be accounted for in any damage assessment. Structural damage usually results in a loss in structural stiffness, which is characterised by a drop in the natural frequency. However, these observations of wandering natural frequencies due to ambient and small motions should serve to caution us that not all changes in natural frequency can be attributed to structural damage. This phenomena needs to be accounted for by any damage assessment methodology with any claims of robustness.

Chapter 7 Source Time Functions

7.1 Introduction

Inverting seismic waveforms to determine the spatial and temporal rupture history of earthquakes has emerged as one of the key tools towards understanding the physics of the rupture process. Source inversions are now common for most California earthquakes larger than M6. These inversions are used to determine rupture dimensions, average slip, rupture velocity and slip heterogeneity. Unfortunately, such parameters are not systematically available for earthquakes smaller than M6. Waveform inversion requires knowledge of the response of the medium to impulses of slip in the source region (Green's functions). At periods longer than about 1*s*, a layered space model can often be used to calculate Green's functions that approximate the response of the Earth. Unfortunately, it has not yet been feasible to synthesize Green's functions at periods much shorter than 1*s* — waveforms often have multiple scattered arrivals; the anelastic attenuation is unknown; and radiation patterns are commonly different from that of a double couple in a layered space. This means that it is often more difficult to resolve rupture characteristics that are shorter than $\frac{1}{2}s$ in time and 1*km* in space.

One approach to this problem is to use spectral methods (corner frequencies) to calculate source parameters. However, many of the problems just discussed are not addressed by these techniques. In many ways, most spectral techniques essentially assume homogeneous whole space Green's functions (Brune, 1970).

One solution is to utilise the waveforms of aftershocks as empirical Green's functions. This assumption is appropriate as long as —

1. the mainshock and the aftershock are co-located,

2. the mainshock and the aftershock have the same focal mechanism,

3. the source time function of the aftershock is short compared to the mainshock source time function.

A necessary (though not sufficient) condition for this assumption is that at each seismic stations, low-pass filtered displacement records from the mainshock and the aftershock are simple scalar multiples of each other. After identifying potential aftershocks by comparing locations and first motion focal mechanisms, this condition is used to identify an appropriate aftershock.

Obviously, it is also critical that the mainshock and the aftershock are well recorded at the same station. The use of aftershocks as Green's functions has only become practical with the deployment of high dynamic range seismographic networks such as SCSN. Furthermore, there must be a sufficient density of stations to obtain the azimuthal coverage that is necessary to derive directivity from the source time functions.

It is demonstrated in this Chapter that the use of aftershocks as empirical Green's Functions provides a robust method by which the directivity of moderate events can be determined. The successful inversions of the timeseries give stable source time functions at each station that are relatively insensitive to choice of aftershock as long as the aftershock approximates the location and first motion focal mechanism of the mainshock. This is promising for extending this work to invert for the rupture time history.

7.2 Theory and Methodology

The basic theory is straightforward and follows from Heaton (1982) and Hartzell and Heaton (1985):

Begin with the following definitions:

$$
\begin{aligned}
x, y &\equiv \text{Cartesian co-ordinates on the fault plane} \\
S &\equiv \text{rupture surface} \\
D(x,y,t) &\equiv \text{slip history at } (x,y) \text{ on the fault} \\
P &= \text{(average slip over fault rupture) x (rupture area)} \equiv A\overline{D} \equiv \text{potency} \\
\mu &= \text{rigidity, or shear modulus, of rock} \\
M_0 &= \text{seismic moment} \equiv \mu A\overline{D} \equiv \mu P \\
\mathbf{U}^i(t) &\equiv \text{observed vector displacement history at the } i^{th} \text{ station} \\
\mathbf{u}^i(x,y,t) &\equiv \text{vector displacement at the } i^{th} \text{ station due to the} \\
&\qquad\qquad \text{dislocation at } (x,y) \text{ on the fault} \\
\mathbf{G}^i(x,y,t) &\equiv \text{Green's functions for the } i^{th} \text{ station}
\end{aligned}
$$

Let x and y run along the fault strike and plunge, respectively. The Green's function is defined as the displacement at the receiver station due to a unit step function point dislocation at (x,y).

A schematic of the fault geometry is in Figure 7.1.

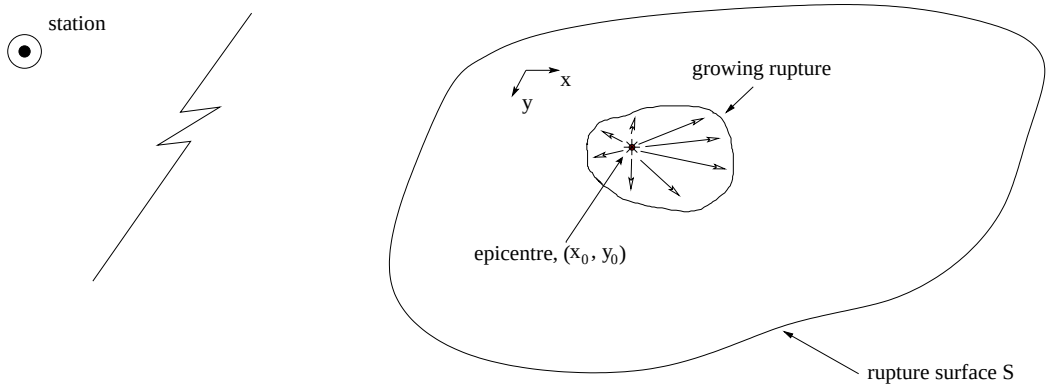

Figure 7.1: Simplified finite fault geometry for the mainshock

If a linear system is assumed, then the observed station displacement from the main-

shock is simply:

$$\mathbf{U}_M^i(t) = \iint_S \mathbf{u}^i(x,y,t)d\mathbf{S} \tag{7.1}$$

and if it is also assumed the dislocation vectors are everywhere parallel over the length of the fault (and thus the focal mechanism is invariant for all the dislocation), we may write:

$$\mathbf{U}_M^i(t) = \iint_S \dot{D}_M(x,y,t) * \mathbf{G}^i(x,y,t)d\mathbf{S} \tag{7.2}$$

where $\cdot$ and $*$ are the differentiation and convolution operators, respectively.

Now further make the assumption that over a small fault region, the Green's function at a point (x,y) is simply related to the Green's function at a single point on the fault (x_0,y_0) (in order to ensure our point is on the fault, we choose the epicentre). The Green's function will be the same but offset with a time lag $T^i(x,y)$, which is associated with the difference in travel time to the station (between the epicentre (x_0,y_0) and the point (x,y)) between key phases of the Green's functions.

$$\mathbf{G}^i(x,y,t) \approx \mathbf{G}^i(x_0,y_0,t) * \delta(t - T^i(x,y)) \tag{7.3}$$

or,

$$\mathbf{G}^i(x,y,t) \approx \mathbf{G}^i[x_0,y_0,t - T^i(x,y)] \tag{7.4}$$

This assumes that the key phases have the same apparent velocity with respect to the station as either the direct P-wave or the direct S-wave (depending on which wave group is being modelled). This is a critical approximation and it is important that individual records are investigated to ensure that we are primarily modelling wave groups with the appropriate velocity. In other words, we deconvolve the P- and S- wave trains separately. In practice, for this work, only the S-wave is deconvolved separately. The S-wave source time functions are found to be very similar to those determined from the deconvolution of the entire wave train at once.

Combining Equations 7.2 and 7.3 we obtain:

$$\mathbf{U}_M^i(t) \approx \iint_S \dot{D}_M(x,y,t) * \mathbf{G}^i(x_0,y_0,t) * \delta(t - T^i(x,y)) d\mathbf{S} \tag{7.5}$$

$$\approx \iint_S \dot{D}_M[x_0,y_0,t - T^i(x,y)] * \mathbf{G}^i(x_0,y_0,t) d\mathbf{S} \tag{7.6}$$

which can be rewritten as:

$$\mathbf{U}_M^i(t) \approx \mathbf{G}^i(x_0,y_0,t) * F_M^i(t) \tag{7.7}$$

where $F_M^i(t)$is the source time function for the i^{th} station given by:

$$F_M^i(t) \equiv \iint_S \dot{D}_M[x_0,y_0,t - T^i(x,y)] d\mathbf{S} \tag{7.8}$$

In this representation, the potency of the mainshock, P_M, is:

$$P_M \approx \int F_M^i(t) dt, \text{ for all } i \tag{7.9}$$

Now assume that the time function of the aftershock is sufficiently short so that it can be approximated by a δ-function times the potency of the aftershock, P_A, and hence:

$$\mathbf{U}_A^i(t) \approx P_A \mathbf{G}^i(x_0,y_0,t) \tag{7.10}$$

To examine the validity of this assumption, consider the definition of the moment magnitude, M_w:

$$M_w = \left[\frac{logM_0}{1.5}\right] - 10.73 \qquad , M_0 \text{ in units of dyne/cm} \tag{7.11}$$

$$\propto logM_0 \tag{7.12}$$

$$\propto log(P) \tag{7.13}$$

$$\propto log(A\bar{D}) \tag{7.14}$$

$$\propto logA^{3/2} \tag{7.15}$$

assuming a constant stress drop, and $\bar{D} \propto \sqrt{A}$:

$$M_w \propto 3/2 log A \tag{7.16}$$

so if the mainshock is an M4.5, and the aftershock being used as a Green's Function is a M2.5, then:

$$\frac{4.5}{2.5} = \frac{log(A_{4.5})}{log(A_{2.5})} \tag{7.17}$$

and so in this case the area of the mainshock is 100 times that of the aftershock. This is why the aftershock can be assumed to be a δ-function of the mainshock if they are sufficiently separated in magnitude.

Combining Equations 7.7 and 7.10 we obtain:

$$\mathbf{U}_M^i(t) \approx \left[\frac{1}{P_A}\right] \mathbf{U}_A^i(t) * F_M^i(t) \tag{7.18}$$

We can then deconvolve the aftershock motion from the mainshock motion to obtain a source time function for each station. Anyone with experience of deconvolutions of this sort will recognize that this deconvolution is typically numerically unstable. Probably the most important issue for stability is whether or not the aftershock and mainshock do indeed have similar Green's functions. This is best established by (i) ensuring that the two events are co-located and have similar first motion focal mechanisms, and by (ii) checking whether the low-pass filtered displacement records are simple scalar multiples of each other. We can then use the damped linear least squares inversion procedure to perform the deconvolution to reveal the source time function for each station. Hartzell and Heaton (1985) used a variation of this technique to derive source time functions from the teleseismic body waves of large subduction earthquakes. This formulation is similar to a serial product and is discussed by Bracewell (1965). Equation 7.18 can be rewritten in the classic form:

$$\mathbf{Ax} = \mathbf{b} \tag{7.19}$$

where in this case:

$$\mathbf{A_{jk}} = \left[\frac{1}{P_A}\right]\mathbf{U}_A^i[(j-k)\Delta t] \tag{7.20}$$

$$\mathbf{x}_j = F_M^i(j\Delta t) \tag{7.21}$$

$$\mathbf{b}_k = \mathbf{U}_M^i(k\Delta t) \tag{7.22}$$

Equation 7.19 can now be solved for the source time functions using standard linear inversion techniques. This formulation can easily be adapted to invert each component of ground motion individually, or all three components simultaneously, by a simple rewriting of the matrix equations (though inversion speeds will of course differ considerably). The method used in this Chapter is a simple least squares inversion, following Menke (1989). The deconvolution method has been discussed in detail in Chapter 1.

7.2.1 Directivity

The first-order effect we expect to see on a deconvolved source time function at a particular station is directivity. This discussion follows Heaton (2003) and ammends Lay and Wallace (1995).

The source time function can be defined as the shape of the body-wave pulses which are caused by the earthquake rupture. At distances beyond a few fault lengths, the near-field effects are dominated by far-field effects, and so only these far-field terms are considered in this case.

The far-field displacement for the P-wave, $u_r(r,t)$ (as in the radial orientation), is:

$$u_r(r,t) = \frac{1}{4\pi\rho\alpha^3}\frac{R^P}{r}\dot{M}\left(t-\frac{r}{\alpha}\right) \tag{7.23}$$

and for the SH-wave, $u_t(r,t)$ (transverse orientation), and SV-wave, $u_v(r,t)$ (vertical orien-

tation):

$$u_t(r,t) = \frac{1}{4\pi\rho\beta^3}\frac{R^{SH}}{r}\dot{M}\left(t-\frac{r}{\beta}\right) \tag{7.24}$$

$$u_v(r,t) = \frac{1}{4\pi\rho\beta^3}\frac{R^{SV}}{r}\dot{M}\left(t-\frac{r}{\beta}\right) \tag{7.25}$$

in these equations, r is distance from fault, α and β are the speed of the P- and SH/SV-waves, and R^P, R^{SH} and R^{SV} are the radiation patterns of the P-, SH- and SV- waves respectively. $\dot{M}$ is the moment rate function, the time derivative of the moment, $M = \mu A(t)\bar{D}(t)$. The radiation patterns are complex functions of the rake, strike and dip, as well as the take-off angle of the ray being considered.

For a small earthquake, the fault is considered to be single point source. As a simple approximation, displacement on this fault can be considered to occur as a ramp function. The source time function arising from a ramp time history on a single point source is a box-car of length τ_r, which is the rise time of the ramp function. For finite length faults, the rupture plane can be approximated as the summation of a number of earthquake point sources that rupture with the appropriate time delays considering the progressive rupture of the fault (see Figure 7.2). This simple line source is the Haskell Fault Model.

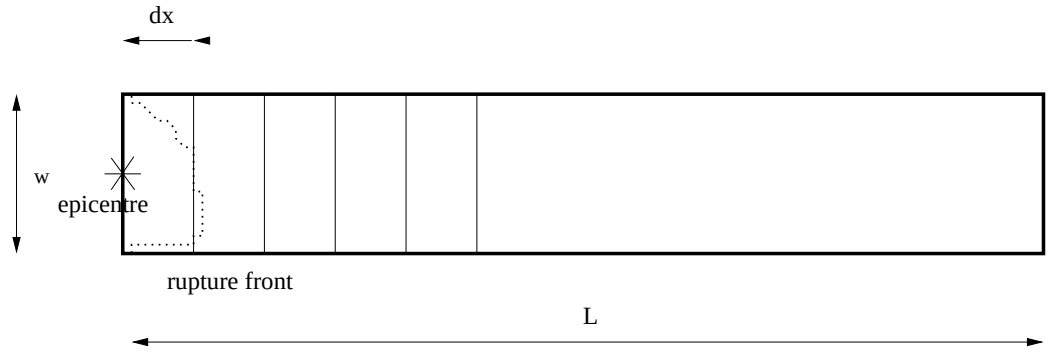

Figure 7.2: Simplified fault geometry for fault of width w and length L, with unilateral slip. Rupture plane is divided into sub-event slices of length Δx.

For the displacement field, this corresponds to:

$$u(r,t) = \sum_{i=1}^{N} u_i\left(r_i, t-\Delta t_i\right) \tag{7.26}$$

where i is an index of sub-events evenly distributed along the fault length. Δt_i is the delay time between sub-events, and if the rupture has a constant rupture velocity, v_r, and the displacement time history is the same ramp function everywhere on the fault, then $\Delta t_i = i\Delta x/v_r = x_i/v_r$. Now $\dot{M}_i$ is $\mu A_i \dot{D}_i(t)$, or $\mu w dx \dot{D}_i(t)$ if the sub-events are assumed to be over a length dx and width w. Thus, for the P-wave, combining Eqns 7.23 and 7.26 gives:

$$u_r(r,t) = \frac{\mu}{4\pi\rho\alpha^3} w \sum_{i=1}^{N} \frac{R_i^P \dot{D}_i}{r_i}(t - \Delta t_i - \frac{r_i}{\alpha})\Delta x \tag{7.27}$$

At large distance from the fault, R_i^P is approximately constant, and $r_i = r - x_i cos\theta$ (see Figure 7.3). In Equation 7.27, the r_i term in the denominator is an amplitude scaling term, and as such small changes in this denominator term will not lead to large changes in the displacements. As the length of the fault from these small events is always small in comparison to the distance of the station to the fault, the $x_i cos\theta$ term is small and aproximates zero. The r_i term in the timing cannot assumed to be constant, as the arrival times are very sensitive to these small changes in travel distances:

$$u_r(r,t) = \frac{R^P \mu}{4\pi\rho\alpha^3} \frac{w}{r} \sum_{i=1}^{N} \dot{D}\left(t - \frac{x_i}{v_r} - \frac{r - x_i cos\theta}{\alpha}\right)\Delta x \tag{7.28}$$

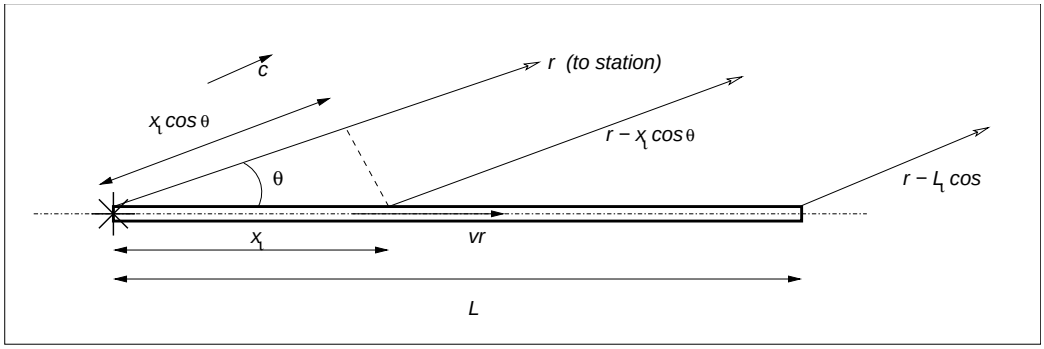

Figure 7.3: Azimuthal dependency of arrival times, for fault plane rupturing from left to right

Noting the shift property of the δ-function, and taking the limit of the sum as $\Delta x \to 0$:

$$u_r(r,t) = \frac{R^P \mu}{4\pi\rho\alpha^3} \frac{w}{r} \int_0^L \dot{D}(t) * \delta\left(t - \frac{x}{v_r} - \frac{r - x cos\theta}{\alpha}\right) dx \tag{7.29}$$

now $\dot{D}$ is independent of x and let $z = t - (x/v_r) - ([r - xcos\theta]/\alpha$:

$$u_r(r,t) = \frac{R^P \mu}{4\pi\rho\alpha^3}\frac{w}{r}\dot{D}(t) * \int_{t-r/\alpha}^{t-L/v_r-(r-Lcos\theta)/\alpha}\left[\frac{\alpha v_r}{v_r cos\theta - \alpha}\right]\delta z dz \quad (7.30)$$

$$= \frac{R^P \mu}{4\pi\rho\alpha^3}\frac{w}{r}\dot{D}(t) * \left[\frac{\alpha v_r}{v_r cos\theta - \alpha}\right] H(z)\Big|_{t-(L/v_r)-[r-Lcos\theta]/\alpha}^{t-r/\alpha} \quad (7.31)$$

$$= \frac{R^P \mu}{4\pi\rho\alpha^3}\frac{w}{r}\dot{D}(t) * B(t;\tau_c) \quad (7.32)$$

where H is the Heavyside step function, and $B(t;\tau_c)$ is a boxcar of duration τ_c ($= L/v_r + [r - Lcos\theta]/\alpha - r/\alpha$) starting at time t.

A similar form can be derived for the SV- and SH- wave displacements, using the shear wave velocity, β, and the respective radiation patterns, R^{SV} and R^{SH}.

Thus the far-field displacement source time function is determined by the convolution of 2 boxcars, one which represents the point source and the second representing the effects of the finite fault. This convolution results in a trapezoid, with duration equal to the sum of the 2 boxcar lengths, and the rise and fall of the trapezoid, equal to the duration of the shortest boxcar (see Figure 7.4).

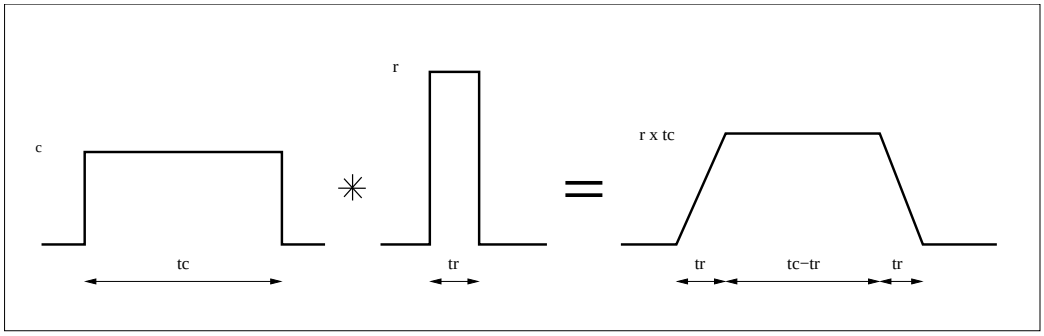

Figure 7.4: Convolution of two box-cars gives a trapezoid.

Now τ_c depends not only on the rupture speed and the fault dimensions, but also on the orientation of the observer relative to the fault. In general, the rupture speed, v_r, is less than the S-wave velocity, β. Figure 7.3 shows how the azimuth affects the arrival times — the

arrivals will reach the station from a rupture at point x at:

$$t_x = \frac{x}{v_r} + \frac{r - x\cos\theta}{c} \tag{7.33}$$

and so the time τ_c, the duration of rupture for this unilateral case, as observed at the station at (r,θ), is:

$$\tau_c = \left[\frac{L}{v_r} + \frac{r - L\cos\theta}{c}\right] - \frac{r}{c} \tag{7.34}$$

$$= \frac{L}{v_r} - \frac{L\cos\theta}{c} \tag{7.35}$$

This is consistent with the length of the boxcar determined for the case of the P-wave, by Equation 7.32. So if a station is located along the direction of rupture propagation, $\theta = 0^o$ and τ_c is short, especially in the case of the shear wave speed ($c = \beta$), as v_r is typically $\sim 0.8\beta$. As the area under the trapezoid is constant, the amplitude will be high. A station behind the rupture propagation ($\theta = 180^o$) has a long τ_c and small amplitude. Stations located perpendicular to the rupture ($\theta = 90^o$) are not affected by the directivity.

A schematic showing how source time functions are affected by a unilaterally rupturing strike-slip fault is in Figure 7.5.

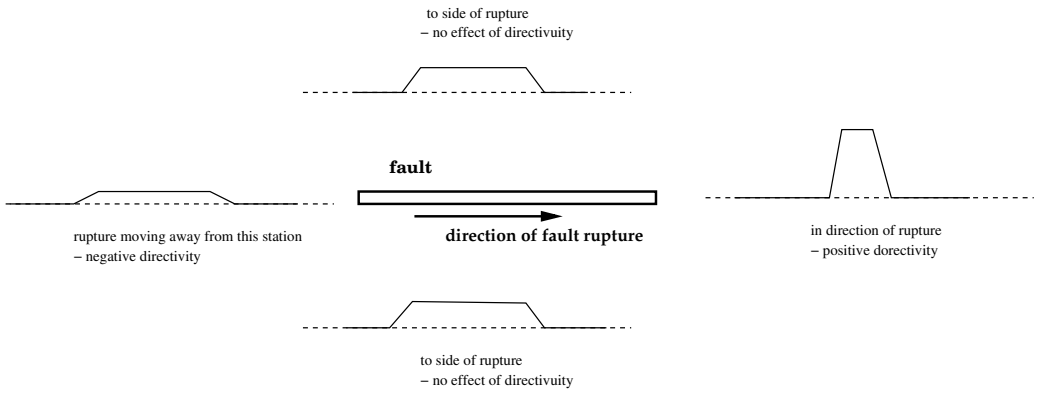

Figure 7.5: Simplified azimuthal variations for source time functions in a unilaterally strike-slip fault rupture. Note that the area under the source time function (proportional to the seismic moment, M_o) is constant, but the time, and the amplitudes, vary widely.

Observing differences in the azimuthal variation of source time functions is fundamen-

tally how we can distinguish between the real and auxiliary focal plane. Of course if the rupture is not unilateral (such as bilateral, or circular faulting), the effect of directivity will be reduced, and it will be more difficult to distinguish the true focal plane using this source time function approach.

7.3 Sample Events

In the relatively young history of the dense CISN, only a small number of earthquakes in the magnitude range of interest (M4—M6) have occurred in regions with dense high dynamic range instrumentation. Some of these earthquakes are investigated in detail. They are the 3 September 2002 M_L4.8 Yorba Linda earthquake, the 30 October 2001 M_L5.1 Anza earthquake, and the 22 Feb 2002 M_L5.4 Big Bear earthquake.

7.3.1 Yorba Linda

The M_L4.8 Yorba Linda earthquake occurred to the South East of the LA basin at 00:08:51 PDT on the 3^{rd} of September, 2002. The earthquake was accompanied by several small foreshocks (the largest a M_L2.6 at 21:50PDT the previous day), and a typical aftershock sequence (the largest a M_L2.9 at 00:15PDT). First motion analysis indicates that the earthquake was primarily strike-slip on a vertical plane striking N30^{o}W. This might be consistent with a location on the Whittier Fault. Depth was estimated to be 12.92*km*. First motion analysis of the aftershocks show many of these also have similar focal mechanisms and locations. Many SCSN stations are located nearby, with good azimuthal coverage. This is the ideal earthquake to test the deconvolution method.

Figure 7.6 shows the location and focal mechanism of the mainshock, and some aftershocks (as well as a foreshock) which are good candidates for use a Green's Functions as they have similar locations and focal mechanisms. Locations and focal mechanisms are from Egill Hauksson (*personal communication*).

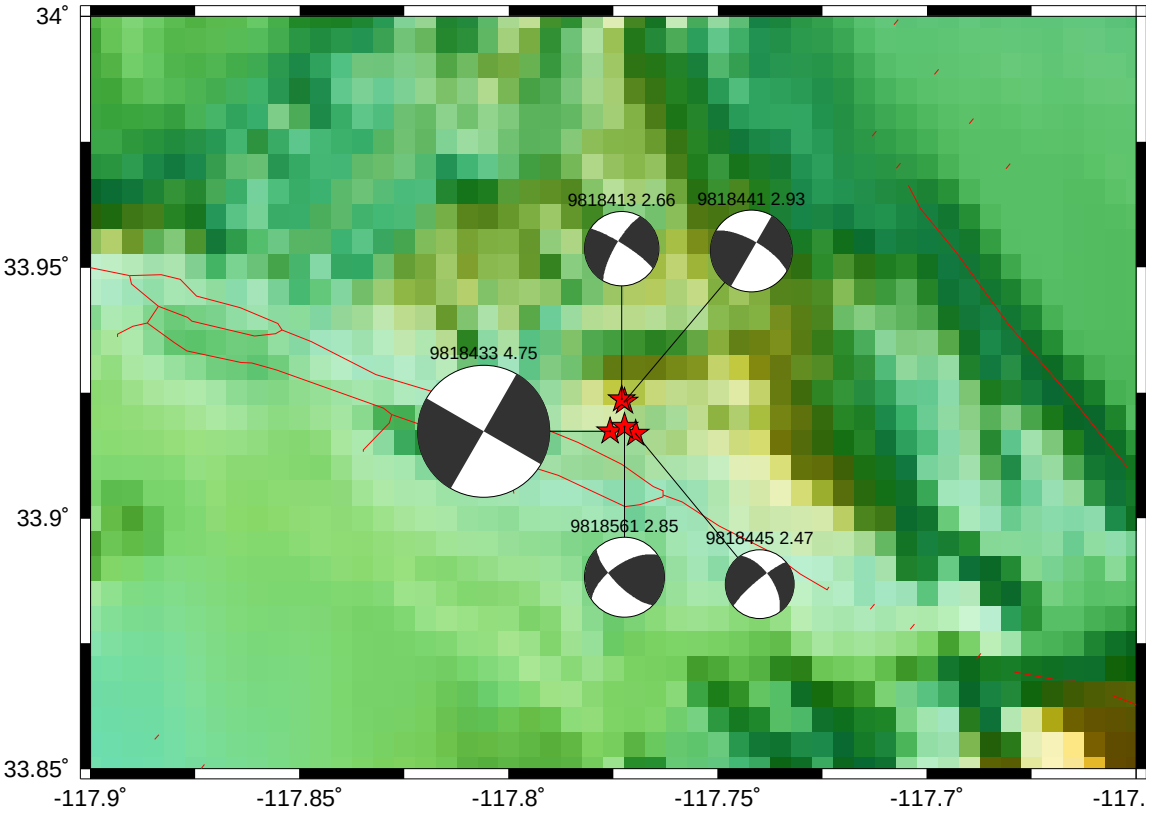

Figure 7.6: Comparison of focal mechanisms (*from Hauksson, personal comm.*) for the mainshock, a foreshock and three aftershocks in Yorba Linda sequence.

M2.85 Aftershock, 04:28:39PST 9818561, Depth = $10.27km$

Although there were other large aftershocks which occurred shortly after the mainshock, this aftershock occurred sufficiently long after the mainshock ensuring the basin waves had attenuated. First motions show the location and focal mechanisms are very similar to the mainshock. SCSN station azimuthal coverage, including all the stations that well recorded both events and are within $40km$ of the mainshock, is shown in Figure 7.7. Also on the Figure are the timeseries at each station for the components transverse to the mainshock coordinates, bandpassed between $5Hz$ and $2s$ (removing the microseismic energy which is comparable to the aftershock excitation at many stations). Even considering wave scattering, the transverse component of motion will have the highest amplitudes of SH motion, which are the waves likely to contain most information about any directivity effect for a vertical strike-slip rupture. In this Figure (as well as all subsequent Figures that display timeseries) the peak amplitude of the aftershock is scaled to the peak amplitude of the mainshock. Note the similarity of the motions, which can be better observed in Figures 7.8 and 7.9. Differences in arrival times are generally consistent with the difference in location. The deconvolution of the source time function for this component at each station is on Figure 7.9. A short duration large amplitude pulse is clearly present in stations to the NNE from the epicenter. This is consistent with the one of the focal planes as observed in the focal sphere, and is indicative of directivity in this direction.

Figures 7.11- 7.12 and 7.13- 7.14 present similar timeseries and source time functions for the radial and transverse directions. Similar directivity is obvious towards the NNE direction, even though the SH motions may not be as large for these components. Figure 7.15 compares the source time functions from all 3 components at each station, showing good repeatability from all three components at most stations.

A final investigation with this aftershock is a comparison of source time functions derived from the entire record at each station ($50s$ of data beginning with the rupture start time is used for both events), and the S-wave only (for this case, a $10s$ data segment beginning about $1s$ before the S-wave arrival is selected only). All data presented thus far has been from the whole record. Both records are tapered and padded with zeros before

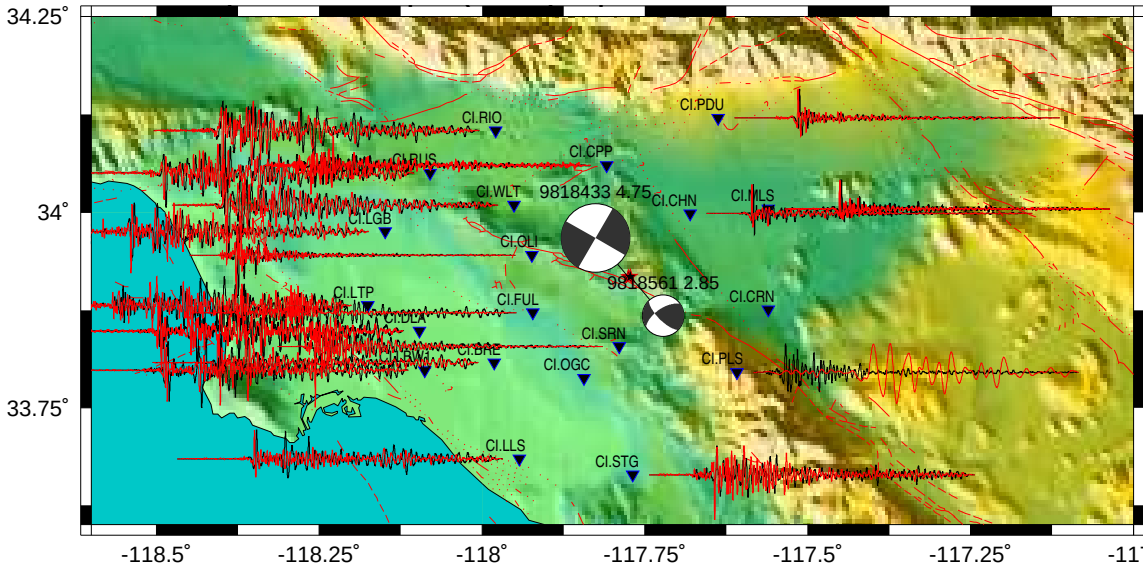

Figure 7.7: Comparison of aftershock and mainshock for Yorba Linda: Transverse component timeseries. All timeseries are scaled to the same amplitude. Black: mainshock; Red: aftershock

the inversion. Figure 7.16 shows the transverse timeseries for the S-wave only. This compares to Figure 7.8 for the entire timeseries. Figures 7.17 - 7.19 compare each component time-functions.

It is clear from these Figures there is little difference between the results of the deconvolutions using the entire tineseries and only the dominant S-wave arrivals. This is likely because the S-wave arrivals in fact dominate the response for all the components. All subsequent timeseries analysis uses data from the entire waveforms.

M2.66 Foreshock, 21:50:48PST 9818413, Depth = 13.62*km*

Figure 7.20 again shows similar timeseries shapes for the transverse components for both this foreshock and the mainshock.

Figure 7.21 shows a very similar shapes for the source time functions at most stations. Amplitude variance to other source time functions is due to difference in size of foreshock (the potency of the foreshock is not removed from the calculation).

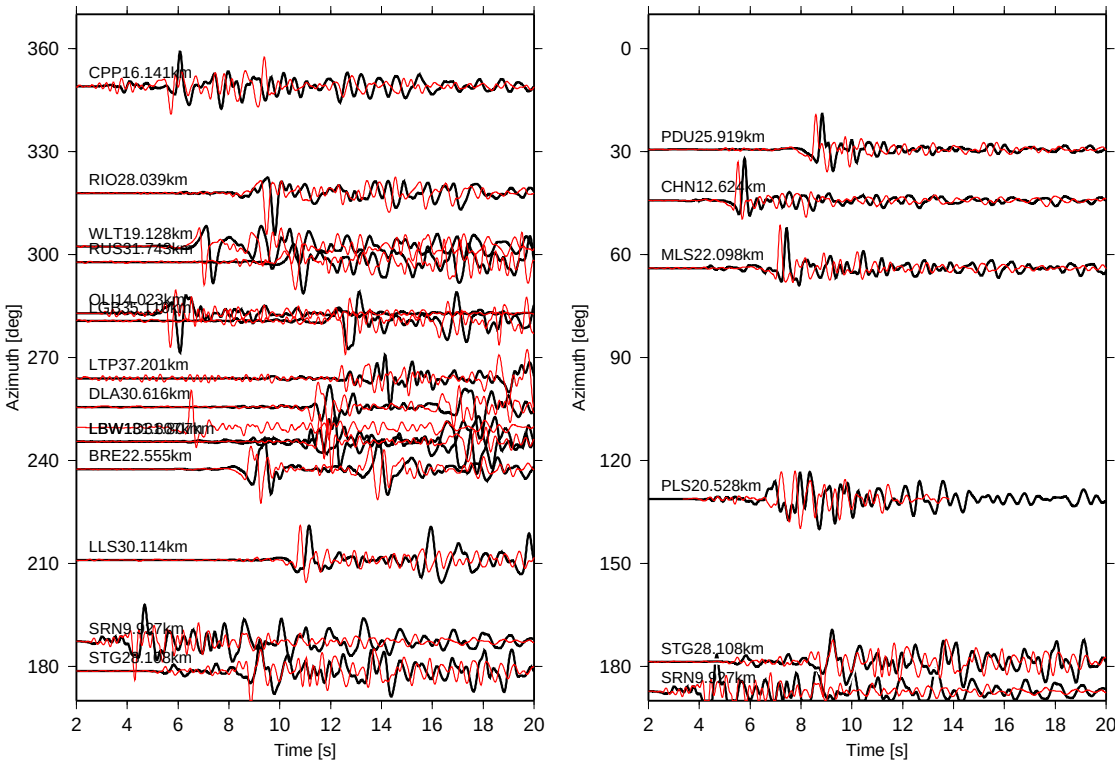

Figure 7.8: Comparison of aftershock and mainshock for Yorba Linda: Transverse component timeseries. All timeseries scaled to same amplitude. Black: mainshock; Red: aftershock

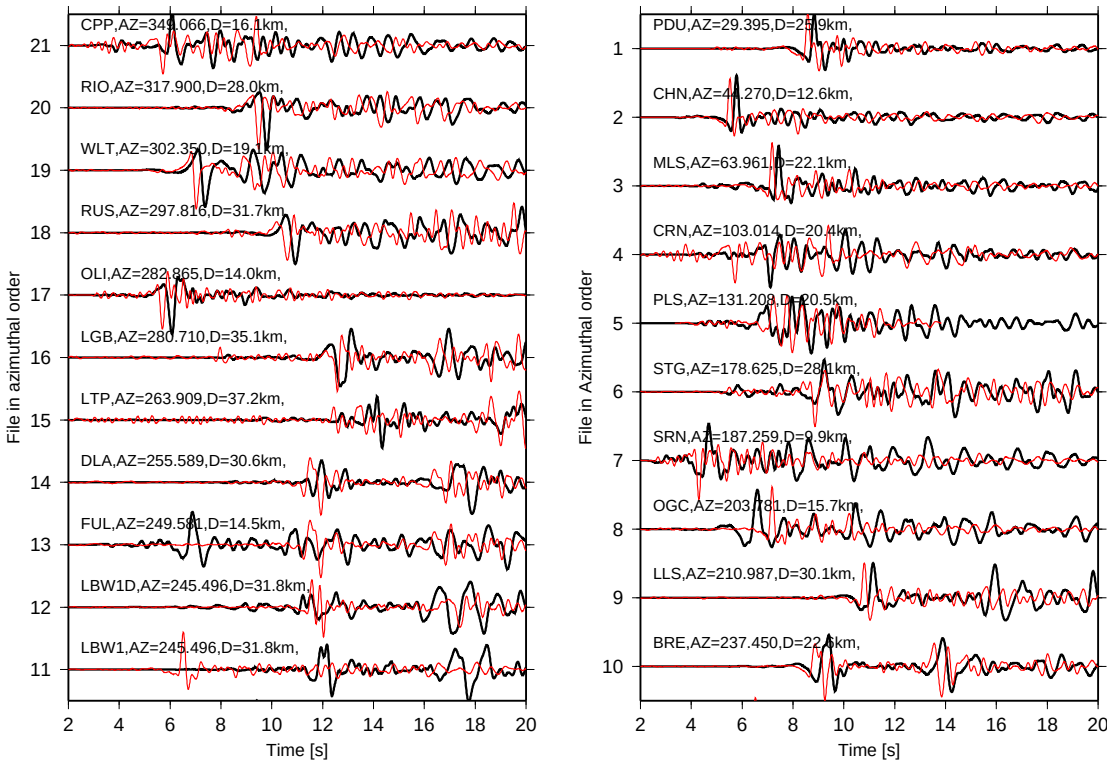

Figure 7.9: Comparison of aftershock and mainshock for Yorba Linda: Transverse component timeseries. All timeseries scaled to same amplitude. Black: mainshock; Red: aftershock

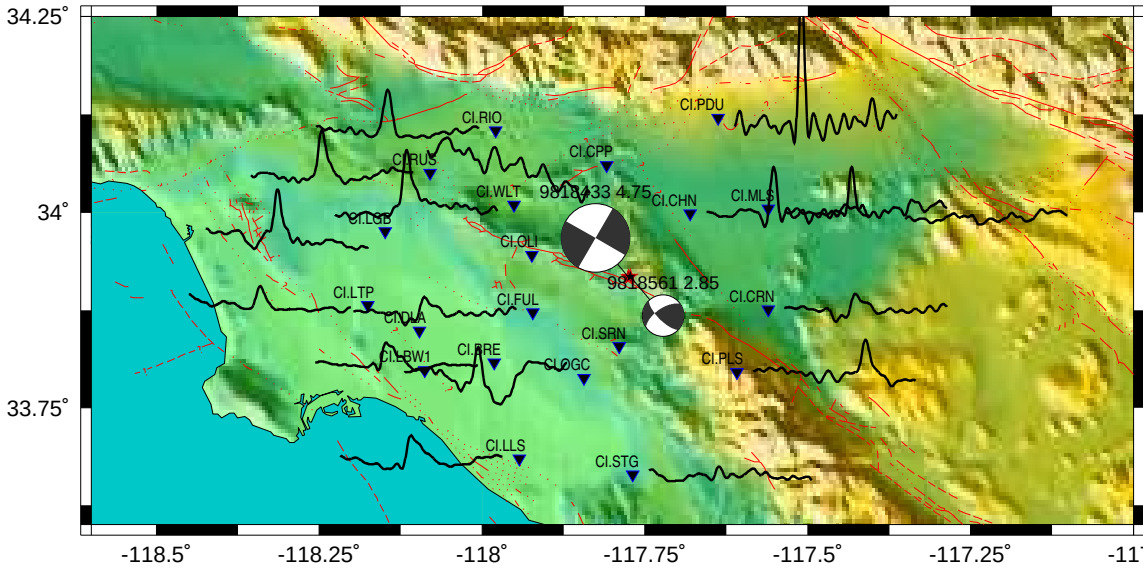

Figure 7.10: Transfer Functions for Yorba Linda from M2.85 — Transverse components. Each timeseries is 4s long, with time from $-1s$ to $+3s$. No relative scaling of amplitudes.

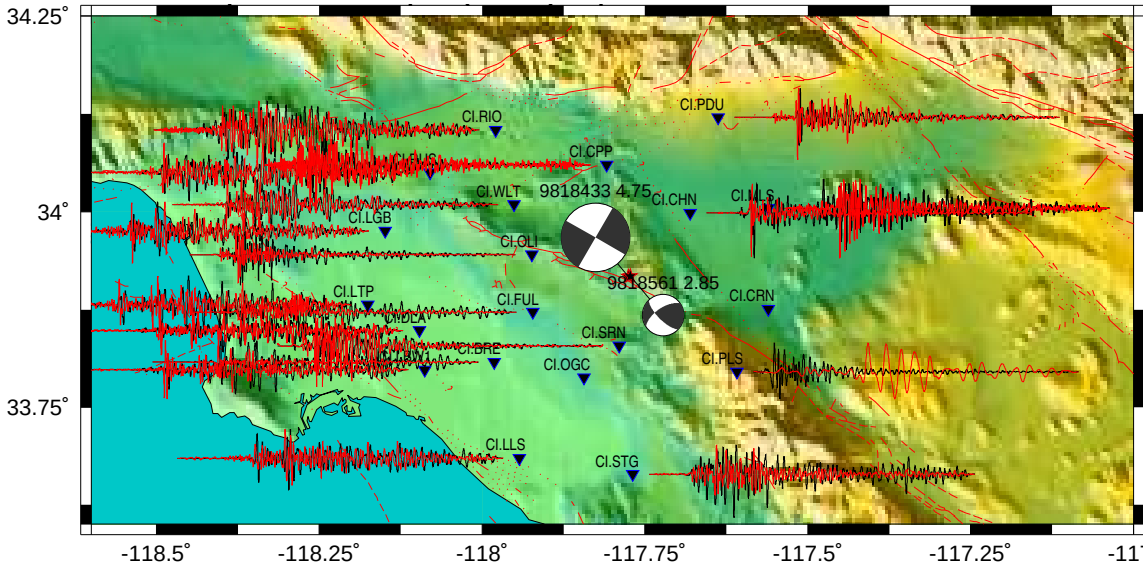

Figure 7.11: Comparison of Aftershock, Mainshock for Yorba Linda: Timeseries from M2.85 — Radial. All timeseries are scaled to same amplitude. Black: mainshock; Red: aftershock

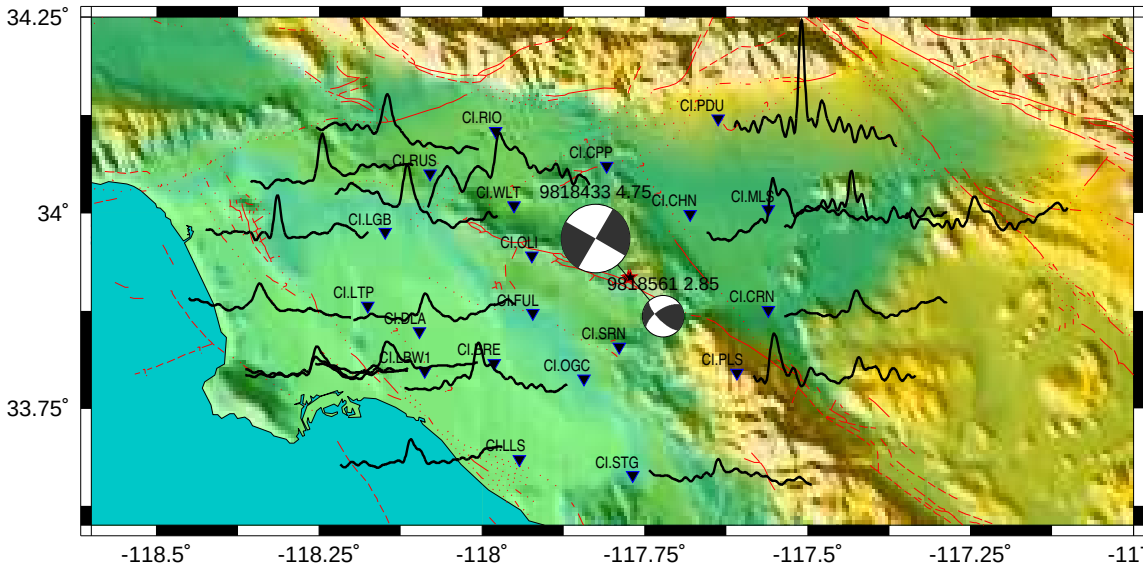

Figure 7.12: Transfer Functions for Yorba Linda from M2.85 — Radial. Each timeseries is 4s long, with time from $-1s$ to $+3s$. No relative scaling of amplitudes.

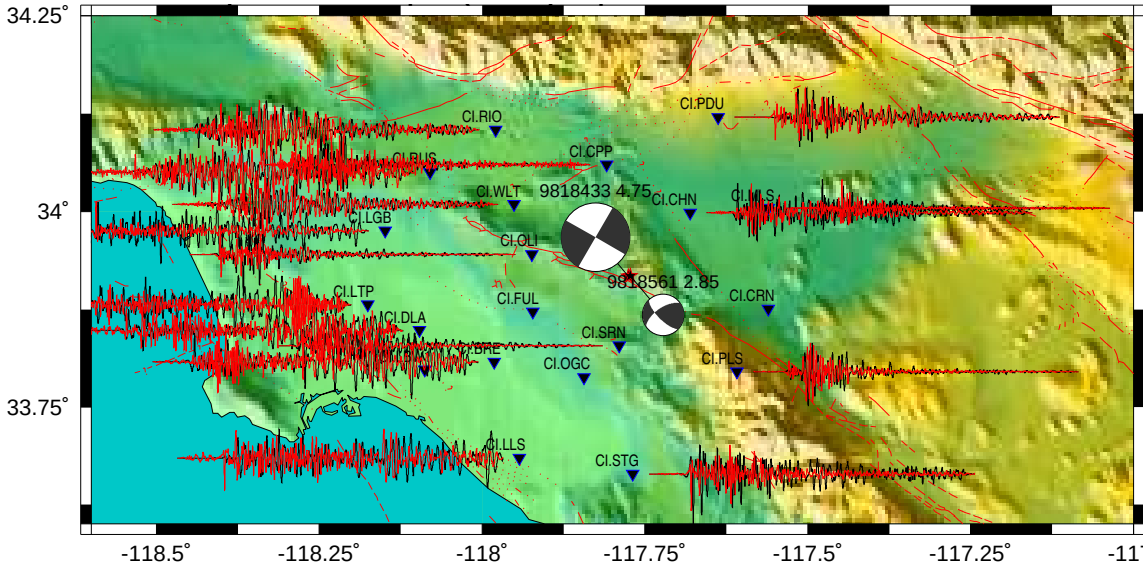

Figure 7.13: Comparison of Aftershock, Mainshock for Yorba Linda: Timeseries from M2.85 — Vertical. Black: mainshock; Red: aftershock

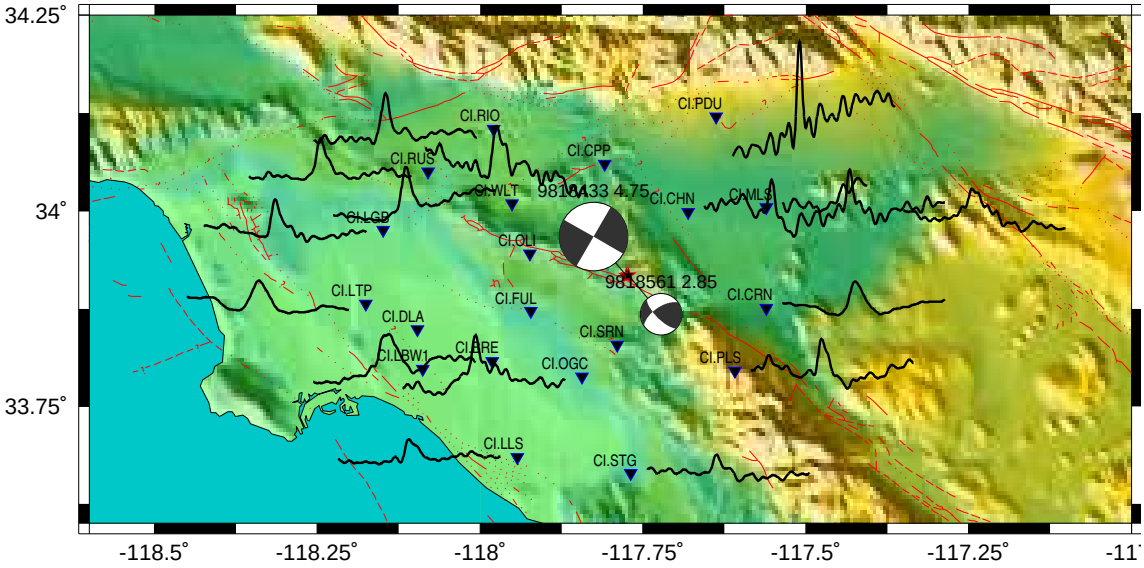

Figure 7.14: Transfer Functions for Yorba Linda from M2.85 — Vertical. Each timeseries is 4s long, with time from $-1s$ to $+3s$. No relative scaling of amplitudes.

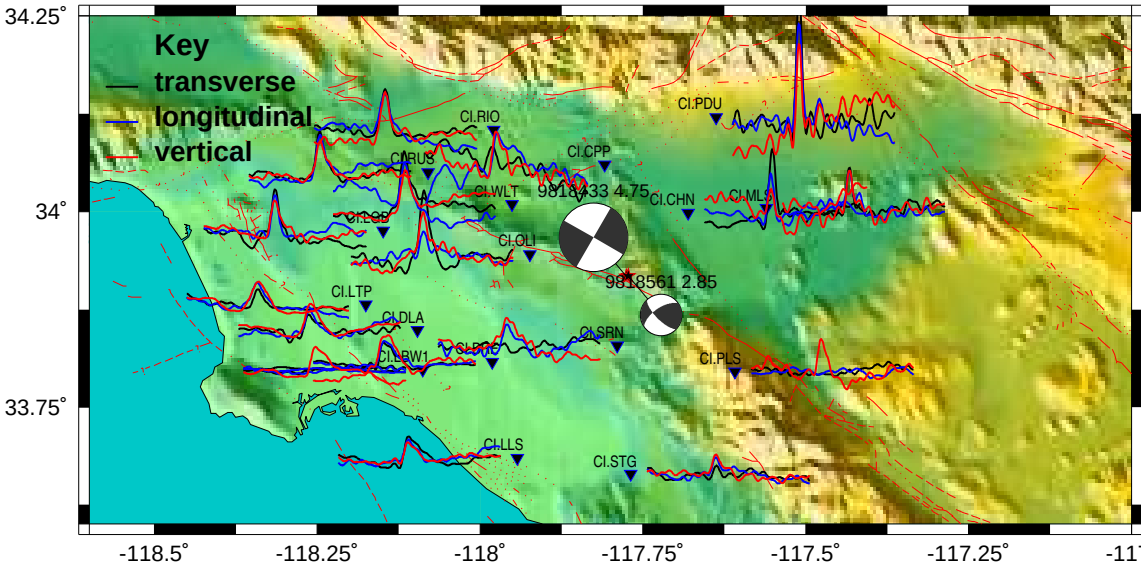

Figure 7.15: Transfer Functions for Yorba Linda from M2.85 — all components

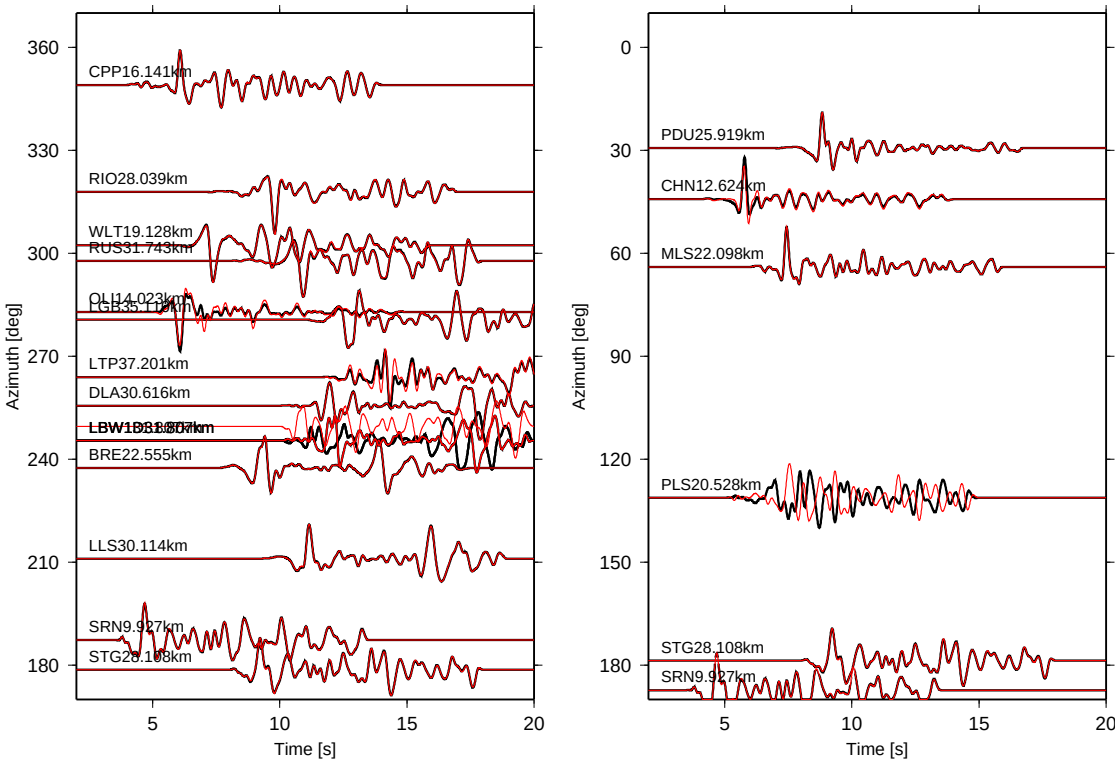

Figure 7.16: Comparison of aftershock, mainshock for Yorba Linda: Transverse S-wave timeseries. All timeseries scaled to same amplitude. Black: mainshock; red: aftershock. Compare to Figure 7.8.

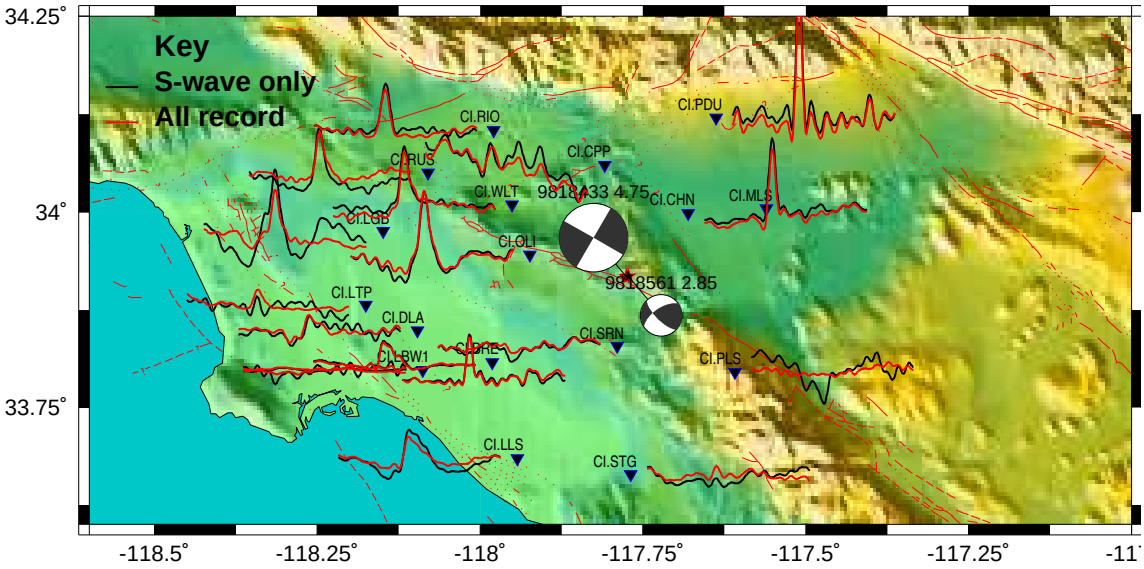

Figure 7.17: Transfer Functions for Yorba Linda from M2.85 — S-wave only vs. all waveform, Transverse components. Each timeseries is 4s long, with time from $-1s$ to $+3s$. No relative scaling of amplitudes.

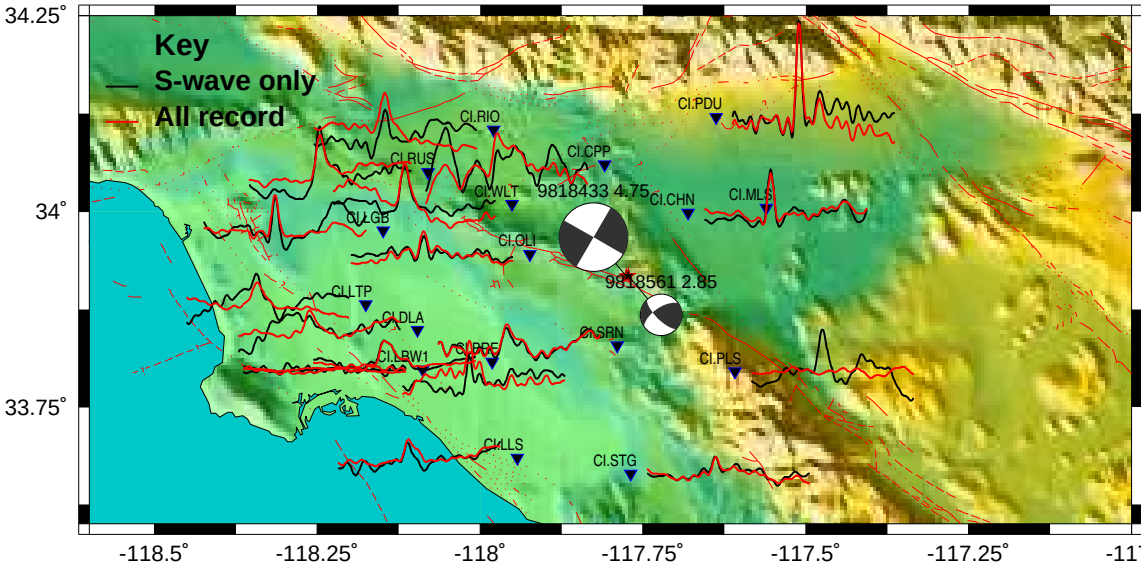

Figure 7.18: Transfer Functions for Yorba Linda from M2.85 — S-wave only vs. all waveform, Radial. Each timeseries is 4s long, with time from $-1s$ to $+3s$. No relative scaling of amplitudes.

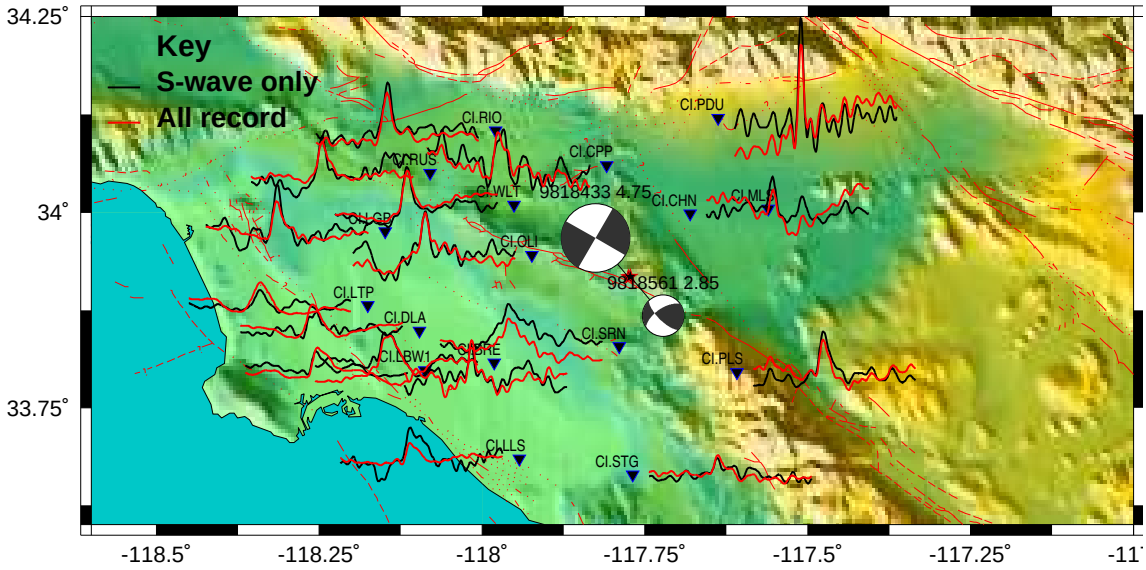

Figure 7.19: Transfer Functions for Yorba Linda from M2.85 — S-wave only vs. all waveform, Vertical. Each timeseries is 4*s* long, with time from $-1s$ to $+3s$. No relative scaling of amplitudes.

M2.93 Aftershock, 00:15:51PST 9818441, Depth = 11.72*km*

Figures 7.22 and 7.23 again show similar timeseries shapes in the transverse components for both this aftershock and the mainshock, with source time functions from all components also similar to the previous aftershock results. Amplitude variance to other source time functions is due to difference in size of aftershock (the potency of the aftershock is not removed from the calculation)

Though this earthquake occurred very soon after the mainshock (7*mins*), in the $2s-5Hz$ bandpasses used for the timeseries and thus also the source time function, the 'noise' from the mainshock is low.

M2.47 Aftershock, 00:17:09PST 9818445, Depth = 11.85*km*

Figure 7.24 again shows similar timeseries shapes for both this aftershock and the mainshock. This M2.47 event occurred just 78*s* after a M2.93 aftershock discussed previously, and so the smaller motions generated by this event are somewhat swamped by the coda from the previous aftershock. This is very clear in the stations to the west of the epicenter,

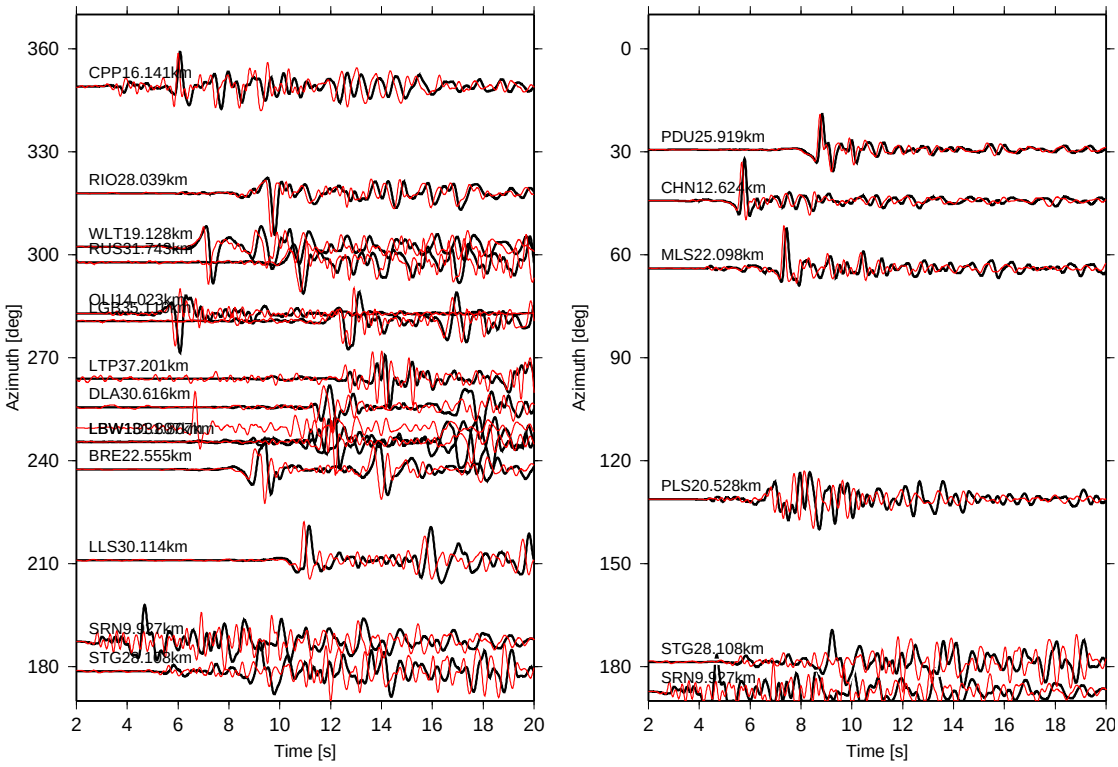

Figure 7.20: Displacement timeseries comparison with M2.66 and mainshock — Transverse component. Black: mainshock; red: aftershock

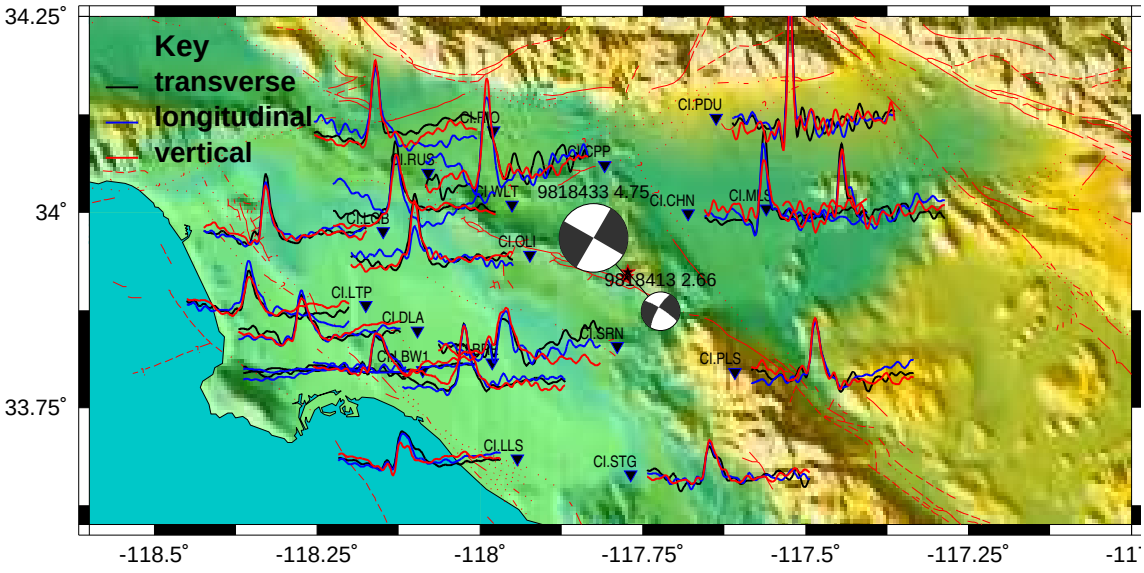

Figure 7.21: Transfer Functions for Yorba Linda from M2.66 — all components. Each timeseries is 4*s* long, with time from $-1s$ to $+3s$. No relative scaling of amplitudes.

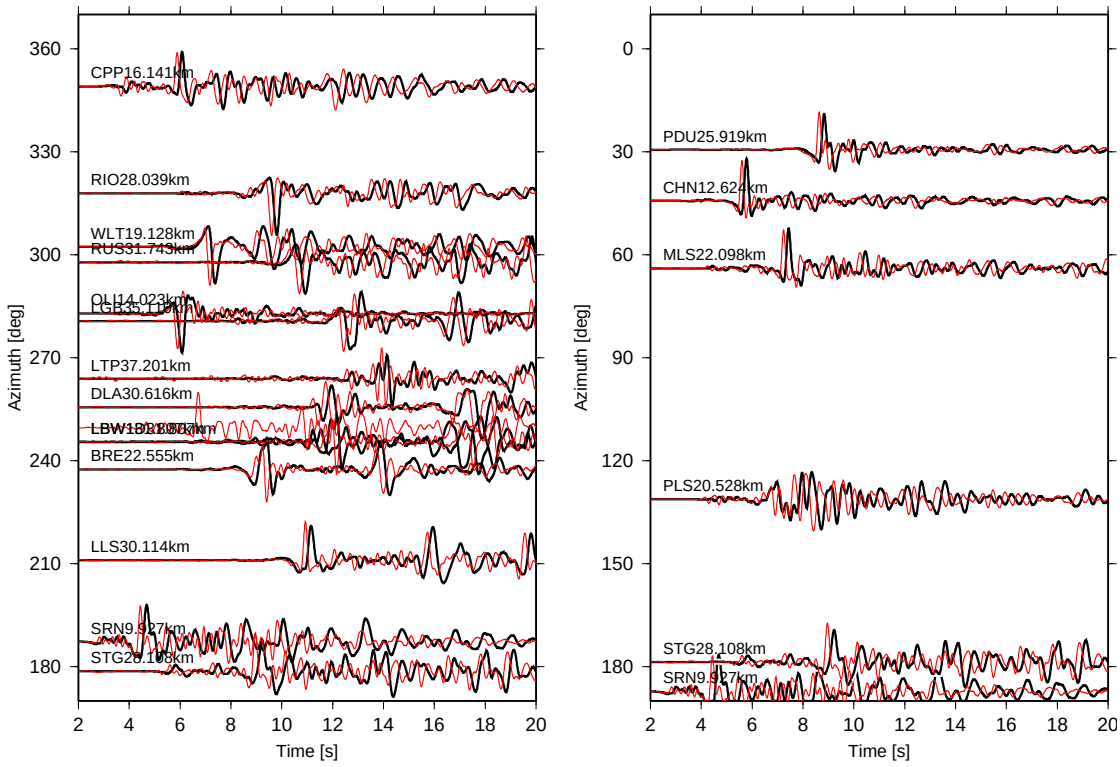

Figure 7.22: Displacement timeseries comparison with M2.93 and mainshock — Transverse component. Black: mainshock; red: aftershock

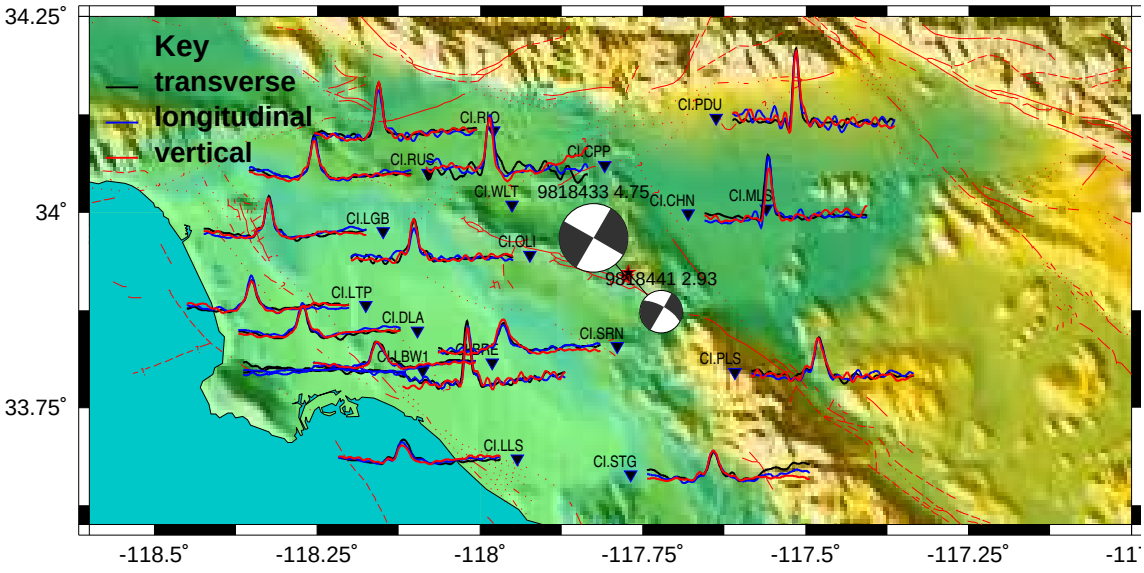

Figure 7.23: Transfer Functions for Yorba Linda from M2.93 — all components. Each timeseries is 4*s* long, with time from $-1s$ to $+3s$. No relative scaling of amplitudes.

which are predominantly basin sites. The rock sites to the east do not appear to have this effect.

Figure 7.25 shows a much poorer source time function for most stations, with a very noisy timeseries. This is likely due to the residual basin waves from the M2.93 event, that are not attenuated, and are of similar order of magnitude to the M2.47 body wave magnitudes. This event is the smallest investigated, and all the source time function map figures employ the same scaling, which explains the larger amplitudes of the source time functions in this Figure. The potency is not removed from these plots.

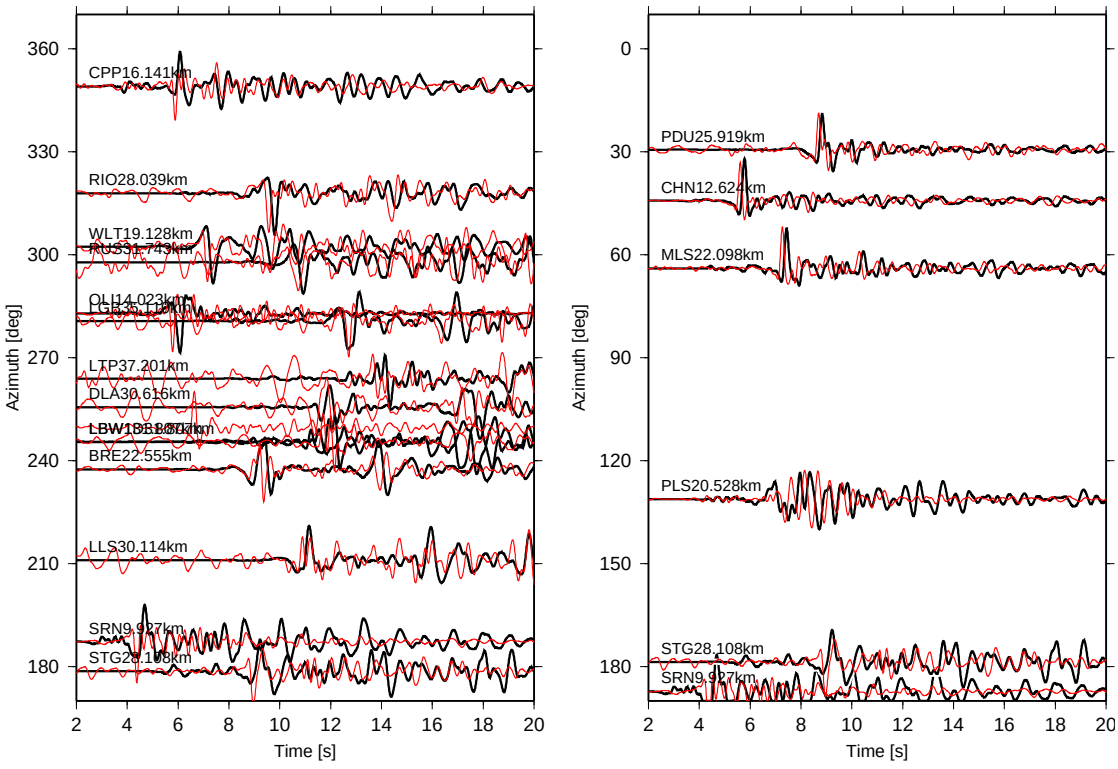

Figure 7.24: displacement timeseries comparison with M2.47 and mainshock — Transverse component

In general, it appears the accuracy of the method is relatively insensitive to the choice of aftershock, as long as the focal mechanisms, locations, and depths are similar. Signal to noise should also be good for the foreshock to minimise noise in the resulting source time functions, which is shown to be problematic if events are small and occur shortly after

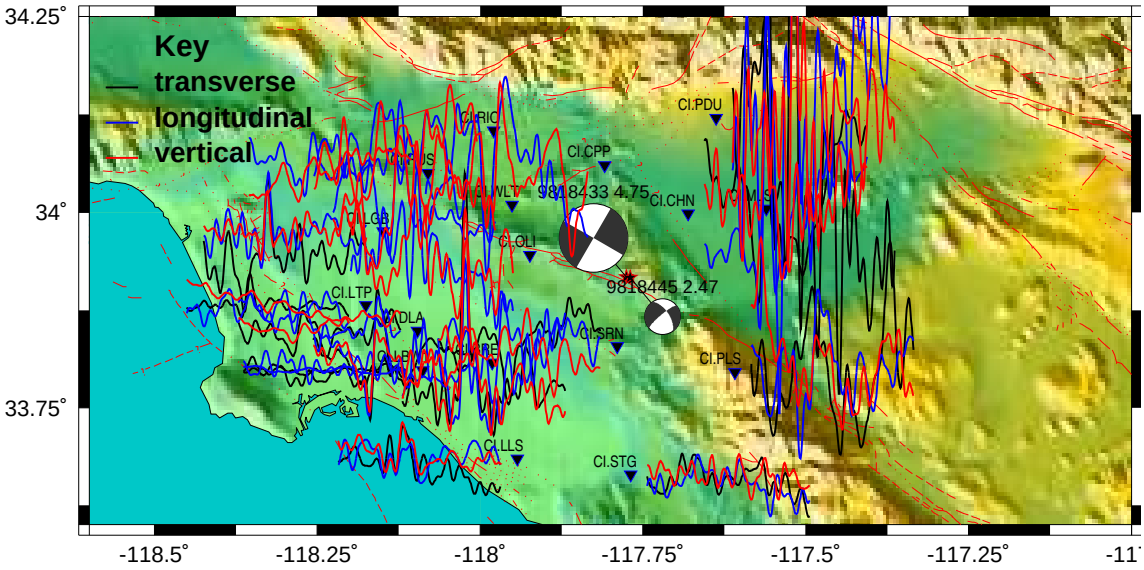

Figure 7.25: Transfer Functions for Yorba Linda from M2.47 — all components

larger events.

Figures 7.26 and 7.27 compare the timeseries and time-functions from all aftershocks at the stations in the apparent forward directivity direction (PDU), to the sides (WLT, PLS) and behind the directivity pulse (PLS). Magnitudes are as expected, with larger amplitudes for source time functions derived from smaller magnitude aftershocks. Time offsets can be explained by the small differences in locations between all the events. The strange timing and amplitude at Station PLS for the M2.85 aftershock is likely a data processing/archiving problem rather than a true reflection of the data. Ignoring the smallest aftershock, which had problems with signal-to-noise, there is significant similarity in all the 'Green's Functions' for the differing aftershocks. These results are very similar to the simplified theoretical solution shown in Figure 7.5. Figure 7.28 presents the same data as Figure 7.27, but has the amplitudes scaled by their potency, relative to the M2.93, which is determined from the magnitudes, following Equations 7.15 and 7.17.

7.3.2 Big Bear

A M_L5.4 earthquake struck the region of Big Bear Lake on the 22^{nd} of February, 2002, at 04:19PST. Depth was estimated to be 1.23km. The event was located 5km north of

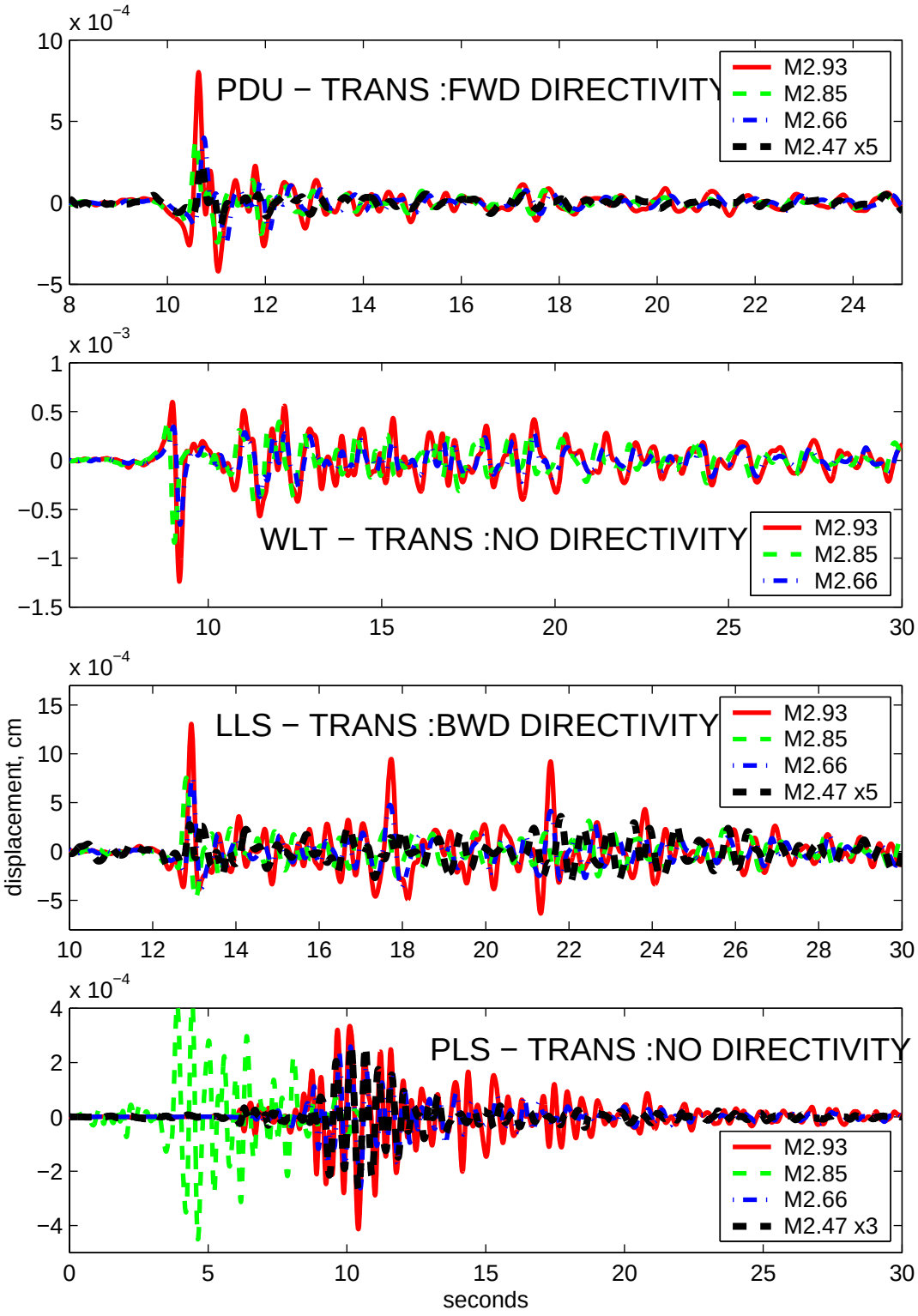

Figure 7.26: Yorba Linda: individual station timeseries comparison.

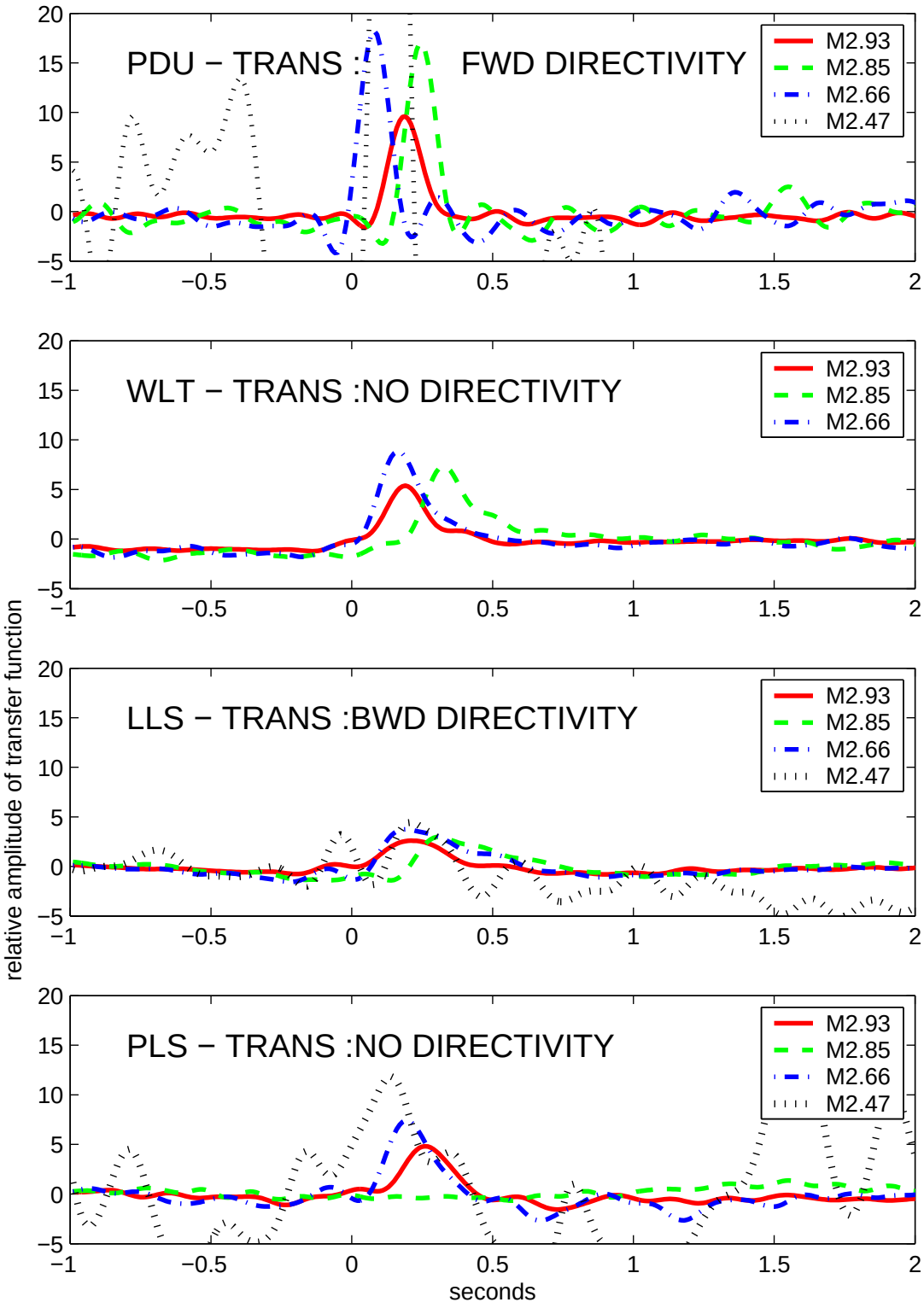

Figure 7.27: Yorba Linda: individual station source time series comparison.

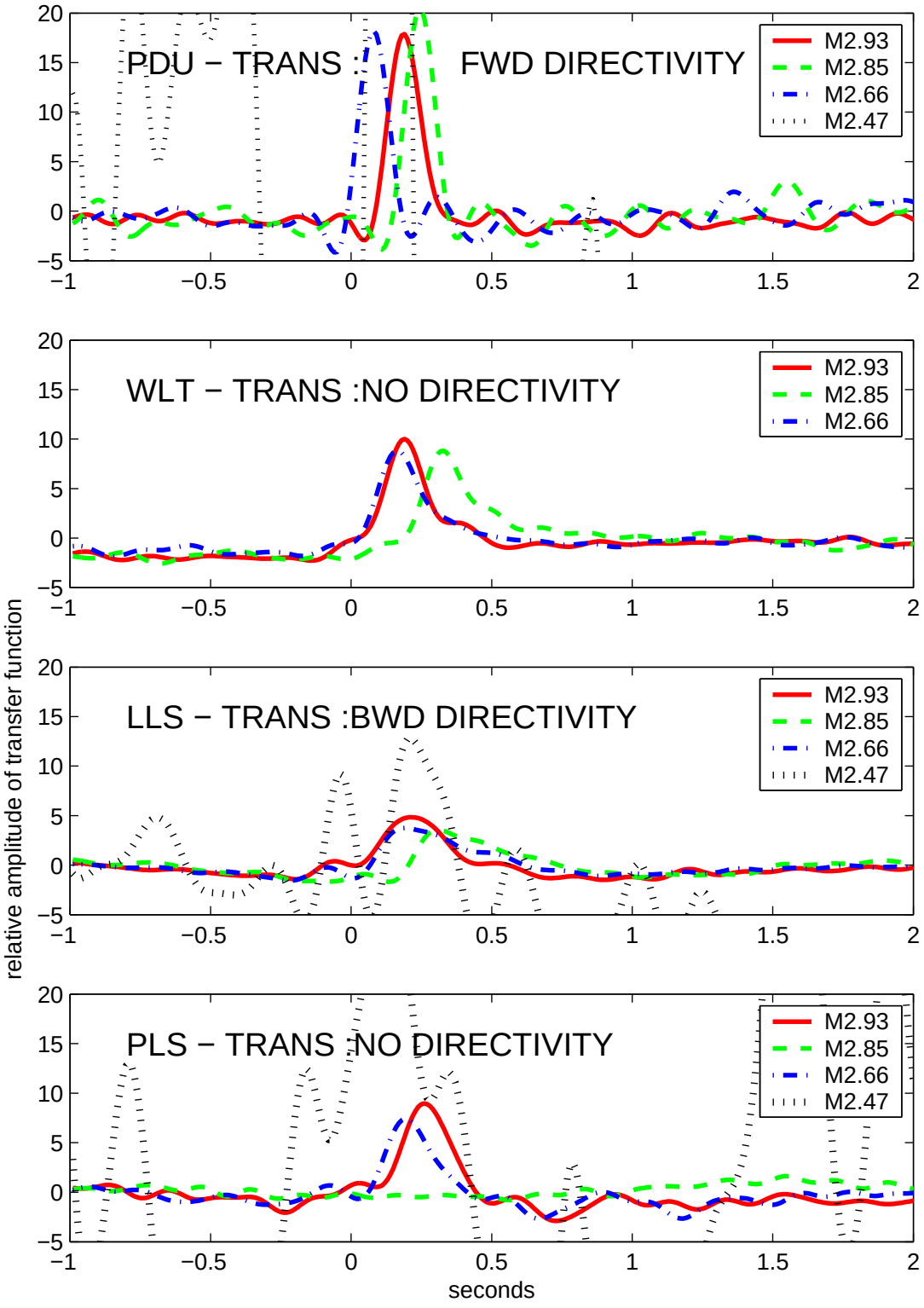

Figure 7.28: Yorba Linda: individual station source time series comparison. All events are scaled by potency, relative to M2.93 event.

Big Bear and thus north of the aftershock zone of the 1992 Big Bear earthquake (M6.2). The mainshock exhibited strike-slip faulting (horizontal movement) on a steeply dipping (80^o) plane striking N40^{o}W, sub-parallel to the local strike of the Helendale fault. This mechanism is consistent with the mainshock being near the Helendale fault.

Figure 7.29 presents the focal mechanism of the mainshocks and some selected aftershocks. Locations and focal mechanisms are again from Egill Hauksson (*personal communication*).

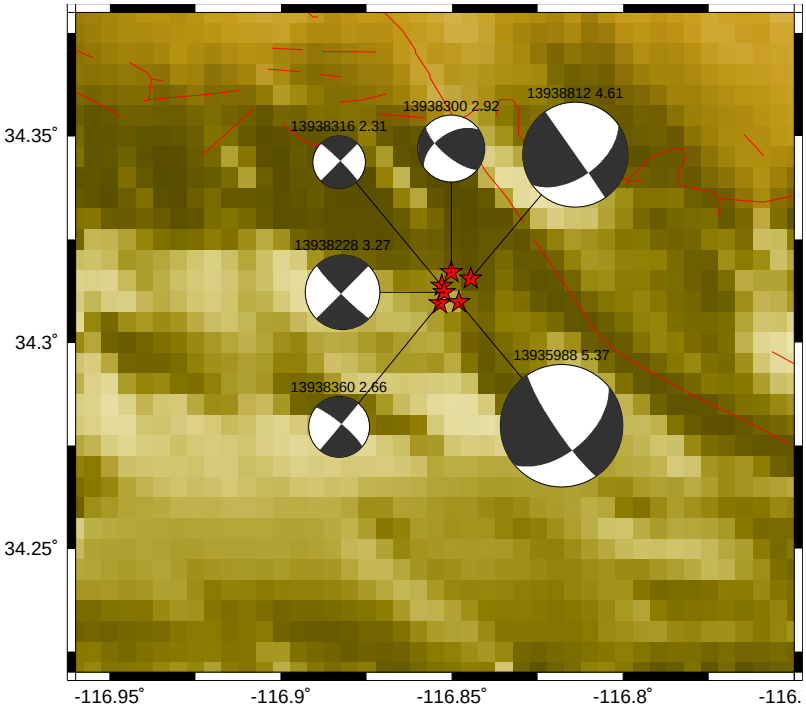

Figure 7.29: Comparison of focal mechanisms (*from Hauksson, personal comm.*) for the mainshock, a foreshock and three aftershocks in Big Bear sequence.

The aftershocks investigated all occurred at least 15 hours after the mainshock, and range in size from M_L2.31 to M_L4.61. They are:

1. M_L3.27, 20:03:59PST (23Feb2004) 13938228, Depth = 6.16*km*
2. M_L2.92, 00:27:00PST (24Feb2004) 13938300, Depth = 4.62*km*
3. M_L2.31, 01:31:07PST (24Feb2004) 13938316, Depth = 6.11*km*
4. M_L2.66, 04:15:39PST (24Feb2004) 13938360, Depth = 5.84*km*
5. M_L4.61, 20:03:04PST (25Feb2004) 13938812, Depth = 2.71*km*

Figures 7.30–7.34 show the source time functions as determined for the three components. The station density is not as good as observed in the Yorba Linda earthquake, especially to the North and East, where the desert and San Bernadino mountains lie respectively. Nonetheless, there does appear to be directivity to the North-East.

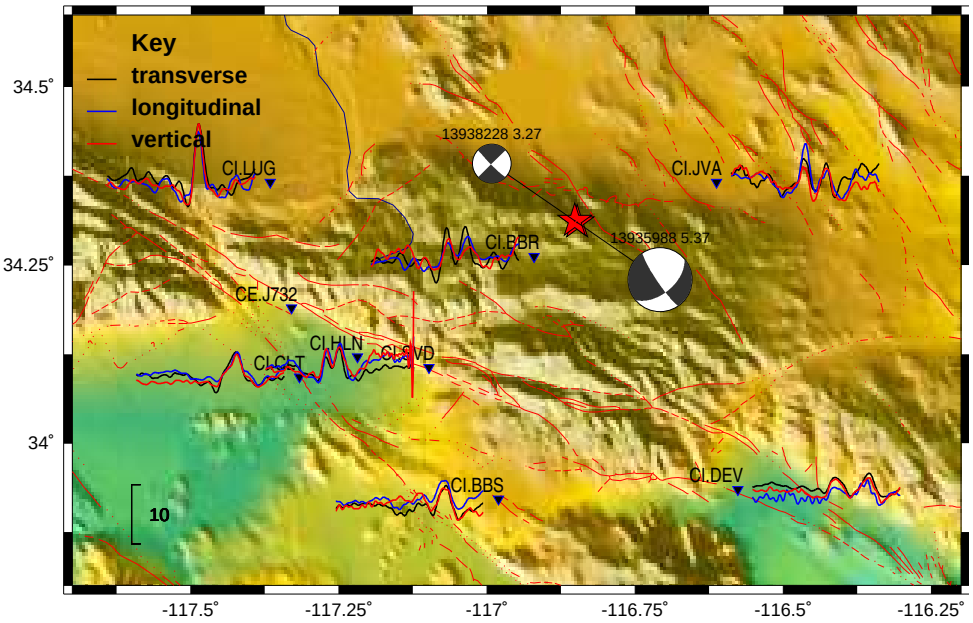

Figure 7.30: Transfer Functions for Big Bear from M3.27 — all components. Each timeseries is 4s long, with time from $-1s$ to $+3s$. Black: mainshock; red: aftershock

From the shape of the source time functions, it appears most likely the rupture plane is the NE-SW trending plane. This is inconsistent with the nearby Helendale fault. Directivity is towards the North-West. Figure 7.35 presents comparisons of the source time functions for stations approximately in the line of directivity (LUG), behind the rupture front (DEV) and to the sides (JVA, SVD). Figure 7.36 shows the displacement time series from these stations. Due to the very wide variability in amplitude, all timeseries are scaled to unit amplitude.

7.3.3 Anza

A M_L5.1 earthquake occurred at 23:56PST, on the 30^{th} of October, 2001, 10 miles southeast of the town of Anza in northern San Diego County. It was located within the 5 km wide

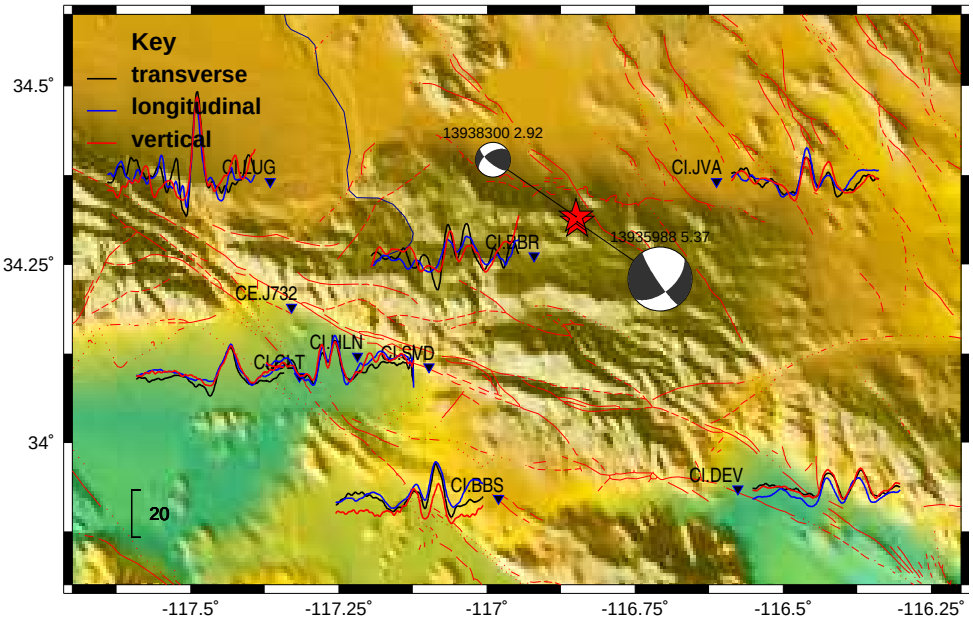

Figure 7.31: Transfer Functions for Big Bear from M2.92 — all components. Each time-series is 4s long, with time from $-1s$ to $+3s$.

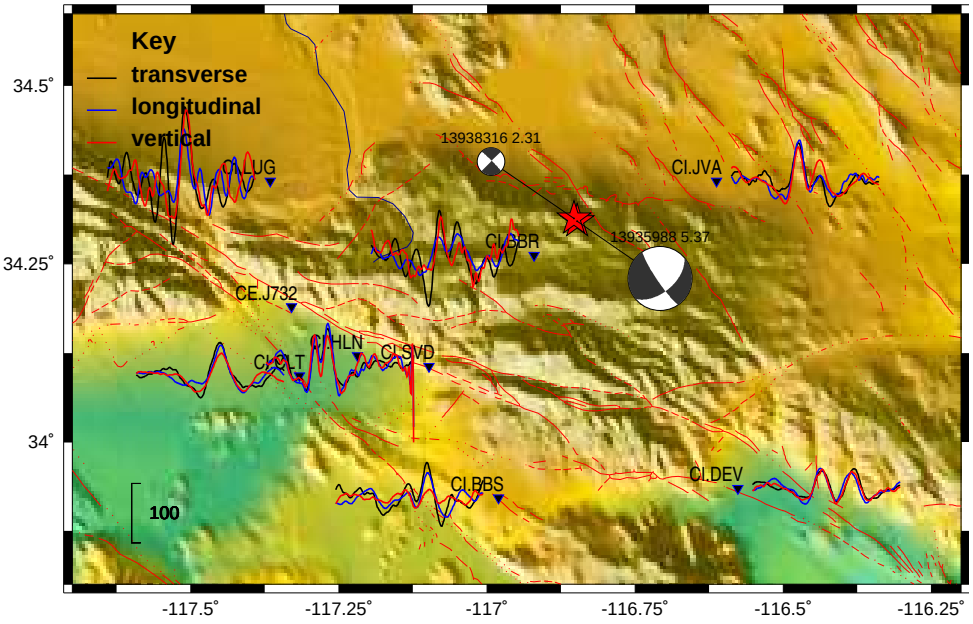

Figure 7.32: Transfer Functions for Big Bear from M2.31 — all components. Each time-series is 4s long, with time from $-1s$ to $+3s$.

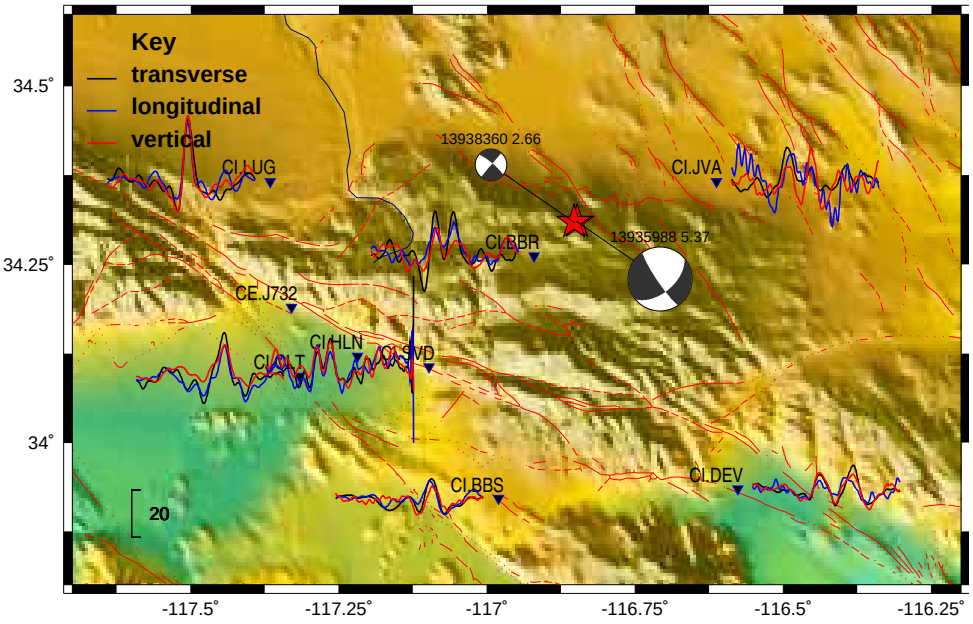

Figure 7.33: Transfer Functions for Big Bear from M2.66 — all components. Each time-series is 4s long, with time from $-1s$ to $+3s$.

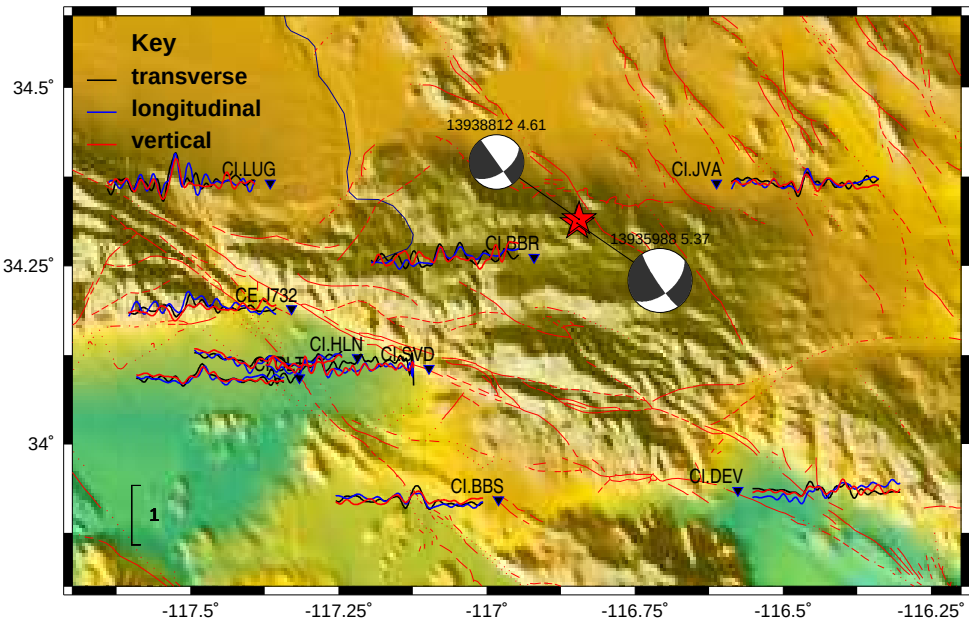

Figure 7.34: Transfer Functions for Big Bear from M4.61 — all components. Each time-series is 4s long, with time from $-1s$ to $+3s$.

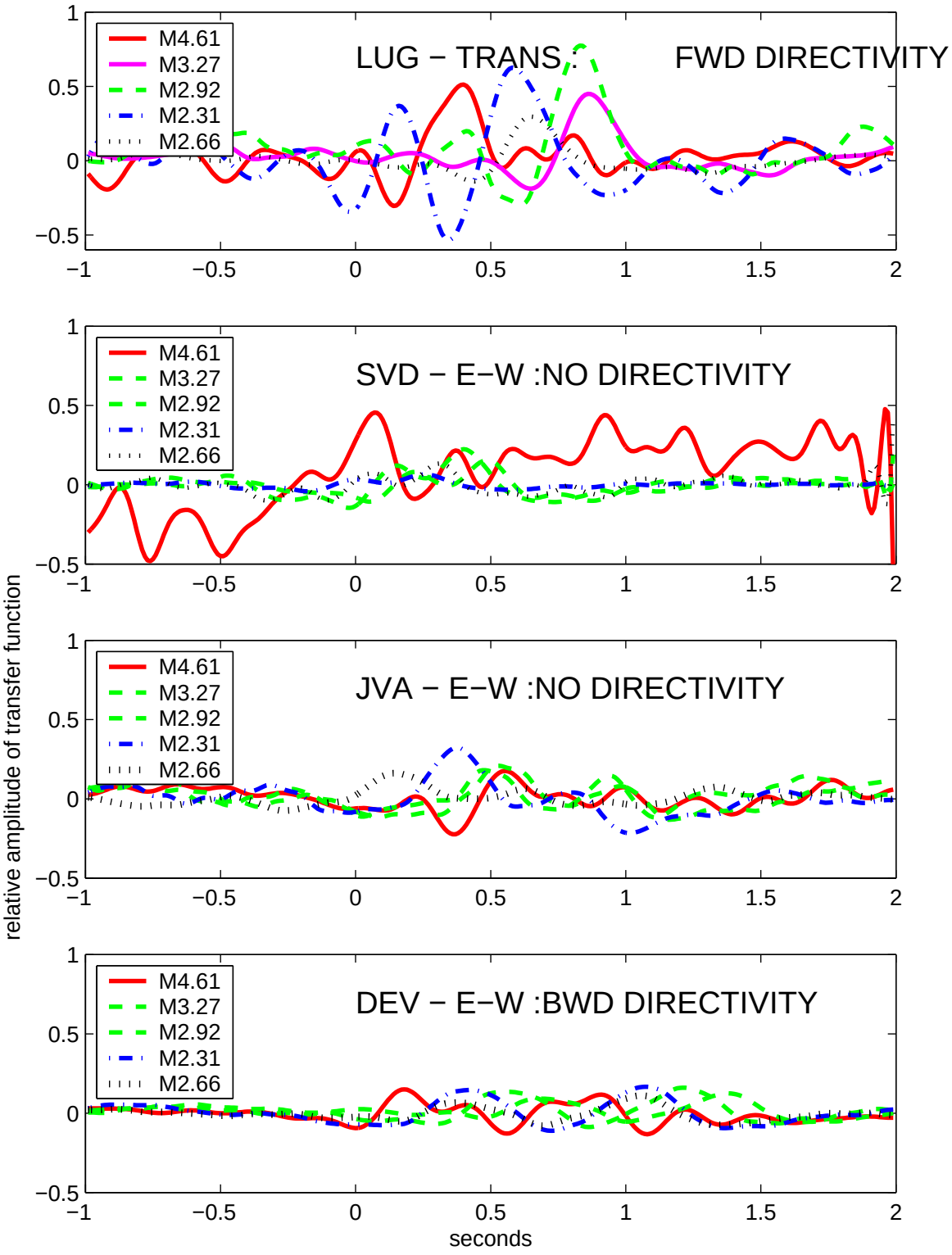

Figure 7.35: Big Bear: individual station source time series comparison. All events are scaled by potency, relative to M4.61 event.

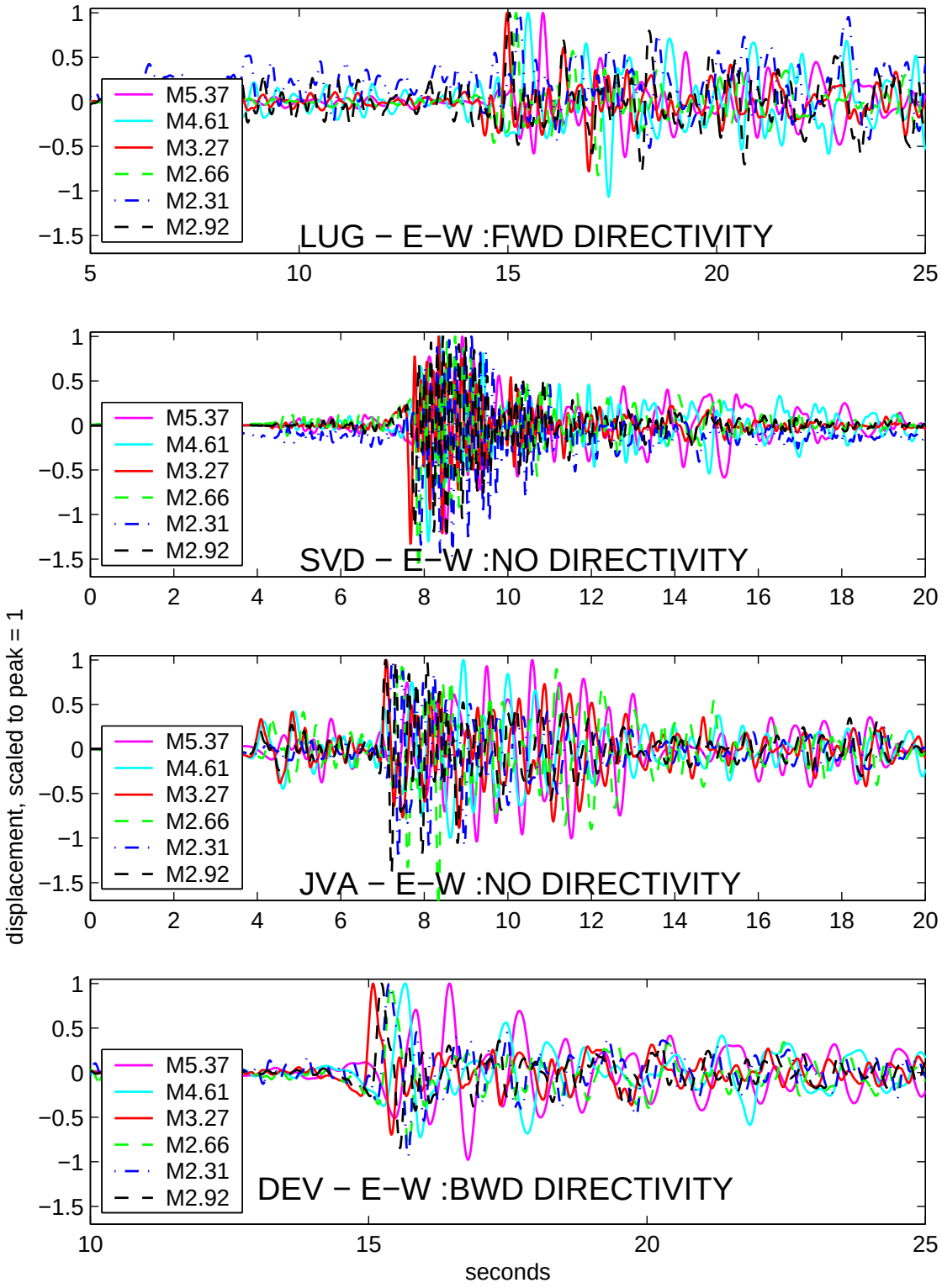

Figure 7.36: Big Bear: individual station timeseries comparison. all timeseries scaled to unit amplitude.

San Jacinto fault zone, a member of the San Andreas fault system, at a depth of 14.5*km*.

The earthquake focal mechanism exhibited mixed left-lateral strike-slip and thrust motion on a vertical fault striking N35^{o}E. This trend that is orthogonal to the strike of the San Jacinto fault suggests that the earthquake occurred on a restraining bend in the San Jacinto fault zone. Such geometrical complexities (bends) inhibit the movement on the main fault strand that shows strike-slip motion and strikes northwest. The aftershocks also show a northeast trend and mostly occur in the depth range of 13 to 16*km*, extending over a zone about 4*km* wide.

Unfortunately few of the aftershocks have similar first motion focal mechanisms and are closely located to the mainshock. An example of one aftershock with a similar focal mechanism is the M_L2.9 at 02:27PST the next day, (31 October 2001), with a depth of 15.2*km*. Figures 7.37 and 7.38 present the timeseries and source time functions for this aftershock / mainshock. The source time functions do not clearly indicate any directivity. This may be due to a variety of reasons; the mainshock focal mechanism is not as simple as the essentially strike-slip motion for the Yorba Linda event, and so the expected pattern may not be easily recognisable; the mainshock rupture may be bi-lateral; or the aftershock selected may not be a good selection as a Green's function. To further complicate matters, the events occurred in a more sparsely instrumented region, and so less data is available with good signal to noise.

7.4 Conclusions and Discussion

The revolutionary nature of the data that is systematically collected by TriNet allows development of new methodologies for studying the source process. Past source studies of earthquakes in the M4 range have primarily been based on spectral techniques (e.g corner frequencies and the Brune stress drop (Brune, 1970)). Unfortunately, these spectral techniques do not generally consider the particular source-station geometry, nor do they consider the particular effects introduced by complex wave propagation. These complex effects include the interference of multiple phases, diffraction and head waves. While there are still simplifying assumptions in the methodology outlined in this Chapter, this proce-

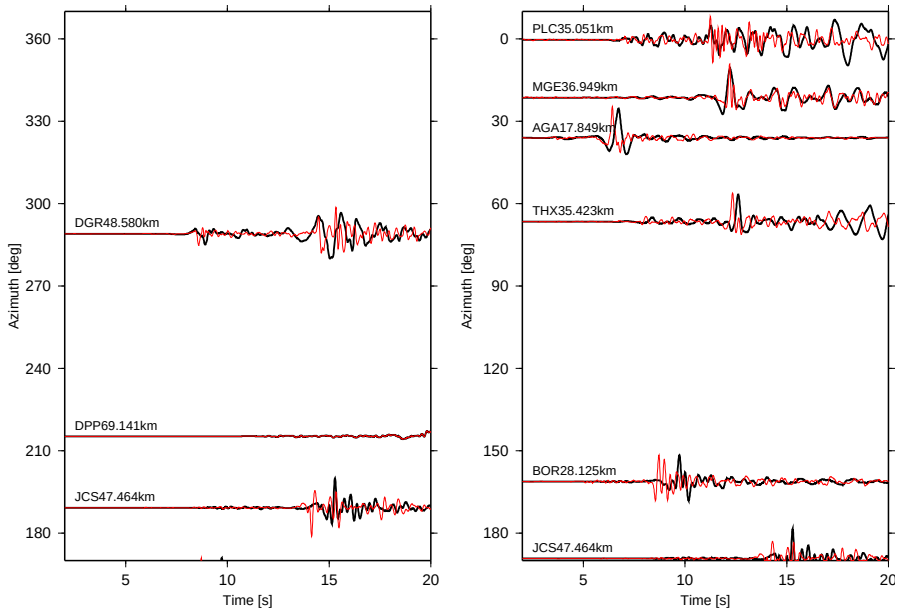

Figure 7.37: Displacement timeseries comparison with M2.90 and Anza mainshock — E-W component.

dure is likely to provide a more meaningful quantification of the source.

Now that the method has been shown to produce source time functions consistent with the expected rupture pattern, the next step would be to invert the source time functions from all the stations to derive the source parameters (fault plane, rupture dimension etc.). Unfortunately, such an inversion is not well enough conditioned to allow a general sub-fault inversion of the type usually employed for larger magnitude earthquakes (e.g Hartzell and Heaton (1983)). Instead, a much simpler parameterisation could be employed. We would begin by assuming one of the conjugate planes derived from the first-motion studies. We then assume that the source consists of a an ellipsoidal patch (2 degrees of freedom), a rupture velocity, and a rise time. This gives a total of 7 degrees of freedom to describe the source. We then would use a neighbourhood algorithm to perform the nonlinear inversion for the 7 parameters that best predict the source time functions. This process would be repeated for the other conjugate fault from the first motion analysis. The conjugate plane that produces the smallest residual would then be chosen as the preferred fault plane. Stress drop would be calculated from the rupture dimensions and the average slip.

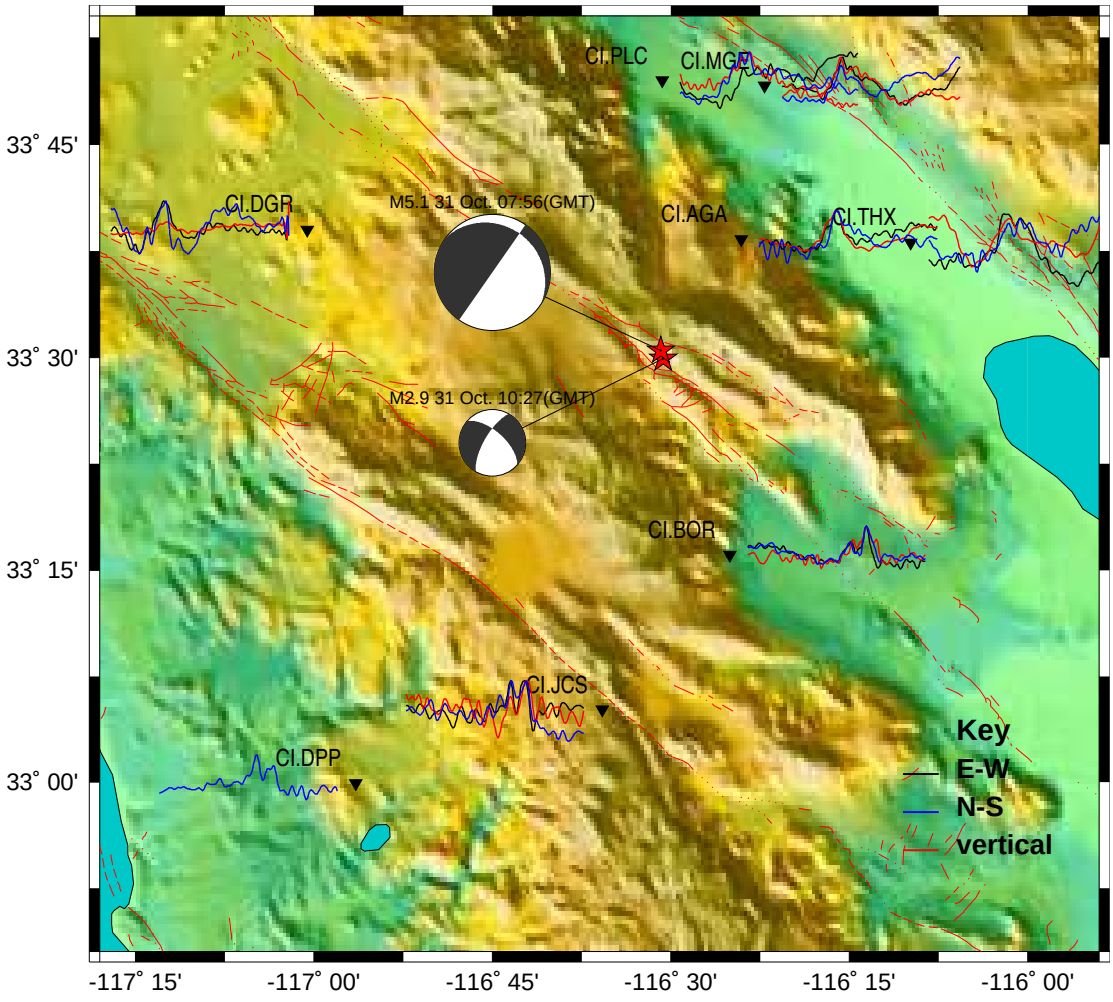

Figure 7.38: Transfer Functions for Anza from M2.90 — all components

As previously mentioned, the underlying assumption of this method is that the Green's function represented by the aftershock is valid for the mainshock. The implications of this for the choice of aftershock have been discussed, but it is this assumption that also places a bound on the application of this method for larger earthquakes. The mainshock to be modelled using an aftershock as a Green's function must possess a simple source time function. In particular it requires that the source-plane is two-dimensional with a constant rake, so that the initial focal-mechanism will be consistent through-out the event. Furthermore, as the rupture length becomes large, the path followed by waves from dislocations far from the epicentre become less similar to the path of the Green's function defined for that epicentre. Large magnitude events which tend to have a complicated rupture pattern over a large length, will likely violate the method's assumptions.

Stress Drop The non-linear inversion of the source time functions which locates the conjugate focal planes on which rupture took place also provides an estimate of the length of the rupture, L, the velocity of rupture, v_r, and a duration for the event, $\Delta T_f = LV_r$.

To calculate the event stress drop, $\Delta\sigma$, we know that:

$$\Delta\sigma = \Delta\varepsilon \cdot \mu \tag{7.36}$$

where $\Delta\varepsilon$ is the strain drop, and μ is the rigidity,

but:

$$\Delta\varepsilon = \frac{\overline{D}}{L} \tag{7.37}$$

where $\overline{D}$ is the average slip over the length of the fault,

also, recall from the definition of seismic moment, M_0, assuming the area is roughly a square with length L:

$$\overline{D} = \frac{M_0}{\mu L^2} \tag{7.38}$$

So we have:

$$\Delta\sigma = \frac{M v_r^3}{T_f^3} \tag{7.39}$$

It is particularly interesting to quantify the variability of stress drop for these smaller

earthquakes. That is, we know that the average stress drop of larger earthquakes is generally less than $10 MPa$. Can we demonstrate that a wider range of stress drops occur for smaller earthquakes? The answer to this question has important consequences for the friction and fracture energy that is used in dynamic rupture models.

Bibliography

Aki, K. and P. G. Richards (1980). *Quantative Seismology: Theory and Methods*, Volume 1, Chapter 10, pp. 477–524. Freeman, San Francisco.

Alves, S. W. and J. F. Hall (2003). Nonlinear modeling of Pacoima Dam using earthquake recordings to assess the effect of topographic nonuniformity in ground motion. Technical report, Data Utilization Report, CSMIP (in print).

Beck, J. L. and E. Chan (1995). Comparison of the Response of Millikan Library to San Fernando and Whittier Narrows Earthquakes. Unpublished Report, Caltech.

Beck, J. L., B. S. May, and D. C. Polidori (3-5 August 1994). Determination of Modal Parameters from Ambient Vibration Data for Structural Health Monitoring. In *First World Conference on Structural Control*, Los Angeles, California, USA.

Benz, H. and J. Filson (1998). *Requirement for an Advanced National Seismic System*. U. S. Geological Survey Circular 1188.

Blandford, R., V. R. McLamore, and J. Aunon (1968). Analysis of Millikan Library from Ambient Vibrations. Technical report, Earth Teledyne Co.

Boore, D. M. (2001, October). Effect of Baseline Corrections on Displacements and Response Spectra for Several Recordings of the 1999 Chi-Chi, Taiwan, Earthquake. *Bulletin of the Seismological Society of America 91*(5), 1199–1211.

Bracewell, R. (1965). *The Fourier Transform and Its Applications*. McGraw-Hill, Inc.

Bradford, S. C., J. F. Clinton, J. Favela, and T. H. Heaton (2004). Results of Millikan Library Forced Vibration Testing. Technical report, California Institute of Technology.

Brune, J. N. (1970). Tectonic Stress and the Spectra of Seismic Shear Waves from Earthquakes. *J. Geophys. Res. 75*, 4997–5009.

Camelo, V. S. (2003). *Dynamic Characteristics of Woodframe Buildings*. Ph.D. thesis, California Institute of Technology.

Chopra, A. K. (1995). *Dynamics of Structures - Theory and Applications to Earthquake Engineering*, Chapter 11, pp. 409–414, 514–515. Prentice Hall.

Clinton, J. F., S. C. Bradford, T. H. Heaton, and J. Favela (2004). The Observed Wander of the Natural Frequencies in a Structure. *in preparation*.

Cua, G. (2004). *Creating the Virtual Seismologist: Developments in Ground Motion Characterization and Seismic Early Warning*. Ph.D. thesis, California Institute of Technology.

Foutch, D. A. (1976). *A Study of the Vibrational Characteristics of Two Multistory Buildings*. Ph.D. thesis, California Institute of Technology, Earthquake Engineering Research Laboratory, Pasadena, California.

Foutch, D. A. and P. C. Jennings (1978). Foundation Response of a Nine-Storey Reinforced Concrete Building. *Bulletin of the Seismological Society of America 68*(1), 219–229.

Foutch, D. A., J. E. Luco, M. D. Trifunac, and F. E. Udwadia (1975). Full Scale, Three Dimensional Tests of Structural Deformation During Forced Excitation of a Nine-Storey Reinforced Concrete Building. In *Proceedings, U.S. National Conference on Earthquake Engineering*, Ann Arbor, Michigan, pp. 206–215.

Hartzell, S. and T. Heaton (1983). Inversion of Strong Ground Motion and Teleseismic Waveform Data for the Fault Rupture History of the 1979 Imperial-Valley, California, Earthquake. *Bulletin of the Seismological Society of America 73*(6), 1553–1583.

Hartzell, S. and T. Heaton (1985). Teleseismic Time Functions for Large, Shallow Subduction Zone Earthquakes. *Bulletin of the Seismological Society of America 75*(4), 965–1004.

Hauksson, E., L. M. Jones, and A. F. Shakal (2003). *International Handbook of Earthquake and Engineering Seismology*, Volume B, Chapter 78, pp. 1275 – 1284. Academic Press.

Hauksson, E., P. Small, K. Hafner, R. Busby, R. Clayton, J. Goltz, T. Heaton, K. Hutton, H. Kanamori, J. Polet, D. Given, L. M. Jones, and D. Wald (2001). Southern California Seismic Network: Caltech/USGS Element of TriNet 1997-2001. *Seismological Research Letters 72*(6), 690–74.

Heaton, T. (1982). The 1971 San-Fernando Earthquake - a Double Event. *Bulletin of the Seismological Society of America 72*(6), 2037–2062.

Heaton, T. H. (2003). CE/GE181 Engineering Seismology. California Institute of Technology.

Heaton, T. H., D. L. Anderson, W. J. Arabasz, R. Buland, W. L. Ellsworth, S. H. Hartzell, T. Lay, and P. Spudich (1989). *National Seismic System Science Plan*. U. S. Geological Survey Circular 1031.

Hudson, D. E. (1962). Synchronized Vibration Generators for Dynamic Tests of Full-Scale Structures. Technical report, Earthquake Engineering Research Laboratory, California Institute of Technology.

Iemura, H. and P. C. Jennings (1973). Hysteretic Response of a Nine-Story Reinforced Concrete Building During the San Fernando Earthquake. Technical report, Earthquake Engineering Research Laboratory, California Institute of Technology.

Iwan, W. D. (1998). CE 151 Dynamics and Vibrations. California Institute of Technology.

Iwan, W. D., M. A. Moser, and C. Y. Peng (1985). Some Observations on Strong-Motion Earthquake Measurement Using a Digital Accelerograph. *Bulletin of the Seismological Society of America 75*(5), 1225–1246.

Jennings, P. C. and J. H. Kuroiwa (1968). Vibration and Soil-Structure Interaction Tests of a Nine-Storey Reinforced Concrete Building. *Bulletin of the Seismological Society of America 58*(3), 891–916.

Kanamori, H., E. Hauksson, and T. Heaton (1991). TERRAscope and CUBE Project at Caltech. *Eos, Trans. Am. Geophys. U. 72*, 564.

Kanamori, H. K. (2002). GE 264 Physics of Earthquakes. California Institute of Technology.

Kuroiwa, J. H. (1967). *Vibration Test of a Multistorey Building*. Ph.D. thesis, California Institute of Technology, Earthquake Engineering Research Laboratory, Pasadena, California.

Larson, K. M., P. Bodin, and J. Gomberg (2003). Using 1-Hz GPS Data to Measure Deformations Caused by the Denali Fault Earthquake. *Science 300*, 1421–1424.

Lay, T. and T. C. Wallace (1995). *Modern Global Seismology*. Academic Press.

Lee, W. H. K., T. C. Shin, K. W. Kuo, and K. C. Chen (1999). *CWD Free-Field Strong-Motion Data From 921 Chi-Chi Earthquake*, Volume 1. Digital Acceleration Files on CD-ROM, Pre-Publication Version, Seismology Center, Central Weather Bureau, Taipei, Taiwan.

Levine, M. B., J. L. Beck, W. D. Iwan, P. C. Jennings, and R. Relles (1988). Accelerograms Recorded at Caltech During the Whittier Narrows Earthquakes of October 1 and 4, 1987 : a Preliminary Report. Technical report, California Institute of Technology. http://resolver.caltech.edu/CaltechEERL:1988.EERL-88-01.

Luco, J., M. Trifunac, and H. Wong (1987). On the Apparent Change in Dynamic Behavior of a 9- Story Reinforced-Concrete Building. *Bulletin of the Seismological Society of America 77*(6), 1961–1983.

Luco, J. E., W. H. L., and T. M. D. (1986, September). Soil-structure interaction effects on forced vibration tests. Technical Report Report 86-05, University of Southern California, Department of Civil Engineering, Los Angeles, California.

McVerry, G. H. (1980). *Frequency Domain Identification of Structural Models from Earthquake Records*. Ph.D. thesis, California Institute of Technology.

Menke, W. (1989). *Geophysical Data Analysis: Discrete Inverse Theory*. Academic Press.

Okada, Y., K. Kasahara, S. Hori, K. Obara, S. Sekiguchi, H. Fujiwara, and A. Yamamoto (2003, Oct). Recent Progress of Seismic Observation Networks in NIED. In *New Technologies for Urban Safety of Mega Cities in Asia*, Tokyo.

Peterson, J. (1993). Observations and Modeling of Background Seismic Noise. *Open File Report 92-302, U. S. Geological Survey, Albuquerque, NM*.

Scherbaum, F. (2001). *Of Poles and Zeros*. Kluwer Academic Publishers.

Strang, G. and K. Borre (1997). *Linear Algebra, Geodesy, and GPS*. Wellesley-Cambridge Press.

Streckeisen, G. and A. G. Messgerate. *STS-2 Portable Very-Broad-Band Triaxial Seismometer*. Dattlikonerstrasse 5, CH-8422 Pfungen, Switzerland.

Teledyne-Geotech-West (1972). Post Earthquake Vibration Measurements Millikan Library. Technical report, Teledyne Geotech West, Monrovia, California.

Tokyo Sokushin Co. Ltd. (2002a). *Broadband Velocity Type Feedback Seismometer - VSE of Tokyo Sokushin Co. and STS of Streckeisen Co*. Office: 2-22-9, Nishi-Nippori, Arakawa-Ku, Tokyo, 116-0013 Japan: Tokyo Sokushin Co. Ltd.

Tokyo Sokushin Co. Ltd. (2002b). *Servo Velocity Meter (VSE-355G2) Operation Manual*. Office: 2-22-9, Nishi-Nippori, Arakawa-Ku, Tokyo, 116-0013 Japan: Tokyo Sokushin Co. Ltd.

Trifunac, M. and M. Todorovska (2001a). Evolution of Accelerographs, Data Processing, Strong Motion Arrays and Amplitude and Spatial Resolution in Recording Strong Earthquake Motion. *Soil Dynamics and Earthquake Engineering 21*(6), 537–555.

Trifunac, M. and M. Todorovska (2001b). A Note on the Useable Dynamic Range of Accelerographs Recording Translation. *Soil Dynamics and Earthquake Engineering 21*(4), 275–286.

Trifunac, M. D. (1972). Comparisons Between Ambient and Forced Vibration Experiments. *Earthquake Engineering and Structural Dynamics 1*, 133–150.

Udwadia, F. E. and P. Z. Marmarelis (1976). The Identification of Building Structural Systems: I. The Linear Case. *Bulletin of the Seismological Society of America 66*(1), 125–151.

Udwadia, F. E. and M. D. Trifunac (1973). Ambient Vibration Tests of a Full-Scale Structure. In *Preceedings, Fifth World Conference on Earthquake Engineering*, Rome.

Udwadia, F. E. and M. D. Trifunac (1974). Time and Amplitude Dependent Response of Structures. *Int. J. Earthquake Engineering and Structural Dynamics 2*, 359–378.

Uzarski, J. and C. Arnold (Eds.) (2001, April). *Earthquake Spectra: 1999 Chi-Chi, Taiwan, Earthquake Reconnaissance Report*, Volume 17, Supplement A, Chapter 2, pp. 5–19.

Wielandt, E. and J. M. Steim (1986). A Digital Very-Broad-Band Seismograph. *Annales Geophysicae 4*(B, 3), 227–232.

Wielandt, E. and G. Streckeisen (1982). The Leaf-Spring Seismometer: Design and Performance. *Bulletin of the Seismological Society of America 72*(6), 2349–2367.

Youd, T. L., J. P. Bardet, and J. D. Bray (Eds.) (2000, December). *Earthquake Spectra: 1999 Kocaeli, Turkey, Earthquake Reconnaissance Report*, Volume 16, Supplement A, Chapter 4–6, pp. 65–140.

Appendix A VSE-355G2/3 Testing Regime

A suite of tests were performed at South Mudd on the Caltech Campus (the location of CISN test station DSN), Kresge Lab in the nearby San Raphael Hills (PAS, PASA, PASB), and Robinson Building also on Caltech Campus (CRP, CRPA). We thank David Johnson, Jascha Polet, Wayne Miller, Mike Watkins and Robert Busby for their advice and help in performing the tests, and obtaining data.

Mr. Isamu Yokoi was the principal contact with Tokyo Sokushin. Mr. Masayuki Kurahashi and Mr Soturu Wada from Sokushin also participated in the testing.

A complete chronological presentation of the results from the cart tests, as well as other important data, is at `www.ecf.caltech.edu/~jclinton/vse/VSEtests.html`.

A.1 12 December 2001: DSN — Noise and Track Test

The VSE-355G2 was initially installed at CISN/TriNet test station DSN in the basement of S. Mudd, Caltech. The instrument was mounted on a milling machine alongside an EpiSensor, attached to a Quanterra Q736 data logger. On 12 December 2001 the 2 instruments were moved back and forth along the track of the milling machine, each length taking about $20s$ to run about $25cm$. The objective of the test was to investigate the accuracy of displacement derived from the VSE-355G2, and compare it to that from the EpiSensor.

Unfortunately, over the length of the track, the was some minor tilt, which we discovered dominated the instrument output, and we could only conclude that the test served only to illustrate the sensitivity of the instruments to tilt. It was impossible to accurately determine displacement from this test. Both instruments recorded data that indicated a static offset in the SDOF mass, as seen in Figure A.1, sub-figures B and C. We were able to estimate the magnitude of the tilt from the static offset — in both cases this was found to be about $0.0007 rads$, or 0.04^o. This was enough to dwarf the relatively small translational displacement derived from each instrument, as is clearly seen in sub-figure B of Figure A.1.

We modeled the tilt as a step at the starting time of the milling machine displacement, which from sub-figures A and D of Figure A.1, is clearly only accurate in estimating final offset (seen in sub-figures B and C of Figure A.1), and not in modeling the motion recorded during the test themselves. In this case, the tilt is likely to occur non-linearly along the track, and is extremely difficult to model.

In sub-figure A of Figure A.1, the thick solid line represents the VSE-355G2 response to a δ-function impulse in acceleration, $V(t)$, which is defined by Eqn. 3.20 in Section 3.2. A positive δ-function at time $t = 0s$ with a negative δ-function at $t \sim 22s$. This is the expected result from the translational movement along the track - we assume an instantaneous rise to a constant velocity, and an instantaneous fall to rest (similar to Figure 3.9). The dashed-dotted line is the same, but includes the VSE-355G2 response to a step in acceleration (Eqn. 3.19, Figure 3.6) at time $t = 0$.

Sub-figure B is the integral of data in sub-figure A, representing the displacement of the VSE. We see a large constant offset of $160cm$. The size of the step in sub-figure A was chosen so as to match this final offset. The final displacement of the VSE-355G2 does indeed look like a sum of the acceleration step function (Figure 3.6) and a static offset in displacement (Figure 3.9).

Sub-figures C and D present the data from and simulation of the EpiSensor in the same test. A tilt is again required to map the offsets. The thick solid line again is the model without tilt, only with a δ-function in acceleration at the beginning and end of the test. In this case response is given by Eqn 3.19, which is also the SDOF response to a δ-function in acceleration. We use this here instead of Eqn 3.20 as the EpiSensor instrument has a displacement transducer, not a velocity transducer as with the VSE. Note the EpiSensor has a natural frequency of $180Hz$ and is critically damped. The dashed-dotted line also includes a step in acceleration (Eqn 3.21). We note again a tilt is required to fit the permanent offset.

An investigation into the noise levels of the VSE-355G2 was made by comparing the sensor output with data from a co-located CMG-40T at DSN. Unfortunately, the site proved too noisy to measure instrument resolution, even when placed on a bed of sand. Some parasitic resonances at high frequencies ($> 10Hz$) were observed. It was decided to move the instrument to a quieter location, and co-locate it with a better long-period instrument to

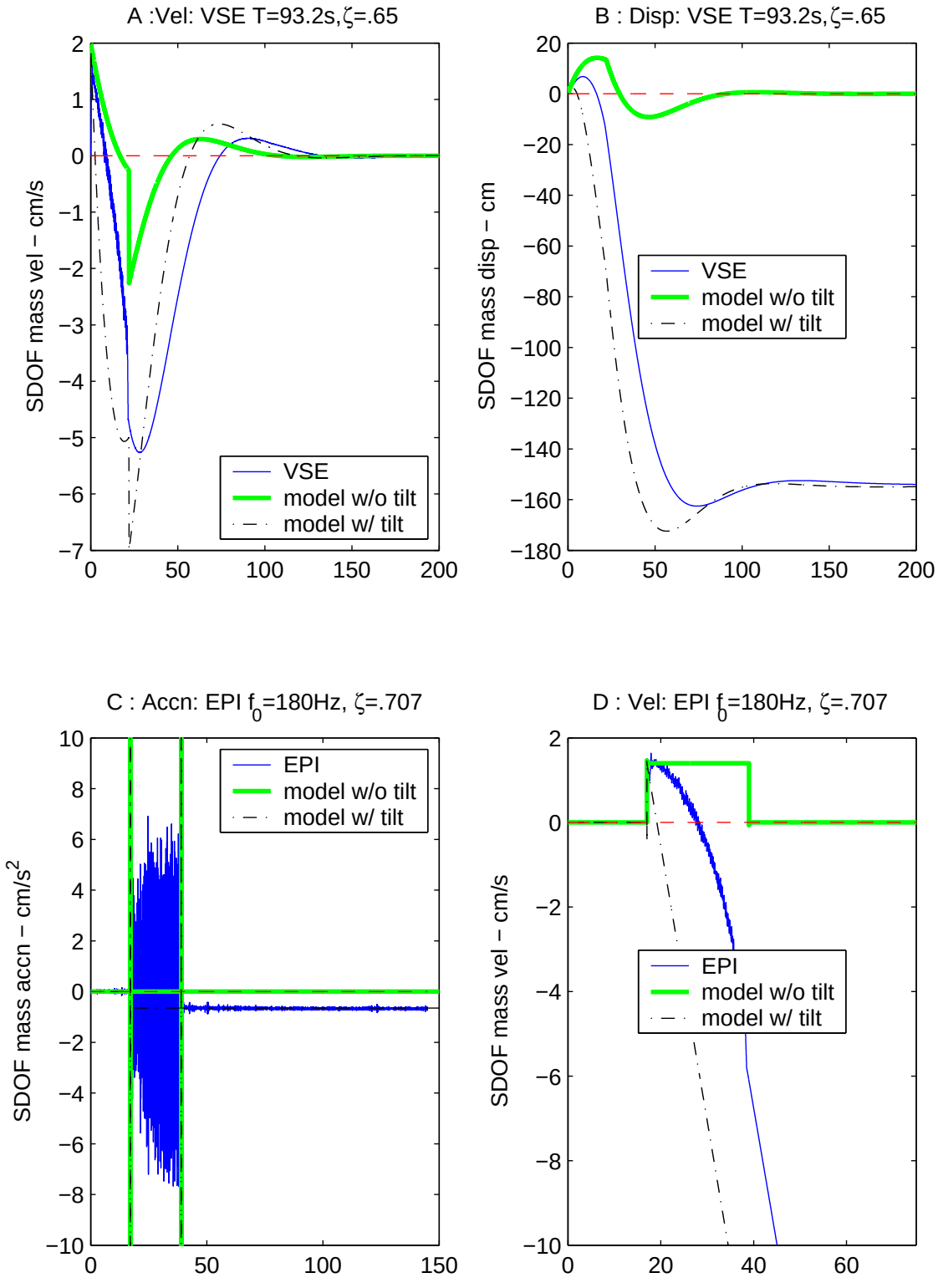

Figure A.1: Data and model from VSE-355G2 and EpiSensor: Milling machine test at DSN, December 2001.

better understand the frequency response.

A.2 February - March 2002: PASA — Noise and Screw Test

The VSE-355G2 was moved to the nearby Kresge lab in the San Rafael Hills, site of the TriNet stations PAS, in order to better measure the noise floor of the instrument. It was installed about 10*m* from PAS (PAS is located in the inner vault at Kresge). It was recorded on a Q4128 as PASA, with an STS-2 (#99713) also being recorded on the digitiser located on the pier in the anteroom. On 4 March, 2002, we performed a 'screw' test, in which a levelling screw was twisted slightly, imparting a step in acceleration on the horizontal components of the instrument. This test was not successful, as in order to use the screw, we had to loosen a locked bolt at the instrument footing which imparted an instrument response into the transient, which had not fully damped out before we adjusted the levelling screw. Further, the twisting was not instantaneous, and it was difficult to model exactly. To rectify the first problem, a further screw test was performed on 7 March, 2002, in which the loosening of the bolt was performed the previous day. It was still difficult to model the resulting data with confidence, due to the transience of the twisting excitation which we modeled as a step. From this analysis it was clear that the calibration coil test would likely provide a more satisfactory estimate of the equivalent SDOF response. We also tried to adjust the levelling screw of the STS-2, but were unable to keep the instrument on scale. Figure A.2 shows the timeseries data from the 4 March screw test.

A.3 March 2002: PASB — Noise and Calibration Coil Test

The VSE-355G2 was moved from the inner vault area to the ante-room at Kresge, and was placed on the pier alongside the STS-2 from the test above. Both instruments were recorded on the same Q4128 as before, and the station was renamed PASB. On 13 March, 2002,

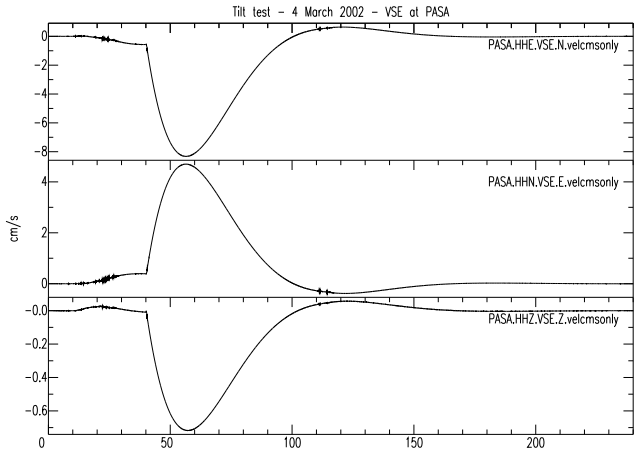

Figure A.2: Tilt test for VSE-355G2 using levelling screws in normal operation, from 4 March 2002. Unlocking of sensor, and transient tilting signal prove difficult to model exactly, so a calibration test was performed (see Figure 3.12). Contrast with tilt test performance for VSE-355G3 in November 2003 and January 2004 (Figures A.9 and A.12)

calibration tests for all 3 components of the VSE-355G2 were performed (see Figure 3.12). The calibration test involved applying a signal generated current in the form of a step function with a period of a few minutes to the calibration coil. It was observed during the test that unless we used much greater resistance than indicated in the Operation Manuel, the system was over-driven (increasing the resistance decreases the applied current, which reduces the equivalent applied velocity). We noted that when smaller resistances were used, which effectively leads to larger output voltages, the clip occurred at about $600,000 cts$, equivalent to $1.43 Volts$, or a velocity of $14.3 cm/s$. The clip velocity should be $2 m/s$. Unfortunately none of the other mechanical tests performed so far (mill test, tilt test) had driven the instrument above this level, so at this stage we were unable to tell whether this was isolated to a problem with the calibration coil, or something that would affect the instruments ability to record motions up to $200 cm/s$ / $2g$ (recall that the VSE sensor clips if either a maximum velocity or acceleration is recorded).

Seismic waveforms from some small local events were recorded, which were useful in calibrating the sensitivity of the instrument (see Figure 3.11), as well as noise data from

which we estimated the instrument's minimum resolution (see Figures 3.14, 3.15 and 3.16).

A.4 8 March 2002: DSN — Cart Test I

The VSE-355G2 was moved back to South Mudd. As there were some problems observed during the calibration test regarding saturation at Voltage significantly lower the published, it was decided to check whether, under real motion, the instrument was performing near its published capacity, which would make it capable of recording on-scale motions near $2m/s$ and $2g$. On 8 March 2002, the instrument was placed on a cart alongside an EpiSensor, and attached to the Q4128 we operated as PASB above. We moved the cart up to $10m$ along the floor at a range of speeds for durations of $\sim 8s$. We observed similar clipping at $\pm 15cm/s$ or $\pm 1.3V$ as in the calibration tests. Once the instrument reached this level ,there would be a spike in velocity, then the instrument would 'flat-line' at $15cm/s$ for some seconds. We performed multiple tests to ensure the spike was not at $2m/s$ and then just fell back to $15cm/s$. Figure 3.21 illustrates this well, where the accelerometer data indicates the maximum velocity is at about $60cm/s$, and the VSE-355G2 does not nearly reach this level..

A.5 June 2002: DSN — Cart Test II

After correspondence with the manufacturer, the source of the low clipping was identified as a problem with the power regulator, which prevented the final stage amplifier from working correctly. The Vice-President of the company, Mr. Isamu Yokoi, visited Caltech on the 18^{th} and 19^{th} of June, 2002, to rectify the problem. Once this problem had been corrected, we repeated our cart test as described in the section above. The test showed improved performance, with excellent VSE correspondence with the EpiSensor data up to $40cm/s$ (see Figure 3.23). On tests that went above this speed, clipping once again occurred (see Figure 3.24). Mr. Yokoi returned to Japan to study the situation.

A.6 June - September 2002: Japan

Tokyo Sokushin developed a new model which they believed was capable of recovering broadband ground motions up to and beyond $2m/s$, with similar noise resolution.

A.7 11 - 12 November 2002: DSN — Cart Test III

On 11-12 November 2002 Mr. Isamu Yokoi and Mr. Sotoru Wada, a engineer from Tokyo-Sokushin, visited Caltech. On 11 November, Mr Wada replaced the 3 seismometers and the feedback circuits. The new instrument was labeled the VSE-355G3. Noise tests performed in Japan indicate comparable performance from the new components to the VSE-355G2. Analysis from subsequent cart tests showed the horizontal channels could resolve motion beyond $2m/s$. However, a low clipping level, as before at about $30cm/s$, was observed on the vertical channel. Furthermore, significant cross-axis sensitivity between all components was observed during strong motion cart tests.

A.8 27 November 2002: DSN — Cart Test IV

After the poor performance from the tests on 12 November, Mr Yokoi suggested rotating the sensor to see if cross-coupling would re-occur under different conditions. We re-ran the cart tests and observed similar flawed patterns to those of the 12 November tests.

A.9 12 March 2003: DSN — Cart Test V

After the poor performance from the tests on 12 and 27 November, Mr Yokoi returned to Caltech. We discussed whether high frequency clipping ($> 2g$ at $> 200HZ$) was responsible for the cross-coupling. Using an oscilloscope and a hammer impulse, Mr, Yokoi demonstrated this high frequency clipping indeed gave an impulse response at about $100s$. It was thought that this does not adequately explain the cross-coupling as the out-of-plane and vertical components follow the velocity as observed in the in-plane motion very closely,

at a $\sim 10s$ period.

No modification was made to the instruments. We re-ran the cart tests. Data showed some flawed patterns. Some sample data showing low vertical clipping is in Figure A.3(a) and the cross-coupling between horizontal channels in Figure A.3(b)

A.10 26 March 2003: DSN — Cart Test VI

We became aware of a potential corruption of data files from 12 March test arising from an extra instrument and datalogger being attached to DSN in a laboratory in the Sub-Basement of S. Mudd. Consequently, we repeated the cart tests as in 12 March. Again, the same flaws were observed.

A.11 April - June 2003: Japan

Tests at Sokushin revealed the Z-axis suspension spring could not linearly resist large velocity ground motions. This defect was deemed responsible for the low vertical component clip levels previously observed, as well as the cross-coupling observed between all channels. Replacement components were made for all three channels. Noise tests performed in Japan also indicate comparable performance from the new VSE-355G3 components to the old VSE-355G2. In order to observe possible low clip levels, a similar setup to the Cart Test, but in an elevator, was performed. Vertical velocities up to $1m/s$ were observed without error, as can be seen in Figure A.4.

A.12 15 - 16 September 2003: DSN — Cart Test VI

Mr. Soturu Wada replaced the original VSE-355G3 components with the new VSE-355G3 components for all three channels. We repeated the Cart Test, and performed a calibration test. Results from the Cart Test were very encouraging, with no low clipping observed in the horizontal channels, and no cross-talk between any channels. No large velocities were observed in the vertical direction as only a horizontal test is practical with the setup

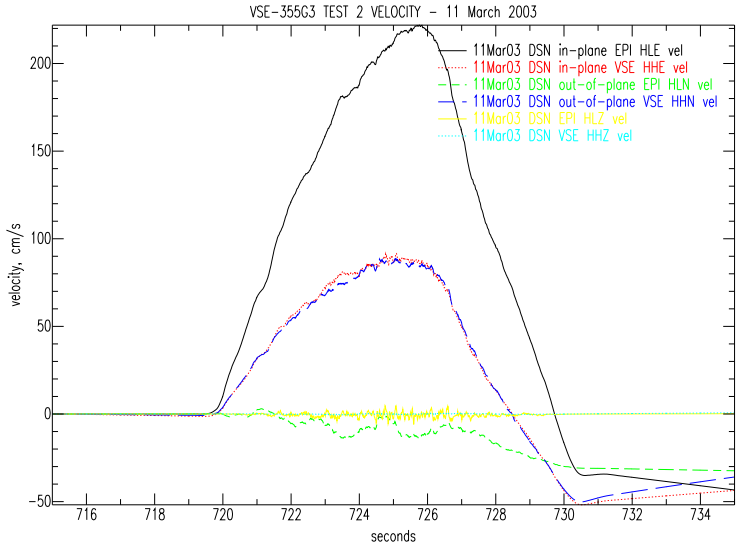

(a) Cross-coupling

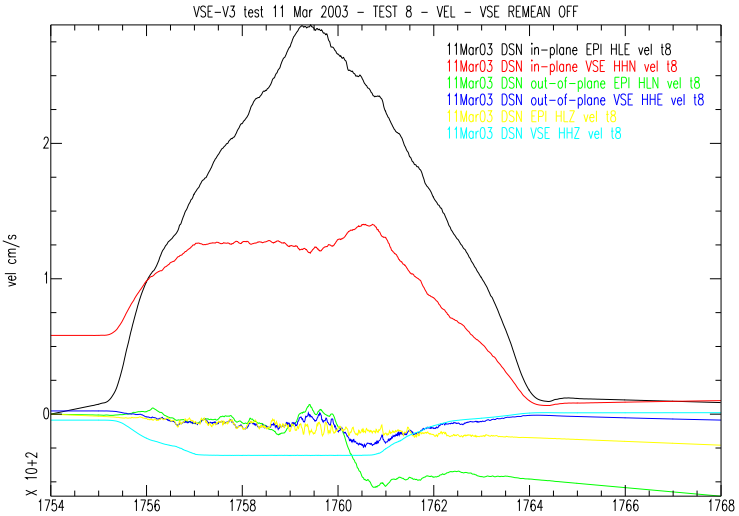

(b) Vertical clipping at $30cm/s$. Also very low in-plane VSE-355G2 velocity

Figure A.3: Errors observed from cart test, 11 March 2003, for VSE-355G3.

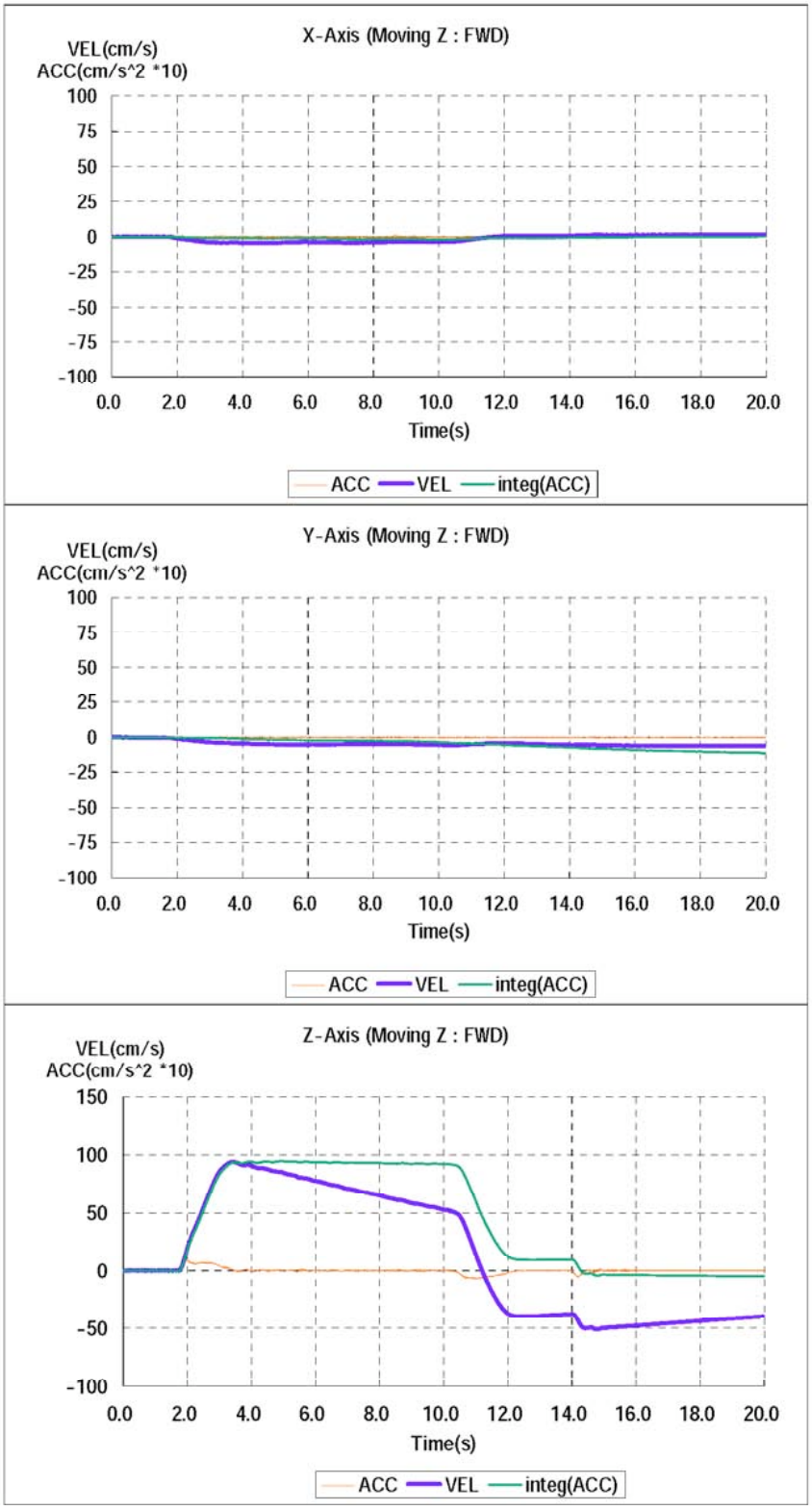

Figure A.4: Elevator test, performed in Japan by Tokyo Sokushin, June 2003, showing ability of VSE-355G3 vertical component to resolve large vertical velocities. No deconvolution of data.

at Caltech. A typical record with a large peak velocity is in Figure A.5. In this Figure, the pre-event mean is not removed, and the 'raw' velocity is shown to clip at $243 cm/s$. At this stage, we became concerned with large offsets after tests, which do not return back to zero. Figure A.6 illustrates the problem. These are discussed in the next section, but basically are caused by tilting of the instrument during testing.

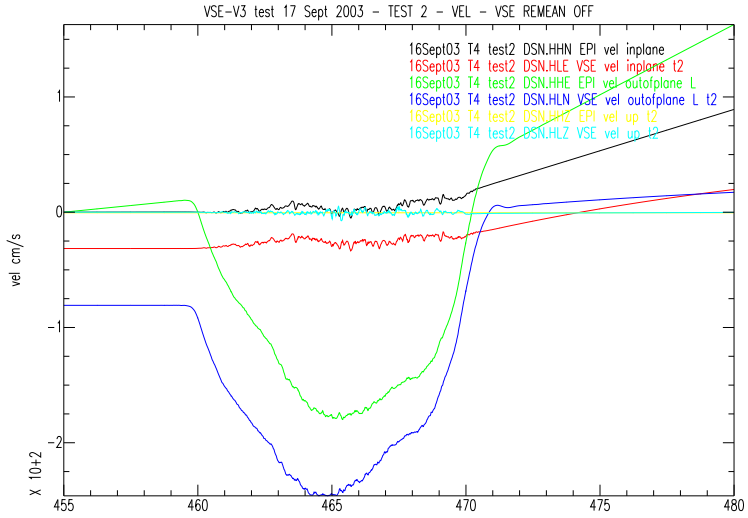

Figure A.5: Cart test, 16 September 2003 - observe VSE-355G3 clipping at $243 cm/s$. Note all data has pre-event mean left on, and VSE-355G3 has significant offsets. In-plane/out-of-plane mix up is due to errors in channel assignments for both sensors.

The VSE-355G3 test regime shown in Figure A.6 does not include levelling in between tests and rotations, which results in large permanent velocity offsets, and so the raw output gives insight into the clipping level of the instrument. Before the cart test at 720*s*, the E-W background velocity is at $-166 cm/s$, indicating the instrument is severely tilted. The ensuing motions decrease the velocity further until a minimum velocity of $-252 cm/s$ is reached (which corresponds to $-10584 cts$ or $2^{23.335}$, $140 dB$ of counts), whereupon the output flatlines until the motion ends. The N-S component is observed to have a similar flatline at $-243 cm/s$ during the test at 460*s*, as seen in Figure A.5. Note this is raw sensor response, and has not been deconvolved to obtain corrected velocity response.

The clip level was not reached in tests where care is taken to level the instrument, as

the speeds upwards of $240 cm/s$ were not reached.

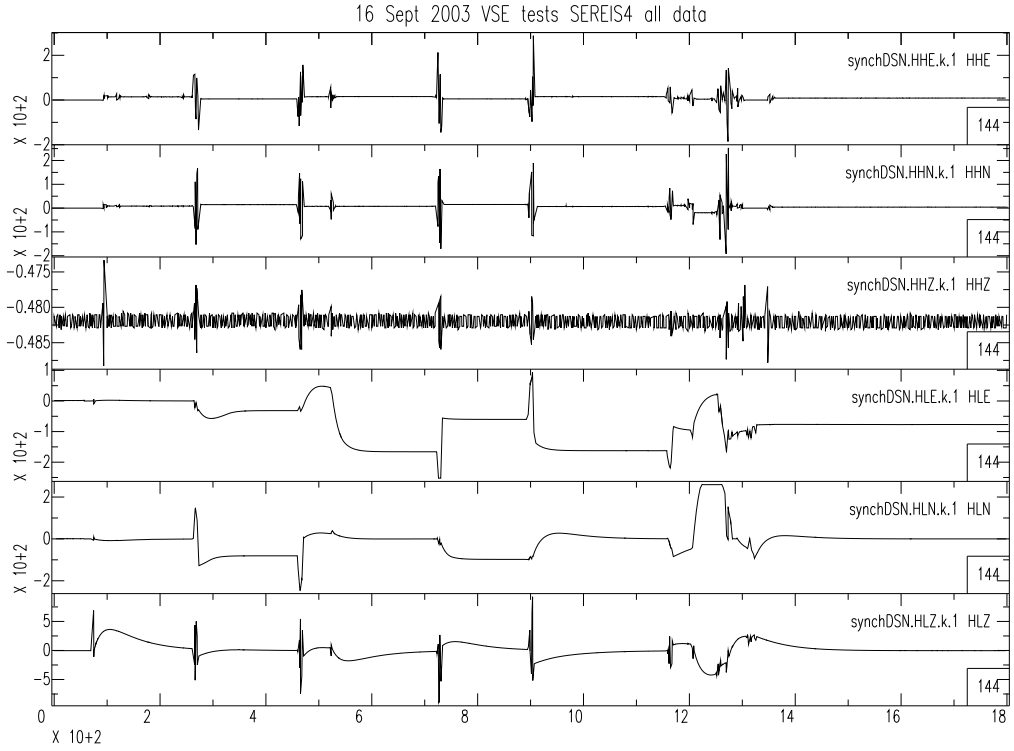

Figure A.6: Cart test — duration of a test sequence, 16 September 2003. Top 3 channels are EpiSensor acceleration (cm/s^2), bottom 3 are the VSE-355G3 raw velocity output (cm/s). X-axis: time in seconds. Note after tests, the VSE-355G3 sometimes exhibits static offset in output, due to tilting. Data from Figure A.5 is from the test occurring between 400 and 500s. Spikes at 80s are due to turning power on. Forward test at 270s, backward at 470s. VSE rotated 90^o anti-clockwise at 515s, with 2 more tests following. Transients after 1150s are of unknown origin, possibly from changing pin connections or modifying the power source. VSE-355G3 E-W channel is observed to clip during the test occurring at 720s, at $-252 cm/s$. At 470s, the N-S channels clips at $-243 cm/s$.

Results from the calibration test are in Figure A.7. A problem was also identified in this test, with behaviour not commensurate with a velocity meter observed in the 2 horizontal channels. This test was performed under the instruction of the manufacturer. A signal generator applied a step function in current, with a period of 5$mins$. A capacitor was placed in the circuit between the signal generator and the calibration coil, which had the effect of

differentiating the input signal to the calibration coil, so the current applied to calibration coil was in the form of an impulse, or δ-function. Thus the input to each channel was an impulse in acceleration. The expected output should be as in Equation 3.20 and as seen Figure 3.5. For each of the three components, the best fit model was determined, varying $t_0, H(t-t_0), \omega_0$ and β, for the observed VSE output. Also included is the expected model to the integrand and double integrand of the output, as given in Eqns. 3.19 and 3.21. Figure A.7 provides a graphical comparison for the best fit and observed VSE data for such an acceleration impulse input. The vertical channel can be well modelled as an SDOF, but the EW and NS deviate from this idealised behaviour.

In summary the best fit SDOF solution is $T_0 = 110s, \zeta = 0.64$ E-W component, $T_0 = 107s, \zeta = 0.60$ N-S, and $T_0 = 105.8s, \zeta = 0.64$ Vertical. These free periods are significantly longer than those of the VSE-355G2. The variation in these solutions were larger than expected, and the horizontal channels cannot be approximated by this SDOF solution.

A.13 October - November 2003: CRP

Ambient noise tests and simple calibration tests using only the levelling screws were performed with the instrument deployed alongside an STS-2 and a CMG-1T at the Robinson Pit CISN station CRP. The system was observed to behave well during the small M3.6 Simi Valley earthquake $55km$ from the site, and during ambient noise analysis (see Figure 5.8). Unfortunately, the screw test, shown in Figure A.8 revealed very strange instrument response to a simple step in acceleration, with permanent offsets in the E-W component, and a response longer in period than that from a $100s$ SDOF.

CRP was logged using a Q680, CRPA with a Q330. As CRPA, and to some extent CRP, are test sites, sensors and dataloggers are interchanged quite frequently.

A.14 24 - 26 November 2003: CRP and DSN

Mr. Yokoi visited Caltech again, to investigate the cross-coupling problems, and faulty output from calibration tests. On 24 November 2003, after reviewing and modifying the

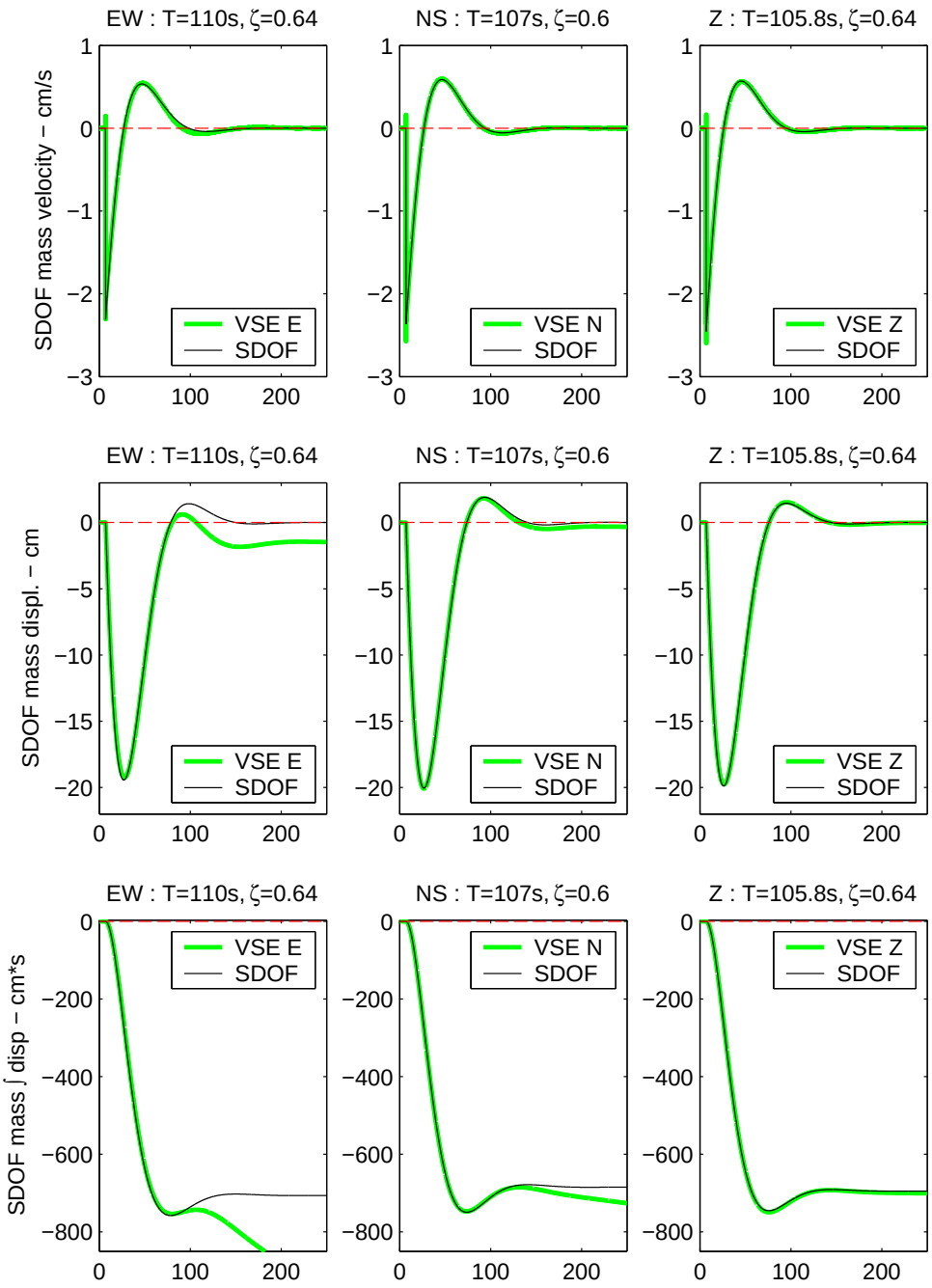

Figure A.7: Calibration coil response test, VSE-355G3, September 2003

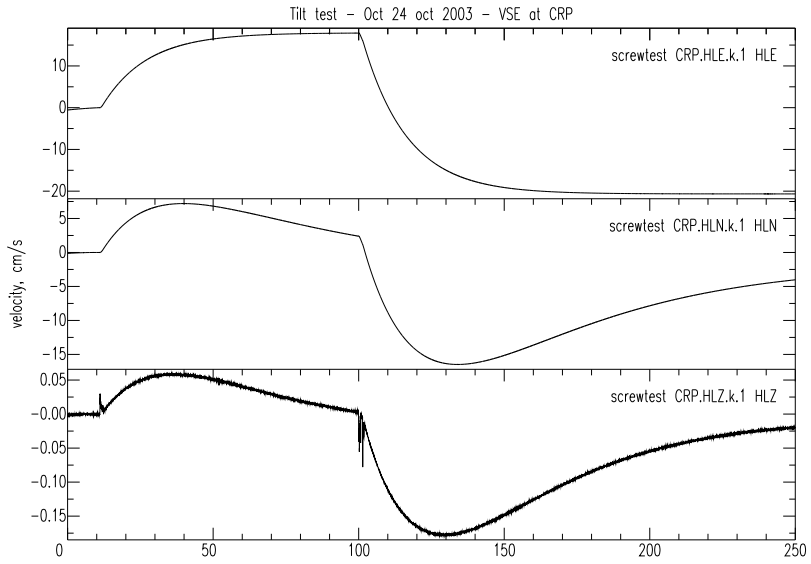

Figure A.8: Tilt test using levelling screws in normal operation, October 2003, VSE-355G3 model. Contrast with VSE-355G2 performance in March 2002 (Figure A.2). Screw turned anti-clockwise 1/4 turn at 10*s*, then 1/2 turn clockwise at 100*s*. Note: $\sim 100s$ SDOF should return to zero offset after $\sim 100s$, as in Figure 3.6. E-W component has permanent offset; all 3 components take $> 100s$ for the transient to settle.

pin connections, data was collected from tilt tests, and simple battery input tests to the calibration coils. Figure A.9 shows results from the screw test, which shows good operation, very similar to the expected result seen in Figure 3.6. All three components have a corner at approximately 105s, with more variability in the damping, ranging from 0.555 to 0.64. Figure A.10 shows results from the battery test, where the connections to the input for the calibration coil are 'touched' briefly to a standard AA battery, which simulates a δ-function input. All output is compared to the models determined in Figure A.9. The N-S and Vertical performance is very similar, but the E-W channel output is very different from that expected. This prompted a complete review of the pin connections. Once this was complete, the battery test indicated good compatibility with the tilt test results for all three components.

As the calibration tests were satisfactory, the instrument was moved back to South Mudd and the Cart Test was run again on 25 November 2003. In the morning a suite of tests were run, and though the clip level was observed to be above $2m/s$, and cross-coupling was not observed, it was noted that after certain runs, and after an instrument rotation (done to identify any cross coupling, and check if each horizontal channel was capable of reaching the large velocities), there were large static offsets in the velocity timeseries. It was determined this was due to tilting of the instrument. In the afternoon, tests were performed with care taken to re-level the instrument if the bubble had been observed to move. Figure A.11 plots the timeseries for the afternoon tests, and includes the E-W component of the FBA-23, and all three components of the VSE-355G3. It was noted that the bubble level did indeed move around, especially after a rotation. Once this was corrected, the baseline velocity re-zeroed. A self levelling device in the instrument saturates when tilts become too large, meaning the instrument cannot re-center. This can be monitored externally, as the tilt channels may not re-center if voltages required to re-center rise above 12V. If the tilt voltage reaches this level, it will remain high, if this level is not reached, the tilt voltage will return to zero. It is unlikely this channel will be monitored remotely. However, in the field, this can be observed from static offsets in the baseline velocity output. The instrument needs to be manually re-levelled to remove the effect. It is not known whether the magnitude of tilt required to create this problem are larger than that expected even in

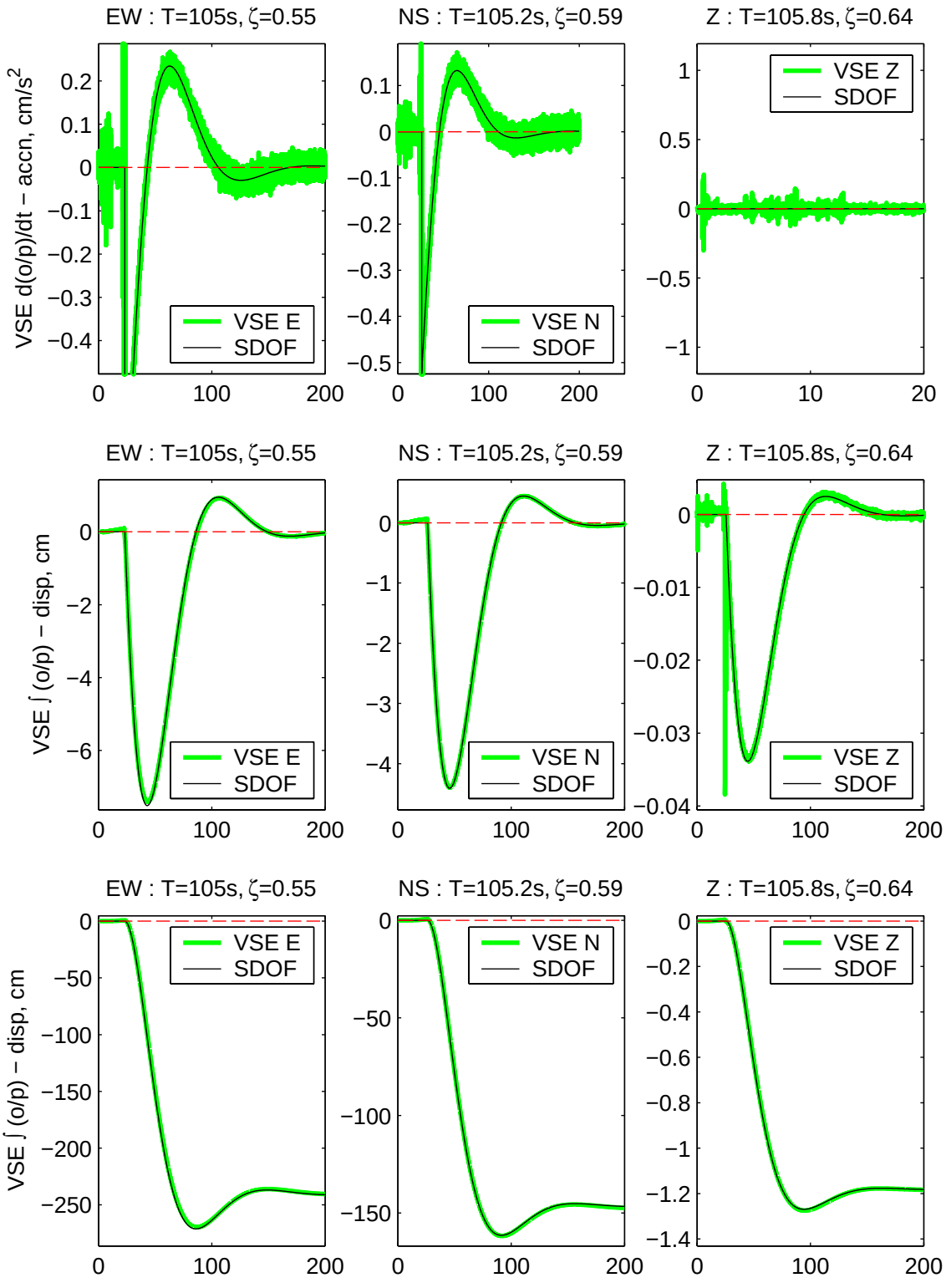

Figure A.9: Tilt test using levelling screws in normal operation, 24 November 2003, VSE-355G3 model. Good performance.

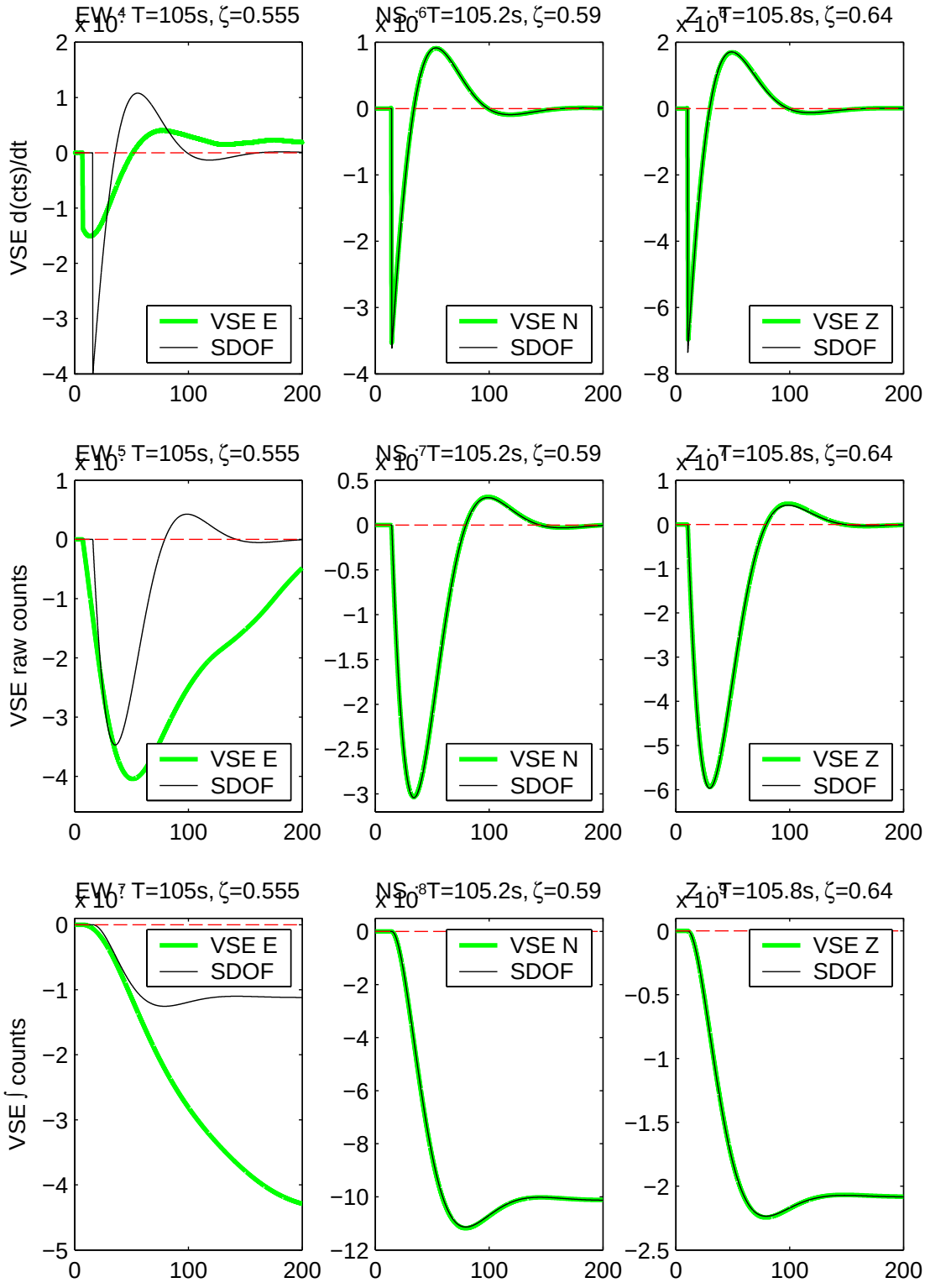

Figure A.10: Battery test using calibration coil input, 24 November 2003, VSE-355G3 model. Poor performance from E-W channel.

severe ground motions. No further research was taken into investigating exactly what tilt magnitude causes the problem. We do note that some large records recorded on Tokyo-Sokushin strong motion velocity instruments during the Tokachi-Oki earthquake do have unexplained offsets in the deconvolved velocity output, which could be due to this effect. This is a clear disadvantage of this instrument compared to an FBA, which can continue to operate with large tilt,

Figure A.11: Cart Test — duration of test sequence, 25 November 2003, with re-levelling after every run. Top channel is E-W EpiSensor acceleration, bottom 3 are the VSE-355G3 raw velocity output. Y-axis is counts. Note after tests, the VSE-355G3 sometimes exhibits static offset in output, due to tilting, which is corrected by re-levelling the instrument. Compare to Figure A.6, without levelling. Forward test at 90*s*, re-levelling at 270*s*, backward at 480*s*, forward at 700*s*. The instrument was rotated 45^o and re-levelled at 830*s*. A backward test at 960*s*, re-levelled at 1100*s*, and forward at 1200*s*. Another 45^o rotation at 1300*s*, backward at1500*s*, re-levelled at 1600*s*. Forward at 1830*s*, re-levelled at 2000*s*. Forward at 2080*s*, backward at 2200*s*.

A.15 23 January 2004: CRP and DSN

After a few months of continuous recording at CRP, another tilt test was performed. Results are in Figure 5.4 and Figure A.12. The equivalent SDOF for the N-S and Z VSE-355G3

channels are identical to the observations from the same test in November 2003, Figure A.9; the E-W component has the same damping, but there is a small increase in free period from 105.0s to 105.5s.

The STS-2 at CRP was removed for use elsewhere in the CISN in late October 2003. This was before the pin connection problems had been resolved. A CMG-1T was the broadband high-gain sensor replacement. Noise and earthquake data (from the San Simeon earthquake, 24 December 2003), have been recorded, and are analysed in Chapter 5. Dynamic range performance was found to be similar to that of the VSE-355G2, with the instrument capable of about 132dB of signal.

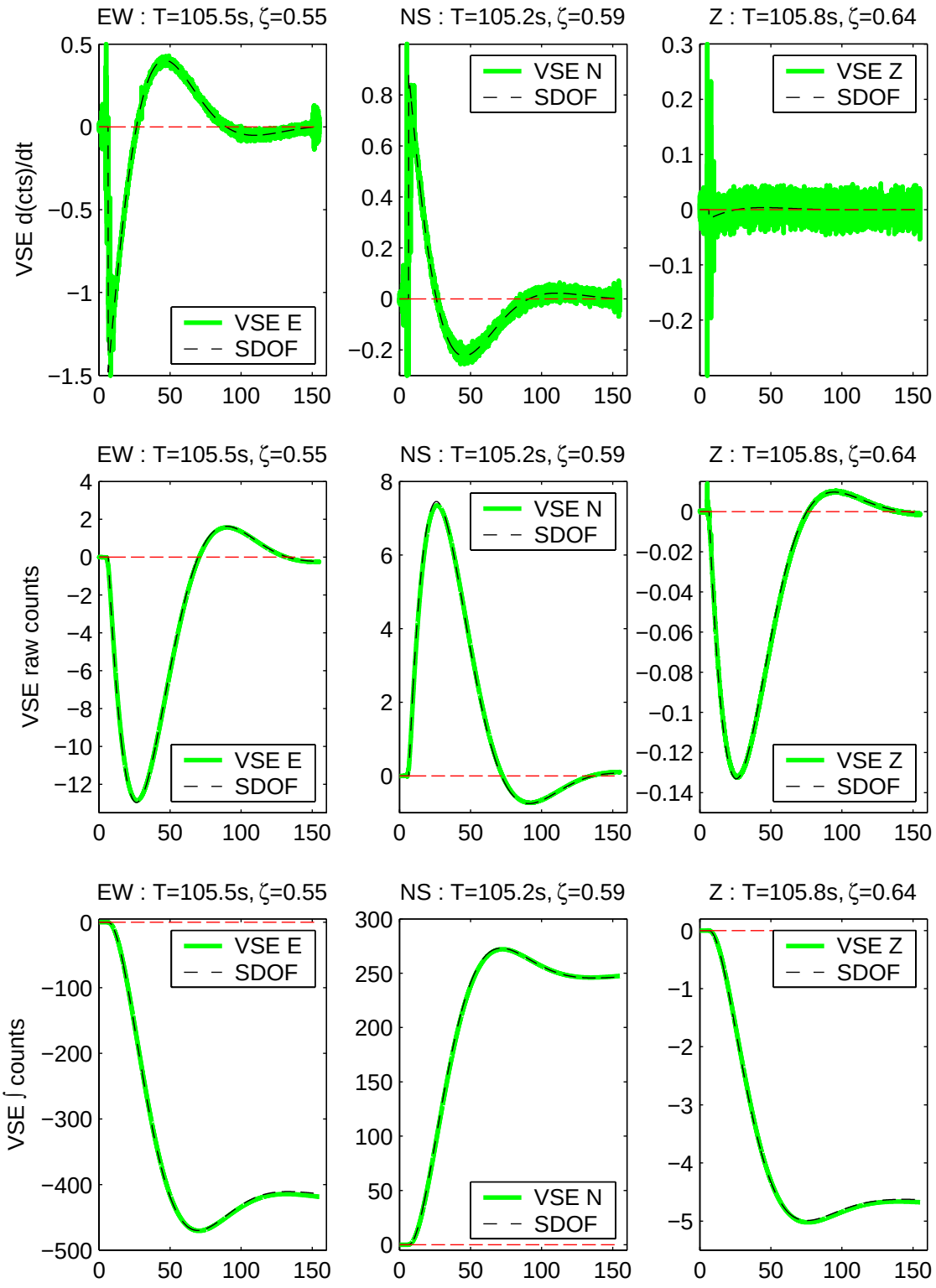

Figure A.12: Response to a tilt, caused by adjusting the levelling screw, January 2004

Appendix B Previous Studies of Millikan Library

Since the completion of the Library in 1966, Millikan has survived (and recorded) numerous moderate earthquakes within and nearby the greater Los Angeles area. Most notable among these are the Borrego Mountain ($M6.5, \Delta = 213km$), Lytle Creek ($M5.3, \Delta = 56km$), San Fernando ($M6.6, \Delta = 39km$), Whittier Narrows ($M5.9, \Delta = 10km$), Pasadena ($M5.0, \Delta = 0km$), Sierra Madre ($M5.6, \Delta = 20km$), Landers ($M7.3, \Delta = 187km$), Big Bear ($M6.5, \Delta = 145km$), Northridge ($M6.7, \Delta = 47km$), and Hector Mine ($M7.1, \Delta = 210km$).

In the decade following its construction, numerous published reports investigated the complex dynamic properties of the structure, with the likely conclusion that the fundamental periods are strongly influenced by soil-structure interaction, and a significant proportion of modal motion is due to rocking and sliding (Luco et al, 1986). It was observed that the building also softened permanently after the strong shaking encountered in the M6.6 1971 San Fernando earthquake.

A complete summary of the various studies into the frequency charateristics of the building may be found in Tables B.1 and B.2. These include both forced and ambient testing of the structure, and indicate an evolution in the frequency and damping of the structure, most notable affected by the $M6.7$ San Fernando event which occured on 9 February 1971 and resulted in the permanent lengthening of the free periods and increased damping for the structure. A permanent shaker installed on the roof allowed forced vibrations at frequencies up to about 10Hz. Table B.3 contains the references used to compile Tables B.1 and B.2. Most years, forced vibration tests are carried out on the building in Caltech Civil Engineering Class 180 — Experimental Mathods in Civil Engineering. Each spring the fundamental modeshapes and natural frequencies are recorded. This provides a‘data point’ for each year. An attempt was made to gather as many of these un-published results as possible.

Figure B.1 presents a summary plot of the tables. It is similar to Figure 6.4, but contains the extra information included in these tables.

Shortly after construction was completed, a PhD study by Kuroiwa (1967) suggested the building behaved non-linearly as a 'softening system', since the natural frequencies reduced as the applied excitation increased. The observed effect was small, with the N-S mode reduced 2.9% as force increased by 3.8, the E-W mode reduced 2.7% as force increased by 7.5, and the torsional mode reduced 1.2% as force increased by 2.1. Damping values also appear to be non-linear, they are observed to increase with increased excitation.

It was also noted that the building is very stiff for its height, but may be readily explained by the very rigid structural system for a building of this height.

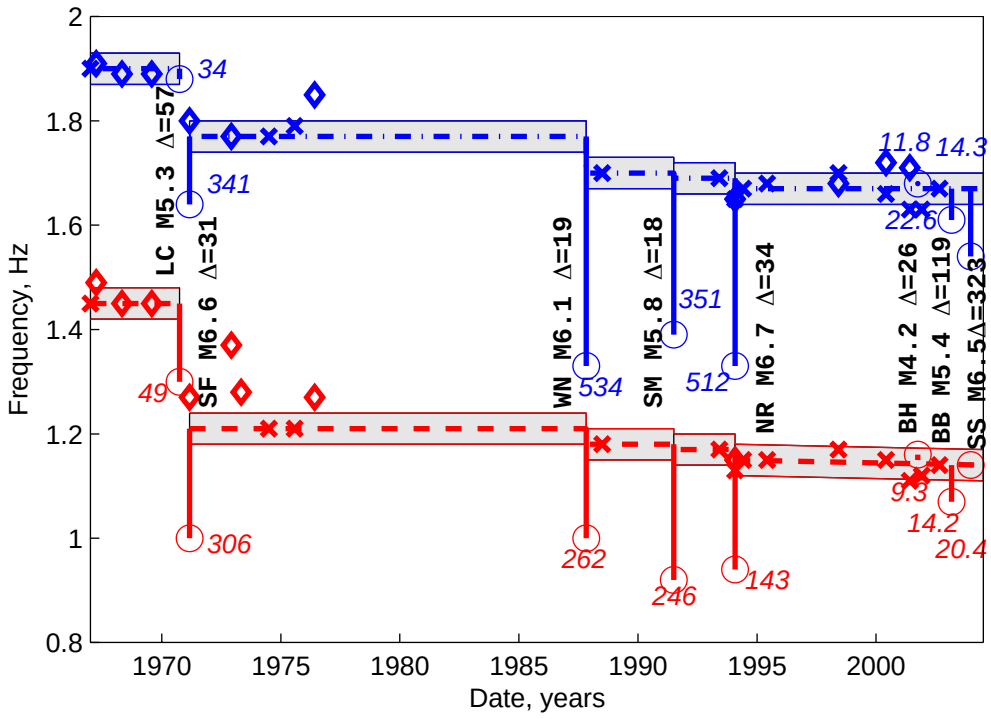

Figure B.1: Graphical interpretation of Tables B.1 and B.2. Dashed lines are E-W natural frequencies, dashed-dotted are N-S natural frequencies, all from forced vibration testing. Shaded area is the likely region of natural frequencies taking into consideration errors in measurement, due to unknown shaker weight configuration and weather conditions for each test, and experimental error. Crosses and diamonds indicate the actual time and frequency of a forced vibration and ambient measurement respectively. Circles indicate natural frequency estimated from the strong motion record of the event, with the number in italics giving the peak acceleration recorded for the event (cm/s^2).

Test	East - West		North - South		Torsional		Remark
	f_0 [ζ_0]	f_1 [ζ_1]	f_0 [ζ_0]	f_1 [ζ_1]	f_0 [ζ_0]	f_1 [ζ_1]	
1966-1967[1]	1.46-1.51 [0.7-1.7]	6.2	1.89-1.98 [1.2-1.8]	-	2.84-2.90 [0.9-1.6]	-	A,F,M
Mar 1967[2]	1.49 [1.5]	6.1	1.91 [1.6]	-	2.88	-	A
Apr 1968[3]	1.45	6.1	1.89	9.18	2.87	9.62	A
Jul 1969[4]	1.45	5.90	1.89	9.10	-	-	A
Sep 12 1970[5]	1.30-1.50	-	1.90-2.10	-	-	-	E (LC)
Sep 12 1970[6]	1.30	-	1.88	-	-	-	E (LC)
∼ M6.7 February 9 1971 San Fernando Earthquake (SF) @ 44km ∼							
Feb 9 1971[5]	1.00-1.50	-	1.50-1.90	-	-	-	E (SF)
Feb 9 1971[7]	0.82-1.43 [1.0-13.0]	-	-	-	-	-	E (SF)
Feb 9 1971[8]	1.02-1.11 [3.5-5.5]	-	-	-	-	-	E (SF)
Feb 9 1971[9]	1.03 [0.07]	4.98 [0.06]	1.61 [0.06]	7.81 [0.06]	-	-	E (SF)
Feb 9 1971[10]	1.02 [0.06]	4.93 [0.05]	1.61 [0.06]	7.82 [0.05]	-	-	E (SF)
Feb 9 1971[6]	1.00	-	1.64	-	-	-	E (SF)
Feb 1971[11]	1.27 [2.5]	5.35 [0.9]	1.8 [3]	9.02 [0.2]	2.65 [2]	9.65 [0.5]	A
Feb 1971[4]	1.30	-	-	-	-	-	A
Dec 1972[4]	1.37	-	1.77	-	-	-	M
Apr 1973[12]	1.28 [1.3]	-	-	-	-	-	A
1974[13]	1.21	-	1.76	-	-	-	F
Jul 1975[14]	1.21 [1.8]	-	1.79 [1.8]	-	-	-	F
May 1976[9]	1.27	-	1.85	-	2.65	-	A
∼ M6.1 October 1 1987 Whittier Narrows Earthquake (WN) @ 19km ∼							
Oct 1 1987[10]	0.932 [0.04]	4.17 [0.08]	1.30 [0.06]	6.64 [0.18]	-	-	E (WN)
Oct 1 1987[6]	1.00	-	1.33	-	-	-	E (WN)
Oct 4 1987[10]	0.98	-	1.43	-	-	-	E(WN M5.3)
Oct 16 1987[10]	1.20	-	1.69	-	-	-	E(WN M2.8)
May 1988[11]	1.18	-	1.70	-	-	-	F
∼ M5.8 June 28 1991 Sierra Madre Earthquake (SM) @ 18km ∼							
June 28 1991[6]	0.92	-	1.39	-	-	-	E (SM)
May 1993[15]	1.17	-	1.69	-	2.44	-	F
∼ M6.7 January 17 1994 Northridge Earthquake (N) @ 34km ∼							
Jan 17 1994[6]	0.94	-	1.33	-	-	-	E (N)
Aug 2002[18]	1.14 [2.28]	4.93	1.67 [2.39]	7.22	2.38 [1.43]	6.57	F

Table B.1: Summary of Millikan Library modal frequency and damping analysis experiments, 1967-1994. f_0 and f_1 are the fundamental frequency and the first overtone, in Hz. ζ_0 and ζ_1 are the corresponding damping ratios, in %. References are found in Table B.3. A: Ambient, M: Man Excited, F: Forced Vibration, E: Earthquake motions [LC: Lytle Creek]

Test	East - West		North - South		Torsional		Remark
	f_0 [ζ_0]	f_1 [ζ_1]	f_0 [ζ_0]	f_1 [ζ_1]	f_0 [ζ_0]	f_1 [ζ_1]	
1966-1967[1]	1.46-1.51	6.2	1.89-1.98	-	2.84-2.90	-	A,F,M
	[0.7-1.7]		[1.2-1.8]		[0.9-1.6]		
Mar 1967[2]	1.49 [1.5]	6.1	1.91 [1.6]	-	2.88	-	A
∼ M6.7 February 9 1971 San Fernando Earthquake (SF) @ 44km ∼							
Feb 9 1971[6]	1.00	-	1.64	-	-	-	E (SF)
May 1976[9]	1.27	-	1.85	-	2.65	-	A
∼ M6.1 October 1 1987 Whittier Narrows Earthquake (WN) @ 19km ∼							
Oct 1 1987[10]	0.932 [0.04]	4.17 [0.08]	1.30 [0.06]	6.64 [0.18]	-	-	E (WN)
Oct 1 1987[6]	1.00	-	1.33	-	-	-	E (WN)
Oct 4 1987[10]	0.98	-	1.43	-	-	-	E(WN M5.3)
Oct 16 1987[10]	1.20	-	1.69	-	-	-	E(WN M2.8)
May 1988[11]	1.18	-	1.70	-	-	-	F
∼ M5.8 June 28 1991 Sierra Madre Earthquake (SM) @ 18km ∼							
June 28 1991[6]	0.92	-	1.39	-	-	-	E (SM)
May 1993[15]	1.17	-	1.69	-	2.44	-	F
∼ M6.7 January 17 1994 Northridge Earthquake (N) @ 34km ∼							
Jan 17 1994[6]	0.94	-	1.33	-	-	-	E (N)
Jan 19 1994[15]	1.13	-	1.65	-	2.39	-	F
Jan 20 1994[15]	1.13	4.40-4.90	1.65	8.22-8.24	2.39	-	A
	[1.2-2.1]	[1.0]	[0.7-1.5]	[0.2-0.3]	[0.3-0.5]		F
May 1994[16]	1.15 [1.38]	-	1.67 [1.46]	-	2.4 [1.18]	-	F
May 1995[16]	1.15 [1.44]	-	1.68 [1.25]	-	2.42 [1.15]	-	F
May 1998[16]	1.17 [1.4]	-	1.70 [1.3]	-	2.46	-	F
May 1998[16]	-	-	1.68	1.5	-	-	M
May 2000[16]	1.15 [3]	-	1.66 [3]	-	2.41 [2.5]	-	F
May 2000[16]	-	-	1.72 [0.8]	-	-	-	A
May 2001[16]	1.11 [3.25]	-	1.63 [3.69]	-	2.31 [2.9]	-	F
May 2001[16]	-	-	1.71 [1.2]	-	-	-	M
Dec 2001[17]	1.12 [1.63]	-	1.63 [1.65]	-	2.34	-	F
Sep 9 2001[6]	1.16	-	1.68	-	-	-	E (BH M4.2)
Aug 2002[18]	1.14 [2.28]	4.93	1.67 [2.39]	7.22	2.38 [1.43]	6.57	F
Feb 22 2003[6]	1.07	-	1.61	-	-	-	E (BB M5.4)

Table B.2: Summary of Millikan Library modal frequency and damping analysis experiments, 1987-2003. f_0 and f_1 are the fundamental frequency and the first overtone, in *Hz*. ζ_0 and ζ_1 are the corresponding damping ratios, in %. References are found in Table B.3. A: Ambient, M: Man Excited, F: Forced Vibration, E: Earthquake motions [BH: Beverly Hills, BB: Big Bear]

Footnote #	Reference	Remarks
1	Kuroiwa (1967)	*forced, ambient, man excitations — during and immediately after construction, Library not full*
2	Blandford et al. (1968)	*ambient*
3	Jennings and Kuroiwa (1968)	*ambient*
4	Udwadia and Trifunac (1973)	*ambient*
5	Udwadia and Trifunac (1974)	*Lytle Creek, San Fernando — based on transfer functions*
6	Clinton et al. (2004), this Thesis	*Earthquakes — estimated from strong motion records*
7	Iemura and Jennings (1973)	*San Fernando*
8	Udwadia and Marmarelis (1976)	*San Fernando — based on linear model*
9	McVerry (1980)	*SanFernando; ambient*
10	Beck and Chan (1995)	*SanFernando, Whittier MODEID*
11	Teledyne-Geotech-West (1972)	*ambient - 1mth after San Fernando — Also Vertical* $f_0 = 3-4Hz$*, high* ζ.
12	Udwadia and Marmarelis (1976)	*San Fernando*
13	Foutch et al. (1975)	*forced*
14	Luco et al. (1987)	*forced*
15	Beck et al. (1994)	*forced, ambient — Also Jan 20 Ambient test: EW3 at 7.83Hz*
16	CE180 Caltech - various students	*forced*
17	Favela, personal communication	*forced*
18	Bradford et al. (2004)	*forced — Also EW3 at 7.83Hz*

Table B.3: References which correspond to footnote numbers in Tables B.1 and B.2

What is more unusual is the ratio of fundamental mode to first overtone for each direction, which, using the recent results of Favela (personal communication, 2002) are ~ 6.6 for the E-W and ~ 5.6 for the N-S direction. From simple theory on beams in pure bending and shear (Iwan, 1998), we expect a ratio of approximately 3 for buildings responding predominantly in shear, and 6.3 for buildings responding predominantly in bending. From the actual values observed in the building, which we expect to respond as a shear building, we must conclude there is a more complicated explanation for the dynamic response of the Library than the simple beam theory allows. This is most likely due to a soil-structure interaction often suggested in the literature, but never fully explained or quantified.

Numerous studies (Kuroiwa, 1967; Foutch, 1976) find a significant portion of roof motion may be accounted for from rocking and translation observed in the basement. Studies after the 1971 San Fernando earthquake find up to 30% of the N-S building motion at resonance may be attributable to foundation compliance (Foutch, 1976), with basement translation increasing by a factor of 2 and basement rotation by a factor of 25 more after the earthquake. (Foutch and Jennings, 1978) suggest the increased foundation compliance may be due to brittle failure of retaining walls, sidewalks and and concrete slabs at the ground floor. They include evidence of compressional spalling and cracking of concrete at the ground level.

Udwadia and Trifunac (1974) employ a moving window analysis of the time-series recorded at Millikan for the 1971 San Fernando event and observe marked reductions in the resonant frequencies in both the N-S and E-W directions within the duration of strong shaking.

Appendix C Millikan Library Dynamic Response to Forced Vibration

During the Summer of 2002, a suite of investigations into the dynamic response of Millikan Library were preformed by myself, Samuel Case Bradford and Javier Favela. An EERL report (Bradford et al, 2004) documents this in detail, but I summarise the important findings here.

In June 2002, we performed a frequency sweep of the building, from below the natural frequencies at $1Hz$ to $9.7Hz$, the upper bound frequency limit of the shaker. Data was recorded on the SCSN Station MIK, and a portable Ranger seismometer placed on the roof. From this sweep, we were able to determine the natural frequencies of the building, and the damping ratios.

The building was shaken in both the E-W and N-S directions. Frequency amplitude plots with force normalisation (different weight configurations were used for different frequencies to maximise building displacement) are presented for both directions in Figures C.1 and C.2.

From these plots we identified the natural frequencies for use in a modal evaluation of the building. For this experiment, we had Arnie Acosta, of USGS, with us to trigger the 36 channel USGS array, which has at least 3 channels per floor (1 E-W, 2 N-S, to dertermine torsion). On 28 August 2002, we shook the building again near these freqencies with frequency increases of about $0.03Hz$, the resolution of the shaker controller. We also shook using differing weight configurations to see if the weight had an effect on the natural frequency.

The results of this experiment is summarised in the Table C.1. The weight configurations vary from full weights, $\sim$ 1/2 weights, and no weights in the shaker. More weight in the shaker, which corresponds to a larger shaking force applied to the building, results in slightly decreased natural frequencies (the bulding appears ‘softer’). From this table, we

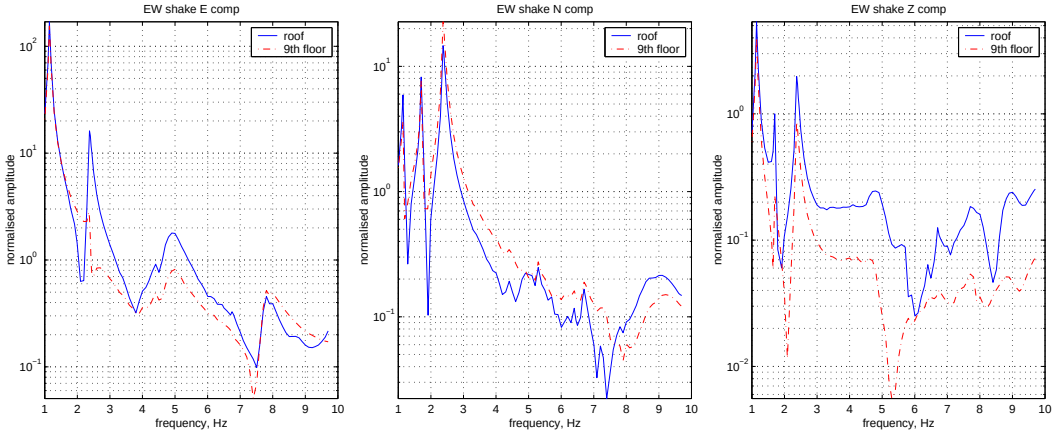

(a) E component (b) N component (c) Z component

Figure C.1: Millikan Library frequency sweep - E-W shake

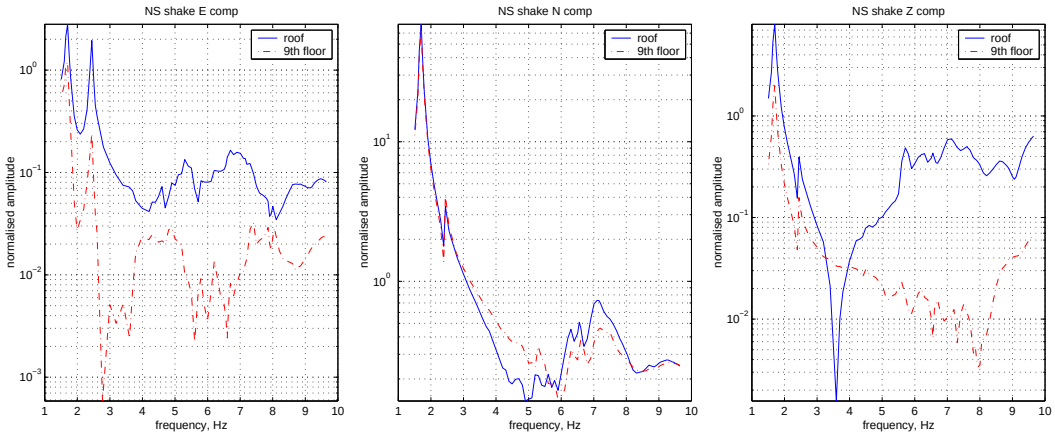

(a) E component (b) N component (c) Z component

Figure C.2: Millikan Library frequency sweep - N-S shake

also see dramatic differences in the amount of soil-structure interaction for the different modes. In this experiment, the interaction is identified by taking the ratio of displacement at the roof which is due to rocking and translation of the basment, to the total roof displacement. Basement rocking is determined using the 3 vertical channels at the basement, and basement displacement from the 3 horizontal basment channels. All 3 identified E-W modes have very little soil-structure interaction ($< 3\%$), and both N-S modes have significant (Fundamental N-S has 30%, first overtone has 21%) soil-structure interaction. For the torsional modes, this soil-structure interaction is defined as proportion of roof rotation due to basment rotation - this ratio is negligible for the fundamental mode, yet is significant for the 2^{nd} mode.

Mode	**Shake / Weights**	**Resonance Peak, *Hz***	**Normalised Displ.**	**% Roof : Basement**
East-West 1	EW / Full EW / 2x2	1.11 1.14	200(EW)	**3**%
North-South 1	NS / Full NS / 2x2	1.64 1.67	80(EW)	**30**%
Torsion 1	EW / 2x2 NS / Full NS / 2x2	2.38 2.35 2.38	25(NS) 5(NS) 5(NS)	**2**%
East-West 2	EW / None	4.53	2(EW)	**1**%
North-South 2	NS / None	7.22	0.8(NS)	**-21**%
Torsion 2	EW / None NS / None	6.57 6.50	0.4(EW), 0.20(NS) 0.5(NS)	**23**%
East-West 3	EW / None	7.83	0.6(EW)	**0**%

Table C.1: Millikan Library forced vibration results

Plots of the important modeshapes follow. More discussion of their shape, and comparison with theoretical modeshapes for homogeneous shear and bending beams, is in (Bradford et al, 2004).

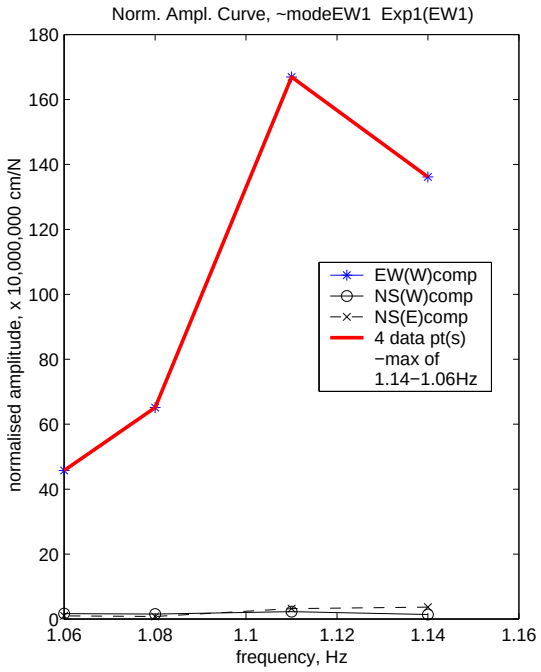

(a) Full weights resonance curve

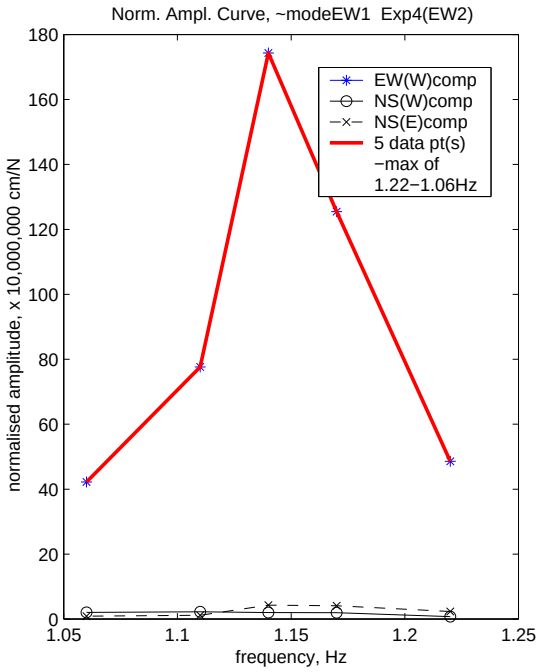

(b) 2x2 weights resonance curve

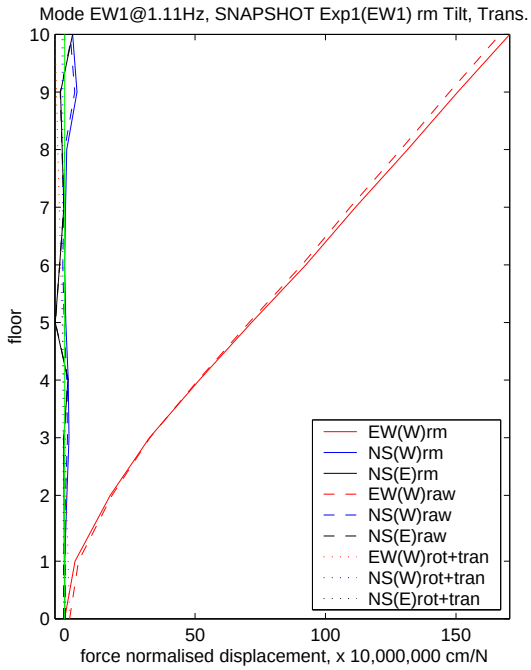

(c) Full weights - 1.11Hz

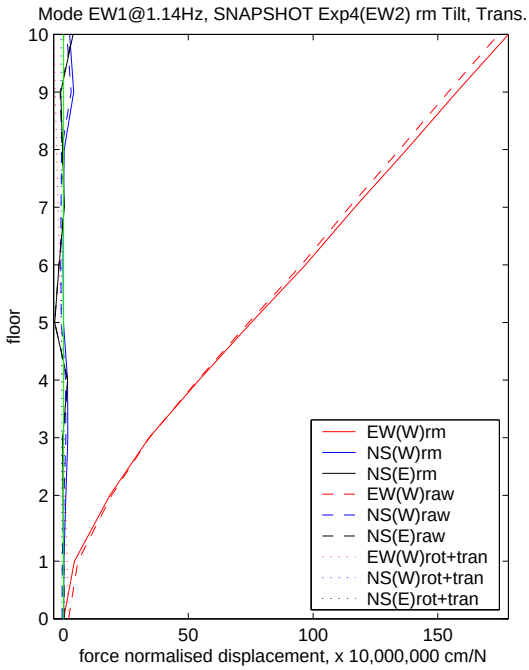

(d) 2x2 weights - 1.14Hz

Figure C.3: Modeshapes and resonance curves for EW 1 Mode. Note shortening of natural frequency when loading increased.

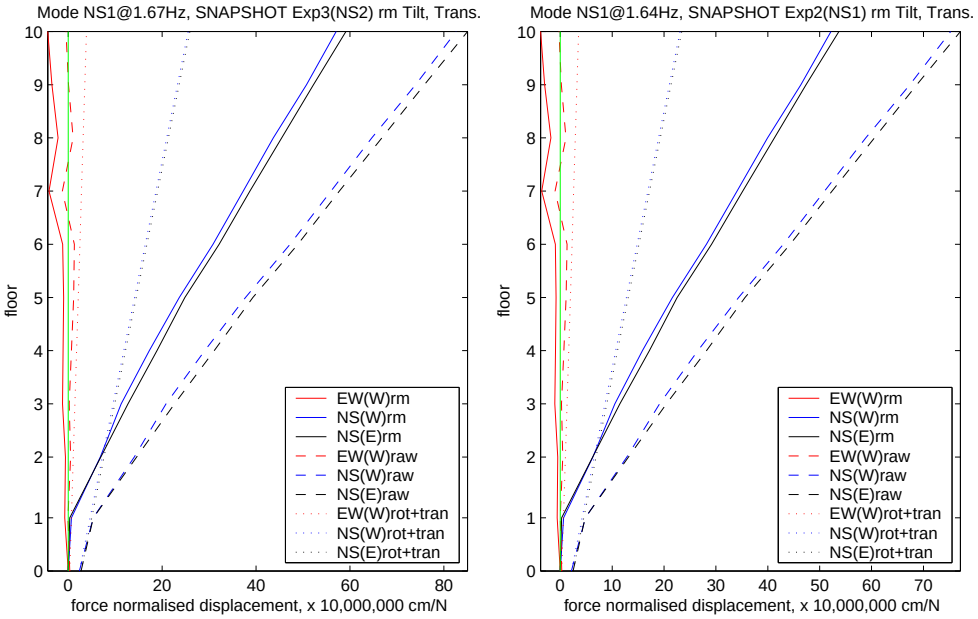

(a) Full weights - 1.64Hz (b) 2x2 weights - 1.67Hz

Figure C.4: Modeshapes for NS 1 mode. Note shortening of natural frequency when loading increased.

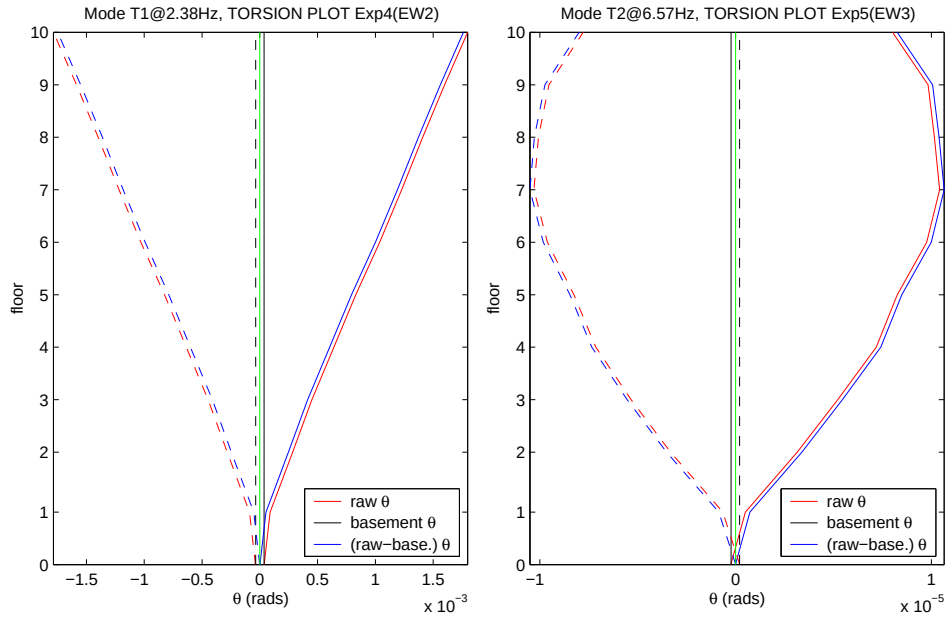

(a) Torsion 1 - 2.37Hz (b) Torsion 2 - 6.57Hz

Figure C.5: Modeshapes for Torsion 1 and 2 modes

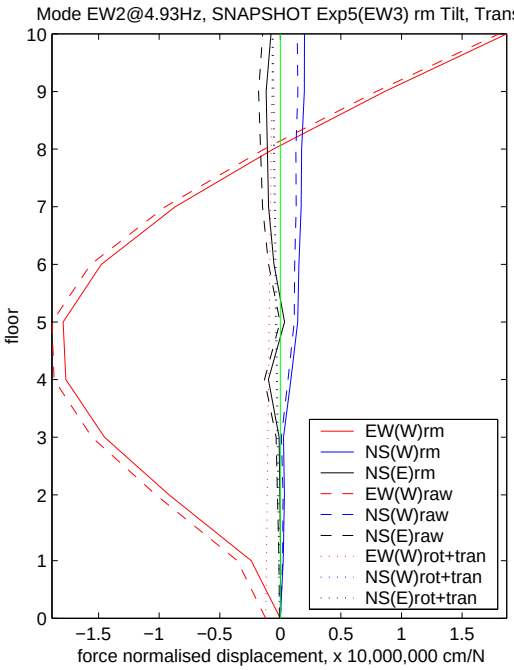

(a) EW 2 - 4.93Hz

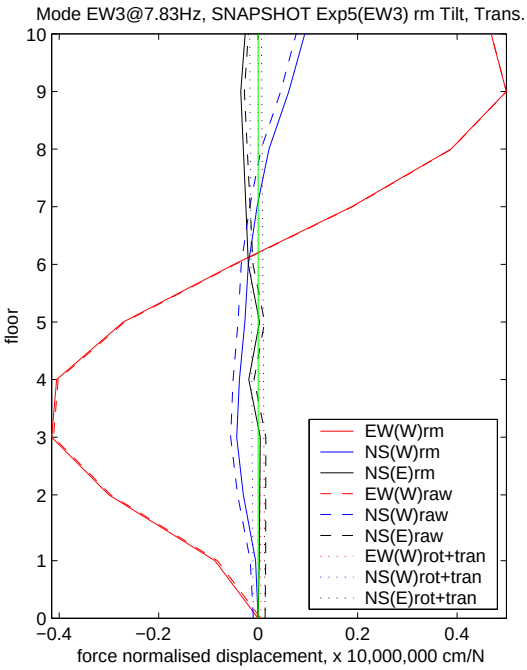

(b) EW 3 - 7.83Hz

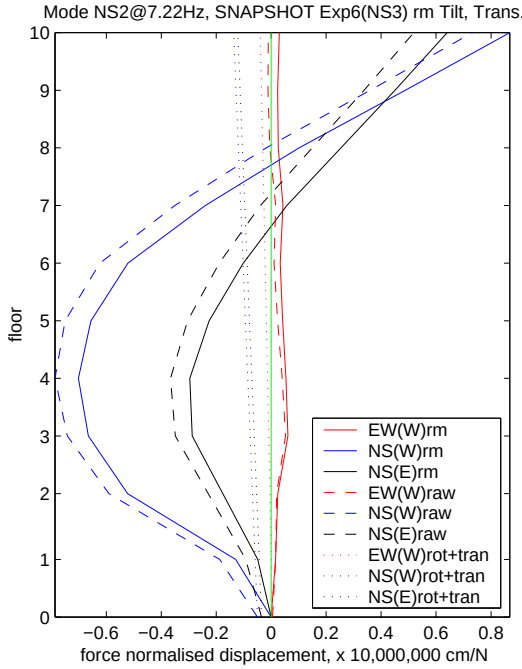

(c) NS 2 - 7.22Hz

Figure C.6: Modeshapes from higher-order modes - EW 2, EW 3, NS 2.